
BASIC MECHANICAL PROPERTIES AND LATTICE DEFECTS OF INTERMETALLIC COMPOUNDS

Edited by

J. H. Westbrook

Brookline Technologies, Ballston Spa, New York, USA

and

R. L. Fleischer

Union College, Schenectady, New York, USA

JOHN WILEY & SONS, LTD

Chichester · New York · Weinheim · Brisbane · Singapore · Toronto

Copyright © 2000 by John Wiley & Sons Ltd,
Baffins Lane, Chichester,
West Sussex PO19 1UD, England

National 01243 779777
International (+44) 1243 779777
e-mail (for orders and customer service enquiries): cs-books@wiley.co.uk
Visit our Home Page on <http://www.wiley.co.uk>
or <http://www.wiley.com>

All Rights Reserved. No part of this publication may be reproduced, stored in a retrieval system, or transmitted, in any form or by any means, electronic, mechanical, photocopying, recording, scanning or otherwise, except under the terms of the Copyright, Designs and Patents Act 1988 or under the terms of a licence issued by the Copyright Licensing Agency, 90 Tottenham Court Road, London W1P 9HE, without the permission in writing of the Publisher

Other Wiley Editorial Offices

John Wiley & Sons, Inc., 605 Third Avenue,
New York, NY 10158-0012, USA

WILEY-VCH Verlag GmbH, Pappelallee 3,
D-69469 Weinheim, Germany

Jacaranda Wiley Ltd, 33 Park Road, Milton,
Queensland 4064, Australia

John Wiley & Sons (Asia) Pte Ltd, 2 Clementi Loop #02-01,
Jin Xing Distripark, Singapore 129809

John Wiley & Sons (Canada) Ltd, 22 Worcester Road,
Rexdale, Ontario M9W 1L1, Canada

Library of Congress Cataloging-in-Publication Data

Basic mechanical properties and lattice defects of intermetallic compounds / edited by
J. H. Westbrook and R. L. Fleischer.
p. cm.

'This volume is one of four now being published, each of which consists of reprints of chapters from the 1995 comprehensive two-volume set—Intermetallic compounds, principles and practice . . . selected sets of chapters are collected, each set being on a single theme . . . reprint volume 2'—Pref.

Includes bibliographical references and index.

ISBN 0-471-61175-1 (pbk. : alk. paper)—ISBN 0-471-60814-9 (set)

I. Intermetallic compounds—Mechanical properties. 2. Crystals—Defects. 3. Crystal lattices. 4. Alloys. 5. Physical metallurgy. I. Westbrook, J. H. (Jack Hall), 1924–
II. Fleischer, R. L. (Robert Louis), 1930– III. Title: Intermetallic compounds.

TA483.B37 2000
620.1'692—dc21

99-052445

British Library Cataloguing in Publication Data

A catalogue record for this book is available from the British Library

ISBN 0 471 61175 1
ISBN 0 471 60814 9 (set)

Typeset by Dobbie Typesetting Ltd, Tavistock, Devon

Printed and bound in Great Britain by Antony Rowe, Chippenham, Wiltshire

This book is printed on acid-free paper responsibly manufactured from sustainable forestry, in which at least two trees are planted for each one used for paper production.

Dedication

To the memory of
John Herbert Hollomon
1919–1985

Wise, vigorous, effective advocate of the relevance and value of scientific research in industry.

His strong belief in the synergetic interaction of Principles and Practice in the field of metallurgy impelled him to assemble an innovative, diverse staff at General Electric, and to inspire independent exploration that benefited both science and engineering.

Contributors

Clyde L. Briant
Division of Engineering
Brown University
Box D, 182 Hope Street
Providence, RI 02912
9104, USA



Joël Douin
Laboratoire d'Etude des
Microstructures, Unité Mixte
CNRS/ONERA, UMR 104,
29 Avenue de la division Leclerc,
92322 Châtillon Cedex, France



Lawrence M. Howe
2 Frontenac Crescent,
P.O. Box 697,
Deep River, Ontario,
Canada K0J 1P0



Han R. P. Inoue (now Kanryu Inoue)
Department of Materials Science
and Engineering, University of
Washington, Seattle,
WA 98195, USA



Morihiko Nakamura
National Research Institute for Metals,
1-2-1 Sengen, Tsukuba-shi,
Ibaraki 305-0047, Japan



Charles de Novion
Laboratoire des Solides Irradiés,
ICEA-CEREM, URA CNRS No.
1380), Ecole Polytechnique,
01128 Palaiseau Cedex, France



Gerhard Sauthoff
Max-Planck-Institut für
Eisenforschung GmbH, D-40074
Düsseldorf, Germany



Yong-Qian Sun
Department of Materials
Science and Engineering,
University of Illinois,
Urbann, IL 61801, USA



Takayuki Takasugi
Institute for Materials Research,
Tohoku University, Katahira
2-1-1, Aoba-ku, Senda 980,
Japan



Patric Veyssiére
Laboratoire d'Etude des
Microstructures, Unité Mixte
CNRS/ONERA, UMR 104,
29 Avenue de la division Leclerc,
92322 Châtillon Cedex, France



C. Marvin Wayman
Department of Materials Science
and Engineering, University of
Illinois, Urbana, IL 61801,
USA



Preface to the 1995 Edition

Intermetallic compounds were last comprehensively reviewed in 1967 in a volume that was edited by one of us (JHW). At that time the field was described as of special interest because it was undergoing 'exponential proliferation'. That trend continues to the present. The number of intermetallic entries in the Permuterm Subject Index shows a doubling period of less than nine years, having reached roughly 1800 entries per year in 1993. Apart from scholarly interest, intermetallics have now become of substantial commercial significance; for some, such as Ni_3Al , world-wide use is in the 1000s of tons; for others, for example III-V semiconducting compounds, although the quantities employed are not in tonnage numbers, their value as vital components of electronic circuits is in the billions of dollars.

From the 1967 book we remind the reader that 'The first published paper dealing with intermetallic compounds appeared in 1839, and more than sixty years elapsed before . . . the first review paper by Neville in 1900. However, new results were then appearing so rapidly that fifteen years later two books were printed, devoted exclusively to this subject, one by Desch in England and one by Giua and Giua in Italy'. More recently, conference volumes that deal exclusively with intermetallics but typically only within specific, limited sub-topical subject areas have become common. The scope of the present work is as broad as that of its 1967 predecessor. However, the increased volume of activity in intermetallics and the increased significance of their applications have necessitated an expansion from the 27 chapters of the earlier work to the 75 chapters of the present treatise.

First, what are intermetallic compounds? Generally, such a compound is a structure in which the two or more metal constituents are in relatively fixed abundance ratios and are usually ordered on two or more sublattices, each with its own distinct population of atoms. Often substantial or complete disorder may obtain, as a result of low ordering energy or the intervention of some external agency, for example extreme cooling rates, radiation, etc. Deviations from precise stoichiometry are frequently permitted on one or both sides of the nominal ideal atomic ratios, necessitating a partial disorder. Here we include as intermetallic compounds all metal-metal compounds, both ordered and disordered, binary and multicomponent. Even the metal-metal aspect of the definition is often relaxed by including some metal-metalloid compounds, such as silicides, tellurides, and semiconductors. We believe this inclusion is appropriate since the phenomenology of many such compounds is nearly identical to metal-metal ones, and they provide useful examples of principles, properties, and practices.

The burgeoning literature on intermetallics and the lack of a comprehensive single source of up-to-date descriptions of where we are, what we need to know, and what we can do with intermetallics created the incentive for the present pair of volumes. This work was planned to provide state-of-the-art assessments of theory, experiment, and practice that will form a solid base for workers who wish to know more than their own particular area. Each author was asked to set forth the principles of his or her subject in terms that are meaningful to scientists and engineers who are not specialists in the author's field, and then to progress to include knowledge that workers in their own areas would wish to have. Concluding sections of most chapters give the authors' critical assessment of the state of their subject and of where they believe further effort is merited.

This work is divided into two volumes in order that each be of manageable size. The first, on the theme Principles, is directed at the science of intermetallics—how do we understand their formation, structure and properties? The Practice volume considers commercial production and engineering applications of intermetallic compounds. The reader who browses carefully will recognize that the immediacy of the practice described ranges from hoped-for use, to beginnings of use, to actual commercial application—depending on the specific subject. Some of the hoped-for uses are fated never to be realized, but the authors have aimed to reveal what the obstacles are so that the reader may make his or her own assessment (and possibly provide a solution!).

We conferred carefully with many people in order to identify authorities for each subject; having recruited contributors for the project, we then strove to assist them in achieving clarity and thoroughness from outline to draft to final manuscript. The contributors cooperated superbly, and we thank them for their hard work and high achievement. We sought experts wherever they were to be found, and our international set of nearly 100 authors turned out to be almost equally divided between the United States and 14 other countries. Manuscripts have in fact come from all inhabited continents.

We planned this work as an aid to both scientists and engineers. It can serve as a base for those who wish to know about intermetallics as an area in which to begin research. Equally it is a resource to workers who are already active in the field and need, or wish, to expand their knowledge of related science or practical technology. We expect that many chapters are appropriate source matter for special topic or seminar courses at the advanced undergraduate and various graduate school levels. It is hoped that passage of the next 25 years will reveal some influence of this treatise on the further development of this field.

As an assist to readers we have provided in the following pages a consolidated acronym list and some crystallographic tables. Nomenclature for crystal structure types is often complex, and some of the authors have introduced their own. Generally we have asked authors to include both of two commonly used types of symbols as they introduce structures. The two-part table following this preface lists many of the common types—by Strukturbericht symbol, prototype name (termed a *structure type*), and Pearson symbol. Strukturbericht symbols are only partly significant and systematic: A's are not compound structures but consist of a single lattice of atoms (except for A15!); B's are equiatomic ordered structures; C's have 2-to-1 atomic abundance ratios, D0's 3-to-1. Structure type compounds are the specific ones used to designate a particular structure. Thus B2 compounds are also referred to as CsCl compounds. Many structures are better known to metallurgists and mineralogists by names other than the formula of the structure type chosen by crystallographers, e.g. Laves, fluorite, Heusler, etc. Such names have been added in selected cases. The Pearson symbols tell the crystal symmetry and the number of atoms per unit cell. Thus, B2, CsCl has a primitive (P) cubic (c) structure with 2 atoms per cell and hence the Pearson symbol (cP2). The Pearson designation is informative, but it is not necessarily unique. Although there is only one cP2 structure, Villars and Calvert list two cP4s, three cF12s and twenty-two hP9s. Thus to be definitive, both the structure type and the Pearson symbol need to be given, or the Pearson and the Strukturbericht symbol.

The index in each volume includes the subjects in *both* volumes of this work, in order that the reader may be able to locate any subject that is addressed. Although the purpose of such combined indices is not to induce the owner of a single volume to purchase the other, it possibly may help to reduce the barrier to such action.

We have benefited from outstanding secretarial help during the three years of this project, first by Phillis Liu, then Constance Remscheid at General Electric, finally Mary Carey at Rensselaer Polytechnic Institute. We appreciate the hospitality of the General Electric Research and Development Center during the inception and middle period of preparing these volumes. Assembling the final product has been eased for us by the continuing efforts and cheerful good counsel at John Wiley of Jonathan Agbenyega, Irene Cooper, Philip Hastings, Vanessa Lutman and Cliff Morgan.

J. H. WESTBROOK, *Ballston Spa, New York*

R. L. FLEISCHER, *Schenectady, New York*

Upon these considerations, we have been induced to undertake the present extensive work, the purpose of which is to instruct rather than to amuse; in which nothing will be omitted that is elegant or great; but the principal regard will be shown to what is necessary and useful.

—Isaac Ware, 1756

Preface to the Reprint Volumes from Intermetallic Compounds: Principles and Practice

This volume is one of four now being published, each of which consists of reprints of chapters from the 1995 comprehensive two-volume set *Intermetallic Compounds: Principles and Practice*. In the present volumes selected sets of chapters are collected, each set being on a single theme. In this format readers who are interested in a particular aspect of intermetallic compounds can have a less weighty volume specific to their subject; a volume that can be produced more economically than the full, original 1900-page set; and that includes a modest updating of the subject matter.

The subjects in most cases are taken from one or more chapter groupings of the original Volume 1 or 2: Hence reprint volume 1, *Crystal Structures of Intermetallic Compounds*, contains the ten chapters from the original work under the heading Crystal Structures; reprint volume 2, *Basic Mechanical Properties and Lattice Defects of Intermetallic Compounds*, contains three from Property Fundamentals, four chapters from Defect Structures, and two from Kinetics and Phase Transformations; reprint volume 3, *Structural Applications of Intermetallic Compounds* contains the thirteen chapters that were under that same topic; and finally reprint volume 4, *Magnetic, Electrical, and Optical Properties and Applications of Intermetallic Compounds*, contains two chapters from the section on Property Fundamentals, seven from Electromagnetic Applications and one from Miscellaneous. Although each chapter is reprinted nearly intact (only typographic and factual errors corrected), the author or authors were given the option of adding a brief addendum in order to add whatever new perspective has arisen over the intervening few years. Some have chosen to do so; some have not, either in the preferred case because they felt none was needed or because the four-month window of opportunity they were given to satisfy our and the publisher's desire for promptness did not fit their work schedule. Corrections to the original chapters that were so lengthy that they would upset the original pagination are to be found in the addenda at the end of each relevant chapter.

Where an addendum is particularly relevant to a portion of the original chapter being reproduced, a margin mark (*) alerts the reader to refer to the added pages at the end of the chapter. Cross-references to other chapters relate to the original 1995 two-volume work, the tables of contents of which appear at the end of this volume.

JHW
RLF

Acronyms

2D	two-dimensional	BH	buried heterostructure
3D	three-dimensional	BIS	bremsstrahlung isochromat spektroskopie
6D	six-dimensional	BM	Bowles-Mackenzie (theory of martensitic transformation)
ACAR	angular correlation of annihilation radiation	BSCCO	bismuth-strontium-calcium-copper oxide
ACPAR	angular correlation of positron annihilation radiation	BSE	back-scattered electrons
AE	atomic environment	BT	Bhatia-Thornton (partial structure factor for liquid alloys)
AES	Auger electron spectroscopy	BW	Bragg-Williams (theory of ordering)
AET	atomic environment type	BZ	Brillouin zone
AIM	argon induction melting		
ALCHEMI	atom location by channeling enhanced microanalysis	CAM	c-axis modulated
ALE	atomic layer epitaxy	CANDU	Canadian deuterium-uranium (power reactor)
AM	air mass	CAP	consolidated under atmospheric pressure
AMT	Advanced Materials Technology, Inc.	CAT	computer-assisted tomography
AN	atomic number	CBLM	cluster Bethe lattice method
AP	atom probe	CC	cluster center
AP	atomic property	CCD	charge-coupled device
APB	antiphase boundary	CCGSE	concentric-circle grating surface- emitting (laser)
APD	antiphase domain	CCIC	cabled conductor in conduit
APD	avalanche photodetector	CCMAI	crystal chemical model of atomic interactions
APE	atomic property expression	c.c.p.	cubic close-packed
APW	augmented plane wave	CCT	continuous cooling transformation
AR	antireflection	CD	compact disc
ARIPES	angle-resolved inverse photoemission spectroscopy	CD	climb dislocation
ARPES	angle-resolved photoemission spectroscopy	CEBAF	continuous electron-beam accelerator facility
ASA	atomic-sphere approximation	CEF	crystalline electric field
ASW	augmented spherical wave	CERN	Centre Européenne Recherche Nucléaire
BC	bond charge	CFT	concentration-functional theory
b.c.c.	body-centered cubic	CMC	ceramic-matrix composite
BCS	Bardeen-Cooper-Schrieffer (theory of superconductivity)	CN	coördination number
b.c.t.	body-centered tetragonal		

CO	cubo-octahedron	ESR	electroslag refined
CP	coördination polyhedron	ETP	electrolytic tough pitch (copper)
CPA	coherent-potential approximation	EXAFS	extended X-ray absorption fine structure
CRSS	critical resolved shear stress		
CS	chemisorption	f.c.c.	face-centered cubic
CSF	complex stacking fault	f.c.t.	face-centered tetragonal
CSL	coincidence-site lattice	FENIX	Fusion Engineering International Experimental Magnet Facility
CSRO	chemical short-range order		
CT	chisel toughness	FET	field effect transistor
CTE	coefficient of thermal expansion	FIM	field ion microscopy
CVD	chemical vapor deposition	FLAPW	full-potential linearized augmented plane wave
CVM	cluster variation method		
CW	cold worked	FLASTO	full-potential linearized augmented Slater-type orbital
CW	concentration wave	FLMTO	full-potential linearized muffin-tin orbital
CWM	Connolly-Williams method (theory of phase transformations)	FOM	figure of merit
		FP	Fabry-Perot (laser)
D-A	donor-acceptor	FT	phase transformation
DB	diffusion bonding	FZ	floating zone
DBTT	ductile-brittle transition temperature		
DC	direct chill (casting)	GB	gain \times bandwidth (product)
DC	direct current	GB	grain boundary
DCA	direct configurational averaging	GFT	glass-forming tendency
DF	density functional	GGA	generalized gradient approximation
DFB	distributed feedback	GITT	galvanostatic intermittent titration technique
DFT	density-functional theory		
DH	double heterojunction	GPM	generalized perturbation method
d.h.c.p.	double hexagonal close-packed	GRPA	generalized random-phase approximation
dHvA	de Haas-van Alphen (effect)		
DLZR	directional levitation zone melting	GS	ground state
DOS	density of states	GT	Goody-Thomas (electronegativity)
DPA	displacement per atom		
DPC	demonstration poloidal coil	HB	horizontal Bridgman
DRP	dense random packing	HBT	heterojunction bipolar transistor
DS	directional solidification	HCF	high-cycle fatigue
DSC	displacement shift complete	h.c.p.	hexagonal close-packed
		HEMT	high-electron-mobility transistor
e/a	electron/atom (ratio)	HIP	hot isostatic pressing
EAM	embedded-atom method	HPT	heterojunction phototransmitter
EBPVD	electron beam physical vapor deposition	HR	high resolution
ECI	effective cluster interaction	HREM	high-resolution electron microscopy
ECM	embedded-cluster method	HRTEM	high-resolution transmission electron microscopy
EDC	electro-optic directional coupler	HSCT	high-speed civil transport
EDM	electrodischarge machining	HTS	high-temperature superconductor
EDX	energy-dispersive X-ray (spectroscopy)	HVEM	high-voltage electron microscopy
		HVTEM	high-voltage transmission electron microscopy
EELS	electron energy-loss spectroscopy		
EMF	electromotive force	IAE	irregular atomic environment
EPI	effective pair interaction	IAET	irregular atomic environment type
ESF	extrinsic stacking fault		

IC	integrated circuit	LO	longitudinal optical (wave)
IC	investment cast	LPCVD	low-pressure chemical vapor deposition
IDOS	integrated density of states	LPE	liquid-phase epitaxy
IEM	interstitial-electron model	LPPS	low-pressure plasma spraying
IGC	Intermagetics General	LPS	long-period superstructure
IHPTET	integrated high-performance turbine engine technology	LRO	long-range order
ILS	invariant line strain	LSDA	local spin-density approximation
IMC	intermetallic compound	LSI	large-scale integration
IMC	intermetallic matrix composite	μ SR	muon spin relaxation
IMC	inverse Monte Carlo (method)	MA	mechanical alloying
IPM	independent-particle method (approximation)	MAPW	modified augmented plane wave
IPS	invariant plan strain	MB	Martinov-Basnov (electronegativity)
IQC	icosahedral quasicrystal	MBE	molecular beam epitaxy
IR	infrared	MBT	metal-base transistor
ISF	intrinsic stacking fault	MC	Monte Carlo
IT	(positive) inner tetrahedron	MCS	Monte Carlo simulation
ITER	International Thermonuclear Experimental Reactor	MD	molecular dynamics
IV	intermediate valence	MEE	migration-enhanced epitaxy
JFET	junction field-effect transistor	MESFET	metal Schottky field-effect transistor
KKR	Korringa-Kohn-Rostoker (bond-calculation method)	MFTF	Mirror Fusion Test Facility
KSV	Khantha-Cserti-Vitek (deformation model)	MISFET	metal-insulator-semiconductor field effect transistor
KTP	potassium titanyl phosphate	MJR	McDonald jelly roll (superconducting cable construction)
KW	Kear-Wilsdorf (dislocation locking mechanism)	MLR	multi-layer reflector
LA	longitudinal acoustic (wave)	MMC	metal-matrix composite
LAPW	linearized augmented plane wave	MN	Mendeleev number
LASTO	linearized augmented Slater-type orbital	MO	magneto-optical
LCAO	linear combination of atomic orbitals	MOCVD	metal-organic chemical vapor deposition
LCF	low-cycle fatigue	MOS	metal-oxide-semiconductor
LCT	large coil task	MOSFET	metal-oxide-semiconductor field effect transistor
LCW	Lock-Crisp-West (radiation analysis)	MOVPE	metal-organic vapor phase epitaxy
LD	laser diode	MQW	multiple quantum well
LDA	local-density approximation	MRI	magnetic resonance imaging
LEC	liquid-encapsulated Czochralski	MRSS	maximum resolved shear stress
LED	light-emitting diode	MRT	orthodontic NiTi alloy
LEED	Low-energy electron diffraction	MT	muffin tin
LEISS	low-energy ion scattering spectroscopy	MTD	martensitic transformation diagram
LHC	Large Hadron Collider	MVA	million volt-amperes
LKKR	Layered KKR (structure calculation)	NASP	National AeroSpace Plane
LME	liquid metal embrittlement	NET	Next European Torus (fusion device)
LMTO	linearized muffin-tin orbital	NHE	normal hydrogen electrode
LNT	liquid nitrogen temperature	NMI	National Maglev Initiative
		NMR	nuclear magnetic resonance
		NN	nearest neighbor
		NNH	nearest-neighbor histogram

NNN	next nearest neighbor	RDS	rate-determining step
NOR	negative OR (logic operator)	RE	rare earth (metal)
NSR	notch/strength ratio	RF	radiofrequency
OAZ	oxidation-affected zone	RHE	reversible hydrogen electrode
ODR	oxygen dissolution reaction	RIM	rigid-ion model
ODS	oxide dispersion-strengthened	RKKY	Ruderman–Kittel–Kasuya–Yoshida (electron interactions)
OEIC	optoelectronic integrated circuit	r.m.s.	root mean square
OH	octahedron	RRR	residual resistivity ratio
ORNL	Oak Ridge National Laboratory	RS	rapidly solidified
OT	(negative) outer tetrahedron	RSP	rapid solidification processing
OTMC	orthorhombic Ti-matrix composites	RSS	resolved shear stress
PAS	positron annihilation spectroscopy	RT	room temperature
PBC	periodic bond chain	RUS	resonance ultrasound spectroscopy
PBT	permeable-base transistor		
PCM	phase-change material	SAD	selected-area diffraction
PCT	pressure–composition–temperature	SAED	selected-area electron diffraction
PD	phase diagram	SAGBO	stress-assisted grain-boundary oxidation
PDF	pair distribution function	SAM-APD	separate absorption and multiplication avalanche photodetector
PDOS	phonon density of states		
PFC	planar flow casting	s.c.	simple cubic
PH	<i>Pearson's Handbook</i>	SC	semiconductor
PHACOMP	phase computation	SCE	standard colomel electrode
PKA	primary knock-on atom	SCH	separate confinement heterostructures
PL	photoluminescence	SDC	specific damping capacity
PM	powder metallurgy	SDW	spin-density wave
PMTC	phenomenological martensite transformation concept	SEM	scanning electron microscopy
PN	periodic number	SESF	superlattice extrinsic stacking fault
pnpn	type of phototransistor	SF	stacking fault
PPDF	partial pair distribution function	SG	spin glass
PPM	path-probability method	SHS	self-propagating high-temperature synthesis
PPV	Paidar–Pope–Vitek ($L1_2$ hardening model)	SI/VLSI	semi-insulating very large-scale integration
PS	Pearson symbol	SIA	self-interstitial atom
PT	phase transformation	SIC	self-interaction correlation
PTMC	phenomenological theory of martensite crystallography	SIM	stress-induced martensite
PVD	physical vapor deposition	SIMS	secondary-ion mass spectrometry
PZT	lead zirconate titanate (ceramic)	SIS	superconductor–insulator– superconductor
QC	quasicrystal(line)	SISF	superlattice intrinsic stacking fault
QCSE	quantum confined Stark effect	SIT	static inductance transistor
QFD	quantum formation diagram	SM	semimetal
QN	quantum number	SMA	second-moment approximation
QSD	quantum structural diagram	SMA	shape-memory alloy
QW	quantum well	SME	shape-memory effect
		SPF	superplastic forming
		SQUID	superconducting quantum interference device
RBS	Rutherford back scattering		
RC	ribbon comminution	SRO	short-range order
RCS	replacement-collision sequence	SSAR	solid-state amorphizing reaction
RDF	radial distribution function	SSD	structural stability diagram

SSF	superlattice stacking fault	ULSI	ultra large-scale integration
STA	<i>Atlas of Crystal Structure Types</i>	USW	ultrasonic wave
STEM	scanning transmission electron microscopy	UTS	ultimate tensile strength
STM	scanning tunneling microscopy	UV	ultraviolet
SV	Sodani-Vitole change of Paidar <i>et al.</i> model	VAR	vacuum arc refined
		VCSEL	vertical-cavity surface-emitting laser
TA	transverse acoustic (wave)	VEC	valence-electron concentration
TB	tight binding	VGf	vertical gradient freezing
TCP	topologically close-packed	VHF	very high frequency
TD	thoria dispersion	VIM	vacuum induction melting
TDFS	temperature dependence of flow stress	VLS	vapor-liquid-solid
TE	thermoelectric	VLSI	very large-scale integration
TE	transverse electric (field)	VPE	vapor phase epitaxy
TEC	thermoelectric cooler	VPS	vacuum plasma spraying
TEG	thermoelectric generator	VUV	vacuum ultraviolet
TEM	transmission electron microscopy	WB	weak beam
TEP	triethylphosphene	WGPD	waveguide photodetector
TGW	Teatum-Gschneidner-Waber (atomic radius)	WLR	Wechsler-Lieberman-Read (theory of martensitic transformation)
TIP	thermally induced porosity	WS	Wigner-Seitz (cell)
TK	Takeuchi-Kuramoto (dislocation locking mechanism)	WSS	Winterbon-Sigmund-Sanders (model of irradiation damage)
TM	transition metal	wt.ppm	weight parts per million
TM	transverse magnetic (field)	XC	exchange-correlation
TMA	titanium-molybdenum-aluminum (alloy)	XD TM	exothermic dispersion (synthesis process)
TO	transverse optical (wave)	XIM	X-ray inspection module
TPA	two-photon absorption	XPS	X-ray photoelectron spectroscopy
TSRO	topological short-range ordering	XRD	X-ray diffraction
TT	truncated tetrahedron	XUV	extreme ultraviolet
TTS	tubular tin source		
TTT	time-temperature-transformation	YAG	yttrium aluminum garnet
UHF	ultra-high frequency	ZIF	zero insertion force
UHV	ultra-high vacuum		

Crystal Structure Nomenclature*

Arranged Alphabetically by Pearson-Symbol Designation

Pearson symbol	Prototype	Strukturbericht designation	Space group	Pearson symbol	Prototype	Strukturbericht designation	Space group
cF4	Cu	A1	$Fm\bar{3}m$	cP6	Ag ₂ O	C3	$Pn\bar{3}m$
cF8	C (diamond)	A4	$Fd\bar{3}m$	cP7	CaB ₆	D2 ₁	$Pm\bar{3}m$
	NaCl (rock salt)	B1	$Fm\bar{3}m$	cP8	Cr ₃ Si (β W)	A15	$Pm\bar{3}n$
	ZnS (sphalerite)	B3	$F\bar{4}3m$		FeSi	B20	$P2_13$
cF12	CaF ₂ (fluorite)	C1	$Fm\bar{3}m$		Cu ₃ VS ₄ (sylvanite)	H2 ₄	$P43m$
	MgAgAs	C1 _h	$F\bar{4}3m$	cP12	FeS ₂ (pyrite)	C2	$Pa\bar{3}$
cF16	AlCu ₂ Mn (Heusler)	L2 ₁	$Fm\bar{3}m$		NiSbS (ullmanite)	F0 ₁	$P2_13$
	BiF ₃ (AlFe ₃)	D0 ₃	$Fm\bar{3}m$	cP20	β Mn	A13	$P4_32$
	NaTi	B32	$Fd\bar{3}m$	cP36	BaHg ₁₁	D2 ₂	$Pm\bar{3}m$
cF24	AuBe ₃	C15 _h	$F\bar{4}3m$	cP39	Mg ₂ Zn ₁₁	D8 _c	$Pm\bar{3}$
	SiO ₂ (β cristobalite)	C9	$Fd\bar{3}m$	cP52	Cu ₂ Al ₄ (γ brass)	D8 _h	$P43m$
	Cu ₂ Mg (Laves)	C15	$Fd\bar{3}m$	hP1	HgSn ₆₋₁₀	A ₁	$P6_3/mmm$
cF32	CuPt ₃	L1 ₁	$Fm\bar{3}c$	hP2	Mg	A ₃	$P6_3/mmc$
cF32	UB ₁₂	D2 ₇	$Fm\bar{3}m$		WC	B _h	$P6_3/mmc$
cF56	Al ₂ MgO ₄ (spinel)	H1 ₁	$Fd\bar{3}m$	hP3	AlB ₂	C32	$P6_3/mmm$
	Co ₂ S ₄	D7 ₂	$Fd\bar{3}m$		CdI ₂	C6	$P3m1$
cF68	Co ₂ S ₈	D8 ₉	$Fm\bar{3}m$		Fe ₂ N	L'3	$P6_3/mmc$
cF80	Sb ₂ O ₃ (senarmontite)	D5 ₄	$Fd\bar{3}m$		LiZn ₂	C ₄	$P6_3/mmc$
cF112	Fe ₃ W ₃ C (η carbide)	E9 ₃	$Fd\bar{3}m$		γ Se	A8	$P3_121$
	NaZn ₁₃	D2 ₃	$Fm\bar{3}c$	hP4	α La	A3'	$P6_3/mmc$
cF116	Cr ₂₃ C ₆	D8 ₄	$Fm\bar{3}m$		BN	B ₁	$P6_3/mmc$
	Mn ₂₃ Th ₆ , Cu ₁₆ Mg ₄ Si ₇ (G-phase)	D8 _h	$Fm\bar{3}m$		C (graphite)	A ₉	$P6_3/mmc$
cI2	W	A2	$Im\bar{3}m$		NiAs	B8 ₁	$P6_3/mmc$
cI16	CoU	B ₂	$I2_13$		ZnS (wurtzite)	B ₄	$P6_3mc$
cI28	Th ₃ P ₄	D7 ₃	$I43d$	hP5	La ₂ O ₃	D5 ₂	$P3m1$
cI32	CoAs ₃ (skutterudite)	D0 ₂	$Im\bar{3}$	hP6	Ni ₂ Al ₃	D5 ₁₃	$P3m1$
cI40	Ge ₂ Ir ₃	D8 ₇	$Im\bar{3}m$		CaCu ₂	D2 ₂	$P6_3/mmm$
	Pu ₂ C ₃	D5 _c	$I43d$		CoSn	B35	$P6_3/mmm$
cI52	Cu ₂ Zn ₄ (γ brass)	D8 ₂	$I43m$		Cu ₂ Te	C ₄	$P6_3/mmm$
	Fe ₃ Zn ₁₀ (γ brass)	D8 ₁	$Im\bar{3}m$		HgS	B9	$P3_121$
cI54	Sb ₂ Tl ₇	L2 ₂	$Im\bar{3}m$		MoS ₂	C7	$P6_3/mmc$
cI58	α Mn (χ -phase)	A12	$I43m$	hP8	Ni ₂ In	B8 ₂	$P6_3/mmc$
cI76	Cu ₁₃ Si ₄	D8 ₆	$I43d$		Na ₃ As	D0 ₁₈	$P6_3/mmc$
cI80	Mn ₂ O ₃	D5 ₃	$Ia\bar{3}$		Ni ₂ Sn	D0 ₁₉	$P6_3/mmc$
cI96	AlLi ₂ N ₂	E9 ₄	$Ia\bar{3}$		TiAs	B ₁	$P6_3/mmc$
cI162	Mg ₃₂ (Al,Zn) ₄₉	D8 ₈	$Im\bar{3}$	hP9	CrSi ₂	C40	$P6_322$
cP1	α Po	A ₁	$Pm\bar{3}m$		Fe ₂ P	C22	$P6_32m$
cP2	CsCl	B2	$Pm\bar{3}m$		{AgZn}	B ₁	$P\bar{3}$
cP4	AuCu ₃	L1 ₂	$Pm\bar{3}m$		SiO ₂ (high quartz)	C8	$P6_322$
	ReO ₃	D0 ₃	$Pm\bar{3}m$	hP10	Pt ₂ Sn ₃	D5 ₃	$P6_3/mmc$
cP5	AlFe ₃ C (perovskite)	L1' ₂	$Pm\bar{3}m$	hP12	CuS	B18	$P6_3/mmc$
	CaTiO ₃ (perovskite)	E2 ₁	$Pm\bar{3}m$		MgZn ₂ (Laves)	C14	$P6_3/mmc$
	Fe ₄ N	L1'	$P43m$		SiO ₂ (β tridymite)	C10	$P6_3/mmc$

continued

*Adapted (with additions and corrections) from *ASM Handbook*, Vol. 3, 10th ed, ASM International, Materials Park, OH.

Arranged Alphabetically by Pearson-Symbol Designation (*continued*)

Pearson symbol	Prototype	Strukturbericht designation	Space group	Pearson symbol	Prototype	Strukturbericht designation	Space group
<i>hP</i> 14	W ₂ B ₅	<i>D</i> 8 _h	<i>P</i> 6 ₃ / <i>mmc</i>	<i>oP</i> 8	βCu ₃ Ti	<i>D</i> 0 _h	<i>P</i> mmn
<i>hP</i> 16	Mn ₃ Si ₃	<i>D</i> 8 _h	<i>P</i> 6 ₃ / <i>mcm</i>		FeB	<i>B</i> 27	<i>P</i> nma
	Ni ₃ Ti	<i>D</i> 0 ₂₄	<i>P</i> 6 ₃ / <i>mmc</i>		GeS	<i>B</i> 16	<i>P</i> nma
<i>hP</i> 18	Al ₃ C ₃ Si	<i>E</i> 9 _h	<i>P</i> 6 ₃ / <i>mc</i>		SnS	<i>B</i> 29	<i>P</i> mcn
	Al ₃ FeMg ₃ Si ₆	<i>E</i> 9 _h	<i>P</i> 6 ₂ / <i>m</i>		MnP	<i>B</i> 31	<i>P</i> nma
	Mg ₂ Ni	<i>C</i> ₆	<i>P</i> 6 ₂ / <i>22</i>		TiB	<i>B</i> ₂	<i>P</i> nma
<i>hP</i> 20	Fe ₃ Th ₃	<i>D</i> 10 ₂	<i>P</i> 6 ₃ / <i>mc</i>	<i>oP</i> 12	Co ₂ Si, NiSiTi (E-phase)	<i>C</i> 23	<i>P</i> nma
	Th ₃ Si ₁₂	<i>D</i> 8 _h	<i>P</i> 6 ₃ / <i>m</i>		Co ₂ Si	<i>C</i> 37	<i>P</i> bnm
<i>hP</i> 24	Cu ₃ P	<i>D</i> 0 ₂₁	<i>P</i> 6 ₃ / <i>cm</i>		HgCl ₂	<i>C</i> 28	<i>P</i> mnb
	MgNi ₂ (Laves)	<i>C</i> 36	<i>P</i> 6 ₃ / <i>mmc</i>	<i>oP</i> 16	Al ₃ Ni	<i>D</i> 0 ₂₀	<i>P</i> nma
<i>hP</i> 28	Co ₂ Al ₃	<i>D</i> 8 ₁₁	<i>P</i> 6 ₃ / <i>mmc</i>		AsMn ₃	<i>D</i> 0 ₄	<i>P</i> mmn
<i>hR</i> 1	αHg	<i>A</i> 10	<i>R</i> 3̄ <i>m</i>		Ba ₃	<i>D</i> 0 ₁₇	<i>P</i> 42 ₁ / <i>m</i>
	βPo	<i>A</i> ₁	<i>R</i> 3̄ <i>m</i>		CdSb	<i>B</i> ₂	<i>P</i> bca
<i>hR</i> 2	αAs	<i>A</i> 7	<i>R</i> 3̄ <i>m</i>		Cu ₂ Sb (wolfsbergite)	<i>F</i> 5 ₆	<i>P</i> nma
<i>hR</i> 3	αSm	<i>C</i> 19	<i>R</i> 3̄ <i>m</i>		Fe ₃ C (cementite)	<i>D</i> 0 ₁₁	<i>P</i> nma
<i>hR</i> 4	NaCrS ₂	<i>F</i> 5 ₁	<i>R</i> 3̄ <i>m</i>	<i>oP</i> 20	Cr ₃ C ₂	<i>D</i> 5 ₁₀	<i>P</i> nma
<i>hR</i> 5	Bi ₂ Te ₃	<i>C</i> 33	<i>R</i> 3̄ <i>m</i>		Sb ₂ S ₃	<i>D</i> 5 ₃	<i>P</i> nma
	Ni ₃ S ₂	<i>D</i> 5 ₁	<i>R</i> 3̄ <i>2</i>	<i>oP</i> 24	Sb ₂ O ₃ (valentinite)	<i>D</i> 5 ₁₁	<i>P</i> ccn
<i>hR</i> 6	CaSi ₂	<i>C</i> 12	<i>R</i> 3̄ <i>m</i>		AuTe ₂ (krennerite)	<i>C</i> 46	<i>P</i> ma2
	NiS (millerite)	<i>B</i> 13	<i>R</i> 3̄ <i>m</i>		CuFe ₂ S ₃ (cubanite)	<i>E</i> 9 ₂	<i>P</i> nma
<i>hR</i> 7	Al ₃ C ₃	<i>D</i> 7 ₁	<i>R</i> 3̄ <i>m</i>		TiO ₂ (brookite)	<i>C</i> 21	<i>P</i> bca
	Mo ₂ B ₃	<i>D</i> 8 ₁	<i>R</i> 3̄ <i>m</i>	<i>oP</i> 40	Cr ₃ C ₃	<i>D</i> 10 ₁	<i>P</i> nma
<i>hR</i> 10	αAl ₂ O ₃ (corundum)	<i>D</i> 5 ₁	<i>R</i> 3̄ <i>c</i>	<i>II</i> 2	αPa	<i>A</i> ₆	<i>I</i> 4/ <i>mmm</i>
<i>hR</i> 12	BaPb ₃		<i>R</i> 3̄ <i>m</i>		In	<i>A</i> ₆	<i>I</i> 4/ <i>mmm</i>
<i>hR</i> 13	Fe ₇ W ₆ (μ-phase)	<i>D</i> 8 ₃	<i>R</i> 3̄ <i>m</i>	<i>II</i> 4	βSn	<i>A</i> 5	<i>I</i> 4 ₁ / <i>amd</i>
<i>hR</i> 15	B ₄ C	<i>D</i> 1 ₄	<i>R</i> 3̄ <i>m</i>	<i>II</i> 6	CaC ₂	<i>C</i> 11 ₄	<i>I</i> 4/ <i>mmm</i>
<i>hR</i> 20	HoAl ₃		<i>R</i> 3̄ <i>m</i>		MoSi ₂	<i>C</i> 11 ₅	<i>I</i> 4/ <i>mmm</i>
<i>hR</i> 26	Cr ₂ Al ₃	<i>D</i> 8 ₁₀	<i>R</i> 3̄ <i>m</i>	<i>II</i> 8	ThH ₂	<i>L</i> ' ₂	<i>I</i> 4/ <i>mmm</i>
<i>hR</i> 32	CuPt	<i>L</i> 1 ₁	<i>R</i> 3̄ <i>m</i>	<i>II</i> 10	Al ₃ Ti	<i>D</i> 0 ₂₂	<i>I</i> 4/ <i>mmm</i>
<i>mC</i> 6	AuTe ₂ (calaverite)	<i>C</i> 34	<i>C</i> 2/ <i>m</i>		Al ₃ Ba	<i>D</i> 1 ₃	<i>I</i> 4/ <i>mmm</i>
<i>mC</i> 8	CuO (tenorite)	<i>B</i> 26	<i>C</i> 2/ <i>c</i>	<i>II</i> 12	MoNi ₄	<i>D</i> 1 ₅	<i>I</i> 4/ <i>m</i>
<i>mC</i> 12	ThC ₂	<i>C</i> ₂	<i>C</i> 2/ <i>c</i>		Al ₃ Cu	<i>C</i> 16	<i>I</i> 4/ <i>mcm</i>
<i>mC</i> 14	δNi ₃ Sn ₄	<i>D</i> 7 ₂	<i>C</i> 2/ <i>m</i>	<i>II</i> 14	ThSi ₂	<i>C</i> ₅	<i>I</i> 4 ₁ / <i>gmd</i>
<i>mC</i> 16	FeKS ₂	<i>F</i> 5 ₄	<i>C</i> 2/ <i>c</i>	<i>II</i> 16	Al ₂ CdS ₄	<i>E</i> 3	<i>I</i> 4
<i>mP</i> 12	AgAuTe ₂ (sylvanite)	<i>E</i> 1 ₃	<i>P</i> 2/ <i>c</i>		Al ₃ Zr	<i>D</i> 0 ₂₃	<i>I</i> 4/ <i>mmm</i>
	ZrO ₂	<i>C</i> 43	<i>P</i> 2 ₁ / <i>c</i>		CuFeS ₂ (chalcopyrite)	<i>E</i> 1 ₁	<i>I</i> 42 <i>d</i>
<i>mP</i> 20	As ₂ S ₃	<i>D</i> 5 ₇	<i>P</i> 2 ₁ / <i>c</i>		Cu ₂ FeSnS ₄ (stannite)	<i>H</i> 2 ₄	<i>I</i> 42 <i>m</i>
<i>mP</i> 22	Co ₂ Al ₃	<i>D</i> 8 ₄	<i>P</i> 2 ₁ / <i>c</i>		Ir ₃ Si	<i>D</i> 0 ₂	<i>I</i> 4/ <i>mcm</i>
<i>mP</i> 24	FeAsS	<i>E</i> 0 ₁	<i>P</i> 2 ₁ / <i>c</i>		MoB	<i>B</i> ₂	<i>I</i> 4 ₁ / <i>amd</i>
<i>mP</i> 32	AsS (realgar)	<i>B</i> ₁	<i>P</i> 2 ₁ / <i>c</i>	<i>II</i> 18	SiU ₃	<i>D</i> 0 ₁	<i>I</i> 4/ <i>mcm</i>
	βSe	<i>A</i> ₁	<i>P</i> 2 ₁ / <i>c</i>	<i>II</i> 26	TiSe	<i>B</i> 37	<i>I</i> 4/ <i>mcm</i>
<i>mP</i> 64	αSe	<i>A</i> ₂	<i>P</i> 2 ₁ / <i>c</i>	<i>II</i> 28	Fe ₃ N	<i>D</i> 2 ₂	<i>I</i> 4/ <i>mmm</i>
<i>oC</i> 4	αU	<i>A</i> 20	<i>C</i> mc <i>m</i>	<i>II</i> 32	Mn ₃ Th	<i>D</i> 2 ₃	<i>I</i> 4/ <i>mmm</i>
<i>oC</i> 8	CaSi	<i>B</i> ₂	<i>C</i> mmc		MnU ₆	<i>D</i> 2 ₄	<i>I</i> 4/ <i>mcm</i>
	αGa	<i>A</i> 11	<i>C</i> mca		Cr ₃ B ₃	<i>D</i> 8 ₁	<i>I</i> 4/ <i>mcm</i>
	CrB	<i>B</i> 33	<i>C</i> mc <i>m</i>	<i>IP</i> 2	Ni ₃ P	<i>D</i> 0 ₁	<i>I</i> 4
	I ₂	<i>A</i> 14	<i>C</i> mca	<i>IP</i> 4	W ₃ Si ₃	<i>D</i> 8 ₂	<i>I</i> 4/ <i>mcm</i>
	P (black)	<i>A</i> 17	<i>C</i> mca		δCuTi	<i>L</i> 2 ₂	<i>P</i> 4/ <i>mmm</i>
<i>oC</i> 12	ZrSi ₂	<i>C</i> 49	<i>C</i> mc <i>m</i>		βNp	<i>A</i> ₈	<i>P</i> 42 ₂
<i>oC</i> 16	BRc ₃	<i>E</i> 1 ₃	<i>C</i> mc <i>m</i>		AuCu	<i>L</i> 1 ₀	<i>P</i> 4/ <i>mmm</i>
<i>oC</i> 20	PdSn ₄	<i>D</i> 1 ₅	<i>A</i> ba2		CuTi ₃	<i>L</i> 6 ₃	<i>P</i> 4/ <i>mmm</i>
<i>oC</i> 24	PdSn ₂	<i>C</i> ₂	<i>A</i> ba2		γCuTi	<i>B</i> 11	<i>P</i> 4/ <i>nm</i>
<i>oC</i> 28	Al ₃ Mn	<i>D</i> 2 ₄	<i>C</i> mc <i>m</i>		PbO	<i>B</i> 10	<i>P</i> 4/ <i>nm</i>
<i>oF</i> 24	TiSi ₃	<i>C</i> 54	<i>F</i> ddd	<i>IP</i> 6	Pb ₃ Sr		<i>P</i> 4/ <i>nm</i>
<i>oF</i> 40	Mn ₃ B	<i>D</i> 1 ₇	<i>F</i> ddd		PtS	<i>B</i> 17	<i>P</i> 4 ₂ / <i>mmc</i>
<i>oF</i> 48	CuMg ₂	<i>C</i> ₂	<i>F</i> ddd		Cu ₂ Sb	<i>C</i> 38	<i>P</i> 4/ <i>nm</i>
<i>oF</i> 72	GeS ₂	<i>C</i> 44	<i>F</i> dd2	<i>IP</i> 10	PbFCl	<i>E</i> 0 ₁	<i>P</i> 4/ <i>nm</i>
<i>oF</i> 128	αS	<i>A</i> 16	<i>F</i> ddd		TiO ₂ (rutile)	<i>C</i> 4	<i>P</i> 4 ₂ / <i>nm</i>
<i>oI</i> 12	SiS ₂	<i>C</i> 42	<i>I</i> bam	<i>IP</i> 16	Pb ₂ Pt	<i>D</i> 1 ₄	<i>P</i> 4/ <i>nbm</i>
<i>oI</i> 14	Ta ₃ B ₄	<i>D</i> 7 ₆	<i>I</i> mmm	<i>IP</i> 20	Si ₃ U ₃	<i>D</i> 5 ₂	<i>P</i> 4/ <i>mbm</i>
<i>oI</i> 20	Al ₃ U	<i>D</i> 1 ₆	<i>I</i> mma	<i>IP</i> 30	PdS	<i>B</i> 34	<i>P</i> 4 ₂ / <i>m</i>
<i>oI</i> 28	Ga ₂ Mg ₅	<i>D</i> 8 ₂	<i>I</i> bam		βU	<i>D</i> 1 ₁	<i>P</i> 4/ <i>mbm</i>
<i>oP</i> 4	AuCd	<i>B</i> 19	<i>P</i> nma	<i>IP</i> 40	σCrFe	<i>A</i> ₈	<i>P</i> 4 ₂ / <i>nm</i>
<i>oP</i> 6	FeS ₂ (marcasite)	<i>C</i> 18	<i>P</i> nn <i>m</i>		Al ₃ Cu ₃ Fe	<i>E</i> 9 ₃	<i>P</i> 4 ₂ / <i>nm</i>
	CaCl ₂	<i>C</i> 35	<i>P</i> nn <i>m</i>	<i>IP</i> 50	Zn ₃ P ₂	<i>D</i> 5 ₃	<i>P</i> 4 ₂ / <i>nm</i>
<i>oP</i> 8	αNp	<i>A</i> ₂	<i>P</i> nma		γB	<i>A</i> ₄	<i>P</i> 4 ₂ / <i>nm</i>
	γNiSi	<i>B</i> ₄	<i>P</i> bn <i>m</i>				

Arranged Alphabetically by Strukturbericht Designation

Struktur- bericht designation	Prototype	Pearson symbol	Space group	Struktur- bericht designation	Prototype	Pearson symbol	Space group
<i>A₂</i>	αPa	<i>tI</i> 2	<i>I</i> 4/ <i>mmm</i>	<i>B</i> 20	FeSi	<i>cP</i> 8	<i>P</i> 2 ₁ 3
<i>A₃</i>	βU	<i>tP</i> 30	<i>P</i> 4 ₂ / <i>mnm</i>	<i>B</i> 26	CuO (tenorite)	<i>mC</i> 8	<i>C</i> 2/ <i>c</i>
<i>A₄</i>	αNp	<i>oP</i> 8	<i>Pnma</i>	<i>B</i> 27	FeB	<i>oP</i> 8	<i>Pnma</i>
<i>A₅</i>	βNp	<i>tP</i> 4	<i>P</i> 4 ₂ 2	<i>B</i> 29	SnS	<i>oP</i> 8	<i>Pmcn</i>
<i>A₆</i>	HgSn ₆₋₁₀	<i>hP</i> 1	<i>P</i> 6/ <i>mmm</i>	<i>B</i> 31	MnP	<i>oP</i> 8	<i>Pnma</i>
<i>A₇</i>	γB	<i>tP</i> 50	<i>P</i> 4 ₂ / <i>nnm</i>	<i>B</i> 32	NaTi	<i>cF</i> 16	<i>Fd</i> 3̄ <i>m</i>
<i>A₈</i>	αPo	<i>cP</i> 1	<i>Pm</i> 3̄ <i>m</i>	<i>B</i> 33(= <i>B₇</i>)	CrB	<i>oC</i> 8	<i>Cmcm</i>
<i>A₉</i>	βPo	<i>hR</i> 1	<i>R</i> 3̄ <i>m</i>	<i>B</i> 34	PdS	<i>tP</i> 16	<i>P</i> 4 ₂ / <i>m</i>
<i>A₁₀</i>	αSe	<i>mP</i> 64	<i>P</i> 2 ₁ / <i>c</i>	<i>B</i> 35	CoSn	<i>hP</i> 6	<i>P</i> 6/ <i>mmm</i>
<i>A₁₁</i>	βSe	<i>mP</i> 32	<i>P</i> 2 ₁ / <i>c</i>	<i>B</i> 37	TiSe	<i>tI</i> 16	<i>I</i> 4/ <i>mcm</i>
<i>A</i> 1	Cu	<i>cF</i> 4	<i>Fm</i> 3̄ <i>m</i>	<i>C₂</i>	Mg ₂ Ni	<i>hP</i> 18	<i>P</i> 6 ₂ 22
<i>A</i> 2	W	<i>cI</i> 2	<i>Im</i> 3̄ <i>m</i>	<i>C₃</i>	CuMg ₂	<i>oF</i> 48	<i>Fddd</i>
<i>A</i> 3	Mg	<i>hP</i> 2	<i>P</i> 6 ₃ / <i>mmc</i>	<i>C₄</i>	ThSi ₂	<i>tI</i> 12	<i>I</i> 4/ <i>amd</i>
<i>A</i> 3'	αLa	<i>hP</i> 4	<i>P</i> 6 ₃ / <i>mmc</i>	<i>C₅</i>	PdSn ₂	<i>oC</i> 24	<i>Aba</i> 2
<i>A</i> 4	C (diamond)	<i>cF</i> 8	<i>Fd</i> 3̄ <i>m</i>	<i>C₆</i>	ThC ₂	<i>mC</i> 12	<i>C</i> 2/ <i>c</i>
<i>A</i> 5	βSn	<i>tI</i> 4	<i>I</i> 4 ₁ / <i>amd</i>	<i>C₇</i>	Cu ₂ Te	<i>hP</i> 6	<i>P</i> 6/ <i>mmm</i>
<i>A</i> 6	In	<i>tI</i> 2	<i>I</i> 4/ <i>mmm</i>	<i>C₈</i>	LiZn ₂	<i>hP</i> 3	<i>P</i> 6 ₃ / <i>mmc</i>
<i>A</i> 7	αAs	<i>hR</i> 2	<i>R</i> 3̄ <i>m</i>	<i>C</i> 1	CaF ₂ (fluorite)	<i>cF</i> 12	<i>Fm</i> 3̄ <i>m</i>
<i>A</i> 8	γSe	<i>hP</i> 3	<i>P</i> 3 ₁ 21	<i>C</i> 1 _b	MgAgAs	<i>cF</i> 12	<i>F</i> 43̄ <i>m</i>
<i>A</i> 9	C (graphite)	<i>hP</i> 4	<i>P</i> 6 ₃ / <i>mmc</i>	<i>C</i> 2	FeS ₂ (pyrite)	<i>cP</i> 12	<i>Pa</i> 3
<i>A</i> 10	αHg	<i>hR</i> 1	<i>R</i> 3̄ <i>m</i>	<i>C</i> 3	Ag ₂ O	<i>cP</i> 6	<i>Pn</i> 3̄ <i>m</i>
<i>A</i> 11	αGa	<i>oC</i> 8	<i>Cmca</i>	<i>C</i> 4	TiO ₂ (rutile)	<i>tP</i> 6	<i>P</i> 4 ₂ / <i>mnm</i>
<i>A</i> 12	αMn (χ-phase)	<i>cI</i> 58	<i>I</i> 43̄ <i>m</i>	<i>C</i> 6	CdI ₂	<i>hP</i> 3	<i>P</i> 3̄ <i>m</i> 1
<i>A</i> 13	βMn	<i>cP</i> 20	<i>P</i> 4 ₃ 2	<i>C</i> 7	MoS ₂	<i>hP</i> 6	<i>P</i> 6 ₃ / <i>mmc</i>
<i>A</i> 14	I ₂	<i>oC</i> 8	<i>Cmca</i>	<i>C</i> 8	SiO ₂ (high quartz)	<i>hP</i> 9	<i>P</i> 6 ₂ 22
<i>A</i> 15	Cr ₃ Si (β-W)	<i>cP</i> 8	<i>Pm</i> 3̄ <i>n</i>	<i>C</i> 9	SiO ₂ (β cristobalite)	<i>cF</i> 24	<i>Fd</i> 3̄ <i>m</i>
<i>A</i> 16	αS	<i>oF</i> 128	<i>Fddd</i>	<i>C</i> 10	SiO ₂ (β tridymite)	<i>hP</i> 12	<i>P</i> 6 ₃ / <i>mmc</i>
<i>A</i> 17	P (black)	<i>oC</i> 8	<i>Cmca</i>	<i>C</i> 11 _a	CaC ₂	<i>tI</i> 6	<i>I</i> 4/ <i>mmm</i>
<i>A</i> 20	αU	<i>oC</i> 4	<i>Cmcm</i>	<i>C</i> 11 _b	MoSi ₂	<i>tI</i> 6	<i>I</i> 4/ <i>mmm</i>
<i>B₁</i>	CoU	<i>cI</i> 16	<i>I</i> 2 ₃	<i>C</i> 12	CaSi ₂	<i>hR</i> 6	<i>R</i> 3̄ <i>m</i>
<i>B₂</i>	†AgZn	<i>hP</i> 9	<i>P</i> 3̄	<i>C</i> 14	MgZn ₂	<i>hP</i> 12	<i>P</i> 6 ₃ / <i>mmc</i>
<i>B₃</i>	CaSi	<i>oC</i> 8	<i>Cmcm</i>	<i>C</i> 15	Cu ₂ Mg	<i>cF</i> 24	<i>Fd</i> 3̄ <i>m</i>
<i>B₄</i>	ηNiSi	<i>oP</i> 8	<i>Pbnm</i>	<i>C</i> 15 _b	AuBe ₃	<i>cF</i> 24	<i>F</i> 43̄ <i>m</i>
<i>B₅</i>	CdSb	<i>oP</i> 16	<i>Pbca</i>	<i>C</i> 16	Al ₃ Cu	<i>tI</i> 12	<i>I</i> 4/ <i>mcm</i>
<i>B₆</i> (= <i>B</i> 33)	CrB	<i>oC</i> 8	<i>Cmcm</i>	<i>C</i> 18	FeS ₂ (marcasite)	<i>oP</i> 6	<i>Pnnm</i>
<i>B₇</i>	MoB	<i>tI</i> 16	<i>I</i> 4 ₁ / <i>amd</i>	<i>C</i> 19	αSm	<i>hR</i> 3	<i>R</i> 3̄ <i>m</i>
<i>B₈</i>	WC	<i>hP</i> 2	<i>P</i> 6̄ <i>m</i> 2	<i>C</i> 21	TiO ₂ (brookite)	<i>oP</i> 24	<i>Pbca</i>
<i>B₉</i>	TiAs	<i>hP</i> 8	<i>P</i> 6 ₃ / <i>mmc</i>	<i>C</i> 22	Fe ₂ P	<i>hP</i> 9	<i>P</i> 6̄2 <i>m</i>
<i>B₁₀</i>	BN	<i>hP</i> 4	<i>P</i> 6 ₃ / <i>mmc</i>	<i>C</i> 23	Co ₂ Si, NiSiTi (E-phase)	<i>oP</i> 12	<i>Pnma</i>
<i>B₁₁</i>	AsS (realgar)	<i>mP</i> 32	<i>P</i> 2 ₁ / <i>c</i>	<i>C</i> 28	HgCl ₂	<i>oP</i> 12	<i>Pmnb</i>
<i>B₁₂</i>	TiB	<i>oP</i> 8	<i>Pnma</i>	<i>C</i> 32	AlB ₂	<i>hP</i> 3	<i>P</i> 6/ <i>mmm</i>
<i>B</i> 1	NaCl (rock salt)	<i>cF</i> 8	<i>Fm</i> 3̄ <i>m</i>	<i>C</i> 33	Bi ₂ Te ₃	<i>hR</i> 5	<i>R</i> 3̄ <i>m</i>
<i>B</i> 2	CsCl	<i>cP</i> 2	<i>Pm</i> 3̄ <i>m</i>	<i>C</i> 34	AuTe ₂ (calaverite)	<i>mC</i> 6	<i>C</i> 2/ <i>m</i>
<i>B</i> 3	ZnS (sphalerite)	<i>cF</i> 8	<i>F</i> 43̄ <i>m</i>	<i>C</i> 35	CaCl ₂	<i>oP</i> 6	<i>Pnnm</i>
<i>B</i> 4	ZnS (wurtzite)	<i>hP</i> 4	<i>P</i> 6 ₃ / <i>mc</i>	<i>C</i> 36	MgNi ₂ (Laves)	<i>hP</i> 24	<i>P</i> 6 ₃ / <i>mmc</i>
<i>B</i> 8 ₁	NiAs	<i>hP</i> 4	<i>P</i> 6 ₃ / <i>mmc</i>	<i>C</i> 37	Co ₂ Si	<i>oP</i> 12	<i>Pbnm</i>
<i>B</i> 8 ₂	Ni ₂ In	<i>hP</i> 6	<i>P</i> 6 ₃ / <i>mmc</i>	<i>C</i> 38	Cu ₂ Sb	<i>tP</i> 6	<i>P</i> 4/ <i>nnm</i>
<i>B</i> 9	HgS (cinnabar)	<i>hP</i> 6	<i>P</i> 3 ₁ 21	<i>C</i> 40	CrSi ₂	<i>hP</i> 9	<i>P</i> 6 ₂ 22
<i>B</i> 10	PbO	<i>tP</i> 4	<i>P</i> 4/ <i>nnm</i>	<i>C</i> 42	SiS ₂	<i>oI</i> 12	<i>Ibam</i>
<i>B</i> 11	γCuTi	<i>tP</i> 4	<i>P</i> 4/ <i>nnm</i>	<i>C</i> 43	ZrO ₂	<i>mP</i> 12	<i>P</i> 2 ₁ / <i>c</i>
<i>B</i> 13	NiS (millerite)	<i>hR</i> 6	<i>R</i> 3̄ <i>m</i>	<i>C</i> 44	GeS ₂	<i>oF</i> 72	<i>Fdd</i> 2
<i>B</i> 16	GeS	<i>oP</i> 8	<i>Pnma</i>	<i>C</i> 46	AuTe ₂ (krennerite)	<i>oP</i> 24	<i>Pma</i> 2
<i>B</i> 17	PtS (cooperite)	<i>tP</i> 4	<i>P</i> 4 ₂ / <i>mmc</i>	<i>C</i> 49	ZrSi ₂	<i>oC</i> 12	<i>Cmcm</i>
<i>B</i> 18	CuS (rovelite)	<i>hP</i> 12	<i>P</i> 6 ₃ / <i>mmc</i>	<i>C</i> 54	TiSi ₂	<i>oF</i> 24	<i>Fddd</i>
<i>B</i> 19	AuCd	<i>oP</i> 4	<i>Pnma</i>	<i>D</i> 0 _a	βCu ₃ Ti	<i>oP</i> 8	<i>Pmmn</i>
				<i>D</i> 0 _c	SiU ₃	<i>tI</i> 16	<i>I</i> 4/ <i>mcm</i>

continued

Arranged Alphabetically by Strukturbericht Designation (*continued*)

Struktur- bericht designation	Prototype	Pearson symbol	Space group	Struktur- bericht designation	Prototype	Pearson symbol	Space group
D0 _c	Ir ₃ Si	<i>tI</i> 16	<i>I4/mcm</i>	D8 _d	Co ₂ Al ₉	<i>mP</i> 22	<i>P2₁/c</i>
D0 _d	AsMn ₃	<i>oP</i> 16	<i>Pmmn</i>	D8 _e	Mg ₃₂ (Al,Zn) ₄₉	<i>cI</i> 162	<i>Im</i> 3
D0 _e	Ni ₃ P	<i>tI</i> 32	<i>I4</i>	D8 _f	Ge ₂ Ir ₃	<i>cI</i> 40	<i>Im</i> 3m
D0 ₂	CoAs ₃ (skutterudite)	<i>cI</i> 32	<i>Im</i> 3	D8 _g	Ga ₂ Mg ₅	<i>oI</i> 28	<i>Ibam</i>
D0 ₃	BiF ₃ , AlFe ₃	<i>cF</i> 16	<i>Fm</i> 3m	D8 _h	W ₂ B ₅	<i>hP</i> 14	<i>P6₃/mmc</i>
D0 ₉	ReO ₃	<i>cP</i> 4	<i>Pm</i> 3m	D8 _i	Mo ₂ B ₅	<i>hR</i> 7	<i>R</i> 3m
D0 ₁₁	Fe ₃ C (cementite)	<i>oP</i> 16	<i>Pnma</i>	D8 _k	Th ₃ Si ₁₂	<i>hP</i> 20	<i>P6₃/m</i>
D0 ₁₇	BaS ₃	<i>oP</i> 16	<i>P4₂/m</i>	D8 _l	Cr ₂ B ₃	<i>tI</i> 32	<i>I4/mcm</i>
D0 ₁₈	Na ₃ As	<i>hP</i> 8	<i>P6₃/mmc</i>	D8 _m	W ₂ Si ₃	<i>tI</i> 32	<i>I4/mcm</i>
D0 ₁₉	Ni ₃ Sn	<i>hP</i> 8	<i>P6₃/mmc</i>	D8 _n	Fe ₃ Zn ₁₀	<i>cI</i> 52	<i>Im</i> 3m
D0 ₂₀	Al ₃ Ni	<i>oP</i> 16	<i>Pnma</i>	D8 ₂	Cu ₂ Zn ₈	<i>cI</i> 52	<i>I43m</i>
D0 ₂₁	Cu ₃ P	<i>hP</i> 24	<i>P6₃/cm</i>	D8 ₃	Cu ₂ Al ₄	<i>cP</i> 52	<i>P43m</i>
D0 ₂₂	Al ₃ Ti	<i>tI</i> 8	<i>I4/mmm</i>	D8 ₄	Cr ₂₃ C ₆	<i>cF</i> 116	<i>Fm</i> 3m
D0 ₂₃	Al ₃ Zr	<i>tI</i> 16	<i>I4/mmm</i>	D8 ₅	Fe ₇ W ₆ (μ -phase)	<i>hR</i> 13	<i>R</i> 3m
D0 ₂₄	Ni ₃ Ti	<i>hP</i> 16	<i>P6₃/mmc</i>	D8 ₆	Cu ₁₅ Si ₄	<i>cI</i> 76	<i>I43d</i>
D1 _a	MoNi ₄	<i>tI</i> 10	<i>I4/m</i>	D8 ₈	Mn ₂ Si ₃	<i>hP</i> 16	<i>P6₃/mcm</i>
D1 _b	Al ₄ U	<i>oI</i> 20	<i>Imma</i>	D8 ₉	Co ₂ S ₂	<i>cF</i> 68	<i>Fm</i> 3m
D1 _c	PdSn ₄	<i>oC</i> 20	<i>Aba2</i>	D8 ₁₀	Cr ₃ Al ₃	<i>hR</i> 26	<i>R</i> 3m
D1 _d	Pb ₃ Pt	<i>tP</i> 10	<i>P4/nbm</i>	D8 ₁₁	Co ₂ Al ₃	<i>hP</i> 28	<i>P6₃/mmc</i>
D1 _e	B ₄ Th	<i>tP</i> 20	<i>P4/mbm</i>	D10 ₁	Cr ₇ C ₃	<i>oP</i> 40	<i>Pnma</i>
D1 _f	Mn ₄ B	<i>oF</i> 40	<i>Fddd</i>	D10 ₂	Fe ₃ Th ₇	<i>hP</i> 20	<i>P6₃/mc</i>
D1 _g	B ₃ C	<i>hR</i> 15	<i>R</i> 3m	E0 ₁	PbFCl	<i>tP</i> 6	<i>P4/nmm</i>
D1 _h	Al ₃ Ba	<i>tI</i> 10	<i>I4/mmm</i>	E0 ₂	FeAsS	<i>mP</i> 24	<i>P2₁/c</i>
D2 _a	Mn ₁₂ Th	<i>tI</i> 26	<i>I4/mmm</i>	E1 _a	MgCuAl ₂	<i>oC</i> 16	<i>Cmcm</i>
D2 _b	MnU ₆	<i>tI</i> 28	<i>I4/mcm</i>	E1 _b	AgAuTe ₄ (sylvanite)	<i>mP</i> 12	<i>P2/c</i>
D2 _c	CaCu ₂	<i>hP</i> 6	<i>P6₃/mcm</i>	E1 _c	CuFeS ₂ (chalcopyrite)	<i>tI</i> 16	<i>I42d</i>
D2 _d	BaHg ₁₁	<i>cP</i> 36	<i>Pm</i> 3m	E2 ₁	CaTiO ₃ (perovskite)	<i>cP</i> 5	<i>Pm</i> 3m
D2 _e	UB ₁₂	<i>cF</i> 52	<i>Fm</i> 3m	E3	Al ₃ CdS ₄	<i>tI</i> 14	<i>I4</i>
D2 _f	Fe ₃ N	<i>tI</i> 18	<i>I4/mmm</i>	E9 _a	Al ₇ Cu ₂ Fe	<i>tP</i> 40	<i>P4/mnc</i>
D2 _g	Al ₃ Mn	<i>oC</i> 28	<i>Cmcm</i>	E9 _b	Al ₃ FeMg ₅ Si ₆	<i>hP</i> 18	<i>P62m</i>
D2 _h	CaB ₆	<i>cP</i> 7	<i>Pm</i> 3m	E9 _c	Mn ₃ Al ₃ Si	<i>hP</i> 26	<i>P6₃/mmc</i>
D2 _i	NaZn ₁₃	<i>cF</i> 112	<i>Fm</i> 3c	E9 _d	AlLi ₃ N ₂	<i>cI</i> 96	<i>Ia</i> 3
D5 _a	Si ₃ U ₃	<i>tP</i> 10	<i>P4/mbm</i>	E9 _e	CuFeS ₃ (cubanite)	<i>oP</i> 24	<i>Pnma</i>
D5 _b	Pt ₂ Sn ₃	<i>hP</i> 10	<i>P6₃/mmc</i>	E9 _f	Fe ₃ W ₃ C (η carbide)	<i>cF</i> 112	<i>Fd</i> 3m
D5 _c	Pu ₂ C ₃	<i>cI</i> 40	<i>I43d</i>	E9 _g	Al ₄ C ₃ Si	<i>hP</i> 18	<i>P6₃/mc</i>
D5 _d	Ni ₃ S ₂	<i>hR</i> 5	<i>R</i> 32	F0 ₁	NiSbS (ullmanite)	<i>cP</i> 12	<i>P2₁/c</i>
D5 _e	As ₂ S ₃	<i>mP</i> 20	<i>P2₁/c</i>	F5 _a	FeKS ₂	<i>mC</i> 16	<i>C2/c</i>
D5 _f	α -Al ₂ O ₃ (corundum)	<i>hR</i> 10	<i>R</i> 3c	F5 _b	NaCrS ₂	<i>hR</i> 4	<i>R</i> 3m
D5 _g	La ₂ O ₃	<i>hP</i> 5	<i>P</i> 3m1	F5 _c	CuS ₂ Sb (wolfsbergite)	<i>oP</i> 16	<i>Pnma</i>
D5 _h	Mn ₂ O ₃	<i>cI</i> 80	<i>Ia</i> 3	H1 ₁	Al ₂ MgO ₄ (spinel)	<i>cF</i> 56	<i>Fd</i> 3m
D5 _i	Sb ₂ O ₃ (senarmontite)	<i>cF</i> 80	<i>Fd</i> 3m	H2 _a	Cu ₃ VS ₃ (sylvanite)	<i>cP</i> 8	<i>P43m</i>
D5 _j	Sb ₂ S ₃	<i>oP</i> 20	<i>Pnma</i>	H2 _b	Cu ₂ FeSnS ₄	<i>tI</i> 16	<i>I42m</i>
D5 _k	Zn ₃ P ₂	<i>tP</i> 40	<i>P4₂/nmc</i>	L1'	Fe ₄ N	<i>cP</i> 5	<i>Pm</i> 3m
D5 _l	Cr ₃ C ₂	<i>oP</i> 20	<i>Pnma</i>	L1 _a	CuPt	<i>cF</i> 32	<i>Fm</i> 3c
D5 _m	Sb ₂ O ₃ (valentinite)	<i>oP</i> 20	<i>Pccn</i>	L1 _b	AuCu	<i>tP</i> 4	<i>P4/nmm</i>
D5 _n	Ni ₃ Al ₃	<i>hP</i> 5	<i>P</i> 3m1	L1 _c (M)	AuCuII	<i>oI</i> 40	<i>Imma</i>
D7 _a	δ -Ni ₃ Sn ₄	<i>mC</i> 14	<i>C2/m</i>	L1 ₁	CuPt	<i>hR</i> 32	<i>R</i> 3m
D7 _b	Ta ₃ B ₄	<i>oI</i> 14	<i>Immm</i>	L1 ₂	AuCu ₃	<i>cP</i> 4	<i>Pm</i> 3m
D7 _c	Al ₃ C	<i>hR</i> 7	<i>R</i> 3m	L1 ₃	AlFe ₃ C (perovskite)	<i>cP</i> 5	<i>Pm</i> 3m
D7 _d	Co ₃ S ₄	<i>cF</i> 56	<i>Fd</i> 3m	L2 _a	δ -CuTi	<i>tP</i> 2	<i>P4/nmm</i>
D7 _e	Th ₃ P ₄	<i>cI</i> 28	<i>I43d</i>	L2 _b	ThH ₂	<i>tI</i> 6	<i>I4/nmm</i>
D8 _a	Mn ₂₃ Th ₆ , Cu ₁₆ Mg ₆ Si ₇ (G-phase)	<i>cF</i> 116	<i>Fm</i> 3m	L2 _c	AlCu ₂ Mn (Heusler)	<i>cF</i> 16	<i>Fm</i> 3m
D8 _b	α -CrFe	<i>tP</i> 30	<i>P4₂/mnm</i>	L3	Sb ₂ Tl ₇	<i>cI</i> 54	<i>Im</i> 3m
D8 _c	Mg ₂ Zn ₁₁	<i>cP</i> 39	<i>Pm</i> 3	L6 ₀	Fe ₂ N	<i>hP</i> 3	<i>P6₃/mmc</i>
					CuTi ₃	<i>tP</i> 4	<i>P4/nmm</i>

Contents

Contributors ix

Preface to the 1995 Edition xi

Preface to Reprint Volumes xiii

Acronyms xv

Crystal Structure Nomenclature xxi

1. Elastic Properties **1**

1.1 Introduction 1

1.2 Elastic Constants of Single Crystals 1

1.3 Anisotropy of Elastic Properties for Single Crystals 2

1.4 Elastic Properties of Dislocations 8

1.5 Elastic Moduli of Polycrystalline Intermetallics 10

1.6 Characteristics of Elastic Moduli 14

1.7 Summary and Conclusion 20

1.8 Acknowledgement 20

1.9 References 20

Addendum 22

2. Intergranular and Cleavage Fracture **25**

2.1 Introduction 25

2.2 L₁ (cP4) Compounds 26

2.3 B2 (cP2) Compounds 34

2.4 Other Intermetallic Compounds 36

2.5 Models for Brittle Fracture 37

2.6 Conclusions 39

2.7 References 39

3. Plastic Deformation	41
3.1 Introduction	41
3.2 Deformation Mechanisms	43
3.3 Stress and Temperature Dependence of Strength and Ductility (Deformation Maps)	48
3.4 Plasticity-Controlling Factors	49
3.5 Perspectives of Materials Developments	58
3.6 Acknowledgements	58
3.7 References	58
Addendum	64
4. Structure of Antiphase Boundaries and Domains	67
4.1 Introduction	67
4.2 The Structure and Energy of APBs	69
4.3 Grown-in APBs and APDs	81
4.4 APBs in Dissociated Dislocations	83
4.5 Concluding Remarks	86
4.6 Acknowledgements	86
4.7 References	87
Addendum	89
5. Dislocations	91
5.1 Introduction	91
5.2 The Fine Structure of Superdislocations in Relation to Crystal Structure	95
5.3 Slip Systems in Intermetallics and Dislocation Cores	113
5.4 Sessile Configurations	115
5.5 Core-Related Mechanical Properties	118
5.6 Dislocations Debris	122
5.7 Conclusion	124
5.8 References	125
6. Point Defects	131
6.1 Introduction	131
6.2 Experimental Techniques for Studying Point Defects	132

6.3	Experimental Studies of the Formation of Vacancies and Antisite Defects	136
6.4	Production and Structure of Interstitials	138
6.5	Theory of Point-Defect Formation Properties	140
6.6	Thermodynamics of Point Defects	142
6.7	Recovery of Point Defects after Irradiation or Quench	145
6.8	Migration Properties of Point Defects	146
6.9	Specific Systems	150
6.10	Influence of Point Defects on Physical Properties	152
6.11	Conclusion	152
	Acknowledgements	153
6.12	References	153
7.	Structure of Grain Boundaries	157
7.1	Introduction	157
7.2	Direct Observations of Structure	158
7.3	Direct Observations of Chemistry	163
7.4	Interpretation of Various Property Measurements by Grain-Boundary Structure and Chemistry	167
7.5	Modeling of Grain-Boundary Structures	170
7.6	Electronic Bonding Aspects	175
7.7	Summary	176
7.8	References	178
8.	Irradiation Damage	181
8.1	Introduction	181
8.2	Point Defects in Intermetallic Compounds	183
8.3	Irradiation-Enhanced Ordering and Irradiation-Induced Disordering of Ordered Alloys	189
8.4	Irradiation-Induced Amorphization	198
8.5	Acknowledgements	212
8.6	References	212
	Addendum	215

9. Crystallographic Transformations 221

9.1 Scope 221

9.2 Crystallography 221

9.3 Kinetics of Martensitic Transformations 225

9.4 Nucleation of Martensite 225

9.5 Stress- and Strain-Induced Martensitic Transformations 225

9.6 Shape-Memory Effects 226

9.7 Martensitic Transformations in Ceramics 229

9.8 Bainite Transformations 229

9.9 Massive Transformations 237

9.10 Twinning 238

9.11 Applications of Phase Transformations to Structural and Functional
Materials 239

9.12 References 240

Addendum 242

Index 249

Chapter 1

Elastic Properties

Morihiko Nakamura

National Research Institute for Metals, 1-2-1 Sengen, Tsukuba-shi, Ibaraki 305-0047

1. Introduction

Elastic constants are fundamental physical constants that are measures of the interatomic forces in materials, and are often used for the estimation of an interatomic potential that is applied in a computer simulation. They give information about the stiffness of the material and are used for understanding of mechanical properties. For example, the properties of dislocations like Peierls stress, self-energy, interaction between dislocations, etc., are explained by elastic theory. The Peierls stress τ_p is given by the following equation (Peierls, 1940; Nabarro, 1947):

$$\tau_p = [2G/(1-\nu)] \exp[-2\pi d/b(1-\nu)] \quad (1)$$

Here, G is the shear modulus, ν is Poisson's ratio, b is the magnitude of the Burgers vector, and d is the distance between slip planes. The fracture strength σ_c of brittle materials is represented by Griffith's relation (Griffith, 1920):

$$\sigma_c = 2(\gamma E/c)^{1/2} \quad (2)$$

where γ is the surface energy, E is Young's modulus, and c is the size of an internal crack.

In this chapter, elastic constants of single crystals are first summarized, and the anisotropy of elastic properties of single crystals is discussed using Young's modulus, Poisson's ratio, etc. Then, the elastic properties of dislocations are discussed using elastic constants of single crystals, followed by a summary of the elastic moduli of polycrystalline intermetallics.

Finally, the effects of various factors like temperature on the elastic moduli are discussed. The experimental details for the determination of elastic constants are not described, since we have a textbook that reviews experimental procedures (Schreiber *et al.*, 1973).

2. Elastic Constants of Single Crystals

Elastic modulus values are classified into two groups: one is the static modulus, and the other is the dynamic modulus. The former is called the 'isothermal modulus' and is obtained from the linear relationship between load and displacement of a specimen. The latter is called the 'adiabatic modulus' and is determined from the resonance frequency or the velocity of an ultrasonic wave (USW) in a specimen. The difference between them is caused by thermal expansion, which results from the adiabatic behavior of the specimen during the propagation of an ultrasonic wave pulse in the latter. Some difficulties cannot be avoided in the determination of the isothermal modulus. For example, a relatively large specimen is needed for the static measurement of a small strain. Thus, the elastic modulus is usually determined from the velocity of an ultrasonic wave in a single crystal of a material, for which it is difficult to prepare a large specimen.

The velocity v of the ultrasonic wave in a material is given by the following equation:

$$v = (M/\rho)^{1/2} \quad (3)$$

Here, ρ is the density and M is the appropriate elastic modulus. The relation between stress σ_{ij} and strain

ϵ_{ij} ($i, j = 1, 2, 3$) for Cartesian coordinates is represented by the generalized Hooke's law. In general, the x_3 -axis is selected for the most symmetrical axis of a crystal structure:

$$\begin{bmatrix} \sigma_{11} \\ \sigma_{22} \\ \sigma_{33} \\ \sigma_{23} \\ \sigma_{31} \\ \sigma_{12} \end{bmatrix} = \begin{bmatrix} c_{11} & c_{12} & c_{13} & c_{14} & c_{15} & c_{16} \\ & c_{22} & c_{23} & c_{24} & c_{25} & c_{26} \\ & & c_{33} & c_{34} & c_{35} & c_{36} \\ & & & c_{44} & c_{45} & c_{46} \\ \text{symmetry} & & & & c_{55} & c_{56} \\ & & & & & c_{66} \end{bmatrix} \begin{bmatrix} \epsilon_{11} \\ \epsilon_{22} \\ \epsilon_{33} \\ \epsilon_{23} \\ \epsilon_{31} \\ \epsilon_{12} \end{bmatrix} \quad (4)$$

Here, c_{ij} is the Voigt notation for the components of the elastic stiffness tensor. The number of independent components c_{ij} decreases with increase of symmetry from 21 for a triclinic crystal to two for an isotropic material. The number of independent c_{ij} is three for a cubic structure like $L1_2$ (cP4), $B2$ (cP2), etc.: $c_{11} = c_{22} = c_{33}$, $c_{44} = c_{55} = c_{66}$, $c_{12} = c_{13} = c_{23}$, and $c_{ij} = 0$ for $i > 3$ or $j > 3$ and $i \neq j$. It is six for a tetragonal structure like $D0_{22}$ (tI8), $D0_{23}$ (tI16), $C11_b$ (tI6), etc.: $c_{11} = c_{22}$, $c_{33} \neq 0$, $c_{44} = c_{55}$, $c_{66} \neq 0$, $c_{12} \neq 0$, $c_{13} = c_{23}$, and $c_{ij} = 0$ for $i > 3$ or $j > 3$ and $i \neq j$. It is five for a hexagonal structure like $D0_{19}$ (hP8), $C40$ (hP9), etc.: $c_{11} = c_{22}$, $c_{33} \neq 0$, $c_{44} = c_{55}$, $c_{66} = (c_{11} - c_{12})/2$, $c_{12} \neq 0$, $c_{13} = c_{23}$, and $c_{ij} = 0$ for $i > 3$ or $j > 3$ and $i \neq j$. It is two for an isotropic material: $c_{11} = c_{22} = c_{33}$, $c_{44} = c_{55} = c_{66} = (c_{11} - c_{12})/2$, $c_{12} = c_{13} = c_{23}$, and $c_{ij} = 0$ for $i > 3$ or $j > 3$ and $i \neq j$.

The appropriate elastic modulus M , which is determined from the velocity of the longitudinal wave in the $[100]$ direction, is c_{11} . M determined from the velocity of the transverse wave in the $[100]$ direction on (001) and (010) planes is c_{55} and c_{66} , respectively. Thus, by measuring the velocity of the longitudinal wave in some crystal orientations and that of the transverse wave on certain crystal planes in some other orientations, depending on crystal symmetry, an elastic-stiffness-constant matrix $\{c_{ij}\}$ is obtained. Table 1 shows the elastic stiffness constants c_{ij} of some intermetallic compounds at room temperature. Although alloys often exhibit some maxima of Young's modulus at compositions corresponding to intermetallic compounds, intermetallics do not always have higher stiffness constants than those of the constituent elements. For example, MoSi_2 , WSi_2 , TiAl_3 , and ZrAl_3 exhibit higher stiffness constants than their constituent metals. In contrast, Ni_3Al and Ni_3Fe have similar constants to Ni,

and the elastic constants of Cu_3Au are similar to those of Au and Cu, averaged.

The elastic constants are closely related to the potential energies between atoms. When the interatomic force is a central force, Cauchy's relationships hold true for the elastic stiffness constants (Love, 1944):

$$\begin{aligned} c_{23} &= c_{44} & c_{31} &= c_{55} & c_{12} &= c_{66} \\ c_{14} &= c_{56} & c_{25} &= c_{46} & c_{45} &= c_{36} \end{aligned} \quad (5)$$

Table 1 shows that generally the Cauchy relationships are not true for intermetallic compounds, although c_{12} is close to c_{66} ($= c_{44}$) for intermetallic semiconductors like GaAs, etc. Thus, when the elastic constants were calculated using a central-force approximation for the forces between atoms, they disagreed with experimental values (Girifalco and Weizer, 1959). Recently, the elastic constants of Ni_3Al , CoAl , SbY , Pt_3Al , MoSi_2 , etc., have been calculated using an embedded-atom method (EAM) (Foiles and Daw, 1987; Chen *et al.*, 1986), a linear augmented-plane-wave (LAPW) method (Mehl *et al.*, 1990), the first-principles full-potential linearized augmented-plane-wave (F-LAPW) total-energy method (Fu and Yoo, 1989), or an all-electron self-consistent full-potential linear muffin-tin-orbitals (F-LMTO) method (Alouani *et al.*, 1991). The calculated elastic stiffness constants are shown in Table 2. It should be noted that the calculated values are in good agreement with the experimental ones for Ni_3Al and MoSi_2 (see Table 1). The methods of first-principles calculation of elastic constants are summarized in Chapter 9 by Mehl *et al.* in this volume.

The isothermal moduli can be calculated from the adiabatic ones using the thermal expansion coefficient α , specific heat at constant pressure C_p , and density ρ (Garber and Granato, 1975; Kayser and Stassis, 1981; Rausch and Kayser, 1977). Table 3 shows the comparison between the adiabatic and isothermal elastic stiffness constants for cubic crystals. The former are about 2% higher than the latter.

3. Anisotropy of Elastic Properties for Single Crystals

When a tensile or compressive test is carried out, the applied stress is usually controlled, and the strain is measured. Thus, it is more convenient to use the following equation instead of equation (4) for the elastic stress-strain relationship:

Table 1. Elastic stiffness constants (10^2 GPa) of intermetallic compounds at room temperature

Intermetallics	c_{11}	c_{22}	c_{33}	c_{44}	c_{55}	c_{66}	c_{12}	c_{13}	c_{23}	Structure ^a	References
TiAl ₃	2.177	c_{11}	2.175	0.920	c_{44}	1.165	0.577	0.455	c_{13}	D0 ₂₂ , tI8	Nakamura and Kimura (1991)
ZrAl ₃	2.088	c_{11}	2.083	0.872	c_{44}	1.022	0.705	0.491	c_{13}	D0 ₂₂ , tI16	Nakamura and Kimura (1991)
MoSi ₂	4.170	c_{11}	5.145	2.042	c_{44}	1.936	1.042	0.838	c_{13}	C11 _b , tI6	Nakamura <i>et al.</i> (1990)
WSi ₂	4.428	c_{11}	5.523	2.116	c_{44}	2.175	1.217	0.810	c_{13}	C11 _b , tI6	Nakamura <i>et al.</i> (1990)
VSi ₂	3.578	c_{11}	4.223	1.357	c_{44}	c_{66}^b	0.506	0.681	c_{13}	C40, hP9	Nakamura (1991b, 1993)
CrSi ₂	3.722	c_{11}	3.852	1.491	c_{44}	c_{66}^b	0.453	0.826	c_{13}	C40, hP9	Nakamura (1991b, 1993)
Ti ₃ Sn	1.390	c_{11}	2.086	0.398	c_{44}	c_{66}^b	0.612	0.721	c_{13}	D0 ₁₉ , hP8	Nakamura (1991a)
TiSi ₂	3.175	3.204	4.132	1.113	0.758	1.1735	0.2935	0.3845	0.8600	C54, oF24	Nakamura (1994)
CoSi ₂	2.770	c_{11}	c_{11}	0.823	c_{44}	c_{44}	1.766	c_{12}	c_{12}	C1, cF12	Nakamura (1994)
CoSi ₃	2.28	c_{11}	c_{11}	0.83	c_{44}	c_{44}	1.40	c_{12}	c_{12}	C1, cF12	Guenin <i>et al.</i> (1990)
Mg ₂ Si	1.21	c_{11}	c_{11}	0.464	c_{44}	c_{44}	0.22	c_{12}	c_{12}	C1, cF12	Whitten <i>et al.</i> (1965)
Ni ₃ Al	2.23	c_{11}	c_{11}	1.25	c_{44}	c_{44}	1.48	c_{12}	c_{12}	L1 ₂ , cP4	Yoo (1987b)
Ni ₂ Al	1.980	c_{11}	c_{11}	1.179	c_{44}	c_{44}	1.266	c_{12}	c_{12}	L1 ₂ , cP4	Ono and Stern (1969)
Ni ₃ Al	2.210	c_{11}	c_{11}	1.240	c_{44}	c_{44}	1.460	c_{12}	c_{12}	L1 ₂ , cP4	Dickson and Wachtman (1969)
Ni ₂ Fe	2.46	c_{11}	c_{11}	1.24	c_{44}	c_{44}	1.48	c_{12}	c_{12}	L1 ₂ , cP4	Yoo (1987b)
Ni ₂ Fe	2.508	c_{11}	c_{11}	1.230	c_{44}	c_{44}	1.538	c_{12}	c_{12}	L1 ₂ , cP4	Yasuda <i>et al.</i> (1992)
Ni ₃ Ga	1.91	c_{11}	c_{11}	1.07	c_{44}	c_{44}	1.23	c_{12}	c_{12}	L1 ₂ , cP4	Yasuda and Koiwa (1991)
Ni ₂ Ge	2.630	c_{11}	c_{11}	1.030	c_{44}	c_{44}	1.430	c_{12}	c_{12}	L1 ₂ , cP4	Yasuda <i>et al.</i> (1992)
Ni ₂ Mn	2.445	c_{11}	c_{11}	1.450	c_{44}	c_{44}	1.653	c_{12}	c_{12}	L1 ₂ , cP4	Yasuda <i>et al.</i> (1992)
Cu ₃ Au	1.87	c_{11}	c_{11}	0.68	c_{44}	c_{44}	1.35	c_{12}	c_{12}	L1 ₂ , cP4	Yoo (1987b)
Cu ₃ Au	1.907	c_{11}	c_{11}	0.6631	c_{44}	c_{44}	1.383	c_{12}	c_{12}	L1 ₂ , cP4	Siegel (1940)
Al ₃ Li	1.236	c_{11}	c_{11}	0.428	c_{44}	c_{44}	0.372	c_{12}	c_{12}	L1 ₂ , cP4	Miller <i>et al.</i> (1981)
NiAl	2.115	c_{11}	c_{11}	1.121	c_{44}	c_{44}	1.432	c_{12}	c_{12}	B2, cP2	Wasilewski (1966)
AgMg	0.84	c_{11}	c_{11}	0.48	c_{44}	c_{44}	0.56	c_{12}	c_{12}	B2, cP2	Yoo (1987b)
AgMg	0.846	c_{11}	c_{11}	0.485	c_{44}	c_{44}	0.567	c_{12}	c_{12}	B2, cP2	Cheng (1967)
AgMg	0.838	c_{11}	c_{11}	0.4755	c_{44}	c_{44}	0.5635	c_{12}	c_{12}	B2, cP2	Chang <i>et al.</i> (1967)
CuZn	1.29	c_{11}	c_{11}	0.82	c_{44}	c_{44}	1.10	c_{12}	c_{12}	B2, cP2	Yoo (1987b)
CuZn	1.279	c_{11}	c_{11}	0.822	c_{44}	c_{44}	1.091	c_{12}	c_{12}	B2, cP2	Smithells (1976)
AuCd	0.903	c_{11}	c_{11}	0.489	c_{44}	c_{44}	0.829	c_{12}	c_{12}	B2, cP2	Zirinsky (1956)
AuZn	0.50	c_{11}	c_{11}	0.370	c_{44}	c_{44}	0.375	c_{12}	c_{12}	B2, cP2	Zirinsky (1956)
AuZn	1.418	c_{11}	c_{11}	0.5452	c_{44}	c_{44}	1.263	c_{12}	c_{12}	B2, cP2	Schiltz <i>et al.</i> (1971)
YZn	0.9443	c_{11}	c_{11}	0.4731	c_{44}	c_{44}	0.4600	c_{12}	c_{12}	B2, cP2	Schiltz <i>et al.</i> (1971)
CoTi	2.03	c_{11}	c_{11}	0.68	c_{44}	c_{44}	1.29	c_{12}	c_{12}	B2, cP2	Yasuda <i>et al.</i> (1991)
Fe ₃ Al	1.710	c_{11}	c_{11}	1.317	c_{44}	c_{44}	1.306	c_{12}	c_{12}	D0 ₃ , cF16	Leamy <i>et al.</i> (1967)
CaMg ₂	0.5625	c_{11}	0.6163	0.1805	c_{44}	c_{66}^b	0.159	0.15	c_{13}	C14, hP12	Sumer and Smith (1962)
CaAl ₂	0.9702	c_{11}	c_{11}	0.3655	c_{44}	c_{44}	0.2240	c_{12}	c_{12}	C15, cF24	Schiltz and Smith (1974)
YAl ₃	1.7084	c_{11}	c_{11}	0.5622	c_{44}	c_{44}	0.3404	c_{12}	c_{12}	C15, cF24	Schiltz and Smith (1974)
LaAl ₃	1.4366	c_{11}	c_{11}	0.4303	c_{44}	c_{44}	0.3200	c_{12}	c_{12}	C15, cF24	Schiltz and Smith (1974)
GdAl ₃	1.6051	c_{11}	c_{11}	0.5947	c_{44}	c_{44}	0.3679	c_{12}	c_{12}	C15, cF24	Schiltz and Smith (1974)
CeAl ₃	1.47	c_{11}	c_{11}	0.428	c_{44}	c_{44}	0.340	c_{12}	c_{12}	C15, cF24	Mock and Guntherodt (1984)
CeAl ₃	1.47	c_{11}	c_{11}	0.437	c_{44}	c_{44}	0.300	c_{12}	c_{12}	C15, cF24	Penney <i>et al.</i> (1982)
ZrCo ₂	2.3311	c_{11}	c_{11}	0.8366	c_{44}	c_{44}	1.1271	c_{12}	c_{12}	C15, cF24	Shannette and Smith (1969)
HfCo ₂	2.5554	c_{11}	c_{11}	0.9030	c_{44}	c_{44}	1.2330	c_{12}	c_{12}	C15, cF24	Shannette and Smith (1969)
HoCo ₂	1.53	c_{11}	c_{11}	0.401	c_{44}	c_{44}	0.93	c_{12}	c_{12}	C15, cF24	Butler <i>et al.</i> (1982)
MgCu ₂	1.228	c_{11}	c_{11}	0.412	c_{44}	c_{44}	0.706	c_{12}	c_{12}	C15, cF24	Cheng (1967)
Nb ₃ Sn	2.496	c_{11}	c_{11}	0.406	c_{44}	c_{44}	1.089	c_{12}	c_{12}	A15, cP8	Rehwalder <i>et al.</i> (1972)
Nb ₃ Sn	2.606	c_{11}	c_{11}	0.4013	c_{44}	c_{44}	1.220	c_{12}	c_{12}	A15, cP8	Chang and Barsch (1980)
Nb ₃ Sn	2.538	c_{11}	c_{11}	0.3960	c_{44}	c_{44}	1.124	c_{12}	c_{12}	A15, cP8	Keller and Hank (1967)
V ₃ Ge	2.966	c_{11}	c_{11}	0.6978	c_{44}	c_{44}	1.042	c_{12}	c_{12}	A15, cP8	Rosen and Klimker (1969)
V ₃ Si	2.870	c_{11}	c_{11}	0.8096	c_{44}	c_{44}	1.202	c_{12}	c_{12}	A15, cP8	Testardi <i>et al.</i> (1965)
HgTe	0.5361	c_{11}	c_{11}	0.2123	c_{44}	c_{44}	0.3659	c_{12}	c_{12}	B3, cF8	Miller <i>et al.</i> (1981)
GaAs	1.412	c_{11}	c_{11}	0.7047	c_{44}	c_{44}	0.6253	c_{12}	c_{12}	B3, cF8	Weil and Groves (1971)
GaAs	1.192	c_{11}	c_{11}	0.538	c_{44}	c_{44}	0.599	c_{12}	c_{12}	B3, cF8	Smithells (1976)
GaSb	0.885	c_{11}	c_{11}	0.433	c_{44}	c_{44}	0.404	c_{12}	c_{12}	B3, cF8	Smithells (1976)
InSb	0.672	c_{11}	c_{11}	0.302	c_{44}	c_{44}	0.367	c_{12}	c_{12}	B3, cF8	Smithells (1976)
InP	1.022	c_{11}	c_{11}	0.460	c_{44}	c_{44}	0.576	c_{12}	c_{12}	B3, cF8	Hickernell and Gayton (1966)
GaP	1.412	c_{11}	c_{11}	0.7047	c_{44}	c_{44}	0.6253	c_{12}	c_{12}	B3, cF8	Weil and Groves (1971)
PbS	1.269	c_{11}	c_{11}	0.248	c_{44}	c_{44}	0.297	c_{12}	c_{12}	B3, cF8	Nadgornyi (1988)
ZnS	1.046	c_{11}	c_{11}	0.461	c_{44}	c_{44}	0.653	c_{12}	c_{12}	B3, cF8	Nadgornyi (1988)
CdS	0.907	c_{11}	0.938	0.150	c_{44}	c_{66}^b	0.581	0.570	c_{13}	B4, hP4	Nadgornyi (1988)

^aPearson (1958), Villars and Calvert (1985).^b $c_{66} = (c_{11} - c_{12})/2$.

Table 2. Calculated elastic stiffness constants (10^2 GPa) of intermetallic compounds

Intermetallics	Method	c_{11}	c_{33}	c_{44}	c_{66}	c_{12}	c_{13}	Structure ^a	References
Ni ₃ Al	EAM ^b	2.52	c_{11}	1.26	c_{44}	1.37	c_{12}	L1 ₂ , cP4	Foiles and Daw (1987)
Ni ₃ Al	EAM ^b	2.46	c_{11}	1.23	c_{44}	1.37	c_{12}	L1 ₂ , cP4	Chen <i>et al.</i> (1986)
Ni ₃ Al	F-LAPW ^c	2.35	c_{11}	1.32	c_{44}	1.45	c_{12}	L1 ₂ , cP4	Fu and Yoo (1989)
Pt ₃ Al	F-LAPW ^c	4.36	c_{11}	1.40	c_{44}	2.20	c_{12}	L1 ₂ , cP4	Fu and Yoo (1989)
Al ₃ Li	F-LAPW ^c	1.58	c_{11}	5.77	c_{44}	2.94	c_{12}	L1 ₂ , cP4	Guo <i>et al.</i> (1991)
Al ₃ Sc	F-LAPW ^c	1.89	c_{11}	0.66	c_{44}	0.43	c_{12}	L1 ₂ , cP4	Fu (1990)
TiAl ₃	F-LAPW ^c	2.02	2.43	0.20	1.45	0.88	0.60	D0 ₂₂ , tI8	Fu (1990)
MoSi ₂	F-LMTO ^d	4.01	5.36	2.08	1.98	1.02	0.78	C11 _b , tI6	Alouani <i>et al.</i> (1991)
SbY	LAPW ^e	1.75	c_{11}	0.255	c_{44}	0.15	c_{12}	B1, cF8	Mehl <i>et al.</i> (1990)
CoAl	LAPW ^e	2.57	c_{11}	1.30	c_{44}	1.07	c_{12}	B2, cP2	Mehl <i>et al.</i> (1990)
RuZr	LAPW ^e	3.72	c_{11}	0.78	c_{44}	1.52	c_{12}	B2, cP2	Mehl <i>et al.</i> (1990)
NbIr ^f	LAPW ^e	4.3	4.9	1.75	2.3	2.7	2.5	L1 ₀ , tP4	Mehl <i>et al.</i> (1990)
NbIr ^g	LAPW ^e	5.8	4.9	1.75	0.8	1.2	2.5	L1 ₀ , tP4	Mehl <i>et al.</i> (1990)

^aPearson (1958).^bEmbedded-atom method.^cFirst-principles full-potential linearized augmented-plane-wave total-energy method.^dAll-electron self-consistent full-potential linear muffin-tin-orbitals method.^eLinear augmented-plane-wave method.^fLattice parameters of a face-centered tetragonal lattice are used for a L1₀ (tP4) structure.^gLattice parameters of a body-centered tetragonal lattice are used.

$$\begin{bmatrix} \epsilon_{11} \\ \epsilon_{22} \\ \epsilon_{33} \\ \epsilon_{23} \\ \epsilon_{31} \\ \epsilon_{12} \end{bmatrix} = \begin{bmatrix} s_{11}s_{12}s_{13}s_{14}s_{15}s_{16} \\ s_{22}s_{23}s_{24}s_{25}s_{26} \\ s_{33}s_{34}s_{35}s_{36} \\ s_{44}s_{45}s_{46} \\ \text{symmetry } s_{55}s_{56} \\ s_{66} \end{bmatrix} \begin{bmatrix} \sigma_{11} \\ \sigma_{22} \\ \sigma_{33} \\ \sigma_{23} \\ \sigma_{31} \\ \sigma_{12} \end{bmatrix} \quad (6)$$

Thus, Young's modulus E_1 in the x_1 -direction of a single crystal is represented by the reciprocal of s_{11} . Similarly, the shear modulus G_{12} in the x_1 -direction on the x_2 -plane or in the x_2 -direction on the x_1 -plane is given by the reciprocal of s_{66} . When a uniaxial stress σ_{11} is applied in the x_1 -direction, Poisson's ratio ν_{12} in the x_2 -direction is given by:

$$\nu_{12} = -\epsilon_{22}/\epsilon_{11} = -s_{12}/s_{11} \quad (8)$$

Here, $\{s_{ij}\}$ is the elastic-compliance-constant matrix.

Young's modulus is given by the relation between stress and strain in the direction of the applied load, when a uniaxial stress is applied to the specimen:

$$\epsilon_{11} = s_{11}\sigma_{11} \quad \text{or} \quad \sigma_{11} = (1/s_{11})\epsilon_{11} \quad (7)$$

Therefore, when the rotational transformation of coordinates is given for the compliance-constant matrix $\{s_{ij}\}$, the reciprocal of Young's modulus, that of the shear modulus, and Poisson's ratio are given respectively by s_{11} , s_{66} , and $-s_{12}/s_{11}$ for a single crystal with different orientations.

Table 3. Comparison between adiabatic and isothermal elastic constants (10^2 GPa) at room temperature

Intermetallics	Adiabatic elastic constants			Isothermal elastic constants			Structure ^a
	c_{11}	c_{44}	c_{12}	c_{11}	c_{44}	c_{12}	
Ni ₃ Al ^b	2.23	1.25	1.48	2.20	1.25	1.45	L1 ₂ , cP4
Fe ₃ Si ^c	2.32	1.36	1.57	2.28	1.36	1.53	D0 ₃ , cF16

^aPearson (1958), Villars and Calvert (1985).^bKayser and Stassis (1981).^cRausch and Kayser (1977).

The compliance-constant matrix $\{s_{ij}\}$ is a simplified notation of the tensor $\{s_{ijkl}\}$. When the x_1 -, x_2 -, and x_3 -axes are rotationally transformed to the x'_1 -, x'_2 -, and x'_3 -axes, the components of the compliance tensor $\{s'_{pqrs}\}$ after transformation are given by:

$$s'_{pqrs} = \sum_i \sum_j \sum_k \sum_l \alpha_{pi} \alpha_{qj} \alpha_{rk} \alpha_{sl} s_{ijkl} \quad (9)$$

($i, j, k, l = 1, 2, 3$)

Here, α_{pi} , etc., represent the directional cosines at an

angle between the x_i - and x'_p -axes. Then, the compliance-constant matrix $\{s'_{pqrs}\}$ is obtained for a single crystal with a desired orientation when the tensor $\{s_{pqrs}\}$ is rewritten in the Voigt notation.

Figure 1 shows the orientation dependence of the reciprocal of Young's modulus s_{11} , that of the reciprocal shear modulus s_{66} , and Poisson's ratio ν_{21} , calculated from the elastic stiffness constants shown in Table 1 for a WSi₂ (C11_b, tI6 structure) single crystal (Nakamura, 1991b). In Figure 1(a), for example, the x_1 -axis changes from the $[100]$ to the $[010]$ via the $[110]$ direction, when the crystal is rotated by 90° around the $[001]$ axis. In Figure 1(b), for example, the x_1 -direction on the $(\bar{1}10)$ plane changes from the $[001]$ to the $[110]$ direction, when the crystal is rotated around the axis perpendicular to the $(\bar{1}10)$ plane. Figure 1(c) shows the change of Poisson's ratio ν_{21} with rotation around the x_2 -axis, along which the uniaxial stress is applied. For example, the x_1 -direction changes from the $[001]$ to the $[010]$ direction, when the crystal is rotated around the applied stress axis, i.e. the direction perpendicular to the (100) plane.

It is found for WSi₂ (C11_b, tI6 structure) that in one of the close-packed atomic arrays, i.e. the $[331]$ direction in which W and Si atoms are arranged in a certain order, Young's modulus ($1/s_{11}$) is lower than in the $[001]$ direction. It is highest in the $[001]$ direction, and lowest in the $[100]$ and $[010]$ directions normal to the $[001]$ direction. The shear modulus ($1/s_{66}$) is independent of the stress direction on the (001) plane, and slightly dependent on the stress direction on the (100) and (103) planes. The shear modulus on the $(\bar{1}10)$ plane is, however, remarkably dependent on the stress direction, and is lowest in the $[110]$ direction. This indicates that the shear modulus does not always exhibit a low value in the direction of atomic arrays with a small interatomic distance. When the stress is applied in the direction perpendicular to the (001) or $(\bar{1}10)$ plane, Poisson's ratio is low and is slightly dependent on the crystal orientation. It is, however, dependent on the orientation for the stress direction perpendicular to the (100) plane, and exhibits a low value in the $[001]$ direction and a high value in the $[010]$ direction. Thus, when a round bar specimen prepared from a single crystal is loaded in tension elastically in the $[001]$ or $[1\bar{1}0]$ direction, the cross-section of the specimen hardly changes from a round shape. In contrast, because of the anisotropy of this structure, when the specimen is loaded in tension in the $[110]$ direction, the cross-section changes to an elliptical shape with the major axis in the $[001]$ direction and the minor axis in the $[010]$ one.

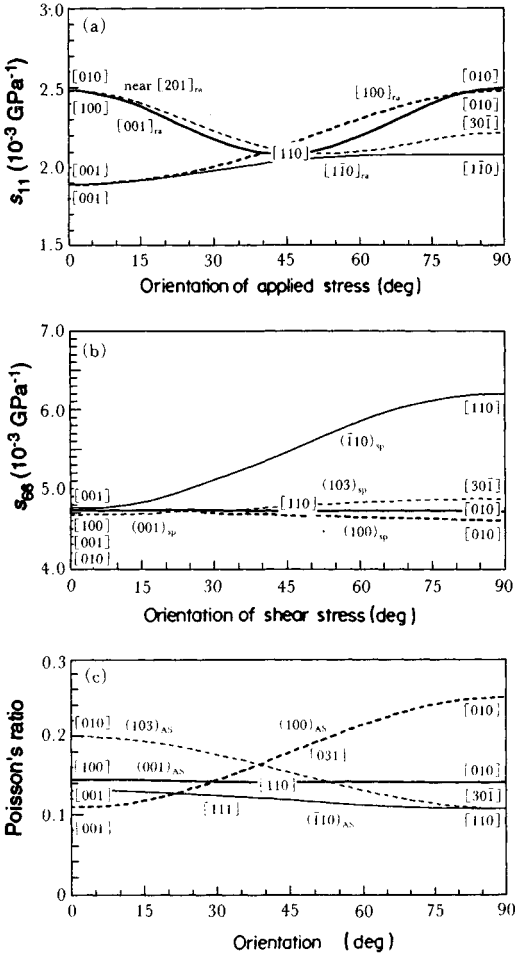


Figure 1. Orientation dependence of the compliances s_{11} and s_{66} and Poisson's ratio for a WSi₂ single crystal; (a) s_{11} , $[h k l]_{ra}$ = direction of rotation axis; (b) s_{66} , $(h k l)_{sp}$ = shear plane; (c) Poisson's ratio, $(h k l)_{AS}$ = direction of applied stress, normal to $(h k l)$ plane (Reproduced by permission of the Japan Institute of Metals from Nakamura, 1991b)

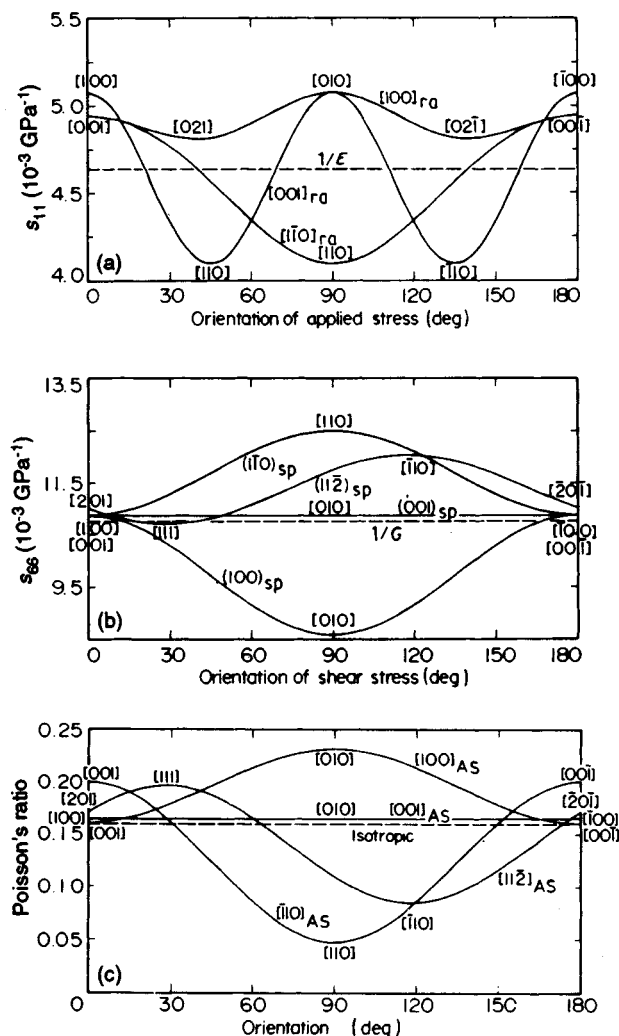


Figure 2. Orientation dependence of the compliances s_{11} and s_{66} and Poisson's ratio for a TiAl₃ single crystal: (a) s_{11} ; (b) s_{66} ; (c) Poisson's ratio $-\nu_{12}/s_{11}$. The values for a polycrystalline material are estimated from the elastic constants for a single crystal. $1/E$ and $1/G$ represent the reciprocals of Young's and the shear moduli, respectively (Reproduced by permission of Chapman & Hall from Nakamura and Kimura, 1991)

Figure 2 for a TiAl₃ single crystal with a tetragonal D₀₂₂ (t18) structure (Nakamura and Kimura, 1991) shows similar relationships to Figure 1. When the stress direction is rotated around the $[001]$ axis, s_{11} depends remarkably upon the crystal orientation, and it is considerably low; that is, Young's modulus is very high in the $[110]$ direction, along which Ti and Al atoms are arranged alternately in close-packed atomic arrays. The value of s_{11} is higher in the $[100]$ direction than in the $[001]$ one. This behavior is not obvious from the fact that the

interatomic distance (0.4296 nm; Villars and Calvert, 1985) in the $[001]$ direction is larger than that (0.3848 nm) in the $[100]$ direction. In the $[021]$ direction, along which Ti and Al atoms are arranged in close-packed arrays, similar to those of the $[110]$ direction, s_{11} is markedly high, compared with that in the $[110]$ direction. That is, Young's modulus in the $[021]$ direction is not so large, and is close to that in the $[001]$ direction. The interatomic distance in the $[021]$ direction (0.2884 nm; Villars and Calvert, 1985) is

considerably smaller than that in the $[001]$ direction (0.4298 nm), and close to that in the $[110]$ direction (0.2721 nm). These facts indicate that Young's modulus is strongly influenced by the arrangement of Ti and Al atoms.

The compliance s_{66} is low on the (100) plane, especially in the $[010]$ direction. It is high on the $(1\bar{1}0)$ plane, especially in the $[110]$ direction, and it is generally higher than on the closest-packed $(11\bar{2})$ plane. That is, it is found that the shear modulus is lower in the $[110]$ direction on the $(1\bar{1}0)$ plane than in the directions of the closest-packed atomic arrays on the closest-packed planes for TiAl_3 as well as for WSi_2 .

When a uniaxial stress is applied in the $[100]$ direction, a large strain is observed in the $[010]$ direction, and a small strain in the $[001]$ direction normal to the $[010]$ one, as shown in Figure 2(c). When the stress direction is perpendicular to the $(\bar{1}10)$ plane, Poisson's ratio is rather dependent on the crystal orientation: Poisson's ratio in the $[001]$ direction, i.e. the maximum value, is four times larger than that in the $[110]$ direction, i.e. the minimum one.

The orientation dependence of the elastic moduli changes with the intermetallic compound, although it has a common trend for single crystals with a tetragonal structure, as shown in Figure 2.

Figure 3 shows the orientation dependence of s_{11} for a Ni_3Al single crystal with a cubic $L1_2$ (cP4) structure for the $[110]$ rotation axis (Nakamura, 1991a). The value of s_{11} is high in the (100) direction, low in the $(\bar{1}11)$ one, and relatively low in the (110) one. That is, Young's modulus is not the highest in the direction along which Ni and Al atoms are arranged alternately in the closest-packed manner; rather it is the highest in the $(\bar{1}11)$ direction.

The orientation dependences of s_{66} and Poisson's ratio were also calculated. The value of s_{66} is

independent of the stress direction on the $\{001\}$ and $\{111\}$ planes. However, on the $\{110\}$ planes, s_{66} is low in the $\langle 001 \rangle$ directions, and high in the $\langle 110 \rangle$ directions. Therefore, the shear modulus is not always lower on the closest-packed $\{111\}$ planes than on the $\{110\}$ planes. When a uniaxial stress is applied in a direction perpendicular to the $\{001\}$ or $\{111\}$ planes, Poisson's ratio is independent of the orientation. For the stress axis perpendicular to the $\{110\}$ planes, it changes remarkably with the crystal orientation, and it is very high (i.e. about 0.8) in the $\langle 001 \rangle$ direction and extremely low (i.e. about -0.2) in the $\langle 110 \rangle$ direction (see Figure 4). The fact that Poisson's ratio exhibits a negative value means that the uniaxial tensile stress perpendicular to the $\{110\}$ planes induces a positive strain in the $\langle 110 \rangle$ direction, although it causes a large negative strain in the $\langle 001 \rangle$ direction normal to the $\langle 110 \rangle$ one. That is, a large elastic distortion is produced in the $\{110\}$ plane normal to the stress direction.

Figure 4 shows examples of the orientation dependences of s_{11} , s_{66} , and Poisson's ratio for Ni_3Al , Ni_3Fe , and Ni_3Ge single crystals with $L1_2$ (cP4, AuCu₃) structures, and compared with a Ni single crystal with an A1 (cF4) structure (Nakamura, 1991a). The values of s_{11} for rotation around the $[110]$ axis, s_{66} on the (110) plane, and Poisson's ratio for the stress direction perpendicular to the (110) plane exhibit remarkable orientation dependences. Here, the curve for Ni_3Ge is coincident with that for Ni. Although Ni_3Fe contains a large amount of Fe, it exhibits an orientation dependence of the elastic moduli extremely similar to that of Ni, and has a smaller orientation dependence than Ni_3Al . The elastic moduli of Ni_3Ge are much less dependent on the orientation than those of Ni_3Al .

Figure 5 shows the orientation dependence of s_{66} for Ti_3Sn (D0₁₉, hP8, Ni_3Sn structure) (Nakamura, 1991a). The radial and angular coordinates represent s_{66} and the crystal orientation, respectively. In this figure, $[\bar{1}100](0001)$ means that the shear stress is applied to the $[\bar{1}100]$ direction on the (0001) basal plane. The compliance s_{66} exhibits no orientation dependence, that is, the shear modulus is constant and low on the (0001) plane. It also exhibits little orientation dependence on the $(1\bar{1}00)$ and $(11\bar{2}0)$ planes. Also, s_{66} is low in the $[11\bar{2}\bar{6}]$ and $[\bar{1}102]$ directions, which contain the component of the c -axis on the $(11\bar{2}1)$ and $(1\bar{1}01)$ planes, respectively. The orientation dependences of s_{11} and Poisson's ratio were also calculated. When the stress direction is rotated around the c -axis, s_{11} is independent of orientation; s_{11} is low in the $[0001]$ direction. Poisson's ratio as well as s_{66} are large and independent

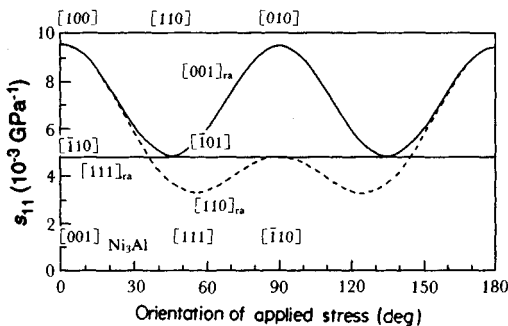


Figure 3. Orientation dependence of the compliance s_{11} for a Ni_3Al single crystal. ra=rotation axis. (Reproduced by permission of the Japan Institute of Metals from Nakamura, 1991a)

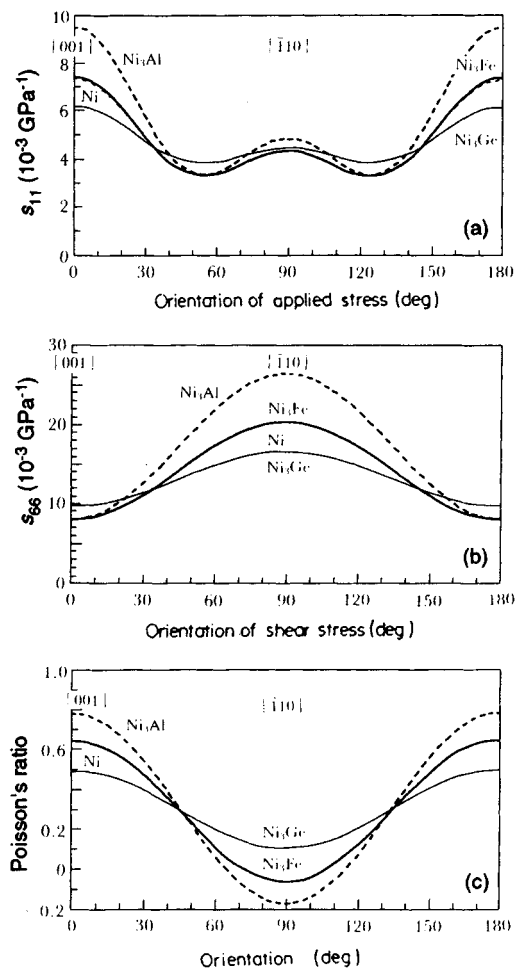


Figure 4. Orientation dependence of s_{11} , s_{66} , and Poisson's ratio for Ni₃Fe, Ni₃Ge, and Ni₃Al single crystals, and Ni: (a) s_{11} for rotation around $[1\bar{1}0]$ axis; (b) s_{66} on $(1\bar{1}0)$ plane; and (c) Poisson's ratio for the stress direction normal to $(1\bar{1}0)$ plane (Reproduced by permission of the Japan Institute of Metals from Nakamura, 1991a)

of orientation when the stress is applied in a direction perpendicular to the (0001) plane. It is found that Poisson's ratio is low and dependent on orientation, when the stress is applied in a direction perpendicular to the $(1\bar{1}00)$ or $(1\bar{1}\bar{2}0)$ plane.

The atomic arrays of intermetallic compounds may affect the orientation dependence of the elastic constants. Table 4 shows the ratio of the interatomic distance in the $[ijk]$ direction to that in the $[001]$ direction, and the associated stiffness-constant and compliance-constant ratios for various intermetallics (Nakamura, 1991a). Here, $c_{[ijk]}$ and $s_{[ijk]}$ represent c_{11}

and s_{11} in the $[ijk]$ direction. In WSi₂ and MoSi₂ the interatomic-distance ratio corresponds relatively well to the ratio of c_{11} , but in TiAl₃, ZrAl₃, NiAl, and CuZn the former does not correspond to the latter. In general, the ratio of s_{11} does not correspond to the interatomic-distance ratio. In TiAl₃ or ZrAl₃, the ratio of c_{11} in the $[1\bar{1}0]$ direction, corresponding to one of the closest-packed atomic arrays, is lower than that in the $[201]$ or $[401]$ direction corresponding to other closest-packed arrays, although the atomic distance in the $[1\bar{1}0]$ direction is approximately equal to that in the $[201]$ or $[401]$ direction. This indicates that the atomic arrangement affects the elastic properties of intermetallics as described before. The value of $c_{[ijk]}$ is related to the tensile or compressive stress, when the elastic deformation causes no strain in directions except for the $[ijk]$ direction. Therefore, in WSi₂ and MoSi₂, for which the ratio of c_{11} is close to the interatomic-distance ratio, the elastic deformation in the direction of the applied strain may be determined mainly by the interatomic force in the strain direction.

4. Elastic Properties of Dislocations

Anisotropy of the elastic constants results in a change of elastic properties of dislocations in intermetallics. We have textbooks for calculation of the elastic properties of dislocations using anisotropic elasticity theory (Hirth and Lothe, 1968; Steeds, 1973). The results calculated from the elastic constants of single crystals are summarized.

Figure 6 shows examples of the elastic fields around a screw dislocation line with a Burgers vector of $\frac{1}{3}[\bar{3}31]$ on the (103) plane for MoSi₂(C11_b, t16 structure) (Nakamura, 1991a). In this figure, the x_3 -axis perpendicular to the figure represents a dislocation line, and the x_2 -axis is perpendicular to the (103) plane. The contour-line maps for σ_{13} and σ_{11} are shown in Figures 6(a) and (b), respectively. The stress field σ_{13} is slightly distorted from that of an isotropic material, and the normal stress field σ_{11} , which does not exist in an isotropic material, appears. The stress fields around an edge dislocation are also slightly distorted.

The elastic stress field around a dislocation affects the elastic energy of a dislocation and the interaction between parallel dislocations. The elastic energy per unit length of dislocation between two cylindrical surfaces of radius r_0 and R is given by:

$$(Kb^2/4\pi)\log(R/r_0) \quad (10)$$

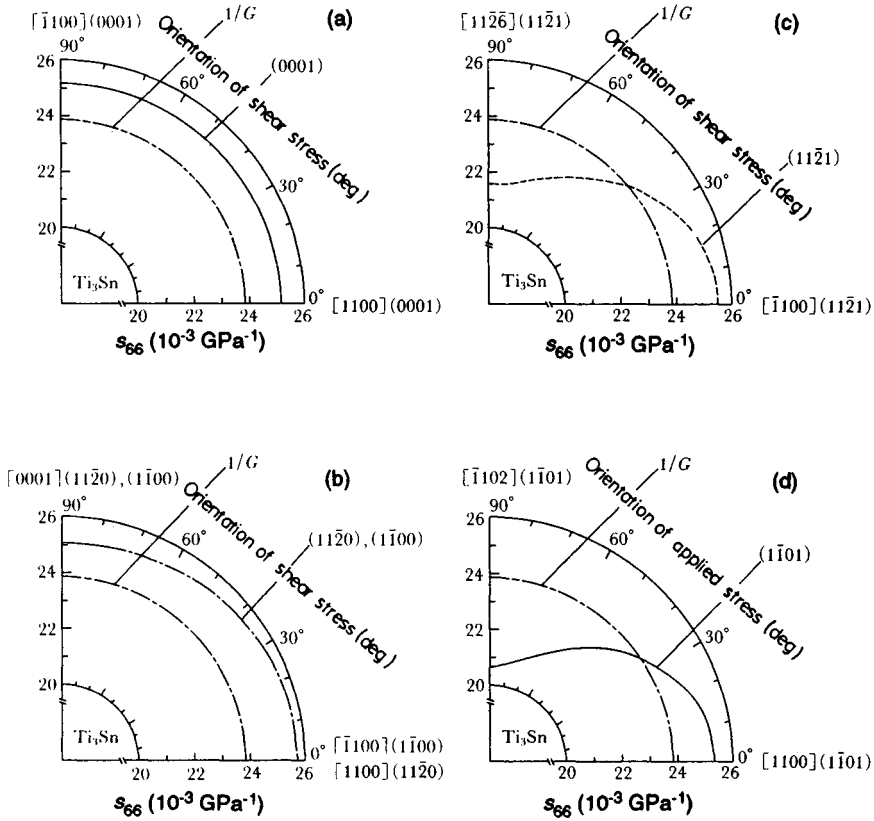


Figure 5. Orientation dependence of the compliance s_{66} for a Ti_3Sn single crystal. The radial and angular coordinates represent s_{66} and orientation, respectively. Shear plane: (a) (0 0 0 1); (b) (1 1 $\bar{2}$ 0) and (1 $\bar{1}$ 0 0); (c) (1 1 $\bar{2}$ 1); and (d) (1 $\bar{1}$ 0 1) planes (From Nakamura, 1991a)

where b is the magnitude of the Burgers vector, and K is the energy factor. In an isotropic material, K equals G and $G/(1-\nu)$ for screw and edge dislocations, respectively. For an anisotropic material, K is calculated using elastic constants c_{ij} (Hirth and Lothe, 1968; Steeds, 1973). Figure 7 shows the elastic energy factor K of a dislocation with a Burgers vector of $\frac{1}{3}[331]$ or $\frac{1}{3}[001]$ for MoSi_2 . Here, the orientation of the dislocation lines varies from the direction of the Burgers vector. The dislocation line with a Burgers vector of $\frac{1}{3}[001]$ has a higher energy factor than that with a Burgers vector of $\frac{1}{3}[331]$. Since the magnitudes of the Burgers vectors are approximately equal ($b=0.2616$ and 0.2615 nm (Villars and Calvert, 1985) for the $\frac{1}{3}[331]$ and $\frac{1}{3}[001]$ Burgers vectors), the elastic energy of the former dislocation is higher than that of the latter, when both dislocation lines lie in the same direction, which is measured from the direction of the Burgers vector. This may correspond to the fact that

dislocations with a Burgers vector of $\frac{1}{3}[001]$ could not be observed for deformed MoSi_2 single crystals (Kimura *et al.*, 1990), although account was also taken of the antiphase boundary (APB) energy. Figure 8 shows the interaction force between parallel dislocation lines with Burgers vector of $\frac{1}{2}[\bar{1}10]$ for Ni_3Al (Yoo, 1987a). A pair of dislocations represent a (1 1 1) APB-type dissociation. Here, a pair of dislocations lie on a (1 1 1) plane, and the orientation of the dislocation lines varies from the direction of the Burgers vector, $[\bar{1}10]$. For an isotropic material, the radial force constant $F_r(\text{iso})$ between a pair of dislocations is finite, but the tangential force constant $F_\theta(\text{iso})$ does not exist. For an anisotropic material, the orientation dependence of the radial force constant F_r is approximately equal to that for an isotropic one. However, the tangential constant F_θ is very large and dependent on the orientation of the dislocation lines. This large tangential force constant may affect dislocation motion, and cause

Table 4. Comparison between interatomic-distance ratio and elastic-constant ratio (Nakamura, 1991a)

Intermetallics	Crystal orientation, $[ijk]$	Interatomic-distance ratio, $[ijk]/[001]$	$c_{[001]}$ $c_{[ijk]}$	$S_{[ijk]}$ $S_{[001]}$
WSi ₂	[100]	1.224	1.247	1.313
WSi ₂	[331]	0.9997	1.064	1.095
MoSi ₂	[100]	1.224	1.234	1.273
MoSi ₂	[331]	0.9993	1.093	1.082
TiAl ₃	[100]	0.895	0.999	1.028
TiAl ₃	[201]	0.671	0.973	0.988
TiAl ₃	[110]	0.633	0.856	0.829
ZrAl ₃	[100]	0.927	0.998	1.063
ZrAl ₃	[401]	0.682	0.965	0.974
ZrAl ₃	[110]	0.656	0.861	0.840
Ni ₃ Al	[110]	0.707	0.718	0.510
Ni ₃ Fe	[110]	0.707	0.766	0.584
Ni ₃ Ge	[110]	0.707	0.859	0.718
NiAl	[111]	0.866	0.672	0.353
CuZn	[111]	0.866	0.572	0.139

the anomalous temperature dependence of the yield strength in Ni₃Al (Yoo, 1987a). In Ni₃Al, there is an increase in the 0.2% flow stress with increasing temperature contrary to the case for ordinary alloys (Copley and Kear, 1967; Thornton *et al.*, 1970; Suzuki *et al.*, 1989).

The stress distribution at the crack tip in a single crystal is also affected by anisotropy of the elastic constants (Sih and Liebowitz, 1968). Figure 9 shows the stress distribution at a crack tip of (100) type under mode I loading for a NiAl single crystal (B2, cP2 structure) (Yoo and Fu, 1991). The x_1 -axis in the

direction of crack extension is the [011] direction, and the x_2 -axis is perpendicular to the (100) crack plane. In the figure, the radial distance from the origin, i.e. the crack tip, represents the relative magnitude of the stresses, σ_r , σ_θ , $\tau_{r\theta}$, and p in the θ direction. The magnitude of the normal stress (σ_r , σ_θ , and p) is in units of $K_I/(2\pi r)^{1/2}$, and that of the shear stress ($\tau_{r\theta}$) is in units of $2K_I/(2\pi r)^{1/2}$, where K_I is the stress intensity factor for mode I loading and r is the radial distance from the crack tip. The stress distribution calculated from the anisotropic elastic constants is different from that calculated from isotropic elastic constants, especially for σ_r and p . This may affect the plastic deformation at the crack tip, and hence the fracture toughness.

5. Elastic Moduli of Polycrystalline Intermetallics

In general, a single crystal is more difficult to prepare than polycrystalline material. Hence, the elastic moduli of many polycrystalline intermetallics have been measured, although it is hard to prepare samples in single-phase condition, especially for intermetallics that permit no deviation from stoichiometry ('line compounds'). The measurement of the ultrasonic wave (USW) velocity is mainly used for the determination of the elastic moduli of polycrystalline materials, while the resonance frequency for different vibrational modes is used for the determination of elastic moduli at elevated

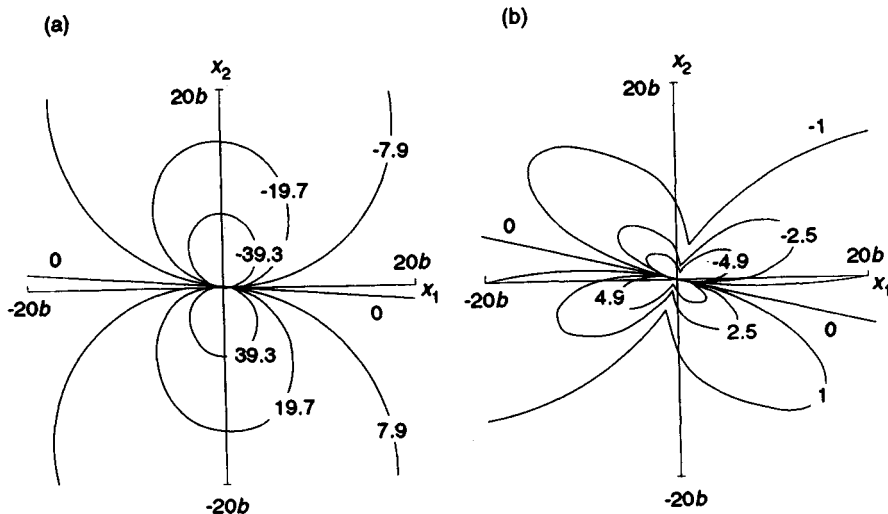


Figure 6. Examples of elastic fields around a screw dislocation line with Burgers vector $\frac{1}{3}[331]$ for MoSi₂: (a) σ_{13} , (b) σ_{11} . The x_3 -axis perpendicular to the figure represents a dislocation line, and the x_2 -axis is normal to the (103) plane. The contour lines are labeled in units of MPa (From Nakamura, 1991a)

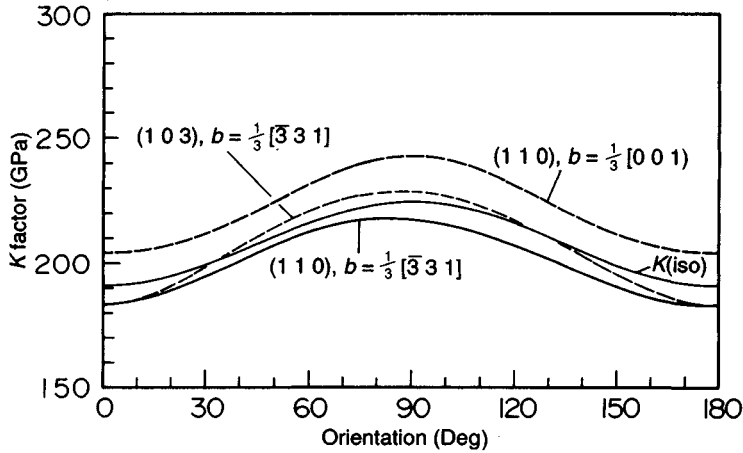


Figure 7. Elastic energy factor K of a dislocation with Burgers vector $\frac{1}{3}[\bar{3}31]$ or $\frac{1}{3}[001]$ for MoSi_2 . The orientation of the dislocation lines varies from the direction of the Burgers vector

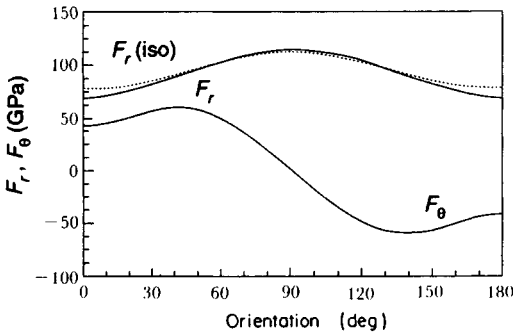


Figure 8. Interaction force between parallel dislocation lines with Burgers vector $\frac{1}{2}[\bar{1}10]$ for Ni_3Al . The radial component F_r , tangential component F_θ , and radial component for an isotropic material $F_r(\text{iso})$ are normalized by $(2\pi r b^2)$, where r is the distance between dislocations and b is the magnitude of the Burgers vector. The orientation of the dislocation lines varies from the direction of the Burgers vector, $[\bar{1}10]$ (Reproduced by permission of Pergamon Press from Yoo, 1987a)

temperatures (Schafrik, 1977), because the coupling materials between a specimen and the ultrasonic-wave transducer cannot usually be used at temperatures above 500–600 °C.

Measurements of elastic moduli have been carried out for many polycrystalline intermetallic compounds by Fleischer and Field (1990). Table 5 shows the elastic moduli of various intermetallic compounds. The elastic properties of intermetallics may be mainly characterized by Poisson's ratio. Poisson's ratio of many intermetallics is lower than that of metals and ordinary alloys, in which it is about 0.25–0.44 (Smithells, 1976). It is low for

VSi_2 , YAl_2 , ZrAl_3 , ZrAl_2 , etc., and remarkably low (<0.1) for Be_{12}Ti (D_{2d} , tI26 structure) and Be_{13}Zr (D_{2d} , cF112 structure). Since Be_{12}Nb (also with a D_{2d} , tI26 structure) exhibits a Poisson's ratio of 0.29, this lattice structure *per se* does not necessarily result in a low Poisson's ratio of 0.099. Fleischer and co-workers have investigated systematically the effects of composition and alloying elements on the elastic moduli at room temperature for Ru–Ta (Fleischer *et al.*, 1991a), Ru–Al (Fleischer *et al.*, 1991b; Fleischer, 1991, 1993a), Ir–Nb (Fleischer *et al.*, 1990), and Be-base (Fleischer and Zabala, 1989) and Ti-base (Fleischer *et al.*, 1988) alloys.

The elastic moduli of a polycrystalline material can be approximately estimated from the elastic constants of the single crystal. First, the maximum and minimum values of the moduli are obtained using Voigt's and Reuss's approximations, respectively. The method in which the average value of the maximum and minimum values is adopted is called Hill's approximation, and the estimated values of Young's modulus are known to be in good agreement with the measured ones (Anderson, 1963).

For all crystal structures, the bulk modulus K of a polycrystalline material is estimated from the following equations (Anderson, 1963):

- For Voigt's approximation

$$K_V = \frac{1}{9}(c_{11} + c_{22} + c_{33}) + \frac{2}{9}(c_{12} + c_{13} + c_{23}) \quad (11)$$

- For Reuss's approximation

$$1/K_R = (s_{11} + s_{22} + s_{33}) + 2(s_{12} + s_{13} + s_{23}) \quad (12)$$

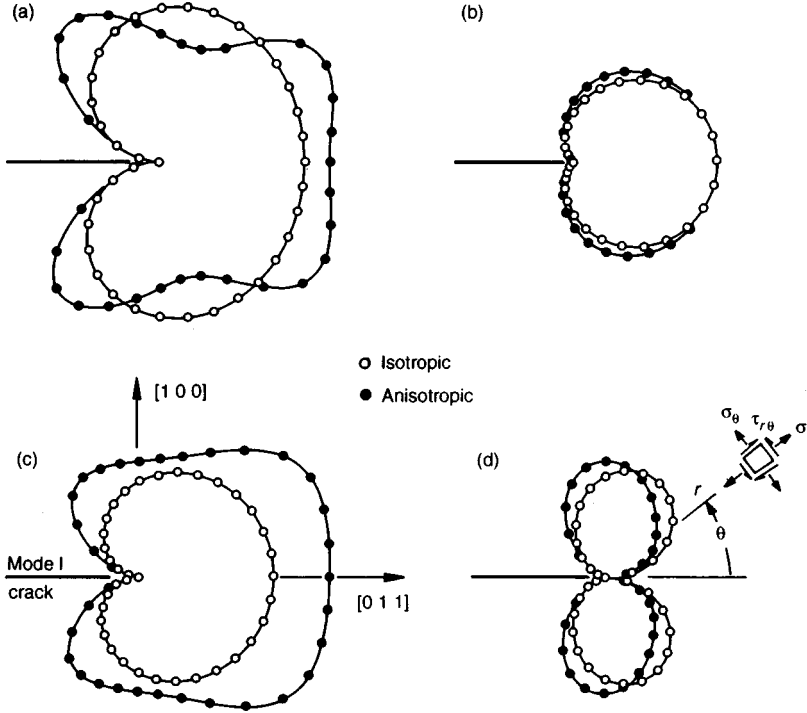


Figure 9. Stress field at a crack tip of (1 0 0) type under mode I loading (tension across the crack) for a NiAl single crystal: (a) radial stress, σ_r ; (b) tangential stress, σ_θ ; (c) positive pressure, p ; and (d) shear component, $\tau_{r\theta}$. (Units: $K_I/(2\pi r)^{1/2}$ for σ_r , σ_θ , and p ; and $2K_I/(2\pi r)^{1/2}$ for $\tau_{r\theta}$.) The radial distance from the origin, i.e. the crack tip, represents the relative magnitude of the stresses, σ_r , σ_θ , $\tau_{r\theta}$, and p in the θ direction (Reproduced by permission of Pergamon Press from Yoo and Fu, 1991)

- For Hill's approximation

$$K_H = \frac{1}{2}(K_V + K_R) \quad (13)$$

The shear modulus G is also estimated from the following equations:

- For Voigt's approximation

$$G_V = \frac{1}{15}(c_{11} + c_{22} + c_{33} - \frac{1}{15}(c_{12} + c_{13} + c_{23})) + \frac{1}{3}(c_{44} + c_{55} + c_{66}) \quad (14)$$

- For Reuss's approximation

$$15/G_R = 4(s_{11} + s_{22} + s_{33}) - 4(s_{12} + s_{13} + s_{23}) + 3(s_{44} + s_{55} + s_{66}) \quad (15)$$

- For Hill's approximation

$$G_H = \frac{1}{2}(G_V + G_R) \quad (16)$$

Then, Young's modulus E and Poisson's ratio ν are given by

$$E = 9KG/(3K + G) \quad (17)$$

and

$$\nu = \frac{1}{2}(3K - 2G)/(3K + G) \quad (18)$$

The elastic-wave velocity in a polycrystalline material is given by the following equations. For the longitudinal wave,

$$v_l = [(K + 4G/3)/\rho_0]^{1/2} \quad (19)$$

and for the transverse wave,

$$v_s = (G/\rho_0)^{1/2} \quad (20)$$

Here, ρ_0 is the density of the material. The average wave velocity v_m is given by the following equation:

Table 5. Elastic moduli of polycrystalline intermetallic compounds at room temperature

Intermetallics	Bulk modulus, K (10^2 GPa)	Young's modulus, E (10^2 GPa)	Shear modulus, G (10^2 GPa)	Poisson's ratio, ν	Structure ^a	References
NbIr	3.01	2.68	0.993	0.352	L1 ₀ , tP4	Fleischer <i>et al.</i> (1990)
Ru ₁₁ Ta ₉	2.55	2.42	0.904	0.341	L1 ₀ , tP4	Fleischer <i>et al.</i> (1991a)
Ru ₄₀ Ta ₅₁	2.55	2.43	0.906	0.341	L1 ₀ , tP4	Fleischer <i>et al.</i> (1991a)
TiAl		1.73	0.700	0.234	L1 ₀ , tP4	Schafrik (1977)
VSi ₂	1.66	3.31	1.42	0.167	C11 _b , t16	Fleischer <i>et al.</i> (1989)
Al ₈ V ₅	1.11	1.55	0.613	0.267	D8 ₂ , c152	Fleischer <i>et al.</i> (1991b)
AlRu	2.07	2.67	1.04	0.286	B2, cP2	Fleischer <i>et al.</i> (1991b)
CoAl		2.59			B2, cP2	Fleischer and Zabala (1990b)
CoAl		2.98			B2, cP2	Harmouche and Wolfenden (1986)
CoAl	1.62	2.78	1.14	0.214	B2, cP2	Fleischer (1993b)
FeAl		2.61			B2, cP2	Harmouche and Wolfenden (1986)
RuSc	1.48	1.55	0.584	0.326	B2, cP2	Fleischer and Zabala (1990b)
RuTi		2.82			B2, cP2	Fleischer and Zabala (1990b)
RuTi	2.47	2.78	1.06	0.31	B2, cP2	Fleischer <i>et al.</i> (1988)
ZrAl ₃	0.954	2.05	0.900	0.141	D0 ₂₃ , t116	Fleischer and Zabala (1990b)
Be ₁₃ Zr	1.22	2.89	1.31	0.033	D2 ₃ , cF112	Fleischer and Zabala (1989)
Be ₁₂ Nb	1.80	2.20	0.86	0.29	D2 _b , t126	Fleischer and Zabala (1989)
Be ₁₂ Ti	1.17	2.82	1.28	0.099	D2 _b , t126	Fleischer and Zabala (1989)
YAl ₂	0.892	1.58	0.655	0.205	C15, cF24	Fleischer and Zabala (1990b)
Cr ₂ Nb	2.00	2.18	0.827	0.318	C15, cF24	Fleischer <i>et al.</i> (1989)
TbFe ₂	0.93	0.94	0.353		C15, cF24	Clark <i>et al.</i> (1973)
ErFe ₂	1.03	1.21	0.462		C15, cF24	Clark <i>et al.</i> (1973)
YFe ₂	0.97	1.27	0.496		C15, cF24	Clark <i>et al.</i> (1973)
ZrAl ₂	1.17	2.22	0.938	0.184	C14, hP12	Fleischer and Zabala (1990b)
TiCr ₂	1.59	1.84	0.71	0.31	C14, hP12	Fleischer <i>et al.</i> (1988)
V ₃ Si	1.75	2.13	0.819	0.298	A15, cP8	Fleischer and Zabala (1990b)
Cr ₃ Si	2.73	3.51	1.37	0.286	A15, cP8	Fleischer and Zabala (1990b)
Ti ₃ Sn		2.07			D0 ₁₉ , hP8	Fleischer and Zabala (1990a)
Ti ₃ Sn	1.35	1.90	0.75	0.27	D0 ₁₉ , hP8	Fleischer <i>et al.</i> (1988)
SbY	0.660	1.01	0.405	0.245	B1, cF8	Fleischer and Zabala (1990b)

^aPearson (1958), Villars and Calvert (1985).

$$\nu_m = \left[\frac{1}{3} (2/\nu_s^3 + 1/\nu_l^3) \right]^{-1/3} \quad (21)$$

$$\theta_D = (h/k) \left[\frac{3}{4} (q/\pi) (N\rho_0/M) \right]^{1/3} \nu_m \quad (22)$$

The Debye temperature θ_D of a material can be calculated by the following equation (Anderson, 1963):

where h is Planck's constant, k is Boltzmann's constant, N is Avogadro's number, M is molecular weight, and q is the number of atoms in the molecule.

Table 6. Elastic moduli of polycrystalline compounds estimated from elastic constants of single crystals using Hill's approximation

Intermetallics	Bulk modulus, K (10^2 GPa)	Young's modulus, E (10^2 GPa)	Shear modulus, G (10^2 GPa)	Poisson's Ratio, ν	Debye temperature, θ_D (K)
TiAl ₃	1.056	2.157	0.930	0.160	681
ZrAl ₃	1.069	2.018	0.851	0.185	577
MoSi ₂	2.097	4.397	1.911	0.151	759
WSi ₂	2.224	4.679	2.036	0.149	625
VSi ₂	1.672	3.426	1.479	0.158	791
CrSi ₂	1.720	3.546	1.533	0.156	793
Ti ₃ Sn	0.975	1.100	0.419	0.312	335
TiSi ₂	1.489	2.778	1.167	0.189	726
CoSi ₂	2.101	1.829	0.675	0.355	528
NiAl	1.660	1.841	0.700	0.315	500
Ni ₃ Al	1.730	2.019	0.773	0.305	478
Ni ₃ Fe	1.806	2.214	0.855	0.296	469

Table 6 shows examples of the elastic moduli of polycrystalline intermetallic compounds estimated from the elastic constants of single crystals using Hill's approximation. The estimated elastic moduli of VSi_2 and ZrAl_3 are approximately equal to the experimental values (see Table 5).

Note that the Young's modulus and the shear modulus for TiAl_3 (D_{022} , t18 structure) and ZrAl_3 (D_{023} , t116 structure) are more than twice those for the constituent elements, Ti, Zr, and Al (Smithells, 1976), although those values are half those for MoSi_2 and WSi_2 (C11_b , t16 structure), the Young's modulus and the shear modulus of which are also higher than those of the constituent elements. The high elastic moduli of intermetallic compounds may be useful for structural elements of machines, etc., because while we have structural alloys with high specific strength like maraging steels, 7000 series aluminum alloys, etc., almost all ordinary structural alloys exhibit similar specific Young's and shear moduli.

6. Characteristics of Elastic Moduli

6.1 Composition Dependence of Elastic Moduli

It is well known that elastic moduli are dependent on alloy composition, and several investigations have been carried out over a wide range of compositions for Cu–Zn, Cu–Al, Cu–Sn (Cabarat *et al.*, 1948a,b), Mg–Pb, and Mg–Sn (Guillet and Le Roux, 1967) alloys. The maximum value of Young's modulus was observed at the composition of the intermetallic compound or ordered phase like CuZn, CuAl, etc. Figure 10 shows the composition dependence of the elastic moduli, $\frac{1}{2}(c_{11}-c_{12})$ and c_{44} , for Fe–Al alloys (Leamy *et al.*, 1967). The elastic moduli exhibit maximum or minimum values at the composition of Fe_3Al with a D_{03} (cF16) structure. Figure 11 shows the composition dependence of Young's modulus for CoAl alloys, which have an extended solubility range for Co and Al (Harmouche and Wolfenden, 1986). The maximum value of Young's modulus is found not at the stoichiometric composition but at a deviation from it. This may be because, even at the stoichiometric composition, intermetallics are not necessarily ideally ordered. Furthermore, off-stoichiometry, the Fe-group aluminides exhibit both a predominant defect type (vacancies, Al-rich; substitutions, Fe-group-rich) and minor types (the reverse or so-called triple defects). On the other hand, the deviation of the maximum modulus from stoichiometry may be an artifact of inexact chemical

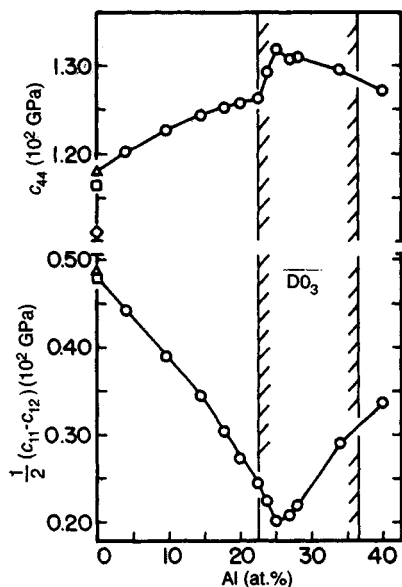


Figure 10. Composition dependence of room-temperature elastic moduli for Fe–Al alloys (from Leamy *et al.*, 1967). The composition range of single-phase (D_{03} , cF16) Fe_3Al is represented by the shaded band, D_{03} . (Reproduced by permission of Pergamon Press)

analysis, because Fleischer (1993) has found that the approximately stoichiometric composition of CoAl intermetallics exhibits the maximum Young's and shear moduli and that the density–composition curve has a break at stoichiometry, indicative of a change of defect type. In polycrystalline AlRu (B_2 , cP2 structure), the

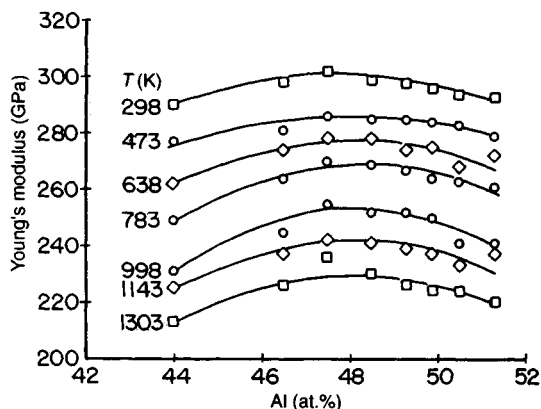


Figure 11. Composition dependence of Young's modulus for CoAl at various temperatures (Reproduced by permission of Elsevier Sequoia from Harmouche and Wolfenden, 1986)

shear modulus at room temperature increases linearly with increase of the Ru content from 47 to 60 at.% (Fleischer, 1991). This behavior of the shear modulus, however, is for a mixture of B2 and A3.

Alloying elements like Ti, Si, V, etc., substitute primarily for Al in Ni_3Al (Guard and Westbrook, 1959). The effect of the alloying element Ti on the elastic constants has been studied for Ni_3Al (Yasuda *et al.*, 1992). The elastic constants of a (nickel-rich) $\text{Ni}_{76}(\text{Al}_{15}\text{Ti}_9)$ single crystal (L1_2 , cP4 structure) are given by $c_{11} = 238$ GPa, $c_{44} = 123$ GPa, and $c_{12} = 141$ GPa. These elastic constants are a little higher than those of Ni_3Al . The substitution of Ti on the Al site hardly causes an increase of the elastic constants, compared with the values in Table 1.

The elastic moduli of RuTi-, RuAl-, and CoAl-base (B2, cP2 structure) and RuTa-base (L1_0 , tP4 structure) compounds have also been studied using polycrystalline alloys (Fleischer *et al.*, 1988, 1991a,b; Fleischer, 1991, 1993a,b). Table 7 shows examples of the effect of alloying elements on the elastic moduli for RuTi-, RuAl-, CoAl-, and RuTa-base intermetallic compounds. The substitutions of Ru by Re or Co, and that of Al by Sc, result in a decrease of the Young's and shear moduli for RuTi and RuAl, respectively. The latter also induces an increase in Poisson's ratio. The substitution of Ru by

Co or Fe also causes a decrease in the Young's and shear moduli, and an increase in Poisson's ratio. The substitutions of Co by Mn or Re, and that of Al by Ti, cause a decrease in the Young's and shear moduli for CoAl. The latter also results in an increase of Poisson's ratio.

6.2 Temperature Dependence of Elastic Moduli

In general, the elastic moduli decrease gradually with increasing temperature for intermetallic compounds without order-disorder transition or phase transformation. Figure 12 shows the temperature dependence of the stiffness constant c_{44} for an Fe_3Si single crystal (Rausch and Kayser, 1977). At temperatures below 77 K, c_{44} is approximately independent of temperature, and above 77 K it decreases almost linearly with increasing temperature. A similar temperature dependence of the elastic moduli is observed for polycrystalline Zr_3Al (Schulson, 1980), single-crystal Fe_3Al (Leamy *et al.*, 1967), single-crystal LaAl_2 (Schiltz and Smith, 1974), and others (Ono and Stern, 1969; Cheng, 1967). In a Laves-phase HfCo_2 single crystal (C15 , cF24 structure), the elastic constants are constant up to about 150 K, and then decrease linearly with increasing temperature (Shannette and Smith, 1969).

Table 7. Effect of alloying elements on elastic moduli

Intermetallics	Bulk modulus, K (10^2 GPa)	Young's modulus, E (10^2 GPa)	Shear modulus, G (10^2 GPa)	Poisson's ratio, ν	Crystal structure ^a	References
RuTi	2.47	2.78	1.06	0.31	B2, cP2	Fleischer <i>et al.</i> (1988)
$\text{Ti}_{50}\text{Ru}_{35}\text{Re}_{15}$	2.19	2.72	1.05	0.29	B2, cP2	
$\text{Ti}_{50}\text{Ru}_{20}\text{Re}_{30}$	2.03	2.53	0.98	0.29	B2, cP2	
$\text{Ti}_{50}\text{Ru}_{40}\text{Co}_{10}$	1.93	2.52	0.98	0.28	B2, cP2	
AlRu	2.07	2.67	1.04	0.286	B2, cP2	Fleischer <i>et al.</i> (1991b)
$\text{Al}_{46}\text{Ru}_{52}\text{Sc}_2$	2.10	2.80	1.10	0.278	B2, cP2	
$\text{Al}_{43}\text{Ru}_{52}\text{Sc}_5$	1.97	2.50	0.97	0.289	B2, cP2	
$\text{Al}_{40}\text{Ru}_{50}\text{Sc}_{10}$	1.85	2.29	0.887	0.291	B2, cP2	
$\text{Al}_{25}\text{Ru}_{50}\text{Sc}_{25}$	1.69	1.91	0.727	0.312	B2, cP2	
AlCo	1.62	2.78	1.14	0.214	B2, cP2	Fleischer (1993b)
$\text{Al}_{50}\text{Co}_{48.5}\text{Mn}_{1.5}$	1.58	2.66	1.09	0.219	B2, cP2	
$\text{Al}_{50}\text{Co}_{45}\text{Mn}_5$	1.38	2.50	1.04	0.198	B2, cP2	
$\text{Al}_{50}\text{Co}_{48.5}\text{Re}_{1.5}$	1.62	2.76	1.13	0.216	B2, cP2	
$\text{Al}_{50}\text{Co}_{45}\text{Re}_5$	1.68	2.65	1.07	0.237	B2, cP2	
$\text{Al}_{48.5}\text{Co}_{50}\text{Ti}_{1.5}$	1.63	2.68	1.10	0.225	B2, cP2	
$\text{Al}_{45}\text{Co}_{50}\text{Ti}_5$	1.68	2.30	0.91	0.230	B2, cP2	
$\text{Ru}_{11}\text{Ta}_9$	2.55	2.42	0.904	0.341	L1_0 , tP4	Fleischer <i>et al.</i> (1991a)
$\text{Ru}_{49}\text{Ta}_{51}$	2.55	2.43	0.906	0.341	L1_0 , tP4	
$\text{Co}_{15}\text{Ru}_{35}\text{Ta}_{50}$	2.29	1.75	0.639	0.372	L1_0 , tP4	
$\text{Co}_{20}\text{Ru}_{30}\text{Ta}_{50}$	2.14	1.47	0.532	0.385	L1_0 , tP4	
$\text{Fe}_{7.5}\text{Ru}_{42.5}\text{Ta}_{50}$	2.21	2.16	0.806	0.338	L1_0 , tP4	
$\text{Fe}_{15}\text{Ru}_{35}\text{Ta}_{50}$	2.30	1.74	0.605	0.374	L1_0 , tP4	

^aPearson (1958), Villars and Calvert (1985).

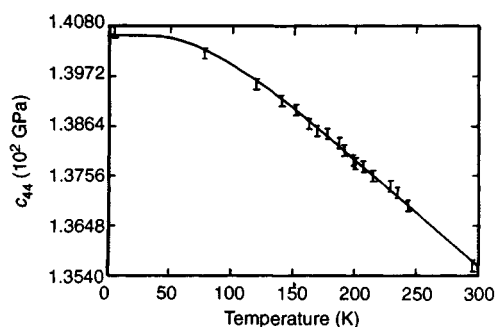


Figure 12. Temperature dependence of the stiffness c_{44} for a Fe_3Si single crystal (Reproduced by permission of the American Institute of Physics from Rausch and Kayser, 1977)

The elastic moduli are measured at temperatures above 500–600 °C by the sonic resonant frequency for different vibrational modes using long cylindrical rods of circular cross-section (Schafrik, 1977). The

temperature dependence of the elastic moduli was measured from 25 to 940 °C for polycrystalline TiAl ($L1_0$, tP4 structure) (Schafrik, 1977). The elastic moduli decrease linearly with increasing temperature, and Young's modulus E , shear modulus G , and Poisson's ratio ν are given at temperature T (°C) by

$$E = 173.59 - 0.0342T \quad (25-935 \text{ } ^\circ\text{C}) \quad (23)$$

$$G = 70.9 - 0.0141T \quad (25-935 \text{ } ^\circ\text{C}) \quad (24)$$

$$\nu = 0.234 + 0.0000067T \quad (25-847 \text{ } ^\circ\text{C}) \quad (25)$$

When alloys exhibit an order–disorder transition or phase transformation with a rise of temperature, an anomalous temperature dependence of the elastic moduli is observed. Figure 13 shows the temperature dependence of the compliance constants s_{11} , s_{44} , and $-s_{12}$ for Cu_3Au ($L1_2$, cP4 structure) (Siegel, 1940). A discontinuity in the modulus versus temperature curves

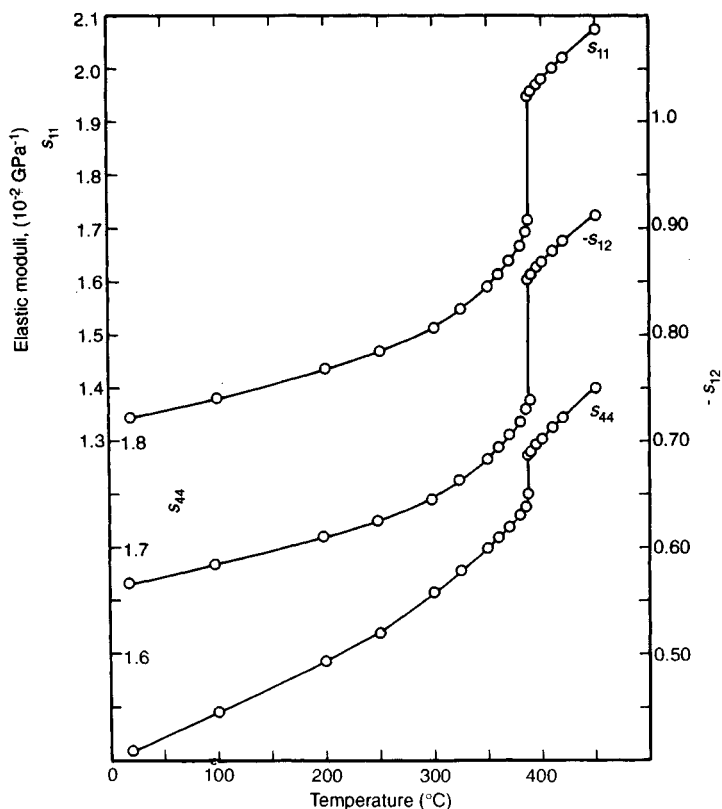


Figure 13. Temperature dependence of the compliances s_{11} , s_{44} , and $-s_{12}$ for a Cu_3Au single crystal (Reproduced by permission of the American Institute of Physics from Siegel, 1940)

is observed at 387.5 °C, above which the compliance constants exhibit high values. This is because Cu_3Au has an order-disorder transition at 387.5 °C, above which it becomes disordered. A similar temperature dependence of the elastic constants is reported in CuZn (B2, cP2 structure) by Young and Bienenstock (1971). Guillet and Le Roux (1967), in a review, showed that for intermetallic compounds like CuZn , Cu_3Au , etc., the order-disorder phase transformation is often accompanied by abrupt variations in Young's modulus.

The intermetallic compounds that have a magnetic transition also exhibit an anomalous temperature dependence of the elastic moduli. Figure 14 shows the temperature dependence of the elastic constant c_{44} for Laves-phase LaAl_2 and GdAl_2 (C15, cF24 structure) (Schiltz and Smith, 1974). GdAl_2 , which has a magnetic transition from a disordered to an ordered phase with decreasing temperature, exhibits a change in slope of the c_{44} versus temperature curve near 170 K, and has higher c_{44} values in the magnetically ordered phase than the extrapolation from the disordered phase. In comparison, for LaAl_2 , which has no magnetic ordering in this temperature range, c_{44} increases continuously with decreasing temperature.

The temperature dependence of the elastic moduli has been investigated from 4.2 to 300 K for various polycrystalline rare earth-cobalt (Klimker *et al.*, 1979), rare earth-iron (Klimker *et al.*, 1974) Laves-phase

compounds, etc. (Rosen *et al.*, 1973). For the rare earth-iron compounds RFe_2 , like DyFe_2 , YFe_2 , GdFe_2 (C15, cF24 structure), etc., for which the Curie temperatures are below room temperature, the elastic moduli decrease monotonically with increasing temperature as do those for LaAl_2 (Klimker *et al.*, 1974). CeFe_2 and HoFe_2 (C15, cF24 structure), however, exhibit anomalies in the elastic moduli in the temperature range from 227 K (i.e. the magnetic ordering temperature) to room temperature, and from 14 to 90 K, respectively. That is, the elastic moduli decrease with decreasing temperature in the noted temperature range, and this behavior is indicative of a lattice softening process preceding the magnetic phase change (Klimker *et al.*, 1979). The rare earth-cobalt Laves-phase compounds RCo_2 , like NdCo_2 , PrCo_2 (C15, cF24 structure), etc. (Klimker *et al.*, 1979), and rare earth-iron Laves-phase (Ho,Tb) Fe_2 (Rosen *et al.*, 1973) exhibit similar behaviors in the temperature dependence of the elastic moduli, i.e. a lattice softening accompanying the magnetic ordering and/or spin reorientation process. Figure 15 shows the temperature dependence of Young's modulus for the rare earth-cobalt Laves-phase compounds (Klimker *et al.*, 1979). It has been noted (Figure 16) that, for the rare earth-iron or rare earth-cobalt Laves-phase compounds in the magnetically ordered state, the elastic moduli are also dependent on magnetic field (Klimker *et al.*, 1974, 1979; Rosen *et al.*, 1973). The moduli increase rapidly with increasing magnetic field, followed by saturation.

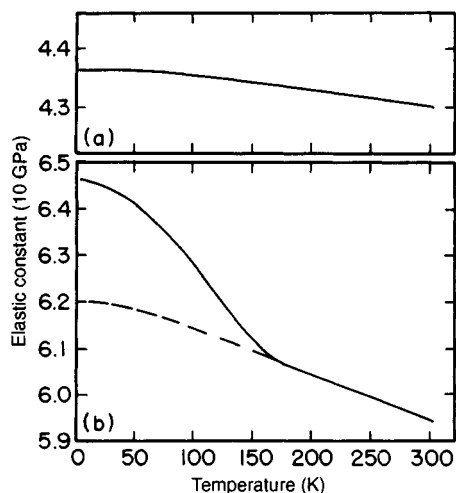


Figure 14. Temperature dependence of the stiffness c_{44} for (a) LaAl_2 and (b) GdAl_2 single crystals. The broken curve represents an extrapolation of the behavior of the magnetically disordered phase (Reproduced by permission of the American Institute of Physics from Schiltz and Smith, 1974)

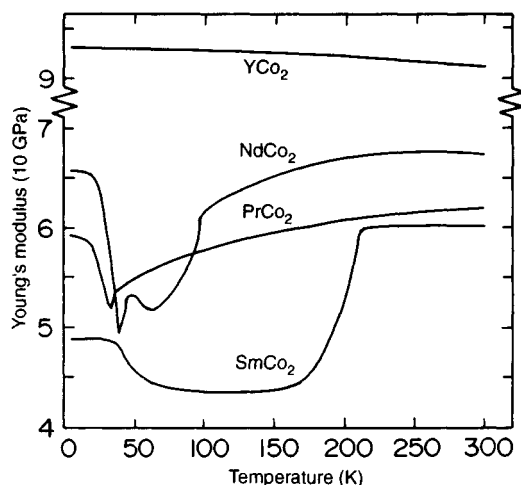


Figure 15. Temperature dependence of Young's modulus for rare earth-cobalt Laves compounds (Reproduced by permission of Pergamon Press from Klimker *et al.*, 1979)

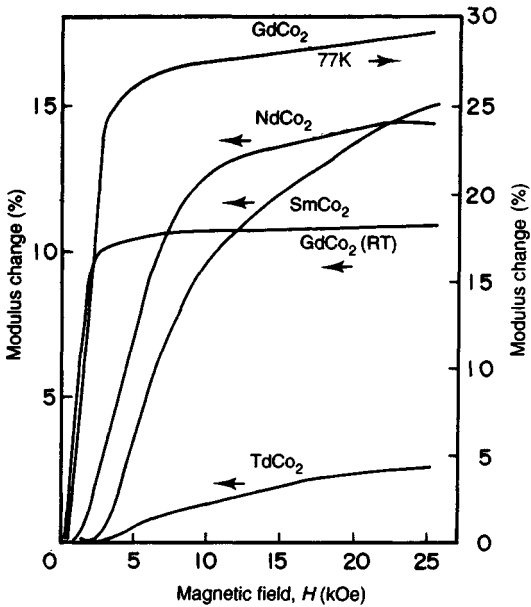


Figure 16. Magnetic-field dependence of the modulus change $(E_H - E_0)/E_0$ for $R\text{Co}_2$ compounds at 77 K. E_H and E_0 are Young's modulus at magnetic field H and 0, respectively (Reproduced by permission of Pergamon Press from Klimker *et al.*, 1979)

Contrary to the normal behavior in metals, the elastic constants c_{11} and c_{44} decrease and the shear modulus $\frac{1}{2}(c_{11} - c_{12})$ vanishes with decreasing temperature in Nb_3Sn (A15, cP8 structure) (Keller and Hank, 1967; Chang and Barsch, 1980) and V_3Si (A15, cP8 structure) (Testardi *et al.*, 1965). These compounds have high superconducting transition temperatures, T_c , of 17 and 18 K, respectively. Figure 17 shows the temperature dependence of the elastic constants for a Nb_3Sn (A15, cP8 structure) single crystal (Keller and Hank, 1967). Below 32 K, c_{11} becomes equal to c_{12} , because a shear wave with the modulus $(c_{11} - c_{12})/2$ cannot be propagated. That is, Nb_3Sn exhibits a lattice softening as temperature is reduced. Thus, one shear wave cannot be propagated below the temperature at which a crystallographic phase transformation may take place (Keller and Hank, 1967). A similar temperature dependence of the elastic constants is observed for V_3Si (A15, cP8 structure) single crystals (Chang and Barsch, 1980). In this compound the shear modulus $(c_{11} - c_{12})/2$ also decreases with decreasing temperature, and vanishes near the critical temperature, 17 K.

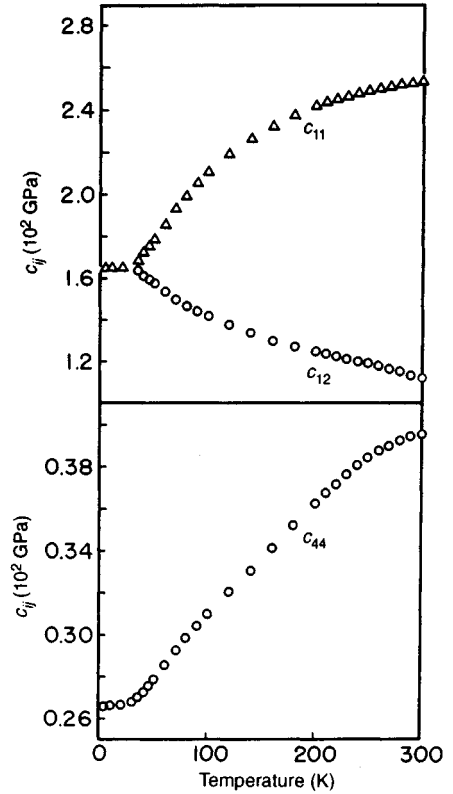


Figure 17. Temperature dependence of the elastic constants for a Nb_3Sn single crystal (Reproduced by permission of the American Institute of Physics from Keller and Hank, 1967)

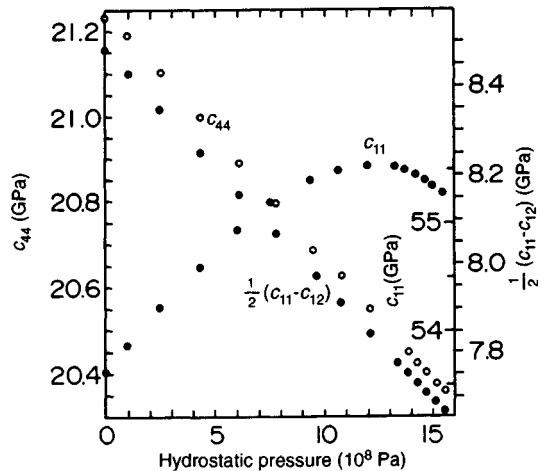


Figure 18. Effect of hydrostatic pressure on the elastic constants c_{11} , c_{44} , and $\frac{1}{2}(c_{11} - c_{12})$ for a HgTe single crystal (Reproduced by permission of Taylor & Francis from Miller *et al.*, 1981)

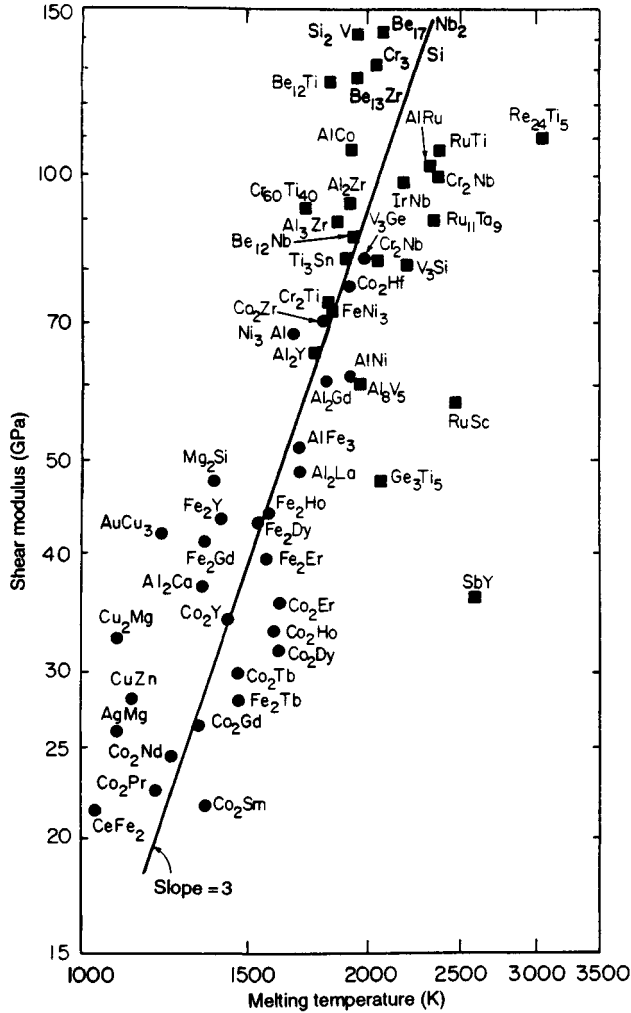


Figure 19. Relationship between the shear modulus and the melting temperature (Reproduced by permission of the Japan Institute of Metals from Fleischer, 1991)

6.3 Pressure Dependence of the Elastic Moduli

HgTe (B3, cF8 structure) has been investigated under hydrostatic pressure up to 1.55 GPa, below which it has no phase transformation. Figure 18 shows the effect of hydrostatic pressure on the elastic constants, c_{11} , c_{44} , and $(c_{11} - c_{12})/2$, for single-crystal HgTe (Miller *et al.*, 1981). The values of c_{44} and the shear modulus $\frac{1}{2}(c_{11} - c_{12})$ decrease linearly with increasing pressure, but c_{11} goes through a maximum at about 1.33 GPa. For Nb₃Sn (A15, cP8 structure) single crystals, the pressure dependence of the elastic constants has been investigated from about 13 to 300 K (Chang and Barsch, 1980).

6.4 Relation Between the Elastic Moduli and Melting Temperature

The elastic moduli are considered to be related to the interatomic forces in intermetallic compounds. Thus, the elastic moduli at room temperature have been related to melting temperatures for various intermetallic compounds (Fleischer, 1991; Skinner and Zedalis, 1988). Figure 19 shows the shear modulus G at room temperature versus melting temperature for polycrystalline intermetallics (Fleischer, 1991). This indicates that the probability of a high shear modulus increases remarkably with melting temperature. The correlation presented in Figure 19 may indicate that

the melting temperature can be used to predict approximately the elastic moduli of intermetallic compounds. The elastic moduli of SbY, RuSc, etc., fall significantly below the scatter band in Figure 19, and no explanation for these anomalous elastic moduli has been given.

7. Summary and Conclusion

The elastic properties of many intermetallic compounds have been investigated extensively since 1967, the year in which the first edition of *Intermetallic Compounds*, edited by Westbrook, was published. In the present chapter, the elastic constants of single-crystal intermetallic compounds have been summarized, and the elastically anisotropic behaviors of single crystals have been discussed. The elastic properties of dislocations as calculated from the anisotropic elasticity have been shown. The elastic moduli of polycrystalline materials have also been summarized. Finally, the effects of various factors like composition, temperature, etc. on the elastic moduli were described.

Knowledge of the elastic constants of a single crystal is necessary to calculate or estimate various elastic properties like elastic anisotropy, elastic properties of dislocations, etc., of intermetallic compounds. Such information is also necessary to estimate or check the potential energy between different atoms, which is used for computer simulations like molecular dynamics, etc., although the elastic constants themselves can be calculated using various methods like EAM, F-LAPW, etc. The temperature dependence of the elastic moduli may also be further used for the investigation of various kinds of transformations, since they are sensitive to composition, temperature, etc.

8. Acknowledgement

The author would like to thank Dr R. L. Fleischer for contributing many references on the elastic moduli of intermetallic compounds.

9. References

- Alouani, M., Albers, R. C., and Methfessel, M. (1991). *Phys. Rev.*, **B43**, 6500.
- Anderson, O. L. (1963). *J. Phys. Chem. Solids*, **24**, 909.
- Butler, B., Grivord, D., Grivord, F., and Palmer, S. B. (1982). *J. Phys.*, **F12**, 2813.
- Cabarat, R., Guillet, L., and Le Roux, R. (1948a). *C. R. Acad. Sci. Paris*, **226**, 1374.
- Cabarat, R., Guillet, L., and Le Roux, R. (1948b). *C. R. Acad. Sci. Paris*, **227**, 681.
- Chang, Y. A., Himmel, L., and Neumann, J. P. (1967). *J. Appl. Phys.*, **38**, 649.
- Chang, Z. P., and Barsch, G. R. (1980). *Phys. Rev.*, **B22**, 3242.
- Chen, S. P., Voter, A. J., and Srolovitz, D. J. (1986). *Scripta Metall.*, **20**, 1389.
- Cheng, C. H. (1967). *J. Phys. Chem. Solids*, **28**, 413.
- Clark, A. E., Belson, H. S., and Strakana, R. E. (1973). *J. Appl. Phys.*, **44**, 2913.
- Copley, S. M., and Kear, B. H. (1967). *Trans. Metall. Soc. AIME*, **239**, 977.
- Dickson, R. W., and Wachtman, J. B., Jr (1969). *J. Appl. Phys.*, **40**, 2276.
- Fleischer, R. L. (1991). In *Proc. Intl. Symp. on Intermetallic Compounds (JIMIS-6)* (ed. O. Izumi). Japan Institute of Metals, Sendai, p. 157.
- Fleischer, R. L. (1993a). *Metall. Trans.*, **24A**, 227.
- Fleischer, R. L. (1993b). *J. Mater. Res.*, **8**, 49.
- Fleischer, R. L., and Field, R. D. (1990). Report, WRDC-TR-90-4046.
- Fleischer, R. L., and Zabala, R. J. (1989). *Metall. Trans.*, **20A**, 1279.
- Fleischer, R. L., and Zabala, R. J. (1990a). *Metall. Trans.*, **21A**, 2709.
- Fleischer, R. L., and Zabala, R. J. (1990b). *Metall. Trans.*, **21A**, 1951.
- Fleischer, R. L., Gilmore, R. S., and Zabala, R. J. (1988). *J. Appl. Phys.*, **64**, 2964.
- Fleischer, R. L., Gilmore, R. S., and Zabala, R. J. (1989). *Acta Metall.*, **37**, 2801.
- Fleischer, R. L., Field, R. D., Denike, K. K., and Zabala, R. J. (1990). *Metall. Trans.*, **21A**, 3063.
- Fleischer, R. L., Field, R. D., and Briant, C. L. (1991a). *Metall. Trans.*, **22A**, 129.
- Fleischer, R. L., Field, R. D., and Briant, C. L. (1991b). *Metall. Trans.*, **22A**, 403.
- Foiles, S. M., and Daw, M. S. (1987). *J. Mater. Res.*, **2**, 5.
- Fu, C. L. (1990). *J. Mater. Res.*, **5**, 971.
- Fu, C. L., and Yoo, M. H. (1989). In *High-Temperature Ordered Intermetallic Alloys III* (eds C. T. Liu, A. I. Taub, N. S. Stoloff, and C. C. Koch). Materials Research Society, Pittsburgh, p. 81.
- Garber, J. A., and Granato, A. V. (1975). *Phys. Rev.*, **B11**, 3990.
- Girifalco, L. A., and Weizer, V. G. (1959). *Phys. Rev.*, **114**, 687.
- Griffith, A. A. (1920). *Phil. Trans. R. Soc.*, **A221**, 163.
- Guard, R. W., and Westbrook, J. H. (1959). *Trans. AIME*, **215**, 807.
- Guenin, G., Ignat, M., and Thomas, O. (1990). *J. Appl. Phys.*, **68**, 6515.
- Guillet, L., and Le Roux, R. (1967). In *Intermetallic Compounds* (ed. J. H. Westbrook). Wiley, New York, p. 453.

- Guo, X.-Q., Podlousky, R., and Freeman, A. J. (1991). *J. Mater. Res.*, **6**, 324.
- Harmouche, M. R., and Wolfenden, A. (1986). *Mater. Sci. Eng.*, **84**, 35.
- Hickernell, F. S., and Gayton, W. R. (1966). *J. Appl. Phys.*, **37**, 462.
- Hirth, J. R., and Lothe, J. (1968). *Theory of Dislocations*. McGraw-Hill, New York.
- Kayser, F. X., and Stassis, C. (1981). *Phys. status solidi*, **A64**, 335.
- Keller, K. R., and Hank, J. J. (1967). *Phys. Rev.*, **154**, 628.
- Kimura, K., Nakamura, M., and Hirano, T. (1990). *J. Mater. Sci.*, **25**, 2487.
- Klimker, H., Rosen, M., Dariel, M. P., and Atzmony, U. (1974). *Phys. Rev.*, **B10**, 2968.
- Klimker, H., Dariel, M. P., and Rosen, M. (1979). *J. Phys. Chem. Solids*, **40**, 195.
- Leamy, H. J., Gibson, E. D., and Kayser, F. X. (1967). *Acta Metall.*, **15**, 1827.
- Love, A. E. (1944). *A Treatise on the Mathematical Theory of Elasticity*, 4th Edn. Dover, New York, p. 100.
- Massalski, T. B. (ed.) (1986). *Binary Alloy Phase Diagrams*, Vol. 1. American Society for Metals, Metals Park, OH, p. 112.
- Mehl, M. J., Osburn, J. E., Papaconstantopoulos, D. A., and Klein, B. M. (1990). *Phys. Rev.*, **B41**, 10311.
- Miller, A. J., Saunders, G. A., and Yogurtcu, Y. K. (1981). *Phil. Mag.*, **A43**, 1447.
- Mock, R., and Guntherodt, G. (1984). *J. Phys.*, **C17**, 5635.
- Nabarro, F. R. (1947). *Proc. Phys. Soc.*, **59**, 256.
- Nadgornyi, E. (1988). *Prog. Mater. Sci.*, **31**, 1.
- Nakamura, M. (1991a). *Bull. Japan Inst. Metals*, **30**, 404.
- Nakamura, M. (1991b). In *Proc. Intl. Symp. On Intermetallic Compounds (JIMIS-6)* (ed. O. Izumi). Japan Institute of Metals, Sendai, p. 655.
- Nakamura, M. (1994). *Met. Trans.*, in press.
- Nakamura, M., and Kimura, K. (1991). *J. Mater. Sci.*, **26**, 2208.
- Nakamura, M., Matsumoto, S., and Hirano, T. (1990). *J. Mater. Sci.*, **25**, 3309.
- Ono, K., and Stern, R. (1969). *Trans. TMS AIME*, **245**, 171.
- Pearson, W. P. (1958). *A Handbook of Lattice Spacings and Structures of Metals and Alloys*. Pergamon, London.
- Peierls, R. (1940). *Proc. Phys. Soc.*, **52**, 34.
- Penney, T., Barbara, B., Plaskett, T. S., King, H. E., Jr, and LaPlaca, S. J. (1982). *Solid State Commun.*, **44**, 1199.
- Rausch, J. B., and Kayser, F. X. (1977). *J. Appl. Phys.*, **48**, 487.
- Rehwal, W., Rayl, M., Cohen, R. W., and Cody, G. D. (1972). *Phys. Rev.*, **B8**, 363.
- Rosen, M., and Klimker, H. (1969). *Phys. Rev.*, **184**, 466.
- Rosen, M., Klimker, H., Atzmony, U., and Dariel, M. P. (1973). *Phys. Rev.*, **B8**, 2326.
- Schafrik, R. E. (1977). *Metall. Trans.*, **8A**, 1003.
- Schiltz, R. J., Jr, and Smith, J. F. (1974). *J. Appl. Phys.*, **45**, 4681.
- Schiltz, R. J., Jr, Prevender, T. S., and Smith, J. F. (1971). *J. Appl. Phys.*, **42**, 4680.
- Schreiber, E., Anderson, O. L., and Soga, N. (1973) *Elastic Constants and Their Measurement*. McGraw-Hill, New York.
- Schulson, E. M. (1980). *Rev. High Temp. Mater.*, **4**, 195.
- Shannette, G. W., and Smith, J. F. (1969) *J. Appl. Phys.*, **40**, 79.
- Siegel, S. (1940). *Phys. Rev.*, **57**, 537.
- Sih, G. C., and Liebowitz, H. (1968). In *Fracture—An Advanced Treatise*. Vol. II (ed. H. Liebowitz). Academic Press, New York, p. 68.
- Skinner, D. J., and Zedalis, M. (1988). *Scripta Metall.*, **22**, 1783.
- Smithells, C. J. (ed.) (1976). *Metals Reference Book*, 5th Edn. Butterworths, London, p. 975.
- Steeds, J. W. (1973). *Introduction to Anisotropic Elasticity Theory of Dislocations*. Clarendon, Oxford.
- Sumer, A., and Smith, J. F. (1962). *J. Appl. Phys.*, **33**, 2283.
- Suzuki, T., Mishima, Y., and Miura, S. (1989) *ISIJ Intl.*, **29**, 1.
- Testardi, L. R., Bateman, T. B., Reed, W. A., and Chirba, V. G. (1965). *Phys. Rev. Lett.*, **15**, 250.
- Thornton, P. H., Davies, R. G., and Johnston, T. L. (1970). *Metall. Trans.*, **1**, 207.
- Villars, P., and Calvert, L. D. (1985) *Pearson's Handbook of Crystallographic Data for Intermetallic Phases*. American Society for Metals, Metals Park, OH.
- Wasilewski, R. J. (1966). *Trans. TMS AIME*, **236**, 455.
- Weil, R., and Groves, W. O. (1971). *J. Appl. Phys.*, **42**, 4049.
- Westbrook, J. H. (ed.) (1967). *Intermetallic Compounds*. Wiley, New York.
- Whitten, W. B., Chung, P. L., and Danielson, G. C. (1965). *J. Phys. Chem. Solids*, **26**, 49.
- Yasuda, H., and Koiwa, M. (1991). *J. Phys. Chem. Solids*, **52**, 723.
- Yasuda, H., Takasugi, T., and Koiwa, M. (1991) *Mater. Trans. Japan Inst. Metals*, **32**, 48.
- Yasuda, H., Takasugi, T., and Koiwa, M. (1992). *Acta Metall.*, **40**, 381.
- Yoo, M. H. (1987a). *Acta Metall.*, **35**, 1559.
- Yoo, M. H. (1987b). In *High-Temperature Ordered Intermetallic Alloys II* (eds N. S. Stoloff, C. C. Koch, C. T. Liu, and O. Izumi). Materials Research Society, Pittsburgh, p. 207.
- Yoo, M. H., and Fu, C. L. (1991). *Scripta Metall.*, **25**, 2345.
- Young, P. L., and Bienenstock, A. (1971). *J. Appl. Phys.*, **42**, 3008.
- Zirinsky, S. (1956). *Acta Metall.*, **4**, 164.

Addendum

A1. Elastic Constants at Room Temperature

Recently, elastic constants of single crystals as well as polycrystalline materials have been determined for many intermetallic compounds using a resonance ultrasound spectroscopy (RUS) method (Maynard, 1996). Since this method does not require large single crystals for measuring elastic constants, elastic constants of single crystals have been measured for intermetallic compounds with tetragonal structures as well as cubic structures. Table 8 shows the elastic constants, c_{ij} , of single crystals at room temperature for several intermetallic compounds. TiAl-based intermetallic alloys are considered promising light-weight materials for high temperature structural applications.

Although TiAl is obtained over a large range of chemical composition from about 49 to 56 at% at room temperature (Massalski *et al.*, 1990), TiAl single crystals have been prepared, not at the stoichiometric composition, but at an Al-rich composition. Thus a single crystal of Ti-56 at% Al was used for measurement of elastic constants (Tanaka *et al.*, 1996a; He *et al.*, 1995).

Table 9 shows the elastic moduli of polycrystalline compounds estimated from the elastic constants in Table 8 using the Hill approximation. Table 10 shows the elastic moduli of polycrystalline NbCr₂ and Hf₂₅V₆₀Nb₁₅ (C15, cF24) measured by a RUS method at room temperature (Chu *et al.*, 1994, 1995).

Table 8. Elastic constants (10² GPa) of intermetallic compounds at room temperature

Intermetallics	c_{11}	c_{22}	c_{33}	c_{44}	c_{55}	c_{66}	c_{12}	c_{13}	c_{23}	Structure ^a	References
MoSi ₂ ^c	4.037	c_{11}	5.054	2.027	c_{44}	1.948	1.145	0.880	c_{13}	C11 _b , tI6	Tanaka <i>et al.</i> (1997)
NbSi ₂ ^c	3.802	c_{11}	4.680	1.453	c_{44}	c_{66}^b	0.759	0.883	c_{13}	C40, hP9	Chu <i>et al.</i> (1996)
TaSi ₂ ^c	3.753	c_{11}	4.767	1.437	c_{44}	c_{66}^b	0.784	0.901	c_{13}	C40, hP9	Chu <i>et al.</i> (1996)
TiAl ^c	1.83	c_{11}	1.78	1.05	c_{44}	0.784	0.741	0.744	c_{13}	L1 ₀ , tP4	Tanaka <i>et al.</i> (1996a)
TiAl ^c	1.86	c_{11}	1.76	1.01	c_{44}	0.77	0.72	0.74	c_{13}	L1 ₀ , tP4	He <i>et al.</i> (1995)
Ti ₃ Al ^c	1.762	c_{11}	2.187	0.624	c_{44}	c_{66}^b	0.878	0.612	c_{13}	D0 ₁₉ , hP8	Tanaka <i>et al.</i> (1996b)
Zr ₂ Ni ^d	1.5477	c_{11}	1.4480	0.2399	c_{44}	0.0966	1.282	0.857	c_{13}	C16, tI12	Eshelman and Smith (1975)
Al ₂ Cu ^d	1.7966	c_{11}	1.7023	0.2798	c_{44}	0.4464	0.7270	0.757	c_{13}	C16, tI12	Eshelman and Smith (1978)
CeNi ₅ ^d	2.15(8)	c_{11}	2.65(9)	0.64(3)	c_{44}	c_{66}^b	1.078	0.948	c_{13}	D2 _d , hP6	Butler <i>et al.</i> (1980)

^aPearson (1958); Villars and Calvert (1985)

^b $c_{66} = (c_{11} - c_{12})/2$

^cRUS method

^dpulse echo technique

Table 9. Elastic moduli of polycrystalline compounds estimated from the elastic constants in Table 8 using the Hill approximation

Intermetallics	Bulk modulus K (10 ² GPa)	Young's modulus E (10 ² GPa)	Shear modulus G (10 ² GPa)	Poisson's ratio ν	Debye temperature θ_D (K)
MoSi ₂	2.099	4.318	1.866	0.157	751
NbSi ₂	1.915	3.628	1.532	0.184	688
TaSi ₂	1.925	3.590	1.510	0.189	552
TiAl	1.100	1.847	0.757	0.220	587
TiAl	1.098	1.829	0.748	0.22	584
Ti ₃ Al	1.11	1.44	0.563	0.283	475
Zr ₂ Ni	1.157	0.556	0.196	0.42	210
Al ₂ Cu	1.086	1.045	0.390	0.34	406
CeNi ₅	1.433	1.638	0.625	0.309	372

Table 10. Elastic moduli of polycrystalline compounds measured by a RUS method

Intermetallics	Bulk modulus K (10^2 GPa)	Young's modulus E (10^2 GPa)	Shear modulus G (10^2 GPa)	Poisson's ratio ν	Structure	References
NbCr ₂	2.294	2.141	0.796	0.34	C15, cF24	Chu <i>et al.</i> (1995)
Hf ₂₅ V ₆₀ Nb ₁₅	1.461	0.8442	0.3007	0.404	C15, cF24	Chu <i>et al.</i> (1994)

Table 11. Elastic constants (10^2 GPa) of intermetallic compounds at different temperatures

Intermetallics	Temperature	c_{11}	c_{33}	c_{44}	c_{66}	c_{12}	c_{13}	Structure	References
NbSi ₂	120 K	3.84	4.73	1.468	c_{66}^a	0.759	0.786	C40, hP9	Chu <i>et al.</i> (1996)
	300 K	3.802	4.680	1.453	c_{66}^a	0.759	0.883		
MoSi ₂	0 K ^b	4.100	5.140	2.065	1.996	1.149	0.875	C11 _b , tI6	Tanaka <i>et al.</i> (1997)
	290 K	4.037	5.053	2.027	1.948	1.145	0.880		
TiAl	0 K ^b	1.87	1.82	1.09	0.812	0.748	0.748	LI ₀ , tP4	Tanaka <i>et al.</i> (1996a)
	298 K	1.83	1.78	1.05	0.77	0.741	0.744		
TiAl ^c	theoretical	1.90	1.85	1.20	0.50	1.05	0.90	LI ₀ , tP4	Fu and Yoo (1990)
TiAl ^d	theoretical	1.88	1.9	1.26	1.00	0.98	0.96	LI ₀ , tP4	Mehl <i>et al.</i> (1991)
Ti ₃ Al	3.3 K	1.862	2.251	0.641	0.471	0.890	0.626	DO ₁₉ , hP8	Tanaka <i>et al.</i> (1996b)
	270 K	1.762	2.187	0.624	0.442	0.878	0.612		

^a $c_{66} = (c_{11} - c_{12})/2$ ^bextrapolated value^ctheoretical, F-LAPW (First-principles full-potential linearized augmented-plane-wave total-energy method)^dtheoretical, LAPW (linear augmented-plane-wave method)

A2. Temperature Dependence of Elastic Constants

Temperature dependence of elastic constants can also be measured using a RUS method, because the method does not require glue, which is usually used to connect a sample with an ultrasonic wave transducer when using conventional ultrasonic methods. The temperature dependence of the elastic constants was measured for a MoSi₂ (C11_b, tI6) single crystal in a temperature range of 4 to 1373 K by a RUS method (Tanaka *et al.*, 1997). c_{11} , c_{33} , c_{44} and c_{66} decrease from about 410, 514, 206 and 200 GPa to 352, 436, 174 and 163 respectively, with increasing temperature from 4 to 1373 K. They decrease linearly with increasing temperature above room temperature, although they are almost saturated at low temperatures as shown for a Fe₃Si (DO₃, cF16) single crystal in Figure 12. c_{12} and c_{13} hardly depend on temperature in this temperature range. A similar tendency was observed for TiAl (LI₀, tP4) and Ti₃Al (DO₁₉, hP8) single crystals in a temperature range from 4 K to room temperature (Tanaka *et al.*, 1996a, 1996b). Table 11 shows the elastic constants of some intermetallic compounds at low temperatures, compared with those at room temperature and theoretical values, where the values at 0 K were extrapolated from the temperature dependence of the elastic constants.

With increasing temperature from 70 K to room temperature the shear and Young's moduli of polycrystalline Hf₂₅V₆₀Nb₁₅ (C15, cF24) increase linearly from about 26 and 75 GPa to 30 and 85 GPa, respectively, and its Poisson's ratio decreases linearly from about 0.42 to 0.405. Its bulk modulus is hardly dependent on temperature (Chu *et al.*, 1994). The temperature dependence of the elastic moduli for this intermetallic compound are remarkably different from those of the elastic constants for usual intermetallics like TiAl, Fe₃Si, MoSi₂, etc. (see Figure 12). That is, the bulk, shear and Young's moduli of polycrystalline MoSi₂ (C11_b, tI6), which were estimated from the elastic constants of single crystals, decrease; and Poisson's ratio increases with increasing temperature from 4 to 1373 K (Tanaka *et al.*, 1997). Chu *et al.* reported that Hf₂₅V₆₀Nb₁₅ (C15, cF24) has no phase transformation at low temperatures and that the anomalous temperature dependence can be understood from the electronic structure (Chu *et al.*, 1994).

A3. References

- Butler, B., Givord, D., Givord, F., and Palmer, S. B. (1980). *J. Phys. C: Solid St. Phys.*, 13, L743.

- Chu, F., Lei, M., Migliori, A., Chen, S. P., and Mitchell, T. E. (1994). *Phil. Mag. B*, **70**, 867.
- Chu, F., He, Y., Thoma, D. J., and Mitchell, T. E. (1995). *Scripta Metall. Mater.*, **33**, 1295.
- Chu, F., Lei, M., Maloy, S. A., Petrovic, J. J., and Mitchel, T. E. (1996). *Acta Mater.*, **44**, 3035.
- Eshelman, F. R. and Smith, J. F. (1975). *J. Appl. Phys.*, **46**, 5080.
- Eshelman, F. R. and Smith, J. F. (1978). *J. Appl. Phys.*, **49**, 3284.
- Fu, C. L. and Yoo, M. H. (1990). *Phil. Mag. Lett.*, **62**, 159.
- He, Y., Schwarz, B., and Migliori, A. (1995). *J. Mater. Res.*, **10**, 1187.
- Maynard, J. (1996). *Physics Today*, **49-1**, 26.
- Massalski, T. B. (ed.) (1990). *Binary Alloy Phase Diagrams*, 2nd edition, Vol. 1. American Society for Metals, Metals Park, Ohio, p. 225.
- Mehl, M. J., Osburn, J. E., Papaconstantopoulos, D. A. and Klein, B. M. (1991). In *Alloy Phase Stability and Design* (eds G. M. Stock, D. P. Pope and A. F. Giamei), *Mater. Res. Soc. Symp. Proc.*, Vol. 186, Mater. Res. Soc., Pittsburgh, p. 277.
- Tanaka, K., Ichitsubo, T., Inui, H., Yamaguchi, M., and Koiwa, M. (1996a). *Phil. Mag. Lett.*, **73**, 71.
- Tanaka, K., Okamoto, K., Inui, H., Minonishi, Y., Yamaguchi, M., and Koiwa, M. (1996b). *Phil. Mag. A*, **73**, 1475.
- Tanaka, K., Onome, H., Inui, H., Yamaguchi, M., and Koiwa, M. (1997). *Mater. Sci. Eng.*, **A239-240**, 188.

Chapter 2

Intergranular and Cleavage Fracture

Clyde L. Briant

*General Electric Company, Research and Development Center, PO Box 8,
Schenectady, New York 12301, USA*

*(now at Division of Engineering, Brown University, Box D, 182 Hope St,
Providence, Rhode Island 02912-9104, USA)*

1. Introduction

One of the most limiting properties of many intermetallic compounds is their brittleness at room temperature. These compounds are often very lightweight, remain strong at high temperatures, and therefore should be attractive for many engineering applications; but their brittleness prevents their use. The fracture mode for these brittle compounds is either cleavage, i.e. fracture along specific crystallographic planes in either a single-crystal or polycrystalline sample, or intergranular, i.e. fracture along the grain boundaries in a polycrystalline sample. Examples are shown in Figure 1. Significant research efforts in recent years have been directed at trying to ductilize these compounds so that they can be used. These efforts have focused primarily on trying to find alloying additions that will impart ductility to the matrix or, specifically for compounds that fail intergranularly, an additive that will segregate to the grain boundaries and increase cohesion across them.

A review of the literature shows that the details of the fracture process and the attempts to improve ductility vary from system to system, and that there are many individual reports on ductility and fracture in specific compounds. To bring all of this information together in a comprehensive way, we have organized this chapter as follows. We will first summarize the research that has been done on compounds with either the L1₂ (cP4) structure or the B2 (cP2) structure. These are emphasized because, as far as fracture and ductility are concerned, they have been investigated the most

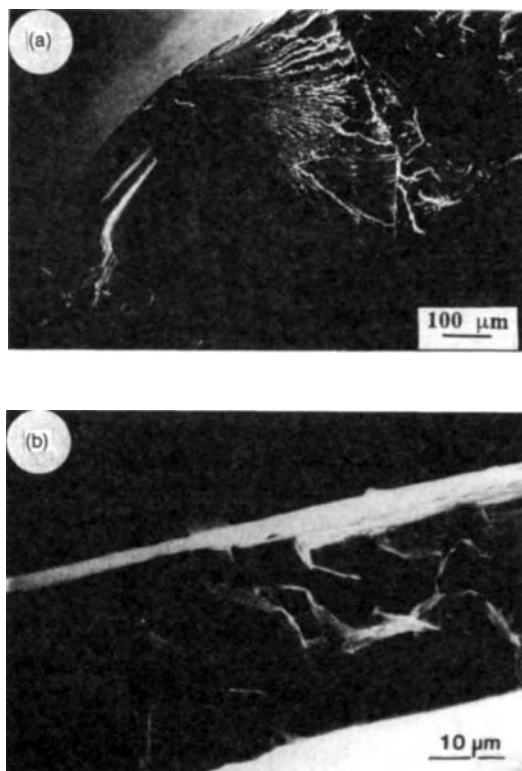


Figure 1. Examples of the two brittle fracture modes found in intermetallic compounds: (a) cleavage in NiAl; (b) intergranular fracture in Ni₃Ge

thoroughly. We will then summarize the results for compounds from other crystallographic systems. These summaries will be followed with a description of the mechanisms that have been proposed to explain the brittleness of these compounds. We end the chapter by listing the general conclusions that we can make, by pointing out areas where further research would be valuable, and by discussing general guidelines that should be followed in investigating fracture modes in these compounds. To make these summaries we have also had to define certain limits for what we will discuss. We will consider only single-phase alloys for which the fracture mode was determined in either a room-temperature tensile, bending, or notch impact test. We will almost exclusively present results on polycrystals, since most studies in the literature are on samples of this type.

We note that several of these topics are also discussed in Chapter 24 by Takasugi in this volume. These common items are used in that chapter to discuss grain-boundary chemistry and structure, whereas here they are used to discuss intergranular fracture.

2. $L1_2$ (cP4) Compounds

In recent years the causes of brittleness and the characterization of brittle fracture have been most extensively studied in the $L1_2$ class of intermetallic compounds. Within this class Ni_3Al has received by far the greatest amount of attention. Single crystals of Ni_3Al are ductile (Copley and Kear, 1967; Mulford and Pope, 1973), but polycrystals are very brittle (Davies and Stoloff, 1965). The fracture in polycrystalline samples occurs along the grain boundaries. Aoki and Izumi (1979) reported that boron additions made polycrystalline Ni_3Al ductile. This finding raised the possibility that a number of brittle intermetallic compounds might be made ductile through additions of boron or some other element, and work in many laboratories began on this topic.

A review of this work is best divided up into the general areas that reflect the types of research that have been carried out. We will first examine the fracture modes in a number of $L1_2$ compounds. We will then report which of those compounds that normally fail in a brittle fashion have been shown to gain ductility through alloying additions. Finally, we will look more closely at the improvement of ductility in Ni_3Al caused by boron additions and discuss the possible mechanisms by which it occurs.

$L1_2$ compounds have a crystal structure that is analogous to the face-centered cubic structure of

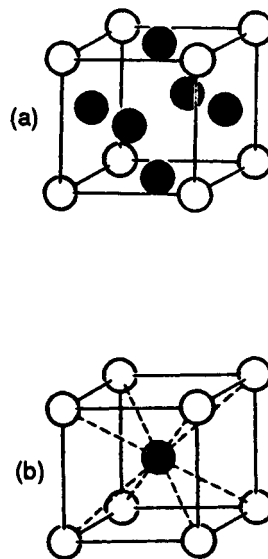


Figure 2. (a) The $L1_2$ (cP4) crystal structure and (b) the B2 (cP2) crystal structure

disordered alloys, as shown in Figure 2(a). They have the stoichiometry A_3B with the A atoms located on the cube faces and the B atoms at the corners. They also have a sufficient number of independent slip systems for polycrystals of these compounds to be ductile. However, the results listed in Table 1 show that most binary polycrystals are brittle. Among the brittle binary compounds, Al_3Sc and Si_3U fail by cleavage and all others fail by intergranular fracture. (There are other $L1_2$ compounds that fail by cleavage and that are formed by making significant alloying additions to non- $L1_2$ -based compounds. These will be considered in the fourth section of this chapter.) The few compounds that are ductile are usually composed of two transition metals.

Given that these compounds should be ductile, based on slip requirements, one must explain why so many of them are brittle. It is easy to explain how intergranular fracture might occur. A stress concentration builds up at the grain boundary from dislocation pile-ups and nucleates an intergranular crack. If the grain boundaries are weak, the crack propagates along them and failure occurs before yielding across the grain boundary takes place (Khadkikar *et al.*, 1987). It is important to note that, unlike the situation in many disordered alloys (Briant, 1988), research has shown that intergranular fracture in these compounds occurs in the absence of any segregated embrittling impurity such as sulfur or phosphorus (Takasugi *et al.*,

Table 1. Fracture mode of $L1_2$ binary compounds

Compound	Ductile (D) or brittle (B)	Fracture mode ^a	References
Ni ₃ Al	B	IG	Takasugi and Izumi (1985a)
Ni ₃ Si	B	IG	Takasugi and Izumi (1985a)
Ni ₃ Ga	B	IG	Takasugi and Izumi (1985a)
Ni ₃ Ge	B	IG	Takasugi and Izumi (1985a)
Fe ₃ Ga	B	IG	Takasugi and Izumi (1985a)
Zr ₃ Al	B	IG	Schulson (1984)
Cu ₃ Pd	D	TD	Takasugi and Izumi (1985a)
Ni ₃ Fe	D	TD	Takasugi and Izumi (1985a)
Cu ₃ Au	D	TD	Vidoz <i>et al.</i> (1963)
Ni ₃ Mn	D	TD	Takasugi and Izumi (1985a)
Co ₃ Ti	D	IG + TD	Takasugi and Izumi (1985a), Takasugi <i>et al.</i> (1987)
Pt ₃ Ga	B	IG	Briant <i>et al.</i> (1990)
Al ₃ Sc	B	C	George <i>et al.</i> (1990, 1991)
Si ₃ U	B	C	Fleischer (personal communication)

^aIG, intergranular; TD, transgranular ductile; C, cleavage.

1985; Huang *et al.*, 1985; Liu *et al.*, 1985). These studies, which employed Auger electron spectroscopy to measure grain-boundary segregation, failed to reveal any elements present on the boundaries except the constituent elements of the compound. One must recall that Auger electron spectroscopy does not detect hydrogen, and that elements must be present at a level greater than approximately 0.1% to be detected; but with these reservations, one can conclude that the grain boundaries in these compounds are intrinsically weak.

Cleavage fracture requires more consideration. When this fracture mode is observed in disordered compounds, it usually nucleates at a specific microstructural constituent (McMahon and Cohen, 1965). The cracks form within this constituent at a low stress and then propagate through the matrix. Al₃Sc is a line compound, i.e. it cannot exist outside perfect stoichiometry. Micrographs show that the structure almost always contains some second phases or casting voids (George *et al.*, 1990, 1991). It seems likely that these second phases might provide nucleation sites for cleavage in this compound. However, no research has been directed at identifying these nucleation sites in either Al₃Sc or Si₃U.

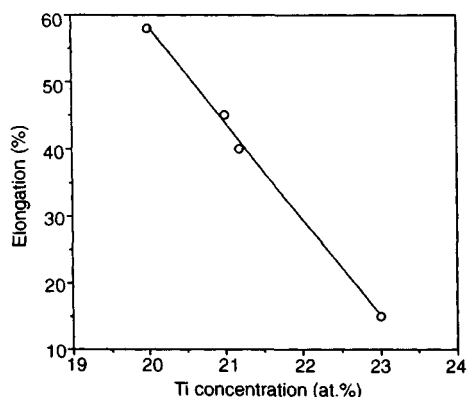


Figure 3. The total elongation of Co₃Ti plotted as a function of titanium content. Data were taken from tensile tests run in the air (From Takasugi *et al.*, 1987)

The listings in Table 1 are for compounds that have compositions very close to the stoichiometric ratio A₃B. The exact composition can vary over some range for most of these compounds without causing a change in crystal structure. These changes in stoichiometry have been shown to affect the mechanical properties of many intermetallic compounds (Wood and Westbrook, 1962), so one must ask whether the fracture mode and ductility of these compounds will also vary with composition. Ni₃Al and Ni₃Ga in the as-cast condition are reportedly brittle over their entire stoichiometric range and the fracture is intergranular (Takasugi *et al.*, 1987). In contrast, Co₃Ti shows a very marked change in ductility as the stoichiometry changes (Takasugi *et al.*, 1987). Figure 3 shows that alloys containing 20% Ti fail with an elongation of 58% whereas alloys with 23% Ti fail with less than 20% elongation. (Note that, unless specifically stated, all compositions will be given in atomic percent.) The fracture mode changes from predominantly ductile, transgranular fracture in samples containing 20 and 21% Ti to predominantly intergranular fracture in samples containing 23% Ti. To our knowledge, the effect of stoichiometry on fracture mode has not been investigated in other binary L1₂ compounds.

In addition to changes in stoichiometry, the test environment has been found to affect ductility and fracture mode. Figure 4 compares tensile elongation data for samples of Co₃Ti tested in air and vacuum. In all cases the ductilities measured in the tests run in air are lower than those measured in vacuum tests, and the fracture surfaces of the samples tested in air contained more intergranular fracture. It has been assumed that this environmental degradation in ductility is a form of hydrogen embrittlement. This interpretation is

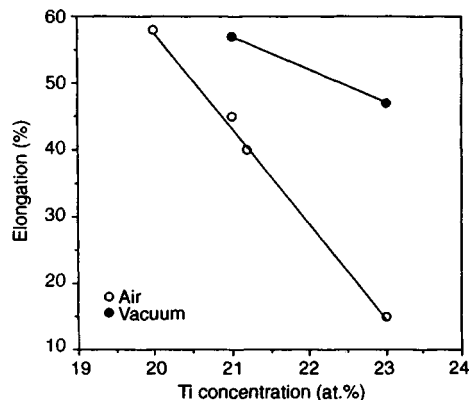


Figure 4. The total elongation of Co_3Ti plotted as a function of titanium content for tensile tests run in air and in vacuum (Data taken from Takasugi *et al.*, 1987)

reasonable, since these alloys tend to be susceptible to hydrogen embrittlement, and hydrogen is the one environmental constituent that could easily move into the lattice at room temperature. However, a hallmark of hydrogen embrittlement, and other forms of environmental embrittlement, is the occurrence of slow, stable crack growth (Briant, 1985). In these tensile tests the fracture occurs quite rapidly. Therefore, the environmental constituent responsible for degrading ductility must do so by affecting the nucleation of a crack. Once this crack has formed, it propagates rapidly and independently of the environment.

The final variable that can affect ductility is the processing history of the sample. For example, $\text{Ni}_{76}\text{Al}_{24}$ has been found to be brittle in as-cast samples (Takasugi *et al.*, 1987), in samples prepared from powder consolidation and subsequent extrusion (Schulson *et al.*, 1991), and in samples prepared by rapid solidification (Taub and Briant, 1987b). George *et al.* (1992, 1993) have recently reported that samples of this composition prepared by cold-forging and recrystallization gave elongations of approximately 2.5%, and samples prepared by recrystallizing a worked single crystal gave elongations of 11 to 13%. However, these latter alloys contained small amounts of zirconium. When the zirconium was removed, the elongations in air were only 3.1 to 4.8%. In all cases where the fracture mode was reported, it was intergranular and appeared to be brittle. Another processing variable that can affect elongation is the environment used for the heat treatment. An extreme example of this effect is the pest phenomenon described by Westbrook and Wood (1964) in which oxygen apparently penetrates the grain boundaries during the heat treatment and causes the sample to turn into a powder.

We now turn our attention to the work that has sought to find additives that will ductilize brittle, polycrystalline L_{12} compounds. These additives can be grouped into two categories. One we will term *major alloying additions*. The concentration of the additive is usually greater than 1% and it is generally presumed, though not proven, that these alloying additions primarily make the matrix more ductile, so that yielding across a grain boundary will occur before a crack can nucleate. The other group of additives we will term *trace-element additions*. These elements are usually added at a concentration well below 1% and often as low as 0.05 to 0.1%. These elements have been shown to segregate to the grain boundaries. In this way they apparently improve cohesion at the grain boundaries and prevent crack formation from occurring before general yielding takes place, or aid slip nucleation at the grain boundaries.

Table 2 summarizes the studies that have examined the effects of additives on ductility. In addition, the fourth column lists the elements that were found not to improve ductility. One general point to note is that an element that is beneficial for one compound may not be beneficial for another.

In the category of alloying additions, manganese and iron have been found to improve the ductility of Ni_3Al (Takasugi and Izumi, 1985b; Takasugi *et al.*, 1987; Masahashi *et al.*, 1988b). The effect of iron on Ni_3Al ductility has been studied much less than that of manganese, so we will not dwell on it here. The effect of manganese on the ductility of Ni_3Al is shown in Figure 5(a). These data, taken from Masahashi *et al.* (1988b), are for the stoichiometric alloy $\text{Ni}_{75}\text{Al}_{25-x}\text{Mn}_x$. One can observe that manganese additions cause an improvement in ductility, relative to pure Ni_3Al , although the fracture remained completely intergranular. Takasugi *et al.* (1987) showed that variation in stoichiometry also affects the elongation in $\text{Ni}_x(\text{Al}_{0.52}\text{Mn}_{0.48})_{100-x}$ alloys, as shown in Figure 5(b). They reported room-temperature tensile elongations approaching 20% in the Ni-rich samples. The fracture mode for these Ni-rich samples was transgranular and ductile.

Titanium additions have been shown to improve ductility in Ni_3Si (Takasugi *et al.*, 1990). To obtain single-phase alloys, these compounds have to be made with the nickel concentration above 75%. Titanium additions as great as 9% provide little improvement in ductility as long as the nickel concentration is below 78%. If the nickel concentration is allowed to increase to 80%, an improvement in ductility is measured, as shown in Figure 6. These data were obtained from tensile tests run in room-temperature air. This figure

Table 2. The effect of boron and other elements on the ductility of $L1_2$ compounds

Compound	Does boron improve ductility		Other elements that improve ductility		Elements that do not improve ductility	
	Yes/No	Reference	Element	References	Element	References
Ni_3Al	Yes	Aoki and Izumi (1979), Takasugi <i>et al.</i> (1987), Taub <i>et al.</i> (1984), Liu <i>et al.</i> (1985), Masahashi <i>et al.</i> (1988a)	Fe	Takasugi and Izumi (1985b)	C	Masahashi <i>et al.</i> (1988a), Huang <i>et al.</i> (1986)
			Mn	Takasugi and Izumi (1985b), Takasugi <i>et al.</i> (1987), Masahashi <i>et al.</i> (1988b)	S	Taub <i>et al.</i> (1986b)
			Be	Masahashi <i>et al.</i> (1988a)	Sb, Co, Cu, Si, Ge, Ga, Ti, V, Cr, Sc	Takasugi and Izumi (1985b)
			Pd	Chiba <i>et al.</i> (1991)		
			Zr	Aoki and Izumi (1979)		
Ni_3Ga	Yes	Takasugi <i>et al.</i> (1987), Taub and Briant (1987a)				
Ni_3Si	Yes	Taub and Briant (1987a)	Ti	Takasugi <i>et al.</i> (1990)		
			C	Taub and Briant (1990a)		
Ni_3Ge	No	Taub and Briant (1987a)				
Pt_3Ga	No	Briant <i>et al.</i> (1990)				
Co_3Ti	Yes	Takasugi <i>et al.</i> (1987)				

also shows that the tensile elongation improves when the alloys are tested in vacuum.

A much greater effort has been devoted to studying the effect of trace-element additions on ductility in $L1_2$ compounds. The results reported in Table 2 show that carbon improves ductility in Ni_3Si and that beryllium, palladium and zirconium have a small but beneficial effect in Ni_3Al . But it has been boron, which significantly improves ductility in Ni_3Al and Ni_3Ga and provides smaller improvements in Ni_3Si and Co_3Ti , that has received the most attention by researchers. Since a large fraction of this work has been devoted to the study of boron in Ni_3Al , we will begin our discussion by describing this effect in some detail and then showing how results for other compounds fit into this description.

The general results from a number of studies of boron in Ni_3Al are the following:

- Boron additions can increase the ductility of polycrystalline Ni_3Al from essentially zero to approximately 50%, as shown in Figure 7. This increase in ductility is accompanied by a change in fracture mode from intergranular fracture to ductile, transgranular fracture (Aoki and Izumi, 1979; Liu *et al.*, 1985; Takasugi *et al.*, 1987; Taub *et al.*, 1984).
- The improvement produced by boron is very dependent on alloy stoichiometry, as shown in

Figure 8. As the amount of aluminum decreases below 25%, the ductility improvements produced by boron additions increase. At aluminum concentrations of 25% and above, boron additions do not produce ductility improvements (Taub and Briant, 1987b; Liu *et al.*, 1985; Masahashi *et al.*, 1988a; Takasugi *et al.*, 1987).

- Boron segregates to the grain boundaries in Ni_3Al . The amount of segregation increases as the bulk boron concentration in the alloy increases, provided that all boron is in solid solution. It is supposed that this segregation improves cohesion at the grain boundaries. Therefore, the segregation is required to produce the beneficial effect (Liu *et al.*, 1985; Briant and Taub, 1988; Huang *et al.*, 1985).
- There is an optimal boron concentration for producing the ductility improvements in the Ni-rich compounds (Taub *et al.*, 1984; Liu *et al.*, 1985). This effect can be observed from the data shown in Figure 7.
- Boron additions increase the hardness and yield strength of the compound (Huang *et al.*, 1984). The amount of solid-solution hardening produced by boron is consistent with it occupying an interstitial site in the matrix. It is also assumed that one reason why improvements in ductility begin to decrease when boron is added beyond some optimal concentration

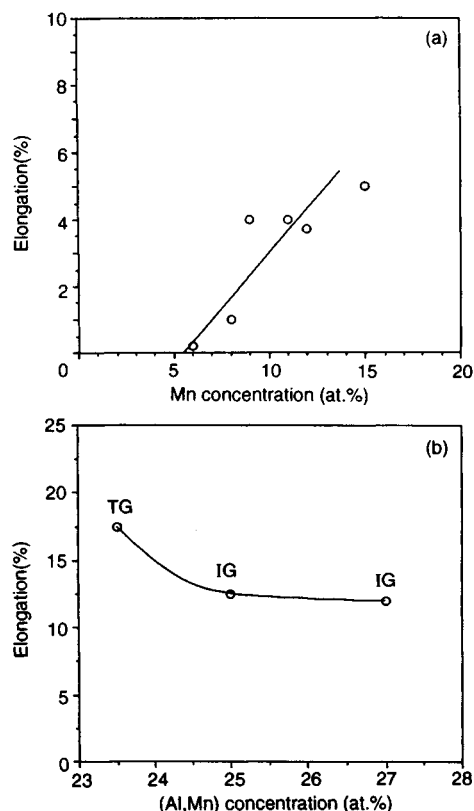


Figure 5. (a) The total elongation of $\text{Ni}_3(\text{Al,Mn})$ plotted as a function of manganese content. The data are taken from room-temperature tensile tests (From Masahashi *et al.*, 1988b). (b) The total elongation of $\text{Ni}_3(\text{Al}_{0.52}\text{Mn}_{0.48})_{100-x}$ plotted as a function of the (Al,Mn) content; IG denotes intergranular and TG transgranular fracture (from Takasugi *et al.*, 1987)

is because the matrix has become so hard that ductility is inherently limited (Liu *et al.*, 1985).

- The test environment affects ductility. This result is demonstrated by the data in Figure 9 (Masahashi *et al.*, 1988a; George *et al.*, 1992, 1993).

These fundamental observations have led to much additional research on the mechanisms by which boron provides this ductility improvement. They have addressed the questions of how boron exerts its beneficial effect and why this effect is so dependent on alloy stoichiometry. We will now consider these mechanisms.

One of the initial theories used to explain why the boron effect was observed only in Ni-rich compositions was that boron segregation was increased in the Ni-rich compounds (Liu *et al.*, 1985). The data used to make this point are shown in Figure 10(a). If one plots these

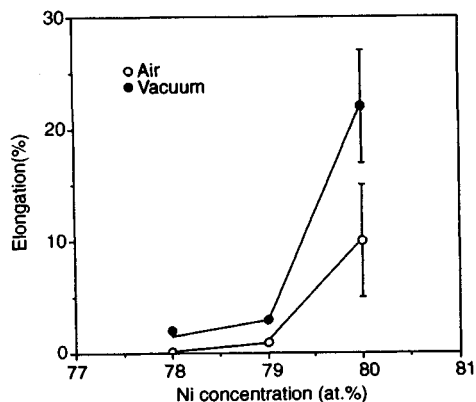


Figure 6. The effect of changes in nickel concentration on ductility in Ni_3Si compounds containing 9% titanium. The data were taken from room-temperature tensile tests performed in air and in vacuum (From Takasugi *et al.*, 1990)

data for boron grain-boundary composition as a function of ductility, as shown in Figure 10(b), it is clear that there can be a significant change in ductility without a significant change in boron concentration on the grain boundaries. Briant and Taub (1988) also examined this question and used hydrogen charging to increase the amount of intergranular fracture in Ni-rich samples. Their results are shown in Figure 11. In this figure the plastic strain to failure is plotted as a function of the boron grain-boundary concentration. The open circles represent data for Ni-rich alloys, and the full circles represent data for stoichiometric or Al-rich compositions. These results show that, for the same grain-boundary concentration of boron, a Ni-rich alloy

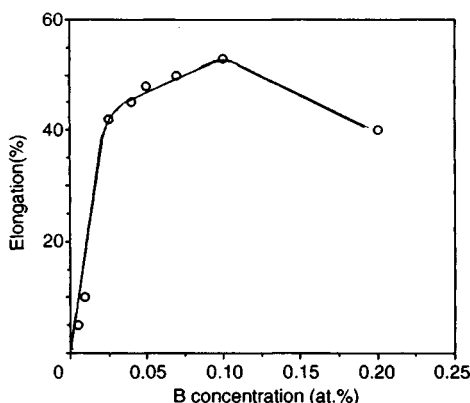


Figure 7. The effect of boron concentration on elongation of polycrystalline Ni_3Al . The data were obtained from room-temperature tensile tests run in air (From Liu *et al.*, 1985)

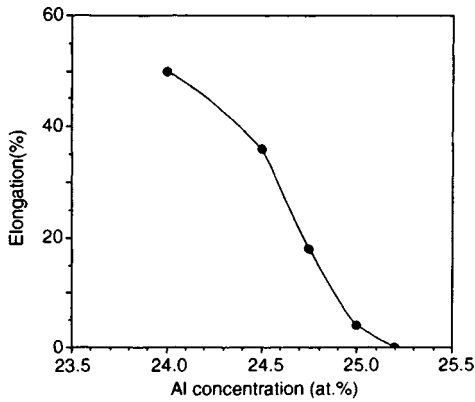


Figure 8. The effect of aluminum concentration on elongation in Ni_3Al . The alloys contained 0.05 wt.% boron. The data were obtained from room-temperature tensile tests run in air (From Liu *et al.*, 1985)

has more ductility than a stoichiometric or Al-rich alloy. This result is corroborated by atom probe/field ion microscopy measurements of boron grain-boundary segregation, which show that boron segregation does not depend on stoichiometry (Brenner and Hua, 1991).

Two other questions that have been raised are whether or not the nickel and aluminum concentrations at the grain boundary are different from the bulk concentration and whether they are affected by the presence of boron. If boron causes a significant change in the grain-boundary composition of the constituent elements, then that

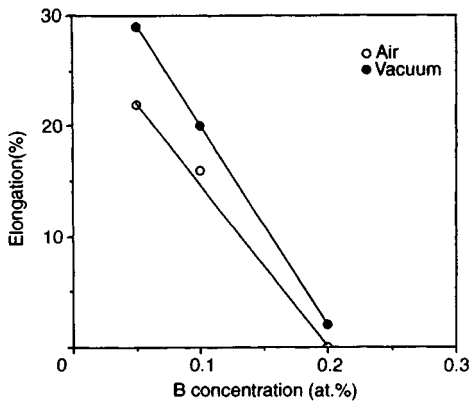


Figure 9. A comparison of the room-temperature elongation of Ni_3Al obtained from tests run in air and in vacuum plotted as a function of the boron concentration (From Masahashi *et al.*, 1988a)

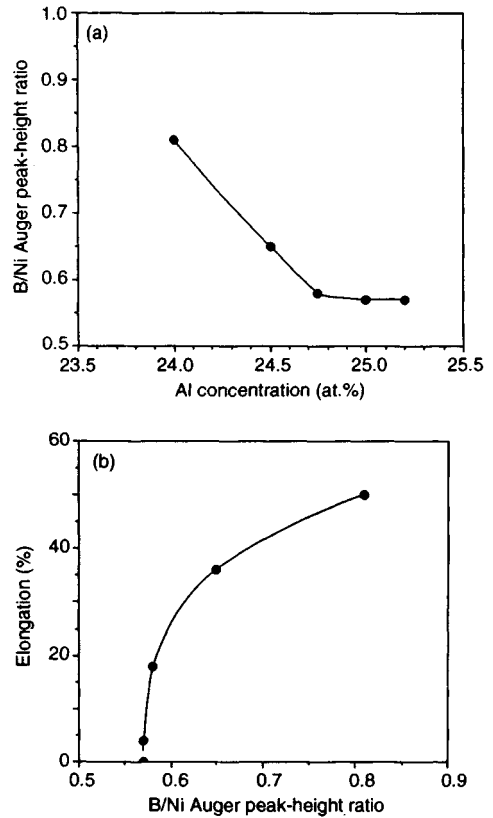


Figure 10. (a) The boron on the grain boundary plotted as a function of the aluminum concentration in Ni_3Al . The bulk boron concentration was 0.05 wt.%. The grain-boundary boron composition was obtained from Auger electron spectroscopy, and is expressed as a ratio of the boron 180 eV peak height to the nickel 102 eV peak height. These numbers are not atomic percents but, as the boron on the grain boundaries increases, this ratio should increase. (b) The boron on the grain boundary plotted as a function of the tensile elongation. The elongation data were obtained from room-temperature tensile tests run in air (From Liu *et al.*, 1985)

change could possibly explain why boron improves ductility. George *et al.* (1989) have examined this question, and their results are summarized in Table 3. The grain boundaries and the bulk have essentially identical compositions in the stoichiometric alloy. This result holds for both boron-containing and boron-free compounds. In the Ni-rich alloys the grain boundaries have less aluminum than the bulk, but this change again appears to be independent of the presence of boron. Therefore, we conclude that changes in bulk alloy composition may affect the grain-boundary composition of the constituent elements in the compound, but that this change is not affected by boron segregation. This result

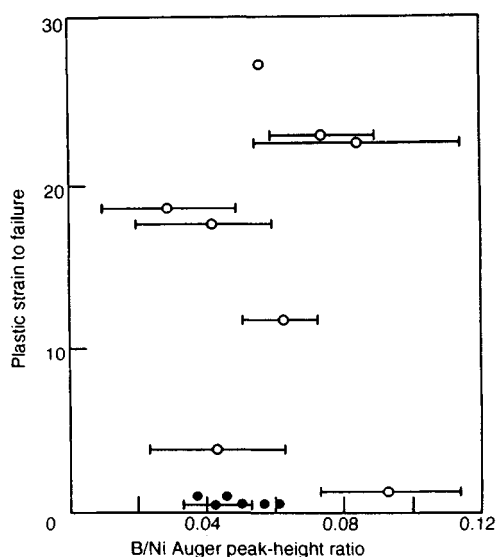


Figure 11. The boron on the grain boundaries plotted as a function of tensile elongation. The full circles represent data for alloys that were on stoichiometry or were Al-rich. The open circles represent data for alloys that were Ni-rich. The Auger peak height ratio used was B 180 eV/Ni 848 eV (From Briant and Taub, 1988)

is not in agreement with results obtained by analytical electron microscopy reported by Baker *et al.* (1988, 1990). They found that the presence of boron did not affect composition in Al-rich alloys, but that in stoichiometric and Ni-rich alloys the presence of boron produced very low aluminum concentrations at the grain boundaries. These results do not agree with the Auger data discussed above, and at present there is no explanation for this discrepancy. Although for a given sample there appears to be some correlation between low aluminum concentration and a low total number of X-ray counts taken in the analytical electron microscope, the fact that the authors used the same counting time for each condition should eliminate any effect of total counts on measured composition. Briant and Taub (1988) reported very high aluminum concentrations for the grain boundaries in the alloys that they studied. However, these concentrations were obtained using an Auger sensitivity factor that was too low. When their uncorrected data were compared with those obtained by George *et al.* (1989), the results from both studies were found to be in excellent agreement (Taub and Briant, 1990b).

Another possible mechanism that has been proposed to explain why boron improves ductility is that it enhances slip transmission across grain boundaries. The

Table 3. A comparison of the aluminum concentration on grain boundaries and bulk for Ni₃Al (Data taken from George *et al.*, 1989)

Alloy composition	Al on grain-boundary fracture surface (%)	Al on trans-granular fracture surface (%)
Ni-25Al	25.7 ± 3.2	25.1 ± 2.4
Ni-25.2Al-0.24B	24.9 ± 3	25.7 ± 1.6
Ni-24Al	22.4 ± 2.3	25.3 ± 3
Ni-24Al-0.24B	21.8 ± 2.2	24.9 ± 1.4

picture that is presented is that, when dislocations pile up at a grain boundary, yielding will take place across the grain boundary and relieve stress before fracture occurs. This stress relief could occur because the boron facilitates the transmission of the dislocations through the boundary or because it aids in nucleation of dislocations in the grain boundary. This possibility can be tested by measuring the yield strength as a function of grain size. The slope of this plot is known as the Hall-Petch slope. An increase in the slope indicates that slip transmission across grain boundaries is more difficult. Schulson and co-workers (Schulson *et al.*, 1986, 1991; Schulson and Baker, 1991; Weihs *et al.*, 1987) have pioneered this work on Ni₃Al, and their results are plotted in Figure 12. The results suggest that, for both the Ni-rich alloy and the stoichiometric alloy, the presence of boron lowers the slope of the line drawn through the data points, whereas in the Al-rich compound the slopes are identical. Schulson has interpreted these results to mean that boron enhances slip transmission across grain boundaries in the stoichiometric and Ni-rich compounds, and that this improvement in slip transmission is the mechanism by which boron improves ductility. This interpretation has been described on a more atomistic scale by Frost (1988), who suggested that, if boron lowers the difference between different ordering configurations at the boundary, then it could aid in the accommodation of stress concentrations by the motion of grain-boundary dislocations.

The next possible mechanism that we wish to consider is based on the following idea. It was noted above that in disordered alloys grain boundaries are usually strong and that an embrittling impurity is required to cause them to be weak fracture paths. Consequently, it has been thought that if the material near the grain boundaries became disordered in these compounds, an improvement in ductility would be realized. King and Yoo (1987) formally demonstrated that disorder would allow many additional dislocation reactions to occur at

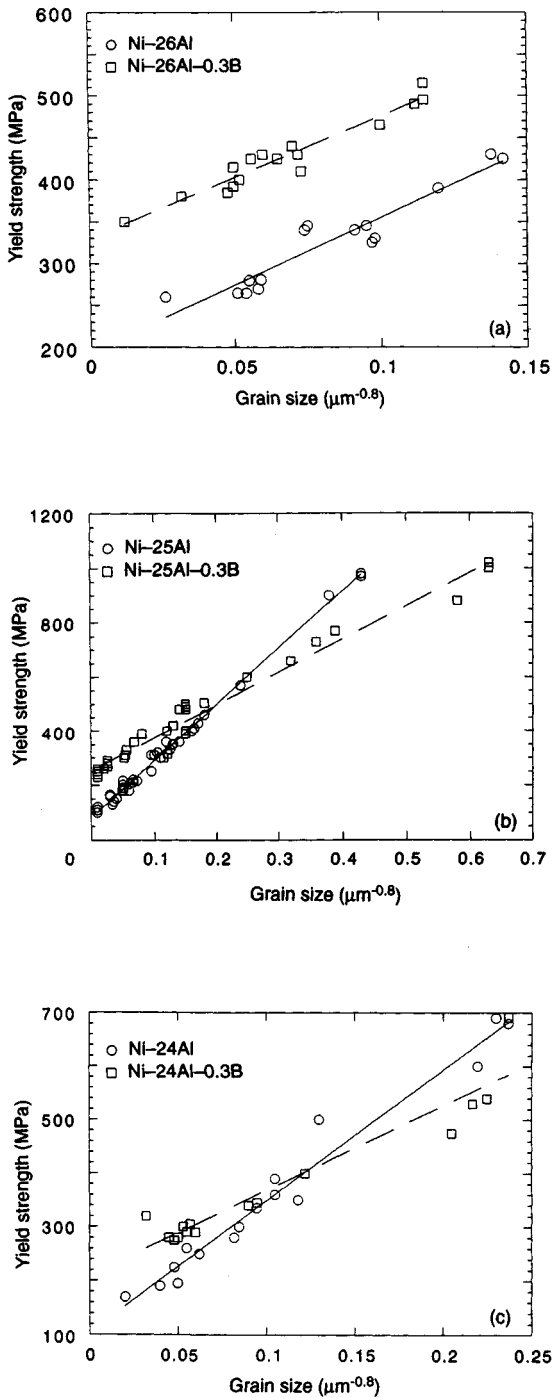


Figure 12. The room-temperature yield strength of Ni₃Al plotted as a function of grain size for (a) Al-rich alloys, (b) stoichiometric alloys, and (c) Ni-rich alloys (Data taken from Schulson and Baker, 1991)

the grain boundaries and thus aid in slip transmission across grain boundaries and improve ductility. One possible way for disorder to be created might be through boron segregation.

Whether or not disordering occurs at the grain boundaries and whether or not boron affects it have been hotly debated issues, primarily because this work must be done with high-resolution transmission electron microscopy. Although this technique is very powerful, the chance of observing artifacts in the images is very great unless extreme care is taken with the experiment and the interpretation. Mackenzie and Sass (1988) first reported that such disordered regions exist with an observation on a single grain boundary in Ni₃Al. Work by Baker *et al.* (1988, 1990) and Baker and Schulson (1989) also suggested that this disordered region existed, and they reported that in some cases the width of the region was as great as 20 nm. They also showed z-contrast images to support their interpretation, but they did not compare calculated and experimental images. Mills (1989) and Mills *et al.* (1991) have also examined this problem in some detail, and have carefully compared experimental images with calculated ones. In all cases they found that order existed to within one atomic layer of the grain boundary. Furthermore, these samples were taken from bi-crystals that were then mechanically tested so that one could be sure that the grain boundary that was examined in transmission electron microscopy was also the one that was tested for ductility. One can conclude from this study that a grain boundary that is completely ordered to within one atomic plane of the interface can also be ductile.

In conclusion, it would appear that there is no convincing evidence that boron produces its beneficial effect either by causing disorder over several atomic layers at the grain boundary, or by affecting the aluminum or nickel concentration at the grain boundary, or by changing its own segregation behavior with changes in alloy stoichiometry. However, there is evidence that it affects dislocation transmission within and across the grain boundary or dislocation generation at the boundary. This effect may well be related to the changes that boron causes in chemical bonding at the boundary (Frost, 1988). The changes in chemical bonding that boron must make, since it is not a hard sphere, might also simply improve cohesion across the grain boundary. With either of these mechanisms one must try to understand chemical bonding at the grain boundary and the effect of boron on it. These ideas will be discussed further in Section 5 of this chapter.

As a result of the significant improvement in ductility that boron produces in Ni₃Al, there has been a tendency

to put boron in all brittle intermetallic compounds to determine if it will improve their ductility. The results have been mixed. Boron appears to have the same effect in Ni_3Ga as it does in Ni_3Al (Takasugi *et al.*, 1987; Taub and Briant, 1987a). Its solubility in both compounds is similar, it segregates to the grain boundaries in both compounds, and as long as the compound is Ni-rich it improves ductility. Small additions of boron (<0.1 at. %) also improve ductility in Ni_3Si (Taub and Briant, 1987a). At boron concentrations greater than this amount, borides precipitate along the grain boundaries. These borides provide sites for crack nucleation and counteract the beneficial effect of the segregated boron. The solubility of boron in Ni_3Ge is so low that even at concentration of $<0.01\%$ borides form along the grain boundaries (Taub and Briant, 1987a). Therefore, little boron segregates and no improvement in ductility is observed. Finally, no boron segregation is observed in Pt_3Ga , and there is no improvement in ductility (Briant *et al.*, 1990).

Although boron can improve ductility in several L1_2 compounds, its beneficial effect can also be counteracted. We mentioned above that boron can increase the hardness of these compounds and that, if boron is added above some optimal level, ductility will begin to decrease because of this increased strength. Sulfur additions have also been shown to counteract the improvements produced by boron (Taub *et al.*, 1986b). Sulfur is a strong embrittling element at grain boundaries in many metallic systems (Mulford, 1983). It segregates to the grain boundaries in Ni_3Al and lowers cohesion across the grain boundary, even in the presence of boron. It does not appear to compete with boron for grain-boundary sites (Briant and Taub, 1988); rather, it simply destroys in some way the improved bonding produced by boron. Finally, Briant and Taub (1989) showed that ductility will be destroyed if boron is added in concentrations beyond its solubility limit, so that borides begin to precipitate along the grain boundaries. The grain-boundary borides help in either the nucleation and/or the propagation of the intergranular crack.

3. B2 (cP2) Compounds

Another class of intermetallic compounds that has received considerable attention are those with the crystal structure designated as B2. Figure 2(b) shows that this structure is analogous to the body-centered cubic structure of disordered alloys. These compounds have the stoichiometry AB, where one atom type is at the center of the unit cell and the other is at the eight corners.

Within this class of compounds, NiAl and FeAl have been the most thoroughly studied. Therefore, our discussion will center on them.

Single crystals of NiAl have been reported to exhibit elongations on the order of 1–2%, but this value is very dependent on orientation (Darolia, 1991; Wasilewski *et al.*, 1967). Recent work has also shown that small additions of iron, molybdenum, and gallium provide some additional ductility to the single crystals (Darolia, 1991). Polycrystalline samples of NiAl show a very small amount of ductility (1–2%) if the composition is precisely on stoichiometry. Deviations from stoichiometry will induce extreme brittleness, and in all cases, both on and off stoichiometry, the fracture is intergranular (Vedula *et al.*, 1989; George and Liu, 1990). Because boron counteracts grain-boundary brittleness in Ni_3Al , work was performed to determine if it would produce a similar improvement in NiAl. The results are summarized in Table 4. Boron segregates to the grain boundaries in NiAl and causes the fracture mode to become transgranular cleavage (George and Liu, 1990). However, boron also increases the strength of this compound significantly, and the material shows no tensile elongation. The increased strength counteracts any potential improvement produced by the boron segregation and makes the material more brittle.

In addition to boron, George and Liu (1990) have investigated the effects of carbon and beryllium on the ductility of NiAl. Carbon does not segregate to the grain boundaries, and the fracture mode of carbon-doped samples remains intergranular. The results in Table 4 show that carbon also raises the yield strength of NiAl, and that any ductility possessed by pure NiAl is lost. Beryllium additions have no effect on the fracture of NiAl. In summary, no additive elements have been found that improve ductility of polycrystalline NiAl.

FeAl can exist over a relatively wide range of stoichiometry, and some of the early reported results

Table 4. Room-temperature tensile properties of NiAl with and without additions of trace elements (except where noted data taken from George and Liu, 1990)

Composition	Yield strength (MPa)	Ultimate tensile strength (MPa)	Tensile elongation (%)
Ni–50Al	154	229	2.2, 2.0 ^a
NiAl + 300 wppm B		329	0
NiAl + 300 wppm C		336	0
NiAl + 500 wppm Be	178	307	3.0

^aVedula *et al.* (1989).

Table 5. Room-temperature tensile properties for FeAl tested in air (except where noted data taken from Liu and George, 1991)

Composition	Yield strength (MPa)	Tensile strength (MPa)	Elongation (%)	Fracture mode ^a
Fe-35Al	347	442	3.4	C
Fe-36.5Al	360	412	2.2	C
Fe-40Al	390	406	1.2	IG
Fe-43Al	229	229	<0.3	IG
Fe-48.5Al		530	0	IG ^b
Fe-40Al + 300 wppm B	391	577	4.3	C
Fe-46Al + 0.7B		972	0	C ^b

^aIG, intergranular; C, cleavage.

^bFrom Crimp and Vedula (1986).

for the binary alloy seemed to be contradictory. Recently, Liu and George (1991) examined the effect of stoichiometry on fracture mode and found that, as the aluminum concentration increases from 30 to 50%, the fracture mode changes from cleavage to intergranular. Their results are summarized in Table 5. Crimp and Vedula (1986) and Liu and George (1991) have also found that boron additions in the higher-aluminum-content compounds can change the fracture mode from intergranular to cleavage. These results for the boron-containing compounds are also summarized

in Table 5. They are quite similar to those reported for NiAl. Boron additions cause the fracture mode to change to cleavage, but they also cause a significant increase in yield strength and very little improvement in ductility.

Liu *et al.* (1989) have reported that the test environment plays a significant role in determining the ductility of FeAl. Their first report was for an Fe-36.5% Al alloy, and the results are shown in Figure 13. Tensile elongation was the least when the material was tested in air or water vapor. Tests in Ar + H₂, oil, and vacuum gave intermediate elongations, and tests in dry oxygen gave the greatest amount of elongation. They also found that, as the elongation increased, the fracture mode changed from transgranular cleavage to intergranular fracture. They attributed the detrimental effect of testing in air and water vapor to hydrogen. Liu and George (1991) continued this work and examined four different aluminum concentrations. Their results are summarized in Table 6. At the two aluminum concentrations that fractured by transgranular cleavage in air, the effects were similar to those described above. However, for the samples that contained more aluminum and failed by intergranular fracture in air, the effect of test environment on elongation was much less. A boron-doped alloy containing 40% aluminum, which failed by transgranular cleavage in air, did show

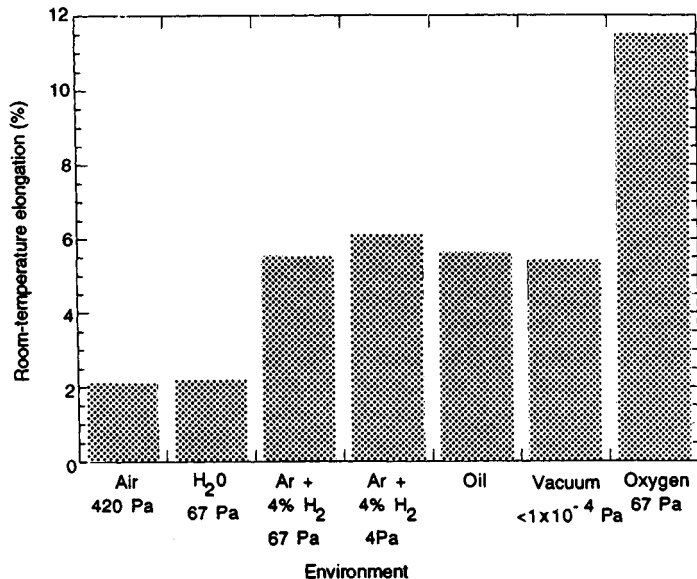


Figure 13. The effect of environment on the elongation of Fe-36.5% Al alloy. The abscissa gives the test environment and the ordinate the room-temperature elongation (Data taken from Liu *et al.*, 1989)

Table 6. The effect of test environment on room-temperature ductility of FeAl (data taken from Liu and George, 1991)

Composition	Test environment	Yield strength (MPa)	Tensile strength (MPa)	Elongation (%)	Fracture mode ^a
Fe-35Al	Air	347	442	3.4	C
Fe-35Al	Air/oil coating	344	570	7.4	—
Fe-35Al	Vacuum	341	558	7.3	C
Fe-35Al	Oxygen	345	785	18.1	C + IG
Fe-36.5Al	Air	360	412	2.2	C
Fe-36.5Al	Air/oil coating	356	524	5.6	—
Fe-36.5Al	Vacuum	351	496	5.4	C + IG
Fe-36.5Al	Oxygen	360	805	17.6	Mostly IG
Fe-40Al	Air	390	406	1.2	IG
Fe-40Al	Air/oil coating	402	466	2.4	IG
Fe-40Al	Oxygen	402	537	3.2	IG
Fe-43Al	Air	229	229	<0.3	IG
Fe-43Al	Air/oil coating	313	313	<0.3	IG
Fe-43Al	Oxygen	327	327	<0.3	IG
Fe-40Al + 300 wppm B	Air	391	577	4.3	C
Fe-40Al + 300 wppm B	Air/oil coating	398	751	8.5	C
Fe-40Al + 300 wppm B	Oxygen	392	923	16.8	C

^aIG, intergranular; C, cleavage.

a significant improvement in ductility when tested in oxygen, but in contrast to the results on Fe-36.5% Al the fracture mode remained transgranular.

These results are certainly intriguing, but they are also puzzling. As mentioned above, the environment must affect crack nucleation, since once the crack is propagating it seems unlikely that the environmental constituent causing the loss in ductility could keep up with it and continue to cause its damaging effect. Given that assumption, one must explain why this improvement in the lower-aluminum alloys is associated with a change from transgranular to intergranular fracture, whereas in the higher-aluminum alloys the fracture is brittle intergranular in all environments and the ductility is unaffected by the environment. Furthermore, when boron is present in the higher-aluminum alloys, the improved ductility is associated with a transgranular fracture, as opposed to intergranular fracture in the boron-free alloys. More detailed mechanistic ideas need to be worked out to explain these results.

Another alloy that has been investigated in some detail is AlRu (Fleischer *et al.*, 1991). The binary compound is very brittle, but, unlike the case with NiAl and FeAl, boron additions improve toughness, and this improvement is greater for the

Al-rich compositions of this compound. Auger electron spectroscopy has shown that, for compounds with the Al-rich compositions, the aluminum concentration at the grain boundary is greater than its bulk composition.

4. Other Intermetallic Compounds

In addition to the research on L1₂ and B2 compounds described above, ductility and fracture mode have been reported on compounds with other crystal structures. We have chosen not to discuss these alloys in depth because the research on them has not been as broad and because most of the important features of brittle fracture in these compounds have already been described by considering the other systems. Table 7 summarizes these studies. (Note that in the table a crystal structure that is given in parentheses is the structure of the base compound but alloying additions have caused a change in the structure to the one that is listed first.) The main point to note is that, just as with the L1₂ and B2 compounds, these compounds tend to be brittle at room temperature and the fracture is either cleavage or intergranular. Attempts to alloy these compounds have in some cases produced significant

Table 7. Ductility and fracture mode data for various intermetallic compounds

Compound	Crystal structure ^a	Elongation	Fracture mode ^b	References
Fe ₃ Al	D0 ₃	4.8 4 8	C C C	McKamey <i>et al.</i> (1991), Kear (1986), Mendiratta <i>et al.</i> (1987)
Fe ₆₉ Al ₃₁	D0 ₃	5.6	C	Mendiratta <i>et al.</i> (1987)
Fe ₇₀ Al ₂₈ Cr ₂	D0 ₃	9.4	C	McKamey <i>et al.</i> (1989)
Fe _{66.85} Al ₂₈ Cr ₅ Zr _{0.1} B _{0.05}	D0 ₃	16.4	C	McKamey <i>et al.</i> (1991)
TiAl	L1 ₀	> 3.0		Murata <i>et al.</i> (1992)
Al ₆₆ Ti ₂₃ Fe ₆ V ₅	L1 ₂ (D0 ₂₂)	0	C	George <i>et al.</i> (1990)
Al ₃ Ti + Ni, Pd, or Mn + V	L1 ₂ (D0 ₂₂)	0	C	George <i>et al.</i> (1991)
Al ₃ Ti + Cr, Fe	L1 ₂ (D0 ₂₂)	0.5	C	George <i>et al.</i> (1991)
Al _{69.5} Fe _{5.5} Zr ₂₅	L1 ₂ (D0 ₂₃)		IG + C	Schneibel and Porter (1989)

^aA crystal structure in parentheses is that of the base compound; alloying has caused a change to the structure listed first.

^bIG, intergranular; C, cleavage.

improvements in ductility (McKamey *et al.*, 1989, 1991).

5. Models for Brittle Fracture

In all of the results that were presented above, one clear trend seems to stand out. Intermetallic compounds, at least in their polycrystalline, single-phase form, tend to fail with a brittle fracture mode. The actual tensile elongations associated with these fractures may be greater than 20%, but the fracture mode still appears to be brittle. The question that we now wish to consider is why brittle fracture modes are observed.

Most of the modeling studies have dealt with intergranular fracture, so we will begin our discussion with it. As mentioned earlier in the text, intergranular fracture in disordered alloys can almost always be attributed to the presence of an embrittling impurity that segregates to the grain boundaries and weakens them. Examples of these impurities are sulfur, phosphorus, tin, and antimony. Research addressing the question of why these impurities cause embrittlement suggests the following mechanism (Losch, 1979; Messmer and Briant, 1982; Briant and Messmer, 1980; Eberhart *et al.*, 1984; Painter and Averill, 1987). The embrittling impurities are electronegative with respect to the host metal. They draw electronic charge off the host metal and onto themselves. This electronic charge transfer weakens the metal-metal bonds at the grain boundaries, and this bond weakening gives rise to the grain-boundary fracture. Calculations have also suggested that boron would not be electronegative with respect to nickel, and that it might contribute electronic charge to the grain boundaries and thus enhance cohesion (Messmer and Briant, 1982). Although these models suggest that electronegativity differences and electronic

charge transfer are at the heart of this embrittlement, it was pointed out in this work that these concepts were developed based on full-scale quantum-mechanical calculations. Existing tables for electronegativity would not be useful in predicting embrittlement, especially for transition metals.

Most of the work that has sought to explain intergranular fracture in intermetallic compounds has drawn on these models (Takasugi and Izumi, 1985b, 1991; Taub *et al.*, 1986a; Taub and Briant, 1987a; Izumi and Takasugi, 1988; Briant, 1990). However, the models have had to be adapted to the fact that intermetallic compounds have grain boundaries that are intrinsically weak. Fracture will occur along them in the absence of impurities, and, as shown by the data in Table 3, the composition of the boundaries can be identical to that of the bulk. Both Izumi and Takasugi (1988) and Briant (1990) suggested that in ordered intermetallic compounds there is electronic charge transfer between the two elements making up the compound, and that this electronic charge transfer should lead to a directionality in the bonds. Therefore, at a grain boundary where the bonding pattern must be disrupted, one would have regions of electronic charge depletion at points where two electropositive elements attempted to form a bond across a boundary and regions of electronic charge excess at points where two electronegative elements tried to form a bond. Also, because the bonding in these compounds should be more directional than in a disordered alloy, the geometric distortions at the grain boundary would make the bonds between the electropositive and electronegative elements less favorably oriented. All of these factors should lower cohesion across the grain boundary. It was also suggested that the beneficial effects of boron and changes in stoichiometry could be explained through these general ideas. As mentioned above, quantum-mechanical

calculations have shown that boron contributes electronic charge to the grain boundaries in nickel, and therefore its presence might supply electronic charge in regions where two electropositive elements meet at the grain boundary. Most of the ductile binary compounds in the $L1_2$ series are those which are composed of two transition metals (Co_3Ti , Cu_3Au , Ni_3Fe , Ni_3Mn , Cu_3Pd). One would expect little charge transfer between compounds made up of these elements, and results show that changes in stoichiometry that increase the transition-metal content of the alloy usually increase ductility.

Several attempts were made to quantify these arguments using various atomic properties. Taub *et al.* (1986a) and Taub and Briant (1987a) used the Pauling electronegativity scale to explain the effect of boron in Ni_3X , where $\text{X} = \text{Al}$, Ga , Si , or Ge . As noted above, boron provides the greatest improvement in Ni_3Al and Ni_3Ga , less in Ni_3Si , and least in Ni_3Ge . Their results suggested that at an average electronegativity value of 1.9 the materials became ductile. Takasugi and Izumi (1985b, 1991) found that electronegativity differences did not explain very well the brittleness differences that they observed, when they included compounds that were composed entirely of transition metals. They found that valence differences explained their results better, and they suggested that, as the difference in valence between the two elements decreased, more ductility should be observed. Other schemes have also been proposed but exceptions can be found in all cases, and the reason for this is quite clear. It is impossible to assign a single number, such as a value of electronegativity or valence, to describe a complex phenomenon such as chemical bonding. Transition metals, in particular, can take on different valences and bonding characteristics as their environment is changed, so the idea of using a table of numbers that would work in all cases is unreasonable. Instead, one must resort to full-scale quantum-mechanical calculations. Though they are time-consuming and expensive, they do hold out the only possibility for giving us insight into these problems.

Schulz and Davenport (1992) have recently reported the results of quantum-mechanical calculations on FeAl , CoAl , and NiAl . They used linear augmented Slater-type orbitals and solved for the bulk electronic structure within the local-density-functional approximation. They focused on bulk properties rather than grain boundaries, so their results would be specifically applicable to single crystals. However, some of the concepts that emerged from their study help us to reconsider the problem of grain-boundary embrittlement, because they give us general information about the electronic charge transfer

between aluminum and the transition-metal atoms. Among the three compounds that they investigated, FeAl is the least brittle in its single-crystal form and CoAl is the most brittle. Thus we might expect to see some changes in bonding as we proceed from FeAl to NiAl to CoAl .

The results of the calculations were very surprising. First, Schulz and Davenport (1992) found that there was little electronic charge transfer in these compounds from aluminum to any of the three transition metals, and that there was no correlation between what little charge transfer occurred and brittleness of the compound. In fact, both the electropositive aluminum and the electronegative transition metal appeared to draw electronic charge out of the interstitial regions of the structure. They found that there was a directional component to the bonding with a build-up of electrons along the transition metal-aluminum axis. However, it could not be used to distinguish a more brittle compound from a less brittle one.

With this new information we should now rethink the issue of grain-boundary embrittlement. One cannot use the idea of electronic charge transfer as originally thought. Given that both elements may tend to pull electronic charge out of the interstitial region, one could argue that the grain-boundary interstices might be depleted of electronic charge and that this depletion would tend to cause embrittlement. In regions where atoms are found to take up positions with less than the equilibrium distance, there could be added repulsion because of the excess electronic charge on them. The other factor that could play a role here is that the boundary, with its breakdown of geometric order, would cause a breakdown of directional bonding and become weak relative to the matrix. However, these are only general statements, and calculations that specifically consider grain-boundary geometries are required.

All of this discussion has been based on the idea that boron would act primarily by improving cohesion across the grain boundary. It should be noted that these ideas are also completely consistent with boron allowing more movement of grain-boundary dislocations or making the generation of dislocations in the boundary occur more easily and thus aiding in the transfer of slip across the grain boundaries as proposed by Schulson *et al.* (1986, 1991) and Frost (1988). The reason that metals are so ductile derives from their electronic configuration and the fact that electrons can be easily shared between atoms, probably by their movement through interstitial regions of the lattice. If ordering pulls electronic charge out of these interstices, then it would decrease ductility.

An element that supplies electrons and segregates to the grain boundary might contribute electrons to the grain-boundary interstices and thus aid in grain-boundary dislocation motion.

6. Conclusions

There are three different categories of summary statements that can be made concerning this work. The first is the specific conclusions that can be drawn, based on the work that has been published. The second is the type of work that needs to be done. The third is the appropriate way to carry out this research so that the results will be meaningful in the broad context of intermetallic compounds. We will consider each of these in turn.

The primary conclusion to be drawn from the many studies that have been published is that the fracture mode in most intermetallic compounds tends to be one that we associate with brittle fracture and that the ductility of these compounds is often quite limited. However, examples are reported in this chapter where the fracture appears to be brittle but the tensile elongation can be greater than 20%. With alloying, the elongation may be as high as 50%. These alloying additives are often specific to particular compounds. Stoichiometry and test environment can have a major effect on the measured ductility. In general, in compounds where one component is a transition metal, increasing that component increases ductility.

Next we address areas for future research. One surprising point that comes out of reviewing this field is how few compounds have been investigated over their entire range of stoichiometry. Given that stoichiometry can have a major effect on ductility, we need to have this fundamental information as a baseline for many of the other studies that have been carried out. Individual reports of ductility on individual compositions are often hard to interpret and put into the correct context. The role of environment on test results needs to be investigated much more thoroughly, as well as the effect of processing history. The results described above suggest that much of the data reported in the literature may have been obtained under poorly controlled conditions, if the moisture content of the laboratory air can have the effect that these results imply. Further quantum-mechanical calculations are also required to obtain a better description of fracture based on differences in chemical bonding.

Finally, we consider the proper way in which experiments should be carried out. The most successful

studies of fracture in disordered alloys have taken a microstructural approach to the problem. They determine through various techniques the initiation sites for fracture and then determine how the crack propagates through the matrix. Such studies are not difficult to perform and usually involve careful optical and scanning electron microscopy on fracture surfaces and on samples tested to just below the fracture point. Given that there is a very complete literature on this topic for disordered alloys, it is surprising that essentially no studies of this type have been performed on intermetallic compounds. These will be essential for us to describe fully the fracture processes in these alloys. To make comparisons between alloys one needs to run tensile tests and to measure elongations. Samples should be tested in a vacuum to eliminate any environmental effects. One should also test alloys of the composition specified and not add small amounts of third elements to improve processing and then forget about them in the discussion. This rather cavalier practice has been all too common in the past. The results presented by George *et al.* (1992b), which show the great improvement in the ductility of Ni₃Al when 0.26% Zr was added, underscore this point. Finally, for the calculations, it is clear that quantum mechanics will be required, and that through these calculations we can eventually describe the fracture process at a new level of microstructure.

7. References

- Aoki, K., and Izumi, O. (1979). *Nippon Kinzaku Gakkaishi*, **43**, 1190.
- Baker, I., and Schulson, E. M. (1989). *Scripta Metall.*, **23**, 1883.
- Baker, I., Schulson, E. M., and Michael, J. R. (1988). *Phil. Mag.*, **57**, 379.
- Baker, I., Schulson, E. M., Michael, J. R., and Pennycook, S. J. (1990). *Phil. Mag.*, **B62**, 659.
- Brenner, S. S., and Hua, M.-J. (1991). *Scripta Metall. Mater.*, **25**, 1271.
- Briant, C. L. (1985) *Metallurgical Aspects of Environmental Failures*. Elsevier, Amsterdam.
- Briant, C. L. (1988). *J. Physique Coll.*, **49**, C5, 3.
- Briant, C. L. (1990). *Metall. Trans.*, **21A**, 2339.
- Briant, C. L., and Messmer, R. P. (1980). *Phil. Mag.*, **B42**, 569.
- Briant, C. L., and Taub, A. I. (1988). *Acta Metall.*, **36**, 2761.
- Briant, C. L., and Taub, A. I. (1989). *Mater. Res. Soc. Symp. Proc.*, **133**, 281.
- Briant, C. L., Taub, A. I., and Hall, E. L. (1990). *J. Mater. Res.*, **5**, 2841.
- Chiba, A., Hamada, S., and Watanabe, S. (1991). *Acta Metall. Mater.*, **39**, 1799.
- Copley, S. M., and Kear, B. H. (1967). *Trans. TMS AIME*, **239**, 922.

- Crimp, M. A., and Vedula, K. (1986). *Mater. Sci. Eng.*, **78**, 193.
- Darolia, R. (1991). *J. Metals*, **43**(3), 44.
- Davies, R. G., and Stoloff, N. S. (1965). *Trans. TMS AIME*, **233**, 714.
- Eberhart, M. E., Latanision, R. M., and Johnson, K. H. (1984). *Acta Metall.*, **32**, 955.
- Fleischer, R. L., Field, R. D., and Briant, C. L. (1991). *Metall. Trans.*, **22A**, 129.
- Frost, H. J. (1988). *Acta Metall.*, **36**, 2199.
- George, E. P., and Liu, C. T. (1990). *J. Mater. Res.*, **5**, 754.
- George, E. P., Liu, C. T., and Padgett, R. A. (1989). *Scripta Metall.*, **23**, 979.
- George, E. P., Horton, J. A., Porter, W. D., and Schneibel, J. H. (1990). *J. Mater. Res.*, **5**, 1639.
- George, E. P., Pope, D. P., Fu, C. L., and Schneibel, J. H. (1991). *ISIJ Intl.*, **31**, 1063.
- George, E. P., Liu, C. T., and Pope, D. P. (1992). *Scripta Metall. Mater.*, **27**, 365.
- George, E. P., Liu, C. T., and Pope, D. P. (1993). *Mater. Res. Soc. Symp. Proc.*, **288**, 941.
- Huang, S. C., Taub, A. I., and Chang, K. M. (1984). *Acta Metall.*, **32**, 1703.
- Huang, S. C., Taub, A. I., Chang, K.-M., Briant, C. L., and Hall, E. L. (1985). *Proc. 5th Intl. Conf. on Rapidly Quenched Metals* (eds S. Steeb, and H. Warlimont). North-Holland, Amsterdam, p. 1407.
- Huang, S. C., Briant, C. L., Chang, K.-M., Taub, A. I., and Hall, E. L. (1986). *J. Mater. Res.*, **1**, 60.
- Izumi, O., and Takasugi, T. (1988). *J. Mater. Res.*, **3**, 426.
- Kear, W. R. (1986). *Metall. Trans.*, **17A**, 2298.
- Khadkikar, P. S., Vedula, K., and Shabel, B. S. (1987). *Metall. Trans.*, **18A**, 425.
- King, A. H., and Yoo, M. H. (1987). *Scripta Metall.*, **21**, 1115.
- Liu, C. T., and George, E. P. (1991). *Mater. Res. Soc. Symp. Proc.*, **213**, 527.
- Liu, C. T., White, C. L., and Horton, J. A. (1985). *Acta Metall.*, **33**, 213.
- Liu, C. T., Lee, E. H., and McKamey, C. G. (1989). *Scripta Metall.*, **23**, 875.
- Losch, W. (1979). *Acta Metall.*, **27**, 1995.
- Mackenzie, R. A. D., and Sass, S. L., (1988). *Scripta Metall.*, **22**, 1807.
- Masahashi, N., Takasugi, T., and Izumi, O. (1988a). *Acta Metall.*, **36**, 823.
- Masahashi, N., Takasugi, T., and Izumi, O. (1988b). *Metall. Trans.*, **19A**, 345.
- McKamey, C. G., Horton, J. A., and Liu, C. T. (1989). *J. Mater. Res.*, **4**, 1156.
- McKamey, C. G., De Van, J. H., Tortinelli, P. F., and Sikka, V. K. (1991). *J. Mater. Res.*, **6**, 1779.
- McMahon, C. J., Jr, and Cohen, M. (1965). *Acta Metall.*, **13**, 591.
- Mendiratta, M. G., Ehlers, S. K., Chatterjee, D. K., and Lipsitt, H. A. (1987). *Metall. Trans.*, **18A**, 283.
- Messmer, R. P., and Briant, C. L. (1982). *Acta Metall.*, **30**, 457.
- Mills, M. J. (1989). *Scripta Metall.*, **23**, 2061.
- Mills, M. J., Goods, S. H., Foiles, S. M., and Whetstone, J. R. (1991). *Scripta Metall. Mater.*, **25**, 1283.
- Mulford, R. A. (1983). *Metall. Trans.*, **14A**, 865.
- Mulford, R. A., and Pope, D. P. (1973). *Acta Metall.*, **21**, 1375.
- Murata, Y., Morinaga, M., and Takeda, Y. (1992). *Mater. Trans. Japan Inst. Metals*, **33**, 419.
- Painter, G. S., and Averill, F. W. (1987). *Phys. Rev. Lett.*, **58**, 234.
- Schneibel, J. H., and Porter, W. D. (1989). *Mater. Res. Soc. Symp. Proc.*, **133**, 335.
- Schulson, E. M. (1984). *Int. Metals Rev.*, **29**, 195.
- Schulson, E. M., and Baker, I. (1991). *Scripta Metall. Mater.*, **25**, 1253.
- Schulson, E. M., Weihs, T. P., Baker, I., Frost, H. J., and Horton, J. A. (1986). *Acta Metall.*, **34**, 1395.
- Schulson, E. M., Xu, Y., Munroe, P. R., Guha, S., and Baker, I. (1991). *Acta Metall. Mater.*, **39**, 2971.
- Schulz, P., and Davenport, J. (1992). *Scripta Metall. Mater.*, **27**, 629.
- Takasugi, T., and Izumi, O. (1985a). *Acta Metall.*, **33**, 1247.
- Takasugi, T., and Izumi, O. (1985b). *Acta Metall.*, **33**, 1259.
- Takasugi, T., and Izumi, O. (1991). *Scripta Metall. Mater.*, **25**, 1243.
- Takasugi, T., George, E. P., Pope, D. P., and Izumi, O. (1985). *Scripta Metall.*, **19**, 551.
- Takasugi, T., Masahashi, N., and Izumi, O. (1987). *Acta Metall.*, **35**, 381.
- Takasugi, T., Nagashima, M., and Izumi, O. (1990). *Acta Metall.*, **38**, 747.
- Taub, A. I., and Briant, C. L. (1987a). *Acta Metall.*, **35**, 1597.
- Taub, A. I., and Briant, C. L. (1987b). *Mater. Res. Soc. Symp. Proc.*, **81**, 343.
- Taub, A. I., and Briant, C. L. (1990a). *Metall. Trans.*, **20A**, 2025.
- Taub, A. I., and Briant, C. L. (1990b). In *High Temperature Aluminides and Intermetallics* (eds S. H. Whang, C. T. Liu, D. P. Pope, and J. O. Steigler). TMS AIME, Warrendale, PA, p. 153.
- Taub, A. I., Huang, S.-C., and Chang, K.-M. (1984). *Metall. Trans.*, **15A**, 399.
- Taub, A. I., Briant, C. L., Huang, S.-C., Chang, K.-M., and Jackson, M. R. (1986a). *Scripta Metall.*, **20**, 129.
- Taub, A. I., Chang, K.-M., and Huang, S. C. (1986b). *Proc. ASM Conf. on Rapidly Solidified Material*. American Society for Metals, Metals Park, OH, p. 297.
- Vedula, K., Hahn, K. H., and Boulogne, B. (1989). *Mater. Res. Soc. Symp. Proc.*, **133**, 299.
- Vidoz, A. E., Lazarevic, D. P., and Cahn, R. W. (1963). *Acta Metall.*, **11**, 17.
- Wasilewski, R. J., Butler, S. R., and Hanlon, J. E. (1967). *Trans. Metall. Soc. AIME*, **239**, 1357.
- Weihs, T. P., Zinoviev, V., Viens, D. V., and Schulson, E. M. (1987). *Acta Metall.*, **35**, 1109.
- Westbrook, J. H., and Wood, D. L. (1964). *J. Nucl. Mater.*, **12**, 208.
- Wood, D. L., and Westbrook, J. H. (1962). *Trans. AIME*, **224**, 1024.

Chapter 3

Plastic Deformation

Gerhard Sauthoff

Max-Planck-Institut für Eisenforschung GmbH, D-4000 Düsseldorf, Germany

1. Introduction

Much of the present general and still-growing interest in intermetallics results from their potential for applications as structural high-temperature materials (see e.g. Liu *et al.*, 1990; Engell *et al.*, 1991; Sauthoff, 1994). For such applications, a candidate phase must have sufficient strength at the service temperature, which means a sufficient creep resistance, too. The creep resistance scales inversely with the diffusion coefficient and directly with the shear modulus, and both the diffusion coefficient and the shear modulus scale with the melting temperature T_m , as will be discussed later. There are many intermetallics with high melting points; indeed, there are some whose melting points exceed those of the constituent elements, as is exemplified by the familiar NiAl. For conventional high-temperature materials, the maximum service temperature is about (rarely above) $\frac{3}{4}T_m$, i.e. candidate phases should have melting temperatures at or above 1600 °C for service temperatures of 1100 °C or higher.

Density is an additional parameter of high importance. For moving parts, the ratio of rupture strength and specific weight is decisive. This ratio is called 'rupture length' and is about 15 km for advanced superalloys. Phases that contain light elements—e.g. Ti, Al, Si, Mg—may have such a low density that they compare favorably with conventional alloys in spite of lower strength or restricted service-temperature range.

The major problem of strong intermetallics is their brittleness, which, however, should be less severe than that of ceramics because of the different types of atomic bonding. A closer look indeed shows that the

deformability of intermetallics is between those of metals and ceramics, as is exemplified by Figure 1. The intermetallic NiAl, which is a candidate phase for high-temperature applications, softens with rising temperature at about half the melting temperature, which is about the range of covalent Si and is higher than that of the ceramic Al₂O₃. However, the brittle-to-ductile transition of NiAl is at about $0.4T_m$, whereas this transition only occurs above $0.8T_m$ for Si and Al₂O₃. Thus NiAl bridges the gap between metals and ceramics.

Plastic deformation is more difficult in intermetallics than in metals because of the stronger atomic bonding, the ordered atomic distribution, and their possibly less symmetric crystal lattices (Paufler, 1985). Experience indeed shows that the brittleness of intermetallic phases increases with decreasing lattice symmetry and increasing unit-cell size (Paufler, 1976). Thus intermetallic phases with high crystal symmetry—possibly cubic phases—and small unit cells are preferred for developments of structural materials. Candidate phases of interest (in particular, nickel aluminides, titanium aluminides, and iron aluminides) show such simple crystal structures—L1₂ (cP4, Cu₃Au type), L1₀ (tP4, CuAu type), D0₂₂ (tI8, Al₃Ti type), B2 (cP2, CsCl type), D0₃ (cF16, BiF₃ type), L2₁ (cF16, Cu₂AlMn type)—which are produced by atomic ordering in the f.c.c. or b.c.c. lattices and are cubic or only slightly tetragonal (see e.g. Sauthoff, 1989; and Chapters 2–10 by Liu and Pope, by Miracle and Darolia, by Huang and Chesnutt, by Banerjee, by Schulson, by Yamaguchi and Inui, by Das, by Vedula, and by Kumar in Volume 2). It has to be noted, however, that the deformability

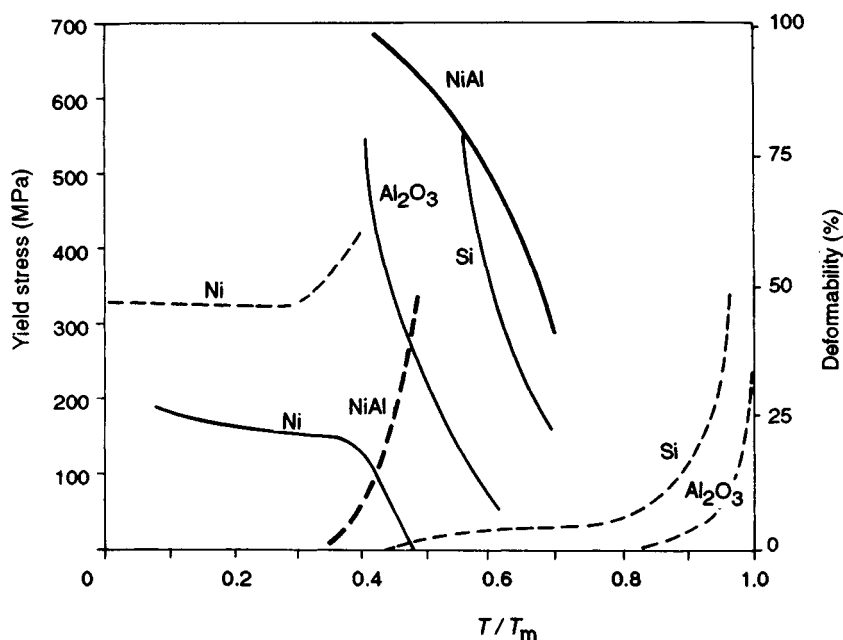


Figure 1. Yield stress (—) and deformability (----) for various materials as a function of homologous temperature T/T_m (T_m = melting temperature) (From Westbrook, 1965)

of intermetallics is a complex function of various other materials parameters besides crystal structure, and indeed there are phases with highly symmetric and small unit cells (e.g. B2) that exhibit insufficient deformability, as well as phases with complex crystal structure that can be deformed plastically, e.g. orthorhombic $AlNbTi_2$.

Intermetallics for high-temperature applications must also be oxidation-resistant in most cases (see Chapter 43 by Doychak in this volume). Oxidation resistance is provided by the presence of elements that can form protective oxide layers. Such elements are first of all Cr, Al, Si, and Be (Aitken, 1967; Hindam and Whittle, 1982). However, chromium oxide and silica are volatile at low oxygen pressures above 1000 °C, silicon oxide may form low-melting silicates, and Be is toxic. Thus aluminides are strongly favored for high-temperature applications. In cases of insufficient oxidation resistance, protective coatings may be applied (see Chapter 22 by Nichols in Volume 2). However, the stability of such coatings decreases with increasing temperature, and therefore phases for applications at 1100 °C and higher should be inherently oxidation-resistant.

Finally the preparation of components with reasonable quality must be possible for the intermetallic alloy in question, i.e. with a sufficiently low content of inherent

macroscopic defects—in particular pores, cracks, and inclusions. The processing of high-strength intermetallics is difficult because of their limited ductility, and thus the development of the necessary processing techniques is a very demanding task. Inherent defects increase the apparent brittleness and decrease the fracture strength, and thus they may preclude any application. Novel methods of alloy synthesis are used to try to circumvent the brittleness problems, including directional solidification, spray casting, mechanical alloying, reactive consolidation, shock synthesis, and rapid solidification, e.g. melt spinning and gas atomization with compaction by hot isostatic pressing or hot extrusion (the latter is also used frequently for thermomechanical processing) (Fischer and Weber, 1990; Sen and Stefanescu, 1991; Kumar, 1991; Thadhani, 1993; Chapter 27 by Martin and Hardwick in this volume).

In view of these difficulties, alloys for mechanical testing have usually been produced only in small quantities. Then strength is studied primarily in compression, which can be done with small specimens of simple shape that are less sensitive to internal cracks. Likewise ductility and toughness are studied by bending tests with small simple specimens instead of by tensile tests. Furthermore, hardness tests are used for studying

the material behavior locally. The indentations can be evaluated with respect to strength at low temperatures and creep at high temperatures, and the cracks that are produced by the indentations can be used to obtain estimates of the fracture toughness (Liang *et al.*, 1990; Davis *et al.*, 1991; Li *et al.*, 1991; Sargent and Ashby, 1992).

Intermetallics have been reviewed repeatedly in the past as well as recently (e.g. Westbrook, 1960, 1977; Stoloff, 1984; Fleischer *et al.*, 1989; Engell *et al.*, 1991; Sauthoff, 1989, 1994), and in particular the deformation behavior has been the subject of recent reviews (Yamaguchi and Umakoshi, 1990; Umakoshi, 1993). In the following the important features of the plasticity of intermetallics are discussed with respect to the basic mechanisms of plastic deformation, which control the strength and ductility of intermetallics. For a detailed discussion of the various intermetallic phases of interest with respect to properties, behavior, and applications, the reader is referred to Sauthoff (1994) as well as to the other chapters of this book.

2. Deformation Mechanisms

2.1 Slip

As in conventional disordered metallic alloys, the plastic deformation of intermetallics usually occurs by the movement of dislocations. However, the crystal symmetry of even the intermetallics with simple crystal lattices is lower than that of conventional alloys because of the particular atomic order—see Section 4.2 and the crystallographic chapters in Part III. Thus in such an intermetallic a perfect single dislocation, which does not affect the order of atoms, has a longer Burgers vector—and thereby a much larger energy—than a dislocation in a disordered alloy. Consequently such dislocations usually dissociate into two or more partial dislocations with antiphase boundaries and/or stacking faults in between in order to reduce their energy.

The resulting complex dislocations are known as superlattice dislocations (or superdislocations) and their energies are composed of the elastic energies and core energies of the partials and of the energies of the antiphase boundaries and/or stacking faults. If such a superdislocation moves, the atomic order across the slip plane is destroyed by the leading partial and restored by the trailing partial of the superdislocation. The particular type of dislocation is determined by the symmetry and energetics of the intermetallic in question.

The observed dislocation types and glide systems have been listed (Marcinkowski, 1974; Paufler, 1976; Baker and Munroe, 1990) for a large number of intermetallic phases with various crystal structures—including the f.c.c. structures B1 (cF8, NaCl type), B3 (cF8, ZnS type) C1 (cF12, CaF₂ type), C15 (cF24, MgCu₂ type), and D0₃ (cF16, BiF₃ type), the simple cubic structures A15 (cP8, W₃O type), B2 (cP2, CsCl type), and L1₂ (cP4, Cu₃Au type), the hexagonal structures A3 (hP2, Mg type), C14 (hP12, MgZn₂ type), and D0₁₉ (hP8, Ni₃Sn type), and the tetragonal structures C11_b (tI6, MoSi₂ type), C16 (tI12, CuAl₂ type), and L1₀ (tP4, CuAu type)—and have been discussed in detail (Yamaguchi and Umakoshi, 1990; Chapter 22 by Veyssi re and Douin in this volume). It is noted that in some B2 (cP2, CsCl type) phases—in particular in FeAl and NiAl—both perfect single dislocations and superlattice dislocations have been observed depending on deformation conditions and composition, i.e. Al content and alloying additions (Baker and Munroe, 1990; Field *et al.*, 1991).

The presence of the more complex superdislocations in intermetallics with their ordered atom distribution affects the strengthening behavior significantly compared with disordered alloys. This is illustrated by the behavior of the ternary phase (Co_{0.7}Fe_{0.3})₃V, which shows an order–disorder transition at about 900 °C, i.e. it exhibits the disordered f.c.c. (cF4, Cu type) structure at higher temperatures and the ordered L1₂ (cP4, Cu₃Au type) structure at lower temperatures—apart from intermediate σ -phase precipitation between 890 and 940 °C (Liu and Inouye, 1979). The disordered state at high temperatures can be retained at room temperature by quenching, and thus Figure 2 shows the strengthening behavior of this phase for various states of atomic order. Clearly the atomic order increases the strain-hardening rate, a behavior that has also been observed for another L1₂-phase Cu₃Au (Sachs and Weerts, 1931), as well as for phases with other crystal structures (Stoloff and Davies, 1964a; Marcinkowski, 1974, 1985), and which has been proposed to be due to the formation of very stable dipoles between superdislocations (Marcinkowski, 1985). In spite of this strengthening effect, the initial flow stress is lower for the ordered state than for the disordered or partially ordered state in Figure 2. This effect is attributed to the presence of short-range order in the disordered or partially ordered state, which makes dislocation movement more difficult than in the fully ordered state (Stoloff, 1984).

Another outstanding effect of atomic order and the presence of superdislocations is the possibility of a positive (i.e. anomalous) temperature dependence of

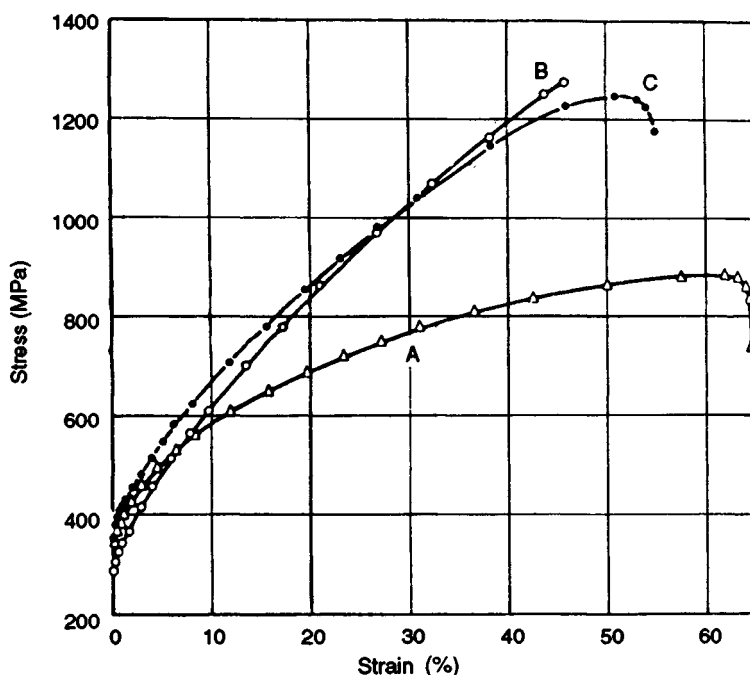


Figure 2. Stress-strain curves of polycrystalline $(\text{Co}_{0.7}\text{Fe}_{0.3})_3\text{V}$ at room temperature for various states of atomic order: curve A, disordered f.c.c., i.e. as-quenched; curve B, ordered L_{12} , i.e. aged 16 000 min at 700°C ; and curve C, partially ordered, i.e. aged 8 min at 700°C (From Liu and Inouye, 1979)

the flow stress. This has been most studied and best understood in the case of the L_{12} (cP4, Cu_3Au type) phase Ni_3Al and is illustrated by Figure 3. Plastic flow of Ni_3Al has been studied by many authors in much detail. The results have been reviewed and discussed intensively and the basic mechanisms are thought to be well understood now (Stoloff and Davies, 1966; Paidar *et al.*, 1981; Liu and Stiegler, 1984; Pope and Ezz, 1984; Stoloff, 1984; Liu and White, 1985; Izumi, 1989; Suzuki *et al.*, 1989; Liu *et al.*, 1990; Yamaguchi and Umakoshi, 1990; Umakoshi, 1993). Between room temperature and about 700°C the flow stress increases with increasing temperature to reach a maximum, and only at higher temperatures does normal softening occur.

As has already been discussed (Sauthoff, 1986), the anomaly results from the anisotropy of the energy and mobility of the superlattice screw dislocations, which determine the plastic deformation of Ni_3Al . The screw dislocations can split on $\{111\}$ planes and on $\{010\}$ planes. The splitting on $\{010\}$ is favored energetically because the energy of the antiphase boundaries (APBs) between the partials is lower on $\{010\}$. However, a superdislocation on $\{010\}$ is sessile because the dislocation cores of the partials spread outside the plane

of the APB. On the other hand, the superdislocation on $\{111\}$ (with higher energy) is glissile because the core spreading is better confined to the slip plane.

This glissile state is metastable since it is thought that the partials must first be coalesced into a single dislocation before cross-slip back to $\{010\}$ can occur. Hence dislocations are generated primarily on $\{111\}$ planes on loading, and slip is confined to $\{111\}$ at low temperatures. With rising temperature, cross-slip to $\{010\}$ becomes possible by thermal activation, resulting in immobilization of the dislocations (Kear–Wilsdorf mechanism). The sessile dislocations act as obstacles and give rise to rapid strengthening with increased flow stress. Thus it is clear that the anomalous temperature dependence of flow stress is observed only with sufficient strain, and indeed the minimum strain for an observable flow-stress anomaly was found to be about 10^{-5} (Thornton *et al.*, 1970). At temperatures above the flow-stress maximum the immobilized dislocations are mobilized again by enhanced thermal activation, which leads to the familiar softening. The details of these mechanisms and reactions have been and still are the subject of specific studies, and the theoretical description becomes more and more elaborate (Pope

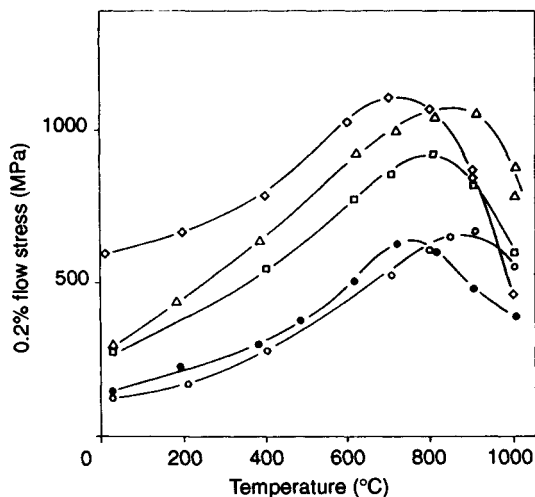


Figure 3. Temperature dependence of flow stress for cast polycrystalline Ni_3Al (●) and Ni_3Al with various alloying additions: (◇) 6 at.% Nb; (□) 10.5 at.% Ti + 2 at.% Cr; (△) 10.5 at.% Ti; (○) 2 at.% Cr (From Thornton *et al.* 1970)

and Ezz, 1984; Yoo *et al.*, 1988; Suzuki *et al.*, 1989; Heredia and Pope, 1991; Vitek and Sodani, 1991; Vitek *et al.*, 1991a,b; Sodani and Vitek, 1991; Pope, 1991; Molenat and Caillard, 1991; Saada and Veyssi re, 1991; Veyssi re, 1991; Yoo and Fu, 1991; Hirsch, 1992; Khantha *et al.*, 1992; Paidar *et al.*, 1992).

From this discussion it is clear that the flow-stress anomaly of Ni_3Al is a function of the binding forces between the atoms. Indeed the anomaly is exhibited by various L_{12} phases to different extents, and the differences are closely correlated with the differences in stability between the L_{12} (cP4, Cu_3Au type) structure and other possible structures, in particular the D_{019} (hP8, Ni_3Sn type) and D_{022} (tI8, Al_3Ti type) structures (Mishima *et al.*, 1985; Suzuki *et al.*, 1989). In Ni_3Si and Ni_3Ge the anomaly is still more pronounced than in Ni_3Al , whereas it is weaker in Co_3Ti , Zr_3Al , Fe_3Ga , and Cu_3Au ; there is a continuous transition from a positive temperature dependence to the familiar negative one in the L_{12} ternary phase $(\text{Ni},\text{Fe})_3\text{Ge}$ when going from Ni_3Ge to Fe_3Ge . Likewise the flow-stress maximum of Ni_3Al can be increased and shifted with respect to temperature by ternary alloying additions, as is exemplified by Figure 3.

Such flow-stress anomalies have also been shown by other phases with different crystal structures—e.g. FeCo-2V (cP2, B2), CuZn (B2), TiAl (tP4, L_{10}), Fe_3Al (cF16, D_{03}), Mg_3Cd (hP8, D_{019}), Ni_3V (tI8, D_{022}), Fe_2B (tI12, C16)—and various mechanisms have been proposed for these phases (Stoloff and Davies,

1964a; Westbrook, 1965; Paufler, 1976; Haasen, 1983; Stoloff, 1984; Kawabata *et al.*, 1985). In the case of phases with an order–disorder transition (e.g. FeCo-2V and Fe_3Al), the flow-stress maximum occurs just below the critical temperature of disordering and is related to the decreased degree of long-range order, which leads to a less strong coupling of the partials of the superdislocations.

The positive temperature dependence of the flow stress, e.g. of Ni_3Al , can be obscured by other concurrent strengthening effects. As an example, the grain size can be reduced to such an extent that the low-temperature flow stress is increased to a level higher than the original flow-stress maximum at high temperature, i.e. a flow-stress maximum is no longer discernible (Schulson, 1985). An analogous effect is produced when C is dissolved in Ni_3Al , gradually increasing the low-temperature flow stress (Jung and Sauthoff, 1989b; Wunnike-Sanders and Sauthoff, 1994).

2.2 Twinning

Besides dislocation slip, twinning is the other principal mode of plastic deformation: it is more important for intermetallics than for disordered alloys since dislocation slip is usually restricted because of the higher energy and lower mobility of dislocations in intermetallics (Yoo, 1989; Yoo *et al.*, 1993). This means that deformation twinning is prevalent not only at high strain rates and/or low temperatures, as for disordered alloys, but also at lower strain rates and higher temperatures.

The process of twinning is a cooperative movement of atoms producing a macroscopic shear (Honeycombe, 1968). The lattice in the twinned region—separated from the matrix by the twinning plane—is usually the mirror image of the parent lattice. The twinning transformation changes the orientation of the twinned region, but it does not alter the symmetry or structure of the crystal. The crystallography of twinning has been discussed in detail by Christian (1975). Twinning is a familiar deformation process in metals where the possible slip systems are severely limited, e.g. the close-packed hexagonal metals, where slip is frequently limited to the unique basal system. It has been found for such metals that twinning is preceded by slip and the resolved shear stress for twinning is substantially higher than that for slip. Twinning has also been observed in b.c.c. and f.c.c. metals, and the propensity for twinning increases with increasing deformation rate and decreasing temperature. The formation of twins during deformation often results in serrations in the stress–strain curve.

Important contributions of deformation twinning to plasticity have been reported for various intermetallic phases with various crystal structures—cubic $L1_2$ (cP4, Cu_3Au type), B2 (cP2, CsCl type), and D0_3 (cF16, BiF_3 type), tetragonal $L1_0$ (tP4, CuAu type), and D0_{22} (tI8, Al_3Ti type), and hexagonal D0_{19} (hP8, Ni_3Sn type) (Yoo, 1989; see also Wayman and Inoue, Chapter 35 in this volume). Important practical examples are the shape-memory phase NiTi with B2 structure (Goo *et al.*, 1985; Chapter 26 by Schetky in Volume 2), the D0_3 phase Fe_3Al (Park and Goo, 1991; Vedula, Chapter 9 in Volume 2), γ -TiAl with $L1_0$ structure (Kim and Dimiduk, 1991; Chapter 4 by Huang and Chesnutt in Volume 2), the D0_{22} phases Al_3Ti (Yamaguchi *et al.*, 1988; Shimokawa *et al.*, 1991; Yamaguchi and Inui, Chapter 7 in Volume 2) and Al_3Nb (Schechtman and Jacobson, 1975; Reip, 1991), and the Laves phase HfV_2 with cubic C15 (cF24, Cu_2Mg type) structure (Livingston and Hall, 1990). The crystallography of twinning—in particular the conjugate relationship between the order twinning and the active slip system at elevated temperatures—has been discussed in detail for the crystal structures $L1_2$, B2, D0_3 , $L2_1$ (cF16, Cu_2AlMn type), $L1_0$, D0_{22} , and D0_{19} (Yoo, 1989) as well as for the cubic A15 (cP8, W_3O type) structure (Khantha *et al.*, 1989). However, the energetics and kinetics of deformation twinning of intermetallic phases have not yet been studied adequately, and correspondingly the effects of deformation twinning on strength and ductility are not yet well understood (Yoo *et al.*, 1993).

2.3 Dislocation Creep

High-temperature deformation of metallic and other materials is controlled by various deformation mechanisms depending on temperature and deformation rate, as is illustrated by the so-called deformation maps (Frost and Ashby, 1982). The comparison of such maps for various materials with different crystal structures and types of atomic bonding shows that the deformation behavior at temperatures above one-third of the melting temperature (order of magnitude) is controlled for many materials by creep processes not only at deformation rates of 10^{-7} s^{-1} and lower, which are used during typical creep experiments, but also at higher rates of say 10^{-3} s^{-1} , which are used during short-term tests for flow-stress determinations, and this may be supposed to be the case for intermetallic phases, too (Sauthoff, 1990b). Thus any discussion of high-temperature deformation behavior has to be centered on creep mechanisms.

The creep behavior of NiAl and NiAl-based alloys has been studied systematically, and the findings have

been the subject of various summarizing reports (e.g. Sauthoff, 1991a, 1992). The following discussion of the main characteristics of the creep behavior of intermetallics refers to NiAl-based intermetallic alloys as typical examples since the understanding obtained there of the rate-controlling mechanisms is thought to be valid for other intermetallics.

The creep of the ternary B2 phase (Ni,Fe)Al exhibits a power-law behavior at high temperatures—e.g. 60% of the melting temperature or higher—with creep rates between about 10^{-8} and 10^{-6} s^{-1} (Rudy and Sauthoff, 1985; Rudy, 1986; Jung *et al.*, 1987), i.e. the observed secondary creep rates, which refer to the steady-state creep stage, are described by the familiar Dorn equation for dislocation creep (Mukherjee *et al.*, 1969):

$$\dot{\epsilon} = A(DGb/kT)(\sigma/G)^n$$

where $\dot{\epsilon}$ is the secondary strain rate, A is a dimensionless factor, D is the effective diffusion coefficient, G is the shear modulus, b is the Burgers vector, k is Boltzmann's constant, T is temperature, and σ is the applied stress, with the exponent n usually between 3 and 5.

Dislocation creep of conventional disordered alloys is produced by gliding and climbing dislocations. If climb is the slower step, as in pure metals, the creep rate is controlled by dislocation climb, which gives rise to a well-defined subgrain structure, and the stress exponent is 4 or 5. Alloys with this characteristic are termed class II alloys. Otherwise, viscous dislocation glide is rate-controlling, which leads to dislocation tangles without subgrain formation and a stress exponent of 3, behavior characteristic of the class I alloys (Sherby and Burke, 1967; Nix and Ilschner, 1979).

The secondary creep behavior of (Ni,Fe)Al shows analogous characteristics. In the Ni-rich phases and in the binary NiAl, a well-defined substructure is found after creep. The subgrain size is of the order of $10 \mu\text{m}$, and the dislocation density within the subgrains is about 10^7 cm^{-2} . In agreement with this, stress exponents between 4 and 4.5 have been found for the Ni-rich phases, i.e. these phases behave like class II alloys with dislocation climb controlling the creep.

In the Fe-rich phases and in FeAl, however, no subgrain formation has been observed even after long creep times. The dislocation density remains high (about 10^{10} cm^{-2}), and the stress exponent varies between 3 and 3.6. This indicates class I behaviour, i.e. here the creep is controlled by the viscous glide of dislocations. In both cases only $\langle 100 \rangle$ dislocations have been observed. Obviously the driving force and the atomic mobility that are necessary for subgrain formation are sufficient only in the Ni-rich phases.

These findings show that dislocation creep of such intermetallic alloys and of conventional disordered Ni-base or Fe-base alloys is controlled by the same mechanisms. Even the observed dislocation densities correspond to those in conventional disordered alloys, as has been shown (Rudy, 1986; Sauthoff, 1991b). This close similarity is surprising since the elementary atomic diffusion processes and the types and numbers of dislocation slip systems are quite different because of the different crystal structures.

Besides dislocation creep, grain-boundary sliding was observed in (Ni,Fe)Al. The process is, of course, not an independent deformation mechanism, since the resulting grain shifts lead to stress concentrations at grain-boundary junctions and must be accommodated by deformation processes within the grains, i.e. by dislocation creep of the grains in the stress-temperature range concerned. For such coupled deformation processes, the total creep rate is controlled by the slower process, which is dislocation creep for not-too-small grain sizes. With decreasing grain size, the contribution of grain-boundary sliding increases, from which a decrease of the total creep resistance results, as is well known for disordered alloys (Frost and Ashby, 1982) and has also been observed for (Ni,Fe)Al (Rudy, 1986; Sauthoff, 1990b).

Secondary creep is preceded by an initial transient primary creep, for which a detailed quantitative physical understanding is still missing, even for conventional metallic alloys. Primary creep has been studied only in a few cases. Early models have been based on simple phenomenological approaches (e.g. Webster *et al.*, 1969; Davies *et al.*, 1969; Ahmadiéh and Mukherjee, 1975) and are not related to microstructural features of plastic deformation. Only recently have creep models been developed that take into account microstructural changes (e.g. Estrin and Mecking, 1984; Derby and Ashby, 1987; Gottstein and Argon, 1987; Mecking and Estrin, 1987). Still such models do not yield the correct prediction for the stress dependence of the total primary strain—i.e. the strain for reaching the secondary stage, as has been shown for a NiAl-base alloy (Klöver and Sauthoff, 1992). Indeed, both positive and negative stress dependences have been found for intermetallic alloys (Reip, 1991; Klöver and Sauthoff, 1992) as well as for conventional metallic alloys (Ilschner, 1973; Schulze and Sauthoff, 1983).

In the case of Ni₃Al, the initial transient creep stage exhibiting normal primary creep, i.e. hardening with decelerating creep rate, is succeeded by a second transient stage with anomalous primary creep, i.e. softening with accelerating creep rate, which is known

as inverse creep (Hemker *et al.*, 1991). The reason for this behavior is again the complexity of the available slip systems, in particular the activation of octahedral slip and cube slip at different stresses (Schneibel and Hazzledine, 1992). Inverse creep is always observed when the number of mobile dislocations is initially insufficient and increases during creep. Another example is the ternary Laves phase NbNiAl with the hexagonal C14 (hP12, MgZn₂ type) structure (Machon, 1992). Inverse creep has been studied and analyzed in detail in the case of Si (Alexander, 1986; Alexander and Haasen, 1968).

In view of the anomalous temperature dependence of the flow stress of Ni₃Al (see preceding section), it is finally to be noted that the creep resistance of Ni₃Al does not show any anomalous temperature dependence (Schneibel and Hazzledine, 1992). The reason for this is that creep occurs at much lower strain rates than used in flow-stress tests, a fact that must be considered when comparing such thermally activated processes, i.e. the strain rate-temperature range of creep corresponds to that above the peak temperature in Figure 3.

2.4 Diffusional Creep

At lower stresses, which produce secondary creep rates below 10^{-8} s^{-1} , the observed stress-strain rate relationship may deviate from the power-law behavior, i.e. the apparent stress exponent is smaller than 3 and decreases with decreasing stress, as has been observed for the ternary B2 phase (Ni,Fe)Al (Jung *et al.*, 1987). This deviation indicates the contribution of diffusional creep, which results from the stress-induced diffusion of atoms (or vacancies) and is a linear function of stress:

$$\dot{\epsilon}_{\text{diff}} = A_{\text{diff}}(\Omega D/kTd^2)\sigma$$

where A_{diff} is a dimensionless factor (usually $A_{\text{diff}} = 14$), Ω is the atomic volume, D is the effective diffusion coefficient, which considers the diffusion both through the grain (Nabarro-Herring creep) and along the grain boundaries (Coble creep), and d is the effective diffusion length, which is usually approximated by the grain size (Frost and Ashby, 1982).

Dislocation creep and diffusional creep are independent creep processes that act in parallel in the grains, and the total creep rate is given by the sum of the partial rates. Because of the stronger stress dependence of dislocation creep, the contribution of diffusional creep becomes more prominent with decreasing stress.

The theory of diffusional creep that results in the above constitutive equation is well established on the

basis of thermodynamics (Nabarro, 1948; Herring, 1950; Coble, 1963; Burton, 1977). It supposes grain boundaries to be ideal sources and sinks of vacancies, and it has been used to consider effects of grain shape and grain growth (Burton and Greenwood, 1985; Mishra *et al.*, 1988) as well as the coupling of diffusional creep with grain-boundary sliding (Ashby, 1972; Stevens, 1972; Burton, 1977). With increasing stress, there is a transition to dislocation creep (Greenwood *et al.*, 1980). If grain boundaries do not act as ideal sources and sinks of vacancies, there is a threshold stress for diffusional creep (Ashby, 1972; Greenwood, 1977). Models are available, but the experimental evidence is still in discussion (Harris *et al.*, 1969; Burton, 1973; Crossland and Clay, 1977; Clegg and Martin, 1982; Arzt *et al.*, 1983; Clegg, 1984; Mishra *et al.*, 1989; Arzt, 1991). Besides grain boundaries, climbing dislocations may act as sources and sinks for vacancies. The resulting diffusional creep, which is known as Harper–Dorn creep, becomes rate-controlling for very large grain sizes; but again the experimental verification of proposed models is still in discussion (Mohamed *et al.*, 1975; Langdon and Yavari, 1982; Nabarro, 1989; Fiala *et al.*, 1991; Wolfenstine *et al.*, 1991).

Diffusional creep is of great practical importance since it controls the long-term creep deformation at very low deformation rates, which correspond to service conditions. Nevertheless, experimental studies of diffusional creep are rare even for conventional disordered alloys. As to ordered intermetallic alloys, diffusional creep has been studied in the case of an advanced Ni₃Al alloy (Schneibel *et al.*, 1986). Much more work is necessary with respect to the various intermetallic alloys being developed. The diffusion data that are needed to analyze the creep behavior are rare or not available at all for the intermetallic phases of interest (see Chapter 32 by Larikov in this volume).

3. Stress and Temperature Dependence of Strength and Ductility (Deformation Maps)

The preceding discussion has shown that plastic deformation is controlled by various different mechanisms depending on stress, temperature, and microstructure. A quick overview on the prevailing deformation mechanisms is given by the deformation mechanism map for a given material (Frost and Ashby, 1982).

Complete deformation maps are available for many metals and alloys as well as for some non-metallic materials (Frost and Ashby, 1982), but not yet for

intermetallic phases. A comparison of one such map for a pure metal, e.g. the transition metal Cr with A2 structure (i.e. b.c.c.), with a map for an only partially metallic interstitial compound, e.g. the refractory carbide ZrC with cubic B1 structure, shows that these maps, when drawn to normalized scales, do not differ too much for these dissimilar materials in spite of the differences in atomic bonding and crystal structure. Figure 4 (Jung *et al.*, 1987) shows the high-temperature part of a deformation map for the ternary intermetallic phase (Ni_{0.8}Fe_{0.2})Al with cubic B2 structure that results from the A2 structure by atomic ordering. Again the behavior of the intermetallic does not differ too much from that of the other two examples. Obviously the normalization of applied stress by the shear modulus and of temperature by the melting temperature is sufficient for a unifying description of the global deformation behavior of various materials including intermetallics.

In the deformation mapping concept just described, the transition from low-temperature deformation, which is controlled by the conservative motion of dislocations, to high-temperature deformation, which is controlled by thermally activated creep processes, is supposed to occur in the temperature range $0.3T_m$ to $0.5T_m$ for intermetallics, where T_m is the melting temperature. This means that the mechanical properties of intermetallic phases at high temperatures are determined by creep processes and depend sensitively on temperature and deformation rate. This understanding is based on detailed studies of the low- and high-temperature deformation studies of various intermetallics, in particular the B2 phases AgMg (Wood and Westbrook, 1962), NiAl (Vandervoort *et al.*, 1966), and (Ni,Fe)Al (Sauthoff, 1990b).

Such deformation maps show the material's response to applied stress and temperature with respect to deformation rate, i.e. its strength. As to ductility and toughness, analogous fracture maps are available only for some metals and alloys and a few other materials (Ashby *et al.*, 1979; Gandhi and Ashby, 1979), but not yet for intermetallics. Fracture of intermetallics has become a subject of systematic research only recently (see e.g. Vehoff, 1992; Chapter 38 by Briant in this volume). Most intermetallics exhibit low or no ductility at low temperatures and become ductile only at elevated temperatures by the thermal activation of deformation processes. The resulting brittle-to-ductile transition temperature in such cases corresponds to the temperature of rapid softening by creep as is visible, for example, in Figure 1 for NiAl and Figure 5 for TiAl. The brittle-to-ductile transition by thermally activated processes

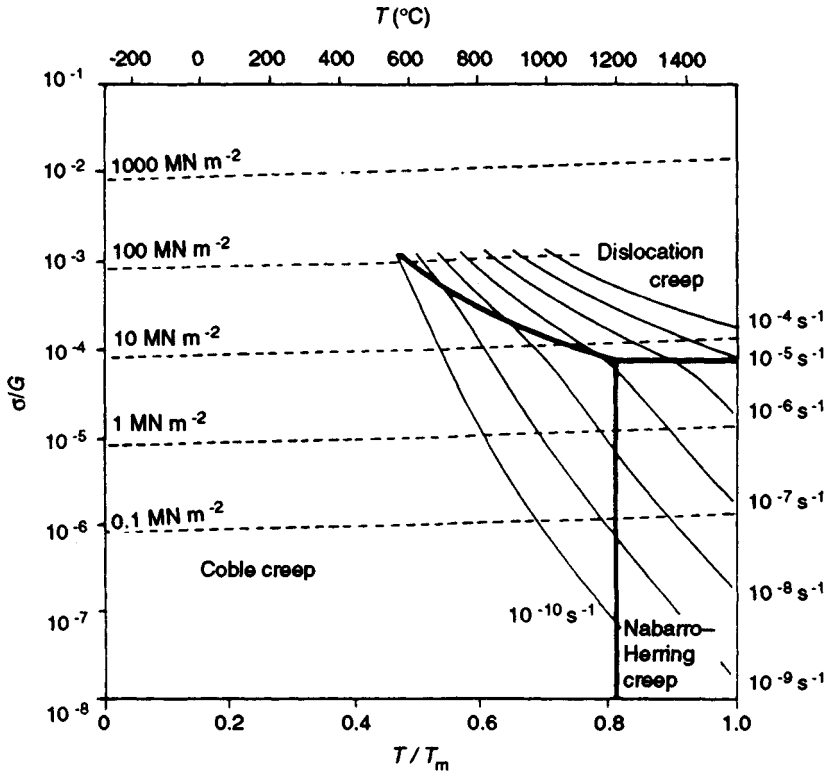


Figure 4. High-temperature deformation map with curves of constant compressive strain rate as a function of normalized compressive stress and temperature (G = shear modulus, T_m = melting temperature) for $(\text{Ni}_{0.8}\text{Fe}_{0.2})\text{Al}$ with 0.1 mm grain size (From Rudy, 1986; Jung *et al.*, 1987)

leads to a strong strain-rate dependence of the brittle-to-ductile transition temperature and of toughness, i.e. the brittle-to-ductile transition temperature increases and toughness decreases with increasing strain rate (Sauthoff, 1990b; Vehoff, 1992).

4. Plasticity-Controlling Factors

4.1 Strength and Character of Bonding

It is generally supposed that a high melting temperature indicates high phase stability and strength of bonding. Indeed, most materials parameters that characterize the deformation behavior are well correlated with the melting temperature (Frost and Ashby, 1982). Examples are the elastic moduli, which not only control the elastic deformation but also are important parameters for describing the plastic deformation, and the diffusion coefficients, which control not only the kinetics of phase reactions but also the kinetics of high-temperature deformation, i.e. creep.

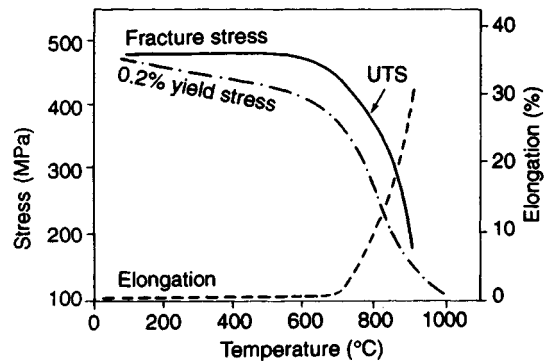


Figure 5. Tensile strength—i.e. fracture stress, ultimate tensile strength (UTS), and 0.2% yield stress—as well as plastic deformability—i.e. tensile elongation—as functions of temperature for single-phase, polycrystalline TiAl with 54 at. % Al (From Lipsitt *et al.*, 1975)

However, a phase melts when the total energy of the solid phase is higher than that of the liquid phase, and thus the melting temperature is a rather complex

Chapter 4

Structure of Antiphase Boundaries and Domains

Yong-Qian Sun

*Department of Materials, University of Oxford, Parks Road, Oxford OX1 3PH, UK
(now at Department of Materials Science and Engineering, University of Illinois,
Urbana, Illinois 61801, USA)*

1. Introduction

Antiphase boundaries (APBs) and antiphase domains (APDs) are microstructural features that are unique to ordered alloys and are not present in disordered alloys. Many of the interesting mechanical and electromagnetic properties of ordered alloys have been interpreted on the basis of the presence of APBs and APDs and their crystallography, energetics, and chemistry. In ordered alloys the mobility of dislocations is often governed by their core structures, which in most cases involve APBs. APBs are also effective barriers to dislocation propagation, and as a result the mechanical properties are influenced by the morphology of APDs, which in many cases can be controlled through heat treatment and alloying. APBs also play an important role in phase transformations involving the generation or elimination of APBs, as well as in the disorder–order transition. The role of alloying elements in intermetallics is sometimes reflected in their effects on the energetics and chemistry of APBs through, for example, their segregation to the APB. Electromagnetic properties are affected by APBs and APDs because of their effects on the band structure. This chapter is concerned with the basic crystallographic, microstructural, and energetic properties of APBs and APDs.

The ordered arrangement of atoms in an intermetallic compound is usually represented in terms of a superlattice and the constituent, identical sublattices. A two-dimensional analog is shown in Figure 1, in which the superlattice (unit cell marked by full lines) is made up of two sublattices (unit cells marked by broken lines). The sublattices are usually named after the types

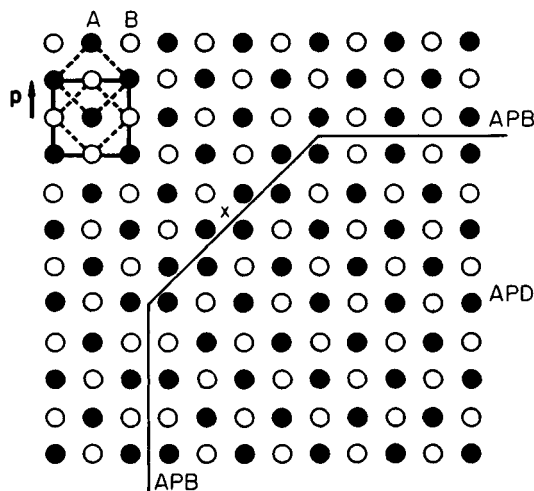


Figure 1. APB and APD in a two-dimensional AB alloy with a square superlattice unit cell. The two sublattices are marked by broken lines and \mathbf{p} is the APB vector. The boundary marked x is a non-conservative APB where there are no B atoms

of atoms that occupy them, e.g. A and B sublattices in Figure 1. The $L1_2$ (CP4) superlattice (composition A_3B), ordered from the face-centered-cubic (f.c.c.) structure, consists of four interpenetrating simple-cubic sublattices, one of which is occupied by B atoms (B sublattice) and the remaining three by A atoms (A sublattices). Similarly, in the $L2_1$ (CF16) superlattice (composition A_2BC), derived from the body-centered-cubic (b.c.c.) structure and also having four simple-cubic sublattices, there are two A sublattices, one B sublattice, and one C sublattice. A vector, within the superlattice unit cell, is referred

to as an antiphase vector if it translates one type of sublattice into coincidence with another type; such a vector, denoted \mathbf{p} , is a lattice vector of the disordered structure, but not of the superlattice. The \mathbf{p} vector in the two-dimensional superlattice is shown in Figure 1. By definition, an antiphase boundary is an interface separating two identically oriented crystals that have been displaced with respect to each other by \mathbf{p} ; there is no crystallographic restriction on the plane normal \mathbf{n} of the interface. An antiphase domain within an ordered crystal is a region that is enveloped by a continuous piece of APB. Figure 1 shows an APD and the enveloping APB in the two-dimensional superlattice. The number of APB or APD variants available in a superlattice is given by the number of antiphase vectors. In some superlattices, e.g. $L1_2$ (cP4), $L1_0$ (tP4), and B2 (cP2), there is just one type of antiphase vector. There are also others in which two (e.g. DO_{22} (tI8), DO_3 (cF16), and $L2_1$ (cF16)) or more (e.g. DO_{19} (hP8)) types of \mathbf{p} vectors are present. See Tables 1–6 for a list of \mathbf{p} vectors in six of the most common superlattice structures. For descriptions of crystal structures in intermetallic compounds, the reader is referred to Chapters 11–20 in this volume.

The arrangement of atom species across an APB is fully characterized by \mathbf{p} and \mathbf{n} ; such an arrangement defines an *ideal* APB, which separates two *rigidly* displaced crystals with uniform composition and degree of order. According to the $\mathbf{p} \cdot \mathbf{n}$ value, the APBs can be classified into two basic types (Marcinkowski, 1963; Beeler, 1967). When $\mathbf{p} \cdot \mathbf{n} = 0$, i.e. when the displacement vector lies within the interface, the APB can be formed by a pure shear without a change of stoichiometry in the boundary; such APBs are called conservative and are involved in the glide dissociation of dislocations. When $\mathbf{p} \cdot \mathbf{n} \neq 0$, the APB can be considered as being formed by a combination of a pure shear and the removal or insertion of a layer of material with a thickness equal to $|\mathbf{p} \cdot \mathbf{n}|$, and such APBs are termed non-conservative. In the latter case the composition in the boundary is different from the bulk if the removed layer does not contain atoms in the stoichiometric proportion. A non-stoichiometric, non-conservative APB is shown marked by x in the two-dimensional superlattice in Figure 1; this APB can be considered as being formed by removing a layer of B atoms parallel to the boundary, and as a result there are no B atoms on either side of the APB. Thus, \mathbf{p} and \mathbf{n} are useful in assessing, on a qualitative basis, the anisotropic nature of the surface energy of the APB by examining the bond changes, across the APB, between nearest neighbors (Flinn, 1960) and higher-order neighbors (Marcinkowski and Brown,

1962; Leamy *et al.*, 1970; Paidar, 1985; Beauchamp *et al.*, 1987; Yamaguchi and Umakoshi, 1990). In the $L1_2$ structure, for example, minimum APB energy is expected to be on the $\{100\}$ planes in which, after the APB displacement, bonding among the nearest neighbors is not changed, as first pointed out by Flinn (1960). For a *real* APB, however, owing to the different bonding environment near the boundary from the interior, the atom positions, the local composition, and the degree of order are all expected to deviate from those for an ideal APB. Deviations from ideal lattice positions are referred to as structural relaxation, or residual or supplementary displacements (Yamaguchi *et al.*, 1981a; Lasalmonie *et al.*, 1988; Ngan, 1992; Fu and Yoo, 1992). Deviations from ideal APBs may also appear in the forms of local disordering (Brown, 1959; Popov *et al.*, 1966; Kikuchi and Cahn, 1979; Sanchez *et al.*, 1987; Korner and Schoeck, 1990; Schoeck and Korner, 1990; Tichelaar *et al.*, 1992) and segregation of vacancies, solute, and excess atoms to the APB (Popov *et al.*, 1966; Cupschalk and Brown, 1968; Wu *et al.*, 1989, 1991); these will be referred to as chemical effects.

In ordered alloys there are two distinctly different processes in which APBs and APDs may be formed, namely disorder–order transformations and the dissociation of dislocations. In disorder–order transformations, occurring during cooling through a certain transition temperature, the widely considered circumstance has been that ordering takes place in an existing disordered or short-range-ordered crystal grain, proceeding first by the nucleation of small ordered regions or nuclei, and followed by the growth of the ordered regions, which become APDs when they eventually come into contact. In dislocation mechanisms, an APB appears in the form of a usually narrow ribbon coupling two or more partial dislocations, and in general the APB vector \mathbf{p} is equal to the Burgers vector of the dislocation that produces the APB. In the classical example first proposed by Koehler and Seitz (1947), and subsequently frequently observed by transmission electron microscopy (TEM) (Marcinkowski, 1963; Ray *et al.*, 1970; Veyssière, 1989; Hazzledine and Sun, 1991), the APB connects two identical superpartial dislocations. Such observations have formed the basis for the experimental measurement of the surface energy of the APB (Section 2.5). Latest experiments using a combination of weak-beam and lattice-resolution TEM have demonstrated that APBs may be involved in more complicated dissociation modes, details of which can be found in Chapter 22 by Veyssière and Douin in this volume. Dislocation mechanisms have also been found to generate a special kind of APD, known as an APB

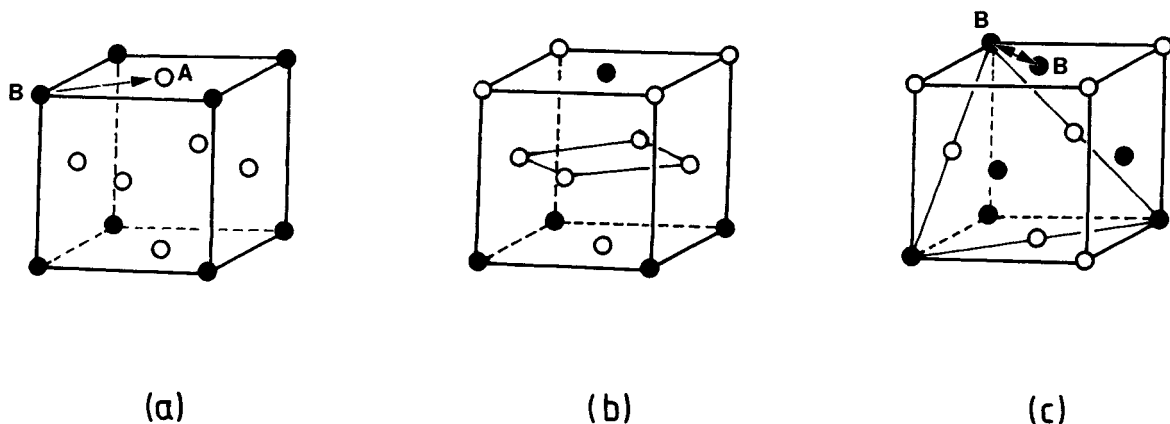


Figure 2. (a) The crystal structure of $L1_2$, $p = \frac{1}{2}\langle 110 \rangle$, represented by the arrow. (b) An APB on $\{001\}$ in which the bonding with the nearest neighbors is not disturbed. (c) An APB on $\{111\}$ in which a nearest B-B bond is created

tube, which is a straight, tubular APD, usually trailing APB-dissociated superdislocations containing jogs; this subject will be dealt with in Section 4.2.

Transmission electron microscopy (TEM) has been used extensively for the observation of APBs and APDs. APBs are usually imaged using the method of dark-field imaging in which only one diffracted beam (denoted g) passes through the imaging lenses. The contrast originates from the interference between the waves diffracted into the g reflection from the crystals on both sides of the APB, and the phase difference between the waves is given by $2\pi g \cdot p$. Contrast is formed when $g \cdot p \neq \text{integer}$ and this is possible only if g is a superlattice reflection (i.e. a reflection forbidden in the disordered counterpart). The image vanishes when $g \cdot p = \text{integer}$, a condition that is satisfied when g is a fundamental reflection or normal to p . The contrast formation of an APB is therefore similar to that of ordinary stacking faults; when the fault plane is inclined to the foil surface, the image consists of an oscillation of dark and light bands. Since in most cases the extinction distances of superlattice reflections are comparable to, or larger than, the foil thickness, thermally formed APBs are often imaged as a single bright or dark band. As for APBs coupling partial dislocations, it is usually impossible to separate the fault contrast from the interference from the strain field of the coupled dislocations; in this case the APB is defined as the space between the dislocations, the images of which are sharp bright lines under the weak-beam condition. The reader is referred to Chapter 22 by Veyssi re and Douin in this volume for examples of TEM observations of APB-dissociated dislocations. Theory and technique for the imaging of APBs have

been well-established, and the reader is referred to the review by Marcinkowski (1963) for the imaging of thermal APBs and to the papers by Cockayne and co-workers (Cockayne *et al.*, 1969; Ray *et al.*, 1970) for the weak-beam method.

2. The Structure and Energy of APBs

2.1 Ideal APBs and APB Energy Anisotropy

An ideal APB is a sharp geometrical plane that separates two identically oriented crystal domains that have been displaced rigidly relative to each other by p . The atoms sit at ideal lattice positions right up to the boundary, and the composition and the degree of order are uniform throughout the domains. Before quantum-mechanical calculations for many-body problems became available in the early 1980s, theoretical estimates for the APB energy were based on the Ising model, in which the increase in the internal energy due to the presence of an APB was derived from the changes in the interaction energies between atom pairs. One of the key assumptions in such calculations is that the pairwise interaction energies are independent of the presence of other atoms. Early calculations considered only the interaction energies among the nearest neighbors (e.g. Flinn, 1960), followed soon by more elaborate treatments that included higher-order interactions (Marcinkowski and Brown, 1962; Leamy *et al.*, 1970; Yamaguchi *et al.*, 1981a; Paidar, 1985; Beauchamp *et al.*, 1987; Lasalmonie *et al.*, 1988). Although such formulations have been largely replaced by modern *ab initio* quantum-mechanical

calculations, their merit still remains in that they provide a clear physical insight into the anisotropic nature of the APB energy. Here we take the $L1_2$ (A_3B) structure as an example. In $L1_2$, shown in Figure 2(a), every atom has 12 nearest neighbors: an A atom has eight nearest B atoms and four nearest A atoms, while a B atom is completely surrounded by 12 A atoms; there is thus no nearest B–B bond. Such a configuration of bonding between the nearest atoms is maintained by a shear APB ($\mathbf{p} = \langle 1\ 1\ 0 \rangle / 2$) on the $\{0\ 0\ 1\}$ plane (Figure 2(b)). For an APB on the $\{1\ 1\ 1\}$ plane, however, two-thirds of the A atoms are still surrounded by eight A atoms and four B atoms, but one-third of the A atoms lose a B atom, which is replaced by an A atom, and at the same time all the B atoms lose an A atom, which is substituted by a B atom; the newly created B–B bond is indicated in Figure 2(c). The energy increase per unit area, which by definition is the APB energy, can be shown to be given by

$$\gamma_{111} = 2V/(\sqrt{3}a^2)$$

where $V = \frac{1}{2}(V_{AA} + V_{BB}) - V_{AB}$ is the ordering energy of the nearest neighbors, and a is the lattice constant. (Here V_{ij} , with $i, j = A, B$, is the interaction energy between nearest neighbors. W_{ij} , which we shall use in later discussions, is the interaction energy between second nearest neighbors.) In general, the number of bonds per unit area (bond density, L_i) across an APB between atoms connected by a vector \mathbf{t}_i can be calculated on the basis of the following consideration. Consider first the plane perpendicular to the bond direction \mathbf{t}_i ; the bond density l_i in that plane is given by

$$l_i = N_0 |\mathbf{t}_i|$$

where N_0 is the number of atoms per unit volume. In a general plane \mathbf{n} , the density of the same bond is given by l_i times the cosine of the angle between \mathbf{n} and \mathbf{t}_i , e.g. $\mathbf{t}_i \cdot \mathbf{n} / |\mathbf{n}| |\mathbf{t}_i|$. This gives

$$L_i = N_0 (\mathbf{t}_i \cdot \mathbf{n}) / |\mathbf{n}|$$

Tables 1–6 contain a list of energies of shear APBs expressed in terms of the ordering energies of the nearest neighbors (V) and the second nearest neighbors (W) (the formulas are taken from Yamaguchi and Umakoshi (1990)). Flinn (1960), who first derived analytical solutions for $L1_2$ and B2 structures, argued that the APB energies should be associated principally with nearest-neighbor interactions since second-neighbor interactions had been estimated to be only one-tenth as

strong as between nearest neighbors (Cowley, 1950; Sutcliffe and Jaumot, 1953). On this basis Flinn predicted that in $L1_2$ the APB energy should be highly anisotropic with a maximum on $\{1\ 1\ 1\}$ and a minimum on $\{0\ 0\ 1\}$. Paidar (1985) more recently included the interaction among second neighbors in $L1_2$ and found that Flinn's result was correct for most of the boundary planes except those with low indices.

The simple estimates based on the pairwise nearest neighbor interactions have been found satisfactory in accounting for the morphological features of thermal APDs observed in some $L1_2$ alloys in which the APD structure has been described as maze-like with the APBs lying preferentially on $\{0\ 0\ 1\}$ planes: Cu_3Au (Fisher and Marcinkowski, 1961), Cu_3Pt (Yodogawa *et al.*, 1980), and Ni_3Al (Horton and Liu, 1985). There are also $L1_2$ alloys, notably Ni_3Fe (Calvayrac and Fayard 1972; Morris *et al.*, 1976), Ni_3Mn (Reynaud *et al.*, 1975), and Pd_3Fe (Yodogawa *et al.*, 1980), in which the morphology of thermal APDs is 'swirl-like' with the APBs adopting random orientations. In these alloys the APB energies are thought to be largely isotropic, in contradiction to the predictions from the nearest-neighbor model.

The APB energy anisotropy also forms the basis for the interpretation of the yield stress anomaly in some $L1_2$ alloys (e.g. Ni_3Al and Ni_3Ga) in which the yield stress exhibits a significant increase with temperature (for reviews, see Pope and Ezz (1984) and Suzuki *et al.* (1989)). In most of the existing models, the rise of the yield stress originates from the formation of Kear–Wilsdorf locks on screw dislocations (Kear and Wilsdorf, 1962; Takeuchi and Kuramoto, 1973; Paidar *et al.*, 1984; Hirsch, 1992), the driving force of which derives partly from the lower APB energy on $\{0\ 0\ 1\}$. Recent weak-beam TEM observations have shown that even in Ni_3Al , which has a very pronounced yield stress anomaly, the $\{0\ 0\ 1\}$ APB energy is often comparable to that on $\{1\ 1\ 1\}$ (Veyssi re *et al.*, 1985; Douin *et al.*, 1986; Korner, 1988; Dimiduk, 1989) (see Table 1). Similar findings have also been made in Ni_3Si (Tounsi, 1988; Yoshida and Takasugi, 1991), Ni_3Fe (Korner and Karnthaler, 1985), and in Co_3Ti (Oliver, 1992). The experimental findings have been further substantiated by the latest quantum-mechanical calculations, which often showed comparable values of APB energies on $\{0\ 0\ 1\}$ and $\{1\ 1\ 1\}$ in Ni_3Al (Stocks *et al.*, 1987; Fu and Yoo, 1989). In the B2-ordered structure, Flinn's calculation (Flinn, 1960) predicted a higher APB energy on $\{1\ 1\ 2\}$ than on $\{1\ 1\ 0\}$ by a factor of $2/\sqrt{3}$. However, Saka *et al.* (1984) observed in $\beta\text{-CuZn}$ that the APB energy on $\{1\ 1\ 0\}$ was in fact higher than on $\{1\ 1\ 2\}$.

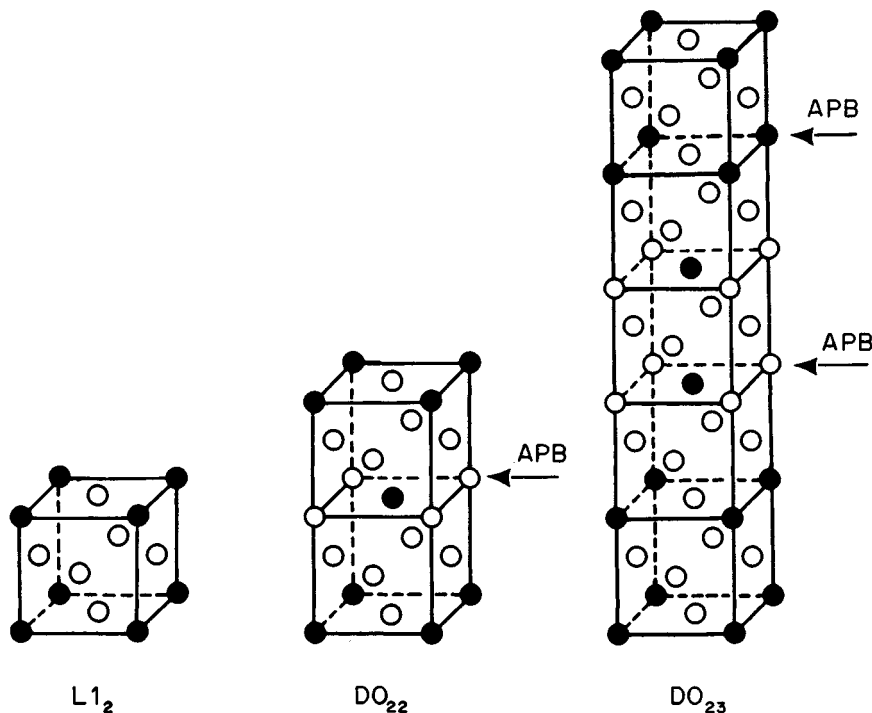


Figure 3. The $D0_{22}$ structure is derived from $L1_2$ by forming an $\{001\}$ APB on every two $\{001\}$ atom layers. The $D0_{23}$ structure is related to $L1_2$ by $\{001\}$ APBs on every four $\{001\}$ atom layers

These departures are usually taken as indications for much stronger interactions among high-order neighbors. Structural relaxations have also been shown to contribute to reducing the degree of APB energy anisotropy in $L1_2$ alloys (Beauchamp *et al.*, 1987).

2.2 APB Energy and Structural Stability

Some superlattice structures are related to each other by introducing APBs periodically on specific crystallographic planes. The $D0_{22}$ structure is obtainable from $L1_2$ by creating an APB on every second $\{001\}$ atom layers; $D0_{23}$ is derived from $L1_2$ by forming an APB on every fourth $\{001\}$ atom layer (Figure 3). In both cases the compound composition remains A_3B but the crystal structure has become tetragonal. It has therefore often been argued that the relative stabilities of $D0_{22}$ and $D0_{23}$ vs. $L1_2$ are reflected in the $\{001\}$ APB energy in $L1_2$, namely, alloys with low $\{001\}$ APB energies are less stable with respect to $D0_{22}$ or $D0_{23}$ than those with high $\{001\}$ APB energies (Wee and Suzuki, 1979; Mishima *et al.*, 1985). In the framework of pair-potential

calculations, if the $D0_{22}$ structure is stable, the $\{001\}$ APB energy in $L1_2$ would be negative (Kikuchi and Cahn, 1979). If the interatomic interactions are included up to the fourth neighbor, the $\{001\}$ APB energy has been shown to be equal to the difference in the internal energies between $L1_2$ and $D0_{22}$ (Nicholson *et al.*, 1989). Yodogawa *et al.* (1980) observed in $\text{Cu}_3\text{Au-Ni}$ alloys that the occurrence of maze-like patterns of thermally formed APDs, suggesting a lower $\{001\}$ APB energy, is often associated with the formation of long-period tetragonal superlattice structures formed by introducing an APB each M $\{001\}$ atom layer, the tetragonality being given by $c/a = 2M$. Using potentials generated from the generalized perturbation method, Nicholson *et al.* (1989) found that, for Al_3Ti , increasing the structural stability of $D0_{22}$ against $L1_2$, by increasing the tetragonality ratio (c/a), was accompanied by a decrease in the $\{001\}$ APB energy. In Al_3Sc , in which the calculated $\{001\}$ APB energy is very high ($\sim 450 \text{ mJ m}^{-2}$), the compound is predicted to be always stable in the $L1_2$ structure (Carlsson and Meschter, 1991; Fu, 1990).

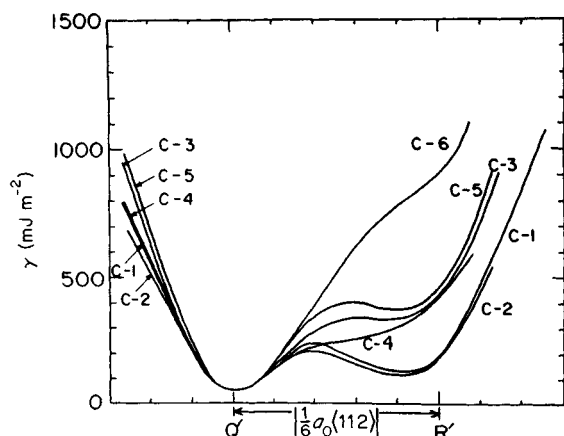


Figure 4. Section of $L1_2$ $\{111\}$ γ -surface containing the supplementary displacement parallel to $\langle 112 \rangle$. R' is the position of ideal APB shear. C-1 to C-6 are from potentials representing increasing A-B ordering energies (Reproduced by permission of Taylor & Francis Ltd from Yamaguchi *et al.*, 1981a)

The APB energy has also been proposed to correlate with the stability of the ordered structure vs. the disordered structure, being reflected, in the Ising model, in the relationship between the APB energy and the critical temperature T_c of the disorder-order transition. Models for the disorder-order transformation based on the nearest-neighbor interactions have yielded in some structures a proportional relationship between the ordering energy V and the transition temperature T_c , i.e.

$$V = kT_c/w$$

where k is the Boltzmann constant and w is a constant that depends on the structure and on the model used (for a review, see Guttman (1956), and also see Tables 1–6 for a list of the relationships between T_c and V and W in six of the most common ordered structures). The ordering energy thus obtained can be directly substituted into the analytical expressions for the APB energies (e.g. Flinn, 1960; Marcinkowski and Brown, 1962), leading to a proportional relationship between γ and T_c of the form $\gamma a^2 \propto T_c$ (see Section 2.5 for more details). Recently, Sparks *et al.* (1991) have used the ordering energy derived from T_c as an indication for the relative phase stability among $L1_2$, $D0_{22}$, and $D0_{23}$. It is on this basis that it is generally believed that, the higher the order-disorder transition temperature, the higher the APB energy. Experimental measurements (see Section 2.5 and Figure 7) show a general trend that is roughly in keeping with the above relationship, but deviations

from the linear relationship can be quite substantial in some alloys.

2.3 Deviations from Ideal APBs— Structural Effects

Owing to the different bonding environment around an APB, atoms near the APB are expected to deviate from ideal lattice positions, as a result of which both the direction and the magnitude of the APB displacement vector \mathbf{p} differ from that for an ideal APB. In general, the deviation vector $\delta\mathbf{p}$ should vary as a function of the position relative to the APB. In most cases, however, a simplification is made in which the APB still separates two rigidly displaced crystals but with a displacement vector in the form

$$\mathbf{p}' = \mathbf{p} + \delta\mathbf{p}$$

with $\delta\mathbf{p}$ being a constant. Yamaguchi *et al.* (1981a) considered for the $L1_2$ structure the supplementary displacement lying in the plane of shear APBs on $\{111\}$ and $\{010\}$. They showed that a rigorous determination of $\delta\mathbf{p}$ would require the construction of the γ surface, which gives the variation of the (general) fault energy as a function of the displacement vector. The equilibrium displacement of the real APB corresponds to a local minimum in the γ surface. However, as demonstrated by Yamaguchi *et al.* (1981a) the directions of such supplementary displacements can be predicted from the symmetry of the atom arrangement in the plane of the fault. In $L1_2$ on the $\{111\}$ plane, the introduction of a $\frac{1}{2}\langle 110 \rangle$ APB destroys the threefold rotational symmetry and the deviation vector $\delta\mathbf{p}$ was shown to be always parallel to the $\langle 112 \rangle$ direction perpendicular to the ideal APB shear \mathbf{p} . Figure 4 shows the section of the $\{111\}$ γ surface that contains the concerned $\langle 112 \rangle$ direction; the curves were calculated using different A-B central-force potentials with C-1 to C-6 representing increasingly larger ordering energies. The ideal APB is represented by R' at which there is no deviation in the $\langle 112 \rangle$ direction. The figure shows that, even with moderate ordering energies, such as those given by C-1 and C-2, the local minimum is already shifted towards Q' , which marks the position of the stable superlattice intrinsic stacking fault (SISF). When the ordering energy is further increased, larger shifts are formed and eventually the $\{111\}$ APB becomes completely unstable for C-6. In the $\{010\}$ plane, the fourfold rotation symmetry is maintained after the APB shear and there is thus no supplementary shear lying within the fault plane. Beauchamp *et al.* (1987), using

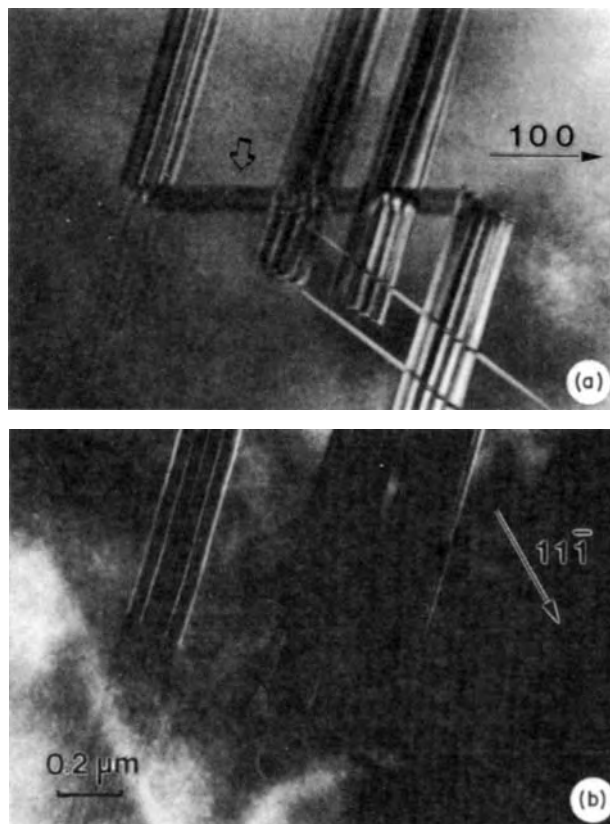


Figure 5. TEM dark-field images of thermal {010} APB in Fe_3Ge . Electron-beam direction is $[001]$. (a) Superlattice reflection $g = 100$, and the {010} APB (indicated by arrow) is in strong contrast. (b) Fundamental reflection $g = 111$, and the APB is in residual contrast (From Ngan, 1992)

pair potentials for Ni_3Al similar to those used by Yamaguchi *et al.* (1981a), calculated the supplementary displacements parallel to shear APBs lying on a range of crystallographic planes and δp was found at maximum on $\{111\}$ with a magnitude approximately equal to $0.06a$. Yamaguchi *et al.* (1981b) also considered the supplementary shears lying within the fault planes in b.c.c. ordered structures ($B2$, $D0_3$, and $L2_1$). In the $B2$ structure, there is no supplementary displacement in the $\frac{1}{2}\langle 111 \rangle$ APB on either $\{110\}$ or $\{112\}$ planes. In $D0_3$ and $L2_1$ the supplementary shears are parallel to $\langle 001 \rangle$ on $\{110\}$ and to $\langle 111 \rangle$ on $\{112\}$. In the $L1_0$ structure, deviations along $\langle 112 \rangle$ directions have been predicted for APBs on $\{111\}$ planes and, similar to the $L1_2$ structure, no deviation is expected in APBs on $\{100\}$ (Yamaguchi *et al.*, 1985). In general, a supplementary displacement lying within the fault plane is expected if the crystal rotation symmetry is destroyed by the introduction of the APB, while supplementary

displacement normal to the fault plane should occur in all cases. Beauchamp *et al.* (1987) found that the effect of relaxations was to reduce significantly the degree of APB energy anisotropy estimated from the nearest-neighbor interactions (e.g. Flinn, 1960). Recently, more sophisticated theoretical calculations have been made for the APB energies, but there has so far been little application of the modern techniques to the extent of structural deviations from ideal APBs. Fu and Yoo (1992), using the full-potential linearized augmented plane-wave (F-LAPW) method, found in NiAl that allowing for relaxation normal to the APB would significantly reduce the APB energies. In NiAl , the $\{110\}$ APB energy (γ_{110}) is 1000 mJ m^{-2} without relaxation, but decreases to 810 mJ m^{-2} after allowing for relaxation.

Supplementary displacement at the APBs has been observed experimentally in TEM in a number of alloys. In TEM an APB is visible if $g \cdot p \neq \text{integer}$ and the

contrast vanishes when $\mathbf{g} \cdot \mathbf{p}$ = integer, the latter happens when \mathbf{g} is a fundamental reflection or perpendicular to \mathbf{p} . Owing to the supplementary displacement $\delta \mathbf{p}$, $\mathbf{g} \cdot \mathbf{p} \neq$ integer even in fundamental reflections or in those normal to the ideal APB shear \mathbf{p} , thus enabling the identification of the direction and magnitude of $\delta \mathbf{p}$ from the *residual contrast*. Figure 5 shows an example of the residual contrast of thermal $\{010\}$ APB observed in $L1_2$ Fe_3Ge (Ngan, 1992). Figure 5(a) is a dark-field image taken with the 100 superlattice reflection in which the $\{010\}$ APB (indicated by an arrow) is in strong contrast (the other fringe patterns are due to superlattice stacking faults). In Figure 5(b), taken with the 111 fundamental reflection, the APB contrast is much weaker but still visible (i.e. showing residual contrast). Comparisons with simulated images show that the residual contrast is formed by a supplementary displacement normal to the APB with a maximum amplitude of the order of 0.3 \AA . Lasalmonie *et al.* (1988) studied the residual contrast of thermal APBs in rapidly solidified Ni_3Al and found that for a non-conservative APB on $\{101\}$ the residual contrast could be accounted for by a supplementary displacement containing components both parallel and normal to the fault plane. The component normal to the fault plane was found to be of the order of $10^{-2}a$ with the component parallel to the APB being much smaller. Thermal APBs in rapidly solidified B2-ordered Fe_3Al have also been found to exhibit residual contrast (Prakash *et al.*, 1991), but in this case the additional displacement was thought to be caused by impurities segregated to the APB.

2.4 Deviations from Ideal APBs— Chemical Effects

Even after allowing for structural relaxations as shown above, an APB is still thermodynamically unstable since it involves an increase in the internal energy but with very little extra entropy to compensate. Therefore, when thermal fluctuations permit, thermodynamic equilibrium configurations would invoke an increase in the degree of randomness near the boundary, which may appear either in a reduction in the local degree of order or in the segregation of impurity or excess (when composition is not exactly stoichiometric) atoms to the boundary. The first treatment was given for a stoichiometric B2-ordered alloy by Brown (1959), who considered the situation in which the entropy increase was effected by a decrease in the degree of order at the APB. On the basis of the Bragg–Williams approximation (Bragg and Williams, 1934, 1935), the

degree of order was found to increase with the vertical distance from the boundary, and the thickness of the APB was defined as the distance at which the degree of order becomes essentially the same as that in the bulk. The thickness of the APB is very small except very close to the transition temperature T_c . At $0.975T_c$, the thickness of the APB is about 10 interplanar spacings. The disordering at APBs in the $L1_2$ -ordered structure was investigated by Popov *et al.* (1966), also using the Bragg–Williams approach. They found that disordering within the first atomic layer adjacent to the APB started at a temperature as low as $0.2T_c$. Similar to the finding of Brown in B2 alloys, disordering was found to extend to approximately 10 atomic layers only when the temperature is just a few degrees below T_c . A more elaborate investigation of the equilibrium structure of APBs in the $L1_2$ -ordered structure was made by Kikuchi and Cahn (1979) using the tetrahedron approximation of the cluster-variation method. They found that a distinct disordered phase may coat the APB, the effect (termed ‘wetting’) being more pronounced in alloys of non-stoichiometric compositions. The above findings have been further substantiated by Sanchez *et al.* (1987), who, using a treatment similar to Kikuchi and Cahn, showed in more detail how the APBs get more diffuse when the temperature approaches that of the transition. In addition, local disordering around the APB was shown to involve an increase near the APB in the concentration of the majority atoms (an increase of 1.2%, from 75 to 76.2%). For off-stoichiometric compositions the disordering is more pronounced, with greater segregation of majority atoms to the APB (increase of up to 6.9%).

Indirect experimental evidence for the thermal disordering at APBs has been provided by TEM observations in which the separation of the APB-coupled partial dislocations was found to increase with annealing temperature, suggesting a lowering of APB energy with temperature. Models for the disordering at the APBs (Popov *et al.*, 1966; Kikuchi and Cahn, 1979) predicted that a decrease in the local degree of order should bring about a corresponding drop in the surface energy. Popov *et al.* (1966) showed that for the $L1_2$ structure the $\{111\}$ APB energy would decrease to about 50% of the low-temperature value when the temperature was raised to $\sim 0.6T_c$; at this temperature the $\{001\}$ APB energy was shown by Kikuchi and Cahn (1979) to exhibit a similar decrease. The decrease of the APB energy with temperature has been observed in a number of ordered alloys, using *in situ* TEM observations in which the width of the APB is monitored during dynamic

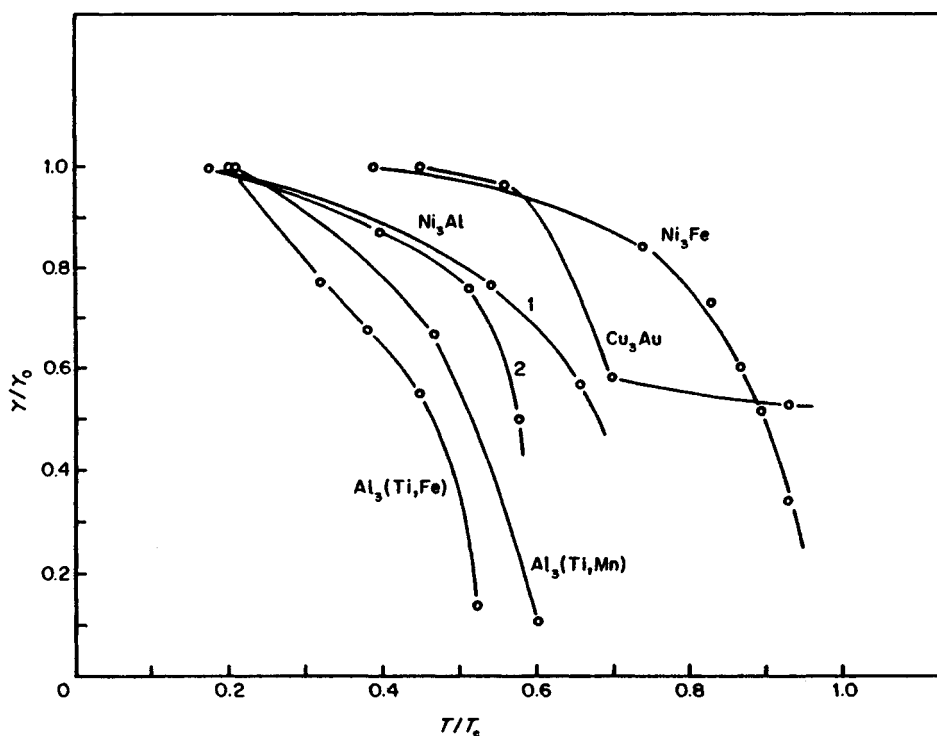


Figure 6. Variation of APB energies with temperature observed in some $L1_2$ compounds. For Ni_3Al the measurements were made for $\{001\}$ APB. Curve 1 was obtained using weak-beam TEM (Veyssi re *et al.*, 1989) and curve 2 was a measurement using lattice-resolution TEM (Crimp, 1989). For other compounds the APB is on $\{111\}$. The APB energies are in fractions of the value at room temperature (γ_0)

annealing, or using *post mortem* examinations. Morris and Smallman (1975) measured the width of $\{111\}$ APB in $L1_2$ Cu_3Au ($T_c = 663$ K) samples that were deformed and subsequently annealed at 623 K ($0.94T_c$) for 5–15 min. From freshly deformed samples, the APB energy was measured at about 48 mJ m^{-2} . In subsequently annealed samples, however, the APB energy was found to have decreased by about 56%, to 27 mJ m^{-2} . Veyssi re *et al.* (1989), using the weak-beam method, observed the variation of the $\{001\}$ APB energy in Ni_3Al in samples deformed at three different temperatures, and the energy was found to have decreased from 126 mJ m^{-2} at room temperature ($0.18T_c$) to 72 mJ m^{-2} at 1100 K ($0.66T_c$). (Ni_3Al is known to remain ordered up to the melting point and here T_c is taken as the melting temperature.) The decrease of $\{001\}$ APB energy with temperature in Ni_3Al was soon confirmed by Crimp (1989) using lattice-resolution TEM. In Ni_3Fe ($T_c = 776$ K), Korner and Schoeck (1990) observed the lowering of $\{111\}$ APB energy with temperature using the TEM *in situ* annealing

technique, and found that the $\{111\}$ APB energy was halved at $0.84T_c$. *In situ* annealing experiments have also been made in $L1_2$ -ordered Al_3Ti containing Fe and Mn by Morris (1992a,b), who reported similar decreases in the $\{111\}$ APB energy. Results of the equilibrium APB energies as a function of temperature in some $L1_2$ alloys are plotted in Figure 6, in which the APB energy at room temperature has been taken as unity and the temperatures are represented in fractions of the transition temperature T_c .

Segregation of vacancies to APBs has also been shown to contribute to the increase in the compensating entropy as well as to a lowering in the internal energy. In quenched β - CuZn with the B2 ordered structure, Cupschalk and Brown (1968) observed in TEM a large density of dislocation loops decorating thermal APBs. The dislocation loops were thought to be formed by the collapse of disks of vacancies that had preferentially migrated to the APBs. In addition to a contribution to an increase in the entropy term, Cupschalk and Brown showed that vacancies sitting at the APB in the B2

structure had lower self-energies. A vacancy in B2 in the bulk is associated with the elimination of eight nearest AB bonds (dangling bonds), but at the APB there are m dangling bonds between AA or BB atoms and $8-m$ dangling bonds between AB atoms, amounting to a reduction of mV in the vacancy self-energy, m being dependent on the orientation of the APB and the specific location in the APB at which the vacancy sits. Vacancies preferentially concentrated at the APB were shown by Cupschalk and Brown to form an important mechanism controlling the kinetics of the migration of thermal APBs.

Segregation of alloying elements to $\{111\}$ APBs in a model $L1_2$ (A_3B) compound containing ternary elements has been investigated theoretically by Wu *et al.* (1989, 1991). The major finding of the work is that the concentration of the elements at the APB depends on the type of sublattice that the ternary elements occupy in the bulk alloy. At the $\{111\}$ APB there is a depletion of A atoms and an enrichment of B atoms if the ternary elements preferentially occupy the B sublattice; conversely, there is a depletion of B atoms and an enrichment of A atoms if the ternary elements preferentially occupy A sublattices. Strengthening models based on the above segregation study were found consistent with the strengthening of Ni_3Al by ternary elements measured experimentally (Wu *et al.*, 1991). There has been little direct experimental observation of segregation of alloying elements to APBs. Horton and Miller (1987), using the atom probe method, observed in B-doped Ni_3Al the segregation of B to APB as well as to dislocations, stacking faults, and grain boundaries.

2.5 Energy of APBs

Early estimates for the surface energy of the APB in ordered alloys were based on the ordering energies V and W obtained from their linear relationships with the transition temperature T_c : B2 (Rachinger and Cottrell, 1956; Potter, 1969/70), Cu_3Au and $CuAu$ (Marcinkowski *et al.*, 1961; Sastry and Ramaswami, 1976), $NiAl$ (Ball and Smallman, 1966), and $TiAl$ (Shechtman *et al.*, 1974). This approach has also been used more recently: Ni_2AlTi , Co_2AlTi (Umakoshi and Yamaguchi, 1985; Umakoshi *et al.*, 1986) and $FeAl$ (Mendiratta and Law, 1987). In the nearest-neighbor approximation, the APB energy γ is related to the ordering energy V via

$$\gamma = F(h, k, l) \frac{V}{a^2} S^2$$

where $F(h, k, l)$ gives the orientation dependence, a is the lattice constant, and S is the long-range order parameter (Marcinkowski, 1963; Leamy *et al.*, 1970). (In $D0_3$ and $L2_1$ $\langle 100 \rangle$ APB energies are related to the ordering energy W of the second-nearest neighbors; see Tables 5 and 6.) In the Ising-type models for the disorder-order transition, the transition temperature T_c is also related to V (and to W in $D0_3$ and $L2_1$) through a proportionality factor, $T_c = wV/k$, where k is the Boltzmann constant and w is a constant that depends on the structure and on the models used. In the B2 structure w varies from 3.1 to 4.0 (for a review, see Guttman, 1956); in $L1_2$, w varies from 0.82 (Yang, 1945), 1.0 (Peierls, 1936), to 1.5 (Cowley, 1950). In $L1_0$, a similar relationship was obtained, giving $w=0.73$ (Li, 1949, 1950). We thus have the following relationship between γ and T_c :

$$\gamma = \frac{k}{a^2} \frac{F(h, k, l) S^2}{w} T_c$$

In $L1_2$ -ordered Cu_3Au , the agreement between the above theoretical estimate and the experimental measurement from the separation of the APB-coupled superpartials is reasonable. Marcinkowski *et al.* (1961) used the APB energy obtained from T_c to calculate the equilibrium separation of the superpartials in Cu_3Au and found that the predicted separation (78–124 Å) was just slightly lower than the experimental measurement using bright-field TEM imaging (90–135 Å), implying that the predicted energy is somewhat higher than the true value. Similar findings have also been made in Cu_3Au by Sastry and Ramaswami (1976) using the weak-beam dark-field method with a higher resolution limit. In the $L2_1$ structure with A_2BC composition, the critical temperature is related to the second-nearest-neighbor ordering energy between B and C atoms, $W_{BC} = kT_c/3.0$ (Murakami *et al.*, 1971). In the $D0_3$ structure (A_3B) the possibility of an additional transition of $D0_3$ to B2 (e.g. in Fe_3Al) enables both V and W to be determined (Rudman, 1960; Crawford, 1971). The relationships of V and W with T_c are summarized in Tables 1–6,* in which APB energies in compounds with the six most common ordered structures are listed. In Tables 1–6 values derived from the transition temperatures are referred to as being obtained by method T_c . For the $L1_2$ structure the variation of $\gamma_{111} a^2$ with T_c is represented by the two straight lines in Figure 7 corresponding to $w=0.82$

*The notation (\dots) and $\{\dots\}$ in some of the tables indicates that all permutations of the first two indices are allowed, whereas the third one is fixed.

Table 1. APB energies in L1₂ compounds: $\mathbf{p} = \frac{1}{2}(1\ 1\ 0)$; $\gamma_{111} = (2V - 6W)/\sqrt{3}a^2$, $\gamma_{010} = -2W/a^2$; $V = kT_c/w$, $w = 0.82$ (Yang, 1945), 1.0 (Peierls, 1936), 1.5 (Cowley, 1950)

*

Composition (at.%)	γ_{111} (mJ m ⁻²)	γ_{010} (mJ m ⁻²)	Method ^a	References
Ni ₃ Al	139–255		T_c	
~ Ni ₃ Al	180 ± 30 (350 °C)	140 (350 °C)	WB	Veyssière <i>et al.</i> (1985)
~ Ni ₃ Al		90 ± 5	WB	Douin <i>et al.</i> (1986)
17.4 Al, 6.16 Ti	250 ± 30	250 ± 30	WB	Korner (1988)
24 Al, 0.24 B		126	WB	Veyssière <i>et al.</i> (1989)
23.5 Al		149 ± 12	HREM	Crimp (1989)
22.9 Al	169 ± 19	104 ± 8	WB	Dimiduk (1989)
24.2 Al	163 ± 21	122 ± 11	WB	Dimiduk (1989)
25.9 Al	190 ± 26	170 ± 21	WB	Dimiduk (1989)
24.1 Al, 0.9 Sn	166 ± 18	129 ± 12	WB	Dimiduk (1989)
21.1 Al, 3.7 Sn	174 ± 20	146 ± 15	WB	Dimiduk (1989)
23.4 Al, 1.0 V	192 ± 26	155 ± 17	WB	Dimiduk (1989)
20.8 Al, 4.0 V	198 ± 32	201 ± 32	WB	Dimiduk (1989)
24.7 Al, 1.0 Ta	165	155	WB	Baluc (1990)
22.7 Al, 0.26 Hf	150 ± 20	120 ± 20	WB	Neveu (1991)
22.7 Al, 1.6 Hf	190 ± 20	170 ± 20	WB	Neveu (1991)
Ni ₃ Al	142	83	EAM(n) ^b	Chen <i>et al.</i> (1986)
Ni ₃ Al	96	28	EAM(n)	Foiles and Daw (1987)
Ni ₃ Al		197	$V_{ij}(n)$	Stocks <i>et al.</i> (1987)
Ni ₃ Al		230	LMTO(n)	Stocks <i>et al.</i> (1987)
Ni ₃ Al	220	140	F-LAPW(n)	Fu and Yoo (1989)
Ni ₃ Ga	123–226		T_c	
Ni ₃ Ga	110 ± 30	17 ± 5	WB(iso.) ^c	Suzuki <i>et al.</i> (1979)
Ni ₃ Mn	62–114		T_c	
22.7 Mn	75		TEM(iso.)	Marcinkowski and Miller (1961)
Ni ₃ Fe	65–119		T_c	
~ Ni ₃ Fe	92	55	WB	Korner and Karnthaler (1985)
Cu ₃ Au	50–92		T_c	
24.8 Au	80 ± 5		TEM(iso.)	Marcinkowski <i>et al.</i> (1961)
24.85 Au	48 ± 5		WB(iso.)	Morris and Smallman (1975)
~ Cu ₃ Au	39 ± 5		WB(iso.)	Sastry and Ramaswami (1976)
Ni ₃ Si	123–225		T_c	
23.1 Si	220	220	WB	Tounsi (1988)
24.5 Si	250	250	WB	Tounsi (1988)
10.9 Si, 10.7 Ti		124	WB	Yoshida and Takasugi (1991)
Co ₃ Ti	119–218		T_c	
23 Ti, 3 Ni	270	210	WB	Oliver (1992)
22 Ti	155	130	WB	Oliver (1992)
Co ₃ Ti		282	LMTO	Pei <i>et al.</i> (1989)
Al ₃ Ti	112–205		T_c	
28 Ti, 8 Fe	310		WB	Morris (1992a)
~ Al ₃ Ti ₂ Mn	270		WB	Morris (1992b)
~ Al ₃ Ti(Fe)	> 430		Ded. ^d	Inui <i>et al.</i> (1992)
Al ₃ Sc	100–184		T_c	
Al ₃ Sc	670	450	F-LAPW(n)	Fu (1990)

^aSee text and/or list of acronyms.^bn, no relaxation allowed at APB.^ciso., fault energy determined using isotropic elasticity.^dDeduced from instability condition of APB vs. SISF.

Table 2. APB energies in $L1_0$ compounds: $\mathbf{p} = \frac{1}{2}\langle 011 \rangle$; $\gamma_{111} = (4V - 12W)/\sqrt{3}a^2$, $\gamma_{100} = -4W/a^2$ (assuming $c/a = 1$) (Yamaguchi and Umakoshi, 1990); $V = kT_c/w$, $w = 0.73$ (Li, 1949, 1950)

Composition (at.%)	γ_{111} (mJ m ⁻²)	γ_{100} (mJ m ⁻²)	Method ^a	References
TiAl	477		T_c	
~TiAl	145 ± 15	100 (600 °C)	WB	Hug <i>et al.</i> (1989)
TiAl	520	435	Calc. ^b	Yamaguchi <i>et al.</i> (1985)
TiAl	670	347	LKKR(n) ^c	Woodward <i>et al.</i> (1991)
TiAl	510	430	F-LAPW(n)	Fu and Yoo (1990)
TiAl	306	66	EAM(n)	Rao <i>et al.</i> (1991)

^aSee text and/or list of acronyms.^bCalculated using pair potential.^cn, no relaxation allowed at APB.**Table 3.** APB energies in $D0_{22}$ structure: $\mathbf{p}_1 = \frac{1}{2}\langle 111 \rangle$, $\mathbf{p}_{11} = \frac{1}{2}\langle 011 \rangle$; $\gamma_{111}^1 = 2(V - W)/\sqrt{3}a^2$, $\gamma_{001}^1 = -2W/a^2$, $\gamma_{111}^{11} = (2V - 4W)/\sqrt{3}a^2$ (Yamaguchi and Umakoshi, 1990); relation with T_c not known

Composition (at.%)	γ_{111}^1 (mJ m ⁻²)	γ_{001}^1 (mJ m ⁻²)	Method ^a	Reference
~Al ₃ Ti	200 (400 °C)	25 (400 °C)	WB	Hug <i>et al.</i> (1989)

^aSee text.**Table 4.** APB energies in B2 structure: $\mathbf{p} = \frac{1}{2}\langle 110 \rangle$; $\gamma_{110} = 4(V - W)/\sqrt{2}a^2$, $\gamma_{112} = 8(V - W)/\sqrt{6}a^2$ (Yamaguchi and Umakoshi, 1990); $V = kT_c/w$, $w = 3.076, 3.278, 3.396, 4.0$ (Guttman, 1956)

Composition (at.%)	γ_{110} (mJ m ⁻²)	γ_{112} (mJ m ⁻²)	Method ^a	References
CuZn	82–107	95–124	T_c	
48.6 Zn	40		TEM	Head <i>et al.</i> (1967)
47.0 Zn	50 ± 10	39 ± 7	WB	Saka <i>et al.</i> (1984)
46 Zn	57 ± 7	62 ±	WB	Dirras <i>et al.</i> (1992)
FeAl	182–237	210–273	T_c	
FeAl	230 ^b		WB	Crawford and Ray (1977)
FeAl	160		Est. ^c	Rudy and Sauthoff (1986)
FeAl	500		F-LAPW(n) ^d	Freeman <i>et al.</i> (1991)
FeAl	650	1040	F-LAPW(n)	Fu and Yoo (1992)
FeAl	300	820	F-LAPW	Fu and Yoo (1992)
NiAl	224–291	260–336	T_c	
NiAl	400		Est. ^c	Rudy and Sauthoff (1986)
NiAl	240	380	EAM	Clapp <i>et al.</i> (1989)
NiAl	1000	950	LMTO(n)	Freeman <i>et al.</i> (1991)
NiAl	425	460	EAM(n)	Rao <i>et al.</i> (1991)
NiAl	1000	1230	LMTO(n)	Fu and Yoo (1992)
NiAl	810	990	LMTO	Fu and Yoo (1992)
Ni ₂ MnAl ₃	740		LMTO(n)	Rao <i>et al.</i> (1991)
Ni ₂ CrAl ₃	510		LMTO(n)	Fu and Yoo (1990)
Ni ₂ Val ₃	250		LMTO(n)	Fu and Yoo (1990)
Ni ₃ Al ₂ Cr	250		LMTO(n)	Fu and Yoo (1990)
Ni ₃ Al ₂ V	550		LMTO(n)	Fu and Yoo (1990)
AlRu	248–322	286–372	T_c	
AlRu	690		LMTO	Freeman <i>et al.</i> (1991)
CoAl	228–297	263–343	T_c	
CoAl	360		Est. ^c	Rudy and Sauthoff (1986)
Fe ₃ Al	45–60	52–68	T_c	
Fe ₃ Al	15 ^b		WB	Crawford and Ray (1977)

^aSee text and/or list of acronyms.^bExtrapolated value.^cOrdering energy estimated from Monte Carlo simulation.^dn, no relaxation allowed at APB.

Table 5. APB energy in D0₃ compounds: $\mathbf{p}_1 = \frac{1}{2}(111)$, $\mathbf{p}_{11} = (111) \langle 100 \rangle$; $\gamma_{110}^I = V/\sqrt{2}a^2$, $\gamma_{112}^I = 2V/\sqrt{6}a^2$, $\gamma_{110}^{II} = 2W/\sqrt{2}a^2$, $\gamma_{112}^{II} = 4W/\sqrt{6}a^2$ (Yamaguchi and Umakoshi, 1990); $V = \frac{1}{2}k(T_c' + 2T_c)$, $W = \frac{2}{3}kT_c'$ when $T_c' \ll T_c$; $V = \frac{1}{2}kT_c$, $W = \frac{2}{3}kT_c$ when $T_c' = T_c$; T_c' is the temperature of transition of D0₃ → B2 (Rudman, 1960; Crawford, 1971)

Composition (at.%)	γ_{110}^I (mJ m ⁻²)	γ_{110}^{II} (mJ m ⁻²)	Method ^a	References
Fe ₃ Al	60	43	T_c	Crawford and Ray (1977)
Fe ₃ Al	70 ^b	100 ^b	WB	
Fe ₃ Si	126	169	T_c	Lakso and Macinkowski (1969)
Fe ₃ Si		225	TEM(iso.) ^c	

^a See text and/or list of acronyms.

^b Extrapolated value.

^c iso., calculated using isotropic elasticity.

Table 6. APB energy in L2₁ (A₂BC) structure: $\mathbf{p}_1 = \frac{1}{2}(111)$, $\mathbf{p}_{11} = (111) \langle 100 \rangle$; $\gamma_{110}^I = (E_1 - 2E_2)/\sqrt{2}a^2$, $\gamma_{112}^I = (2E_1 - 4E_2)/\sqrt{6}a^2$, $\gamma_{110}^{II} = 2W_{BC}/\sqrt{2}a^2$, $\gamma_{112}^{II} = 4W_{BC}/\sqrt{6}a^2$; $E_1 = 2V_{AB} + 2V_{AC} - V_{BC}$, $E_2 = 2W_{AB} + 2W_{AC} - W_{BC}$ (Yamaguchi and Umakoshi, 1990); $W_{BC} = kT_c/3.0$ (Murakami *et al.*, 1971)

Composition (at.%)	γ_{110}^I (mJ m ⁻²)	γ_{110}^{II} (mJ m ⁻²)	Method ^a	References
Ni ₂ AlTi		132	T_c	Umakoshi and Yamaguchi (1985)
Ni _{2.03} Al _{1.11} Ti _{0.86}		115	WB(iso.) ^b	
~Co ₂ AlTi		80	WB(iso.)	

^a See text.

^b iso., fault energy determined using isotropic elasticity.

(Yang, 1945) and $w = 1.5$ (Cowley, 1950) respectively; this is to be compared with values obtained experimentally (full circles) and with those determined by atomistic calculations (open circles).

In theoretical treatments based on the Ising model, the APB energy is affected by the long-range order parameter S via $\gamma = \gamma_0 S^2$, where γ_0 is the APB energy for the case of perfect order; the APB energy is expected to decrease with the decrease in the degree of long-range order. Such a relationship can be used to estimate the effect of composition on the APB energy in non-stoichiometric alloys, in which the maximum order parameter S_M depends on the composition. In the L1₂ structure with composition A_{1-x}B_x, $x \leq 0.25$, the maximum degree of long-range order is given by $S_M = 4x$ (Leamy *et al.*, 1970) and thus $\gamma = 16\gamma_0 x^2$, i.e. the APB energy decreases with decreasing concentration of the minority component. Dimiduk (1989) measured the APB energies in binary Ni₃Al at three compositions containing 22.9, 24.2, and 25.9 at.% Al; the first two compositions were found to have similar $\{111\}$ APB energies, but the APB energy in the third composition is higher by about 20–30 mJ m⁻². In the B2 compound with composition A_{1-x}B_x, $x \leq 0.5$, the maximum degree of long-range order is given by $S_M = 2x$ and thus $\gamma = 4\gamma_0 x^2$ (Leamy *et al.*, 1970; Crawford, 1971). Such a trend was found experimentally in B2-ordered Fe₃Al in which the $\{110\}$ APB energy was found to decrease

from 110 mJ m⁻² at 36 at.% Al to 30 mJ m⁻² at 27 at.% Al (Crawford and Ray, 1977).

Recently, more sophisticated theoretical calculations of APB energies have been made on computers, employing a number of techniques: embedded-atom method (EAM) (Chen *et al.*, 1986; Foiles and Daw, 1987), full-potential linearized augmented plane-wave (FLAPW) method (Fu, 1990; Fu and Yoo, 1990), and linear muffin-tin orbitals (LMTO) method (Hong and Freeman, 1991). Tables 1–6 contain results of APB energies calculated by these methods. For details of atomistic calculation, see Chapters 3 and 4 by Carlsson and Meschter and by Voter in this volume. There is as yet, however, no consistent agreement between the results given by the different techniques or by different workers using the same technique. For example, the $\{111\}$ APB energy in Ni₃Al was calculated to be 142 mJ m⁻² by Chen *et al.* (1986) and 96 mJ m⁻² by Foiles and Daw (1987), both using the embedded-atom method; a similar discrepancy is also found in the $\{001\}$ APB energy, 83 mJ m⁻² by Chen *et al.* and 28 mJ m⁻² by Foiles and Daw. Much higher values of $\{001\}$ APB energy in Ni₃Al were obtained by Stocks *et al.* (1987), 197 mJ m⁻², using the interchange potential method, and still higher at 230 mJ m⁻² by LMTO. Discrepancies of similar magnitude have also been found in calculated APB energies in B2 compounds. The reasons for the discrepancies in the theoretical calculations are not yet

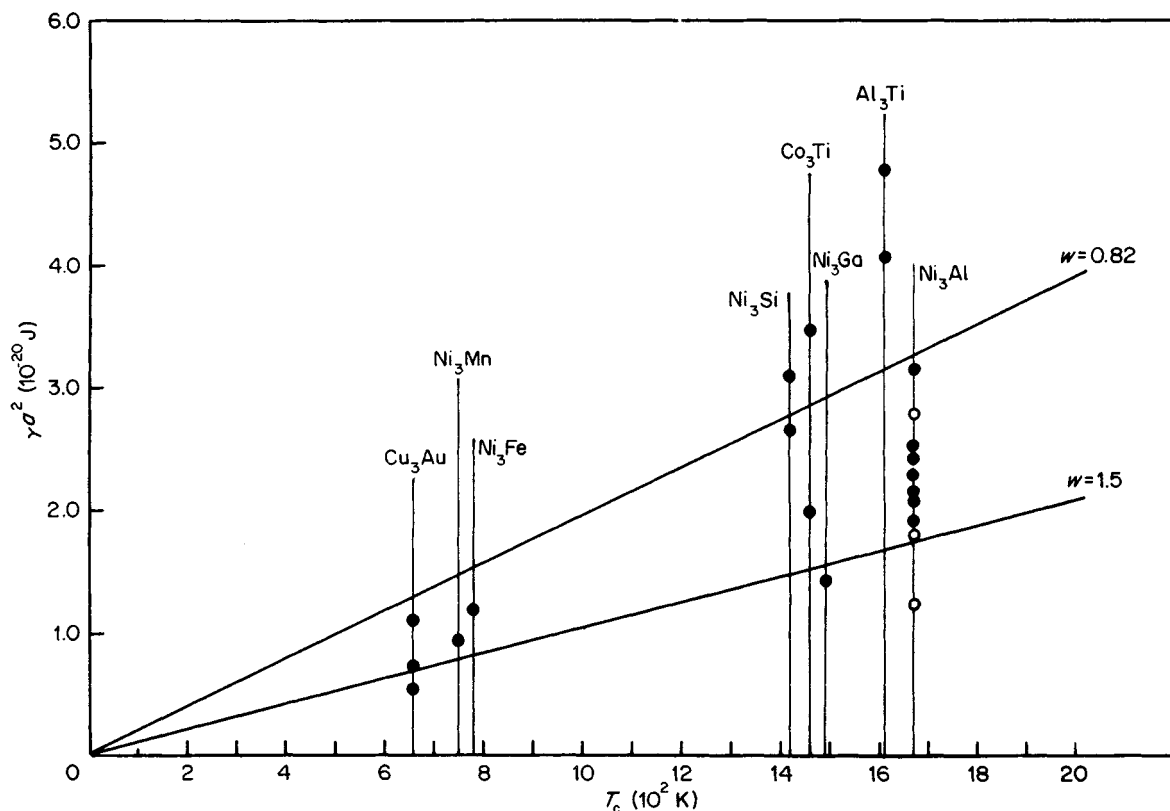


Figure 7. The $\{111\}$ APB energies in $L1_2$ alloys plotted against the disorder-order transition temperature T_c . Full circles represent values determined experimentally using TEM. Open circles represent values given by atomistic calculations. The two straight lines are energies obtained from the nearest-neighbor interaction with the ordering energies derived from T_c using $w=0.82$ and $w=1.5$.

clear. One possible reason could be that very often structural relaxations at the APBs have not been allowed for in the calculations (e.g. Stocks *et al.*, 1987; Chen *et al.*, 1986; Hong and Freeman, 1991). Fu and Yoo (1992) considered the effect of structural relaxation normal to the fault plane on APB energies in FeAl and NiAl. They found that substantial reductions in the APB energies were obtained as a result of allowing for relaxation. The $\{112\}$ APB energies (γ_{112}) decreased from 1230 and 1040 mJ m^{-2} to 990 and 820 mJ m^{-2} for FeAl and NiAl respectively. It should be noted that for $\frac{1}{2}\langle 111 \rangle$ APB in the B2 lattice, structural relaxation within the fault plane is not expected on either $\{110\}$ or $\{112\}$ owing to crystal symmetry in these two planes, while in general relaxation occurs both normal and parallel to the fault plane. If relaxation is the primary source of the discrepancies, the lower values calculated by including relaxation are the more realistic ones.

* The experimental determination of the APB energies is usually made using TEM by measuring the separation

between APB-coupled superpartials. Early measurements were made by TEM bright-field or dark-field imaging under the two-beam condition, which has a rather low resolution limit (Marcinkowski, 1963; Head *et al.*, 1967). The weak-beam technique developed by Cockayne *et al.* (1969) has a resolution limit of the order of 10–15 Å and has been widely used for the measurement of APB energies, as well as surface energies of ordinary stacking faults. The key assumption in this technique is that the APB-coupled superpartials are in equilibrium separation r , which is related to the APB energy γ via

$$\gamma = \frac{K(\theta)b^2}{2\pi r}$$

where b is the Burgers vector of the superpartials bounding the APB and $K(\theta)$ is the energy factor, which is a function of the dislocation character and the elastic constants. In general the line image of a dislocation in

TEM does not coincide exactly with its true position and, under the weak-beam condition, shifts of the order of 10 Å are predicted, the direction of the shift being dependent on the sign of $\mathbf{g} \cdot \mathbf{b}$, where \mathbf{g} is the reflection used for the imaging. Since, in most cases, the partial dislocations bounding the APB have the same Burgers vector, their line images are expected to be shifted in the same direction by approximately the same amount; the true separation can therefore be measured directly from the image. Lattice-resolution TEM, in which the dislocations are imaged end-on in a thin foil, provides a much higher resolution power (< 2 Å) than the weak-beam technique. This technique was used by Crimp (1989) to measure the $\{001\}$ APB energy in Ni_3Al . The difficulty of the lattice imaging method lies in that specimen preparation is more difficult and that in general a very high dislocation density has to be introduced by heavy deformation. The advantage of the weak-beam method is that the APB width can be observed over a wide range of dislocation characters (see Chapter 22 by Veyssi re and Douin in this volume for examples of TEM observations of dislocations). Tables 1–6 contain results of APB energies measured using the weak-beam (WB) method. In most of the measurements the energy factor $K(\theta)$ was calculated using anisotropic elasticity, but some of the early work was based on isotropic elasticity (marked 'iso.' in Tables 1–6). Experimental measurements using the weak-beam method are often subjected to about 10–20% fluctuations, for which several factors may be responsible. One is that the dislocations may not be always in the equilibrium configuration, and this is particularly likely for dislocations that are liable to transform into locked structures (e.g. screw and edge dislocations on $\{001\}$ in L1_2 compounds (Sun *et al.*, 1991)). Another factor that may cause fluctuations in the separation between partial dislocations is inhomogeneous element distribution, which would cause the fault energy to vary with position.

3. Grown-in APBs and APDs

3.1 APD Morphology and Crystallography

Owing to the surface energy of the APB, the thermally formed APDs should vanish when true equilibrium is attained, but it is possible to produce a metastable three-dimensional domain structure in which the annihilation of the domains becomes very slow. Depending on the number of APB variants available, there are two basic types of metastable three-dimensional domain structures. When there are four or more APB variants available, a case that has been known since Bragg (1940),

the post-ordering microstructure can be described as a three-dimensional mosaic or foam built up by the domains, analogous in morphology to a polycrystalline aggregate of grains. The structure becomes metastable when the domains meet along lines in groups of three at mutual angles of 120° , and at corners in groups of four (Bragg, 1940); in this configuration the surface tensions are fully balanced. In a three-dimensional space there is no regular polyhedron that can be stacked with the plane faces meeting at the above angles, although a pentagonal dodecahedron is a close approximation. When there are only two APD variants available, the merging of randomly nucleated ordered domains would lead either to isolated 'islands' of one domain embedded in another domain, or to a configuration, schematically illustrated in Figure 8 (English, 1966), in which intertwining, multiply connected 'pipes' of one domain weave through the primary domain. The 'island' structure is highly unstable with a relatively high shrinking rate (Cupschalk and Brown, 1968). The latter structure, known as the 'Swiss-cheese' structure (English, 1966), may render the domain structure metastable since the surface of the connecting pipes is double-curved or saddle-shaped, i.e. the two principal radii of curvature are opposite in sign (Cupschalk and Brown, 1968). The low annihilation rate results from the surface tension from the two principal curvatures driving the APB in opposite directions. Cupschalk and Brown (1968) examined the rate of the flattening of wavy APB and found that it was much slower than the shrinkage of an isolated spherical domain, but they did not extend their treatment to the double-curved pipes in three dimensions. Both of the above two types of three-dimensional domain structures have been observed experimentally: e.g. Lasalmonie *et al.* (1988), Fisher and Marcinkowski (1961), and Horton and Liu (1985), in L1_2 compounds with four variants; and Marcinkowski and Brown (1962), Cupschalk and Brown (1967), and Crawford (1971), in B2 with two variants.

Another crystallographic factor that affects the morphology of thermal APDs is whether or not the crystal system changes during the disorder–order transition. The transformation is termed 'isostructural' if the crystal system remains the same upon ordering, e.g. in the ordering of most B2 and L1_2 alloys from corresponding cubic disordered systems. If ordering results in a change in the crystal symmetry, e.g. in the ordering of many L1_0 and D0_{22} structures, the transformation is termed 'neostuctural' (Tanner and Leamy, 1974). The morphology of APDs in isostructural ordering transitions is usually well-defined and the preferential orientation of the APBs, or the lack of it,

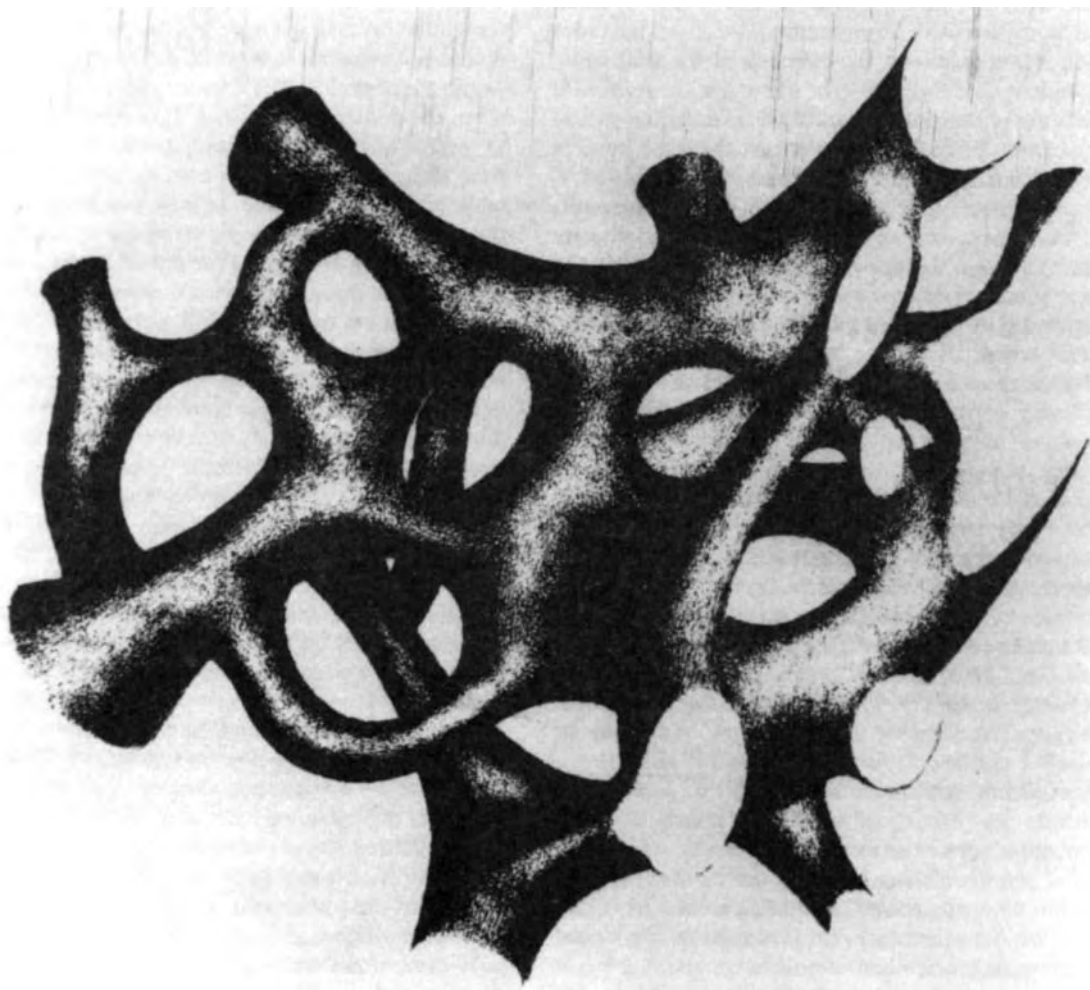


Figure 8. The 'Swiss-cheese' structure of thermal APDs in compounds with two APB variants (English, 1966). (Reprinted with permission from *Transactions of the Metallurgical Society*, 236, 14–18 (1966), a publication of the Minerals, Metals & Materials Society, Warrendale, Pennsylvania 15086)

can usually be interpreted on the basis of the APB energy anisotropy. In neostructural transitions, the domain structure is more complicated because unique axes, e.g. the tetragonal axis in $L1_0$, can have different orientations in different domains, as a result of which neighboring domains may be misoriented. Often the lattice strain caused by the misorientation in neostructural changes can be accommodated by deformation, e.g. twinning in $L1_0$ -ordered CuAu and TiAl (Tanner and Leamy, 1974; Yamaguchi and Umakoshi, 1990).

3.2 APDs and Disorder–Order Transition

The presence of APDs as a result of cooling through the disorder–order transition temperature is usually taken as an indication that the transition is a first-order phase change involving a latent heat. Such a transition starts with the ordered domains being nucleated independently in an *existing solid* disordered crystal, followed by a stage in which the ordered and disordered phases coexist, and finally the disordered phase diminishes and the ordered domains come into contact,

the boundary between them being APBs. In higher-order or continuous transitions, APDs may also be formed but the physical picture is not as clear (Tanner and Leamy, 1974). A rigorous determination of the order of the transition requires that the 'lever rule' be checked from microstructural observations. Ordering occurring in an existing crystal was termed 'sequential ordering' by Cahn (1987) to contrast with 'direct ordering' in which the alloy freezes directly into the ordered state. Cahn emphasized that this distinction was particularly important when the disorder-order transition temperature T_c is very close to the melting point, and that thermal APD should form only in sequential ordering. This view, however, appears to contradict the observation that, in Ni_3Al , which has its T_c near to or above the melting point and in which thermal APDs are not normally observed, thermal APDs are formed most readily in rapidly solidified samples (Horton and Liu, 1985). According to Cahn (1987), the undercooling brought about by the rapid cooling should push the transition further toward the category of direct ordering in which the disordered phase tends to be retained and APD formation should be even more strongly suppressed. Horton and Liu (1985), on the other hand, based their interpretation of APDs in rapidly solidified Ni_3Al alloys on the swiftness of domain growth in this material. Thermal APDs form as a result of the suppression of domain growth by the rapid cooling rate. It is possible that the absence of a three-dimensional domain structure in a given material may result from both strong ordering and the rapid domain growth when the transition temperature is very high. Compositional inhomogeneity brought about by, for example, dendrite formation during solidification has also been found to affect the domain structure. Morris (1992b) has shown recently that the bulk composition of the alloy may significantly change the APD structure in rapidly solidified Ni_3Al in which the element distribution was found to vary substantially across the grain structure. The growth of APDs is in many ways similar to the growth of grains in that both are driven by the reduction in the curvature of the boundary. The main difference is that a misorientation exists at a grain boundary while crystallographic directions are maintained upon crossing an APB. The relatively loose structure at the grain boundary enables easy interchange of atoms during diffusion, while at the APB the atomic registry is maintained, at least in the case of an ideal APB, and the migration of the APB is therefore expected to be much slower than grain growth. Cupschalk and Brown (1968) proposed a mechanism for the growth of APD in which the atom

diffusion controlling the domain migration is essentially the same as the bulk diffusion of substitutional atoms, namely an atom makes a jump only if it is adjacent to a vacancy. The vacancies preferentially segregated to the APB, which were observed experimentally in quenched β -CuZn in the form of collapsed vacancy disks at the APB (Cupschalk and Brown, 1968), enable the boundary migration with short-range diffusion. This model was supported by the experimental measurement of domain growth in Cu_3Au , in which the activation energy for domain growth was found to be very close to that for bulk diffusion (Poquette and Mikkola, 1969).

In disordering, the role of the existing APBs is to act as preferential nucleation sites for the disordered phase, and in this sense the role of the APB is not very different from other interfaces, e.g. grain boundaries or free surfaces. In continuous transitions the domain structure is expected to disappear upon reaching the critical temperature. In first-order or discontinuous transitions, the domains always retain a certain degree of long-range order even at the transition temperature, and the disordering starts with the APBs being coated (wetted) by a layer of the disordered phase. The investigation of Kikuchi and Cahn (1979) using the cluster-variation method showed that the wetting of the APB with the disordered or nearly disordered phase would start well before reaching the true transition temperature. In experiments, wetting with the disordered phase at APBs and other interfaces has been directly observed using TEM (Tichelaar *et al.*, 1992; Morris, 1975; Leroux *et al.*, 1990). Tichelaar *et al.* (1992) observed the wetting of APBs in Cu_3Au by the TEM *in situ* annealing technique and found that the wetted regions became nucleation sites for the disordered phase, which grew when the temperature was brought very close to T_c . Wetting was found particularly pronounced at non-conservative APBs.

4. APBs in Dissociated Dislocations

4.1 Stability of APB Dissociation

In a given material, the selection of the active dislocation system is based on competitions in both the dislocation self-energy and dislocation mobility. The reduction in the self-energy due to APB dissociation is given by

$$E = \frac{b^2 K(\theta)}{2\pi} \ln(\tau_0) - \gamma r_0$$

where $K(\theta)$ is the energy factor, b is the Burgers vector of the bordering superpartials, and r_0 is the equilibrium

separation. In the B2-ordered alloys the competition is usually between APB-dissociated $\langle 111 \rangle$ superdislocations and $\langle 100 \rangle$ ordinary dislocations. On the basis of the b^2 criterion, a $\langle 100 \rangle$ dislocation has a lower self-energy than an undissociated $\langle 111 \rangle$ superdislocation. But the $\langle 111 \rangle$ dislocation may become energetically favored if it can reduce its self-energy sufficiently by dissociating into APB-coupled partials, and this requires that the APB energy is lower than a certain level. In NiAl and CoTi, in which the APB energies are very high, dislocations in deformed samples are usually $\langle 100 \rangle$ type; $\langle 111 \rangle$ dislocations are formed only if the resolved shear stresses on $\langle 100 \rangle$ dislocations are close to zero (Rachinger and Cottrell, 1956; Loretto and Wasilewski, 1971; Takasugi *et al.*, 1990). In β -CuZn and FeAl, the APB energies are relatively low, and this is consistent with the operative dislocations being APB-dissociated $\langle 111 \rangle$ superdislocations. In the $L1_2$ -ordered alloys, a $\langle 110 \rangle$ dislocation dissociated into APB-coupled superpartials on a $\{001\}$ plane is energetically more favorable than the same dissociation on $\{111\}$ owing partly to the lower $\{001\}$ APB energy, but prohibited at low temperatures since on $\{001\}$ the dislocations are locked along both screw and edge orientations (Hazzledine and Sun, 1991; Sun *et al.*, 1991). In the $L1_2$ structure APB-coupled dissociation also competes with the dissociation into SISF-coupled $\frac{1}{2}\langle 112 \rangle$ super-Shockley partials, and the favored dissociation mode depends on the relative magnitudes of the APB and SISF energies. According to Suzuki *et al.* (1979), who treated the relative stability using isotropic elasticity, APB dissociation on screw dislocations is favored if

$$\gamma_{111} < 1.9 \frac{r_0}{b} \gamma_{\text{SISF}}$$

where r_0 is the equilibrium APB width. In addition to the self-energy, the APB dissociation may also be made unstable if the γ surface does not contain a minimum at the position corresponding to an APB shear. Yamaguchi *et al.* (1981a) showed (Figure 4) that, by increasing the ordering energy in the $L1_2$ structure, the $\{111\}$ APB can be made unstable, in which case the stable configuration is the SISF dissociation; this may happen even when γ_{SISF} is not sufficiently low to satisfy the self-energy criterion based on elasticity. An unstable $\{111\}$ APB has been shown to alter the yield behavior of $L1_2$ alloys significantly. In alloys that exhibit the anomalous yield stress, e.g. Ni_3Al and Ni_3Ga , the $\{111\}$ APB is thought to be stable or metastable and the screw dislocation may (temporarily)

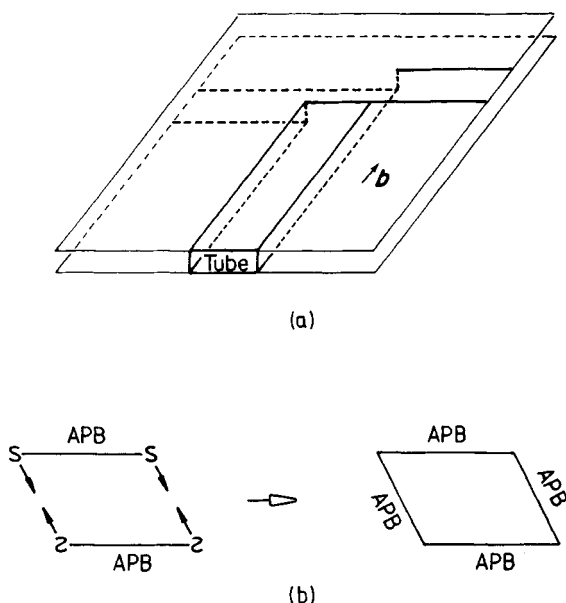


Figure 9. Formation mechanisms of APB tubes. (a) The Vidoz-Brown non-aligned jog mechanism. (b) The cross-slip and annihilation mechanism

assume a planar mobile structure on $\{111\}$, which, with increasing temperature, becomes more likely to be locked into the Kear-Wilsdorf configuration. When the $\{111\}$ APB is unstable, not only is the dissociation mode made into SISF but also the core of the bordering $\frac{1}{2}\langle 112 \rangle$ partials is always non-planar when the dislocation is lying along a $\langle 110 \rangle$ direction, quite similar to the core structure of $\langle 111 \rangle$ screw dislocations in b.c.c. metals. In the latter case the role of the thermal fluctuations is to free the dislocation from the locked structures, and the material therefore becomes softer as the temperature rises. An unstable $\{111\}$ APB has been thought to account for the normal yield stress in Pt_3Al and Pt_3Ga (Tichy *et al.*, 1986).

4.2 APB Tubes

The possibility of APB tubes being produced by dislocation mechanisms was proposed in 1962 (Vidoz and Brown, 1962), but they were not observed until the early 1980s (Chou *et al.*, 1982; Chou and Hirsch, 1983). In the mechanism of Vidoz and Brown (1962) the cross-section of the APB tube is a parallelogram. In this mechanism, when a superdislocation consisting of two APB-coupled superpartials is intersected by a 'forest' dislocation or a dislocation in a secondary slip system,

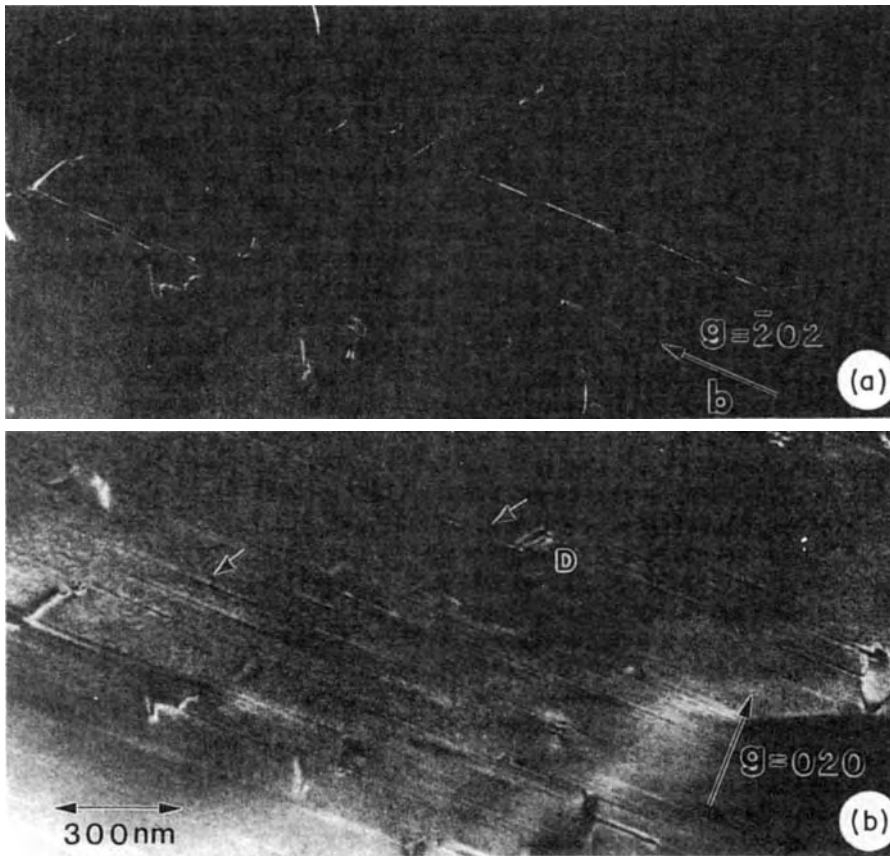


Figure 10. TEM weak-beam images of APB tubes in Ni_3Ga . (a) The reflection $\bar{2}02$ is parallel to the tube axis and the tubes are out of contrast. (b) The reflection 020 is perpendicular to the tube axis and strong tube contrast is observed

two jogs are created, one on each of the two superpartials. The two jogs are not aligned along the direction of the Burgers vector of the primary dislocation if the forest dislocation keeps moving during the intersection. As a result, the APB created by the leading partial is not eliminated by the trailing partial and an APB tube is formed (Figure 9(a)). The key factor in this mechanism is that the forest dislocations must be produced through the activation of the secondary slip systems. The geometrical feature of the APB tubes thus created is that they are connected to superdislocations containing non-aligned jogs.

Chou and Hirsch (1983) carried out systematic calculations of the image contrast of APB tubes in TEM. In their model an APB tube is treated as the equivalent of two overlapping APBs and the tube produces contrast because there is a phase difference of $2\pi\mathbf{g}\cdot\mathbf{p}$ between waves diffracted from inside and

outside of the tube. The contrast criterion is therefore essentially the same as that of the imaging of ordinary APBs; contrast is formed if $\mathbf{g}\cdot\mathbf{p} \neq \text{integer}$, which requires that \mathbf{g} be a superlattice reflection. On the basis of this contrast selection rule, Chou *et al.* (1982) and Chou and Hirsch (1983) successfully observed APB tubes in FeAl (B2) and Ni_3Al (L1_2). More recently Sun (1992) observed APB tubes in lightly deformed L1_2 -ordered Ni_3Ga and found that the contrast formation based on the $\mathbf{g}\cdot\mathbf{p} \neq \text{integer}$ criterion was often violated, since tube contrast was observed in some fundamental reflections, with the contrast being strongest in reflections perpendicular to the tubes axis. Figure 10(a) is a weak-beam image taken with $\bar{2}02$ reflection parallel to the Burgers vector of dislocations in the primary slip system; in this reflection the dislocations are in strong contrast and the APB tubes are invisible. Figure 10(b), in which APB tubes are visible in the form of thin lines, is imaged

using 020, which is also a fundamental reflection but perpendicular to the tube axis. This observation suggests that there are lattice distortions normal to the tube axis, and it led to the proposal (Sun, 1992) that, in addition to the APB displacement, an APB tube also possesses a continuous distortion field that arises as a result of the surface tension of the APB. Simple analytical solutions for the displacement field were obtained (Sun, 1992) for a circular APB tube. Images were simulated and were found to be in qualitative agreement with the experimental observation. For a circular tube in an isotropic material, the surface tension causes a hydrostatic pressure inside the tube and a pure-shear strain field outside. The additional contrast, which leads to the violation of the $g \cdot p$ criterion, arises as a result of the local deviation (as a result of the shear distortion) from the diffraction condition in the bulk; in this sense the tube contrast formation is essentially the same as for dislocations, i.e. strain contrast. Strain contrast of APB tubes has since been observed in Fe_3Ge by Ngan (1992).

The overall arrangement of the APB tubes in deformed samples observed in TEM was, however, found to be inconsistent with the mechanism of Vidoz and Brown (1962). First, APB tubes were observed in slightly deformed samples in which no secondary slip system was activated. Secondly, the tubes were often found to be connected to dislocation dipoles, e.g. the dipole marked D in Figure 10, instead of to jogged dislocations. A new mechanism was proposed by Chou and Hirsch (1983) and Chou *et al.* (1987) based entirely on the dislocations in the primary system. In this mechanism, when two APB-dissociated screw superdislocations having opposite signs pass each other on elevated planes, the attractive elastic interaction drives the two screw dislocations toward each other through cross-slip and they eventually annihilate. The computer simulation of Chou *et al.* shows that during cross-slip the partials do not follow one another along the same path, and as a result the annihilation is not complete and an APB tube is created. A simplistic situation is illustrated in Figure 9(b), viewed along the tube axis, in which the screw partials cross-slip independently during the annihilation; in this case the tube cross-section is a simple parallelogram, while in general the cross-section is more likely to be an irregular polyhedron (Chou *et al.*, 1987). The key feature in this model is that the tubes are connected to both ends of near-edge dipoles, which is consistent with the experimental observations.

5. Concluding Remarks

Much of the discussion in this chapter is developed on the basis of the clear distinction between ideal APBs

and real APBs. The structure of an ideal APB can be fully characterized by the APB displacement vector p and the plane normal n . An ideal APB has been shown to be not necessarily stable, and interesting variations occur when the APB is allowed to relax to reach thermodynamic equilibrium. Owing to the limitations of space, it has not been possible to cover in detail the theoretical treatment, and instead the aim has been to highlight the basic physical origins for the deviations from ideal APB structures. The traditional treatment based on pairwise interactions has the advantage of offering a clear physical picture about the factors governing the structure and energy of APBs. Indeed, the APB energies obtained using the ordering energies derived from their relationship with the disorder-order transition temperature T_c have been found to be in order-of-magnitude agreement with the experimental measurements made by the TEM method (Tables 1–6 and Figure 7). The latest *ab initio* atomistic methods are promising in that they employ more rigorous treatments and that some have been very successful in predicting some of macroscopic properties, e.g. lattice parameters and elastic constants; but clearly further developments are required in the field of fault-energy calculations, judging merely from the fact that different techniques have given very different results and that their agreement with the experimental measurements is usually subject to large variations.

It has also not been possible to cover several other topics closely connected with the structure and energetics of APBs and APDs: these include dislocation locking mechanisms involving APB transformation and disordering (Chapters 22 and 38 by Veysière and Douin and by Briant in this volume); the strengthening by ordered precipitates in which the structure and energy of APBs are the controlling parameters (Chapters 2 and 12 by Liu and Pope and by Ardell in Volume 2); strengthening by thermal APDs (Chapter 39 by Sauthoff in this volume); the work-hardening mechanism involving APB tubes, and the effect of the presence of APBs and APDs on electromagnetic properties (Chapters 40 and 41 by Kouvel and by Braunovic in this volume). It is hoped that the reader will find discussions related to the above subjects in these other chapters.

6. Acknowledgements

The author is grateful to Dr A. H. W. Ngan for permission to use unpublished work (Figure 5), to the SERC for financial support, and to Wolfson College, Oxford, for a Junior Research Fellowship.

7. References

- Ball, A., and Smallman, R. E. (1966). *Acta Metall.*, **14**, 1517.
- Baluc, N. (1990). PhD Thesis, Université de Lausanne.
- Beauchamp, P., Douin, J., and Veyssi re, P. (1987). *Phil. Mag.*, **55A**, 565.
- Beeler, J. R. (1967). In *Intermetallic Compounds* (ed. J. H. Westbrook). Wiley, New York, p. 233.
- Bragg, W. L. (1940). *Proc. R. Soc.*, **51**, 105.
- Bragg, W. L., and Williams, E. J. (1934). *Proc. R. Soc.*, **A145**, 699.
- Bragg, W. L., and Williams, E. J. (1935). *Proc. R. Soc.*, **A151**, 540.
- Brown, N. (1959). *Phil. Mag.*, **4**, 693.
- Cahn, R. W. (1987). In *High Temperature Ordered Intermetallic Alloys II* (eds N. S. Stoloff, C. C. Koch, C. T. Liu, and O. Izumi). *Mater. Res. Soc. Proc.*, **81**, 27.
- Calvayrac, Y., and Fayard, M. (1972). *Mater. Res. Bull.*, **7**, 891.
- Carlsson, A. E., Meschter, P. J. (1991). In *High Temperature Ordered Intermetallic Alloys IV* (eds L. A. Johnson, D. P. Pope, and J. O. Stiegler). *Mater. Res. Soc. Proc.*, **213**, 19.
- Chen, S. P., Voter, A. F., and Srolovitz, D. J. (1986). *Scripta Metall.*, **20**, 1389.
- Chou, C. T., and Hirsch, P. B. (1983). *Proc. R. Soc.*, **A387**, 91.
- Chou, C. T., Hirsch, P. B., McLean, M., and Hondros, E. (1982). *Nature*, **300**, 621.
- Chou, C. T., Hazzledine, P. M., Hirsch, P. B., and Anstis, G. R. (1987). *Phil. Mag.*, **56**, 799.
- Clapp, P. C., Rubins, M. J., Charpency, S., Rifkin, J. A., Yu, Z. Z., and Voter, A. F. (1989). In *High Temperature Ordered Intermetallic Alloys III* (eds C. T. Liu, A. I. Taub, N. S. Stoloff, and C. C. Koch). *Mater. Res. Soc. Proc.*, **133**, 29.
- Cockayne, D. J. H., Ray, I. L. F., and Whelan, M. J. (1969). *Phil. Mag.*, **20**, 1265.
- Cowley, J. M. (1950). *Phys. Rev.*, **77**, 669.
- Crawford, R. C. (1971). PhD Thesis, University of Oxford.
- Crawford, R. C., and Ray, I. L. F. (1977). *Phil. Mag.*, **35**, 549.
- Crimp, M. A. (1989). *Phil. Mag. Lett.*, **60**, 45.
- Cupschalk, S. G., and Brown, N. (1967). *Acta Metall.*, **13**, 847.
- Cupschalk, S. G., and Brown, N. (1968). *Acta Metall.*, **16**, 657.
- Dimiduk, D. M. (1989). PhD Thesis, Carnegie-Mellon University.
- Dirras, G., Beauchamp, P., and Veyssi re, P. (1992). *Phil. Mag.*, **65A**, 815.
- Douin, J., Veyssi re, P., and Beauchamp, P. (1986). *Phil. Mag.*, **54**, 375.
- English, A. T. (1966). *Trans. AIME*, **236**, 15.
- Fisher, R. M., and Marcinkowski, M. J. (1961). *Phil. Mag.*, **6**, 1385.
- Flinn, P. A. (1960). *Trans. AIME*, **218**, 145.
- Foiles, S. M., and Daw, M. S. (1987). *J. Mater. Res.*, **2**, 5.
- Freeman, A. J., Hong, T., Lin, W., and Xu, J. H. (1991). In *High Temperature Ordered Intermetallic Alloys IV* (eds L. A. Johnson, D. P. Pope, and J. O. Stiegler). *Mater. Res. Soc. Proc.*, **213**, 3.
- Fu, C. L. (1990). *J. Mater. Res.*, **5**, 971.
- Fu, C. L., and Yoo, M. H. (1989). In *High Temperature Ordered Intermetallic Alloys III* (eds C. T. Liu, A. I. Taub, N. S. Stoloff, and C. C. Koch). *Mater. Res. Soc. Proc.*, **133**, 81.
- Fu, C. L., and Yoo, M. H. (1990). *Phil. Mag. Lett.*, **62**, 159.
- Fu, C. L., and Yoo, M. H. (1992). *Acta Metall.*, **40**, 703.
- Guttman, L. (1956). *Solid State Phys.*, **3**, 145.
- Hazzledine, P. M., and Sun, Y. Q. (1991). In *High Temperature Ordered Intermetallic Alloys IV* (eds L. A. Johnson, D. P. Pope, and J. O. Stiegler). *Mater. Res. Soc. Proc.*, **213**, 209.
- Head, A. K., Loretto, M. H., and Humble, P. (1967). *Phys. Status Solidi*, **20**, 521.
- Hirsch, P. B. (1992). *Phil. Mag.*, **65A**, 569.
- Hong, T., and Freeman, A. J. (1991). *Phys. Rev.*, **B43**, 6446.
- Horton, J. A., and Liu, C. T. (1985). *Acta Metall.*, **33**, 2191.
- Horton, J. A., and Miller, M. K. (1987). In *High Temperature Ordered Intermetallic Alloys II* (eds N. S. Stoloff, C. C. Koch, C. T. Liu, and O. Izumi). *Mater. Res. Soc. Proc.*, **81**, 105.
- Hug, G., Douin, J., and Veyssi re, P. (1989). In *High Temperature Ordered Intermetallic Alloys III* (eds C. T. Liu, A. I. Taub, N. S. Stoloff, and C. C. Koch). *Mater. Res. Soc. Proc.*, **133**, 125.
- Inui, H., Luzzi, D. E., Porter, W. D., Pope, D. P., Vitek, V., and Yamaguchi, M. (1992). *Phil. Mag.*, **65A**, 245.
- Kear, B. H., and Wilsdorf, H. G. (1962). *Trans. AIME*, **224**, 382.
- Kikuchi, R., and Cahn, J. W. (1979). *Acta Metall.*, **27**, 1337.
- Koehler, J. S., and Seitz, F. (1947). *J. Appl. Mech.*, **14A**, 217.
- Korner, A. (1988). *Phil. Mag.*, **58A**, 507.
- Korner, A., and Karthaler, H. P. (1985). *Phil. Mag.*, **52**, 29.
- Korner, A., and Schoeck, G. (1990). *Phil. Mag.*, **61**, 909.
- Lakso, G. E., and Marcinkowski, M. J. (1969). *Trans. AIME*, **245**, 1111.
- Lasalmonie, A., Chenal, B., Hug, G., and Beauchamp, P. (1988). *Phil. Mag.*, **58**, 543.
- Leamy, H. J., Schwellinger, P., and Warlimont, H. (1970). *Acta Metall.*, **18**, 31.
- Leroux, C., Loiseau, A., Cadeville, M. C., Broddin, D., and Van Tendeloo, G. (1990). *J. Phys.: Condens. Matter*, **2**, 3479.
- Li, Y. Y. (1949). *Phys. Rev.*, **76**, 972.
- Li, Y. Y. (1950). *Phys. Rev.*, **77**, 300.
- Loretto, M. H., and Wasilewski, R. J. (1971). *Phil. Mag.*, **23**, 1311.
- Marcinkowski, M. J. (1963). In *Electron Microscopy and Strength of Crystals* (eds G. Thomas and J. Washburn). Interscience, New York, p. 333.
- Marcinkowski, M. J., and Brown, N. (1962). *J. Appl. Phys.*, **33**, 537.
- Marcinkowski, M. J., and Miller, D. S. (1961). *Phil. Mag.*, **6**, 871.
- Marcinkowski, M. J., Brown, N., and Fisher, R. M. (1961). *Acta Metall.*, **9**, 129.
- Mendiratta, M. G., and Law, C. C. (1987). *J. Mater. Sci.*, **22**, 607.

- Mishima, Y., Oya, Y., and Suzuki, T. (1985). In *High Temperature Ordered Intermetallic Alloys* (eds C. C. Koch, C. T. Liu, and N. S. Stoloff). *Mater. Res. Soc. Proc.*, **39**, 266.
- Morris, D. G. (1975). *Phys. Status Solidi*, **a32**, 145.
- Morris, D. G. (1992a). *Phil. Mag.*, **65A**, 389.
- Morris, D. G. (1992b). In *Ordered Intermetallics—Physical Metallurgy and Mechanical Properties* (Proc. NATO Advanced Research Workshop). Kluwer Academic, Dordrecht, p. 123.
- Morris, D. G., and Smallman, R. E. (1975). *Acta Metall.*, **23**, 73.
- Morris, D. G., Brown, G. T., Piller, R. C., and Smallman, R. E. (1976). *Acta Metall.*, **24**, 21.
- Murakami, Y., Kachi, S., Nakanishi, N., and Takehara, H. (1971). *Acta Metall.*, **19**, 97.
- Neveu, N. (1991). PhD Thesis, Université de Paris-Sud.
- Ngan, A. H. W. (1992). PhD Thesis, University of Birmingham.
- Nicholson, D. M., Stocks, G. M., Temmerman, W. M., Sterne, P., and Pettifor, D. G. (1989). In *High Temperature Ordered Intermetallic Alloys III* (eds C. T. Liu, A. I. Taub, N. S. Stoloff, and C. C. Koch). *Mater. Res. Soc. Proc.*, **133**, 17.
- Oliver, J. O. (1992). PhD Thesis, Université de Paris XI.
- Paidar, P. (1985). *Acta Metall.*, **33**, 1803.
- Paidar, P., Pope, D. P., and Vitek, V. (1984). *Acta Metall.*, **32**, 435.
- Pei, S., Massalski, T. B., Temmerman, W. M., Sterne, P. A., and Stocks, G. M. (1989). *Phys. Rev.*, **B39**(9), 5767.
- Peierls, R. (1936). *Proc. R. Soc.*, **A154**, 207.
- Pope, D. P., and Ezz, S. S. (1984). *Int. Met. Rev.*, **29**, 136.
- Popov, L. E., Kozlov, E. V., and Golosov, N. S. (1966). *Phys. Status Solidi*, **13**, 569.
- Poquette, G. E., and Mikkola, D. E. (1969). *Trans. AIME*, **245**, 743.
- Potter, D. I. (1969/70). *Mater. Sci. Eng.*, **5**, 201.
- Prakash, U., Buckley, R. A., Jones, H., and Sellars, C. M. (1991). *Scripta Metall.*, **25**, 2249.
- Rachinger, W. A., and Cottrell, A. H. (1956). *Acta Metall.*, **4**, 109.
- Rao, S. I., Woodward, C., and Partharathy, T. A. (1991). In *High Temperature Ordered Intermetallic Alloys IV* (eds L. A. Johnson, D. P. Pope, and J. O. Stiegler). *Mater. Res. Soc. Proc.*, **213**, 125.
- Ray, I. L. F., Crawford, R. C., and Cockayne, D. J. H. (1970). *Phil. Mag.*, **21**, 1027.
- Reynaud, F., Lasserre, A., Coulomb, P. (1975). *Acta Metall.*, **23**, 9.
- Rudman, P. S. (1960). *Acta Metall.*, **8**, 321.
- Rudy, M., and Sauthoff, G. (1986). *Mater. Sci. Eng.*, **81**, 525.
- Saka, H., Kawase, M., Nohara, A., and Imura, T. (1984). *Phil. Mag.*, **50A**, 65.
- Sanchez, J. M., Eng, S., Wu, Y. P., and Tien, J. K. (1987). In *High Temperature Ordered Intermetallic Alloys II* (eds N. S. Stoloff, C. C. Koch, C. T. Liu, and O. Izumi). *Mater. Res. Soc. Proc.*, **81**, 57.
- Sastry, S. M. L., and Ramaswami, B. (1976). *Phil. Mag.*, **33**, 375.
- Schoeck, G., and Korner, A. (1990). *Phil. Mag.*, **61**, 917.
- Shechtman, D., Blackburn, M. J., and Lipsitt, H. A. (1974). *Metall. Trans.*, **5**, 1373.
- Sparks, C. J., Specht, E. P., Ice, G. E., Zschack, P., and Schneible, J. H. (1991). In *High Temperature Ordered Intermetallic Alloys IV* (eds L. A. Johnson, D. P. Pope, and J. O. Stiegler). *Mater. Res. Soc. Proc.*, **213**, 363.
- Stocks, G. M., Nicholson, D. M., Pinski, F. J., Butler, W. H., Sterne, P., Temmerman, W. M., Gyorffy, B. L., Johnson, D. D., Gonis, A., Zhang, X.-G., and Turchi, P. E. A. (1987). In *High Temperature Ordered Intermetallic Alloys II* (eds N. S. Stoloff, C. C. Koch, C. T. Liu, and O. Izumi). *Mater. Res. Soc. Proc.*, **81**, 15.
- Sun, Y. Q. (1992). *Phil. Mag.*, **65**, 287.
- Sun, Y. Q., Hazzledine, P. M., Crimp, M. A., and Couret, A. (1991). *Phil. Mag.*, **64**, 311.
- Sutcliffe, C. H., and Jaumot, F. E. (1953). *Acta Metall.*, **1**, 725.
- Suzuki, K., Ichihara, M., and Takeuchi, S. (1979). *Acta Metall.*, **27**, 193.
- Suzuki, T., Mishima, Y., and Miura, S. (1989). *ISI J. Int.*, **29**, 1.
- Takasugi, T., Tsurisaki, K., Izumi, O., and Ono, S. (1990). *Phil. Mag.*, **61**, 785.
- Takeuchi, S., and Kuramoto, E. (1973). *Acta Metall.*, **21**, 415.
- Tanner, L. E., and Leamy, H. J. (1974). In *Order-Disorder Transformation in Alloys* (ed. H. Warlimont). Springer-Verlag, New York, p. 180.
- Tichelaar, F. D., Schapink, F. W., and Li, X. F. (1992). *Phil. Mag.*, **65A**, 912.
- Tichy, G., Vitek, V., and Pope, D. P. (1986). *Phil. Mag.*, **53**, 467.
- Tounsi, B. (1988). PhD Thesis, Université de Poitiers.
- Umakoshi, Y., and Yamaguchi, M. (1985). *Phil. Mag.*, **52A**, 357.
- Umakoshi, Y., Yamaguchi, M., and Yamane, T. (1986). *Phil. Mag.*, **53A**, 221.
- Veyssi re, P. (1989). In *High Temperature Ordered Intermetallic Alloys III* (eds C. T. Liu, A. I. Taub, N. S. Stoloff, and C. C. Koch). *Mater. Res. Soc. Proc.*, **133**, 175.
- Veyssi re, P., Douin, J., and Beauchamp, P. (1985). *Phil. Mag.*, **51**, 469.
- Veyssi re, P., Yoo, M. H., Horton, J. A., and Liu, C. T. (1989). *Phil. Mag. Lett.*, **59**, 61.
- Vidoz, A. E., and Brown, L. M. (1962). *Phil. Mag.*, **7**, 1167.
- Wee, D. M., and Suzuki, T. (1979). *Trans. Japan Inst. Metals*, **20**, 634.
- Woodward, C., Maclaren, J. M., and Rao, S. (1991). In *High Temperature Ordered Intermetallic Alloys IV* (eds L. A. Johnson, D. P. Pope, and J. O. Stiegler). *Mater. Res. Soc. Proc.*, **213**, 715.
- Wu, Y. P., Sanchez, J. M., and Tien, J. K. (1989). In *High Temperature Ordered Intermetallic Alloys III* (eds C. T. Liu, A. I. Taub, N. S. Stoloff, and C. C. Koch). *Mater. Res. Soc. Proc.*, **133**, 119.
- Wu, Y. P., Sanchez, J. M., and Tien, J. K. (1991). In *High Temperature Ordered Intermetallic Alloys IV* (eds L. A. Johnson, D. P. Pope, and J. O. Stiegler). *Mater. Res. Soc. Proc.*, **213**, 87.

- Yamaguchi, M., and Umakoshi, Y. (1990). *Prog. Mater. Sci.*, **34**, 1.
- Yamaguchi, M., Vitek, V., and Pope, D. P. (1981a). *Phil. Mag.*, **43**, 1027.
- Yamaguchi, M., Pope, D. P., Vitek, V., and Umakoshi, Y. (1981b). *Phil. Mag.*, **43**, 1265.
- Yamaguchi, M., Umakoshi, Y., and Yamane, T. (1985). In *Dislocations in Solids* (eds H. Suzuki, T. Ninomiya,

- K. Sumino, and S. Takeuchi). University of Tokyo Press, Tokyo, p. 77.
- Yang, C. N. (1945). *J. Chem. Phys.*, **17**, 66.
- Yodogawa, Y., Wee, D. M., Oya, Y., and Suzuki, T. (1980). *Scripta Metall.*, **14**, 849.
- Yoshida, M., and Takasugi, T. (1991). In *Intermetallic Compounds, Structural and Mechanical Properties* (ed. O. Izumi). Japan Institute of Metals, Sendai, p. 403.

This chapter was originally published in 1995 as Chapter 21 in *Intermetallic Compounds*, Vol. 1: *Principles*, edited by J. H. Westbrook and R. L. Fleischer.

Addendum

On the subject of APB energies, the FLAPW method was recently used by Paxton and Sun (1998) to calculate the APB energies in several $L1_2$ intermetallic compounds. In this work, atomic relaxation, both normal and parallel to the interface planes, was allowed in calculating the final interface energy after full equilibration. The APB energies given by the new calculation are lower than those given by earlier works in which the same method was used but only one mode of relaxation was allowed (e.g. Fu and Yoo, 1989). For Ni_3Al , the calculated APB energies are 115 and 188 mJ/m^2 on {001} and {111} planes, lower than the respective APB energies (140 and 220 mJ/m^2) given by the earlier work (Fu and Yoo, 1989) and closer to the results measured by weak-beam electron microscopy (e.g. Dimiduk, 1989; Neveu, 1991). APB energies in Cu_3Au , Pt_3Al , Ni_3Si , Co_3Ti , Ni_3Ge were also calculated with the same approach and are listed in Table 7.

Notable is the negative {010} APB energy in Ni_3Ge resulting from $L1_2$ being its metastable crystal structure; the first-principles calculation suggests the true ground-state structure of Ni_3Ge to be $D0_{22}$ which is derivable from $L1_2$ by forming {001} APBs on

Table 7 APB energies in $L1_2$ compounds (Paxton and Sun, 1998)

Composition	γ_{111} (mJ/m^2)	γ_{010} (mJ/m^2)	Method
Ni_3Al	188	115	FLAPW
Cu_3Au	129	47	FLAPW
Pt_3Al	349	523	FLAPW
Ni_3Si	682	683	FLAPW
Co_3Ti	692	412	FLAPW
Ni_3Ge	83	-40	FLAPW

alternating planes (Figure 3). The calculated {111} and {001} APB energies were used in predicting the formation of Kear–Wilsdorf locks by the cross-slip of {101} screw superdislocations. The Kear–Wilsdorf locks in $L1_2$ intermetallic compounds and their effects on mechanical properties are discussed by Veyssière and Douin in Chapter 5 in this volume.

Reference

- Paxton, A. T., and Sun, Y. Q. (1998). *Philosophical Magazine*, **78**, 85.

Chapter 5

Dislocations

Patrick Veyssière and Joël Douin

*Laboratoire d'Etude des Microstructures, Unité Mixte CNRS/ONERA, UMR 104,
29 Avenue de la division Leclerc, 92322 Châtillon Cedex, France*

1. Introduction

Individual dislocations, their organization, the chemical effects that take place in their vicinity, and the influence of these on the physical properties of crystals constitute an open field in which investigations have been very active over the years. Some physical properties depend on the long-range elastic stresses and strains of dislocations; others are dictated by the detailed structure of dislocation cores, whose complexity and variety have become increasingly apparent over the last two decades. Dislocations have been and will probably remain primarily studied in connection with plasticity. Nevertheless, knowledge of individual dislocations not only provides information on the variety of plastic behaviors of crystals, but it provides some predictive tools in a wide range of domains covering crystal growth, grain-boundary structure—with deep implications for the electrical properties of semiconducting compounds—and, to a lesser extent, the magnetic, optical, and thermal properties of crystals. Beside technologically oriented studies, dislocations have retained the attention of physicists as examples of solitons and of singularities of an order parameter. Physicists interested in electronic structures can now make more reasonable atomistic studies of dislocations in metals and alloys as well as in ionic-covalent solids, and they can reproduce all sorts of core rearrangements, including the effect of dopants. The organization of dislocation networks has been demonstrated to be fractal in some circumstances.

This chapter on dislocations will focus on plasticity-related analyses; it should be read in close

connection with Sun's contribution in Chapter 21 in this volume. Some of the other topics mentioned above will, however, be addressed in Chapters 24 and 39 by Takasugi and by Sauthoff in this volume and in Section I in Volume 2, where the reader may find complementary specialized information on topics with which the present authors are not particularly familiar.

1.1 Definitions and Tools

It is a fact that a number of macroscopic mechanical properties of intermetallics are governed by the intrinsic mobility of dislocations, which makes the detailed study of their core* structure so important and attractive in this category of alloys. In addition, because of the abundance of available mechanisms, dislocation studies in ordered structures have significantly complemented our overall understanding of dislocation processes for themselves or in relation to plasticity. This chapter focuses on problems that have attracted the attention of the scientific community over the last decade. These problems are often complex, and it is worth realizing that, though many of the most important questions on the plasticity of intermetallic compounds were raised during the late 1950s and the early 1960s, at the beginning of studies of the mechanical properties of this class of materials, they may not all have been reliably answered yet. Dislocations in intermetallics constitute an extremely wide field that cannot be reasonably covered in this chapter; the reader is thus invited to refer

*Here the term *core* refers to the fine structure of a dislocation regardless of its extent.

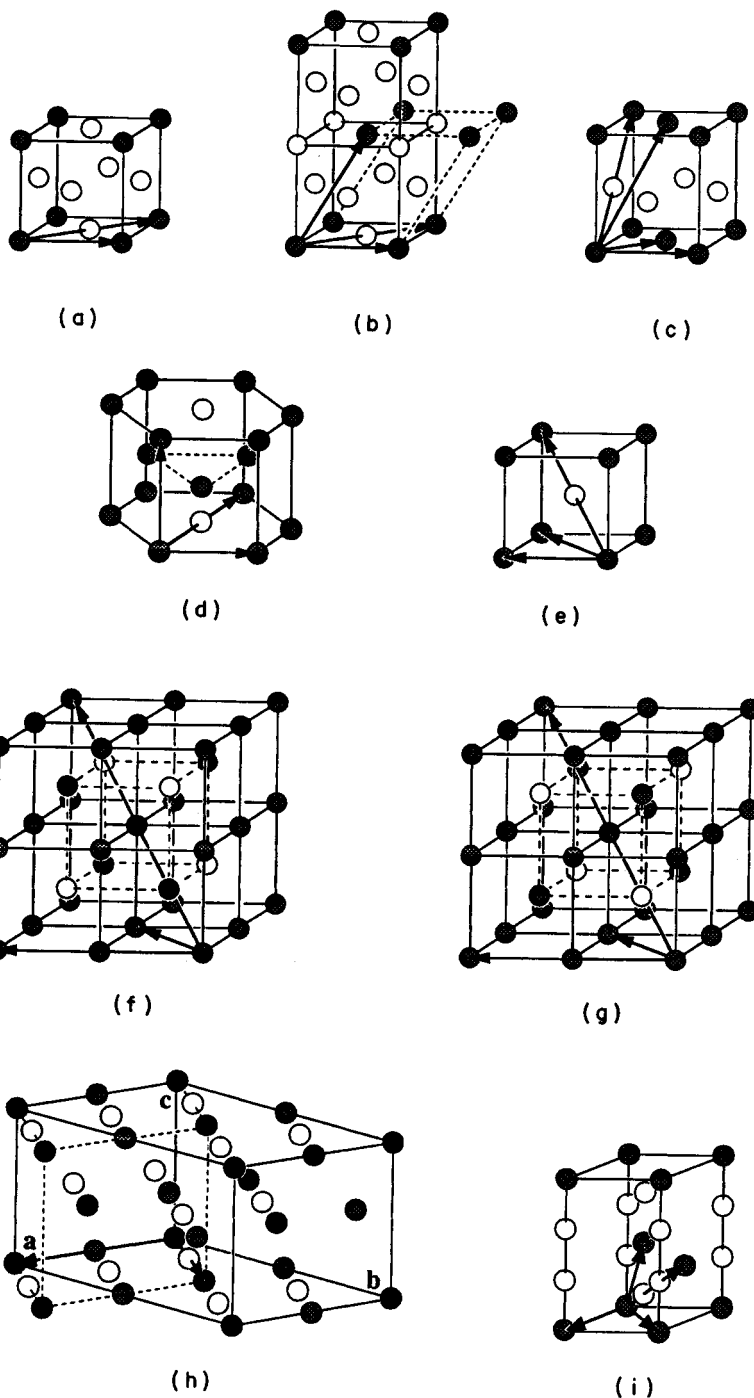


Figure 1. The various ordered structures examined in this review. The thick arrows represent some of the shortest unit Burgers vectors of each structure. (a) $L1_2$ (cP4). (b) $D0_{22}$ (tI8); note that the unit cell consists of two $L1_2$ unit cells shifted by $\frac{1}{2}[110]$ every other (001) plane. (c) $L1_0$ (tP4); compared to $L1_2$, the two cube faces perpendicular to the c-axis contain only like atoms. (d) $D0_{19}$ (hP8). (e) $B2$ (cP2). (f) $L2$, (cF16). (g) $D0_3$ (cF16). (h) phase O (oC16). (i) $C11b$ (tI6); one of the unit translations represented in this structure, $\frac{1}{2}[331]$, terminates on an atom located out of the unit cell

to earlier reviews of interest (Marcinkowski, 1963; Stoloff and Davies, 1966; Brown, 1967; Amelinckx, 1979; Pope and Ezz, 1984; Yamaguchi and Umakoshi, 1990) as well as to the other chapters in Section IV in this volume and Chapter 39 by Sauthoff, where some of the aspects that are discussed below may be developed from different points of views.

The symmetry of an alloy is reduced upon ordering (Figure 1) and the shortest unit translations in the disordered lattice are not in general perfect Burgers vectors of the ordered alloys. Long ago (Marcinkowski, 1963), the expression *superlattice dislocation* was introduced in order to help to identify in ordered alloys these dislocations whose nature would be changed if the crystal became disordered. For instance, $\frac{1}{2}\langle 111 \rangle$ is no longer a perfect Burgers vector in the B2 lattice; on the other hand, $\langle 100 \rangle$ dislocations remain perfect upon ordering in both the B2 and the L1₂ structures. Afterwards, the expression *superlattice* was simplified into the prefix *super*, which is specific to ordered alloys, and this notation has survived over the years, although it is certainly superfluous, as shown by the many similar situations encountered in ceramics.[†] For this reason, this convention will not be respected too carefully in the following.

1.2 Observing the Fine Structure of Dislocations

Macroscopic mechanical tests provide limited direct information on dislocations that consist of essentially the operating slip system and a few microscopic parameters of the deformation such as the activation volume and the activation energy. Understanding the fine structure of dislocations requires, in fact, that direct analyses are conducted at the appropriate resolution level. In the last 30 years, powerful observation techniques have emerged that have benefited from the improved resolution of transmission electron microscopes (TEM), and dislocation studies can now be conducted very accurately. It is worth recalling that one of the early applications of the weak-beam (WB) technique was aimed at demonstrating the fourfold dissociation in Fe₃Al (D0₃ structure) (Crawford and Ray, 1970). At that time, it was not anticipated that under WB one could ever routinely resolve between dislocations separated by, say, 3 to 4 nm. It was only in the early 1980s that materials scientists started to apply WB extensively to dislocation analyses in

intermetallics. Nowadays, WB experiments are used to pinpoint details separated by about 2 nm without the need of drastic precautions; more accurate studies require some expertise with the instrument, and observations are even being conducted at resolutions better than 1 nm. Simultaneously, intermetallics have been studied under high-resolution electron microscopy (HREM), that is, the imaging of lattice columns. Under both WB and HREM, the analysis of dislocation images can be uncertain because of problems associated with contrast artifacts and of difficulties in interpreting images, as well as in deriving physical information from these. Difficulties that are currently encountered in the course of studies of intermetallic alloys have been reviewed elsewhere (Clément *et al.*, 1991a,b; Veyssi re, 1989, 1991a,b, 1992). It should be kept in mind that since a dislocation image results from the interaction between an electromagnetic wave and a distorted lattice, contrast may not always be trivial to understand. This is exemplified in the following results obtained under HREM and WB.

(i) *High-resolution electron microscopy.* It is well-known that boundary conditions at free surfaces are liable to induce peculiar relaxation properties such as the widening or narrowing of the separation between companion Shockley partials (Hazzledine *et al.*, 1975), with the consequence that the sample surface is a favored nucleation site for cross-slip (George *et al.*, 1973; M ller and Haasen, 1976). Less well-known, however, is the so-called Eshelby twist and its implications for the contrast of end-on screw dislocations: Mills (1989) used this effect to point out subtle contrast differences between the pair of $\frac{1}{2}\langle 110 \rangle$ partials in Ni₃Al depending upon whether they form a superdislocation or a dipole (same sign or opposite sign, respectively).

(ii) *Weak-beam technique.* WB images of pairs of partials with collinear Burgers vectors had been used quite carelessly for years until Baluc *et al.* (1991a) showed that, in Ni₃Al, the observed separation between superpartial cores differs from its actual value and that the correction depends upon the dissociation plane, which, in their study, coincided with the projection plane. Though companion partials have the same Burgers vectors and are therefore viewed under the same *g.b* condition, their line images are not shifted by the same amount (Baluc *et al.*, 1991a) and their intensities differ in general (Veyssi re and Morris, 1992). On the other hand, it has been shown recently (Oliver, 1992) that, for particular deviations from the Bragg condition, a pair of peaks could originate from double

[†]See, for instance, the spinel structure, where the dissociation and subdissociation schemes are exactly the same as in L1₂ alloys.

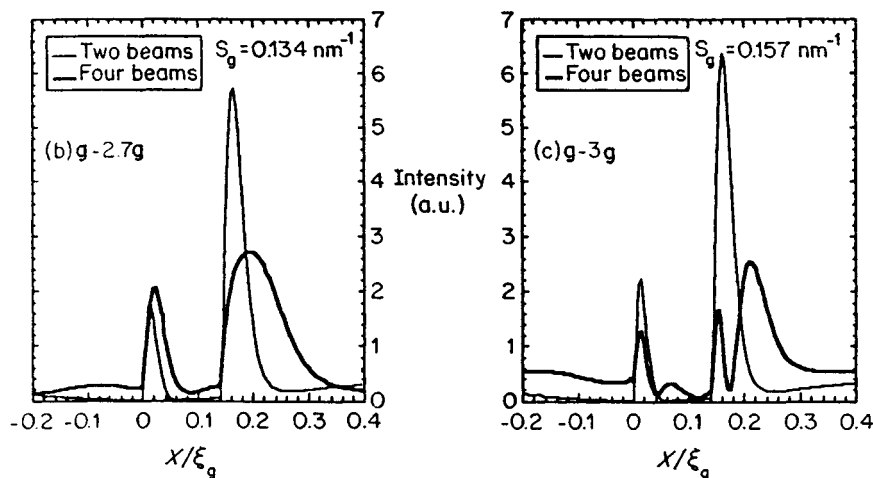
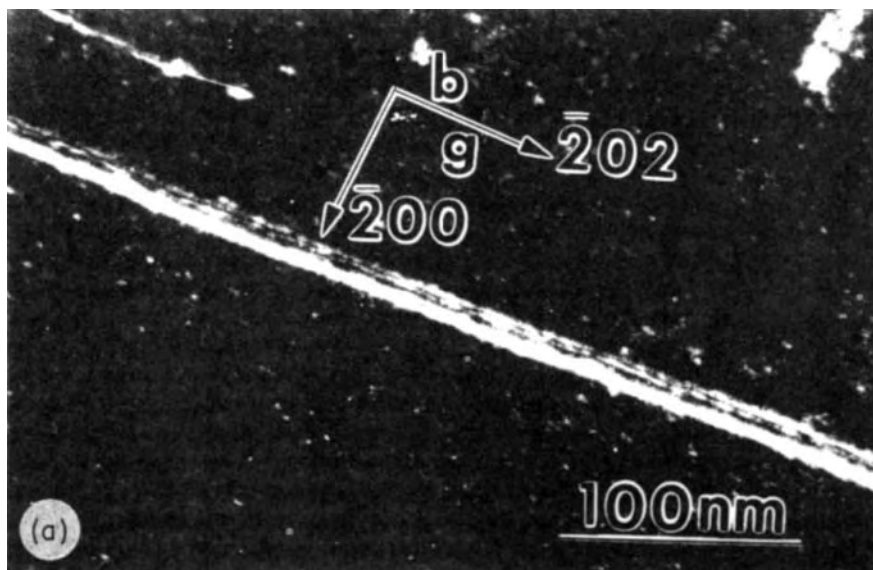


Figure 2. Experimental evidence of the splitting of the peak associated with a $\frac{1}{2}\langle 110 \rangle$ superpartial under conditions where $\mathbf{g} \cdot \mathbf{b} = 2$ and selected deviations from exact Bragg orientation are shown ($\mathbf{g} - n\mathbf{g}$, n is the abscissa of the intersection of the systematic row by the Ewald sphere). (a) Screw superdislocation in Ni_3Al . A splitting appears on the upper superpartial under the $\mathbf{g} - 3\mathbf{g}$ orientation. (b) Simulation of image profiles showing that, under $\mathbf{g} - 2.7\mathbf{g}$, no extra peak appears on either one superpartial (a.u. stands for arbitrary units). (c) Same as in (b) but under $\mathbf{g} - 3\mathbf{g}$ conditions. The simulations demonstrate that, in the appropriate orientation, the splitting appears only when four beams are included in the calculation whereas, with two beams, no extra image arises: the splitting is an artifact that originates from a multibeam effect

diffraction in the core of a $\frac{1}{2}\langle 110 \rangle$ dislocation imaged under conditions such that $\mathbf{g} \cdot \mathbf{b} = 2$ (Figure 2). This may explain why such screw superpartials have been occasionally reported as subdissociated into Shockley partials with separations that are unexpectedly large when compared to the same dislocations viewed under HREM. For additional information on the practice of

the WB technique, see Cockayne (1972), Veyssi re and Hug (1990), Veyssi re (1991a, 1992), and Hemker and Mills (1993).

Finally, knowledge of the mobility of individual dislocations under load is important in analyzing core-controlled mechanical properties. For this purpose, two

techniques that provide direct information should be mentioned: (i) *in situ* straining in the electron microscope, and (ii) the Johnston–Gilman etch-pitting techniques. The former has been applied quite extensively to a variety of solids, and in recent years to intermetallic compounds. Illustrations of such studies can be found in the papers of Baker *et al.* (1987a,b), Baker and Schulson (1989), Caillard *et al.* (1991a,b), Nohara (1991), and Suzuki *et al.* (1977a,b). Its limitations are numerous, but not much more than other TEM techniques of investigation (Clément *et al.*, 1991a,b; Veyssi re, 1991a); not all difficulties encountered during *in-situ* experiments are, in addition, clearly identified. On the other hand, the etch-pitting technique has not been applied to intermetallics studies at least to a level comparable to that of *in situ* straining. There seems to exist a potential of applications for etch-pitting measurements of dislocation mobilities in intermetallics (Nadgorny, 1992). Etch-pitting experiments could be significantly hindered in intermetallics, because dislocation densities are larger in intermetallics than in LiF, MgO, Si, and other ionic-covalent crystals where the etch-pitting method has been successfully applied. Moreover, since in some systems, such as in L1₂ alloys, the flow-stress anomalous behavior occurs only at permanent strains of the order of 0.2% (Section 5.1), it is clear that dislocation densities are then much too large to be tractable by means of surface etch pits.

1.3 Simulating the Fine Structure of Dislocation

Two levels of simulation are used to analyze dislocation cores, from continuum elasticity (see Section 2.1) to atomistic simulation. In the latter, atomic positions in the vicinity of a dislocation are determined using empirical or first-principles calculations of atomic interactions. This can be used either to analyze dislocation properties directly or as an input for image simulation of HREM pictures.

Simulation methods based on first principles are becoming available, but the number of atoms that is tractable at present is significantly fewer than what dislocation studies require (De Fontaine, 1992; Pettifor, 1992), implying approximations at various levels. As with most techniques, simulations are not in general fully reliable (see antiphase-boundary (APB) energy calculations in Ni₃Al and in NiAl (Chapter 21 by Sun in this volume), and the situation does not improve when dealing with more complicated defects such as dislocation cores. Simulations may nevertheless be helpful in solving problems that would otherwise require intuition.

Conclusions based on atomistic simulations of defects in intermetallics are not definitive, but they will evolve with the rapid refinement of approximations to describe atomic interactions from first principles and with the improvement of computational capabilities. Core simulations in intermetallics have been reviewed by Vitek (1985), Vitek *et al.* (1991), Pasianot *et al.* (1991), and Parthasarathy *et al.* (1991).

Most simulations have been conducted using empirical central-force pair potentials and *N*-body potentials (Finnis–Sinclair method (Finnis and Sinclair, 1984), embedded-atom method (Daw and Baskes, 1983; see also Chapter 4 by Voter in this volume)) that are fitted to a number of crystal parameters. They have shed light on the influence of crystal symmetry on dislocation cores (Pasianot *et al.*, 1991; Vitek *et al.*, 1991), on γ surfaces and surface defects (Khantha *et al.*, 1991), on dislocation–solute interactions (Dimiduk *et al.*, 1992), and this for stacking-fault and APB energies which can be adjusted. Simulations based on empirical and semiempirical potentials cannot take the angular dependence of the bonding into account (Pettifor, 1992), which could introduce some serious limitations in dislocation core analysis (Section 2.3.3). Nevertheless, they remain useful to check dislocation core properties based on crystal symmetry. They have provided a number of clarifications, especially in L1₂ alloys. The description of the elemental motion of $\frac{1}{2}\langle 110 \rangle$ partials on the cube plane (Section 2.2.1; see Vitek, 1985) is probably the most spectacular success of atomistic simulations in intermetallics. However, they have strong limitations. In B2 alloys, for instance, the details of the flow-stress anomaly could not be explained from computer simulations. On the other hand, it is still unclear from an experimental standpoint whether a strong negative temperature dependence of the flow stress (TDFS) in L1₂ alloys undergoing octahedral slip at low temperature, implies that the flow stress is governed by the core of $\frac{1}{2}\langle 112 \rangle$ partials (Section 5.2). Finally, it can be noted that the prediction of a yield-stress increase with decreasing temperature in Ti₃Al alloys deformed under prism slip (Vitek *et al.*, 1991) is not verified experimentally (Minonishi *et al.*, 1991).

2. The Fine Structure of Superdislocations in Relation to Crystal Structure

The fact that most ordered alloys are elastically anisotropic (see Chapter 37 by Nakamura in this volume) prevents one from comparing forces or energies analytically and, except for specific crystal directions

Chapter 6

Point Defects

Charles de Novion

Laboratoire des Solides Irradiés, (CEA-CEREM, URA CNRS No. 1380) Ecole Polytechnique,
91128 Palaiseau Cedex, France

1. Introduction

Point defects have a significant role in intermetallic compounds, as they control many properties of technological importance, such as atomic diffusion, high-temperature creep and other mechanical properties, sintering, behavior under irradiation, and in particular irradiation-induced crystalline-to-amorphous transitions. Introduction of point defects by irradiation has even allowed one to obtain an ordered phase (FeNi) in a system where it was hindered by the low atomic mobility (Néel *et al.*, 1964; Koczak *et al.*, 1971).

As in pure metals, point defects in intermetallic compounds include vacancies, interstitials, impurities, and their combinations, but also, in long-range ordered (LRO) alloys, antisite defects; the latter consist, for example in the case of a binary AB alloy, of B atoms wrongly placed on A sublattice sites (see Figure 1), and can form thermally or accommodate non-stoichiometry. A large literature exists concerning point defects in pure metals, dilute alloys, and simple covalent and ionic crystals (Wollenberger, 1983; Crawford and Slifkin, 1972; Abromeit and Wollenberger, 1987). Much less work has been done in the case of intermetallic compounds. In particular, the role of impurities has scarcely been studied, and we shall only mention a few examples in this review, focusing on intrinsic point defects (vacancies, interstitials, antisites).

In most solids, point defects are not found thermodynamically at 0 K: they form at finite temperature T , with concentration $C \approx \exp(-E_F/kT)$, where E_F is the

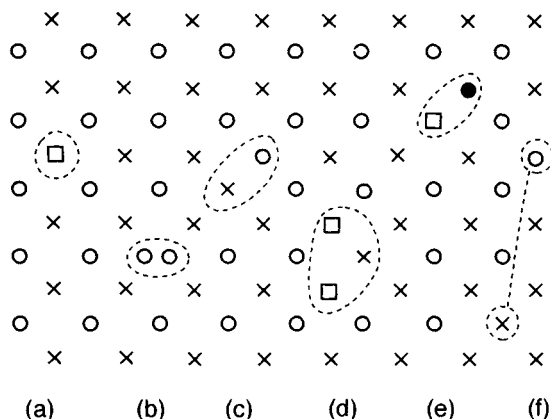


Figure 1. Typical point defects in a binary ordered alloy: (a) vacancy (\square); (b) split interstitial; (c) bound pair of antisite defects; (d) bound triple defect consisting of two vacancies and one antisite atom; (e) vacancy-impurity (\bullet) bound pair; (f) unbound wrong pair. Many other types of defects are possible, as will be discussed for example for B11 (CuTi, Section 5.3) and A15 (Nb₃Sn, Section 9.1) compounds

formation energy* and k is the Boltzmann constant. They can be retained by quenching, or produced by irradiation or cold working. The rate of disappearance of excess point defects is proportional to $\exp(-E_M/kT)$, where E_M is the migration energy. In pure metals,

*The formation energy E_F and the formation volume V_F are defined as the change of energy (volume) of the crystal when displacing an atom from the bulk to the surface (vacancy) or from the surface to the bulk (interstitial) without changing the surface energy. Strictly speaking, one should consider formation and migration enthalpies H_F and H_M . But, at atmospheric pressure p , the values of pV_F and pV_M are typically 10^{-5} eV, negligible compared to E_F and E_M . In the following, we have therefore identified H_F and E_F , H_M and E_M , H_D and E_D .

vacancies have a formation energy E_F^V of the order of 0.5 to 2 eV, leading to a thermodynamic vacancy concentration at the melting point of a few 10^{-4} , and $E_M^V \approx 0.5$ to 1.5 eV. The self-diffusion coefficient is equal to $\exp(-E_D/kT)$, with $E_D \approx E_F^V + E_M^V$.

On the other hand, in some intermetallic compounds that permit off-stoichiometry (see Section 3.2), one finds structural ('constitutional') vacancies, even at low temperatures: the concentration of such defects may be important (several percent) and in some cases the defects order.

Very generally, point defects distort locally and induce electronic perturbations in the crystal: these effects lead to elastic and electronic interactions between them, as well as with other defects (dislocations, grain boundaries, etc.). The complex defects so formed may introduce more distortion into the lattice than simple point defects, and therefore have greater effects on the mechanical properties. With increasing temperature, point defects become more and more randomly positioned, and complex defects (e.g. divacancies, vacancy-impurity or interstitial-impurity bound pairs) dissociate.

From the fundamental point of view, vacancies and interstitials in intermetallic compounds present special features and a much more complex behavior, as compared to pure metals. For example, in a pure metal of simple crystal structure, all the bulk lattice sites are equivalent for the formation of a vacancy. On the contrary, in an LRO concentrated alloy, the various sublattices are not equivalent. Moreover, atoms of a given sublattice may have various atomic environments: in an LRO alloy as well as in a concentrated solid solution, many types of vacancies can be produced. Also, the vacancy formation energy depends on the extent of off-stoichiometry, and the thermal vacancy concentration may be much larger than in pure metals.

In the same way, the migration of vacancies is more complex than in pure metals, because sites are inequivalent; for example, in an LRO alloy, the jump of a vacancy between two neighboring sites belonging to different sublattices changes the LRO parameter, and this will increase the migration energy.

The same arguments apply to interstitials. In pure metals of simple (f.c.c. or b.c.c.) crystal structure, the structure and properties of interstitials are well-known; for example, in many f.c.c. metals, it consists of a dumbbell oriented in a $\langle 100 \rangle$ -type direction, with a large formation energy (several eV) and a small migration energy (typically 0.2 eV). In intermetallic compounds, the structure of interstitials is generally not known: in some cases, several types of complex defects occur

simultaneously. In concentrated solid solutions, the migration properties of interstitials are typical of transport in disordered media, requiring specific concepts such as percolation, localization, and trapping: this leads to a slowing down of the interstitial, which can in some cases show a larger migration energy than the vacancy.

2. Experimental Techniques for Studying Point Defects

2.1 Production of Point Defects

Because their formation energy is generally lower than that of interstitials, the quenching of a stoichiometric intermetallic compound from high temperature, if fast enough, will give isolated vacancies and antisite defects.

The best way to obtain self-interstitials is by low-temperature electron irradiation, which in fact creates isolated vacancy-interstitial pairs (Frenkel pairs) (Wollenberger, 1983). Ion or fast neutron irradiation directly gives defect clusters, so-called 'cascades.' Electron irradiation can be performed either in a high-voltage transmission electron microscope (HVTEM) with direct observation of defect clustering, or in a Van de Graaff accelerator; in the latter case, measurement of defect production and recovery is generally made by electrical resistivity. By varying the incident electron energy, one can determine the threshold displacement energies E_d for various types of atoms. For example, in Cu_3Au (L1_2 (cP4)) and CuAu (L1_0 (tP4)), the minimum electron energies for displacement of (light) Cu and (heavy) Au were found respectively to be 400 and 900 keV ($E_d \approx 18$ eV). By irradiating between 400 and 900 keV, one creates only Cu Frenkel pairs; with an electron energy above 900 keV, gold atoms are also displaced (Alamo *et al.*, 1986).

2.2 Determination of Point-Defect Formation Properties

Structural vacancies in non-stoichiometric intermetallic compounds have been detected by coupled density and lattice-parameter measurements. The measured density is compared to calculated densities in order to choose between several models: antistructure defects, vacancies within a sublattice, interstitials, etc. The application of this method to CoAl alloys is shown in Figure 2 (Fleischer, 1993). Care must be taken to check the absence of porosities and to determine precisely the chemical content of the sample.

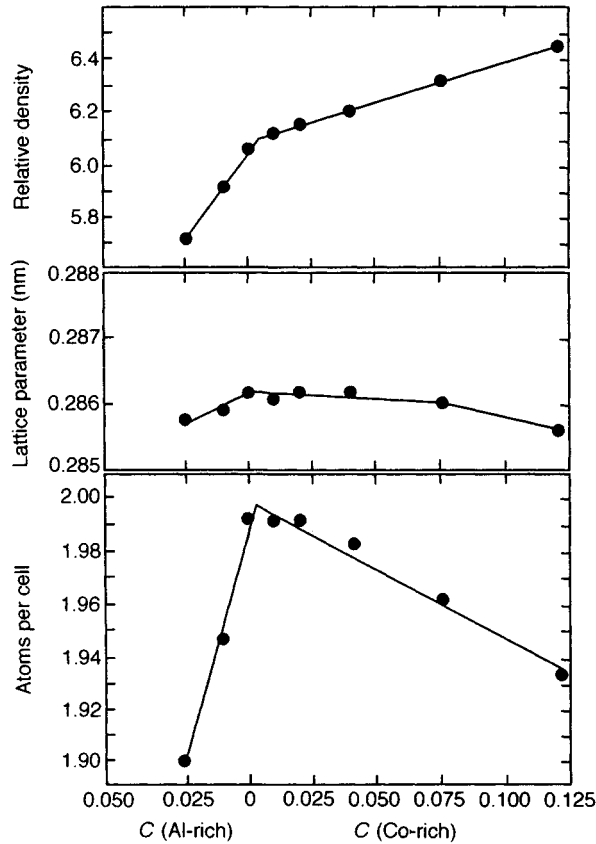


Figure 2. Relative density (specific gravity) and lattice parameter (measured at room temperature) and deduced cell occupancy as a function of composition for CoAl B2 alloys (from Fleischer, 1993). Each excess Al atom produces a vacant lattice site on the Co sublattice. Excess Co leads to lesser vacancy concentrations

The progress of X-ray and especially neutron diffraction techniques now allows one to obtain information on structural vacancies and antisite defects (in the percent concentration range) from the precise determination of structure factors (see for example Kogachi *et al.*, 1992); neutron measurements are possible up to very high temperatures.

To create thermal vacancies, atoms may be thought of as taken out of lattice sites in the interior of the specimen and placed on its surface. This changes the number of sites and the length of the specimen (although the vacancy formation volume is smaller than the atomic volume because of relaxation effects). Therefore, thermal vacancy formation can be studied by the comparison of the relative change of length L and lattice constant a , measured *in situ* at high temperature

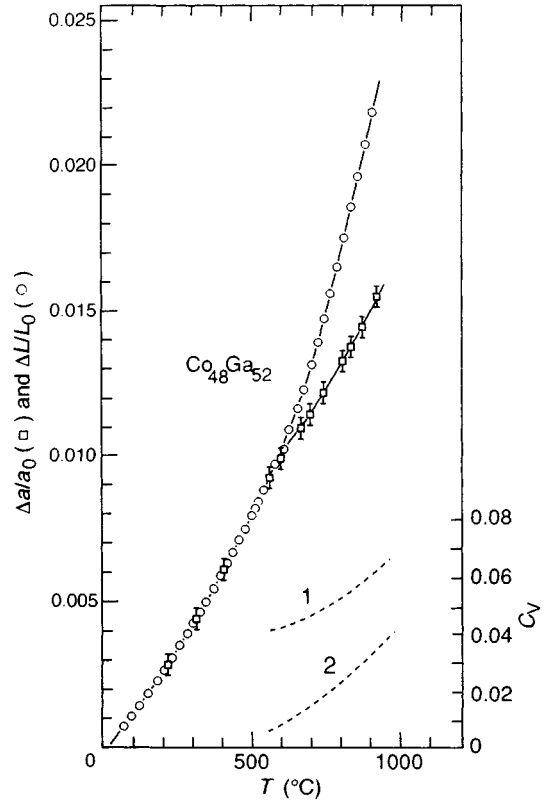


Figure 3. Variation of lattice parameter a (\square) and macroscopic length L (\circ) as functions of temperature in B2 (cP2) $\text{Co}_{48}\text{Ga}_{52}$. Also shown are the deduced vacancy concentration for $\text{Co}_{48}\text{Ga}_{52}$ (broken curve 1) and $\text{Co}_{56}\text{Ga}_{44}$ (broken curve 2) (From Van Ommen *et al.*, 1981)

(Simmons and Balluffi, 1960). The extra thermal vacancy content is given by

$$\Delta C_V(T) = (1 + C_{V0}) \left\{ \frac{[1 + \Delta L(T)/L_0]^3}{[1 + \Delta a(T)/a_0]^3} - 1 \right\}$$

where C_{V0} , L_0 and a_0 are given at room temperature. A typical set of curves, obtained for $\text{Co}_{48}\text{Ga}_{52}$, where deviation from stoichiometry is mainly accommodated by Co structural vacancies (see Section 3.2), is given in Figure 3. Above 560 °C, the formation of thermal vacancies leads to a splitting between $L(T)$ and $a(T)$ and to a deviation from the normal thermal expansion (Van Ommen *et al.*, 1981).

The study of vacancies is now mainly performed by the positron annihilation technique (see for example Corbel, 1987). Because the electron density is weak in a vacancy, the lifetime τ of a positron trapped in it is

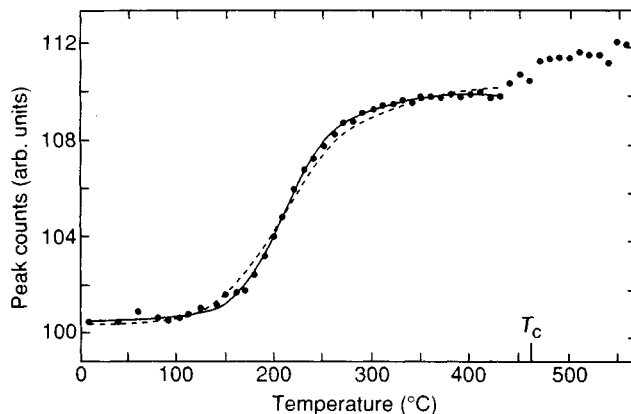


Figure 4. Coincidence counts at the peak of the angular distribution of annihilating photons, measured as a function of temperature in β -brass CuZn, B2 (cP2). Broken curve: fit with a single exponential. Full curve: fit with a T -dependent formation energy (From Kim and Buyers, 1980)

noticeably larger than if itinerant in the bulk of the crystal (typically 180 and 100 ps, respectively). Also, the value h at the peak of the correlated angular distribution of the annihilating photons, or the parameter S of the Doppler broadening line, are very sensitive to the concentration of vacancies (above a threshold of 10^{-7}). The parameters τ , h or S , measured either *in situ* at high temperature, or after quenching, are generally analyzed in a two-state trapping model, where they are assumed to depend linearly on the positron annihilation rate at the defect, which is proportional to the vacancy concentration. In the simplest model, one has, for example

$$L(T) = \frac{h_B + h_V A_V \exp(-E_F^V/kT)}{1 + A_V \exp(-E_F^V/kT)}$$

(where B stands for 'bulk' and V for 'vacancies'). Figure 4 shows, for CuZn (B2 (cP2)), the annihilation rate $h(T)$ plotted as a function of temperature, from which the formation energy E_F^V of an average vacancy has been obtained (Kim and Buyers, 1980) (see Section 3.1).

When lattice defects are generated thermally, their formation energy gives an extra contribution to the heat capacity of the crystal. To our knowledge, such measurements have not been applied in intermetallic compounds.

A frequently used technique to study point-defect creation is electrical conductivity measurement, because of its simplicity and great sensitivity. Indeed, in metallic materials, point defects are scattering centers for electrons: they increase the electrical resistivity. In semiconductors, they introduce localized levels in the

gap and change the number of carriers. The measurements should preferably be performed at low temperature to avoid thermal contributions: for example, determination of the vacancy formation energy on samples quenched from various temperatures or study of the defect production during irradiation.

Information on the structure of interstitials can be obtained from diffuse X-ray scattering (Dederichs, 1973). In particular, the long-range part of the strain field of point defects leads near the Bragg peaks in reciprocal space to a diffuse intensity that diverges as q^{-2} ($q = \tau_{hkl} - Q$, where Q is the scattering vector, and τ_{hkl} the position of the Bragg peak) and is labeled 'Huang' scattering. Its intensity is directly related to the elastic constants and to the formation volume of the defect (in fact, the interstitial in the case of electron irradiation). The symmetry of Huang scattering in reciprocal space is dependent on the defect symmetry in real space. Of course, the information is less clear when several types of defects coexist, which is the general case in alloys. As an example, the X-ray Huang intensity of ordered Fe-40 at% Al is given in Figure 5: it is shown to increase after electron irradiation at 20 K. Analysis of the data suggests that the most probable configuration is the $\langle 110 \rangle$ split interstitial with orthorhombic symmetry. The subsequent increase after annealing at 300 K is due to the formation of very small clusters (10 interstitials) (Beaufort *et al.*, 1986).

2.3 Determination of Point-Defect Migration Properties

The most popular technique for studying the migration of vacancies in a binary alloy AB is the measurement of

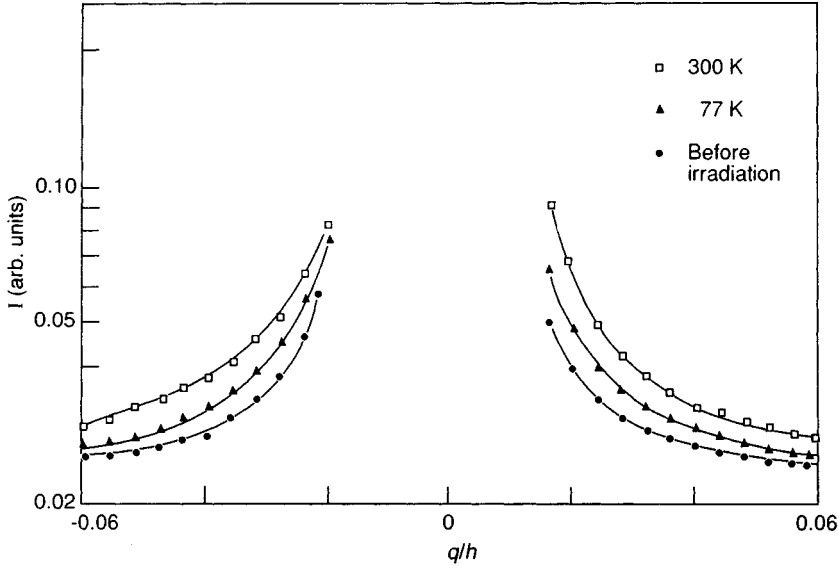


Figure 5. Diffuse X-ray intensity (arbitrary units) measured at 77 K in a single crystal of B2 (cP2) Fe-40 at. % Al near the (200) reflection in the direction $q = [100]$ (q in units of $h = 2\pi/\text{lattice parameter}$) (From Beaufort *et al.*, 1986). ●, data before irradiation; ▲, data for irradiation at 20 K and annealing at 77 K; □, data after annealing at 300 K

atomic self-diffusion coefficients D_A^* and D_B^* by tracer techniques (see Chapter 32 by Larikov in this volume). Atomic diffusion is generally due to vacancies, and the migration energy of A-type vacancies is estimated as the difference between the activation energy for self-diffusion E_D^A and the vacancy formation energy E_F^{VA} . More precise information on migration energies has been obtained from experiments that require only a small number of vacancy jumps:

(i) If one applies an instantaneous small temperature jump $T \rightarrow T \pm \Delta T$, the original vacancy concentration will differ by $\Delta C_V(T)$ from its new equilibrium value and will evolve toward it, with a rate depending on the vacancy mobility. Generally $d(\Delta C_V)/dt$ is proportional to $-\Delta C_V$, whence $C_V(T + \Delta T, t) = C_V(T + \Delta T, t = \infty) + \Delta C_V \exp(-t/\tau)$. Many properties that depend on the vacancy content will evolve linearly with $\Delta C_V(T, t)$ and therefore exponentially with time: electrical resistivity, magnetic susceptibility, length, etc. (see Figure 6). The relaxation time τ generally depends exponentially on temperature: $\tau = \tau_0 \exp(E/kT)$, from which the activation energy E of the process can be determined.

(ii) The detailed analysis of isochronal and isothermal recovery of defects created or retained at low temperature (by quenching or irradiation) allows one to obtain the characteristic activation energy of a given migration stage.

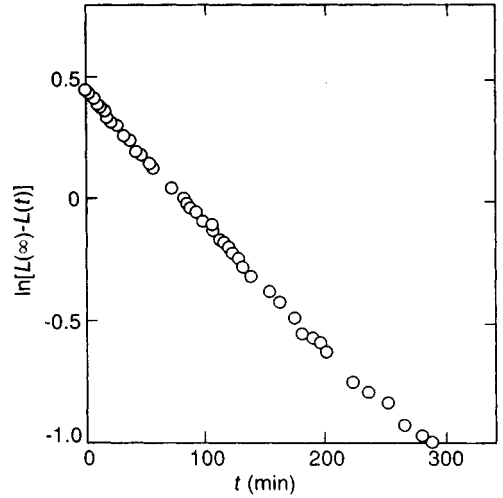


Figure 6. Typical semilogarithmic plot of the length variation $[L(\infty) - L(t)]$ of CoGa measured as a function of time at 773 °C after a 20 °C temperature step increase (From Van Ommen and de Miranda, 1981)

Point-defect migration energies can also be deduced from the growth or shrinkage of dislocation loops during or after irradiation in a HVTEM (see Chapter 22 by Veyssi re and Douin in this volume).

2.4 Recovery and Clustering of Point Defects

Recovery of point defects created at low temperature occurs by several intermediate stages, generally involving clusters, and has been studied by various techniques: electrical resistivity, differential scanning calorimetry, transmission electron microscopy (when the size of defect clusters is larger than 2 nm), positron annihilation (the lifetime of a positron in a three-dimensional vacancy cluster increases with the size of the cluster and can reach 500 ps), and Huang X-ray scattering (it increases when interstitials cluster into dislocation loops).

3. Experimental Studies of the Formation of Vacancies and Antisite Defects

3.1 Alloys with No Structural Vacancies

For most of the intermetallic compounds, deviation from the stoichiometric composition is accommodated by antisite atoms: CuZn, Cu₃Au, NiTi, Ni₃Al. Paired antisite defects are also formed thermally in high concentration for those alloys which present an order-disorder transition in the solid state (Cu₃Au, CuZn): their concentration is directly related to the LRO parameter value. The absence of structural vacancies has been checked by positron annihilation in the case of CuZn (Kim and Buyers, 1980), Cu₃Au (Doyama *et al.*, 1985a, b), Fe₃Al (Schaefer *et al.*, 1990), and TiAl (Shirai and Yamaguchi, 1992). In all cases, thermal vacancies form at high temperature.

3.1.1 Alloys With High Ordering Energies

High ordering energies are exemplified by the case of Ni₃Al, which remains LRO up to the melting point. The homogeneity range of this alloy extends from 23 to 27.5 at.% Al. Coupled lattice-parameter, density, and long-range order parameter *S* (determined by X-ray diffraction) measurements performed at room temperature have shown that the departure from stoichiometry is mainly accommodated by antisite defects, i.e. Ni atoms on Al sites (labelled Ni_{Al}) in Ni-rich alloys, and Al atoms on Ni sites (labelled Al_{Ni}) in Al-rich alloys. The stoichiometric compound Ni₃Al is nearly perfectly ordered at room temperature (*S* = 0.98) (Aoki and Izumi, 1975).

Nevertheless, positron annihilation measurements on polycrystalline samples, either pure or doped with boron, show that at room temperature Ni-rich alloys contain no detectable vacancies, but stoichiometric and

Al-rich alloys contain a small but detectable (Ni) vacancy concentration, roughly a few 10⁻⁶.^{*} The positron trapping increases with boron content; this suggests that boron atoms or clusters are trapped near constitutional Ni vacancies, increasing their concentration and forming stable complex defects. This has interesting consequences for the interpretation of mechanical properties: trapping of boron atoms near vacancies might explain the lack of ductility of B-doped stoichiometric or Al-rich Ni₃Al, whereas in Ni-rich alloys this does not occur, boron enriching the grain boundaries and increasing the ductility (Das Gupta *et al.*, 1987).[†]

In Ni-rich Ni₃Al (76.3 at.% Ni), vacancies form only thermally, very similarly to metals: from the positron trapping rate plotted as a function of the quenching temperature, one obtains the formation energy of a vacancy, $E_F^V = 1.6 \pm 0.2$ eV (Wang *et al.*, 1984). This value is in agreement with recent theoretical calculations for formation of a Ni vacancy (1.47 eV) (Foiles and Daw, 1987).

3.1.2 Alloys with Low Ordering Energies

The influence of long-range ordering on vacancy properties has been studied in some detail in β -brass (CuZn). Positron measurements (angular correlation technique) show an annihilation rate versus temperature with a double S shape (see Figure 4). This unusual shape is probably due to the trapping of two different vacancy-type defects: either (i) Cu and Zn vacancies (Chabik and Rozenfeld, 1981), or (ii) vacancies and divacancies (Kim and Buyers, 1980). The first interpretation seems unlikely as, in the LRO state, the Cu and Zn diffusion coefficients are very near to one another (Kuper *et al.*, 1956). In the second interpretation, a precise fit of the low-temperature data ($T < 430$ °C) requires a temperature-dependent vacancy formation energy (the full curve in Figure 4): $E_F^V = 0.35$ eV in the disordered state, and 0.75 eV in the LRO state. This variation of 0.4 eV corresponds roughly to the increase of Zn diffusion activation energy between the disordered and the ordered phases (Kuper *et al.*, 1956). Nevertheless, it has to be remarked that it is much larger than predicted from a simple Bragg-Williams model, where the vacancy formation energy is related to breaking of the first-neighbor bonds ($E_F^V(\text{ordered}) - E_F^V(\text{disordered})$)

^{*}This result is in apparent contradiction with the conclusion of a diffusion study, which suggests a small Ni vacancy concentration ($\sim 10^{-6}$) on both sides of stoichiometry (Hoshino *et al.*, 1988).

[†]In rapidly quenched stoichiometric Ni₃Al, boron atoms remain in solid solution up to 1.5 at.%, tend to occupy interstitial sites, and strongly increase the strength of the alloy (Huang *et al.*, 1984).

$\approx kT_c/1.54 \approx 0.04$ eV (Girifalco, 1964)). Certainly more experimental and theoretical effort must be made in this direction.

The vacancy formation energy has also been determined in gold-copper alloys by electrical resistivity measurements in quenched samples ($E_F^V = 1.00 \pm 0.06$ eV in Cu_3Au (Benci *et al.*, 1969)) and by positron annihilation (angular correlation-type measurements in the disordered state, 500–900 °C ($E_F^V = 1.05 \pm 0.11$ eV in Cu_3Au , 1.00 ± 0.10 eV in CuAu (Kim, 1987)). In fact, the positron lifetime of the defects in the quenched Cu_3Au sample is 240 ps instead of 200 ps for the single vacancy (obtained by electron irradiation), showing that a quenched foil of thickness 0.4 mm retains small three-dimensional vacancy clusters (\approx six vacancies) (Doyama *et al.*, 1985b).

3.2 Alloys with Structural Vacancies

Bradley and Taylor (1937) observed that the density of Al-rich NiAl was smaller than calculated from the lattice parameter, assuming two atoms per unit cell. They concluded that the excess Al atoms do not substitute on the Ni sublattice, but that vacancies must be created on that sublattice. At room temperature, in $\text{Ni}_{45}\text{Al}_{55}$, 10% of the Ni sites are vacant. These vacancies, determined by composition and not temperature, are called structural (or constitutional). On the other hand, on the Ni-rich side, the extra nickel atoms substitute normally for Al atoms on the Al sublattice. The composition dependence of the vacancy content at room temperature in the NiAl intermetallic compound was checked by positron annihilation (Doyama *et al.*, 1987) and detailed X-ray diffraction studies (Kogachi *et al.*, 1992).

The same behavior was found for a number of other group VIII–IIIA intermetallic compounds with the B2 (cP2) structure (CsCl type) (Neumann *et al.*, 1976), in particular FeAl (Ho and Dodd, 1978), CoAl (Bradley and Seager, 1939; Wachtel *et al.*, 1973; Fleischer, 1993), CoGa (Berner *et al.*, 1975; Van Ommen *et al.*, 1981), and NiGa (Donaldson and Rawlings, 1976; Seybolt and Westbrook, 1964; Wasilewski *et al.*, 1968), as well as for a few other B2-structure compounds (see review by Chang and Neumann, 1982).

Generally, the lattice parameter peaks at or close to the stoichiometric composition (Cooper, 1963). The determination of cell occupancy as a function of composition from measurements of specific gravity and lattice parameter is shown on Figure 2 in the case of CoAl. The vacancy content at room temperature has been shown to depend on the thermal history of the

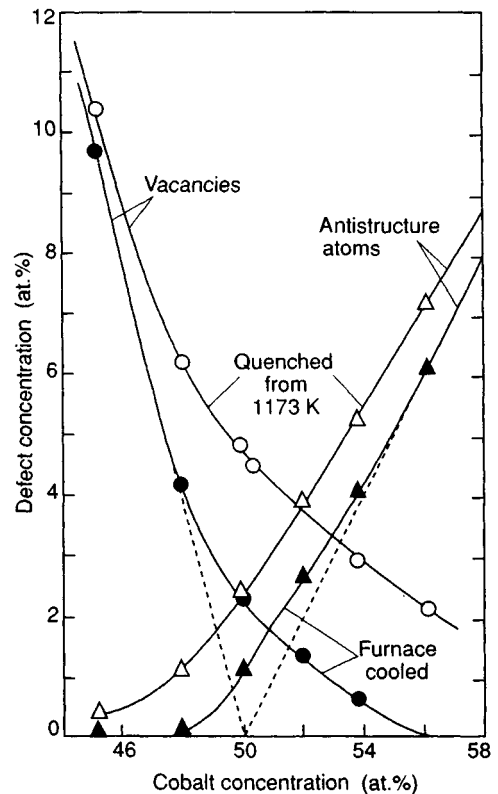


Figure 7. Concentration of vacancies and antisite defects in CoGa alloys as a function of composition and of thermal treatment (From Schwab and Gerold, 1980)

sample. This may be the explanation for some unresolved cases: for example, AgMg has been classified by Chang and Neumann (1982) as an antistructure defect alloy, whereas Hünecke *et al.* (1987) have detected in this compound a small structural-vacancy content.

The CoGa alloy has been the most studied experimentally. The concentrations of vacancies and antisite atoms versus Co content are shown for this compound in Figure 7. It can be seen that the number of defects is higher in alloys quenched from 1173 K than in slowly cooled alloys (Berner *et al.*, 1975; Van Ommen *et al.*, 1981). An important question is the following: are these defects true structural vacancies (i.e. are they stable at 0 K?), or are they frozen-in thermal vacancies? It is generally believed that the broken lines of Figure 7 represent the structural vacancies, and that the full curves represent the total (structural plus thermal) defect concentrations. Thus the observed vacancy concentration

on the Co-rich side would correspond to thermal vacancies, whereas those on the Ga-rich side would be mainly structural vacancies.

Coupled length and lattice-constant measurements (see Section 2.2) were performed between 800 and 1200 K to determine the thermal dependence of vacancy concentration, which is shown as broken curves on Figure 3 for $\text{Co}_{48}\text{Ga}_{52}$ and $\text{Co}_{56}\text{Ga}_{44}$ (Van Ommen *et al.*, 1981). One can see that, even for Co-rich alloys, where no structural vacancies exist, the thermal-vacancy content is much larger than in a metal: 3.5% at 1200 K for $\text{Co}_{56}\text{Ga}_{44}$ (see broken curve 2 in Figure 3).

If we suppose that the thermal vacancies are Co vacancies (just like the structural vacancies), then this creation must be accommodated by another type of defect to maintain a constant composition. It is generally proposed that the creation of two thermal vacancies always occurs in combination with the formation of an antisite atom (Co atom on Ga site): this is the triple-defect structure proposed first by Wasilewski (1968).

On the basis of thermodynamic calculations (Kim, 1986) (see Section 4), it has been supposed that, at least in some compounds, including CoGa, structural vacancies are unlikely, purely thermal vacancies accounting for the observed behavior. In our opinion, strong arguments for the existence of structural vacancies at low Ni or Co content in B2-structure aluminides or gallides are the following:

- The large vacancy content retained at room temperature in Co-rich alloys would require a very large migration energy, much larger than in Ga-rich alloys; this is contrary to diffusion data, Co and Ga self-diffusion coefficients being weakly composition-dependent (Stolwijk *et al.*, 1980).
- $C_V(T)$ for $\text{Co}_{48}\text{Ga}_{52}$ (measured between 800 and 1200 K) extrapolates to a finite value of 3–4% at 0 K (broken curve 1 in Figure 3; data from Van Ommen *et al.*, 1981).
- There exist vacancy-ordered phases in the Ni–Al system (see below).
- The fact that, in the Ni–Al system, the increase of vacancy content below 50% Al at room temperature is very sudden (Doyama *et al.*, 1987; Kogachi *et al.*, 1992).

Structural vacancies have been found in other alloys: ternary alloys such as (Fe,Ni)Al and (Cu,Ni)Al based on the above B2 alloys (Lipson and Taylor, 1939; Jacobi and Engell, 1971), γ -brass phases in the Cu–Al and Cu–Ga systems (above 35% Al or Ga) (Hume-Rothery *et al.*, 1952), and LiAl (Brun *et al.*, 1983).

Intermetallic compounds with the B8_1 (hP4) structure (NiAs type) also contain structural defects; for example, the Ni_{1+x}Sb phase exists at room temperature with $-0.06 < x < 0.06$. When $x < 0$, the compound contains Ni vacancies; and when $x > 0$, Ni interstitial atoms (Leubolt *et al.*, 1986).

The structural vacancies sometimes order. This has been found in the Ni–Al system: the Ni_2Al_3 phase is produced from NiAl (B2) by subtracting a Ni plane every three; for compositions that are intermediate between NiAl and Ni_2Al_3 , vacancies tend to order and prepare the Ni_2Al_3 phase (Delavignette *et al.*, 1972; Taylor and Doyle, 1972). A similar phenomenon is found for NiAs and NiSb, because the B8_2 (hP6, Ni_2In type), B8_1 (NiAs type), and C6 (hP3, NiTe_2 type) structures form a continuous transition: this can be made by subtracting Ni atoms from the Ni sublattice.

In β -LiAl (B32 (cF16), NaTl-type structure), vacancies on the Li sublattice are the dominant defect for Li-deficient compositions (48 to 50 at.%). Neutron diffraction measurements show that these vacancies order on every tenth (840) plane below 97 K. This vacancy ordering is responsible for anomalies observed in several physical properties around 100 K (electrical resistivity, specific heat, nuclear spin–lattice relaxation) (Brun *et al.*, 1983).

Some tetrahedral compounds contain structural vacancies on the cation sublattice, in ordered or disordered fashion. This is, for example, the case for Ga_2S_3 (derived from hexagonal wurtzite structure) or CdGa_2S_4 (derived from cubic zinc-blende structure), where respectively one-third and one-quarter of the cation sites are unoccupied (see Chapter 14 by Parthé in this volume).

4. Production and Structure of Interstitials

It is important to know the elementary properties of self-interstitials, if we want to understand in detail and model the behavior of intermetallic compounds under technological irradiation conditions, e.g. disordering and dissolution of precipitates in steels used in nuclear reactors, or amorphization by implantation.

4.1 Production

As mentioned in Section 2.1, because of the small electron mass, the energy transferred by MeV electrons to nuclei via Rutherford scattering is small and of the order of the displacement threshold energy E_d (~ 20 eV). Therefore, electron irradiation, performed

at low temperature to avoid point-defect migration, is the most suitable for investigation of isolated Frenkel pairs.

Defect production by electron irradiation is more complicated in intermetallic compounds than in pure metals: apart from the existence of different types of interstitials (see Section 1), one must also take into account radiation-induced disordering (Schulson, 1979). This can occur by several mechanisms, in particular uncorrelated mutual recombination between a vacancy on the α sublattice and a B interstitial, or successive replacement collisions along crystal directions where A and B atoms alternate ($\langle 110 \rangle$ in $L1_2$, $\langle 111 \rangle$ in B2-ordered alloys). The latter process is extremely efficient, as the number of replacements per displacement can be typically of the order of 100.

In intermetallic compounds, the production of point defects by electron irradiation has generally been studied by electrical resistivity measurements. This has the advantage that the specific resistivity of a Frenkel pair is one to two orders of magnitude larger than that of an antisite defect.

In a binary alloy A–B, the rate of increase of electrical resistivity ρ with fluence ϕ is, at low fluence,

$$(d\rho/d\phi)_{\phi=0} = \sigma_d^A \rho_F^A + \sigma_d^B \rho_F^B$$

where ρ_F^A and ρ_F^B are the average resistivities of A and B Frenkel pairs, and σ_d^A and σ_d^B are the displacement cross-sections of A and B atoms, taking into account interatomic (A–A, A–B, B–A, B–B) collisions. The values of σ_d^A and σ_d^B depend on the incident electron energy and on the threshold displacement energies of A and B, and can be calculated analytically for isotropic ('amorphous') alloys (Lesueur, 1981).

Figure 8 shows the resistivity increase of ordered and disordered FeCo (B2 cubic structure) during 2.5 MeV electron irradiation (Rivière *et al.*, 1983b). Because of the very similar electronic structure and size of Fe and Co, $\rho_F^{\text{Fe}} \approx \rho_F^{\text{Co}}$. In the case of disordered FeCo, it is reasonable to assume that the damage comes only from Frenkel pairs, whence $\rho_F = 13 \pm 3 \mu\Omega \text{ cm}/\%$ Frenkel pair (assuming $E_d^{\text{Co}} = E_d^{\text{Fe}} = 22 \text{ eV}$). The large damage rate in ordered FeCo is then ascribed to the creation of antisite defects; if ρ is assumed to depend quadratically on the LRO parameter S (Muto, 1936), the data are consistent with a specific resistivity of $0.07 \mu\Omega \text{ cm}/\%$ antisite defect and about 30 replacements per displacement.

On Figure 8, one sees that the defect production rate shows a slight tendency to saturate at high fluence. This is due (i) to the existence of a recombination volume

V_0 within which any vacancy–interstitial pair will spontaneously recombine and (ii) to subthreshold energy transfers inducing athermal migration and annihilation of interstitials (with a cross-section σ_r). It can be shown that the Frenkel-pair production rate obeys the following relation:

$$dc(\phi)/d\phi = \bar{\rho}_F^{-1} d\rho(\phi)/d\phi = \sigma_d(1 - V_0c)^2 - \sigma_r c$$

Therefore from the plot of $dc/d\phi$ versus c for disordered FeCo, Rivière *et al.* (1983b) obtain values for the saturation resistivity and $V_0 \approx 250\Omega_a$ (atomic volumes), which are quite similar to the pure-metal values.

Similar studies have been performed on Fe–40% Al (Rivière *et al.*, 1983a), Cu_3Au , and CuAu (Alamo *et al.*, 1986). In the latter alloys, as discussed in Section 2.1, E_d^{Au} and E_d^{Cu} have been determined experimentally from the dependence of damage rate on incident electron energy. The Frenkel-pair resistivity is probably larger by a factor of 1.5 to 2 in ordered compared to disordered copper–gold alloys (Alamo *et al.*, 1986).

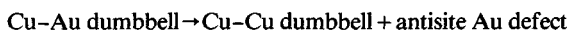
The addition of a third element to an ordered binary alloy can modify considerably the point-defect properties: for example, the behavior of FeCo–2% V is very complex, because vanadium forms a resonant virtual bound state at the Fermi level, the partial filling of which depends strongly on the state of order (Rivière *et al.*, 1983b). Solutes (specifically Mn, Re, and Ti) have also been shown to have complicated effects in CoAl (Fleischer, 1993).

4.2 Experimental Determination of the Self-Interstitial Structure

Structures of self-interstitials can be determined by measuring the X-ray Huang scattering (see Section 2.2). To our knowledge, three ordered alloys have been studied by this technique: the $L1_2$ compounds Ni_3Fe (Bender and Ehrhart, 1982), and Cu_3Au (Urban and Ehrhart, 1987); and the B2 structure Fe–40% Al (Beaufort *et al.*, 1986).

In Ni_3Fe , where both types of atoms are of similar size, the (average) interstitial was found to be very similar to that in f.c.c. metals: a $\langle 100 \rangle$ dumbbell with a relaxation volume of about $1.5\Omega_a$.

In Cu_3Au , the average interstitial relaxation volume is much smaller: $0.8\Omega_a$. This suggests that there is a unique interstitial, the small Cu–Cu dumbbell, the displaced larger gold atoms transferring to a copper site according to the reaction:



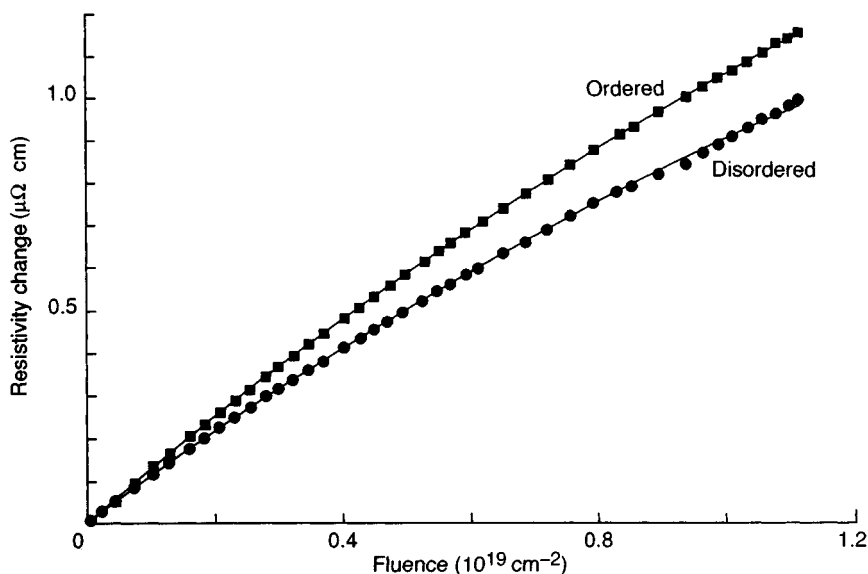


Figure 8. Resistivity increase $\Delta\rho$ during 2.5 MeV electron irradiation at 21 K as a function of the fluence in ordered and disordered FeCo (From Rivière *et al.*, 1983a)

This is confirmed by the isochronal recovery curves, which are very similar for incident electron energies of 0.66 and 2.36 MeV (without and with Au displacements) (see Section 7) (Alamo *et al.*, 1986).

In Fe-40% Al, the asymmetry of the Huang scattering suggests that the most probable interstitial configuration should be a $\langle 110 \rangle$ -oriented dumbbell with orthorhombic symmetry as in b.c.c. Fe or Mo.

5. Theory of Point-Defect Formation Properties

5.1 Empirical Prediction of Structural-Vacancy Compounds

An explanation for the occurrence of structural vacancies has been given from the Hume-Rothery rules. One knows that the ordered B2 compounds exist only if the number of conduction electrons per atom n_e is near to and does not exceed 1.5. This is the case for stoichiometric NiAl, if one admits that Ni, a transition metal, contributes zero electrons. Then, for an aluminum-rich alloy $\text{Ni}_{1-x}\text{Al}_{1+x}$, if non-stoichiometry occurs via Al_{Ni} antisites, $n_e = 1.5(1+x)$; the Fermi surface will enter the second Brillouin zone, strongly increasing the internal energy. The alloy energy can be minimized by creating vacancies in the Ni sublattice, n_e then remaining equal to 1.5. The qualitative validity of this model is confirmed by the behavior of AgMg, where Ag brings one electron and Mg two electrons, n_e being maintained at 1.5 if non-

stoichiometry occurs by an equal number of Ag vacancies and Mg_{Ag} antisites, as found experimentally (Hünecke *et al.*, 1987). The same explanation applies to the γ phase of CuGa, for which n_e should not exceed 21/13.

Although the Hume-Rothery rules explain many experimental facts, other authors have tentatively explained the occurrence of structural vacancies by size-effect arguments (Lipson and Taylor, 1939) or by interionic repulsion (Jacobi and Engell, 1971).

Diamond-like ionic-covalent tetrahedral defect structures are obtained when the valence-electron concentration (VEC) per atom ranges from 4 to 4.8. Because each anion-cation bond is saturated by two electrons, and each non-bonding anion orbital pointing toward a cation vacancy contains also two electrons, the number y of structural vacancies per atom is simply related to VEC: $y = \text{VEC}/4 - 1$ (e.g. $\text{VEC} = 4.8$ and $y = 0.2$ for Ga_2S_3) (Parthé, 1964).

5.2 Empirical Prediction of Vacancy Formation Energies

In pure metals, empirical relationships have been noted between the monovacancy formation enthalpy and either the heat of vaporization, the Debye temperature, or the electron density at the boundary of an atomic cell (Miedema, 1979). In particular, the analogy with a macroscopic hole has suggested the fairly accurate Miedema relationship

$$E_F^V = Q^{-1} \gamma_0^S \Omega_m^{2/3} \quad (1)$$

where γ_0^S is the surface energy and Ω_m the molecular volume, and where the effective value of the constant Q , larger than for a macroscopic hole, includes both electronic and elastic relaxation effects.

Such simple correlations cannot be directly extended to ordered alloys, as we have seen that vacancies on different sublattices have very different properties. In fact, because electronic long-range interactions are screened in metals, the properties of a vacancy are mainly controlled by its immediate neighborhood.

Using this argument, and the analogy with a macroscopic hole previously applied successfully to pure metals, Miedema (1979) suggested that, in a dilute binary alloy $A_x B_{1-x}$ ($x \ll 1$, e.g. LaNi_5) with all A atoms surrounded by B atoms, a vacancy on an α site will be equivalent to a monovacancy in pure metal B: $E_F^{\alpha} \approx E_F^{\text{VB}}$.

Corrections were then introduced in this model (i) to include size effects $\Omega_A \neq \Omega_B$ (the larger the A atom, the larger its vacancy formation energy E_F^{VA} , see formula (1)) and (ii) to extend it to arbitrary concentration values, a vacancy on an α site then being partly surrounded by A and B atoms. The generalized formula may be written as

$$E_F^{\alpha} = (1 - f_{\alpha}^{\text{B}}) E_F^{\text{VA}} + f_{\alpha}^{\text{B}} (\Omega_A / \Omega_B)^{5/6} E_F^{\text{VB}}$$

where E_F^{VA} and E_F^{VB} are pure-metal values, and the factor f_{α}^{B} characterizes the degree to which an α site is surrounded by B atoms ($f_{\alpha}^{\text{B}} = 0.75$ in B2 LRO cubic alloys) (Miedema, 1979).

Qualitatively, the Miedema model explains a certain number of experimental facts, such as the occurrence of a very large vacancy concentration on the Co sublattice of CoGa (the formation enthalpy of vacancies in pure Ga being only ≈ 0.5 eV, correlated to its low melting point, 30°C). But quantitatively, the agreement with the scarce experimental data is not good: for example, in Ni_3Al Miedema estimates $E_F^{\text{Ni}} = 0.4$ eV, whereas the experimental value (see Section 3.1.1) is 1.6 eV. Reasons for these disagreements might be that the Miedema model neglects specific charge transfers near the vacancy as well as the possibility of strong atomic relaxations.

5.3 Theoretical Computation of Point-Defect Formation Properties

Several attempts have been made recently to calculate from first principles the electronic structure of point defects in intermetallic compounds (and from this their

formation and interaction energies), generally the B2 ones (FeAl , NiAl , ...). Local partial densities of states are calculated for each type of defect from the band structure of the stoichiometric compound, either by the tight-binding method (Masuda-Jindo, 1987), or in the framework of the linear muffin-tin orbital method, using Green's function formulas (Koenig *et al.*, 1986; Koch and Koenig, 1986, 1987, 1988; Stefanou *et al.*, 1987) or defect-specified supercells (Gu and Fritsche, 1992). Up to now, these calculations have allowed only qualitative predictions: for example the antisite Fe_{Al} defect in FeAl is correctly predicted to possess a localized magnetic moment (contrary to iron atoms in stoichiometric FeAl) (Gu and Fritsche, 1992). On the other hand, the calculated sign of the interaction energy between Fe vacancies in FeAl is in contradiction with experimental observations (Koch *et al.*, 1987). Difficulties are found when limiting the defect potential to a simple site. These calculations have to be improved to take correctly into account the charge transfer and charge redistribution near the point defect, as well as atomic relaxations (the latter have been shown to decrease considerably the formation energy of antisite defects in Cu_3Au , see Rey-Losada *et al.*, 1993).

Up to now, the main progress in simulating point-defect properties in intermetallic compounds has been made by semiempirical methods. The first detailed papers in this sense concern the A15-structure superconductors (Moseev *et al.*, 1983, 1986; Welch *et al.*, 1984). Although these authors used very simplified pair potentials, qualitative results were obtained, which are discussed in more detail in Section 9.1.

The best results have been obtained by embedded-atom-type methods, applied first with good success to many metallurgical properties of pure metals: surface energy, point-defect properties (see for example Foiles *et al.*, 1986; Chapter 4 by Voter in this volume). In these methods, the energy of each atom is computed from the energy $F_i(\rho_i)$ needed to embed it in the local-electron density ρ_i provided by the other atoms of the alloy (approximated by the superposition of atomic-electron densities: $\rho_i = \sum_{j \neq i} \rho_j(R_{ij})$), plus an additional electrostatic short-range core-core repulsion $\phi_{ij}(R_{ij}) = Z_i(R_{ij})Z_j(R_{ij})/R_{ij}$. The total energy is then written as

$$E_{\text{tot}} = \sum_i F_i(\phi_i) + \frac{1}{2} \sum_{i,j \neq i} \phi_{ij}(R_{ij})$$

The function F is deduced from the equation of state of the pure metals, known from their sublimation energies, atomic volumes, and bulk modulus. Parameters describing the effective charges $Z_i(R_{ij})$ and the numbers of s, p, d electrons of each type of atom involved in the $\rho_j(R_{ij})$ are computed from the fit of

selected properties of the pure metals (elastic constants, vacancy formation energy) and of the ordered alloy.

Two types of calculations are made: (i) energy minimization at 0 K, (ii) Monte Carlo simulations to produce the thermal equilibrium distribution of the atoms at a given temperature. This can be applied to any atomic distribution, disordered or ordered, with or without defects or discontinuities. Calculations are typically performed on box-like volumes of ~ 1000 atoms.

Foiles and Daw (1987) applied the method to Ni_3Al . They could correctly construct the Ni–Al phase diagram, and calculated various point-defect properties: good agreement with experimental data (Wang *et al.*, 1984) was found for the formation and migration energy of the Ni vacancy; the Al vacancy formation energy was found to be lower than that of the complex consisting of a Ni vacancy and a Ni_{Al} antisite defect.

A very detailed work was published recently on CuTi and CuTi_2 body-centered tetragonal structure alloys (Shoemaker *et al.*, 1991), unfortunately systems with no experimental information on point-defect properties. In both compounds, the removal of a Cu or Ti atom results in a vacant Cu site, with an adjacent Ti_{Cu} antisite defect in the latter case. Interstitials have complicated structures of the crowdion type, on a Cu (111) row, which involves seven Cu for six sites (CuTi case) or five Cu for four sites (CuTi_2 case) and the creation of two or three antisite defects in the respective cases of Cu or Ti displacements.

The embedded-atom technique was applied to the study of interstitials in NiAl (Caro and Pedraza, 1991) and Ni_3Al (Caro *et al.*, 1990; Pedraza *et al.*, 1991). In Ni_3Al , the enthalpy differences between dumbbell, octahedral, and crowdion Ni interstitial configurations are small, typically 0.1 to 0.2 eV. The $\langle 100 \rangle$ Ni–Ni dumbbells in pure Ni planes ($E_{\text{F}}^{\text{Ni}} = 3.63$ eV) are favored: Ni–Al and Al–Al dumbbells have larger formation energies (4.45 and 6.22 eV respectively, which is understandable on the basis of size arguments) and hence convert into Ni–Ni dumbbell + Al_{Ni} antisite defects. This behavior is very similar to that studied experimentally in Cu_3Au (see Sections 4 and 7).

Threshold displacement energies were computed for Ni_3Al (Caro *et al.*, 1990); these values should not be considered as quantitative because of their sensitivity to interatomic repulsive potentials, which were determined only from the elastic constants. Nevertheless, it is found (i) that $\langle 100 \rangle$ and $\langle 110 \rangle$ are easy directions for defect production as in f.c.c. pure metals ($E_{\text{d}} \approx 20$ to 30 eV), (ii) that $\langle 110 \rangle$ Ni–Al–Ni–Al collision sequences are efficient, and (iii) that the

displacement process can lead to various metastable interstitial configurations (octahedral, crowdions, . . .).

The spontaneous recombination volumes were calculated for ordered and for disordered Ni_3Al , and were found to be much smaller than in pure metals, which should lead to larger point-defect concentration at saturation (i.e. at high fluence) and have consequences for radiation-induced segregation and amorphization.

6. Thermodynamics of Point Defects

In order to model kinetic properties, it is important to know the nature and concentration of point defects in given experimental conditions. Up to now, there has been no satisfactory theory of the equilibrium number and distribution of point defects in intermetallic compounds as a function of the (long-range or short-range) ordered state. The available models, limited to binary alloys, are all based on the Bragg–Williams mean-field theory of order, assuming (somewhat naively) pair interaction energies, generally limited to first neighbors.

6.1 General Formalism

Let us consider a binary ordered alloy with two sublattices, labeled α and β , preferentially occupied by A and B atoms, respectively. Because of their low equilibrium concentration, interstitials are neglected. We shall adopt the following terminology due to Kim (1984):

N_{α}, N_{β}	number of α or β sites
$N_{\text{A}}, N_{\text{B}}, N_{\text{V}}$	number of A atoms, B atoms, vacancies
N_{Kj}	number of K th species on j th sites ($N_{\text{A}\alpha}, N_{\text{B}\alpha}, N_{\text{V}\alpha}, N_{\text{A}\beta}, N_{\text{B}\beta}, N_{\text{V}\beta}$)
δ	deviation from stoichiometry
η	long-range order parameter

One has

$$\begin{aligned} N_{\text{A}} &= N_{\text{A}\alpha} + N_{\text{A}\beta} & N_{\text{B}} &= N_{\text{B}\alpha} + N_{\text{B}\beta} \\ N_{\alpha} &= N_{\text{A}\alpha} + N_{\text{B}\alpha} + N_{\text{V}\alpha} & N_{\beta} &= N_{\text{A}\beta} + N_{\text{B}\beta} + N_{\text{V}\beta} \end{aligned}$$

In the Bragg–Williams approximation, the configurational entropy is given by

$$S = k_{\text{B}} \ln \left(\frac{N_{\alpha}!}{N_{\text{A}\alpha}! N_{\text{B}\alpha}! N_{\text{V}\alpha}!} \frac{N_{\beta}!}{N_{\text{A}\beta}! N_{\text{B}\beta}! N_{\text{V}\beta}!} \right) \quad (2)$$

We shall restrict discussion to the case of B2-structure alloys, where α sites are at the corners and β sites at the centers of the cubic lattice cells, each α (resp. β) site being coordinated to eight β (resp. α) sites. One then has $N_\alpha = N_\beta = 1/2$, and

$$\eta = \frac{(N_{A\alpha} - N_{B\alpha}) + (N_{B\beta} - N_{A\beta})}{N_A + N_B}$$

$$\delta = \frac{N_A - N_B}{N_A + N_B} = \frac{2(N_{A\beta} - N_{B\alpha}) + (N_{V\beta} - N_{V\alpha})}{N_A + N_B}$$

Introducing the first-neighbor energies ϵ_{AB} , ϵ_{AA} , and ϵ_{BB} , and the ordering energy $\epsilon = \epsilon_{AB} - (\epsilon_{AA} + \epsilon_{BB})/2$, the internal energy is then equal to

$$E = -8[N_{A\alpha}N_{A\beta}\epsilon_{AA} + (N_{A\alpha}N_{B\beta} + N_{B\alpha}N_{A\beta})\epsilon_{AB} + N_{B\alpha}N_{B\beta}\epsilon_{BB}] \quad (3)$$

if one assumes that bonds between a vacancy and its neighbors are broken ($\epsilon_{VA} = \epsilon_{VB} = 0$). Some authors (Neumann *et al.*, 1976; Edelin, 1979) have refined this model, taking into account 'ghost' interaction energies between vacancies and A and B atoms: ϵ_{VA} , ϵ_{VB} .

6.2 Calculation of the Vacancy Concentration in Ordered Alloys

A first approach to this problem is given by the vacancy-energy model of Cheng *et al.* (1967). Although, as discussed below, the model is incorrect in its original form, at least if the vacancy formation energies on α and β sites are very different, it gives interesting information.

The formation free energy g for a vacancy on a given site in an alloy is mainly dependent on its local atomic environment. Let us assume that g depends only on the nature of atoms directly coordinated with the vacancy. Distributing at random $N_{V\alpha}^i$ and $N_{V\beta}^i$ vacancies on α or β lattice sites coordinated with i B atoms and $(z-i)$ A atoms, and giving to each of them a free energy $g_{i\alpha}$ (resp. $g_{i\beta}$), one finds by minimizing the total free energy relative to the vacancy concentrations $N_{V\alpha}^i$ and $N_{V\beta}^i$:*

$$N_{V\beta}^i = \frac{z!}{(z-i)!i!} (1 + \eta - 2\delta)^{z-i} (1 - \eta + 2\delta)^i \exp\left(-\frac{g_{i\beta}}{kT}\right)$$

$$N_{V\alpha}^i = \frac{z!}{(z-i)!i!} (1 - \eta - 2\delta)^{z-i} (1 + \eta + 2\delta)^i \exp\left(-\frac{g_{i\alpha}}{kT}\right)$$

*For disordered dilute alloys $A_{1-c}B_c$ ($\eta = 0$, $c \ll 1$), this reduces to the model developed by Lomer (1958) for vacancy-impurity interactions.

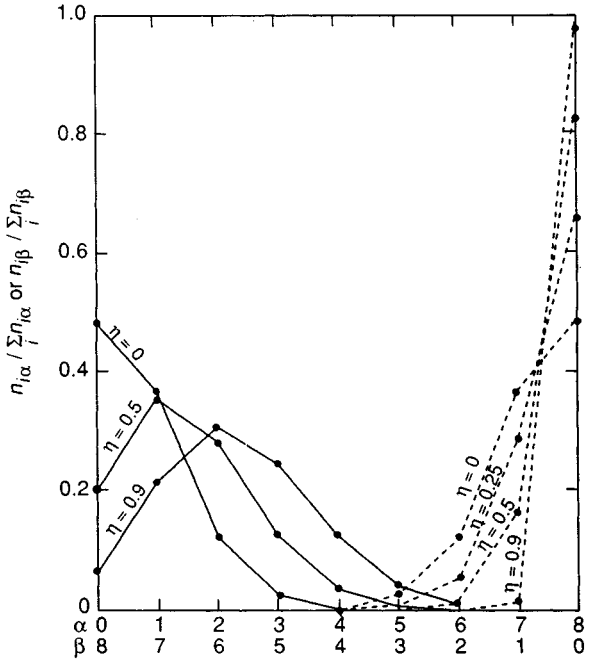


Figure 9. Distribution of the various vacancy concentrations on α (Cu-rich, —) and β (Zn-rich, ----) sites of the stoichiometric CuZn alloy calculated from the modified vacancy-energy model. Each 'curve' corresponds to a value of the LRO parameter η (and of temperature T). The abscissa shows the number of Cu atoms coordinated to the vacancy. Pair interaction energies are given in the text (From Cheng *et al.*, 1967)

As up to now the $2(z+1) g_{i\alpha}$ and $g_{i\beta}$ coefficients cannot be experimentally determined or theoretically calculated, for numerical calculations a simple bond-breaking model has been applied (modified vacancy-energy model of Cheng *et al.* (1967)), where the bond-energy change when displacing an A or B atom from the lattice to the surface is $-[(z-i)\epsilon_{AA} + i\epsilon_{AB}]/2$ or $-[(z-i)\epsilon_{AB} + i\epsilon_{BB}]/2$ respectively.

Applying this model to CuZn, with $\epsilon_{AA} = \epsilon_{ZnZn} = 0.34$ eV, $\epsilon_{BB} = \epsilon_{CuCu} = 0.88$ eV, and $\epsilon_{AB} = 0.62$ eV, it is found that, above the critical ordering temperature T_c , the concentrations of vacancies on α and β sites are indistinguishable, but that, below T_c , $N_{V\alpha}$ and $N_{V\beta}$ become different, with fewer vacancies on α sites. The average vacancy formation energy increases with the LRO parameter η . The distribution of the various vacancy concentrations is given in Figure 9. It is seen that the most populous types of vacancies change with η or temperature. For example, for $\eta = 0.5$ ($T/T_c \approx 0.85$), vacancies on α sites (Zn) are mostly surrounded by one

Cu and seven Zn, and those on β sites (Cu) by eight Zn. The curves of Figure 9 are asymmetric (between α and β) because $\epsilon_{\text{CuCu}} > \epsilon_{\text{ZnZn}}$.

Let us recall that this vacancy-energy model is incorrect, because it does not take into account local rearrangements of atoms around a vacancy after its creation. Indeed, as noted by Kim (1984), as the ratio of the number of surface sites to the total number of atoms in a typical crystal is of the order of 10^{-8} , many pure-B surface layers will be formed when creating $\approx 10^{-3}$ vacancies if $E_F^{\text{V}\beta} \ll E_F^{\text{V}\alpha}$. Another process must occur simultaneously to maintain the nominal superficial composition. The triple-defect model, described in Section 3.2 and depicted in Figure 1, satisfies this requirement. This is taken into account in the model developed by Kim (1984, 1986, 1987). This model is altogether general and simple (Bragg-Williams approximation, pair interactions, bond-breaking model for describing vacancy creation). Starting from equations (2) and (3) of Section 6.1 for configurational entropy S and bond energy E , he shows that the free energy $F = E - TS$ depends on only three independent variables: $N_{\text{A}\beta}$, $N_{\text{B}\alpha}$, and $n = (N_{\text{V}\alpha} + N_{\text{V}\beta})/2$. Minimizing F with respect to these three variables gives a set of equations that have to be solved numerically to obtain the defect concentrations: $N_{\text{V}\alpha}$, $N_{\text{V}\beta}$, $N_{\text{A}\beta}$, $N_{\text{B}\alpha}$.

Kim (1984, 1986, 1987) applied his model to NiGa, FeAl, CoGa, Cu₃Au, and CuAu. Reasonable input parameters ϵ_{AA} , ϵ_{BB} , and ϵ allowed the calculations to reproduce very satisfactorily the total vacancy concentration measured in these alloys for several compositions and temperatures. In the case of the B2 compounds, the vacancies were shown to be entirely on the transition-metal sublattice, and it was suggested that they are thermal vacancies with low formation energies rather than structural vacancies (see discussion in Section 3.2).

In this model, the formation energy of a pair of antisites (B in α and A in β) in the stoichiometric compound is $16\epsilon_{\text{AB}} - 8\epsilon_{\text{AA}} - 8\epsilon_{\text{BB}}$, and that of a triple defect (two vacancies in α , one antisite in β) is $16\epsilon_{\text{AB}} - 8\epsilon_{\text{AA}}$. Therefore, the criterion for preferential disorder by vacancies (triple defects) is $\epsilon_{\text{BB}} < 0$ (repulsive B-B energies). The same criterion is found for accommodating B-rich non-stoichiometry by vacancies on α rather than by B on α antisite defects. Of course, the crudeness of these models requires that they should not be taken too quantitatively.

In the case of small deviation from stoichiometry ($\delta \ll 1$), it can be shown (Edelin, 1979) that the defect concentrations obey mass-action laws: $N_{\text{A}\beta}N_{\text{B}\alpha} = K_1$, $N_{\text{V}\alpha}N_{\text{V}\beta} = K_2$, $N_{\text{B}\alpha}(N_{\text{V}\beta})^2 = K_3$, $N_{\text{A}\beta}(N_{\text{V}\alpha})^2 = K_4$, where the

K 's are composition-independent. In particular, it is found that K_1 varies as $\exp(16\epsilon/kT)$.

6.3 The Triple-Defect Case

As strong experimental arguments exist that in B2 alloys non-stoichiometry is accommodated by vacancies (triple defects) on the B-rich side, and antisite defects on the A-rich side (see Section 3.2), several simplified models have been developed to describe this behavior (Neumann, 1977, 1980; Edelin, 1979; Bakker and Van Ommen, 1978; Van Ommen *et al.*, 1981). In these models, it is assumed that $N_{\text{B}\alpha} = N_{\text{V}\beta} = 0$. The following relations have been found at low defect concentration:

- The α vacancy and β antisite-defect concentrations obey the mass-action law $N_{\text{A}\beta}(N_{\text{V}\alpha})^2 = K_4$, and K_4 is proportional to $\exp(-3Q/kT)$, where $3Q = 2E_F^{\text{V}\alpha} + E_F^{\text{A}\beta}$ is a linear combination of the α vacancy and β antisite-defect formation energies ($E_F^{\text{V}\alpha} = 4\epsilon_{\text{AB}}$, $E_F^{\text{A}\beta} = 8\epsilon_{\text{AB}} - 8\epsilon_{\text{AA}}$ in the bond-breaking model).
- At the stoichiometric composition ($\delta = 0$), $N_{\text{V}\alpha} = 2N_{\text{A}\beta}$, and the vacancy concentration is thermally activated: $N_{\text{V}\alpha}$ varies as $\exp(-Q/kT)$.
- The difference between the relative change of lattice parameter and the linear expansion of the crystal, due to the creation of vacancies (measured in Simmons and Balluffi-type experiments) is

$$3(\Delta a/a - \Delta l/l) = (N_{\text{V}\alpha} + N_{\text{V}\beta})/2N$$

which is proportional to $\exp(-Q/KT)$. Therefore positron annihilation or Simmons and Balluffi-type experiments do not give the vacancy formation energy, but a linear combination of the latter with the antisite-defect formation energy.

- For non-stoichiometric alloys, $\delta = (N_{\text{A}\beta} - N_{\text{V}\alpha}/2)/N$, and the concentration of α vacancies $x_{\text{V}\alpha} = N_{\text{V}\alpha}/2N$ obeys the equation (deduced from the above mass-action law):

$$(x_{\text{V}\alpha})^{3/2} + \delta(x_{\text{V}\alpha})^2 - \exp(-3Q/kT) = 0$$

As long as $\delta \ll 1$, the defect concentrations depend only on the activation energy Q .

This simple model was fitted to the vacancy and antisite-defect concentration data of CoGa and NiGa; the agreement is fairly good with $Q = 0.265$ eV for CoGa and 0.29 eV for NiGa (Edelin, 1979). This low Q value explains the high defect concentrations. The fit of density data gives the formation volume of the defects in CoGa: 0.69 atomic volumes for the Co vacancy, and 0.89 atomic volumes for Co replacing Ga.

The model was also used to calculate thermodynamic activity and partial enthalpy. Good agreement is found with experimental data (Neumann, 1977; Van Ommen *et al.*, 1981; Chang and Neumann, 1982).

7. Recovery of Point Defects After Irradiation or Quench

In pure metals, the recovery of point defects created or retained at low temperature follows a general scheme, evidenced by the study of isochronous annealing of irradiated materials. This is because the mobility of interstitials is much higher than that of vacancies. Typically, in a metal such as copper, interstitials become mobile around 50–100 K ($E_M^i \approx 0.1$ eV), and at 100 K have either recombined with vacancies, or clustered in small dislocation loops, or bound to impurities. Vacancies become mobile above ≈ 250 K and form clusters that dissociate at high temperature (≈ 500 K).

Information on intermetallic compounds is fragmentary. Some behave very similarly to metals, and in others it is clear that interstitials are much less mobile.

The most-studied compound is certainly LRO Cu_3Au . Its recovery stages, measured by electrical resistivity, are practically identical after irradiation by 0.66 and 2.36 MeV electrons (see Figure 10), strongly suggesting a single type of defect, the copper self-interstitial (Alamo *et al.*, 1986). The recovery curves are very similar to that of Cu pure metal, suggesting that the 40 and 70 K stages are due respectively to close Frenkel-pair recombination and free interstitial migration. During stage II (100–250 K), where resistivity decreases only slightly, the analysis of the Huang scattering shows that the interstitial clusters remain very small (single and di-interstitials) (Urban and Ehrhart, 1987). At 250 K:

- The Huang signal disappears, indicating that interstitial clusters have disappeared.
- The positron lifetime increases suddenly, indicating vacancy clustering (Doyama *et al.*, 1985a).
- The resistivity shows a large annealing stage and becomes lower than the unirradiated value (Alamo *et al.*, 1986).

These three observations are consistent with vacancy migration starting from 250 K, vacancies either annihilating on interstitial loops or forming vacancy clusters, and increasing the long-range order of the alloy during their migration. The positron lifetime is maximum at 390 K and is consistent with clusters containing more than six vacancies; above 410 K, these

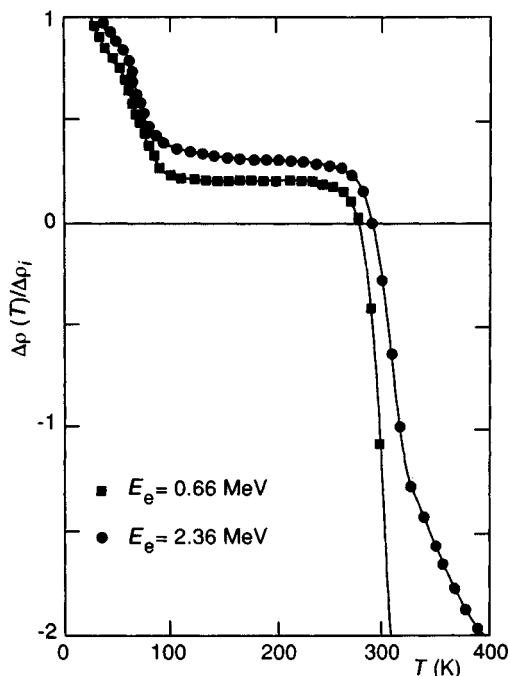


Figure 10. Isochronal recovery of electrical resistivity versus annealing temperature after 0.66 or 2.36 MeV electron irradiation at 21 K for ordered Cu_3Au (From Alamo *et al.*, 1986)

clusters evaporate and single vacancies order the sample during their long-range migration toward sinks (Doyama *et al.*, 1985a).

Electron-irradiated *disordered* Cu_3Au shows a similar behavior concerning vacancy stages; but the low-temperature recovery is very different from that of LRO Cu_3Au . Instead of definite stages, one observes a continuous recovery from 50 to 250 K; this is consistent with a spectrum of energy barriers for the movement of the interstitial (Alamo *et al.*, 1986).

Irradiated CuAu and CuAu_3 have not been studied in detail, but do not behave as does Cu_3Au : CuAu shows a more complex stage behavior (Alamo *et al.*, 1986), and CuAu_3 shows no vacancy clustering (Doyama *et al.*, 1985a).

Other alloys such as Ni_3Al (Dimitrov *et al.*, 1992) and FeCo (Rivière *et al.*, 1983b) behave similarly to Cu_3Au . In the case of $\text{Fe}_{60}\text{Al}_{40}$, the interstitial free-migration stage seems to be around 500 K, which is consistent with an interstitial migration energy of the order of 1 eV, much more than in pure metals (Rivière *et al.*, 1983a).

In FeCo and $\text{Fe}_{60}\text{Al}_{40}$, as in Cu_3Au and CuAu , the vacancy migration leads always to an increase of the

LRO, observed by electrical resistivity (Rivière *et al.*, 1983a, b; Alamo *et al.*, 1986).

Recovery of vacancies retained by quenching has been studied by positron annihilation in Ni-rich NiAl (Wang *et al.*, 1983) and in disordered Cu₃Au (Doyama *et al.*, 1985b).

Vacancy clusters formed during annealing of quenched samples were observed by transmission electron microscopy in Cu₃Au (Condat and Fayard, 1972) and in a number of B2-structure alloys: FeAl (Wechsler, 1957; Junqua *et al.*, 1973; Weber *et al.*, 1977), NiAl (Ball and Smallman, 1968; Eibner *et al.*, 1975; Marshall and Brittain, 1975), CoGa (Schwab and Gerold, 1980), CuZn (Cupschalk and Brown, 1967), and AuCd (Wechsler, 1957); and by small-angle X-ray and neutron scattering in NiAl-based alloys (Epperson *et al.*, 1978; Epperson and Loomis, 1981). Various types of defects are observed: voids, (100) or (111) dislocation loops, and helices. Their occurrence seems to depend on several factors: quenching temperature, surface oxidation, and presence of inclusions (which help nucleation of vacancy loops). In some cases, (111) loops are dissociated into two concentric partials separated by a stacking fault (Junqua *et al.*, 1973; Weber *et al.*, 1977; Cupschalk and Brown, 1967).

The kinetics of vacancy elimination, measured by the time dependence of defect cluster density and size, shows either a simple (single activation energy) or a complex behavior, owing to its heterogeneous character or to competing mechanisms. Its analytical form depends on the existence of defect cluster nuclei in the quenched samples.

8. Migration Properties of Point Defects

8.1 Vacancies

Owing to the values of formation and migration energies, it is generally assumed that, in most cases, atomic transport in intermetallic compounds occurs via vacancy migration. Here, we shall only discuss transport at the atomic level, atomic diffusion being treated in detail in Chapter 32 by Larikov in this volume.

A correct description of vacancy migration in an alloy must take into account its true defect structure, including short- and long-range order, and the different types of jumps with different jump lengths and different exchange rates of the vacancy with its neighbors.

For random disordered binary alloys, the atomic self-diffusion coefficients have been calculated in a mean-field approximation by Manning (1971):

$$D_{A(B)}^* = \lambda s^2 C_V f_{A(B)} W_{A(B)}$$

where s is the first-neighbor jump distance, $f_{A(B)}$ the correlation coefficients, and $W_{A(B)}$ the exchange rates of the vacancy with an A or B neighbor (assumed independent of the local surroundings). The movement of a vacancy is no longer a random walk (as in pure metals), but its successive jumps are correlated. The correlation coefficients have been calculated by various methods, including numerical simulation, which have been extended to short-range ordered alloys (Stolwijk, 1981). Of course, the mean-field approximation is particularly insufficient to describe vacancy migration when $C_A \ll 1$ and $W_A/W_B \gg 1$, i.e. when an A atom and a vacancy trap each other and exchange their positions frequently without long-range migration.

The mean-field expression for self-diffusion coefficients has been extended to several LRO intermetallic structures by Bakker and Westerveld (1988). In this case, one has to take into account jumps within each sublattice as well as between different sublattices. For example, for the f.c.c. L1₂ structure A₃B, assuming near-neighbor jumps, one has

$$D_A^* = \frac{C_A^\alpha f_A}{C_A} \frac{f_A}{2} (p_{AV}^{\alpha\alpha} W_A^{\alpha\alpha} + p_{AV}^{\alpha\beta} W_A^{\alpha\beta}) a^2$$

where $W_A^{\alpha\beta}$ is the exchange rate between a vacancy on a β site and an A atom on an α site and $p_{AV}^{\alpha\beta}$ is the probability of finding a vacancy on a β site near neighbor of an A atom on an α site ($W_A^{\alpha\alpha}$ and $p_{AV}^{\alpha\alpha}$ are defined similarly).

Very different behaviors are observed, depending on the crystal structure and on the type of atom considered:

(i) *L1₂ structure.* In the case of A-type vacancies in A₃B compounds with the L1₂ structure (e.g. Cu vacancy in Cu₃Au, Ni vacancy in Ni₃Al), the vacancy mobility is very similar to that in a pure metal. This is because (i) vacancies of the considered element have a small formation energy and predominate, and (ii) three-dimensional transport of A atoms is possible via first-neighbor jumps of vacancies on the α sublattice as in f.c.c. pure metals.

In Ni₃Al, the sum of Ni vacancy formation and migration energies, determined experimentally (1.6 ± 0.2 and 1.35 ± 0.15 eV, respectively; Wang *et al.*, 1984; Dimitrov *et al.*, 1992), is 15% lower than the Ni self-diffusion activation energy ($E_D \approx 3.5$ eV; Hoshino *et al.*, 1988). As remarked by Bakker (1987), the similarity of these values with those of pure nickel is somewhat fortuitous, as the formation of a Ni vacancy in Ni₃Al

involves the breaking of eight Ni–Ni bonds and four Ni–Al bonds, and its migration to near-neighbor Ni sites involves a saddle point with two Ni and two Al first neighbors. Nevertheless, numerical simulations confirm that a Ni vacancy jumps more easily into a near-neighbor Ni site (1.02 eV) than into a near-neighbor Al site (1.28 eV) (Foiles and Daw, 1987).

(ii) *B2 structure*. In the B2 structure, α sites are entirely surrounded by (eight) β near neighbors and vice versa. In highly ordered alloys, the correlation effects for diffusion will be high ($f_A, f_B \ll 1$). If an A atom jumps on a β (vacant) site, the reverse jump that re-establishes the chemical order will be very easy. One will have many forward and backward jumps of the vacancy, inefficient for mass transport. Thermal disorder (antisite defects) is then important to help atomic diffusion in B2-ordered alloys, as shown by computer simulation of the correlation factor f (Bakker *et al.*, 1976).

Experimentally, self-diffusion has been measured in a few ordered B2 alloys. Let us summarize the main results of these studies:

- In a given alloy, the self-diffusion coefficients of the two atomic species generally only differ by less than one order of magnitude, which suggests that their migrations are coupled; the difference is somewhat larger in alloys containing structural vacancies.
- The correlation factor f deduced from isotope-effect measurements is shown to be small (AuZn; see Hilgedieck and Herzig, 1982) and to decrease with T below the order–disorder critical temperature (FeCo; see Fishman *et al.*, 1970).
- In alloys presenting an order–disorder transition (case of CuZn; see Kuper *et al.*, 1956), the Arrhenius plot of $\ln D$ versus $1/T$ shows a change of slope at the transition and a curvature in the LRO state. This has been tentatively explained by (i) an increase of the vacancy migration energy with the LRO parameter S (Girifalco, 1964), (ii) a decrease of the correlation factor in the LRO state (Bakker, 1984), or (iii) different competing mechanisms (Stolwijk *et al.*, 1980).
- The diffusion coefficients are often minimum and the activation energy maximum at (or near to) the stoichiometric composition. This can be understood (i) by the fact that E_F and E_M increase with S , which is maximum at stoichiometry, and (ii) in some cases by the existence of structural vacancies in non-stoichiometric alloys, which favour diffusion: the composition dependence is then non-symmetrical.

- The activation energy for self-diffusion can be different from the sum of vacancy formation and migration energies (case of AuCd; see Gupta *et al.*, 1967). This can be due to experimental uncertainties, but also to the fact that these energies are averages and apparent energies deduced from a fit within a narrow temperature range.
- The transport of matter can occur preferentially on the sublattice that contains fewer vacancies, because the corresponding migration energy is very low (case of AgMg where $D_{Ag} < D_{Mg}$; see Hagel and Westbrook, 1965).

Various atomic mechanisms have been proposed for diffusion of vacancies in B2-ordered alloys (see Figure 11):

- (a) Vacancy nearest-neighbor (NN) jump between an α and a β site, which does not preserve the local order.
- (b) Vacancy next-nearest-neighbor (NNN) jump between sites of the same sublattice, which preserves the local order.
- (c,d) Six-jump cycle proposed by Elcock and McCombie (1958) and Huntington *et al.* (1961), which allows NN jumps without altering the local order. Numerical Monte Carlo simulations have shown that this mechanism is not very efficient because in fact the various potential barriers oblige the vacancy to perform a large number of backward jumps (Arnhold, 1981).
- (e,f) Triple-defect jump proposed for CoGa by Van Ommen *et al.* (1981). Here the intermediate configuration consists of a NN divacancy ($V_{Co} + V_{Ga}$); as Co_{Ga} antisites are allowed, but Ga_{Co} are forbidden, it is assumed that NN jumps are allowed for Co, but that Ga diffuses via NNN jumps into the divacancy.
- (g) Two correlated NN jumps through a divacancy (pair of vacancies of both sublattices); model proposed for PdIn by Hahn *et al.* (1983).

(iii) *L1₀, B11, and C11₆ structures*. In the tetragonal structures of L1₀ (tP4) CuAu, B11 (tP4) CuTi, and C11_b (tI6) CuTi₂, which are made by stacking pure A and pure B atomic planes along the (001) direction, diffusion of an element in its own sublattice via NN jumps can only occur in two dimensions. Three-dimensional migration involves creation of antisite defects and disorder. Recent computer simulation studies (Shoemaker *et al.*, 1991) have confirmed this for CuTi, where the migration energy of the Cu vacancy (via NN jumps) is calculated to be 0.19 eV within Cu

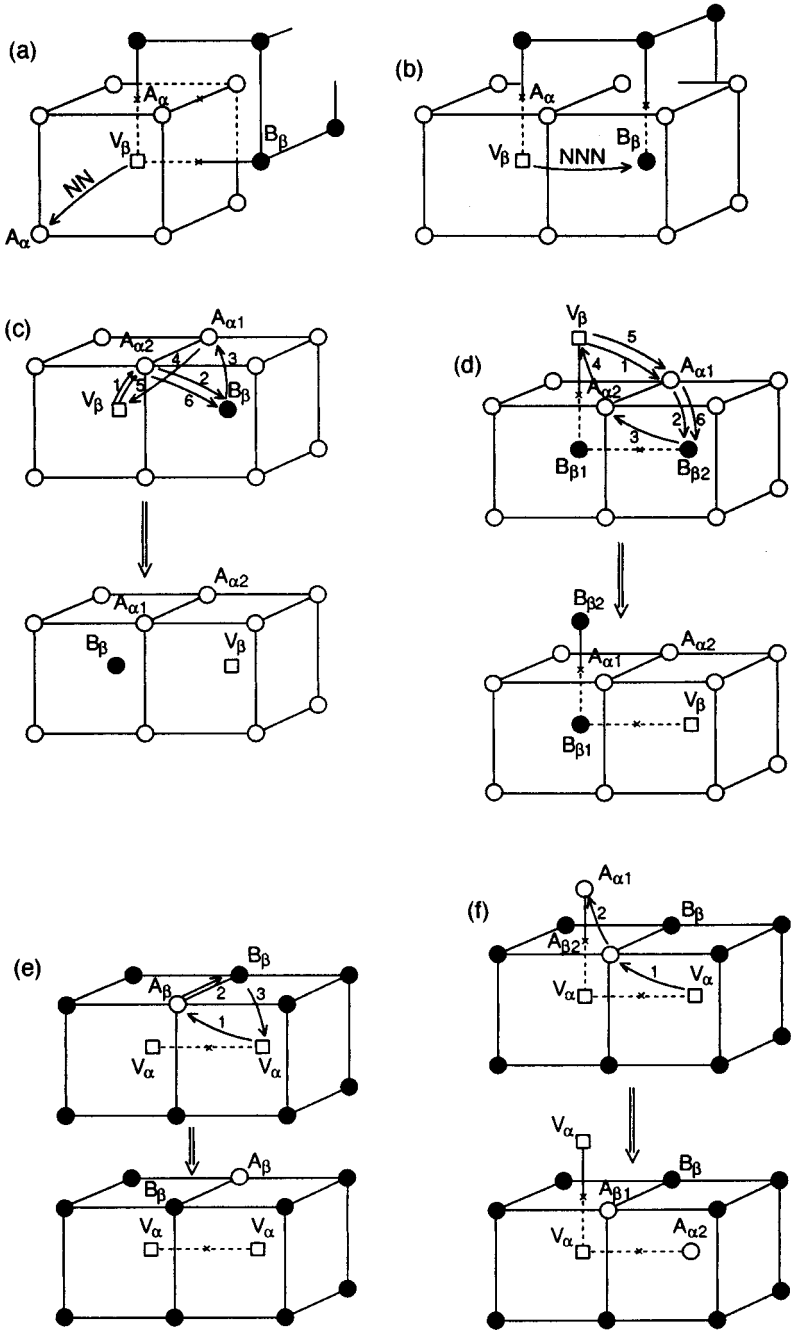


Figure 11. Jump mechanisms for ordered B2 alloys: (a) nearest-neighbor jump; (b) next-nearest-neighbor jump; (c,d) six-jump cycles; (e,f) possible jumps for a triple defect. (●) B atoms; (○) A atoms; (□) vacancies (From Bocquet *et al.*, 1983)

- Cu
● Ti
□ Vacancy

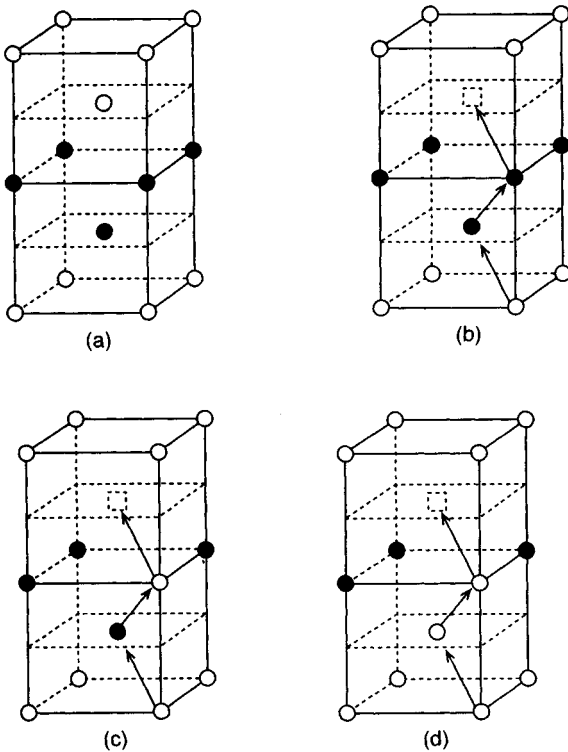


Figure 12. Vacancies in CuTi: (a) the perfect crystal. (b) migration path of Cu vacancy through the Ti (001) planes; (c,d) the same, assisted by one or two Cu_{Ti} antisite defects (From Shoemaker *et al.*, 1991)

sheets and 1.32 eV across Ti sheets. The latter value is lowered to 0.75 or 0.66 eV if one or two Cu antisite defects are present on the Ti sublattice (see Figure 12).

As the Ti vacancy is calculated to be unstable relative to the complex (Cu vacancy)+(Cu_{Ti} antisite), Ti migration requires first creating a vacancy on the Ti sublattice.

In a few cases, vacancy migration energies have been determined by isothermal variations of a physical property measured during the thermal recovery of a quenched or electron-irradiated sample:

- Differential scanning calorimetry experiments on NiAl (480 °C stage, $E_M^V \approx 1.75$ eV; Doyama *et al.*, 1987) and NiSb (285 °C stage, $E_M^V \approx 1.15$ eV; Jennane *et al.*, 1992).

- Electrical resistivity measurements in FeAl (610 °C stage, $E_M^V = 1.20 + 0.61 S^2$; Rivière and Grilhé, 1974) and Cu₃Au (250 °C stage, $E_M^V = 0.71 + 0.36 S^2$; Benci and Gasparrini, 1966). The increase of E_M^V with long-range order parameter S is in qualitative agreement with the theoretical predictions of Girifalco (1964).
- Resistivity and positron trapping rate measurements in Ni₃Al (120 °C stage, $E_M^V = 1.35 \pm 0.15$ eV; Sitaud *et al.*, 1991).

Vacancy mobility was also studied by isothermal after-effect measurements following small temperature increments, as described in Section 2.2:

- Magnetic after-effect in CoGa (Van Ommen *et al.*, 1977).
- Length after-effect in CoGa (Van Ommen and de Miranda, 1981; see Figure 6). In the latter experiment, measurements were performed over a relatively large temperature interval (600–800 °C) and showed the existence of at least two processes with different activation energies ($E_M^V \approx 1.5$ –2 and 3.5–4 eV) attributed respectively to NN cobalt→vacancy and NNN gallium→vacancy jumps. Self-diffusion activation energies (Stolwijk *et al.*, 1980), vacancy migration energies (Van Ommen and de Miranda, 1981), and formation energies (Van Ommen *et al.*, 1981) measured in CoGa form a consistent set of data.

8.2 Interstitials

The migration energy of interstitials has been measured by various techniques in a few irradiated ordered or disordered concentrated alloys:

- In disordered f.c.c. AgZn_x by Zener relaxation (Beretz *et al.*, 1981): $E_M^I \approx 0.8$ eV.
- In disordered f.c.c. Fe–Cr–Ni austenites with various Ni and Cr contents by electrical resistivity (Dimitrov and Dimitrov, 1984; Dimitrov *et al.*, 1987) and TEM measurement of the depleted zone at the edge of a thin foil (Housseau and Pellissier, 1983): $E_M^I \approx 0.5$ to 0.9 eV.
- In ordered b.c.c. Fe–40% Al by electrical resistivity (Rivière *et al.*, 1983a) and TEM study of the growth of dislocation loops (Kinoshita *et al.*, 1982): $E_M^I \approx 1$ to 1.3 eV.
- In ordered f.c.c. Cu₃Au by electrical resistivity (Gilbert *et al.*, 1973): $E_M^I \approx 0.2$ eV.
- In stoichiometric Ni₃Al, two activation energy values were determined in the resistivity recovery stage, assigned to interstitial-defect migration: 0.16 ± 0.02 eV and 0.28 ± 0.02 eV (Sitaud *et al.*, 1991).

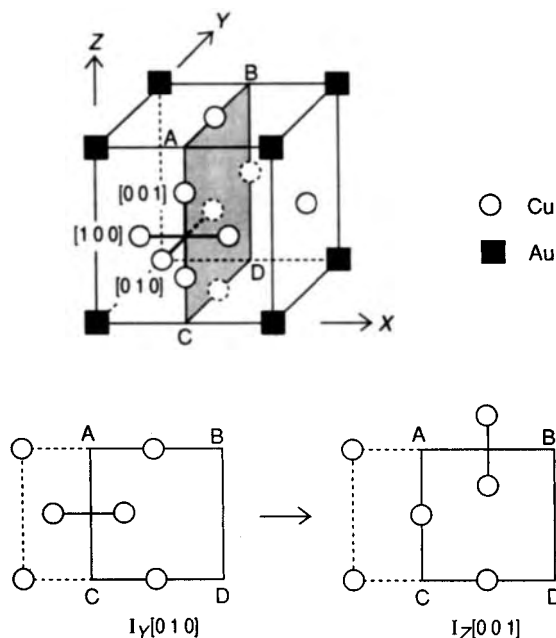


Figure 13. Configuration and migration of the Cu-Cu split interstitial proposed for ordered Cu_3Au . The labelling $I_X[010]$ means the dumbbell is oriented along the $\langle 010 \rangle$ direction, and centered on the cube face perpendicular to the X axis (From Alamo *et al.*, 1986)

With the exception of LRO Cu_3Au and Ni_3Al , this activation energy is much larger than in pure metals ($E_M^I \approx 0.1$ to 0.2 eV) and of the order of the vacancy migration energy, indicating a strong slowing of the interstitial.

Models have been developed for the migration of $\langle 100 \rangle$ dumbbells in disordered f.c.c. solid solutions A_{1-x}B_x , in an effective-field approximation (Bocquet, 1986). If the B-B interstitial configuration is of lowest energy, as long as the B clusters do not extend to the whole lattice (i.e. typically for $x < 0.3$), B interstitials are trapped in the clusters and their long-range migration requires detrapping. Beyond a percolation threshold $x_0 \approx 0.3$, the interstitial mobility greatly increases toward typical pure-metal values.

In the case of LRO Cu_3Au , we have seen (Section 4) that the interstitial probably has a unique structure, the $\langle 100 \rangle$ Cu-Cu dumbbell. We can see in Figure 13 that the interstitial centered in the middle of the cube face Y , with $[010]$ orientation, can migrate toward a configuration of the same energy centered on one of its eight Cu first neighbors, by the same mechanism as in pure f.c.c. metals, i.e. by a rotation of 90° (for example, $I_Y[010] \rightarrow I_Z[001]$), explaining therefore

the existence of a well-defined recovery stage at 70 K (Alamo *et al.*, 1986).

In B2-ordered alloys, such as Fe-40% Al, where fragmentary Huang scattering data suggest a similar interstitial as in b.c.c. Fe or Mo ($\langle 110 \rangle$ dumbbell), the migration of this interstitial requires changes of configuration such as $\text{A-A} \rightleftharpoons \text{A-B}$, or $\text{A-B} \rightleftharpoons \text{B-B}$, and therefore a high activation energy consistent with experimental data.

In other ordered alloys, complex structures (i.e. crowdion type) have been proposed for the interstitial, suggesting a high activation energy for three-dimensional migration.

9. Specific Systems

Up to now, we have discussed mostly 'model' intermetallic compounds with simple crystal structures (generally cubic: L1_2 , B2, . . .) and containing two metal species. We shall now present briefly some properties of point defects in more exotic systems, of considerable interest: the A15 superconductors, transition-metal carbides and nitrides, and III-V semiconductors (e.g. GaAs).

9.1 A15 Compounds

The superconducting properties of A15 compounds are extremely sensitive to point defects. For example, in V_3Ga , the superconducting critical temperature T_c is maximum at the stoichiometric composition and decreases after a quench (Bakker, 1987). This can be understood in the frame of the model of Labbé and Friedel (1966), where the superconducting properties are due to narrow bands formed with the 3d orbitals of the transition-metal chains. Point defects in the chains decrease the electronic relaxation time and, according to the uncertainty principle, broaden the narrow bands, causing a decrease in the density of states at the Fermi level $N(E_F)$, of the electron-phonon coupling, and of the critical temperature T_c . This was clearly demonstrated by low-temperature electron irradiation experiments on Nb_3Ge (Rullier-Albenque and Quéré, 1981). When increasing the incident electron energy E_e , one encounters three domains: for $E_e < 0.5$ MeV, no damage; for $0.5 < E_e < 0.8$ MeV, only the lighter Ge atoms are displaced, the electrical resistivity ρ increases but the critical temperature remains unchanged; for $E_e > 0.8$ MeV, when the transition metal Nb is also displaced, both ρ and T_c change during irradiation. This is direct proof that point defects in the Nb chain

are responsible for the decrease of T_c . A detailed analysis shows that both vacancies and antisite defects contribute to this, antisite defects being mostly created by short, focused collision sequences along $\langle 120 \rangle$ -type crystal directions ($\cdots \text{Nb-Ge-Nb} \cdots \text{Nb-Ge-Nb} \cdots$). Similar effects were observed on V_3Si , where the T_c decrease is $\sim 2 \text{ K/at.}\%$ V displaced (Rullier-Albenque and Sénateur, 1986).

In fact, irradiation induces large lattice distortions, as shown by the increase of the static Debye-Waller factor. This certainly plays a role in the decrease of $N(E_F)$ and T_c .

The atomic configuration of point defects and the surrounding lattice distortions have been computed numerically in Nb_3Sn and Mo_3Si (Moseev *et al.*, 1983, 1986; Welch *et al.*, 1984) using pair interactions. The structure calculated by Welch *et al.* (1984) for the Nb sublattice vacancy in Nb_3Sn is interesting: the Nb vacant site is suggested to split into two 'partial vacancies' separated by a segment of Nb chain translated by $a/4$ (half the Nb-Nb distance) and forming a sort of stacking fault. The Sn vacancy is found to be metastable and to convert into a split Nb vacancy plus an antisite Nb_{Sn} .

Vacancy migration is complex in an A15 compound such as Nb_3Sn , as several types of jumps must be taken into account: within the Nb chain (jump distance $a/2$), between Nb chains (jump distance $a\sqrt{6}/4$), between Sn first-neighbor sites (distant by $a\sqrt{3}/2$), and from Nb to Sn site or vice versa (jump distance $a\sqrt{3}/4$). In the split vacancy model of Welch *et al.* (1984), the Nb vacancy migration is found to be nearly one-dimensional, with a much lower migration energy along the Nb chain ($< 1 \text{ eV}$) than between chains ($\sim 4 \text{ eV}$).

9.2 Transition-Metal Carbides and Nitrides

Many refractory transition-metal carbides and nitrides can be described as a close-packed metal lattice (f.c.c. of B1 (cF8) NaCl type or h.c.p.), with the carbon or nitrogen atoms in the center of the octahedral interstices. A large fraction of these octahedral sites (up to 50% in the cases of $\text{TiC}_{0.5}$ and $\text{TiN}_{0.5}$) are unoccupied and may be considered as 'structural' vacancies. Chemical bonding and transport properties depend strongly on the structural-vacancy content.

Vacancies and metalloid atoms form a pseudo-solid solution with order-disorder phenomena analogous to those encountered in metallic solid solutions A_{1-x}B_x , i.e. long-range order for special compositions (V_8C_7 , Ti_2C , and V_6C_5 cubic carbides; V_2C , Nb_2C , and Ta_2C hexagonal hemicarbides) below a critical temperature,

with superlattice reflections, antiphase domains, etc. (de Novion and Landesman, 1987; de Novion *et al.*, 1987, 1990; Epicier, 1990).

In the disordered state, very short-range local order remains, limited to a few neighbor shells, which gives rise to diffuse streaks in the electron and neutron diffraction patterns (de Novion *et al.*, 1990). For example, in $\text{NbC}_{0.83}$, vacancies tend to remain third neighbors on the f.c.c. carbon sublattice and each Nb atom tends to be surrounded by five carbons and one vacancy. Effective interatomic ordering energies have been deduced from the elastic neutron diffuse scattering spectra and are in qualitative agreement with those deduced by Landesman *et al.* (1985) from a theoretical analysis of the band structure; the main interaction is a repulsive one between second-neighbor carbon vacancies that are distant by $\langle 100 \rangle a$.

Detailed X-ray scattering (Dunand *et al.*, 1985), channeling (Kaufmann and Meyer, 1983), and extended X-ray absorption fine structure (EXAFS) (Moisy-Maurice and de Novion, 1988) experiments have also allowed local structural distortions around a carbon vacancy to be determined.

Atomic diffusion has been extensively studied in some of the cubic carbides in the disordered state (see review by Davis, 1987). Both atom species (metal and carbon) diffuse by independent, random migration of defects on the respective sublattice of each component. For carbon, owing to the large concentrations of carbon vacancies, the activation energy for self-diffusion is a pure migration energy $E_D = E_M^V (\approx 3 \text{ to } 4 \text{ eV})$; in TiC_x , the C atomic diffusion coefficient is simply proportional to the vacancy content. Metal diffusion requires a vacancy-creation term as in simple f.c.c. metals; the low value of the metal diffusion coefficient and the high activation energy ($E_D \sim 6 \text{ to } 7 \text{ eV}$) are related to the strong bonding in these compounds (the melting point of TaC is 4000°C).

9.3 GaAs and Other III-V Semiconductors

Bulk point defects have a considerable importance in III-V semiconductors such as gallium arsenide GaAs, because they interact with free carriers, acting as scattering centers, traps and recombination centers, and have a large effect on electronic transport, even at very low concentration. Surface and interface defects due to processing are also important.

Owing to their non-metallic character and to the very low defect concentrations, the techniques for studying point defects in these materials are quite different from those presented in Section 2: they consist mainly of electrical measurements (conductivity, Hall effect,

deep-level transient spectroscopy, . . .), optical measurements, and electron paramagnetic resonance. Positron annihilation is of much more complex interpretation than in metals, because the positron trapping depends on the state of charge of the vacancy, which can change with temperature and doping (Corbel *et al.*, 1988).

A detailed review of native defects in GaAs has been published recently (Bourgoin *et al.*, 1988). Some point defects have been clearly identified and characterized, in particular in electron-irradiated single crystals: the As vacancy, interstitial and Frenkel pair, the antisites Ga_{As} and As_{Ga} , and small defect clusters (such as the divacancy $V_{\text{Ga}} + V_{\text{As}}$). The charge state of the As vacancy shows two transitions controlled by the position of the Fermi level: $V_{\text{As}}^{2-} \rightarrow V_{\text{As}}^{-}$ and $V_{\text{As}}^{-} \rightarrow V_{\text{As}}^0$. V_{As}^0 does not trap (or only very weakly traps) positrons. There is a common agreement that the Ga vacancy is stable when the Fermi level is high in the gap, but presents an instability $V_{\text{Ga}} \rightarrow V_{\text{As}} + \text{As}_{\text{Ga}}$ in semi-insulating materials.

Native defects in GaAs depend strongly on the cooling rate after processing. They are not simple intrinsic defects (except the antisites Ga_{As} and As_{Ga} which accommodate non-stoichiometry), but complexes involving vacancies, antisites, impurities, and perhaps interstitials. The vacancy-type defect concentration is typically 10 to 100 ppm in bulk materials.

The major defect, which recently received considerable interest and many interpretations (simple As_{Ga} antisite, or $\text{As}_{\text{Ga}} + \text{As}$ interstitial, . . .) is the so-called EL2 defect, which is a donor largely responsible for the semi-insulating behavior of undoped GaAs. This defect shows an interesting metastable behavior, induced optically at low temperature, the origin of which has not yet achieved a consensus—see discussion by Dabrowski and Scheffler (1992).

Strong interactions of native defects with dislocations, and As-rich clusters (up to 100 Å diameter) have been detected in GaAs. The inhomogeneous distribution of native defects in the material has a great influence on its electrical properties.

10. Influence of Point Defects on Physical Properties

Up to now, we have mostly emphasized the structure and energetics of point defects, with only occasional reference to their effects on properties. In the present section, we briefly summarize the latter.

(i) The effect on atomic diffusion has been discussed in Section 8.1: generally, the diffusion coefficient is a minimum at the stoichiometric composition.

(ii) Point defects generally soften the elastic constants.

(iii) The effect on plastic properties is very important: point defects may strengthen or weaken the compound, depending on temperature. At low temperature (compared to the melting point), structural vacancies and antistructure defects induce point-defect hardening via strain-field effects or elastic-modulus effects (Fleischer, 1987): for example, the hardness of NiAl and CoAl is a minimum at the stoichiometric composition (Westbrook, 1956). On the contrary, at high temperature, the strength is greatest at stoichiometry, because mobile point defects associated with off-stoichiometry favor dislocation climb. Increases of hardness and yield strength were also observed after vacancy quenching (as predicted by Rudman, 1962) or irradiation.

(iv) Finally, point defects increase the electrical resistivity (as discussed in Section 4.1 and Figure 8), and decrease the thermal conductivity and the superconducting critical temperature (Section 9.1). This has been studied experimentally in detail in the case of transition-metal carbides (Toth, 1971; Williams, 1971).

11. Conclusion

Point defects in intermetallic compounds present a great variety of behavior. In a case such as Cu_3Au , the geometry of the Cu sublattice allows rather simple structures and migration mechanisms of vacancies and interstitials, similar to those in f.c.c. metals. In a simple, cubic semiconductor such as GaAs, one finds already a much more complicated situation, in particular because each type of defect can have several charge states, each with a specific relaxation of its atomic surroundings. In some alloys with low crystal symmetry, computer simulation supports defect structures not found in metals: the split Nb vacancy in Nb_3Sn , or the seven-Cu-atom crowdion for the interstitial in CuTi.

In fact, only a few compounds of simple crystal structure (mainly B2- or L1_2 -ordered alloys) have been studied experimentally. Our knowledge of the type of defects, and of their structure, formation, and migration properties, is very fragmentary or even completely lacking in many compound families (e.g. Laves phases) (see discussion by Wever, 1992). This is partly due to the lack of single crystals of good quality and sufficient purity.

The possible point-defect structures, migration properties, . . . are so numerous in intermetallic compounds that experiment alone cannot solve the problem. Unfortunately, theory here is still in its infancy. For example, the commonly used Miedema and bond-breaking semiempirical models to estimate point-defect formation energies are quite contradictory. It is only recently, since the 1980s, that more sophisticated theoretical methods have been developed and seem to be able to predict point-defect structures and properties with some accuracy. Great progress can be expected from the combined use of Monte-Carlo and molecular-dynamics simulations (Rey-Losada *et al.*, 1993).

Some good papers have been published recently. Unfortunately the corresponding experimental data are most often lacking. The point-defect properties calculated from the electronic structure will have to be integrated in a proper thermodynamic theory. Such knowledge will also allow study in important fields that are practically unexplored up to now in intermetallic compounds: point defect–impurity interaction, point defect–dislocation interaction, and consequences on the mechanical properties, etc. Considerable work is still required.

Acknowledgements

The author wishes to thank Dr O. Dimitrov for a critical reading of the manuscript.

12. References

- Abromeit, C., and Wollenberger, H. (1987). *Vacancies and Interstitials in Metals*. Trans Tech Publications, Zürich.
- Alamo, A., de Novion, C. H., and Desarmot, G. (1986). *Rad. Effects*, **88**, 69.
- Aoki, K., and Izumi, O. (1975). *Phys. Status Solidi*, **A32**, 657.
- Arnhold, V. (1981). Thesis, Westfälische Wilhelms Universität, Münster, Germany.
- Bakker, H. (1984). *Mater. Res. Soc. Symp. Proc.*, **21**, 319.
- Bakker, H. (1987). *Mater. Sci. Forum*, **15–18**, 1155.
- Bakker, H., and Van Ommen, A. H. (1978). *Acta Metall.*, **26**, 1047.
- Bakker, H., and Westerveld, J. P. A. (1988). *Phys. Status Solidi*, **B145**, 409.
- Bakker, H., Stolwijk, N. A., Van Der Meij, L., and Zuurendonk, T. J. (1976). *Nucl. Metall.*, **20**, 96.
- Ball, A., and Smallman, R. E. (1968). *Acta Metall.*, **16**, 233.
- Beaufort, M. F., Guillot, J. P., and Rivière, J. P. (1986). *Rad. Effects*, **100**, 263.
- Benci, S., and Gasparrini, G. (1966). *J. Phys. Chem. Solids*, **27**, 1035.
- Benci, S., Gasparrini, G., and Germagnoli, E. (1969). *Nuovo Cimento*, **31**, 1165.
- Bender, O., and Ehrhart, P. (1982). In *Point Defects and Their Interaction in Metals* (eds J. Takamura, M. Doyama, and M. Kiritani). University of Tokyo Press, Tokyo, p. 639.
- Beretz, D., Hillairet, J., and Halbwachs, M. (1981). *J. Physique Coll.*, **42**, C5, 747.
- Berner, D., Geibel, G., Gerold, V., and Wachtel, E. (1975). *J. Phys. Chem. Solids*, **36**, 221.
- Bocquet, J. L. (1986). *Acta Metall.*, **34**, 571.
- Bocquet, J. L., Brebec, G., and Limoge, Y. (1983). In *Physical Metallurgy*, 3rd Edn. (eds R. W. Cahn and P. Haasen). North-Holland, Amsterdam, p. 385.
- Bourgoin, J. C., Von Bardeleben, H. J., and Stievenard, D. (1988). *J. Appl. Phys.*, **64**, R65.
- Bradley, A. J., and Seager, G. C. (1939). *J. Inst. Metals*, **64**, 81.
- Bradley, A. J., and Taylor, A. (1937). *Proc. R. Soc.*, **A159**, 56.
- Brun, T. O., Susman, S., Dejus, R., Graneli, B., and Skold, K. (1983). *Solid State Commun.*, **45**, 721.
- Caro, A., Victoria, M., and Averback, R. S. (1990). *J. Mater. Res.*, **5**, 1409.
- Caro, J. A., and Pedraza, D. F. (1991). *Nucl. Instrum. Methods Phys. Res.*, **B59/60**, 880.
- Chabik, St., and Rozenfeld, B. (1981). *Appl. Phys.*, **25**, 143.
- Chang, Y. A., and Neumann, J. P. (1982). *Prog. Solid State Chem.*, **14**, 221.
- Cheng, C. Y., Wynblatt, P. P., and Dorn, J. E. (1967). *Acta Metall.*, **15**, 1045.
- Condat, M., and Fayard, M. (1972). *Acta Metall.*, **20**, 115.
- Cooper, M. J. (1963). *Phil. Mag.*, **8**, 805.
- Corbel, C. (1987). *Scanning Microsc.*, **1**, 545.
- Corbel, C., Stucky, M., Hautajarvi, P., Saarinen, K., and Moser, P. (1988). *Phys. Rev.*, **B38**, 8192.
- Crawford, J. H., Jr, and Slifkin, L. M. (1972). *Point Defects in Solids*. Plenum, New York.
- Cupchalk, S. G., and Brown, N. (1967). *Acta Metall.*, **15**, 847.
- Dabrowski, J., and Scheffler, M. (1992). *Mater. Sci. Forum*, **83–87**, 735.
- Das Gupta, A., Smedskjaer, L. C., Legnini, D. G., and Siegel, R. W. (1987). *Mater. Sci. Forum*, **15–18**, 1213.
- Davis, R. F. (1987). In *Advances in Ceramics*, Vol. 23, *Non-Stoichiometric Compounds*. American Ceramic Society, Columbus, OH, p. 529.
- Dederichs, P. H. (1973). *J. Phys.*, **F3**, 471.
- Delavignette, P., Richel, H., and Amelinckx, S. (1972). *Phys. Status Solidi*, **A13**, 545.
- de Novion, C. H., and Landesman, J. P. (1987). In *Advances in Ceramics*, Vol. 23, *Non-stoichiometric Compounds*. American Ceramic Society, Columbus, OH, p. 499.
- de Novion, C. H., Beuneu, B., Priem, T., Lorenzelli, N., and Finel, A. (1990). In *The Physics and Chemistry of Carbides, Nitrides and Borides* (NATO ASI Series E, Appl. Sci., Vol. 185) (ed. R. Freer). Kluwer Academic, Dordrecht, p. 329.
- Dimitrov, C., and Dimitrov, O. (1984). *J. Phys.*, **F14**, 793.
- Dimitrov, C., Benkaddour, A., Dimitrov, O., Corbel, C., and Moser, P. (1987). *Mater. Sci. Forum*, **15–18**, 1275.
- Dimitrov, C., Sitaud, B., Zhang, X., Dimitrov, O., Dedek, V., and Dworschak, F. (1992). *J. Phys.: Condens. Mater.*, **4**, 10199, 10211.

- Donaldson, A. T., and Rawlings, R. D. (1976). *Acta Metall.*, **24**, 811.
- Doyama, M., Moser, P., Huguenin, D., Alamo, A., and Corbel, C. (1985a). In *Positron Annihilation* (eds P. C. Jain, R. M. Singru, and K. P. Gopinathan). World Scientific, Singapore, p. 903.
- Doyama, M., Moser, P., and Hillairet, J. (1985b). In *Positron Annihilation* (eds P. C. Jain, R. M. Singru, and K. P. Gopinathan). World Scientific, Singapore, p. 906.
- Doyama, M., Wang, T. M., Shimotomai, M., and Iwata, T. (1987). *Mater. Sci. Forum*, **15-18**, 1305.
- Dunand, A., Flack, H. D., and Yvon, K. (1985). *Phys. Rev.*, **B31**, 2299.
- Edelin, G. (1979). *Acta Metall.*, **27**, 455.
- Eibner, J. E., Engell, H. J., Schultz, H., and Jacobi, H. (1975). *Phil. Mag.*, **31**, 739.
- Elcock, E. W., and McCombie, C. W. (1958). *Phys. Rev.*, **109**, 605.
- Epicer, T. (1990). In *The Physics and Chemistry of Carbides, Nitrides and Borides* (NATO ASI Series E, Appl. Sci., Vol. 185) (ed. R. Freer). Kluwer Academic, Dordrecht, p. 215.
- Epperson, J. E., and Loomis, B. A. (1981). *J. Nucl. Mater.*, **108-109**, 476.
- Epperson, J. E., Gerstenberg, K. W., Berner, D., Kostorz, G., and Ortiz, C. (1978). *Phil. Mag.*, **A38**, 529.
- Fishman, S. G., Gupta, D., and Lieberman, D. S. (1970). *Phys. Rev.*, **B2**, 1451.
- Fleischer, R. L. (1987). *Scripta Metall.*, **21**, 1083.
- Fleischer, R. L. (1993). *J. Mater. Res.*, **8**, 49.
- Foiles, S. M., and Daw, M. S. (1987). *J. Mater. Res.*, **2**, 5.
- Foiles, S. M., Baskes, M. I., and Daw, M. S. (1986). *Phys. Rev.*, **B33**, 7983.
- Gilbert, J., Herman, H., and Damask, A. C. (1973). *Rad. Effects*, **20**, 37.
- Girifalco, L. A. (1964). *J. Phys. Chem. Solids*, **25**, 323.
- Gu, Y. M., and Fritzsche, L. (1992). *J. Phys.: Condens. Matter*, **4**, 1905.
- Gupta, D., Lazarus, D., and Lieberman, D. S. (1967). *Phys. Rev.*, **153**, 863.
- Hagel, W. C., and Westbrook, J. H. (1965). *Diffusion in Body Centered Cubic Metals*. American Society for Metals, Metals Park, OH, p. 197.
- Hahn, H., Fromberg, G., and Wever, H. (1983). *Phys. Status Solidi*, **A79**, 559.
- Hilgedieck, R., and Herzig, C. (1982). *Z. Metallk.*, **74**, 38.
- Ho, K., and Dodd, R. A. (1978). *Scripta Metall.*, **12**, 1055.
- Hoshino, K., Rothman, S. J., and Averback, R. S. (1988). *Acta Metall.*, **36**, 1271.
- Housseau, N., and Pelissier, J. (1983). *J. Nucl. Mater.*, **119**, 317.
- Huang, S. C., Taub, A. I., and Chang, K. M. (1984). *Acta Metall.*, **32**, 1703.
- Hume-Rothery, W., Betterton, J. O., and Reynolds, J. (1952). *J. Inst. Metals*, **80**, 609.
- Hünecke, J., Kim, I., Froberg, G., and Wever, H. (1987). *Mater. Sci. Forum*, **15-18**, 1311.
- Huntington, H. B., Miller, N. C., and Nerses, V. (1961). *Acta Metall.*, **9**, 749.
- Jacobi, H., and Engell, H. J. (1971). *Acta Metall.*, **19**, 701.
- Jennane, A., Bernardini, J., Hatem, G., and Moya, G. (1992). *Phil. Mag. Lett.*, **65**, 71.
- Junqua, N., Desoyer, J. C., and Moine, P. (1973). *Phys. Status Solidi*, **A18**, 387.
- Kaufmann, R., and Meyer, O. (1983). *Phys. Rev.*, **B28**, 6216.
- Kim, S. M. (1984). *Phys. Rev.*, **B29**, 2356.
- Kim, S. M. (1986). *Phys. Rev.*, **B33**, 1509.
- Kim, S. M. (1987). *Mater. Sci. Forum*, **15-18**, 1257.
- Kim, S. M., and Buyers, W. J. L. (1980). *Phys. Rev. Lett.*, **45**, 383.
- Kinoshita, C., Mukai, T., and Kitajima, S. (1982). In *Point Defects and Their Interactions in Metals* (eds J. Takamura, M. Doyama, and M. Kiritani). University of Tokyo Press, Tokyo, p. 857.
- Koch, J. M., and Koenig, C. (1986). *Phil. Mag.*, **54**, 177.
- Koch, J. M., and Koenig, C. (1987). *Phil. Mag.*, **55**, 359.
- Koch, J. M., and Koenig, C. (1988). *Phil. Mag.*, **57**, 557.
- Koch, J. M., Stefanou, N., and Koenig, C. (1987). *Mater. Sci. Forum*, **15-18**, 1329.
- Koczak, M. J., Herman, H., and Damask, A. C. (1971). *Acta Metall.*, **19**, 303.
- Koenig, C., Stefanou, N., and Koch, J. M. (1986). *Phys. Rev.*, **B33**, 5319.
- Kogachi, M., Minamigawa, S., and Nakahigashi, K. (1992). *Acta Metall. Mater.*, **40**, 1113.
- Kuper, A. B., Lazarus, D., Manning, J. R., and Tomizuka, C. T. (1956). *Phys. Rev.*, **104**, 1536.
- Labbé, J., and Friedel, J. (1966). *J. Physique*, **27**, 153.
- Landesman, J. P., Treglia, G., Turchi, P., and Ducastelle, F. (1985). *J. Physique*, **46**, 1001.
- Lesueur, D. (1981). *Phil. Mag.*, **A44**, 905.
- Leubolt, R., Isper, H., and Komarek, K. L. (1986). *Z. Metallk.*, **77**, 284.
- Lipson, A., and Taylor, A. (1939). *Proc. R. Soc.*, **A173**, 232.
- Lomer, W. M. (1958). In *Vacancies and Other Point Defects in Metals and Alloys* (Institute of Metals Monograph and Report Series, no. 23). Institute of Metals, London, p. 85.
- Manning, J. R. (1971). *Phys. Rev.*, **B4**, 1111.
- Marshall, G. W., and Brittain, J. O. (1975). *Metall. Trans.*, **A6**, 921.
- Masuda-Jindo, K. (1987). *Mater. Sci. Forum*, **15-18**, 1299.
- Miedema, A. R. (1979). *Z. Metallk.*, **70**, 345.
- Moisy-Maurice, V., and de Novion, C. H. (1988). *J. Physique*, **49**, 1737.
- Moseev, N. V., Chudinov, V. G., Goshchitskii, B. N., and Protasov, V. I. (1983). *Phys. Status Solidi*, **A79**, 67.
- Moseev, N. V., Chudinov, V. G., Goshchitskii, B. N., and Protasov, V. I. (1986). *Phys. Status Solidi*, **A94**, 147.
- Muto, T. (1936). *Inst. Phys. Chem. Res. Sci. Papers, Tokyo*, **30**, 99.
- Néel, L., Pauleve, J., Pauthenet, R., Laugier, J., and Dautreppe, D. (1964). *J. Appl. Phys.*, **35**, 873.
- Neumann, J. P. (1977). *Scripta Metall.*, **11**, 969.

- Neumann, J. P. (1980). *Acta Metall.*, **28**, 1165.
- Neumann, J. P., Chang, Y. A., and Lee, C. M. (1976). *Acta Metall.*, **24**, 593.
- Parthé, E. (1964). *Crystal Chemistry of Tetrahedral Structures*. Gordon and Breach, New York.
- Pedraza, D. F., Caro, A., and Farkas, D. (1991). *Rad. Effects Defects Solids*, **118**, 143.
- Rey-Losada, C., Hayoun, M., and Pontikis, V. (1993). *Mat. Res. Soc. Symp. Proc.*, **291**, 549.
- Rivière, J. P., and Grilhé, J. (1974). *Phys. Status Solidi*, **A25**, 429.
- Rivière, J. P., Dinhut, J. F., and Dural, J. (1983a). *Rad. Effects*, **69**, 47.
- Rivière, J. P., Dinhut, J. F., and Desarmot, G. (1983b). *Rad. Effects*, **71**, 137.
- Rudman, P. S. (1962). *Acta Metall.*, **10**, 195.
- Rullier-Albenque, F., and Quéré, Y. (1981). *Phys. Lett.*, **81A**, 232.
- Rullier-Albenque, F., and Sénateur, J. P. (1986). *Rad. Effects*, **88**, 17.
- Schaefer, H. E., Wurschum, R., Sob, M., Zak, T., Yu, W. Z., and Eckert, W. (1990). *Phys. Rev.*, **B41**, 11869.
- Schulson, E. M. (1979). *J. Nucl. Mater.*, **83**, 239.
- Schwab, R., and Gerold, V. (1980). *Acta Metall.*, **28**, 433.
- Seybolt, A. U., and Westbrook, J. H. (1964). *Acta Metall.*, **12**, 449.
- Shirai, Y., and Yamaguchi, M. (1992). *Mater. Sci. Eng.*, **A152**, 173.
- Shoemaker, J. R., Lutton, R. T., Wesley, D., Wharton, W. R., Dehrl, M. L., Herte, M. S., Sabochik, M. J., and Lam, N. Q. (1991). *J. Mater. Res.*, **6**, 473.
- Simmons, R. O., and Balluffi, R. W. (1960). *Phys. Rev.*, **117**, 1.
- Sिताud, B., Dimitrov, C., Dai, G., Moser, P., and Dimitrov, O. (1991). *Proc. Intl. Symp. Intermetall. Compounds, Structure and Mechanical Properties (JIMIS-6)* (ed. O. Izumi). Tohoku University, Sendai, Japan, p. 69.
- Stefanou, N., Keller, R., and Dederichs, P. H. (1987). *Phys. Rev.*, **B35**, 2705.
- Stolwijk, N. A. (1981). *Phys. Status Solidi*, **B105**, 223.
- Stolwijk, N. A., Van Gend, M., and Bakker, H. (1980). *Phil. Mag.*, **A42**, 783.
- Taylor, A., and Doyle, N. J. (1972). *J. Appl. Crystallogr.*, **5**, 201.
- Toth, L. E. (1971). *Transition Metal Carbides and Nitrides*. Academic Press, New York.
- Urban, R., and Ehrhart, P. (1987). *Mater. Sci. Forum*, **15-18**, 1251.
- Van Ommen, A. H., and de Miranda, J. (1981). *Phil. Mag.*, **A43**, 387.
- Van Ommen, A. H., Reckman, A. P. F. M., Van Feggelen, M., and Bakker, H. (1977). *J. Physique Coll.*, **38**, C7, 337.
- Van Ommen, A. H., Waegemaekers, A. A. H. J., Moleman, A. C., Schlatter, H., and Bakker, H. (1981). *Acta Metall.*, **29**, 123.
- Wachtel, E., Linse, V., and Gerold, V. (1973). *J. Phys. Chem. Solids*, **34**, 1461.
- Wang, T. M., Shimotomai, M., and Doyama, M. (1983). *Phil. Mag.*, **A48**, L5.
- Wang, T. M., Shimotomai, M., and Doyama, M. (1984). *J. Phys.*, **F14**, 37.
- Wasilewski, R. J. (1968). *J. Phys. Chem. Solids*, **29**, 39.
- Wasilewski, R. J., Butler, S. R., and Hanlon, J. E. (1968). *J. Appl. Phys.*, **39**, 4234.
- Weber, D., Meurtin, M., Paris, D., Fourdeux, A., and Lesbats, P. (1977). *J. Physique Coll.*, **38**, C7, 330.
- Wechsler, M. S. (1957). *Acta Metall.*, **5**, 150.
- Welch, D. O., Dienes, G. J., Lazareth, O. W., Jr, and Hatcher, R. D. (1984). *J. Phys. Chem. Solids*, **45**, 1225.
- Westbrook, J. H. (1956). *J. Electrochem. Soc.*, **103**, 54.
- Wever, H. (1992). In *Diffusion in Solids: Unsolved Problems* (ed. G. E. Murch). Trans Tech Publications, Zürich, p. 55.
- Williams, W. S. (1971). *Prog. Solid State Chem.*, **6**, 57.
- Wollenberger, H. J. (1983). In *Physical Metallurgy*, 3rd Edn (eds R. W. Cahn and P. Haasen). North-Holland, Amsterdam, p. 1140.

This chapter was originally published in 1995 as Chapter 23 in *Intermetallic Compounds*, Vol. 1: *Principles*, edited by J. H. Westbrook and R. L. Fleischer.

Chapter 7

Structure of Grain Boundaries

Takayuki Takasugi

Institute for Materials Research, Tohoku University, Katahira 2-1-1, Aoba-ku, Sendai 980, Japan

1. Introduction

Just as with grain boundaries in pure metals and disordered alloys, grain boundaries in intermetallic compounds play important roles in various properties of polycrystalline materials, such as mechanical properties, recrystallization, electronic conductivity, and corrosion resistance (Chadwick and Smith, 1976; Johnson and Blakely, 1977). There are numerous variables that can affect the structure and properties of a grain boundary. For example, there are the crystallographic parameters that describe the orientations of the neighboring grains and the interface, the nature of the atomic accommodation, and the distributions of the primary compositional atoms and the impurity atoms (Chadwick and Smith, 1976; Johnson and Blakely, 1977).

There are some indications that grain boundaries in intermetallic compounds behave uniquely and thus present some very interesting properties, which are technologically and scientifically important. In perfect lattices of intermetallic compounds, i.e. mostly ordered alloys, atoms of one component prefer to bind with atoms of the other component atom as their nearest neighbors owing to their chemical bonding nature. However, in the grain-boundary region of intermetallic compounds, normal bonds between unlike atoms may not be conserved or may be distorted; also, wrong bonds between like atoms may be introduced, though because of the energetic requirement these defects are minimal. Thus, grain boundaries in intermetallic compounds may involve the influence of bond defects in addition to the lattice distortion. It has been recognized in pure metals and alloys that many properties of a grain boundary

depend strongly upon the chemical composition at grain-boundary planes. Therefore, understanding of the chemical composition at grain boundaries of intermetallic compounds, which essentially consist of multi-components in contrast to pure metals, is particularly important. In grain boundaries of intermetallic compounds, the concentration of component atoms at a grain boundary can vary depending on the stoichiometric range in the bulk, and can deviate from its stoichiometry in the matrix, and also the component atoms can interact with the impurity atoms. These compositional perturbations at grain boundaries can affect many material properties, such as grain-boundary fracture, grain-boundary corrosion, grain-boundary sliding, and the electronic conductivity of intermetallic compounds. Furthermore, the atomic structure and chemical composition of grain boundaries in intermetallic compounds result in a unique charge distribution of the electrons. This electronic structure and the nature of the chemical bond at grain boundaries can influence the cohesion of a grain-boundary plane, which is closely related to the mechanical properties of intermetallic compounds.

During the last decade, extensive progress has been made on experimental observations and theoretical understanding of grain boundaries in intermetallic compounds, and these techniques and theories have also been applied to grain boundaries of pure metals and disordered alloys. However, many problems still remain. In this chapter, we review direct observations using transmission electron microscopy (TEM), high-resolution transmission electron microscopy (HRTEM), and field ion microscopy (FIM). Next, concerning the chemistry on grain boundaries of intermetallic compounds, direct

observations using Auger electron spectroscopy (AES), TEM combined with energy-dispersive X-ray (TEM-EDX), and FIM combined with atom-probe (FIM-AP) techniques are presented. In the last part of this chapter, geometrical and atomistic computer models for the structure of grain boundaries of intermetallic compounds are presented. Some unique characteristics of grain-boundary structures in intermetallic compounds are mentioned. Finally, the nature of the chemical bonds and the associated electronic structure are discussed in relation to the atomistic structure and the composition of grain boundaries. In this chapter, the terminology 'grain boundaries' is used in a wide sense, i.e. it involves to some extent regions adjoining the grain-boundary plane because it has been shown that these regions also affect the properties of intermetallic compounds. Also, wherever the terminologies commonly used in the field of grain boundaries and their physical meanings are not described in sufficient detail, the reader is referred to textbooks (Chadwick and Smith, 1976; Johnson and Blakely, 1977; Westbrook, 1975; Williams *et al.*, 1992). These textbooks contain numerous references not only on the terminology of grain boundaries but also on the terminology of the microscopy technique described in this chapter.

2. Direct Observations of Structure

HRTEM and FIM can offer the most direct information for the structure of grain boundaries. The lattice points (or fringes) at or near a grain boundary can be imaged, and then the possible atomic configurations can be constructed. Less-direct observations are done using conventional TEM, by which contrast images of features such as geometrical defects or grain-boundary dislocations are observed, and these can then be discussed in relation to the grain-boundary structure. HRTEM observation is generally applicable only when lattices in either or both of the grains adjoining the grain-boundary plane are parallel to the electron beam, i.e. when the grain-boundary plane is parallel to the electron beam. In contrast, FIM observation is free from this geometrical restriction and offers spatial information on the atoms at or near a grain boundary. Many observations by HRTEM, conventional TEM, and FIM have been reported, mostly on alloys with $L1_2$ -type structure.

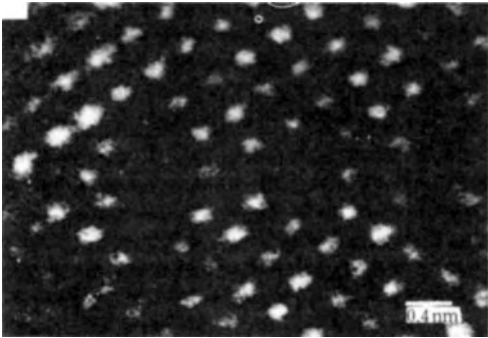
2.1 HRTEM and TEM Observations

Concerning the atomic configuration at a grain boundary, Sasaki *et al.* (1980) showed an HRTEM

image of a grain boundary prepared from a bicrystal of the $L1_2$ -type $Ni_3(Al,Ti)$ compound, which is supposed to have a high ordering energy. When two cubic lattices with the same lattice parameter, which have one lattice point in common, are related by any of a series of special rotations through the common point, they can introduce a three-dimensional superlattice of common lattice points. These are called coincidence-site lattices, and the fraction of lattice points in common is usually written as $1/\Sigma$, where Σ is an odd integer (Chadwick and Smith, 1976; Johnson and Blakely, 1977). Figures 1(a) and (b) show an atomic image and the corresponding atom distribution observed in the $\Sigma = 13$, 67.38° coincidence-site lattice (CSL) boundary with $[1\ 0\ 0]$ rotation axis. The atomic positions consisting of all the Ni atoms are imaged in this figure. This observation reveals that the grain-boundary structure attained a symmetrical configuration without a substantial rigid translation along x and y directions (i.e. along the interface) and also that an almost ideal $L1_2$ order is preserved up to the grain-boundary plane. However, the expected two Al(Ti) atoms, i.e. wrong bond pairs across the boundary (see Figure 1(b)), were not detected in this image, and were apparently replaced with vacancies. Consequently, it is suggested that chemical ordering is primarily sustained without locally accommodating the atoms with a possible chemical disordering, leading to the energy minimum. In this figure, it is also noted that distinct columnar cavities occur in grain boundaries owing to the depleted bond pairs.

Extensive HRTEM observations have been performed on grain boundaries of Ni_3Al , with and without boron, which were prepared as oriented bicrystals (Kung *et al.*, 1991a, b, 1992; Mills *et al.*, 1991) or solidified polycrystals (Mackenzie and Sass, 1988; Kung *et al.*, 1991a, 1992; Mills, 1989; Krzanowski, 1989; Baker *et al.*, 1990). The major interest in these studies has been directed to determination of the existence of structural disordering (or ordering) at or near the grain-boundary plane, because this feature was postulated to relate to the mechanical response of the grain boundary in this type of alloy. In other words, the objective in these observations was to understand the intrinsic brittleness of Ni_3Al in its polycrystalline form and the beneficial effect of boron addition on grain-boundary brittleness. Various types of grain boundaries, such as low- and high-angle tilt and twist boundaries, special CSL and random (general) boundaries have been observed. It was found that small-angle twist, tilt and mixed boundaries, and large-angle CSL boundaries were primarily ordered up to very close to the grain-boundary plane, regardless of the addition of boron (Kung *et al.*, 1991a, b, 1992;

(a)



(b)

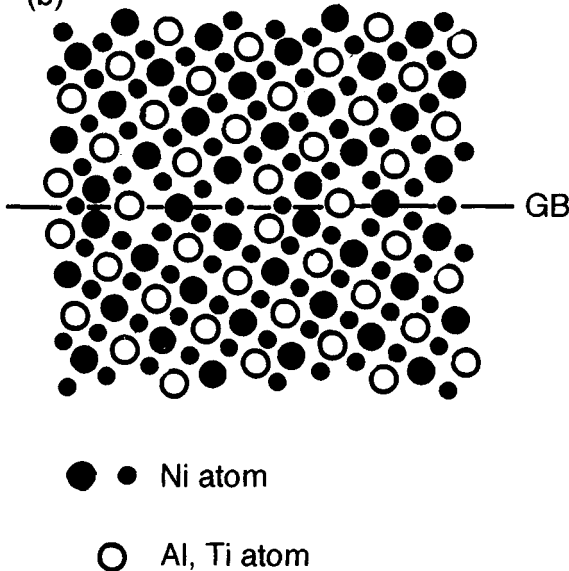


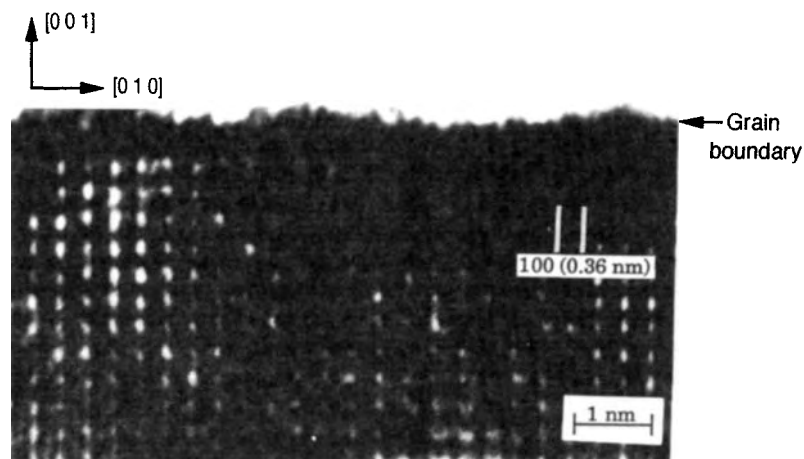
Figure 1. (a) Atomic lattice image and (b) the corresponding atom distribution observed in the $\Sigma=13$, 67.38° CSL tilt boundary with $[100]$ rotation axis of $\text{Ni}_3(\text{Al,Ti})$ bicrystal. Note that large and small circles represent atoms distributed on the first (100) atomic plane and the second (100) atomic plane, respectively (Reprinted with permission from Sasaki *et al.*, *Acta Metall. Mater.*, **38**, 1417. Copyright (1990) Pergamon Press Ltd)

Mills, 1989; Mills *et al.*, 1991; Krzanowski, 1989). For example, Figure 2 shows HRTEM images of two large-angle twist boundaries (with $\Sigma=5$ orientation) in Ni_3Al bicrystals with boron and without boron (Kung *et al.*, 1992). A square array of 0.36 nm lattice fringes, corresponding to the (100) and (010) planes, i.e. superlattice fringes, is present up to close to the interface plane in both cases. In these observations, the lattice

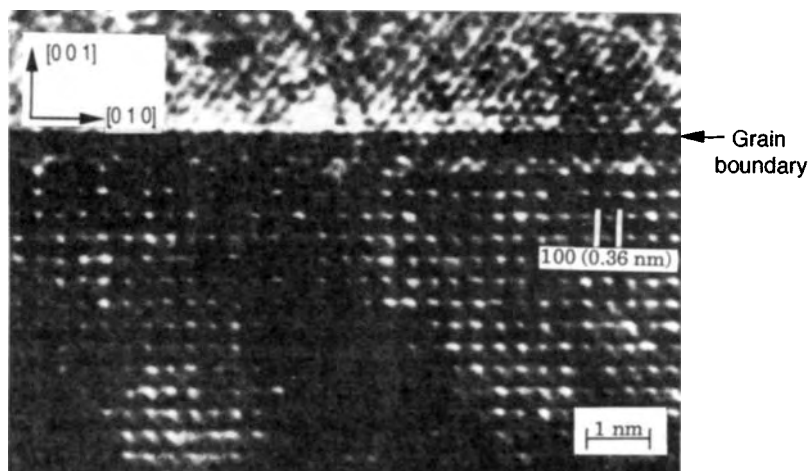
images at the interface itself were not clear. This is mostly due to the grain boundary being inclined to the beam direction. Therefore, whether the lattice is ordered just at the interface is inconclusive. Also, discussion of the detailed atomic configuration at the interface, e.g. how much translational and local lattice accommodation takes place at the interface, was impossible from these observations. There are other examples: a compositionally disordered region $\sim 1.5\text{ nm}$ thick, which was not an imaging artifact, was found to be present in the vicinity of a large-angle general boundary in boron-doped Ni_3Al (Mackenzie and Sass, 1988; Kung *et al.*, 1992). Also, it was found that a disordered phase up to 20 nm wide, which is a discrete phase with a distinct interface with the matrix, exists along portions of grain boundaries in boron-free Ni_3Al , and this phase was found to cover all the boundary regions in boron-doped Ni_3Al that was prepared by powder processing (Baker *et al.*, 1990). However, arc-melted and well-recrystallized Ni_3Al materials did not have such a thick disordered phase and regardless showed very high ductility. Thus, the structure and the associated composition at grain boundaries of Ni_3Al depend on the material processing, stoichiometry, alloying of boron, and also the orientation parameters.

There are no HRTEM observations of grain boundaries for other intermetallic alloys, for example, for a weakly ordered L_{12} alloys. To get a generalized conclusion for grain boundaries in L_{12} structure, more studies are needed. HRTEM observations for grain boundaries in other kinds of crystal structure are also needed.

The atomic configuration at a grain boundary and the existence of its multiplicity, i.e. variants, were demonstrated for coherent (Tichelaar and Schapink, 1986) and incoherent (Tichelaar and Schapink, 1988) $\Sigma=3$ twin boundaries of Cu_3Au -ordered alloy using the conventional TEM method of α fringes. Figure 3 shows that two structures consisting of symmetric (denoted S in Figure 3(b)) and asymmetric (denoted A in Figure 3(b)) configurations were separated by an antiphase boundary (APB) on one side of the boundary plane. Here, a symmetric configuration is defined as the structure where each sublattice occupied by Cu and Au atoms in one component crystal is fully symmetrical to the corresponding sublattice occupied by Cu and Au atoms in the other component crystal. On the other hand, an asymmetric configuration is defined as a structure where one sublattice occupied by Cu atoms in one component crystal is symmetrical to a sublattice occupied by Au atoms. Tichelaar and Schapink (1986) demonstrated that these structures can be generated by



(a)



(b)

Figure 2. HRTEM images of two large-angle twist boundaries (with $\Sigma = 5$ orientation) in Ni_3Al bicrystals (a) with boron and (b) without boron (Reprinted with permission from Kung *et al.*, *Acta Metall. Mater.*, **40**, 81. Copyright (1992) Pergamon Press Ltd)

rigid translations of the type $\frac{1}{2}\langle 110 \rangle$ or the type $\frac{1}{6}\langle 211 \rangle$ parallel to the boundary plane. The latter translation is generated by a dislocation in the boundary.

The dislocation structures of grain boundaries in intermetallic compounds have also been observed using the conventional TEM technique (Kung and Sass, 1992; Buis *et al.*, 1989, 1991). It was shown that small-angle $[001]$ twist boundaries and small-angle $[011]$ tilt boundaries in L1_2 -type Ni_3Al contain dislocations with Burgers vectors corresponding to APB-coupled

$\frac{1}{2}[110]$ superpartials. Figure 4 represents the diffraction image of a $[001]$ small-angle boundary in Ni_3Al with a twist component of 1.0° and a tilt component of 0.4° . The structures of these boundaries were thus shown to be in agreement with theoretical models proposed by Marcinkowski (1968) and also with the CSL theory summarized by Balluffi *et al.* (1972). Also, it was found that boron additions to Ni_3Al reduced the APB energy at the interface (Kung and Sass, 1992).

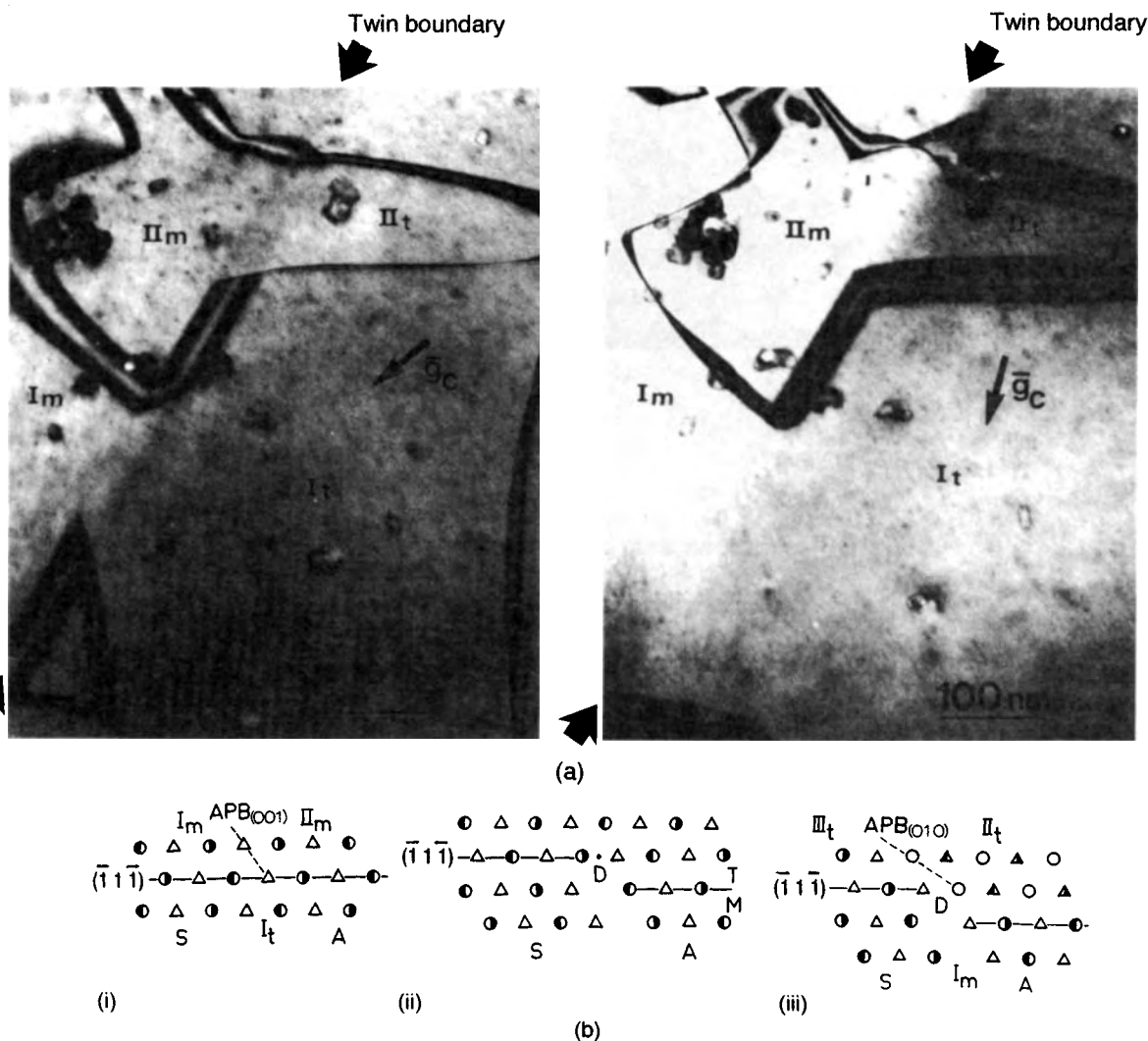


Figure 3. (a) TEM bright-field electron micrographs showing two structures consisting of a symmetric and an asymmetric configuration separated by an antiphase boundary (APB) on one side of the $(\bar{1}1\bar{1})$ boundary plane (indicated by arrows) in ordered Cu_3Au (Reproduced by permission of Taylor & Francis from Tichelaar and Schapink, 1986). Numbers are assigned to different domains. The m and t correspond to 'matrix' and 'twin' orientations, respectively. (b) Grain-boundary structures corresponding to TEM images. The left (i) is a projection of a $(\bar{1}1\bar{1})$ twin boundary in an $\text{L}_{12}\text{A}_3\text{B}$ ordered alloy along $[110]$, while the center (ii) and right (iii) are projections along $[011]$. S and A indicate symmetrical or asymmetrical structures. Projections (ii) and (iii) contain a dislocation (marked D) with $b = \frac{1}{6} [21\bar{1}]$ and line direction $u = [110]$. \circ and Δ represents A atoms at heights zero and $a/2\sqrt{2}$ above the plane of paper respectively. \bullet represents an A atom at height zero and B atom at height $a/2\sqrt{2}$ above the plane of the paper. Δ represents a B atom at level $a/2\sqrt{2}$ below the paper and A atom at height $a/2\sqrt{2}$ above the plane of the paper.

The dislocation structures of grain boundaries in B2 (cP2)-type ordered Fe_3Al alloys have been observed (Buis *et al.*, 1989, 1991). It was shown that a symmetrical low-angle tilt boundary consisted of a regular array of $\langle 111 \rangle$ -type superdislocations in large areas, accompanied

by ordinary dislocations (i.e. $\frac{1}{2}\langle 111 \rangle$) in small areas. The spacing of the superdislocations distributed at the interface was larger than the value calculated from anisotropic elasticity theory. This discrepancy was attributed to changes in the APB energy due to

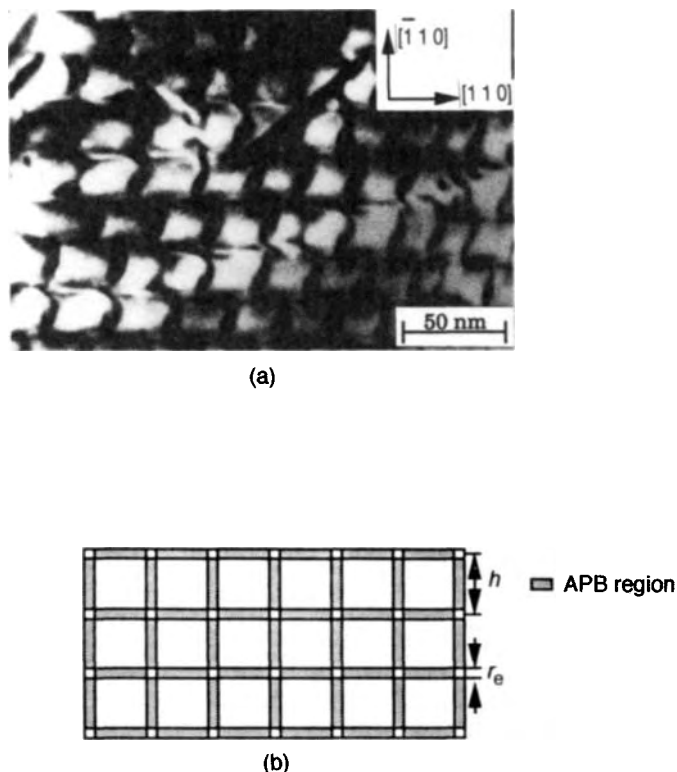


Figure 4. (a) Diffraction ($g = 0\ 2\ 0$) image of $[0\ 0\ 1]$ small-angle boundary in Ni_3Al with θ (twist) = 1.0° and θ (tilt) = 0.4° . (b) Schematic diagram showing the structure modeled using APB-coupled superpartial dislocations (Reprinted with permission from Kung and Sass, *Acta Metall. Mater.*, 40, 99. Copyright (1992) Pergamon Press Ltd)

segregation of solute atoms to the APBs associated with the superdislocations. On the other hand, asymmetrical tilt boundaries consisted of two types of $\langle 1\ 1\ 0 \rangle$ dislocations. Some of these dislocations were dissociated into ordinary dislocations. Also, the asymmetrical $\Sigma = 3$ boundary, which involves an extra 4° misorientation, was shown to consist of a hexagonal dislocation network accommodating the deviation from the CSL misorientation. However, the Burgers vectors of these dislocations were not the expected smaller DSC (displacement shift complete) lattice vectors (Bollmann, 1967) but the lattice vectors.

The kinetics of the order–disorder phase transition at twin boundaries (of $\Sigma = 3$, $\{1\ 1\ 1\}$ and $\{2\ 1\ 1\}$ types) has been observed in the L1_2 -type Cu_3Au alloy using an *in situ* TEM technique (Antonopoulos *et al.*, 1990; Tichelaar *et al.*, 1992). It was shown that the order–disorder phase transition occurs in these boundaries prior to the phase transition in the bulk. The temperature difference between the transition temperature of both twin boundaries and the bulk was demonstrated to range from 0.5 to 2 K.

However, differences in the transition temperature for the two types of twin boundaries were not explained.

2.2 FIM Observations

FIM observations have been performed on grain boundaries of Ni_3Al polycrystals by two laboratories: Oak Ridge National Laboratory (ORNL) (Miller and Horton, 1986a, b, c; Horton and Miller, 1987a, b) and the University of Pittsburgh (Brenner *et al.*, 1986; Sieloff *et al.* 1986, 1987a, b; Brenner and Hua, 1990a, b, 1991). The major interest in the FIM observations as in the HRTEM observations was the detection of the state of order (or disorder) in the boundary region and the effect of boron on it. Various types of grain-boundary structures and the associated compositions were observed, depending on material processing and thermomechanical treatment. Disordered phases were occasionally detected in boundaries of these alloys, but most of those phases were probably non-equilibrium phases, e.g. introduced by powder processing. In the

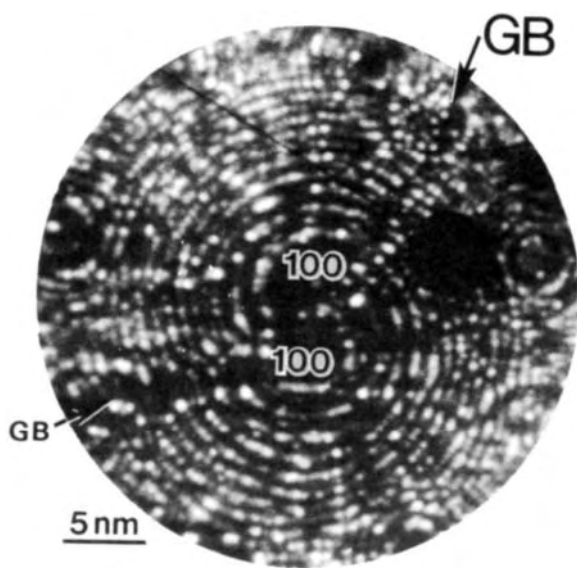


Figure 5. FIM image of a grain boundary of Ni_3Al with 0.35 wt.% boron showing bright and dim contrast features of edges of superlattice planes on both sides. This result indicates ordering of the matrix right up to the boundary (Reprinted with permission from Brenner and Ming-Jian, *Scripta Metall. Mater.*, 24, 671. Copyright (1990) Pergamon Press Ltd). Note that the black circle corresponds to the area where atom-probe (AP) analysis has been done

equilibrium case, the ordered L1_2 structure persisted in the near-vicinity of the interface in Ni_3Al polycrystals without boron and also even in those with boron. Figure 5 shows an FIM image of a grain boundary of Ni_3Al with 0.35 wt.% boron (Brenner and Hua, 1990a, 1991). In this image, alternating bright and dim lattice-plane edges were visible at the two $\{002\}$ superlattice poles that are in close proximity to the boundary at opposite sides of the interface, giving strong evidence for ordering right up to the boundary. More quantitative evidence of ordering was given in an atom-probe (AP) analysis, which showed the successive superlattice planes on the two sides of the boundary. It was demonstrated from these observations that the limiting thickness of an ordered layer that can be resolved is approximately 1 nm (Brenner and Hua, 1990a), meaning that only a few atomic layers in the vicinity of a grain boundary have the possibility of a disordered structure.

As will be described later, FIM observations were indeed successful in the determination of grain-boundary chemistry when they were combined with AP analysis, but were not successful in the determination of the local atomic positions. It is generally known that the resolution obtainable by FIM is insufficient to

determine the exact site of atoms because of geometrical and field-effect constraints. Therefore, concerning the atomic configuration and linear defects, such as dislocations at grain boundaries of intermetallic compounds, there are no reliable FIM observations at the present time.

3. Direct Observations of Chemistry

The chemical composition of grain boundaries in intermetallic compounds as well as in ordinary metals strongly affects material properties. Since intermetallic compounds by definition consist of components of two or more elements, the chemical compositions at grain boundaries are not so simple. At least two kinds of atomic species, i.e. the constituent atoms, and solute or impurity atoms are considered for the chemistry of grain boundaries in intermetallic compounds. The stoichiometry at grain boundaries may be different from the stoichiometry of the matrix; enrichment or depletion of the constituent atoms at grain boundaries relative to the matrix may take place owing to a McLean (1957) form of grain-boundary segregation or variants for configurations with different atomic composition but with nearly equal energy. On the other hand, the segregation of solute atoms and impurity atoms to the grain boundaries of intermetallic compounds may be influenced by the alloy stoichiometry at the grain boundary or in the matrix. For both kinds of segregation species, two types of equilibrium and non-equilibrium segregations are considered.

Three direct observation techniques have been adopted for the chemistry at grain boundaries of intermetallic compounds: Auger electron spectroscopy (AES) (White *et al.*, 1984; Takasugi *et al.*, 1985; Liu *et al.*, 1985; Ogura *et al.*, 1985; White, 1986; Briant and Taub, 1988; George *et al.*, 1989, 1991a, b; Horton and Liu, 1990; Suzuki and Masahashi, 1991; Choudhury *et al.*, 1992; George and Liu, 1990); transmission electron microscopy combined with energy-dispersive X-ray techniques (TEM-EDX) (Baker and Schulson, 1988; Krzanowski, 1989); and field ion microscopy combined with atom-probe methods (FIM-AP) (Miller and Horton, 1986a, b, c; Horton and Miller, 1987a, b; Brenner *et al.*, 1986; Sieloff *et al.*, 1986, 1987a, b; Brenner and Hua, 1990a, b).

3.1 AES and TEM-EDX observations

It was discovered by Aoki and Izumi (1979) that Ni_3Al polycrystals were ductilized by addition of a small

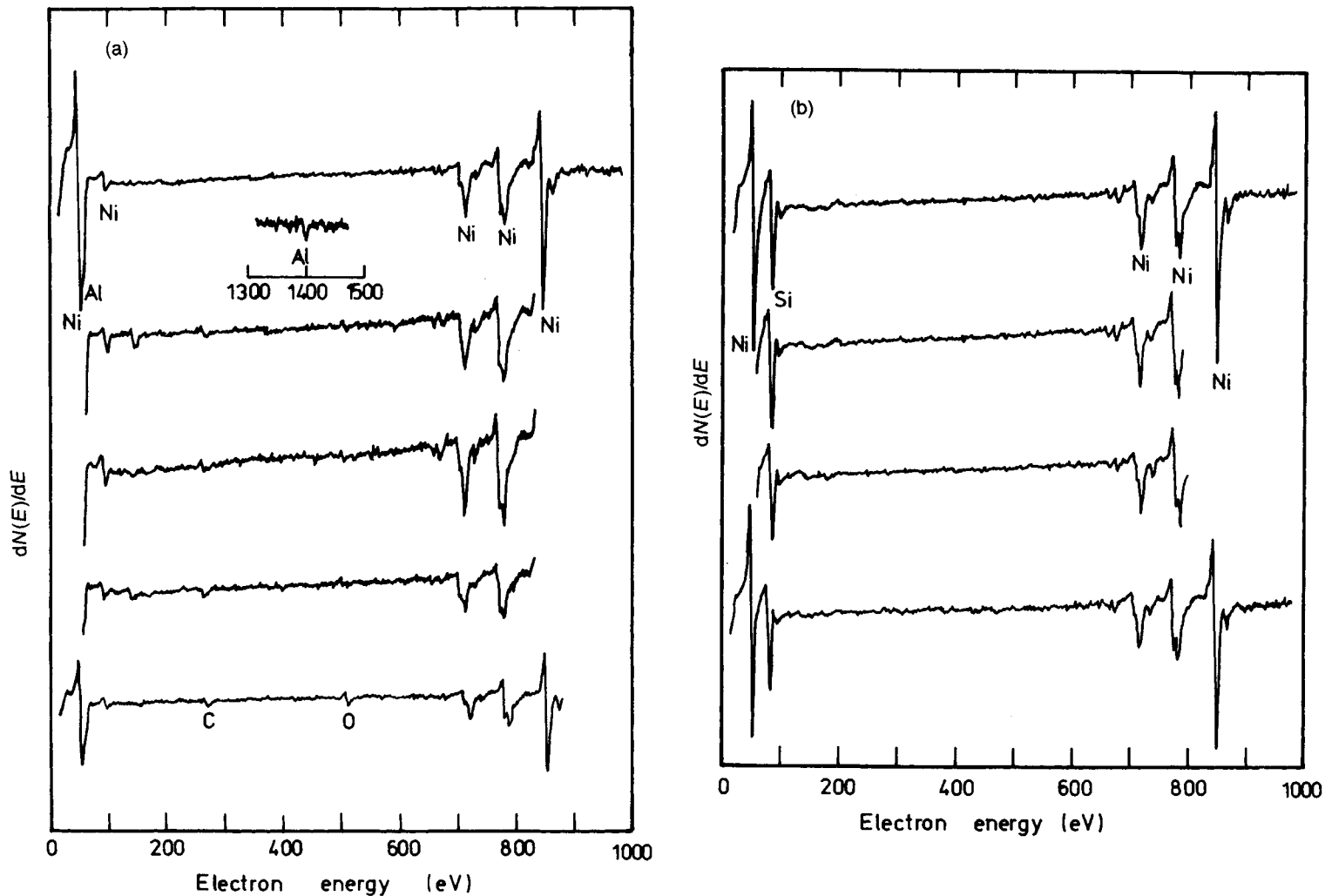


Figure 6. AES spectra from intergranular fracture facets of (a) Ni_3Al (water-quenched, 25 at. % Al) and (b) Ni_3Si (water-quenched, 23.7 at. % Si) compounds. Each spectrum was measured from each grain-boundary facet. Note that signals of carbon and oxygen detected in a few spectra were due to contamination from the vacuum pump system (Reprinted with permission from Takasugi *et al.*, *Scripta Metall.*, **19**, 551. Copyright (1985) Pergamon Press Ltd)

amount of boron. Without boron, Ni_3Al compounds fail in an extremely brittle manner along their grain boundaries. Therefore, the first inquiries using AES were directed to determine whether or not the grain boundaries of Ni_3Al are contaminated by a harmful species and thereby embrittled. AES results on fractured grain boundaries of Ni_3Al (Takasugi *et al.*, 1985; Liu *et al.*, 1985; Ogura *et al.*, 1985) and Ni_3Si (Takasugi *et al.*, 1985), which were prepared from high-purity raw materials, showed no impurity atoms on these grain boundaries, for example, as shown in Figure 6 (Takasugi *et al.*, 1985). Thus, AES results showed that the grain-boundary brittleness of Ni_3Al cannot be associated with the grain-boundary segregation of impurities. Also, clean grain boundaries were observed on stoichiometric NiAl (with B2 (cP2) structure), which similarly fails in a predominantly intergranular manner (George and Liu, 1990). No impurities were detected on the fractured grain boundaries of NiAl (George and Liu, 1990).

Concerning the segregation of unintentionally included impurity atoms to grain boundaries, a number of AES results have been accumulated on fractured grain boundaries of Ni_3X (X = Al, Si, Ga, and Ge) and NiAl with and without boron. The segregation of sulfur, oxygen, and carbon into the grain-boundary facets of Ni_3X has been reported (White *et al.*, 1984; Takasugi *et al.*, 1985; Liu *et al.*, 1985). These atoms, except for carbon, are likely to be embrittling elements in intermetallic compounds as well as in ordinary metals and alloys. Hence, it has to be noted that the elimination or control of these unintentionally included impurity elements is still an important technological method to improve the mechanical properties of intermetallic compounds. The distribution of the segregated atoms was not uniform from boundary facet to boundary facet, thus indicating the orientation dependence of the grain-boundary segregation of the impurity atoms. The sulfur peak in Auger spectra in the grain boundaries of Ni_3Al and Ni_3Si disappeared immediately upon the start of sputtering, indicating that the sulfur enrichment is due to equilibrium-type segregation (Takasugi *et al.*, 1985).

During the last decade, extensive efforts have been made using AES to understand the behavior of the segregation of boron into grain boundaries in Ni_3X , particularly in Ni_3Al , in relation to its ductilization effect (White *et al.*, 1984; Takasugi *et al.*, 1985; Liu *et al.*, 1985; Ogura *et al.*, 1985; White, 1986; Briant and Taub, 1988; Horton and Liu, 1990; George *et al.*, 1989, 1991a, b; Suzuki and Masahashi, 1991; Choudhury *et al.*, 1992). The solubility of boron in the matrix (i.e. the perfect lattice) of Ni_3Al was approximately

1.4 at.% (0.3 wt.%) (Sieloff *et al.*, 1987a) and the enrichment factor of boron at grain boundaries of Ni_3Al ranged between 5 and 50, depending on the bulk concentration of boron, of course, as well as on heat-treatment temperature and orientation of the grain-boundary facets (Liu *et al.*, 1985; Briant and Taub, 1988; Choudhury *et al.*, 1992). Many AES results showed that the signals of boron were removed by sputter etching of the fracture surfaces, revealing equilibrium-type segregation. The equilibrium type of segregation of boron in Ni_3Al was also demonstrated by the experimental results that the boron content at grain boundaries increased with decreasing temperature and with increasing bulk boron content, as shown in Figure 7 (Choudhury *et al.*, 1992). Based on these AES measurements, the binding energy of boron atoms to a grain boundary was estimated as 14–43 kJ mol⁻¹, depending on temperature and bulk boron content. As a result, an enthalpy of adsorption of boron to a grain boundary of 13 kJ mol⁻¹ was calculated (Choudhury *et al.*, 1992). Also, the kinetics of boron segregation to grain boundaries of Ni_3Al was evaluated based on the experimental data, as shown in Figure 8. Consequently, it was shown that the diffusion coefficients at 973 and 773 K were 10⁻¹⁶ to 10⁻¹⁷ m² s⁻¹ and 5 × 10⁻²¹ m² s⁻¹, respectively, and the activation energy for diffusion

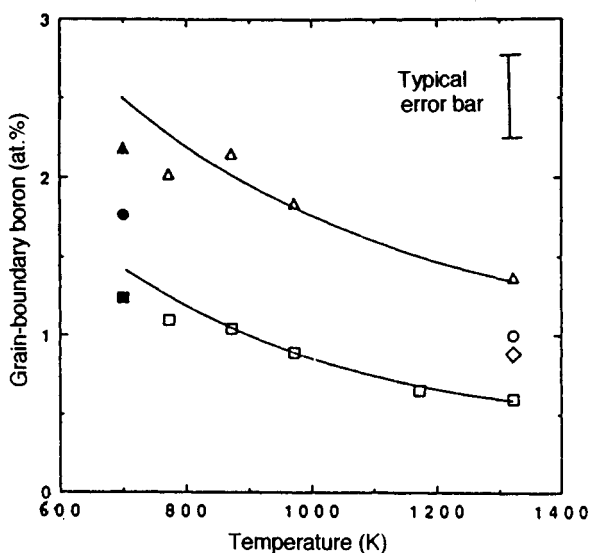


Figure 7. The equilibrium grain-boundary boron content vs. temperature. (Reprinted with permission from Choudhury *et al.*, *Acta Metall. Mater.*, **40**, 57. Copyright (1992) Pergamon Press Ltd) Bulk boron content (at. %): (□) 0.048, (◇) 0.144, (○) 0.240, and (△) 0.480; (■) 0.048, (●) 0.240, and (▲) 0.480. ■, ● and ▲ were slowly cooled

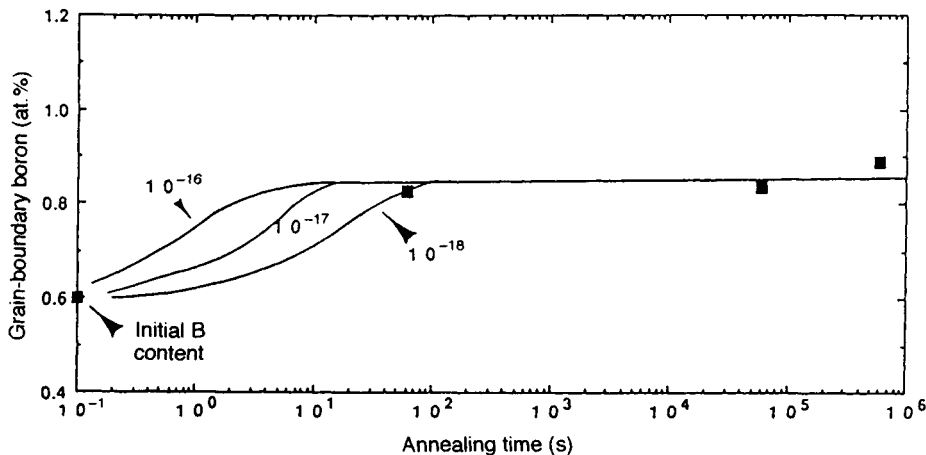


Figure 8. The variation of boron concentration on the grain boundary with annealing time at 973 K for an Ni_3Al alloy with 0.048 at.% boron (100 wt. ppm). (Reprinted with permission from Choudhury *et al.*, *Acta Metall. Mater.*, **40**, 57. Copyright (1992) Pergamon Press Ltd). Calculated curves were drawn on the assumption of three values of the diffusion coefficient

of boron in Ni_3Al was between 200 and 300 kJ mol^{-1} (Choudhury *et al.*, 1992). The diffusion coefficient and the associated activation energy for boron in Ni_3Al are considerably smaller and larger, respectively, than those for interstitial solutes in typical face-centered cubic metals (e.g. Ni, Cu, and $\gamma\text{-Fe}$). For example, the diffusion coefficient at 773 K and the associated activation energy were reported to be $4.7 \times 10^{-15} \text{ m}^2 \text{ s}^{-1}$ and 150 kJ mol^{-1} for carbon in Ni (Massaro and Petersen, 1971), $2.3 \times 10^{-3} \text{ m}^2 \text{ s}^{-1}$ and 88 kJ mol^{-1} for boron in $\gamma\text{-Fe}$ (Busby *et al.*, 1953), and $6.9 \times 10^{-15} \text{ m}^2 \text{ s}^{-1}$ and 142 kJ mol^{-1} for carbon in $\gamma\text{-Fe}$ (Ananyn *et al.*, 1970). Also, site competition between sulfur and boron at grain boundaries of Ni_3Al was detected (White *et al.*, 1984; Liu *et al.*, 1985). That is, boron has a strong tendency to segregate to grain boundaries but not to free surfaces (White *et al.*, 1984; Liu *et al.*, 1985). On the other hand, sulfur tends to segregate more strongly to free surfaces than to grain boundaries (White *et al.*, 1984; Liu *et al.*, 1985). However, more recent observation indicated no clear competition of boron with sulfur for grain-boundary sites (Briant and Taub, 1988).

The solubilities of boron in Ni_3Si and Ni_3Ge were shown to be very much lower than that in Ni_3Al (Briant and Taub, 1988). Correspondingly, the enrichment factor of boron at grain boundaries of these compounds was very large, i.e. more than 50 (Briant and Taub, 1988). Thus, the general form of behavior observed in conventional alloys, i.e. that the grain-boundary enrichment factor is proportional to the inverse of the solid solubility of the species in the

matrix (Seah and Hondros, 1973), also holds in the L_{12} -type intermetallic compounds.

The most interesting result for boron segregation obtained by AES observations is the correlation of segregation between the constituent atom, Ni (or Al), and the dopant, B. The intensity of boron segregated to grain boundaries increased, and also the amount of grain-boundary Ni increased significantly, with increasing bulk Ni (decreasing Al) concentration, as shown in Figure 9 (Liu *et al.*, 1985). On the other hand, it was demonstrated by FIM-AP (Sieloff *et al.*, 1987a, b) and TEM-EDX (Baker and Schulson, 1988; Krzanowski, 1989) observations that grain boundaries in Ni_3Al without boron had almost the bulk composition, being independent of the stoichiometry of the bulk (Sieloff *et al.*, 1987a, b). This result suggests the co-segregation of B and Ni. Thus, the alloy stoichiometry may strongly influence the segregation of the boron atoms either through its bulk concentration or through its grain-boundary concentration. However, it was recently claimed that their results may have been influenced by rapid solidification or insufficient equilibration, and may not be generally applicable. Recent observations using AES indeed showed that grain boundaries in similarly processed Ni_3Al alloys, with and without boron, were only slightly Ni-enriched relative to the bulk (George *et al.*, 1989; Suzuki and Masahashi, 1991), but by about the same amount in the two alloys, thus indicating that boron did not attract so much excess Ni to grain boundaries and also did not introduce a disordered phase at grain boundaries. More work is needed to provide a general conclusion for the

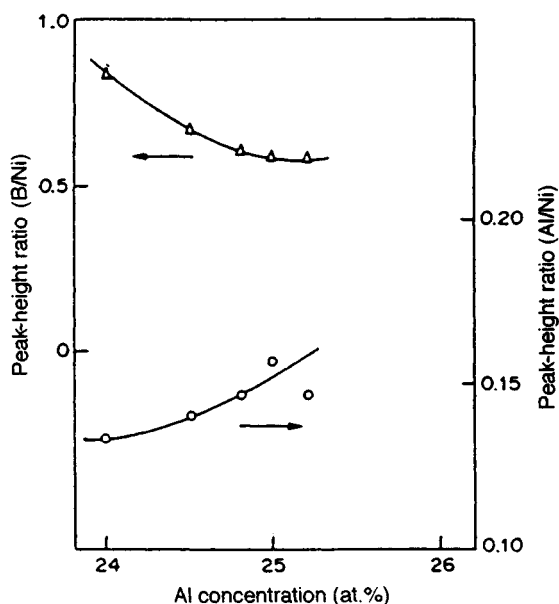


Figure 9. Variations of boron and Al concentrations with Ni (or Al) concentration at grain boundaries of $\text{Ni}_3\text{Al}-0.05 \text{ wt. \% boron}$ (Reprinted with permission from Liu *et al.*, *Acta Metall. Mater.*, 33, 213. Copyright (1985) Pergamon Press Ltd)

correlation of the segregation of boron with the alloy stoichiometry at the grain-boundary plane in these intermetallic compounds.

Boron segregation to the grain boundaries was detected in stoichiometric B2 (cP2)-type NiAl polycrystals at a bulk level of 0.12 at. % (300 wt. ppm) and was shown to suppress intergranular fracture (George and Liu, 1990). However, there was no attendant improvement in tensile ductility because boron is an extremely potent solid-solution strengthener in NiAl . Also, it was shown by the compressive test and the fracture test with chisel and hammer that boron has a tendency to segregate to the grain boundaries in stoichiometric and Al-rich B2 (cP2)-type AlRu , thereby resulting in the suppression of the intergranular brittleness (Fleischer *et al.*, 1991).

3.2 FIM-AP Observations

FIM combined with AP analysis provides a large number of results for the chemistry and for the associated grain-boundary structure of Ni_3Al with and without boron, a part of which has already been described in the previous section. Boron segregation to grain boundaries can be generally identified as the bright

images at grain boundaries and also can be quantitatively measured by AP analysis. Figures 10(a) and (b) show the FIM image and the AP result on grain boundaries of L1_2 -type $\text{Ni}_{3.19}(\text{Si}_{0.53}\text{Ti}_{0.47})_{0.81}$ containing 16 wt. ppm boron, the solid solubility of boron in which has been shown to be less than 50 wt. ppm (Takasugi *et al.*, 1990). In this case, the relative area of the grain boundary to the matrix in the probe was taken into the calculation and then a grain-boundary enrichment factor for boron ranging from 2000 to 3000 was obtained (Takasugi *et al.*, 1993). Concerning the boron segregation and the alloy stoichiometry in the matrix (or at grain boundaries), FIM-AP observation indicated that boron segregates to grain boundaries both in Ni-rich as well as in Ni-poor Ni_3Al . The co-segregation of Ni and boron to grain boundaries was difficult to ascertain because of the considerable concentration fluctuations. However, the consensus for the results obtained by FIM-AP was that there was an enrichment of Ni at least at some of the boundary planes and its zone was of the order of 2 nm wide. Careful AP examination of boundaries that are oriented perpendicular or parallel to the direction of analysis is required to get the most accurate results.

4. Interpretation of Various Property Measurements by Grain-Boundary Structure and Chemistry

It is considered likely that the grain-boundary structure and chemistry play significant roles in the various properties of many intermetallic compounds. Among these properties, during recent decades, intergranular fracture has been well-interpreted based on a number of experimental data described in the previous sections and also with help of theoretical calculation. They will be briefly discussed in the following sections and also in detail in Chapter 38 by Briant in this volume.

In early work, a large number of properties associated with the grain boundaries of many intermetallic compounds (for example, microhardness at or near grain boundaries, electrical conductivity, and corrosion behavior) have been observed to be very interesting and specific (e.g. Westbrook, 1967).

In many intermetallic compounds, including Ni_3Al , NiAl , NiGa , and AgMg , grain-boundary hardening of up to 30% relative to the matrix (the grain interior) has been detected by means of microhardness measurements and has been summarized by Westbrook (1965). The degree of hardening is generally more severe in alloys containing an excess of the more electropositive element,

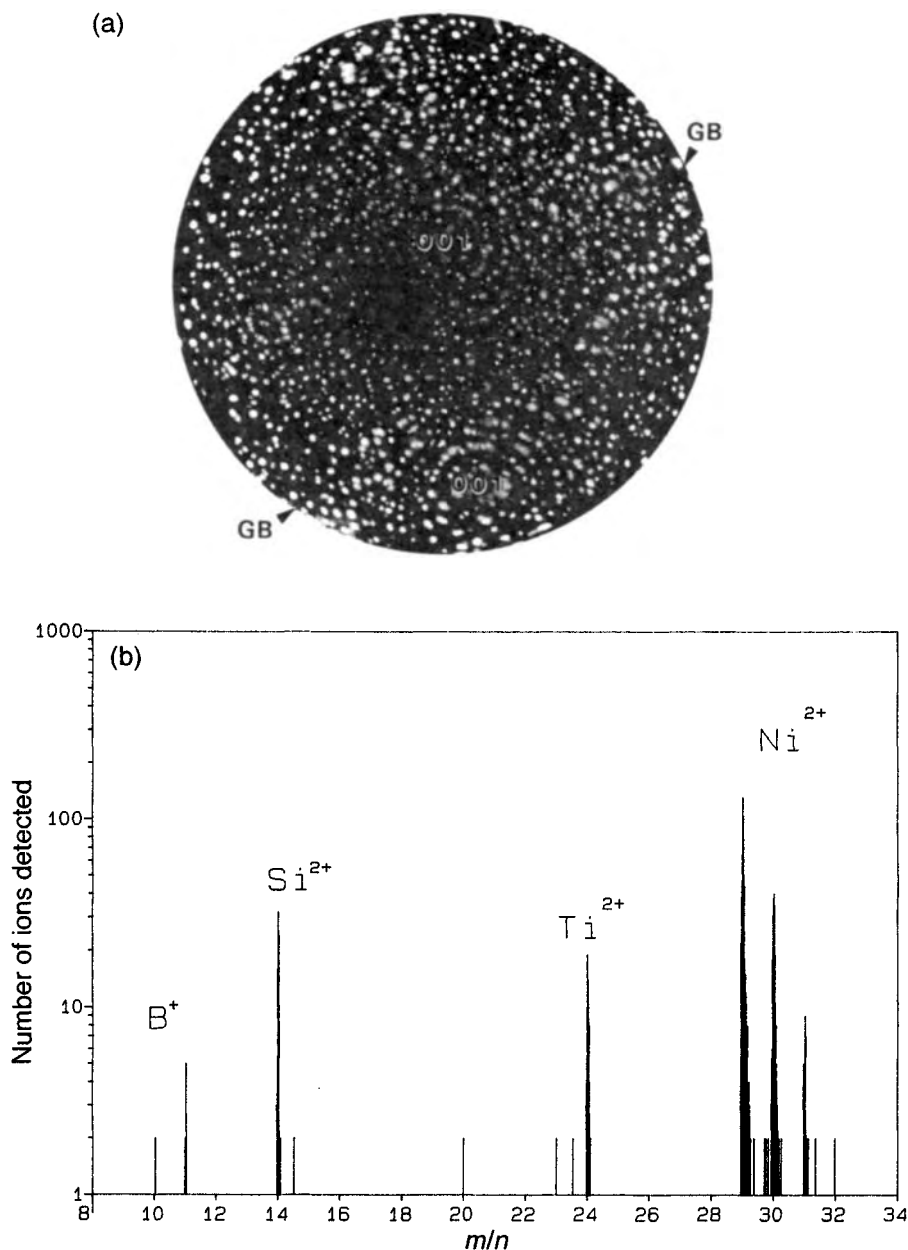


Figure 10 (a) FIM image and (b) the AP result on grain boundaries of $L1_2$ -type $Ni_{3,19}(S_{0.53}Ti_{0.47})_{0.81}$ containing 16 wt. ppm boron in the bulk (Reprinted with permission from Takasugi *et al.*, 1993)

e.g. Mg-rich AgMg, as shown in Figure 11 (Westbrook and Wood, 1963). Grain-boundary hardening has been eliminated by several means; drastic quenching treatments from above a minimum temperature (e.g. 225 °C for AgMg and 900 °C for NiGa) or, alternately,

adding third elements such as Zr to FeAl, have been successfully employed to restore ductility (Westbrook, 1965). Also, the intermetallic compounds that exhibited grain-boundary hardening underwent disintegration at intermediate temperature, the so-called 'pest effect.'

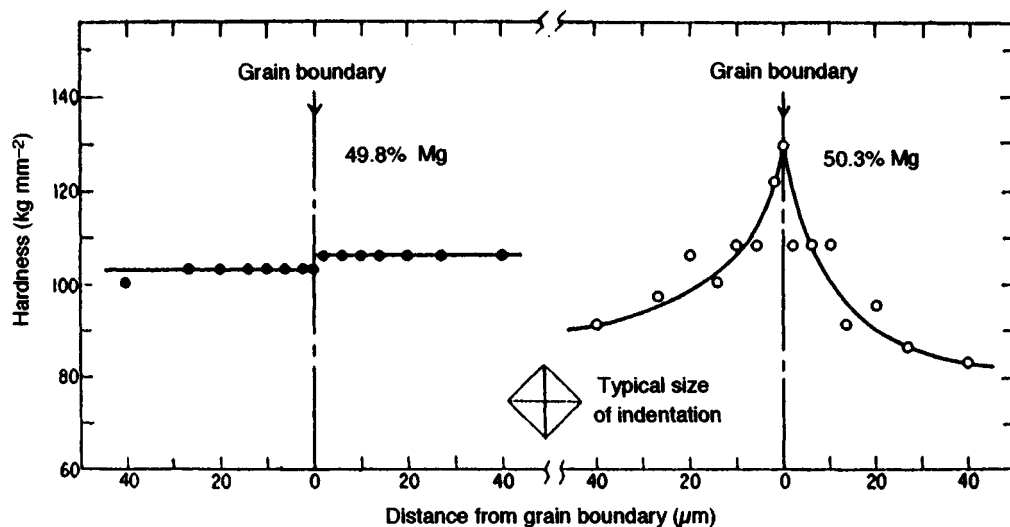


Figure 11. Grain-boundary hardening in AgMg, illustrating hardening only with a stoichiometric excess of the more electropositive element (Mg) (From Westbrook and Wood, 1963)

It was shown by several observations that there is a close correlation between the upper temperature limit for the disappearance of grain-boundary hardening and the temperature limit for the disappearance of the disintegration effect in intermetallic compounds, e.g. NiAl, MoSi₂, and ZrBe₁₃. Westbrook and Wood (1963) proposed a model based on preferential grain-boundary diffusion of a reactive gaseous element and segregation of the element in the lattice structure near the grain boundary. At intermediate temperatures harmful elements like oxygen segregated in the region near the boundary, lead to hardening and embrittlement. On the other hand, at low temperatures the oxygen diffusion from the environment is too low to penetrate to the grain boundaries. At high temperatures, because the bulk diffusion and grain-boundary diffusion rates for oxygen become comparable, hardening and embrittlement are relieved. Westbrook (1965) has demonstrated that these phenomena were associated with the impurity distribution at the grain boundaries by, for example, segregation of oxygen, nitrogen, and other impurities, or complex defects (or compounds) with vacancies (or component elements). However, direct measurements for the chemical composition of the grain boundaries of these intermetallic compounds had not been made at that time. Indeed, a recent study for polycrystalline MoSi₂ showed that 'pest' disintegration occurs through transport of oxygen into the interior of the specimen along pre-existing cracks and/or pores (grain boundaries), where it reacts to form MoO₃ and SiO₂. The internal

stress produced during the formation of MoO₃ results in disintegration to powder (McKamey *et al.*, 1992). Also, it was shown that near stoichiometry, the susceptibility to pest disintegration increases with increasing Mo content. Silicon-rich compositions did not disintegrate, nor did they form the pest oxide (MoO₃); instead, a continuous dark-gray protective oxide (SiO₂) formed on the surface. Thus, these previous experimental observations for grain-boundary hardening indicate that there is a strong correlation between grain-boundary hardening (and also the associated grain-boundary brittleness) and alloy stoichiometry and impurity atoms (such as gaseous elements or impurities at the grain-boundary planes). However, in spite of Westbrook's (1965) claims, unfortunately much time has passed without any direct observations of the structure and compositions at the grain boundaries of these intermetallic compounds. Extensive studies beyond those directed toward the boron effect on the intergranular fracture of Ni₃Al are required to solve these phenomena entirely.

Also, indirect insight into the chemistry of the grain boundaries can be obtained by referring to early work by Westbrook (1967), in which electrochemical potentials and the grain-boundary corrosion properties are affected. These results could be explained by direct observation of the chemical compositions at the grain-boundary plane. Thereby, the controlling element would be identified and also the correlation between these chemical properties and the chemistry at the grain boundary would be understood.

5. Modeling of Grain-Boundary Structures

In spite of a large number of direct observations by HRTEM, TEM, and FIM, the grain-boundary structure in intermetallic compounds is not well-understood, owing to experimental limitations, including limitations in resolution. Therefore, modeling of the grain-boundary structures and the implications deduced from such modeling become very important to the understanding of the properties of grain boundaries in intermetallic compounds, as they have been quite useful in disordered alloys. The early investigations of the structure of grain boundaries in intermetallic compounds were based on geometric and crystallographic concepts (Takasugi and Izumi, 1983, 1987; Farkas, 1985; Farkas and Rangarajan, 1987; Frost, 1987; Schapink and Tichelaar, 1988). Recently a number of atomistic modeling studies have been carried out (Chen *et al.*, 1986, 1987, 1989a, 1990; Foiles, 1987; Kruisman *et al.*, 1988; Ackland and Vitek, 1989; Vitek *et al.*, 1989; Vitek and Chen, 1991). Also, interaction of lattice dislocations with grain boundaries was studied (Pestman *et al.*, 1990, 1991).

5.1 Geometric and Crystallographic Models

A quantitative description of grain boundaries in pure metals and disordered alloys has been achieved in the framework of the coincidence-site lattice (CSL) and the O-lattice theories (Bollman, 1967; Ranganathan, 1966; Brandon *et al.*, 1964; Brandon, 1970; Grimmer *et al.*, 1974). The conclusions of these theories regarding the existence of special coincidence boundaries and the determination of possible Burgers vectors of dislocations in these boundaries have been confirmed in a number of experimental studies (Buis *et al.*, 1989; Schober and Balluffi, 1970; Schober, 1970; Bollmann *et al.*, 1972; Pond and Smith, 1977). These theories do not succeed in describing the energetics and thus the detailed atomic structure of grain boundaries. On the other hand, computer simulation permits the minimization of the energy of an assembly of a large number of atoms and therefore gives a stable structure in the grain-boundary region. However, this limitation does not diminish the significance of the application of CSL and O-lattice theories to grain boundaries of intermetallic compounds. The CSL theory can give physical and geometrical meaning to the results obtained and has the possibility of showing any crystallographic nature that might be unique in grain boundaries of intermetallic compounds. Also, the favored configuration of the grain boundary as determined by the CSL theory can give us a model

of the periodic boundary, which will be used in computer calculations in order to accommodate atoms.

The CSL grain-boundary structures of the A_3B $L1_2$ -type and the AB $B2$ -type intermetallic compounds have been considered for two extreme cases of geometry, i.e. the tilt boundary (Takasugi and Izumi, 1983) and the twist boundary (Takasugi and Izumi, 1987). Considerations of symmetry in the lattice and of the geometric degrees of freedom in the grain boundary generally require two 'macroscopic' parameters and two 'microscopic' parameters to describe grain boundaries. The former are the 'relative orientation' and the 'grain-boundary inclination', while the latter are the 'relative translation' and the 'position of the grain boundary,' associated with the atomic 'core' structure of grain boundaries. First, the 'relative translation' parameter yields two different types of configurations for the CSL grain boundary in the case of a pure tilt misorientation. One is a fully symmetrical configuration and the other is a pseudosymmetrical configuration. The parameter describing the 'position of the grain boundary' similarly yields several configurations, and then produces different atomic compositions of A and B atoms at the grain-boundary plane. As an example, Figure 12 shows eight configurations deduced for the $\Sigma=5$, 53.13° tilt boundary with $[100]$ rotation axis of an A_3B $L1_2$ -type intermetallic compound. In this case, it was shown that there are two types of configuration (i.e. type S and type PS) about the 'relative translation' and also two types of configurations (i.e. type II and type III) about the 'position of grain boundary.' For the former type configuration, type S is the fully symmetrical configuration, where the sublattices in one half of the crystal are really symmetrical to the sublattices in the other, forming with the same kind of atoms as each other; while type PS is the pseudosymmetrical configuration, where one of the three sublattices forming the A atoms in one half of the crystal is symmetrical to the sublattice forming the B atoms in the other half. For the latter type configurations, type II consists of the plane where A atoms and B atoms are evenly distributed; while type III consists of the plane where the lattice positions are all occupied by A atoms.

Thus, geometrical consideration of the grain-boundary structures of intermetallic compounds reveals the possibility of the existence of variants for the atomic configurations if their energies are not too different. Indeed, TEM observations for twin boundaries of $L1_2$ -type Cu_3Au indicated the existence of variants of the atomic configuration at grain boundaries (Tichelaar and Schapink, 1986, 1988), as described in an earlier section. From these analyses, it was also deduced that

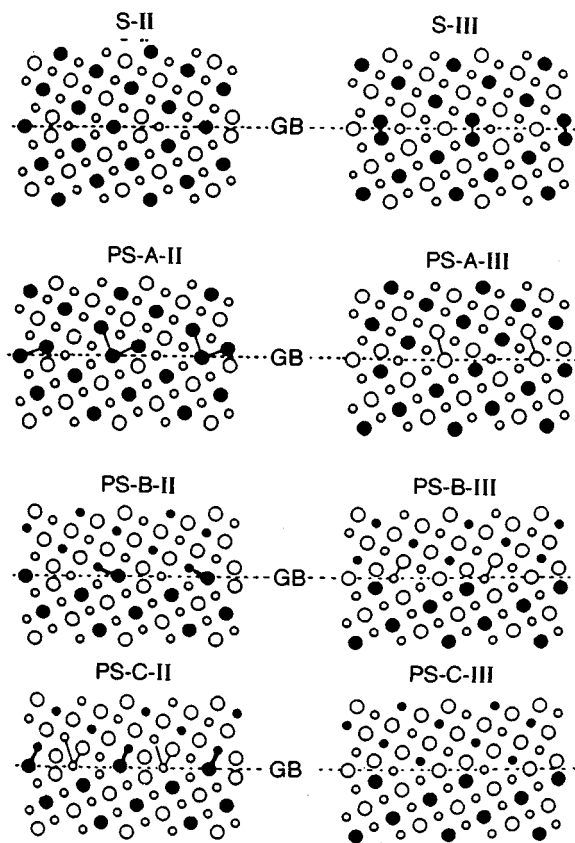


Figure 12. Eight atomic configurations constructed on the $\Sigma = 5$, 53.13° tilt boundary with a $[100]$ rotation axis as an example of the A_3B $L1_2$ -type intermetallic compounds (Reprinted with permission from Takasugi and Izumi, *Acta Metall.*, 31, 1987. Copyright (1983) Pergamon Press Ltd. Note that large and small circles represent atoms distributed on the first (100) atomic plane and the second (100) atomic plane, respectively. Also, open and full symbols correspond to A atoms and B atoms, respectively. The linkages shown are wrong-atom pairs between two atoms

the number of configurations created depends upon the type of crystal structure, rotation axis, and misorientation. Thus, the existence of different ordering configurations at grain boundaries may create different chemistry- and structure-related properties even for the same grain-boundary facet. Also, it was predicted that, if the chemical ordering is dominant, i.e. unless wrong bonds are permitted at grain boundaries, distinct columnar cavities will occur in grain boundaries owing to the depleted bond pairs or undistorted but mis-oriented lattices meeting at the grain-boundary plane. This prediction agrees with direct observation of grain

boundaries of an $L1_2$ -type $Ni_3(Al,Ti)$ compound (Figure 1) (Sasaki *et al.*, 1990), as described in an earlier section.

In the grain-boundary region of intermetallic compounds, proper bonds with unlike atoms may sometimes not be conserved or can be distorted; also, wrong bonds between like atoms may be introduced, although energetic requirements dictate that these defects are minimal. Thus, grain boundaries in intermetallic compounds may involve the incidence of bond defects in addition to lattice distortion. Geometrical analysis gave good insight into this problem (Takasugi and Izumi, 1983, 1987). Wrong pair bonds across the boundary were usually recognized in these geometrical analyses. For example, the wrong bonds are visualized by the full lines between the two atoms in Figure 12. Depending on the portion of the two types of wrong pair bonds, A-A and B-B pairs, three types of faults were defined in analogy with the planar faults in the perfect lattice of the ordered structure. These are the antiphase boundary (APB) fault, the stacking fault (SF), and the complex stacking fault (CSF). For example, in Figure 12, the S-II and PS-C-III configurations did not contain any planar faults. On the other hand, the S-III, PS-A-II, PS-A-III, PS-B-II, and PS-B-III configurations contained a SF, and the PS-C-II configuration contained an APB. Thus, the existence of different near-neighbor bonds at the grain boundary may produce different electrochemically related properties. The excess energies of the different configurations due to the wrong bonds were estimated by counting the wrong pair bonds across the grain boundary (Takasugi and Izumi, 1983, 1987). It was shown that:

- The excess energy does not systematically depend on the misorientation (or the value of Σ).
- The excess energy usually depends on the type of configuration, and the excess energy differences between these types become less in the high-angle (general) boundaries, suggestive of multiple structures with nearly the same energy.
- The excess energy in grain boundaries of the A_3B $L1_2$ structure, reflecting a large anisotropy of the APB energy on several crystallographic planes in the perfect lattice, shows widely different values relative to those of the AB B2 structure.

An extended analysis of geometrical considerations for grain boundaries in ordered structures has been carried out by Frost (1987). The variations for different configurations in atomistically flat or stepped grain-boundary planes in the $L1_2$ structure were discussed, and again the possible ordering configurations were

presented (Frost, 1987). A more sophisticated geometrical crystallographical method, in which a modified hard-sphere model and CSL theory were involved, was used to analyze possible configurations in the $L1_2$ -type intermetallic compounds (Farkas and Rangarajan, 1987). Two distinctly different intermetallic compounds, i.e. Cu_3Au and Ni_3Al , were analyzed. For the weakly ordered alloy, Cu_3Au , consisting of atoms of similar size, the grain-boundary structures obtained were similar to those reported for pure f.c.c. metals like the constituent Cu atoms. However, for the strongly ordered alloy, Ni_3Al , consisting of atoms of different sizes, the configurations of grain boundaries that are most dense were found to be generally different from, and less dense than, those in pure f.c.c. metals and Cu_3Au . Based on these facts, it was demonstrated that the segregation of elements of smaller size would be strongly favored. In both intermetallic compounds, several boundaries were found to present two possible structures, thus suggesting the existence of variants of the atomic configurations at the grain boundary.

Geometrical analysis in the frame of the CSL theory also indicated that the possible atomic structure in $L1_2$ -ordered alloys can be generally altered by interface dislocations with DSC^o or DSC^d vectors as Burgers vectors (where DSC^o or DSC^d vectors are ordered or disordered DSC vectors, respectively) (Schapink and Tichelaar, 1988). For example, for the $\Sigma = 5$ (1 3 0) tilt boundary, the shortest DSC^o parallel to the (1 3 0) boundary plane was given by $\frac{1}{2}$ [3 1 0]. Indeed, these interfacial dislocations were observed to exist in the Cu_3Au alloy in agreement with theory (Tichelaar and Schapink, 1992). Thus, it was demonstrated that a step in the boundary is associated with an interfacial glide dislocation and also that larger steps in the boundary can only occur for such dislocations if additional shuffling of atoms occurs (Schapink and Tichelaar, 1988).

5.2 Computed Atomic Models

Most of the calculations of atomic structure of grain boundaries in intermetallic compounds have been made on the $L1_2$ structure, using pair potentials (Kruisman *et al.*, 1988), local-volume potentials (Chen *et al.*, 1989a; Pestman *et al.*, 1991), and N -body potentials (Ackland and Vitek, 1990). These potentials were all empirical and were fitted to reproduce the properties of the alloys studied. The major interests of these calculations have been directed toward the compositional effect, such as

the selection of component elements (i.e. dependence on alloy system), the stoichiometric effect, and the alloying effect in crystallographically identical boundaries, rather than the misorientation dependence.

Previous hard-sphere models indicated that the difference in size between the constituent atoms and in the associated ordering energy is a significant factor controlling the grain-boundary structure of $L1_2$ alloys (Farkas and Rangarajan, 1987). Quite a similar result was obtained by computer calculation (Ackland and Vitek, 1989). Grain boundaries of pure f.c.c. metals and of $L1_2$ alloys with low and high ordering energies were calculated using N -body potentials (Ackland and Vitek, 1990; Ackland *et al.*, 1987; Vitek *et al.*, 1991). As alloys with low and high ordering energies, Cu_3Au and Ni_3Al were calculated as examples. Figure 13(a), (b), and (c) show the structures of the $\Sigma = 5$ (3 1 0)[0 0 1] symmetrical tilt boundaries in pure Cu, Cu_3Au , and Ni_3Al alloys, respectively (Ackland and Vitek, 1989). Figure 13(a) shows the energetically most favorable structure in Cu, being practically the same as that found in Ni. In Cu_3Au and, of course, in Cu and Ni, the relaxation of atoms in the boundary region is substantial, and the atoms in the boundary region cannot be uniquely assigned to either one grain or the other. On the other hand, in Ni_3Al , all atoms can be regarded as uniquely attached to either one or the other grain, so that the ideal $L1_2$ structure is practically undisturbed on either side of the boundary up to the boundary plane. This structural difference was attributed to a distinct difference in ordering energy: in the case of the strongly ordered alloy (Ni_3Al), the chemical order is the principal controlling factor of the energy of the system; while in the case of the weakly ordered alloy (Cu_3Au) and also for pure f.c.c. metals, a more relaxed grain-boundary structure with a possible chemical disordering is energetically favored. Also, it was demonstrated that the results shown in Figure 13 are applicable to other [0 0 1] symmetrical tilt boundaries. Calculations for still other tilt and twist boundaries reveal their general validity (Ackland and Vitek, 1989). Indeed, the HRTEM observation on $\text{Ni}_3(\text{Al}, \text{Ti})$ alloy described in an earlier section suggested that there was little relaxation of atoms, and the atoms in the grain-boundary region persisted in the ideal ordered structure by removing wrong bonds and also by preserving right bonds (Sasaki *et al.*, 1990).

Concerning the stoichiometric effect on the grain-boundary structures of A_3B $L1_2$ alloys with high ordering energy, the symmetrical $\Sigma = 5$ (3 1 0)[0 0 1] and (2 1 0)[0 0 1] tilt boundaries and other CSL boundaries were studied in detail using appropriate pair

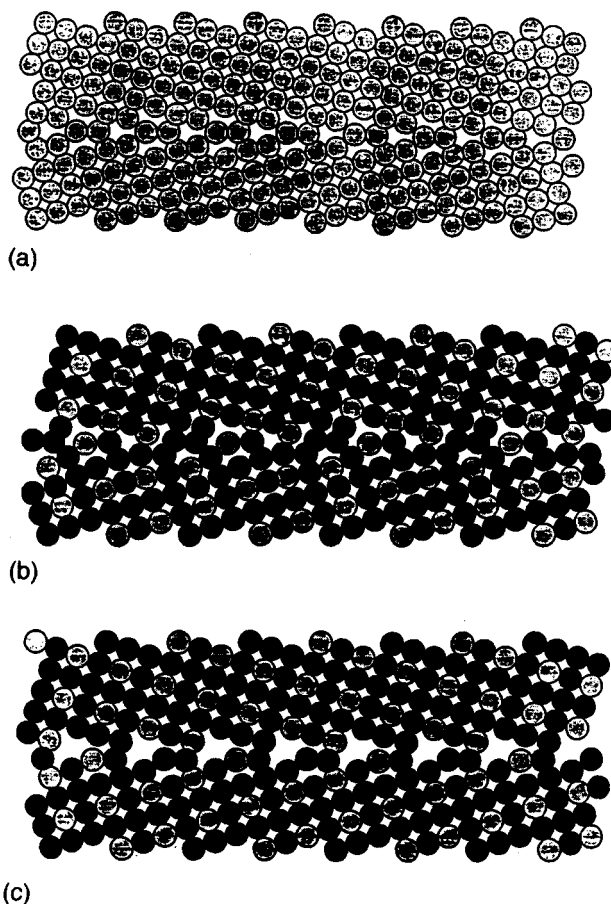


Figure 13. Structures of the $\Sigma=5$ $(3\ 1\ 0)[0\ 0\ 1]$ symmetrical tilt boundaries in (a) pure Cu, (b) Cu_3Au , and (c) Ni_3Al alloys, respectively (Reproduced with permission from Ackland and Vitek, 1989)

potentials (Kruisman *et al.*, 1988). Figures 14, 15 and 16 show the relaxed atomic structures at grain boundaries in compounds with stoichiometric composition, with A-atom-rich composition, and with A-atom-poor composition, respectively. Here, in Figure 15 a surplus of two A atoms was added per period and in Figure 16 two A atoms were removed per period. Calculations showed that the concept of structural units, originally developed for pure metals (Sutton and Vitek, 1983; Sutton, 1984; Wang *et al.*, 1984), was still applicable to the grain-boundary structure of ordered alloys, i.e. intermetallic compounds. These figures clearly indicate that the structural units in the stoichiometric boundaries were more distorted than those of either A-atom or B-atom-rich boundaries. Thus, away from stoichiometry the structures resemble more closely the corresponding structures in single-

component systems. Consequently, the structural changes associated with the deviation from stoichiometry toward Ni-rich compositions can explain the fact that the ductilization of Ni_3Al was observed in Ni-rich compositions, but cannot explain the fact that the same effect was not observed in Ni-poor compositions. Energetic considerations for the segregation of surplus atoms to the grain boundaries of Ni_3Al answered this inconsistency; Ni enrichment at the grain boundary can be reached without any significant difficulty, while this is not the case for Al enrichment at the grain boundaries (Kruisman *et al.*, 1988). Also, it has been shown, in fact, that Al-rich grain boundaries have higher energy (Chen *et al.*, 1986, 1987, 1989a, 1990). Furthermore, extended calculations for other types of grain boundaries (i.e. other CSL boundaries) showed that the multiplicity of the grain-boundary structure types was much more

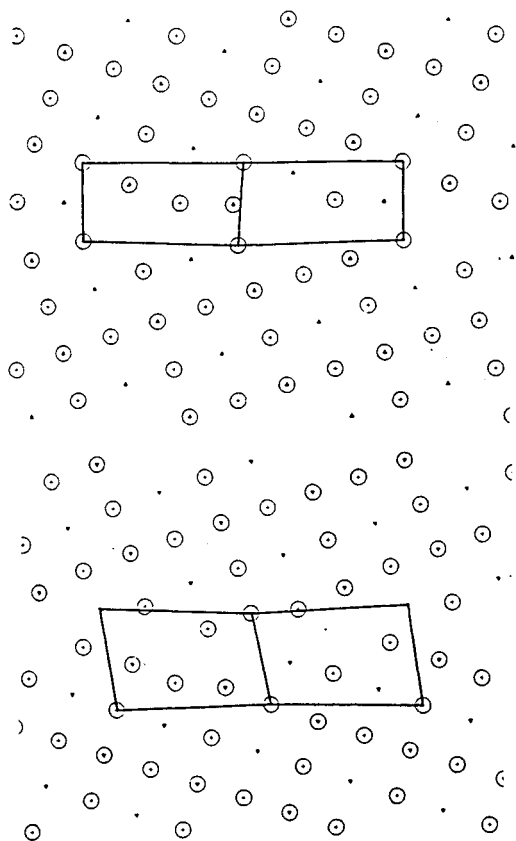


Figure 14. $\Sigma = 5$ (3 1 0) boundary structures in $A_3B L_{12}$ with stoichiometric composition. Two structures with nearly equal energy are shown (Reprinted with permission from Kruisman *et al.*, *Acta Metall.*, **36**, 2729. Copyright (1968) Pergamon Press Ltd)

extensive compared to pure metals. This was attributed to the fact that the grain-boundary structures of ordered alloys differ not only topologically but also compositionally (Kruisman *et al.*, 1988), as has already been predicted from geometrical analysis of intermetallic compounds.

The effects of boron doping on the grain-boundary structures and energies of L_{12} -type Ni_3Al alloys have been calculated using appropriate potentials (Chen *et al.*, 1989a, b, c, 1990), the fitting of which has been done by linear muffin-tin orbital (LMTO)-based quantum calculations for a number of Ni-B and Al-B compounds and f.c.c. boron. In Ni-rich alloys the segregation energy was 13 kJ mol^{-1} , and thus Ni segregation is favored, though not very strongly. However, when boron is present in grain boundaries, the segregation energy of Ni was found to be 44 kJ mol^{-1} , showing the enhanced

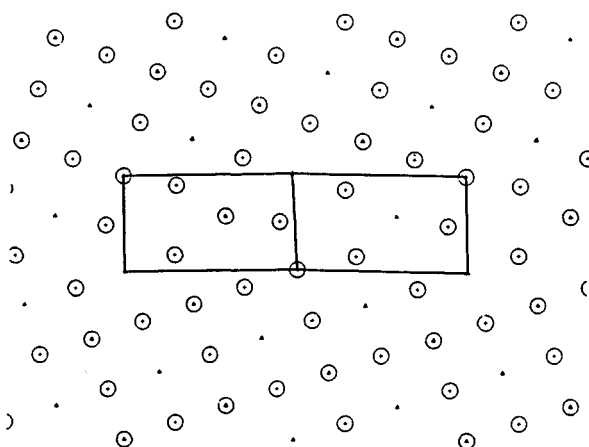


Figure 15 $\Sigma = 5$ (3 1 0) boundary structures in $A_3B L_{12}$ with a surplus of two A atoms per period relative to the stoichiometric composition (Reprinted with permission from Kruisman *et al.*, *Acta Metall.*, **36**, 2729. Copyright (1988) Pergamon Press Ltd)

segregation propensity. The fracture strength of boundaries that consist of various compositions involving surplus of Ni or Al and boron in interstitial sites was calculated, with the results shown in Figure 17, where the maximum stress needed to break a bicrystal consisting of a $\Sigma = 5$ (2 1 0) symmetrical tilt boundary is plotted for various chemical compositions of the grain boundaries. The stress was the highest in the case of the Ni-rich boundary with boron and the

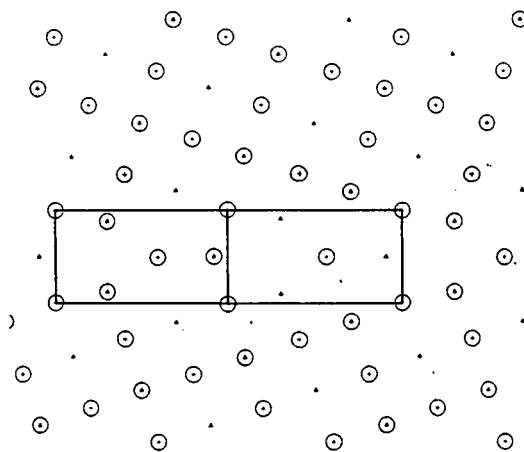


Figure 16. $\Sigma = 5$ (3 1 0) boundary structures in $A_3B L_{12}$ with a deficit of two A atoms per period relative to the stoichiometric composition (Reprinted with permission from Kruisman *et al.*, *Acta Metall.*, **36**, 2729. Copyright (1988) Pergamon Press Ltd)

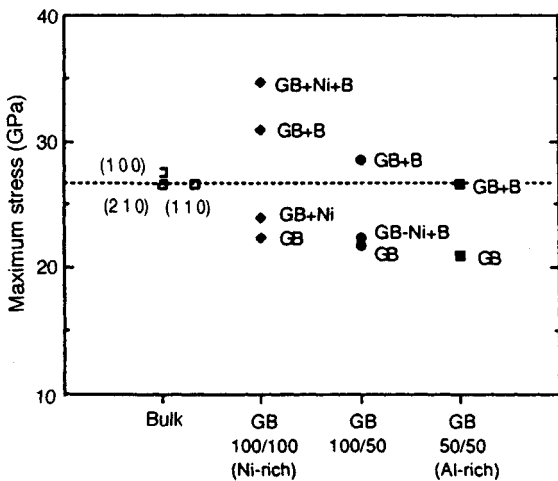


Figure 17. Maximum stress needed to break a bicrystal of Ni_3Al consisting of a $\Sigma = 5$ (2 1 0) symmetrical tilt boundary plotted for various chemical compositions of the grain boundary (Reproduced with permission from Chen *et al.*, 1990). The chemical compositions at the grain boundary are denoted as (1 0 0/1 0 0) or Ni-rich when both sides of the grain boundary comprise 100% Ni layers. The other two cases are denoted as (1 0 0/5 0) or stoichiometric, and (5 0/5 0) or Al-rich

lowest in the case of the Al-rich boundary without boron. It was thus suggested that Al-rich grain boundaries are more likely to fail than those which have the stoichiometric composition or the constituent Ni or Al metals. Also, substitutional sulfur was shown to be a very deleterious element in reducing the fracture stress (Chen *et al.*, 1989a).

Thus, several principal grain-boundary structures and their properties in L1_2 -type intermetallic compounds are recognized from these computer simulations:

- The grain-boundary structures with least energy are not necessarily similar to those of the corresponding boundaries in pure f.c.c. metals.
- Variants with different ordering configurations exist in ordered alloys and are much more extensive than those in disordered alloys.
- The structure and energy of grain boundaries are very much affected by the stoichiometry of the component atoms and by the addition of interstitial atoms.

Few calculations have been done for grain-boundary structures and energies in intermetallic compounds with other than L1_2 crystal structures. Only one example is presented: the grain-boundary structures of B2-type NiAl were calculated using many-body potentials (Chen *et al.*, 1989b, c). $\Sigma = 5$ (2 1 0) and (3 1 0) symmetrical tilt

boundaries were studied in terms of the stoichiometric effect and the boron doping effect. Calculation showed that both Ni-rich and Al-rich compositions led to grain-boundary vacancies, thereby resulting in columnar cavities, while the stoichiometric composition was more homogeneous and less distorted. Also, it was shown that segregated boron appears to decrease the intergranular cohesion and therefore does not have a beneficial effect on the ductility. However, the experimental result is somewhat different from this prediction: when boron is added to stoichiometric NiAl , such that a sufficient amount of boron segregates to the grain boundaries without introducing significant solid-solution hardening, then grain-boundary fracturing was suppressed (George and Liu, 1990). This experimental result showed that boron in NiAl behaves in a similar way, i.e. has the same beneficial effect as in Ni_3Al .

Using many-body potentials representing an L1_2 -ordered alloy with low ordering energy (i.e. Cu_3Au) and high ordering energy (i.e. Ni_3Al), the interactions (e.g. absorption, attraction, and transmission) between $\frac{1}{2}\langle 110 \rangle$ screw dislocations and grain boundaries with symmetric [1 1 0] tilt boundaries were calculated under an applied shear stress or with no applied shear stress (Pestman *et al.*, 1991). It was shown that transmission of the dislocation through the boundary occurs at high stress levels, and the superpartials constituting the arriving dislocation decrease their separation in response to the applied stress, thus creating a higher stress concentration near the grain boundary than that in disordered alloys (Pestman *et al.*, 1991).

6. Electronic Bonding Aspects

The chemical bonding nature and the corresponding electronic structure in grain boundaries, which are primarily associated with their crystal structure and chemical composition, strongly affect not only grain-boundary properties but also bulk properties. Some arguments for the chemical bonding and the electronic structures in grain boundaries of intermetallic compounds have been made in relation to the intrinsically brittle/ductile properties of L1_2 alloys. Since a detailed discussion of this subject will be given in the chapter by Briant in this volume, in this section only a brief description is given.

A first qualitative consideration was based on geometrically constructed grain boundaries with the L1_2 structure and some principal features were demonstrated (Izumi and Takasugi, 1987). In a strongly ordered A_3B L1_2 alloy involving the contribution of

strong covalent bonds, the bond may be characterized by the 'directionality' and the 'heteropolarity' of the electronic charge distribution. From the point of view of the 'directionality' (Gelatt *et al.*, 1983; Miedema, 1976; Shao and Machlin, 1983; Losh, 1979), A-B bonds (i.e. covalent bonds) prefer to be at a 90° angle, for which the non-central contribution to the energy of formation is at a minimum (i.e. most stable). It seems unlikely that, across a grain boundary, the angle between A-B bonds from a given B atom will always be close to the desired 90° value. This situation is schematically shown in Figure 18, where the atomic configuration and bond nature in a geometrically constructed $\Sigma=5$ CSL boundary with $[100]$ axis is drawn. Thus, A-B covalent bonds perpendicular to the grain-boundary plane, which are supposed to sustain the grain-boundary cohesion, should be limited, resulting in a lower grain-boundary cohesion. Next, from the point of view of the 'heteropolarity,' the B atom withdraws electron density from the A-A (metal-metal) bonds and forms ionic A(metal)-B bonds. It was then demonstrated that the reduction of charge density in A-A bonds results in reduction of the grain-boundary cohesive strength. Thus, the 'heteropolarity' of electron charge density due to A-B bonds at the boundary plane introduces something like a penny-shaped cavity into the locality. This idea originally stems from the mechanism by which grain-boundary brittleness has been proposed to arise in a grain boundary to which impurity atoms are segregated (Losh, 1979; Briant and Messmer, 1980; Messmer and Briant, 1980; Hashimoto *et al.*, 1984a,b; Wakeyama *et al.*, 1984). Consequently, the valency difference and the electronegativity criterion can generally be justified as measures of transfer of electrons between constituent

atoms and thus as predictors of grain-boundary brittleness. When the valency difference between A and B atoms is larger (or component atom B is more electronegative with respect to the other component, atom A), B atoms have a greater tendency to pull electron charge out of A-A bonds. Based on this concept, it was demonstrated that alloying effects (such as component atoms, stoichiometry, addition of substitutional atoms, and the doping of boron) on the grain-boundary strength (and resultant fracture) of $L1_2$ -ordered A_3B intermetallic compounds can be interpreted by the electronic modification of the electronic structure and atomic bonds through compositional modification at the grain boundary (Izumi and Takasugi, 1987, 1988; Takasugi and Izumi, 1988).

Some attempts to understand the electronic nature of the grain boundary have recently been performed based on theoretical calculations (Chen *et al.*, 1986; Eberhart and Vvedenski, 1986; Masuda-Jindo, 1988). Cluster calculation of the density of states was done for $L1_2$ -ordered A_3B intermetallic compounds (Eberhart and Vvedenski, 1986); Figure 19 shows the density of states calculated for crystals in the bulk and polyhedra at a grain boundary in Ni_3Si and Cu_3Pd alloys. For brittle Ni_3Si , there was a markedly enhanced hybridization with s orbitals on both Si and Ni throughout the bands for the grain-boundary structure of Ni_3Si (Figure 19(a)). However, for Cu_3Pd , which is ductile, the grain-boundary polyhedron developed directional Pd levels above the Fermi energy, in contrast to the diffuse sp levels of the parent crystal. Evidently, the grain boundaries of Cu_3Pd are better able to accommodate the bond misorientation (i.e. bond directionality) concomitant with grain-boundary structure than are those of Ni_3Al and Ni_3Si . Based on this calculation, the relative s-orbital electronegativity of the constituent atoms was predicted to provide a reliable indication of the grain-boundary cohesion, being consistent with experimental data.

7. Summary

In this chapter, the structures of grain boundaries of intermetallic compounds observed by transmission electron microscopy (TEM), high-resolution transmission electron microscopy (HRTEM), and field ion microscopy (FIM) were presented. Of these direct observations, the HRTEM technique especially provided very significant information: for example, preservation of the ordering close to the boundary plane, preservation of the chemical ordering without significant local atomic

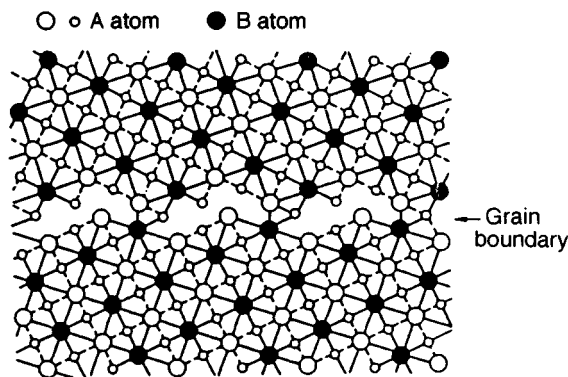


Figure 18. Schematic representation of the bond pairs at a grain boundary of the A_3B $L1_2$ alloy (Reproduced with permission from Izumi and Takasugi, 1987)

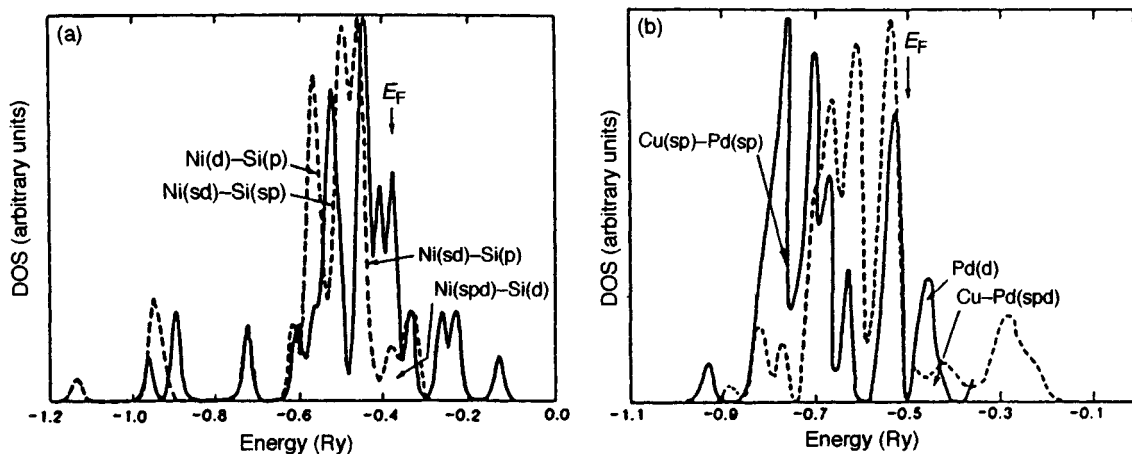


Figure 19. Density of states (DOS) calculated for crystals in the bulk (----) and polyhedron at a grain boundary (—) in (a) Ni_3Si and (b) Cu_3Pd alloys, respectively (Reproduced by permission of the American Physical Society from Eberhart and Vvedenski, 1986)

accommodation, and the existence of variants of the atomic configurations. Next, the chemistry of grain boundaries of intermetallic compounds observed by Auger electron spectroscopy (AES), TEM combined with energy-dispersive X-ray technique (TEM-EDX), and FIM combined with atom-probe method (FIM-AP) were presented. Among these direct measurements, AES and FIM-AP techniques provided very distinct results, e.g. for the interrelation between alloy stoichiometry and doping atoms such as boron. Then geometrical and atomistic computer models for the structure of grain boundaries of intermetallic compounds were presented. These models predicted that variants exist, i.e. a multiplicity of possible atomic configurations, and also established that the grain-boundary strength and the associated brittleness depend on the ordering energy, alloy stoichiometry, and the doping with interstitials. Finally, the nature of the chemical bonds and the associated electronic structure were discussed in relation to the atomistic structure and the composition of grain boundaries.

Understanding of grain-boundary structures in intermetallic compounds has progressed much since the early 1980s. This progress is due to some exciting findings, particularly that Ni_3Al , which has high potential as a high-temperature structural material, was ductilized by boron doping. These findings stimulated many researchers. Not only experimental work but also basic theoretical approaches were required to understand the associated mechanism. However, a number of

problems still remain unresolved and therefore many more studies are needed before well-founded conclusions can emerge. Particularly, the electronic structures in grain boundaries of intermetallic compounds must be studied. Thus far, studies of grain boundaries of intermetallic compounds have been limited to the L_{12} (cP4) structure. A number of other types of intermetallic compounds have their own attractive properties, for which more general grain-boundary information is needed.

It is well-known that the antiphase boundaries (APBs) in intermetallic compounds affect many material properties, such as the dislocation structures, the associated plastic deformation, and microstructures of many intermetallic compounds. APBs are two-dimensional defects, i.e. intercrystalline interfaces similar to grain boundaries. Therefore, the phenomenology of APBs has many parallels with that of grain boundaries. The structure and chemistry of APBs are discussed in Chapter 21 by Sun in this volume.

A significant body of work from both experimental and theoretical points of view has been done on grain boundaries in covalently bonded III-V and II-VI compounds, the structure and the associated electronic structures of which strongly affect electronic properties of devices. Specific grain-boundary structures have been observed by the HRTEM technique, and also a number of sophisticated methods of calculation have been provided to determine structural and electronic properties. However, a detailed description is beyond the scope of this chapter.

8. References

- Ackland, G. J., and Vitek, V. (1989). *Mater. Res. Soc. Symp. Proc.*, **133**, 105.
- Ackland, G. J., and Vitek, V. (1990). *Phys. Rev.*, **B41**, 10324.
- Ackland, G. J., Tichy, G., Vitek, V., and Finnis, M. W. (1987). *Phil. Mag.*, **A56**, 735.
- Ananyin, V. M., Glakov, V. P., Zotov, V. P., and Skorov, D. M. (1970). *At. Energy*, **29**, 220.
- Antonopoulos, J. G., Schapink, F. W., and Tichelaar, F. D. (1990). *Phil. Mag. Lett.*, **61**, 195.
- Aoki, A., and Izumi, O. (1979). *J. Japan Inst. Metals*, **45**, 1190.
- Baker, I., and Schulson, E. M. (1988). *Phil. Mag.*, **B57**, 379.
- Baker, I., Schulson, E. M., Michael, J. R., and Pennycook, S. J. (1990). *Phil. Mag.*, **B62**, 659.
- Balluffi, R. W., Komem, Y., and Schober, T. (1972). *Surf. Sci.*, **31**, 68.
- Bollmann, W. (1967). *Phil. Mag.*, **16**, 363, 383.
- Bollmann, W., Michaut, B., and Sainfort, G. (1972). *Phys. Status Solidi*, **A13**, 637.
- Brandon, D. G. (1970). *Crystal Defects and Crystalline Interfaces*. Springer, Berlin.
- Brandon, D. G., Ralph, B., Ranganathan, S., and Wald, M. S. (1964). *Acta Metall.*, **12**, 813.
- Brenner, S. S., and Hua, M.-J. (1990a). *Scripta Metall. Mater.*, **24**, 667.
- Brenner, S. S., and Hua, M.-J. (1990b). *Scripta Metall. Mater.*, **24**, 671.
- Brenner, S. S., and Hua, M.-J. (1991). *Scripta Metall. Mater.*, **25**, 1271.
- Brenner, S. S., Sieloff, D., and Burke, M. G. (1986). *J. Physique*, **47**, C2, 215.
- Briant, C. L., and Messmer, R. P. (1980). *Phil. Mag.*, **B42**, 569.
- Briant, C. L., and Taub, A. I. (1988). *Acta Metall.*, **36**, 2761.
- Buis, A., Tichelaar, F. D., and Schapink, F. W. (1989). *Phil. Mag.*, **A59**, 861.
- Buis, A., Tichelaar, F. D., and Schapink, F. W. (1991). In *Structure and Property Relationships for Interface* (eds J. L. Walter, A. H. King, and K. Tangri). ASM International, pp. 97–119.
- Busby, P. E., Wargu, M. E., and Wells, C. (1953). *J. Metals*, **5**, 1463.
- Chadwick, G. A., and Smith, D. A. (1976). *Grain Boundary Structure and Properties*. Academic Press, London.
- Chen, S. P., Voter, A. F., and Srolovitz, D. J. (1986). *Scripta Metall.*, **20**, 1389.
- Chen, S. P., Voter, A. F., and Srolovitz, D. J. (1987). *Mater. Res. Soc. Symp. Proc.*, **81**, 45.
- Chen, S. P., Srolovitz, D. J., and Voter, A. F. (1989a). *J. Mater. Res.*, **4**, 62.
- Chen, S. P., Voter, A. F., Albers, R. C., Boring, A. M., and Hay, P. J. (1989b). *Scripta Metall.*, **23**, 217.
- Chen, S. P., Voter, A. F., Albers, R. C., Boring, A. M., and Hay, P. J. (1989c). *Mater. Res. Soc. Symp. Proc.*, **133**, 149.
- Chen, S. P., Voter, A. F., Albers, R. C., Boring, A. M., and Hay, P. J. (1990). *J. Mater. Res.*, **5**, 955.
- Choudhury, A., White, C. L., and Brooks, C. (1992). *Acta Metall. Mater.*, **40**, 57.
- Eberhart, M. E., and Vvedenski, D. D. (1986). *Phys. Rev. Lett.*, **58**, 61.
- Farkas, D. (1985). *Scripta Metall.*, **19**, 467.
- Farkas, D., and Rangarajan, V. (1987). *Acta Metall.*, **35**, 353.
- Fleischer, R. L., Field, R. D., and Briant, C. L. (1991). *Metall. Trans.*, **22A**, 403.
- Foiles, S. M. (1987). *Mater. Res. Soc. Symp. Proc.*, **81**, 51.
- Frost, H. J. (1987). *Acta Metall.*, **35**, 519.
- Gelatt, C. D., Jr, Williams, A. R., and Moruzzi, V. L. (1983). *Phys. Rev.*, **B27**, 2005.
- George, E. P., and Liu, C. T. (1990). *J. Mater. Res.*, **5**, 754.
- George, E. P., Liu, C. T., and Padgett, R. A. (1989). *Scripta Metall.*, **23**, 979.
- George, E. P., Liu, C. T., and Liao, J. J. (1991a). *Mater. Res. Soc. Symp. Proc.*, **186**, 375.
- George, E. P., White, C. L., and Horton, J. A. (1991b). *Scripta Metall. Mater.*, **25**, 1259.
- Grimmer, H., Bollmann, W., and Warrington, D. H. (1974). *Acta Crystallogr.*, **A30**, 197.
- Hashimoto, M., Ishida, Y., Yamamoto, R., and Doyama, M. (1984a). *Acta Metall.*, **32**, 1.
- Hashimoto, M., Ishida, Y., Wakayama, S., Yamamoto, R., Doyama, M., and Fujiwara, T. (1984b). *Acta Metall.*, **32**, 13.
- Horton, J. A., and Liu, C. T. (1990). *Scripta Metall. Mater.*, **24**, 1251.
- Horton, J. A., and Miller, M. K. (1987a). *Mater. Res. Soc. Symp. Proc.*, **81**, 105.
- Horton, J. A., and Miller, M. K. (1987b). *Acta Metall.*, **35**, 133.
- Izumi, O., and Takasugi, T. (1987). *Mater. Res. Soc. Symp. Proc.*, **81**, 173.
- Izumi, O., and Takasugi, T. (1988). *J. Mater. Res.*, **3**, 426.
- Johnson, W. C., and Blakely, J. M. (1977). *Interfacial Segregation*. American Society for Metals, Metals Park, OH.
- Kruisman, J. J., Vitek, V., and DeHosson, J. Th. M. (1988). *Acta Metall.*, **36**, 2729.
- Krzanowski, J. E. (1989). *Scripta Metall.*, **23**, 1219.
- Kung, H., and Sass, S. L. (1992). *Acta Metall. Mater.*, **40**, 99.
- Kung, H., Rasmussen, D. R., and Sass, S. L. (1991a). In *Intermetallic Compounds—Structure and Mechanical Properties (JIMIS-6)* (ed. O. Izumi). Japan Institute of Metals, Sendai, pp. 347–70.
- Kung, H., Rasmussen, D. R., and Sass, S. L. (1991b). *Scripta Metall. Mater.*, **25**, 1277.
- Kung, H., Rasmussen, D. R., and Sass, S. L. (1992). *Acta Metall. Mater.*, **40**, 81.
- Liu, C. T., White, C. L., and Horton, J. A. (1985). *Acta Metall.*, **33**, 213.
- Losh, W. (1979). *Acta Metall.*, **27**, 1885.
- McKamey, C. G., Tortorelli, P. F., Devan, J. H., and Carmichael, C. A. (1992). *J. Mater. Res.*, **7**, 2747.
- Mackenzie, R. A. D., and Sass, S. L. (1988). *Scripta Metall.*, **22**, 1807.
- McLean, D. (1957). *Grain Boundaries in Metals*. Oxford University Press, Oxford, ch. 1.

- Marcinkowski, M. J. (1968). *Phil. Mag.*, **17**, 159.
- Massaro, T. A., and Petersen, E. E. (1971). *J. Appl. Phys.*, **42**, 5534.
- Masuda-Jindo, K. (1988). *J. Physique*, **49**, C5, 557.
- Messmer, R. P., and Briant, C. L. (1980). *Acta Metall.*, **30**, 457, 1811.
- Miedema, A. R. (1976). *J. Less-Common Metals*, **46**, 67.
- Miller, M. K., and Horton, J. A. (1986a). *Scripta Metall.*, **20**, 789.
- Miller, M. K., and Horton, J. A. (1986b). *J. Physique*, **47**, C2, 209.
- Miller, M. K., and Horton, J. A. (1986c). *J. Physique*, **47**, C7, 263.
- Mills, M. J. (1989). *Scripta Metall.*, **23**, 2061.
- Mills, M. J., Goods, S. H., Foiles, S. M., and Whetstone, J. R. (1991). *Scripta Metall. Mater.*, **25**, 1283.
- Ogura, T., Hanada, S., Masumoto, T., and Izumi, O. (1985). *Metall. Trans.*, **A16**, 441.
- Pestman, B. J., DeHosson, J. Th. M., Vitek, V., and Schapink, F. W. (1990). *J. Physique*, **51**, C1, 311.
- Pestman, B. J., DeHosson, J. Th. M., Vitek, V., and Schapink, F. W. (1991). *Mater. Res. Soc. Symp. Proc.*, **213**, 429.
- Pond, R. C., and Smith, D. A. (1977). *Phil. Mag.*, **36**, 353.
- Ranganathan, S. (1966). *Acta Crystallogr.*, **21**, 197.
- Sasaki, G., Shindo, D., Hiraga, K., Hirabayashi, M., and Takasugi, T. (1990). *Acta Metall. Mater.*, **38**, 1417.
- Schapink, F. W., and Tichelaar, F. D. (1988). *Phys. Status Solidi*, **A106**, 433.
- Schober, T. (1970). *Phil. Mag.*, **22**, 1063.
- Schober, T., and Balluffi, R. W. (1970). *Phil. Mag.*, **21**, 109.
- Seah, M. P., and Hondros, E. D. (1973). *Proc. R. Soc.*, **A335**, 191.
- Shao, J., and Machlin, E. S. (1983). *J. Phys. Chem. Solids*, **44**, 289.
- Sieloff, D. D., Brenner, S. S., and Burke, M. G. (1986). *J. Physique*, **47**, C7, 289.
- Sieloff, D. D., Brenner, S. S., and Burke, M. G. (1987a). *Mater. Res. Soc. Symp. Proc.*, **81**, 87.
- Sieloff, D. D., Brenner, S. S., and Ming-Jian, H. (1987b). *Mater. Res. Soc. Symp. Proc.*, **133**, 155.
- Sutton, A. P. (1984). *Intl. Metals Rev.*, **29**, 377.
- Sutton, A. P., and Vitek, V. (1983). *Phil. Trans. R. Soc.*, **A309**, 1.
- Suzuki, S., and Masahashi, N. (1991). *Bull. Japan Inst. Metals*, **30**, 993.
- Takasugi, T., and Izumi, O. (1983). *Acta Metall.*, **31**, 1187.
- Takasugi, T., and Izumi, O. (1987). *Acta Metall.*, **35**, 823.
- Takasugi, T., and Izumi, O. (1988). *Mater. Forum*, **12**, 8.
- Takasugi, T., George, E. P., Pope, D. P., and Izumi, O. (1985). *Scripta Metall.*, **19**, 551.
- Takasugi, T., Shindo, D., Izumi, O., and Hirabayashi, M. (1990). *Acta Metall. Mater.*, **38**, 739.
- Takasugi, T., Hono, K., Suzuki, S., Hanada, S., and Sakuri, T. (1993). *Scripta Metall. Mater.*, **29**, 1587.
- Tichelaar, D. D., and Schapink, F. W. (1986). *Phil. Mag.*, **A54**, L55.
- Tichelaar, D. D., and Schapink, F. W. (1988). *J. Physique*, **49**, C5, 293.
- Tichelaar, F. D., and Schapink, F. W. (1992). *Mater. Res. Soc. Symp. Proc.*, **238**, 145.
- Tichelaar, F. D., Schapink, F. W., and Li, X.-F. (1992). *Phil. Mag.*, **A65**, 913.
- Vitek, V., and Chen, S. P. (1991). *Scripta Metall. Mater.*, **25**, 1237.
- Vitek, V., Chen, S. P., Voter, A. F., Kruisman, J. J., and DeHosson, J. Th. M. (1989). *Grain Boundary Chemistry and Intergranular Fracture* (eds G. S. Was and S. M. Bruemmer); *Mater. Sci. Forum*, **46**, 237.
- Vitek, V., Ackland, G. J., and Cserti, J. (1991). *Mater. Res. Soc. Symp. Proc.*, **186**, 237.
- Wakayama, S., Hashimoto, M., Ishida, Y., Yamamoto, R., and Doyama, M. (1984). *Acta Metall.*, **32**, 21.
- Wang, G.-J., Sutton, A. P., and Vitek, V. (1984). *Acta Metall.*, **32**, 1093.
- Westbrook, J. H. (1965). *Metall. Rev.*, **9**, 415.
- Westbrook, J. H. (1967). *Intermetallic Compounds* (ed. J. H. Westbrook). Wiley, New York, p. 1.
- Westbrook, J. H. (1975). *Grain Boundaries in Engineering Materials* (Proc. Fourth Bolton Landing Conf.). Claitor's, Baton Rouge, pp. 671–88.
- Westbrook, J. H., and Wood, D. L. (1963). *J. Inst. Metals*, **91**, 174.
- White, C. L. (1986). *J. Vac. Sci. Technol.*, **A4**, 1633.
- White, C. L., Padgett, R. A., Liu, C. T., and Yalisove, S. M. (1984). *Scripta Metall.*, **18**, 1417.
- Williams, D. B., Alan, R. P., and Gronsky, R. (1992). *Images of Materials*. Oxford University Press, New York.

This chapter was originally published in 1995 as Chapter 24 in *Intermetallic Compounds*, Vol. 1: *Principles*, edited by J. H. Westbrook and R. L. Fleischer.

Chapter 8

Irradiation Damage

Lawrence M. Howe

*AECL Research, Reactor Materials Research Branch, Chalk River Laboratories,
Chalk River, Ontario K0J 1J0, Canada*

(Present address: 2 Frontenac Crescent, P.O. Box 697, Deep River, Ontario, K0J 1P0, Canada)

1. Introduction

There is considerable interest in irradiation effects in intermetallic compounds from both the applied and fundamental aspects. Initially, this interest was associated mainly with nuclear reactor programs but it now extends to the fields of ion-beam modification of metals, behavior of amorphous materials, ion-beam processing of electronic materials, and ion-beam simulations of various kinds.

From the applied point of view, significant mechanical (Chapter 6 by Schulson in Volume 2; Hillairet, 1989; Povolo and Hillairet, 1990), physical (Rest *et al.*, 1990; Piercy, 1963; Hillairet, 1989; Rullier-Abenque and Senateur, 1986), and microchemical (Griffiths, 1988; Yang *et al.*, 1986) changes have been observed during irradiation of various alloys that are in service or have potential use in an irradiation environment. For example, candidate reactor fuel materials such as U_3Si ($D0_c$ ($tI16$) structure) and U_6Fe ($D2_c$ structure) reveal extraordinary large voids at low and medium fuel burn-up (Rest *et al.*, 1990). This accelerated swelling phenomenon was attributed to an irradiation-induced crystalline-to-amorphous transformation associated with an enhancement of diffusion and plastic flow in the amorphous material (Rest *et al.*, 1990; Birtcher *et al.*, 1991). The ordered alloy Zr_3Al ($L1_2$ ($cP4$) structure) has some very attractive properties (low absorption cross-section for thermal neutrons, good mechanical properties at elevated temperatures, and acceptable corrosion behavior) for its use in a nuclear reactor, particularly for the CANDU (Canadian

deuterium-uranium) system (Schulson, 1974; Chapter 6 by Schulson in Volume 2). However, its use in a nuclear reactor is somewhat questionable, as an irradiation-induced ordered \rightarrow disordered \rightarrow amorphous phase transformation occurs below ~ 700 K (Howe and Rainville, 1977, 1979, 1980; Schulson *et al.*, 1979). Further information on the potential use of Zr_3Al as a structural material in nuclear reactors can be found in Chapter 6 by Schulson in Volume 2).

The irradiation behavior of the various intermetallic compounds of zirconium containing Fe, Cr, Ni, Nb, Sn, and Si, which are contained in the fuel cladding and pressure tubes (e.g. Zircaloy-2, Zircaloy-4, and Zr-2.5Nb alloys) in water-cooled nuclear reactors, is of considerable interest. An irradiation-induced crystalline-to-amorphous transformation was found for $Zr(Cr,Fe)_2$ and $Zr_2(Ni,Fe)$ precipitates in Zircaloy-2 and Zircaloy-4 (Gilbert *et al.*, 1985; Griffiths, 1988, 1990; Yang, 1988; Yang *et al.*, 1986; Lefebvre and Lemaignan, 1989; Motta *et al.*, 1991, 1993a; Motta and Lemaignan, 1992a, b). Depending upon the precipitate, temperature of irradiation, and nature of the bombarding projectile, the transformation could occur with or without a concurrent preferential depletion of Fe from the precipitates. Yang (1990) and Yang *et al.* (1986) also reported on the phase instabilities in neutron-irradiated Zircaloy-4, which included the amorphous transformation and the dissolution of the intermetallic precipitate $Zr(Fe,Cr)_2$ in the α -recrystallized matrix and the dissolution of the metastable precipitate $Zr_2(Fe,Cr)$ in the β -quenched matrix. Some of the above effects appear to be associated with the macroscopic irradiation

response of these alloys in service, and it is essential, therefore, to understand fully the mechanisms involved. Crystalline-to-amorphous transitions are discussed * further in Chapters 31 and 29 by Greer and by Johnson in this volume, and Okamoto and Meshi (1990).

The good structural stability and creep resistance at high temperatures of nickel-based γ/γ' superalloys result from the presence of a hardening γ' phase (an $L1_2$ type intermetallic compound, dispersed in a short-range-ordered f.c.c. nickel-based solid solution); see Chapter 1 by Anton in Volume 2. The atomic mobilities (via vacancy diffusion) in the two phases control the high-temperature properties (Voorhees, 1985). For example, the creep rate is mainly controlled by dislocation climb either in the γ phase or in the γ' phase, and thus depends on the diffusion rate in the corresponding phase. Irradiation damage studies on Ni-Al alloys provide pertinent information on the defect properties (Dimitrov *et al.*, 1992a,b).

Various A15 compounds (e.g. Nb_3Sn , V_3Si , and Nb_3Ga) have possible applications in superconducting magnets in controlled thermonuclear reactors. However, during irradiation, the critical temperature T_c for the transition from the superconducting to the normal state can be reduced appreciably due to irradiation-induced disordering (Brown *et al.*, 1978a). Adequate shielding from the irradiation would be needed to prevent appreciable depression of T_c if the above A15 compounds were used in practice. See Chapter 16 by Stekly and Gregory in Volume 2 on superconducting applications.

The development and refinement of metallic glass-forming techniques, such as electrodeposition (Brenner *et al.*, 1950), vapor and sputter deposition (Büchel and Hilsch, 1952, 1954), and the rapid quenching of alloy melts (Klement *et al.*, 1960; Duwez, 1967), have resulted in extensive investigations of the properties of metallic glasses and a considerable growth in applications (Steeb and Warlimont, 1985; Wagner and Wright, 1988). Crystalline materials can undergo solid-state amorphizing transformations by interdiffusion reactions, mechanical alloying, hydrogenation, or the application of pressure (Johnson, 1986). Even though amorphous alloys are metastable materials, they often exhibit properties that are superior to those of the corresponding crystalline material (Johnson, 1986). Consequently there is a strong impetus to obtain a detailed understanding of the factors controlling the crystalline-to-amorphous transformation. Other examples of where intermetallic compounds are sustained in non-equilibrium conditions by external forcing are (i) compounds produced by ion-beam mixing (Banerjee *et al.*, 1984), (ii) intermetallics in superalloys

under cyclic loading where there is sustained shearing (and sometimes dissolution) of the precipitates (Brechet *et al.*, 1987), (iii) intermetallics undergoing phase transformations during ball-milling (Martin and Gaffet, 1990), and (iv) ordered compounds when formed by vapor-phase deposition (Bellon *et al.*, 1988). Investigations of the nature of the damage produced during irradiation have proven to be quite useful in understanding the behavior of intermetallic compounds that are driven far from equilibrium.

Ion implantation is now used quite extensively for modifying the properties of metals, particularly in the near-surface region. This procedure can give rise to a considerable improvement of the corrosion, wear, and fatigue properties. This frequently involves the formation of an intermetallic compound in the implanted region. Compound formation using ion implantation and annealing is a powerful technique for forming multilayer structures (Celler and White, 1992). Full exploitation of the above techniques requires a detailed understanding of phase stability during irradiation as well as the properties of the irradiation-produced defects.

From a fundamental point of view, the study of irradiation damage in intermetallic compounds offers an interesting challenge. Antisite defects (atoms occupying wrong sites) need to be considered in addition to Frenkel defects (interstitial atoms and vacancies); see Figure 1. Ion-beam mixing can also occur, and in general there is a more complex behavior of the irradiation-produced defects than in elemental metals. On the other hand, special features of the intermetallic compounds (e.g. ordered alloys) allow for some rather sophisticated studies of irradiation damage (Piercy, 1963; Kirk *et al.*, 1977; Rullier-Albenque and Senateur, 1986). Improvements in the determination of interatomic potentials has also resulted in more detailed calculations of point-defect properties in intermetallic compounds, particularly using molecular-dynamics simulations (Caro *et al.*, 1990; Sabochik and Lam, 1991a,b; Lam *et al.*, 1993; Devanathan, 1993; Devanathan *et al.*, 1993a,b,c).

The field of irradiation damage in intermetallic compounds is rapidly expanding, and no attempt will be made in this chapter to cover all of the various aspects. Instead, attention will be focused on some specific areas and, hopefully, through these, some insight will be given into the physical processes involved, the present state of our knowledge, and the challenge of obtaining more comprehensive understanding in the future. The specific areas that will be covered are:

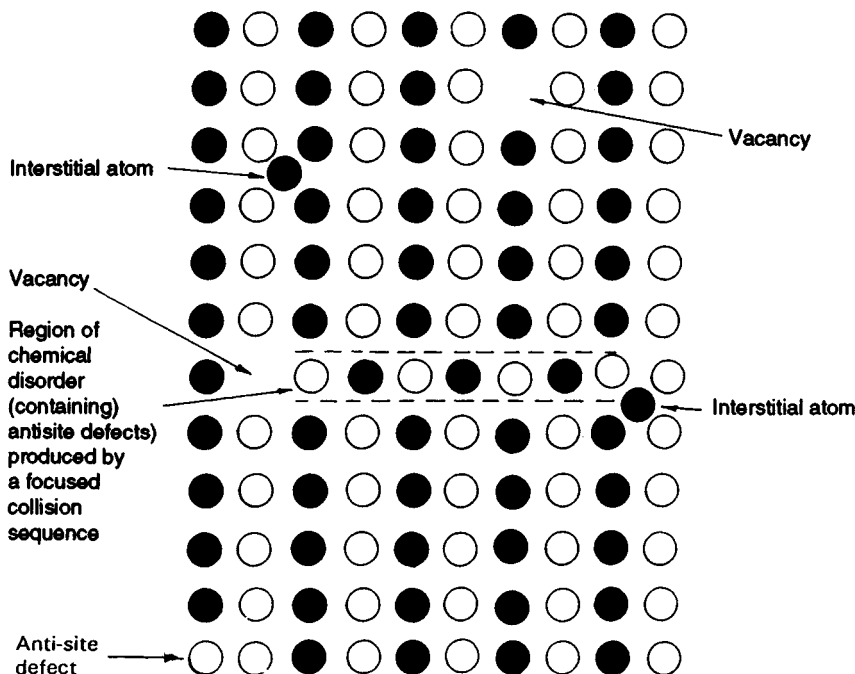


Figure 1. Schematic of a lattice of an intermetallic compound containing Frenkel defects (vacancies and interstitial atoms) as well as regions of chemical disorder in which there are antisite defects

- Point defects in intermetallic compounds.
- Irradiation-enhanced ordering and irradiation-induced disordering of ordered alloys.
- Irradiation-induced amorphization.

2. Point Defects in Intermetallic Compounds

2.1 Experimental Investigations

A variety of experimental methods have been used to elucidate the properties of point defects in intermetallic compounds. The specific examples given below are relevant to understanding the irradiation behavior of these compounds. More detailed information on point defects in intermetallic compounds can be found in Chapter 23 by de Novion in this volume.

The most extensive studies of point defects in intermetallic compounds have been performed in ordered alloys. In such alloys both irradiation-induced disordering and irradiation-enhanced ordering can occur, as will be discussed in Section 3 (also see the review by Schulson, 1979). The principal objective of many of these studies was to attempt to elucidate the mechanisms responsible for the irradiation-induced

disordering or irradiation-enhanced ordering. In many cases, changes in electrical resistivity were monitored during the irradiation and subsequent annealing. Consider, for example, the experiments on the electron irradiation of Cu_3Au by Gilbert *et al.* (1973). Ordered and disordered Cu_3Au samples were irradiated with 1.0 and 1.5 MeV electrons at ~ 20 K and subsequent isochronal anneals were performed from 30 to 450 K. Electron irradiations were used in order to produce fairly simple defects, i.e. isolated pairs of vacancies and interstitial atoms. For electron irradiation, the maximum energy transferred per primary collision is given by

$$E_{T,\max} = 2E_0(E_0 + 2m_0c^2)/M_2c^2 \quad (1)$$

where E_0 is the energy of the incident electron, m_0 is the rest mass of the electron, c is the velocity of light, and M_2 is the mass of the struck atom in the sample. The purpose of selecting electron energies of 1.0 and 1.5 MeV was that at the former energy only Cu atoms were expected to be displaced in the Cu_3Au lattice, whereas both Cu and Au atoms should be displaced at the higher energy. In disordered specimens irradiated with 1.0 MeV electrons, four annealing stages were

detected, centered at about 90, 130, 330, and 410 K. These were assigned to recombination of an interstitial gold atom I_{Au} with a copper vacancy V_{Cu} close pair, I_{Cu} migration, V migration, and trapped V migration, respectively. Following irradiation with 1.5 MeV electrons, a disordered specimen exhibited the four above stages, plus ones at 55 and 190 K that were attributed to $I_{Au}-V_{Au}$ close-pair recombination and I_{Au} migration, respectively. For both 1.0 and 1.5 MeV ion irradiations, the ordered Cu_3Au exhibited only three stages at 75, 240, and 410 K that were assigned to I_{Cu} migration, V migration, and migration of vacancies initially trapped at antiphase domain boundaries, respectively. It was proposed that focusons dissipate the energy in the ordered specimens such that Au interstitials cannot form (a focuson is a focused energy packet in which energy is only transferred along a particular direction). In the Cu_3Au superlattice ($L1_2$ structure) as shown in Figure 2, Cu atoms are nearest neighbors in $\langle 110 \rangle$ directions on $\{111\}$ planes. Lines of Cu atoms can therefore serve as focusons to dissipate the energy given to a primary knock-on atom. Computer studies of irradiation damage in ordered Fe_3Al (Jackson *et al.*, 1972) show such a mechanism operating.

Minimum displacement threshold energies for Cu atoms in ordered and disordered Cu_3Au and $CuAu$ were determined at 20 K by Alamo *et al.* (1986) using 0.66 and 2.36 MeV electron irradiations and electrical resistivity measurements. It was found that the minimum displacement threshold energy is $E_{d,min}^{Cu} = 18$ eV in all

cases. Post-irradiation annealing studies in the ordered compounds showed the same recovery stages regardless of the energy of the incident electrons (see Figure 3). It was argued that a single type of interstitial (Cu) was migrating freely at 70 K in both $L1_2$ -ordered Cu_3Au and $L1_0$ -ordered $CuAu$. Proposed $\langle 100 \rangle$ Cu-Cu split interstitial configurations and their migrations are depicted in Figure 4. The Au interstitial is believed to take the place of a Cu atom and to produce a Cu interstitial associated with an antisite defect. The assignment of the other stages shown in Figure 3 was as follows: recovery of close vacancy-interstitial pairs at ~ 40 K in Cu_3Au and $CuAu$, interstitial cluster growth at ~ 140 K in Cu_3Au and ~ 130 K in $CuAu$, and vacancy migration above 300 K in both alloys. Positron annihilation experiments by Doyama *et al.* (1985) indicate that in ordered Cu_3Au vacancies migrate and form three-dimensional clusters at 260–400 K, and break-up of the vacancy clusters occurs at 400–500 K.

Damage production by electron irradiation and its subsequent annealing have been investigated in solid solutions of $NiAl$ and $Ni(Al,Ti)$ as well as ($L1_2$) Ni_3Al intermetallic compounds by Dimitrov *et al.* (1992a, b) using electrical resistivity measurements. Frenkel-pair resistivities deduced from the comparative analysis of the initial damage rates in the solid solutions and in pure nickel were $6.5\text{--}9.4 \mu\Omega \text{ cm}/\%$, which are similar to that for pure nickel. In the Ni_3Al intermetallic compounds the Frenkel-pair resistivities ranged from 97 to $109 \mu\Omega \text{ cm}/\%$, and this was correlated with the large ideal resistivity of these materials. In the solid solutions, long-range defect migration resulted in increases of local order; self-interstitial atoms were found to be mobile above 110 K and vacancies to be mobile above 330 K. The recovery spectrum of the irradiated Ni_3Al compounds was similar to Ni but with a smaller amount of fine structure. The mobility of self-interstitials (corresponding mainly to Ni-Ni dumbbells) occurred at a higher temperature (75 K) than in Ni (50 K) and did not induce significant ordering. The Ni vacancies in Ni_3Al , which appeared to be the dominant vacancy species, were slightly less mobile than in Ni and promoted some increase of long-range order.

The critical temperature T_c of A15 (cP8) compounds like Nb_3Ge or V_3Si is very sensitive to lattice disorder and decreases under irradiation by neutrons, α particles, heavy ions or electrons. In the above A15 compounds the Si (or Ge) atoms constitute a b.c.c. lattice and the V (or Nb) atoms are arranged in linear chains along the $\langle 100 \rangle$ directions. Labbé and Friedel (1966) have developed a model of A15 compounds in which the one-dimensionality of transition-metal atoms gives rise to

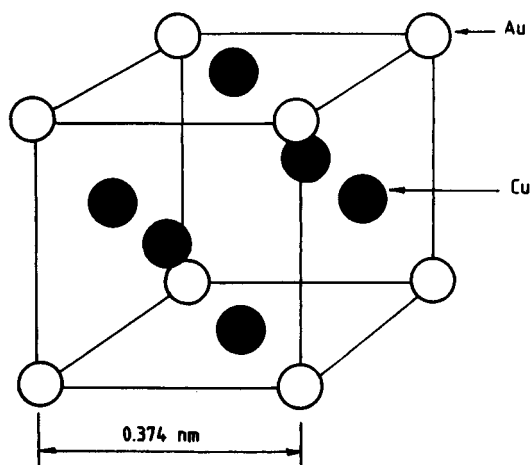


Figure 2. Schematic of the ordered Cu_3Au lattice ($L1_2$ (cP4)-structure). Other ordered compounds having this structure are Zr_3Al , Ni_3Al , Ni_3Mn , Ni_3Fe , and Pt_3Fe

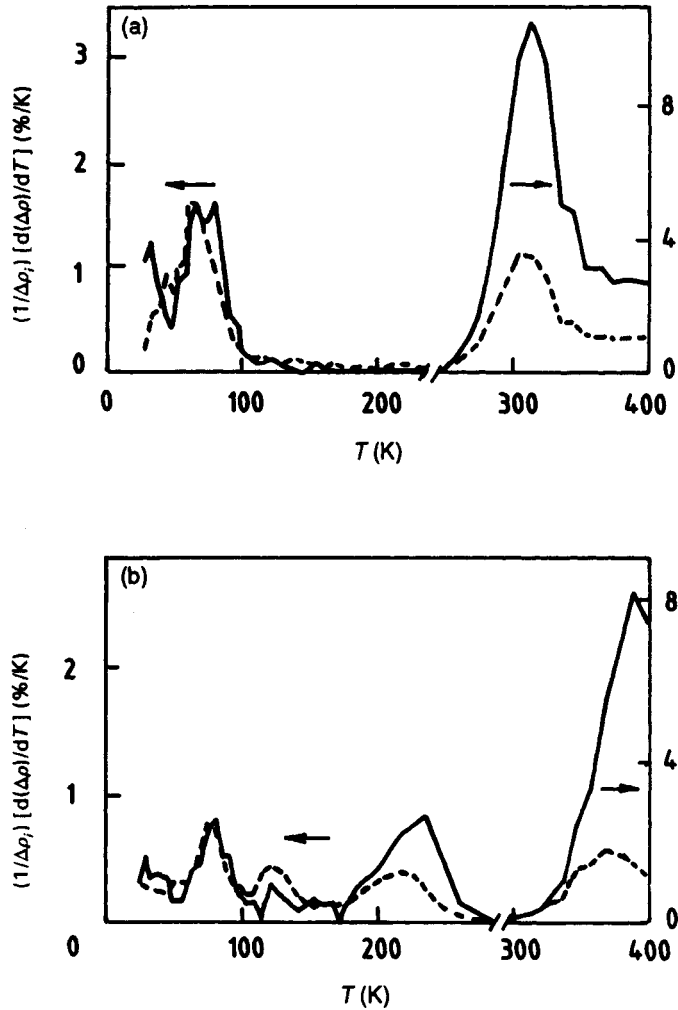


Figure 3. Recovery stages in (a) ordered Cu_3Au and (b) ordered CuAu following electron irradiation at 20 K, at $E_e = 0.66$ MeV (—) and 2.36 MeV (----). For both graphs, the left and right vertical axes are for $(1/\Delta\rho_i)[d(\Delta\rho)/dT]$, but have different scales (From Alamo *et al.*, 1986)

a high density of electronic states near the Fermi level, a condition favorable to a high T_c . On the basis of this model, essentially no change of T_c should occur when disorder is created in the b.c.c. sublattice, leaving the transition-metal rows unaltered. Combining measurements of electrical resistivity ρ and critical temperature T_c can provide information on the displacement threshold energies E_d (i.e. the minimum energy that has to be transferred to an atom to produce a point defect) for specific atoms in the lattice and can also be used to obtain specific Frenkel-pair resistivities. For example, Rullier-Albenque and Senateur (1986) have measured ρ and T_c in V_3Si irradiated with electrons

at ~ 21 K and analyzed their results within the framework of the linear chain model of Labbé and Friedel (1966). The results indicated that Si atoms were displaced at an electron energy $E = 0.20$ MeV, leading to an increase in ρ , but T_c was only affected when V atoms were displaced at $E = 0.35$ MeV. Values of E_d were 25 ± 1 eV for both Si and V, and specific Frenkel-pair resistivities were $\rho_{\text{FP}}^{\text{Si}} = 4.2 \pm 0.5 \mu\Omega \text{ cm/at.}\%$ and $\rho_{\text{FP}}^{\text{V}} = 27 \pm 3 \mu\Omega \text{ cm/at.}\%$ for Si and V respectively. The production of antisite defects occurred at $E \geq 0.50$ MeV. In general, the most efficient mechanism for producing antisite defects under electron irradiation is the replacement-collision sequence. In the A15 structure,

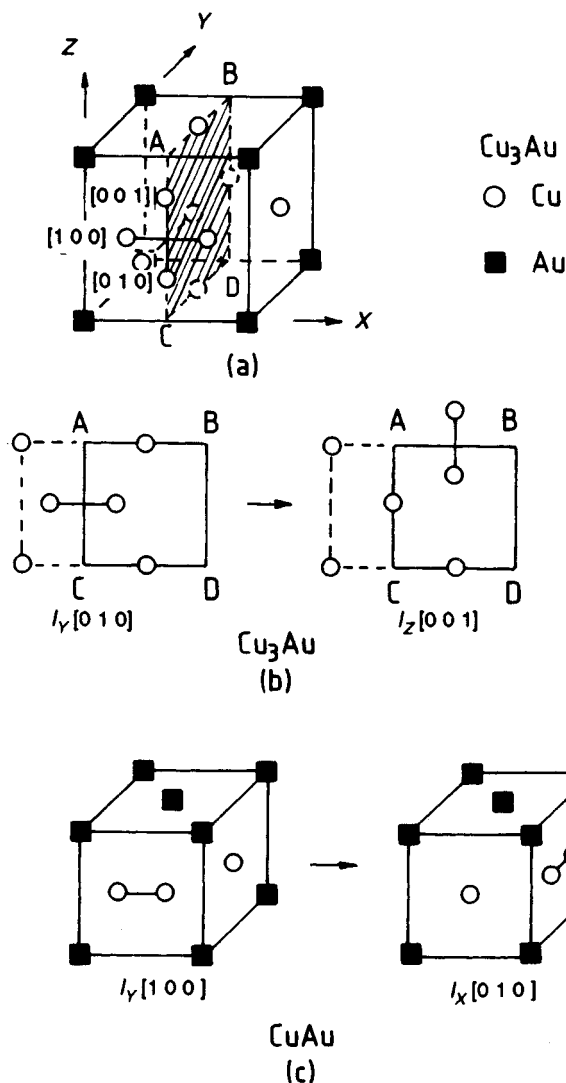


Figure 4. Proposed $\langle 1\ 0\ 0 \rangle$ Cu-Cu split interstitial configurations before and after migration in ordered Cu_3Au and CuAu (From Alamo *et al.*, 1986)

the diatomic rows along which atom displacements can produce antisite defects are the $\langle 1\ 2\ 0 \rangle$ rows (see Figure 5). Long-range collision sequences are unlikely in these directions because of the 'void' between the V-Si-V atomic sequences.

In all of the investigations discussed above, electron irradiations were employed and isolated Frenkel pairs were produced. For bombardment with ions and neutrons, a more complex damage cascade is produced, usually with a vacancy-rich core region and interstitial atoms (either single or in small clusters) in the peripheral

regions. The maximum energy $E_{T,\max}$ that can be transferred to a lattice atom of mass M_2 by an incident particle of mass M_1 and energy E_0 is given by

$$E_{T,\max} = 4M_1M_2E_0/(M_1 + M_2)^2 \quad (2)$$

The number of displacements per cascade, n_d , is given approximately by (Sigmund, 1969):

$$n_d = 0.8\nu(E)/2E_d \quad (3)$$

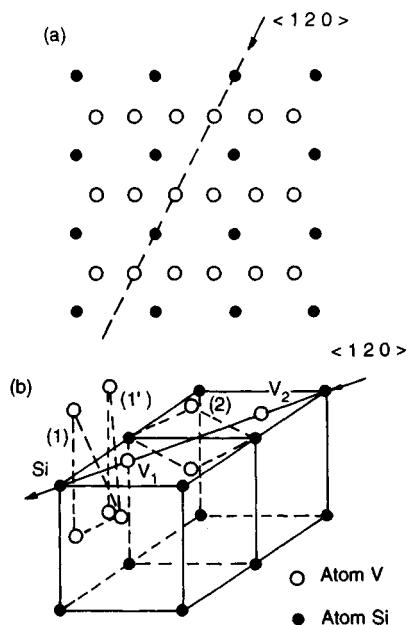


Figure 5. Schematic sketch illustrating (a) the (0 0 1) plane of the A15 structure of V₃Si and the <1 2 0> direction along which atom replacements can produce disorder, and (b) the atomic configuration around the <1 2 0> direction. In order to make a replacement, an atom V₁ (or Si) has to go through two barriers ((1) and (1')) and an atom V₂ has to pass the barrier (2) (From Rullier-Albenque and Senateur, 1986)

where $\nu(E)$ is the portion of the energy that goes into nuclear collisions (remainder gives rise to electronic excitations) and E_d is the threshold displacement energy required to displace an atom from its normal lattice site. As an example, for zirconium irradiated by 1.0 MeV neutrons, $n_d = 675$, i.e. $\nu(E) \sim 0.04$. It should be noted, however, that, due to recombination events the number of point defects that actually survive in the initial cascade event is considerably less than the calculated number. It is also convenient to consider the number of times each atom has been displaced during irradiation, or displacements per atom (DPA), particularly at high fluences where considerable overlap of the displacement cascades occurs. The quantity DPA is given by

$$\text{DPA} = n_d \sigma_s \phi t \quad (4)$$

where σ_s is the scattering cross-section, ϕ is the flux of bombarding projectiles, and t is the time of bombardment. For neutron irradiation of many metals, for $E > 1.0$ MeV and $E_d \sim 25$ eV, 1 DPA corresponds to a fluence of $\sim 1.0 \times 10^{25}$ neutrons/m².

Information on the long-range migration of self-interstitial atoms (SIA) produced in collision cascades in Ni₄Mo and Pt₃Co was obtained by Aidelberg and Seidman (1987) using the field-ion microscope (FIM) technique. The specimens were irradiated *in situ* with either 30 keV Kr ions or 30–60 keV Xe ions to fluences of $(2-10) \times 10^{12}$ ions/cm². The surface of the FIM specimen served as a sink for the SIA, and the arrival of the SIA was detected when it reached the surface. No long-range migration of SIA was observed between 6 and 30 K, while uncorrelated long-range migration was detected above 30 K. In the case of L1₂ (cP4) D1_a (tI10) Pt₃Co a broad peak centered at ~ 37.5 K was attributed to long-range SIA migration, and for D1_a (tI10) Ni₄Mo peaks centered at ~ 37.5 and ~ 77.5 K were attributed to long-range migration of interstitial atoms.

2.2 Theoretical modeling

With the establishment of suitable potentials for interatomic compounds (see Chapter 23 by de Novion in this volume) and large memory and fast computers (particularly for molecular-dynamics calculations), more detailed theoretical information is now emerging on point defects in intermetallic compounds. Several examples are given below.

Caro and Pedraza (1991) have used the embedded-atom potentials for Ni and Al, developed by Daw and Baskes (1984) and Foiles and Daw (1987), to calculate the energy of formation of antisite defects, of vacancies, and of various possible interstitial configurations in the ordered B2 (cP2) alloy NiAl. The <1 1 1> crowdion incorporating an extra Ni atom was found to be the lowest-energy interstitial configuration (a crowdion is an interstitial atom that is constrained to move in one direction). The Ni–Al <1 1 0> mixed dumbbell at an Al site was the second lowest-energy configuration; although it contains an Al atom, it still contains an extra Ni atom. If an extra Al atom is incorporated, the lowest-energy stable configuration is a <1 1 1> crowdion that incorporates an extra Ni atom plus a Ni antisite defect (that the Al atom moves into), as shown in Figure 6. The displaced Al atoms may be the main contributors to the loss of long-range order under irradiation when their mobility is low, either when they recombine with nearby vacancies that are not of their own sublattice or when they occupy a Ni site upon driving the Ni atom into a crowdion configuration, as in Figure 6. In the ordered alloy, the Ni interstitial will tend to be quite stable since all its neighbors are Al atoms. Only when an adjacent site becomes vacant will the extra Ni atom move in and create an antisite defect. The distance for

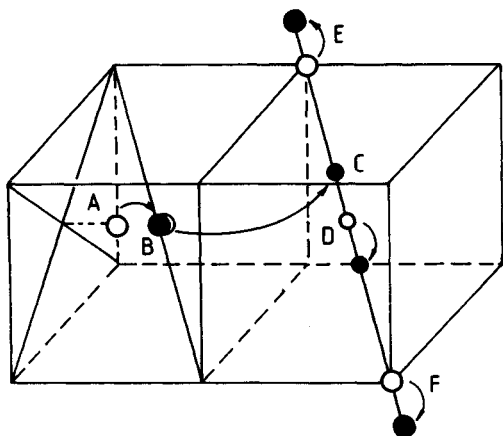


Figure 6. Schematic for defects in the (B2) NiAl lattice showing the relaxed atomic positions attained when an Al atom is added at site A ($\frac{1}{4}, \frac{1}{2}, \frac{1}{2}$). The Al atom at A moves into site B, which is a Ni sublattice site, generating an antisite defect. The Ni atom initially at B moves into position C, displacing the Ni atom at D, as indicated, and causing the Al atoms at E and F to be displaced. A crowdion with an extra Ni atom along a $\langle 111 \rangle$ direction is produced. Open circles show initial positions, filled circles final ones (From Caro and Pedraza, 1991)

spontaneous recombination of Frenkel pairs was found to be third-nearest neighbor provided the chemical order was maintained, i.e. in ordered alloys the recombination of close pairs was favored, even though antisite defects were created. In disordered alloys, however, interstitial trapping occurred in the vicinity of a vacancy and thereby enhanced the survival of Frenkel pairs.

Threshold displacement energies for atomic displacement along $\langle 110 \rangle$, $\langle 100 \rangle$, and $\langle 111 \rangle$ directions, and formation enthalpies of several symmetrical interstitial atom configurations, have been computed in ordered $L1_2$ (cP4) Ni_3Al by Caro *et al.* (1990), also using embedded-atom potentials developed by Daw and Baskes (1984) and Foiles and Daw (1987). The stacking of the $L1_2$ structure (Figure 2) along the $\langle 100 \rangle$ direction is ABAB..., where A is a plane containing 50% Ni and 50% Al and the B plane contains 100% Ni. Besides two types of vacancies and two types of antisite defects, several types of interstitials are possible (i.e. six possible dumbbell configurations, four octahedrals, and four proper crowdions). In the Al sublattice, an extra Al or Ni atom generates a dumbbell, which has eight Ni atoms as nearest neighbors regardless of its orientation along any of the three major crystallographic axes. For the Ni sublattice, a Ni atom can belong to either an A or B plane, depending on the direction of

stacking. The dumbbell interstitial with the lowest enthalpy was found to be Ni-Ni(B), whereas the Al-Al(A) dumbbell had the highest enthalpy. The most mobile dumbbell appears to be the Ni-Ni(B), whereas an Al interstitial is immobile since it converts into an antisite defect. Among the octahedral interstitials, the Ni(B) had the lowest enthalpy. The results also predict crowdion formation at the end of replacement-collision sequences along $\langle 110 \rangle$ for A planes as well as the usual $\langle 100 \rangle$ dumbbell for B planes. The simulations also showed that the spontaneous recombination volume for some defects in Ni_3Al can be much smaller than in pure metals. It was argued that this may have important implications for irradiation-induced amorphization of intermetallic compounds, since each Frenkel pair makes a large contribution to the total enthalpy of the crystalline phase.

Molecular-dynamics calculations provide valuable insight into the evolution with time of defect structures created in the collision cascade. Consider, for example, the molecular-dynamics simulations of low-energy displacement cascades in the B11-ordered compound CuTi (Figure 7) by Zhu *et al.* (1992). Figure 8 shows the number of Frenkel pairs produced by a Cu primary knock-on atom (PKA) as a function of recoil energy at the end of the collisional phase (0.2 ps) and at the end of the cooling phase (2.5 ps). The number of Frenkel

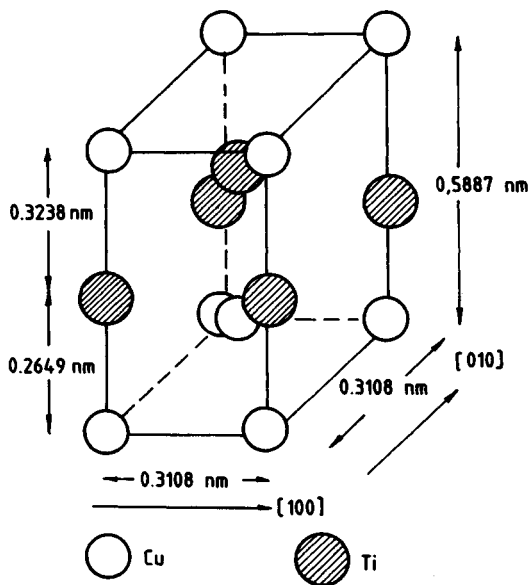


Figure 7. The B11 (tP4) structure of ordered CuTi (From Zhu *et al.*, 1992)

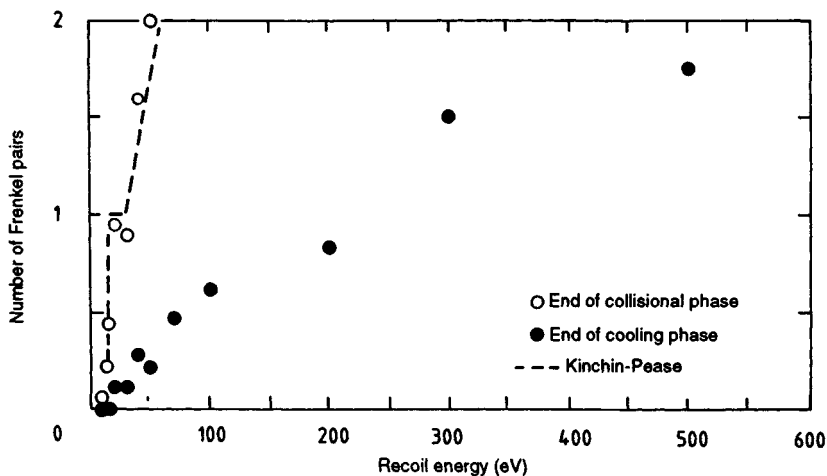


Figure 8. Average number of Frenkel pairs produced by a Cu PKA as a function of recoil energy at 0.2 ps (○) and 2.5 ps (●). The Kinchin–Pease function (equation (3)) for $E_d = 15$ eV is shown for comparison (From Zhu *et al.*, 1992)

defects predicted by equation (3) (i.e. the modified Kinchin–Pease function) is also shown for $E_d = 15$ eV. It can be seen that there is an appreciable reduction in the number of Frenkel pairs during the cooling phase. For example, considering both Cu and Ti PKAs and a recoil energy of 500 eV, about half the number of replacement atoms that had been produced in the collisional phase returned to their original lattice sites in the cooling phase. At the end of the cooling phase, half of the replacements are antisite defects. It was also found that when the PKA was a Ti atom, the directional dependence of E_d was similar to that in pure metals (i.e. E_d was small in low-index directions); whereas if the PKA was a Cu atom, this behavior was not observed in $\langle 110 \rangle$ and $\langle 112 \rangle$. On average, the threshold energy with Ti as a PKA was greater than that with Cu as a PKA by a factor of 1.67. The effective threshold energy calculated by averaging over all the directions and both Cu and Ti PKAs was 62 eV. For detailed information on the computation of the energies and configurations of vacancies and interstitial atoms in CuTi and CuTi₂, using embedded-atom potentials, see Shoemaker *et al.* (1991).

The energies and configurations of interstitials and vacancies in the B2 (cP2) ordered compounds NiTi and FeTi have been calculated by Lutton *et al.* (1991) using atomistic simulation. In NiTi, the stable configuration of a vacancy after the removal of a Ni atom was a vacant Ni site, and in FeTi the removal of an Fe atom resulted in a vacant Fe site. In both compounds, removal of a Ti atom led to the creation of a vacant Ni or Fe site

and an adjacent antisite defect. Interstitial atoms in NiTi formed split $\langle 111 \rangle$ configurations consisting of a Ni–Ni dumbbell with one or two adjacent antisite defects. The Fe interstitial atom in FeTi was of the Fe–Fe $\langle 111 \rangle$ dumbbell type, and the Ti interstitial formed a $\langle 110 \rangle$ Fe–Fe dumbbell. All of the interstitial configurations contained antisite defects and probably have large migration energies. Consequently the interstitial atoms in these compounds may be much less mobile than those in pure metals.

3. Irradiation-Enhanced Ordering and Irradiation-Induced Disorder of Ordered Alloys

3.1 Irradiation-Enhanced Ordering

The Bragg–Williams description (Bragg and Williams, 1934) of long-range atomic order S in a binary alloy is given as follows:

$$S = (P_\alpha^A - X_A)/(1 - X_A) = (P_\beta^B - X_B)/(1 - X_B) \quad (5)$$

where the parameters P_α^A and P_β^B are the probabilities of an A atom residing on an α site and a B atom residing on a β site, respectively, and X_A and X_B are the atomic fractions of the respective species. For complete order, $P_\alpha^A = P_\beta^B = 1$ and $S = 1$, whereas for complete disorder $P_\alpha^A = X_A$ and $P_\beta^B = X_B$ and $S = 0$.

An increase in the degree of order in a disordered or partially ordered alloy corresponds to an increase in the

number of correct atomic bonds, i.e. to an increase in the probability that an A atom occupies an α site and that a B atom occupies a β site. It has been demonstrated in numerous experiments (see the review by Schulson, 1979) using a variety of experimental techniques that this increase in S during irradiation involves the thermally activated migration of irradiation-produced point defects. The phenomenon can be suppressed if the temperature of irradiation is sufficiently low and accelerated if the temperature is raised above ambient. It also occurs under irradiation conditions where isolated Frenkel pairs are created (electron irradiation) as well as when there are more complex displacement cascades (heavy-ion and neutron irradiation).

Consider, for example, the study of ordering and disordering in Cu_3Au during 600 keV electron irradiation (in a high-voltage electron microscope (HVEM)) by Hameed *et al.* (1982). The rate of ordering and disordering was determined between 140 and 400 K by measuring the ratio of the intensities of the superlattice and fundamental reflections in electron diffraction patterns. Specifically, the degree of order was obtained from the relation,

$$S = (I_s/I_f)^{1/2} / (I_s/I_f)^{1/2}_{S=1} \quad (6)$$

where I_s and I_f are the intensities of the superlattice

and fundamental reflections, respectively. Figure 9 and 10 show the way S varies for initially ordered (L1_2) Cu_3Au and initially disordered Cu_3Au samples during electron irradiation at various temperatures. The final state of the alloy at any irradiation temperature is independent of the initial condition, as can also be seen in Figure 11, which contains measurements obtained from both initially ordered and initially disordered specimens. At all irradiation temperatures a steady-state degree of order was developed.

The most comprehensive models of irradiation-induced ordering and disordering, which have been used to analyze data of the type shown in Figures 9–11, are those due to Liou and Wilkes (1979), Zee and Wilkes (1980), Butler (1979), and Banerjee and Urban (1984). In Butler's model, only AB alloys are considered; Liou and Wilkes, and Zee and Wilkes consider AB_3 alloys (Cu_3Au in particular); and Banerjee and Urban's model has been developed for alloys with B2 , L1_2 , and D1_2 structures. In general, in these models two competitive processes are occurring simultaneously, i.e. irradiation-enhanced ordering and irradiation-induced disordering. In the above models, it is assumed that interstitial atoms do not contribute significantly to the ordering and that disordering takes place athermally.

The irradiation-induced disordering is expressed by Zee and Wilkes (1980) as follows:

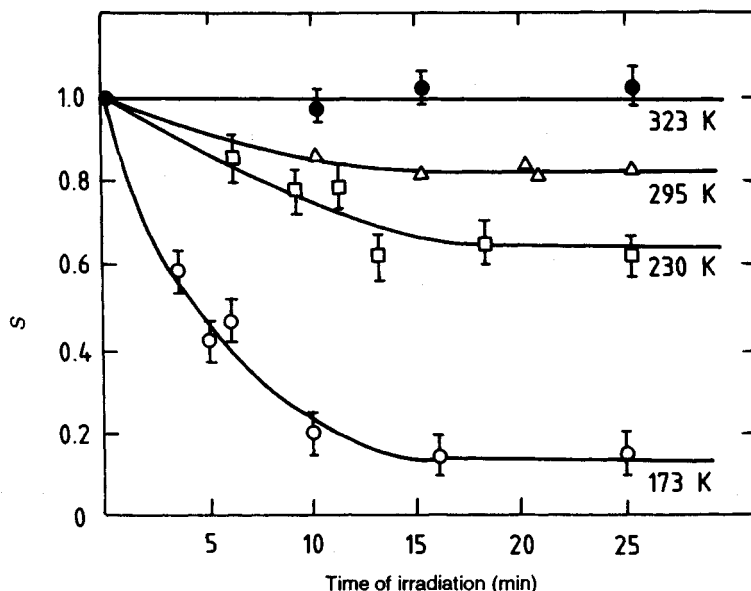


Figure 9. Variation of the degree of long-range order S for initially ordered Cu_3Au for various irradiation temperatures as a function of time of irradiation with 600 keV electrons (From Hameed *et al.*, 1982)

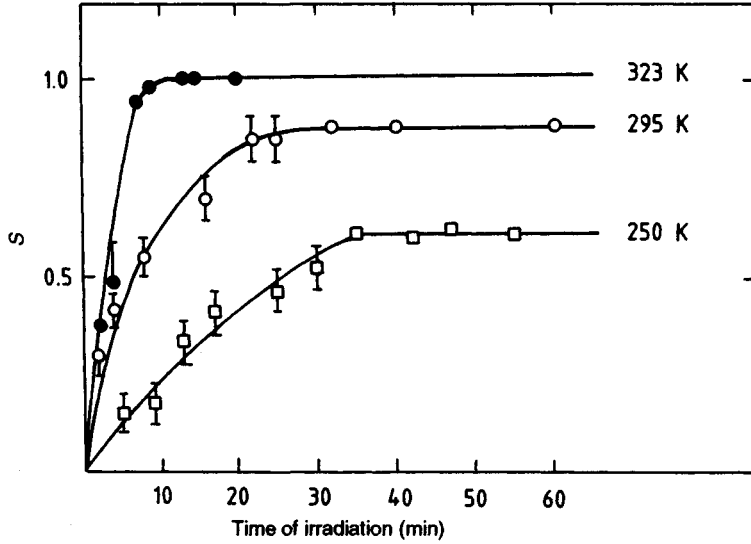


Figure 10. Variation of the degree of long-range order S for initially disordered Cu_3Au for various irradiation temperatures as a function of time of irradiation with 600 keV electrons (From Hameed *et al.*, 1982)

$$(dS/dt)_{\text{irr}} = -\epsilon kS \quad (7)$$

where ϵ is the number of replacements per displacement, K is the displacement rate, and S is the instantaneous degree of order. Under electron irradiation and near threshold $\epsilon \sim 1$, whereas for fast-neutron irradiation Zee and Wilkes (1980) use $\epsilon = 80$. To describe the rate of change of order due to thermally activated processes during irradiation, Zee and Wilkes (1980) use the equation:

$$(dS/dt)_{\text{ord}} = [(Z_\alpha + Z_\beta - 2)(\nu_v/2)(Z_\beta/X_B)C_v \exp(-E_m^0/k_B T) \{ X_A X_B (1-S)^2 - \exp(-V_0 S/k_B T) [S + X_A X_B (1-S)^2] \}] \quad (8)$$

Where Z_α is the number of A atoms around β sites, Z_β is the number of B atoms around α sites, ν_v is the vacancy jump attempt frequency, X_A and X_B are the fractions of A and B atoms, C_v is the steady-state

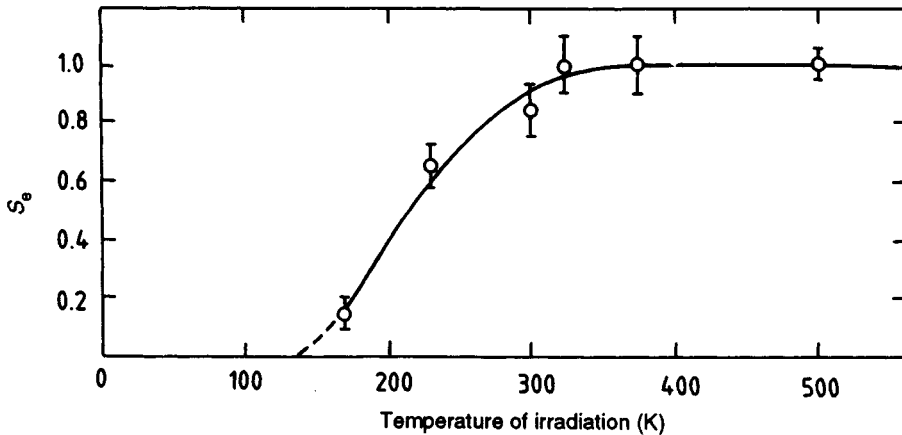


Figure 11. Variation of the steady-state degree of order S_e developed during irradiation at various temperatures with 600 keV electrons at a displacement rate of $\sim 10^{-3}$ DPA/s (From Hameed *et al.*, 1982)

vacancy concentration, E_m^0 is the ordering jump energy, k_B is Boltzmann's constant, T is the absolute temperature, S is the degree of long-range order, and $V_0 = V/S$ (V is the ordering energy). The actual ordering rate dS/dt is a balance between the irradiation-induced disordering rate $(dS/dt)_{irr}$ and the irradiation-enhanced ordering rate $(dS/dt)_{ord}$. Thus:

$$(dS/dt) = (dS/dt)_{irr} + (dS/dt)_{ord} \quad (9)$$

The steady state of order S_c is developed at any temperature when

$$(dS/dt)_{irr} + (dS/dt)_{ord} = 0 \quad (10)$$

Zee and Wilkes (1980) applied their model to data that had been obtained by various investigators on fast- and thermal-neutron irradiations of Cu_3Au , and claimed that there was reasonably good agreement between their model and the experimental results, particularly for irradiation times beyond the initial transient stage. The parameters used in fitting the theoretical model to the experimental data were $E_m = 0.8$ eV for vacancy motion, E_m^0 for ordering vacancy jumps, $\epsilon = 80$ for fast neutrons and 20 for thermal neutrons, and a survival rate for vacancy production of 5% for fast neutrons and 100% for thermal neutrons.

Hameed *et al.* (1982) applied the model of Zee and Wilkes (1980) to their experimental data, shown in Figures 9–11, on the rates of ordering and disordering in electron-irradiated Cu_3Au . Reasonable agreement with these experimental data was obtained if minor modifications were made to the theory. Values of E_m and E_m^0 of 0.6 and 0.62 eV, respectively, were used in place of the 0.8 and 0.84 eV values used by Zee and Wilkes (1980). A value of $E_m = 0.60$ eV is considerably less than that expected for vacancy migration in Cu_3Au , and may indicate that point-defect mobility is considerably increased during irradiation due to irradiation-enhanced diffusion or by the formation of divacancies. In the case of electron irradiations in a HVEM, the role of the nearby surfaces acting as sinks for the migrating defects (which might affect the above analysis) still has to be assessed.

In the model by Banerjee and Urban (1984), the net ordering rate under irradiation is given by

$$dS/dt = (dS/dt)_c + (dS/dt)_r + (dS/dt)_l \quad (11)$$

where $(dS/dt)_c$ is the rate of disordering due to collision sequences, $(dS/dt)_r$ is the total disordering

rate by random defect annihilation, and $(dS/dt)_l$ is the thermal ordering rate. Specifically,

$$(dS/dt)_c = -\chi m_e PS / C_A C_B \quad (12)$$

$$(dS/dt)_r = -PS \quad (13)$$

$$(dS/dt)_l = K_+ C_A^\beta C_B^\alpha - K_- C_A^\alpha C_B^\beta \quad (14)$$

In the above equations, χ is a geometrical factor, m_e is the effective number of pair exchanges produced in a collision sequence, P is the atom displacement rate (DPA/s), S is the long-range order parameter, C_A and C_B are the concentrations of A and B atoms in the alloy, K_+ and K_- are rate coefficients for ordering and disordering, respectively (these are related to the concentration of vacancies on the α and β sublattices of the ordered alloy), and C_A^β , C_B^α , C_A^α , and C_B^β refer to the concentrations of either A or B atoms on α or β lattice sites. The above model was applied by Banerjee and Urban (1984) to analyze the results obtained by Banerjee *et al.* (1984) on the electron irradiation of Ni_4Mo (D1_a (t110) structure). The calculated temperature dependence of the steady-state degree of long-range order was in good agreement with the experimental observations, although the values used for the diffusion behavior as well as the displacement threshold energies were those for Ni, as pertinent data for Ni_4Mo were not available.

It is obvious that, in order to apply models of the above type to study the irradiation behavior of ordered compounds in general, detailed information is required on the configurations and migration energies of the vacancies and interstitial atoms. Computations of the type described in Section 2.2, along with corresponding experimental investigations, are certainly required. In the analysis of the Cu_3Au and Ni_4Mo results described above, it was assumed that only the migration of vacancies is contributing to the ordering, which may be quite a reasonable assumption for those particular alloys for the temperature regime used for the analysis. It also may be true for many other ordered alloys. However, as shown in Section 2.2, there are some ordered alloys in which the migration energy for interstitial migration may be quite high, and may be even higher than that for vacancies (i.e. the reversal of that normally found in most elemental metals). There is also evidence for this reversal from studies of mechanical relaxation effects in the irradiated substitutional alloy Ag-24 at. \% Zn (Halbwachs and Beretz, 1980). This effect was attributed to the marked slowing-down of the self-interstitials by the undersized solute atoms and may also

occur in other solid solutions where a marked size difference exists between the constituent elements.

It is also of interest to obtain information on changes of short-range order (SRO) during irradiation as well as of long-range order (LRO). The state of SRO is usually given by the Cowley-Warren parameters α_i that describe the conditional probability P'_{AB} (P'_{BA}) of finding B (A) atoms on the successive coordination shells around A (B) atoms, and which have the form

$$\alpha_i = 1 - (P'_{AB}/C_B) = 1 - (P'_{BA}/C_A) \quad (15)$$

As an example, consider the study by Banerjee *et al.* (1984) on the effect of electron irradiation on the order-disorder transformation in (D1_a) Ni₄Mo. Electron micrographs and diffraction patterns were obtained during *in situ* electron irradiations at 50–1050 K in a HVEM. At temperatures below 200 K, the alloy completely disorders. At 200–450 K, only SRO was observed, and the transition between LRO and SRO, which occurs via the completely disordered state, is consistent with the concentration-wave description of the SRO structure and supports the concept of spinodal ordering. It is believed that an interstitial mechanism is responsible for maintaining the SRO. Above 450 K, LRO persisted for samples initially in this state and SRO was only preserved up to 550 K for samples initially in that state. Between 550 and 720 K, a mixed SRO–LRO state occurred, and at temperatures above 720 K a complete transition to SRO was obtained. It is believed that maintenance of LRO requires a vacancy mechanism. At temperatures below 800 K the SRO–LRO transition occurred in a continuous fashion, while above 800 K a nucleation and growth mechanism was operative. This behavior is characteristic of an ordering transition of the first kind below and above the coherent instability temperature.

3.2 Irradiation-Induced Disorder

From measurements on the changes in electrical resistivity, lowering of the transition temperature for superconductivity as well as the magnetic saturation in ferromagnetic materials and decreased intensity in the diffraction intensity in superlattice reflections, it has been shown that irradiation-induced disordering occurs in alloys that were initially ordered. For a general review of some of these aspects, see Schulson (1979).

In investigations on the L1₂ compounds Ni₃Mn (Aronin, 1954), Cu₃Au (Siegel, 1949), Zr₃Al (Carpenter and Schulson, 1978), and Pt₃Fe (Piercy, 1963), the D1_a compound Ni₄Mo (Banerjee *et al.*,

1984; Banerjee and Urban, 1984), the A15 compounds Nb₃Sn and Nb₃Ge (Brown *et al.*, 1978b) as well as Nb₃Al (Sweedler and Cox, 1975), the degree of long-range order S decreased exponentially with the irradiation fluence. In general, this dependence can be expressed as

$$S = S_0 e^{-K\phi t} \quad (16)$$

where S_0 is the initial degree of long-range order, K is a parameter expressing the effectiveness with which the incident particle disorders the material, and ϕt is the irradiation fluence. The disordering occurs for bombardments with electrons, ions, and thermal and fast neutrons. In general, at temperatures below which irradiation-enhanced ordering can occur, complete disordering occurs at lower calculated DPA levels (see equation (4)) for cascade-producing irradiations (ions and fast-neutron irradiation) than for irradiations where only Frenkel pairs are produced (electrons and thermal neutrons). In Zr₃Al and Ni₃Al, ~1–3 DPA was required with electron irradiation to reduce S to ~0.1, whereas in Zr₃Al, Ni₃Al, Pt₃Fe, Cu₃Au, Ni₃Mn, Nb₃Sn, and Nb₃Al, ~0.1–0.3 DPA was required with heavy-ion and neutron irradiation to reach $S \sim 0.1$ (see Schulson, 1979). A more detailed comparison, however, should also take into account the large amount of spontaneous recombination that occurs promptly in dense cascades. Irradiation also increased the lattice parameter a , as indicated by studies on Zr₃Al, Nb₃Sn, V₃Ga, Nb₃Ge, Nb₃Al, Nb₃Pt, and Mo₃Os, by amounts ranging from 0.1 to 1.25% in these materials (see tabulation by Schulson, 1979). Many of these increases were considerably larger than those observed in intermetallic compounds that can be disordered thermally in the absence of irradiation, where $\Delta a/a \sim 0.1$ –0.2%. Hence under irradiation, as disordering occurs in an ordered alloy, the observed volume changes arise from the creation of wrong bonds (i.e. disordering) and lattice dilations arising from the presence of point defects and defect clusters.

Various mechanisms have been proposed for the rearrangement of atoms from their correct positions in an ordered lattice to a random distribution of the atoms as irradiation proceeds. These include thermal spikes by Seitz (1949), replacement collisions by Kinchin and Pease (1955), plastic spikes by Seitz and Koehler (1956), collapse of cascades to vacancy loops by Jenkins and Wilkens (1976), and random recombination by vacancies and interstitials by Carpenter and Schulson (1978). Some examples will now be given of experiments that have been undertaken in an attempt to elucidate some of the mechanisms of irradiation-induced disordering.

Piercy (1963) performed magnetic measurements on ($L1_2$) ordered Pt_3Fe that had been neutron irradiated (3.4×10^{17} – 6.4×10^{19} fission neutrons/cm²) at ~ 333 K. Pt_3Fe was chosen because it is normally paramagnetic above the antiferromagnetic Néel temperature of 70 K but becomes ferromagnetic when disordered. Hence the size of small disordered regions (~ 5 nm) in an ordered matrix could be detected since they were ferromagnetic regions with a low magnetic anisotropy contained in a non-ferromagnetic matrix. It was concluded that an average of 2.3 disordered regions were produced per fission neutron and that approximately 3300 atoms were disordered on average in these regions. The results also indicated that there was a region of partial disorder surrounding each completely disordered region. From an estimation of the temperature ($\sim 1.5 \times 10^4$ K) and duration ($\sim 4 \times 10^{-11}$ s) of the thermal spikes produced during each neutron collision, Piercy (1963) concluded that purely thermal effects could account for the disordering of about 3100 atoms contained within a radius $1.125r_0$ and the partial disordering of a further 1200 atoms contained within a radius of $1.25r_0$. The above calculation was based on an average energy of 8.6 keV being available in a thermal spike that disordered 3300 atoms, this energy being initially distributed uniformly over a radius r_0 of 1.97 nm. A normal Arrhenius equation for the atomic jump frequency, with a frequency factor of 10^{14} s^{-1} and an energy of 3 eV for interchanging two atoms, was used for calculating the number of jumps per atom for the short time interval that the spike was heated.

Detailed information on the role of replacement collision sequences in producing disordering was obtained by Kirk *et al.* (1977, 1978) and Kirk and Blewitt (1982) from magnetic saturation experiments performed on the $L1_2$ alloy Ni_3Mn . The atomic structure of ordered Ni_3Mn is shown in Figure 12, along with a representation of a Ni–Mn (100) plane before and after the passage of a $\langle 110 \rangle$ replacement-collision sequence (RCS). According to the model of ferromagnetism in Ni_3Mn by Marcinkowski and Poliak (1963), each Mn atom will align ferromagnetically with its nearest-neighbor Ni atoms unless three or more nearest-neighbor Mn atoms are present, in which case the central Mn atom will align antiferromagnetically. The passage of a $\langle 110 \rangle$ RCS in the fully ordered alloy will not change the state of magnetic order, whereas the passage of a $\langle 110 \rangle$ RCS in a partially ordered alloy will have some probability of placing a Mn atom into a position with three nearest-neighbor Mn atoms, thus causing a spin flip and a decrease in saturation magnetization. In one series of experiments, they irradiated Ni_3Mn samples

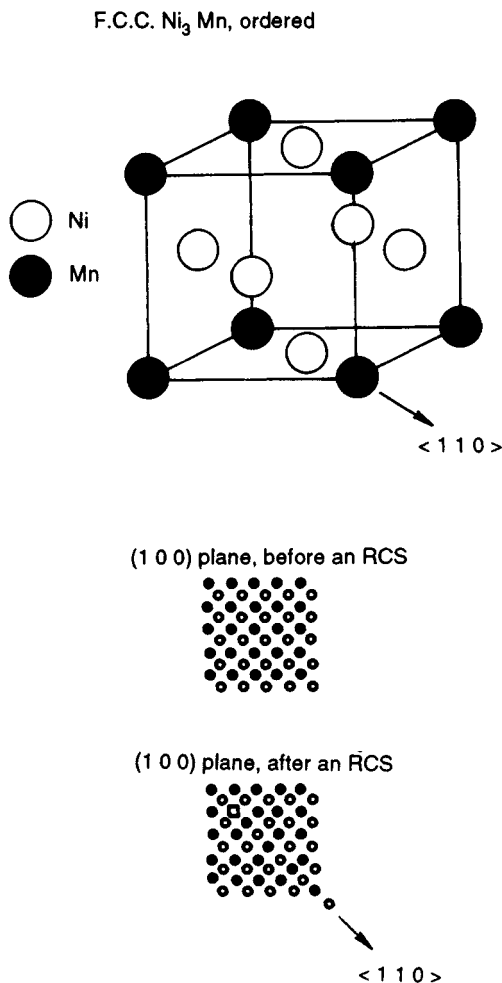


Figure 12. Unit cell of ordered Ni_3Mn and (100) Ni–Mn planes before and after occurrence of a replacement collision sequence RCS (From Kirk *et al.*, 1977)

containing different degrees of order S and measured the decrease in magnetization during irradiation with thermal neutrons at 5–6 K. The magnetic changes were related to the production of $\langle 110 \rangle$ RCSs by (n, γ) recoils, through the unique dependence on sample order (as discussed above). A comparison of the experimental data with a computer analysis of the magnetic model is shown in Figure 13. It was concluded that 112–150 $\langle 110 \rangle$ replacements occur, within one or two sequences, per (n, γ) recoil with an average energy of 492 eV. This is to be compared with the results of molecular-dynamics computer calculations by King and Benedek (1982). They found 56 $\langle 110 \rangle$ replacements at a 450 eV recoil

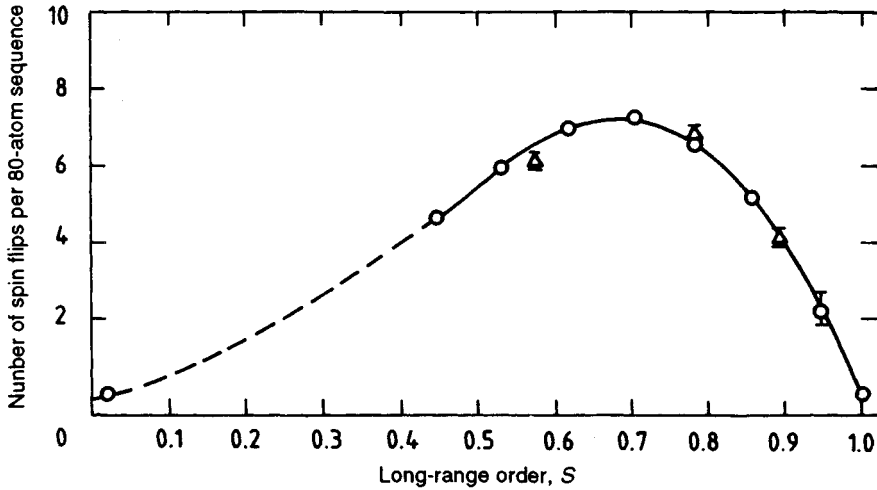


Figure 13. The dependence of the number of Mn atom spin flips per 80-atom sequence on the degree of long-range order in Ni_3Mn . Experimental results obtained for thermal neutron irradiation (Δ) are compared with a computer model calculation (\circ) (From Kirk *et al.*, 1977)

energy and much branching of sequences to yield an average maximum number of 4–5 replacements per sequence.

Kirk *et al.* (1978) and Kirk and Blewitt (1982) also studied the effect of fission neutrons on the saturation magnetization of Ni_3Mn . From equation (16), they obtained

$$d\Delta S/d\phi t = K(S_0 - \Delta S) \quad (17)$$

where K is now related to the number of random replacements per neutron. Equation (17) shows that the initial disordering rate (KS_0) is an increasing and linear function of the initial degree of order. Furthermore, they argued that long $\langle 110 \rangle$ RCSs produce a decreasing magnetization change per unit neutron fluence with increasing order ($S > 0.7$), while random replacements produce an increasing magnetization change per unit neutron fluence with increasing order. An irradiation experiment on two samples of different degrees of order (as shown in Figure 14) was performed to try to separate the effects of the two types of disordering. The ratio of the slopes (KS_0) of the two curves in Figure 14 was within 1% of the ratio of the degrees of order, thus implying that very few ($\sim 4\%$) of the replacements that were measured can be attributed to long-range $\langle 110 \rangle$ RCSs. The number of Ni–Mn interchanges per high-energy primary knock-on (average energy 30 keV) was 3400, and there were 60 replacements per displacement (as determined experimentally). Their results also suggest that in the cascades produced by the fission

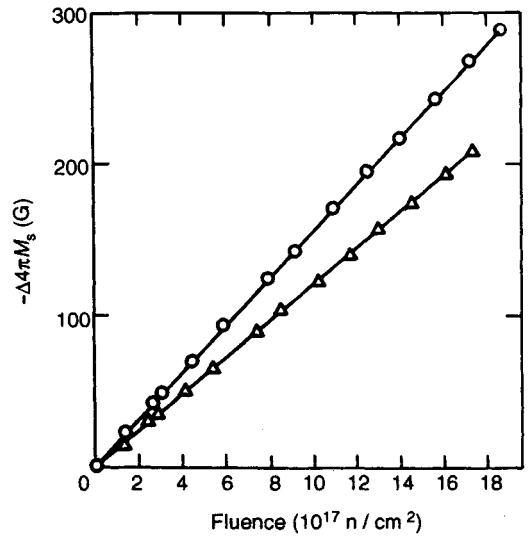


Figure 14. Decrease in saturation magnetization with fission-neutron fluence ($E > 0.1$ MeV) for two simultaneously irradiated samples of Ni_3Mn with long-range order parameters $S_0=0.93$ (\circ) and $S_0=0.72$ (Δ) (From Kirk *et al.*, 1978)

neutron irradiations, the distribution of the interstitial atoms is spatially quite compact just outside of the vacancy-rich core. The absence of long-range RCSs in even the peripheral regions of the cascade suggests that thermal agitation of the atoms within the cascade may prevent this from occurring.

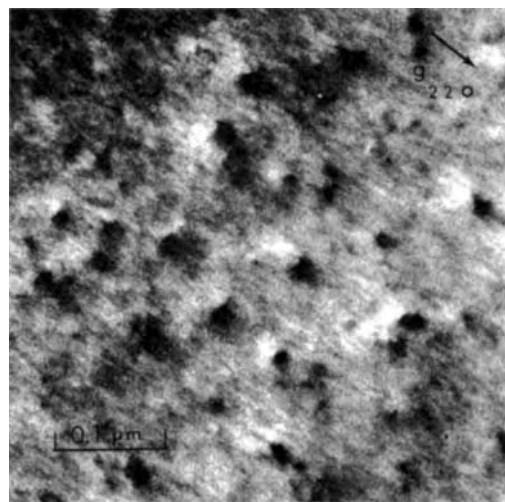
The damage produced within a reasonably dense collision cascade in ordered alloys can be observed directly in the electron microscope. The principle of the method has been described by Jenkins *et al.* (1976) and Jenkins and Wilkens (1976). Within individual cascade regions the long-range order is disrupted, giving rise to zones of reduced long-range order within the ordered matrix. This technique has been used for studying the disordering of the $L1_2$ compounds Cu_3Au , Cu_3Pd , Zr_3Al , Ni_3Si , and Ni_3Mn , the D0_3 compounds Fe_3Al and Fe_3Si , and the A15 compound Nb_3Sn , under various irradiation conditions. Described next are some specific results on Zr_3Al , Cu_3Au , and Nb_3Sn .

Zr_3Al is an $L1_2$ alloy that under various irradiation conditions can be disordered and then eventually amorphized (Howe and Rainville, 1977, 1979, 1980; Schulson *et al.*, 1979). The nature of the damaged regions formed in individual collision cascades has been investigated using low-fluence ($\sim 1 \times 10^{11}$ ions/cm²) bombardments with Ar ions (Howe and Rainville, 1977, 1979, 1980) as well as Cu ions (Howe and Rainville, 1991), and the results of the latter study will be described here. It is also of interest to describe these results in the context of the average deposited-energy density within a collision cascade. $\bar{\theta}_v$ is defined as follows for monatomic implants:

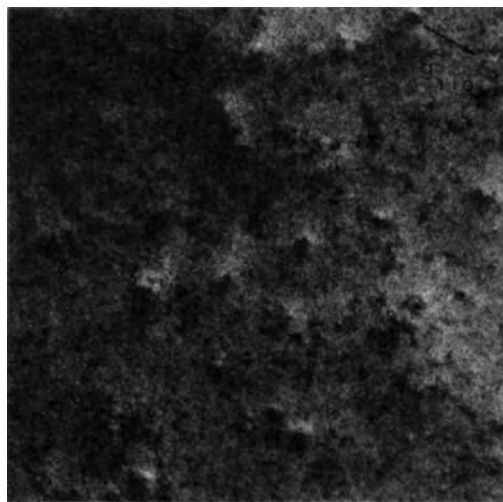
$$\bar{\theta}_v = 0.2\nu(E)/N_v V_R \quad (18)$$

where $\nu(E)$ is the portion of the monatomic ion energy that is lost in nuclear collision events, N_v is the number of lattice atoms contained within a spheroid whose axes are determined by the longitudinal $\langle \Delta X^2 \rangle^{1/2}$ and transverse $\langle Y^2 \rangle^{1/2}$ straggling components of the statistical damage distribution (Winterbon *et al.*, 1970; Winterbon, 1975), and V_R is the volume ratio defining the fraction of the statistical cascade volume filled on average by an individual cascade. Based upon the Monte Carlo damage simulations of Walker and Thompson (1978), for various implants in Si and Ge, a value of $V_R = 0.18$ was chosen by Howe and Rainville (1991) for ^{63}Cu ion implants in Zr_3Al .

Ion bombardments were performed at 295 K with 15–120 keV ions, which corresponded to $\bar{\theta}_v$ varying from 1.33 to 0.09 eV/atom (i.e. $\bar{\theta}_v$ decreases with increasing ion energy). Using the (1 1 1), (2 0 0), (2 2 0), and (1 1 3) fundamental reflections, the damaged regions exhibited black-white features (see Figure 15(a)) that indicate that these regions have a spherically symmetrical strain field. The average diameter \bar{D}_{sc} of these regions was 5.1–8.1 nm. The strain-contrast features indicate that they are probably three-dimensional clusters of interstitial atoms, although the possibility of amorphous regions being produced directly in the cascade cannot be ruled out. Centres of dilation would be consistent with the 5% volume increase observed (Schulson *et al.*,



(a)



(b)

Figure 15. Damaged regions produced in Zr_3Al by 100 keV Cu ions. Dark-field electron micrographs taken of the same area under two-beam dynamical conditions with a fundamental (2 2 0) reflection (a) and a superlattice (1 1 0) reflection (b). Zone axes near [0 0 1] (From Howe and Rainville, 1991)

1979) for the crystalline-to-amorphous transformation in Zr_3Al . When the same areas of the foil previously imaged with fundamental reflections were imaged under dynamical conditions with (110) superlattice reflections, many damaged regions were present in addition to those revealed using the fundamental reflections; as shown in Figure 15(b). These additional damaged regions appeared as black spots and were considerably smaller than the strain-contrast regions. Their average diameters \bar{D}_d were in the range 2.4–3.7 nm. They represent regions within the damage cascade in which sufficient disorder of the ordered lattice has occurred to give rise to a visible region using a superlattice reflection, but which do not contain a sufficiently high concentration of vacancies or interstitials to give rise to a strain-contrast effect. The contrast arises from the difference in structure factor (for superlattice reflections) between the disordered zone and the ordered matrix, i.e. due to a local reduction in the long-range order parameters. The number of observed regions per incident ion increased with increasing ion energy (decreasing $\bar{\theta}_c$) for the defects having a spherically symmetrical strain field as well as for the disordered regions. At the lower ion energies (15

and 30 keV), there was essentially one disordered region produced in each collision cascade, whereas at higher energies there were multiple disordered regions produced within a single cascade. As shown in Figure 16, the ratios $\bar{D}_{sc}/2\langle Y^2 \rangle^{1/2}$ (strain-contrast regions) and $\bar{D}_d/2\langle Y^2 \rangle^{1/2}$ (disordered regions) both decreased with increasing ion implantation energy. Even taking into account the increase in the number of damaged regions per incident ion with increasing ion energy, the fraction of the theoretical collision cascade volume occupied by the total volume of the damaged regions still decreased appreciably with increasing ion energy (decreasing $\bar{\theta}_c$).

The collapse of defect cascades to dislocation loops in (L1₂) ordered Cu_3Au has been studied quite extensively (Jenkins and English, 1982). Black *et al.* (1987) have performed a systematic transmission electron microscopy (TEM) study of the conditions leading to the formation of vacancy dislocation loops at the sites of defect cascades produced by irradiating with Ar, Cu, and Kr ions (50 and 100 keV) at 30 and 300 K. The disordered zones were imaged using superlattice reflections and dislocation loops using fundamental reflections. It was found that all dislocation loops were associated with disordered zones, but not

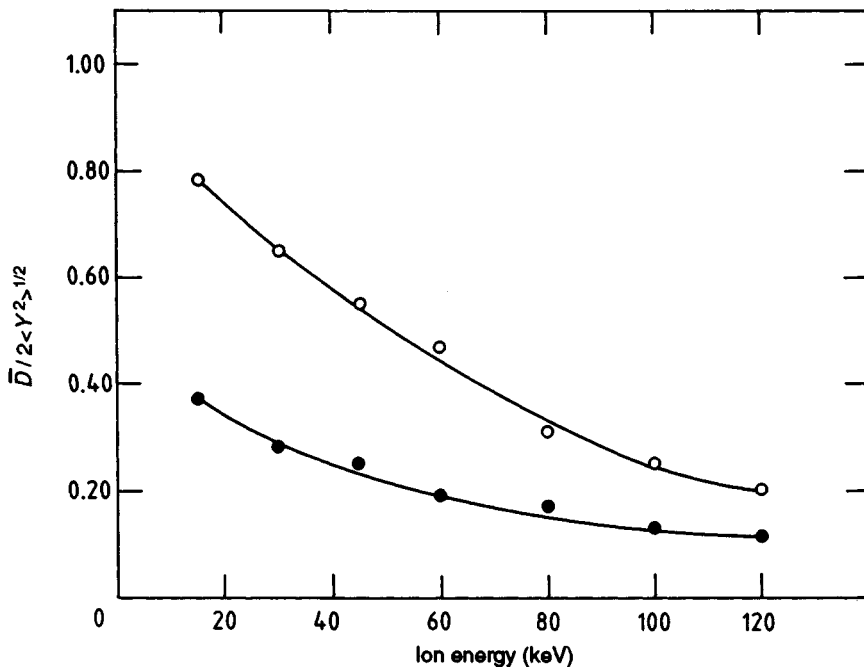


Figure 16. Variation of $\bar{D}_{sc}/2\langle Y^2 \rangle^{1/2}$ (strain-contrast regions) (○) and $\bar{D}_d/2\langle Y^2 \rangle^{1/2}$ (disordered regions) (●) with energy of implantation for ^{63}Cu ions in Zr_3Al (From Howe and Rainville, 1991)

vice versa. For all of the bombardments, collapse of the displacement cascades to dislocation loops occurred with high probability at temperatures as low as 30 K. Since vacancies do not undergo long-range thermal migration at 30 K, the collapse is occurring during the phase of collision cascades when extensive vacancy motion is possible, i.e. in the thermal spike phase that occurs within about 10^{-11} s of cascade initiation (Guinan and Kinney, 1981). Following the 30 K irradiation, no additional cascade collapse was observed during warming to 300 K. This observation, along with the high values of defect yield at 30 K, suggests that directed motion of vacancies toward the cluster nucleus occurs during the collapse process. Displacement cascades were observed to collapse with a significantly higher probability at 300 K than at 30 K, and the effect was more pronounced the higher the mass of the incident ion. Within a thermal spike model, an increase in ambient temperature might be expected qualitatively to decrease the cooling rate within the cascade region and therefore to increase the thermal spike lifetime.

Irradiation-induced disordering and defect production in Cu_3Au and Ni_3Al (both L_{12} structures) were studied by molecular-dynamics simulation for a 5 keV recoil atom at 10 K (Diaz de la Rubia *et al.*, 1993). They observed that the loss of the underlying crystalline structure and the loss of the chemical short-range order were controlled by different timescales. The crystalline order parameter decreased to ~ 0 within 1 ps, whereas the fast quenching occurring in the core of the cascade did not allow for a comparable loss of the chemical SRO. The transition between the disordered region produced by the cascade and the surrounding ordered region was sharper for Ni_3Al than for Cu_3Au , with perfect order being recovered within shells of 0.5 and 1.5 nm for Ni_3Al and Cu_3Au , respectively. The size of these disordered regions was consistent with those found by Black *et al.* (1987) in their TEM studies of Cu_3Au bombarded with 50 keV Cu ions at 30 K. Diaz de la Rubia *et al.* (1993) found evidence for vacancy clustering in the core of the displacement cascade, but there were no signs of interstitial cluster production in the intracascade regions.

The effects of fast-neutron irradiation on some bulk properties of A15 superconductors are fairly well-established, but the basic mechanism responsible for these irradiation-induced changes (e.g. critical current density J_c) are not well-understood (Weber, 1986). Experiments by Brown and Blewitt (1979) and Guinan *et al.* (1984) suggest that defects produced by collision cascades in A15 compounds are capable of pinning magnetic flux lines and thus initially increasing the

critical current densities during ion or neutron irradiation at low fluences. However, there is also considerable evidence that the enhancement of J_c is related to the irradiation-induced disorder. Support for this view also comes from experiments on the irradiation-produced change of J_c in pure and alloyed Nb_3Sn conductors and their comparison with the alloying effect in unirradiated samples (Suenaga, 1985). Kirk *et al.* (1990) performed 50 keV Xe-ion and 1.5 MeV Kr-ion irradiations on Nb_3Sn at 13–15 K and observed the damage evolution in a high-voltage electron microscope (HVEM). Initially, the martensitic structure in Nb_3Sn was observed at 12–30 K and then images of the irradiation-produced defects were obtained using either fundamental or superlattice reflections. At ion doses of 8.0×10^{11} Xe ions/cm² visible strain centres were observed that appeared to be regions of high concentration of point defects but which contained relatively little atomic disorder (i.e. antisite disorder). It was postulated that the centers of strain can be associated with pinning sites of magnetic flux and the corresponding increase in J_c . At higher ion doses of either Xe or Kr ions, overlap of the collision cascades produced regions of stronger disorder and possibly even amorphous zones. By a dose of 5×10^{12} Kr ions/cm², the characteristic contrast of the martensitic structure had disappeared, thus suggesting that a revision to the pre-transformation cubic structure had occurred due to the strain associated with the defects produced by the irradiation. Upon irradiating to 3.5×10^{13} Kr ions/cm², there appeared to be evidence for the onset of amorphization. The disordered or amorphous zones may be associated with decreases in J_c and the critical temperature T_c , as observed under neutron irradiation at comparable damage levels.

4. Irradiation-Induced Amorphization

4.1 Experimental Observations

The irradiation-induced amorphization of intermetallic compounds is of scientific interest and technological importance, as it entails the complete loss of measurable crystalline order. It is an extreme response of the solid to a combination of a large external input of energy and the presence of kinetic constraints that preclude the formation or the maintenance of the stable intermetallic phase. The kinetic path taken by the material to arrive at this large departure from equilibrium depends not only on the characteristics of the material but on the irradiation conditions as well. The spatial and temporal balance between irradiation damage and annealing can

Chapter 9

Crystallographic Transformations

C. Marvin Wayman

Department of Materials Science and Engineering, University of Illinois, Urbana, Illinois 61801, USA

Han R. P. Inoue

Department of Materials Science and Engineering, University of Washington, Seattle, Washington 98195, USA

1. Scope

By 'crystallographic transformations' one generally means that, when a new phase (product) forms from the old (parent), it bears certain definite geometrical relationships. The most widely studied crystallographic transformation is the martensitic transformation, the prototype of which occurs in quenched steels. Actually, martensite (in honor of Professor A. Martens) was the name given by Osmond in 1895 to the microstructure observed in quenched steels, but in more modern times the word 'martensite' designates a transformation mechanism, now known to be associated with many metals, alloys, ceramics, and even some polymers. These transformations occur in a variety of intermetallics, most notably the Hume-Rothery electron compounds as found, for example, in β -brass of near-equiatomic composition, and many similar alloys of Cu, Ag, and Au.

This chapter begins with a general consideration of the crystallographic features of martensitic transformations. The principles are general, and thus detailed descriptions of the crystal structures and substructures for individual alloy systems such as Ni–Al versus Cu–Sn are avoided. A brief survey of shape-memory phenomena within the framework of martensite crystallography is presented; this subject and the various martensite crystal structures are presented in detail in Chapter 26 by Schetky in Volume 2. Martensitic transformations and shape-memory phenomena are common to many

intermediate phases of the β -brass type, which also undergo massive and bainitic transformations; these transformations are also considered, even though massive transformations are non-crystallographic. The bainite transformation is highly controversial despite its martensitic crystallographic features. Some mechanical aspects of martensitic transformations have been considered for their insight into stress-induced transformations. Twinning is a shear process without phase transformation; however, it is considered in this chapter because of its intimate relationships with crystallography. Finally, brief mention is made of optical applications in connection with phase transformations.

2. Crystallography

2.1 The Lattice Correspondence and Bain Deformation

A great scientific and atomistic step was taken by Bain (1924) when he proposed a rather simple, albeit elegant, scheme for f.c.c. austenite to transform into b.c.t. martensite (Figure 1). The Bain distortion relates corresponding unit cells in the two structures and specifies the 'upsetting' strain, by means of which martensite is formed. This picture is too simple in itself but has remained an integral part of the more sophisticated theories that have ensued.

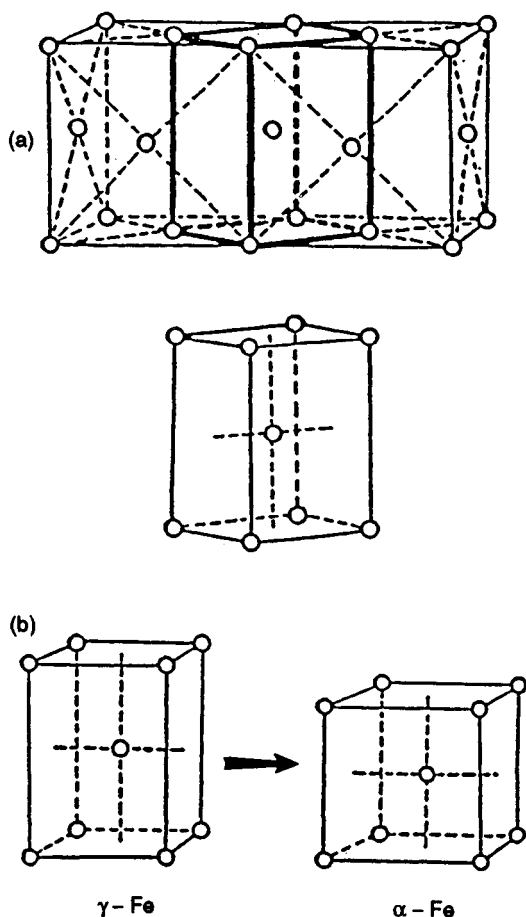


Figure 1. Bain's model for the formation of martensite in steels showing (a) a b.c.t. lattice delineated in the f.c.c. austenite structure and (b) the b.c.c. lattice of iron produced by the upsetting of the former (After Bain, 1924)

Note that the Bain strain implies a lattice orientation*, which from Figure 1 is

$$\begin{aligned} (001)_M &\parallel (001)_P \\ [001]_M &\parallel [001]_P \\ [010]_M &\parallel [110]_P \\ \text{etc.} \end{aligned}$$

Actually this simple orientation relationship is not observed; instead, the above planes and directions are not exactly parallel. In other words, the f.c.t.

prism delineated in the two f.c.c. unit cells is both compressed and 'rigidly' rotated during the course of the austenite–martensite transformations, as known from X-ray diffraction (Kurdjumov and Sachs, 1930; Nishiyama, 1934). Clearly, the rotation taken aside, the Bain distortion precisely accounts for the f.c.c. to b.c.t. structural change.

2.2 The Shape Change

It has been known for some time that the formation of martensite causes roughening (in Bain's words) of a prepolished surface, as shown in Figure 2. Careful analysis of the tilted martensite platelets shows, however, that an invariant plane strain (IPS) has occurred (Bowles, 1951). Such a distortion resembles a shear but also includes a volume-change component. In an IPS the displacement of any point is in a common direction and is proportional to its distance from the undistorted and unrotated invariant plane.

We now face a dilemma: in the case of iron alloys or steels (or in general), the measured IPS is inconsistent with the correct structural change as given by the Bain strain; on the other hand, the 'upsetting' produced by the Bain strain is not an IPS. Incidentally, the invariant plane is the habit plane of the martensite plates, as shown in Figure 2. Modern crystallographic theories of martensite formation such as those of Bowles and Mackenzie (1954) (BM) and Wechsler *et al.* (1953) (WLR) rectify these apparent inconsistencies, so we will proceed to discuss these BM and WLR theories, which are fundamentally identical but differ in mathematical order.

2.3 The Phenomenological Theory of Martensite Crystallography (PTMC)

Modern crystallographic theories suppose that, in addition to the Bain strain (the 3×3 matrix **B**) and rotation (**R**) alluded to earlier, a simple shear (**S**) occurs simultaneously (actually, no temporal sequence is implied by these operations). These three operations taken together are equivalent to the IPS shape deformation (**P**), or in matrix form

$$\mathbf{P} = \mathbf{SRB}$$

or equivalently

$$\mathbf{P} = \mathbf{RBS}$$

and

$$\mathbf{PS}^{-1} = \mathbf{RB}$$

*Subscripts P and M designate the parent phase and martensite respectively.

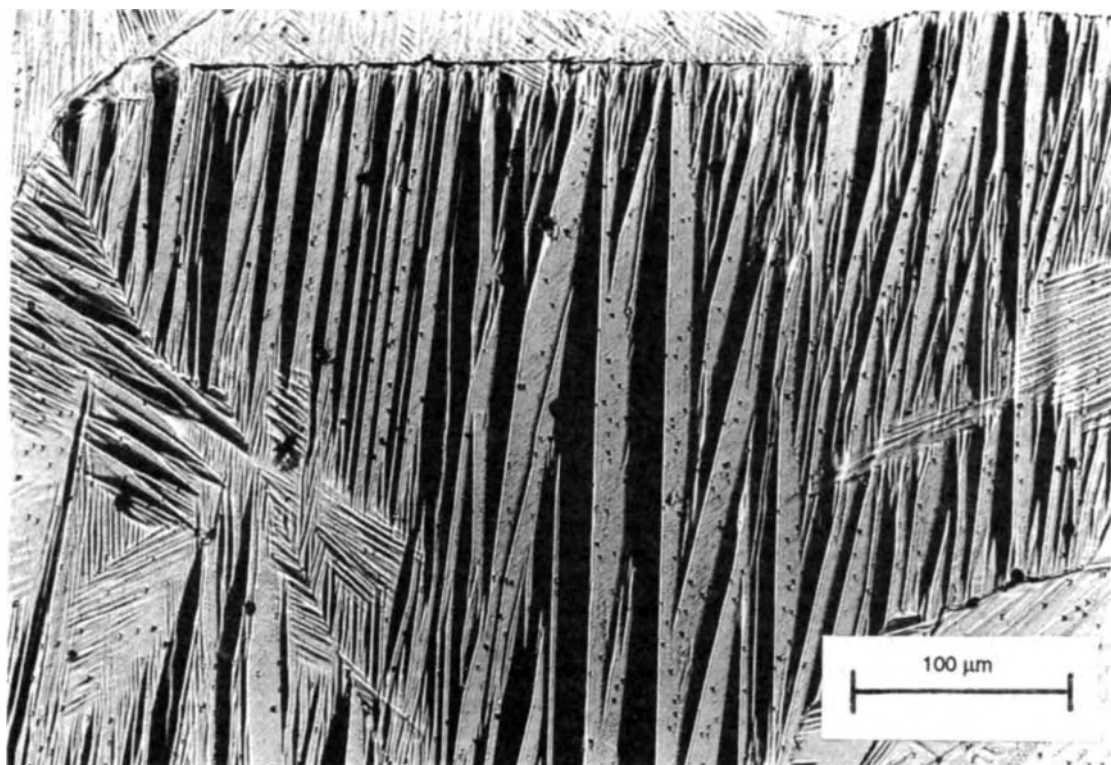


Figure 2. Optical micrograph showing an Fe-24Pt alloy partially transformed to martensite. The surface upheavals caused by martensite formation are analyzed to be an invariant plane strain. Both phases are ordered

Since S^{-1} is also a shear (but in the opposite direction), its combination with the IPS P produces an invariant line strain (Bowles and Mackenzie, 1954). That is, the combined rotation and Bain strain RB are also the identical invariant line strain (ILS). The ILS reduces to an eigenvalue problem with input data:

- Lattice parameters of the phase (hence strain magnitudes).
- Assumed Bain correspondence (hence the strain axes).
- Assumed plane p and direction d for S .

Out of this, the habit plane, lattice orientation relationship, and magnitude of the shape deformation P (surface tilt) are predicted.

At this point we must address the third item listed above, the simple shear. If the theory has any physical basis, then one would expect a fine-scale corrugation within the martensite as shown schematically in Figure 3. In other words, the martensite contains a substructure consisting of adjacent domains that are either slipped

or twinned relative to each other, an example of which is shown in Figure 4 for internally twinned martensite.

The basic PTMC presented above and the notion of an internally modulated martensite phase applies to all known martensitic transformations. The idea of a shape change and lattice (Bain) correspondence is also universal. We may, therefore, conclude that martensitic transformations are shear-like (displacive) in nature, involving cooperative atomic movements. There will, accordingly, be predictable interactions with mechanical stresses, as will be seen later.

2.4 What is a Martensitic Transformation?

The 'shear-like', 'cooperative', and 'military' (Christian, 1965) characteristics of martensitic transformations are universally recognized, but few explicit definitions exist. As late as the 1950s some refused to recognize that a martensitic transformation could occur in materials other than steels (Crussard and Philibert, 1956). More recently Cohen *et al.* (1979) concluded that:

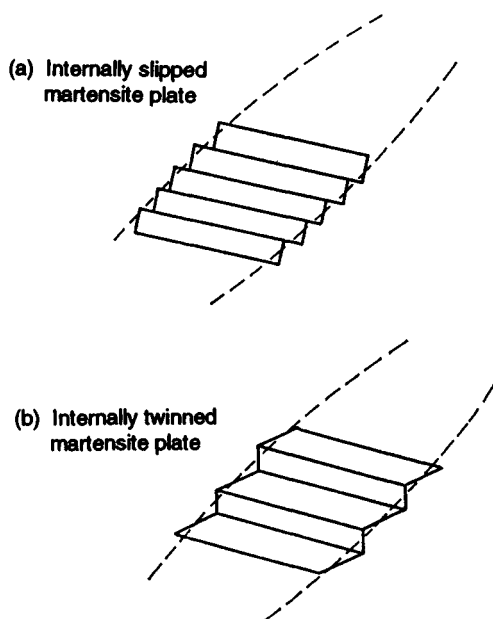


Figure 3. Schematic sketch showing (a) internally slipped and (b) internally twinned martensite. The alternate serrations at the habit plane average the strain out to zero on a macroscopic scale

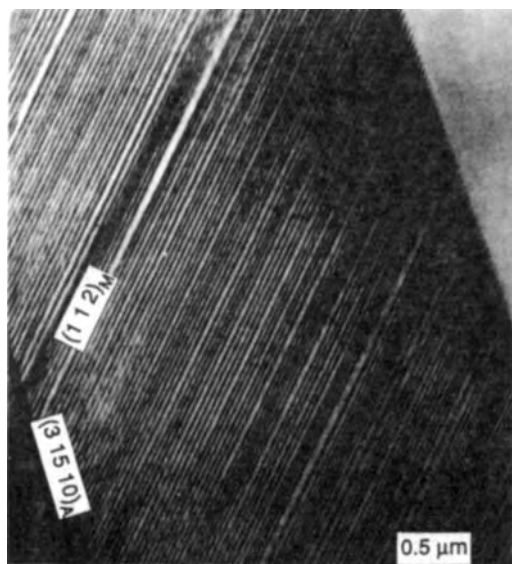


Figure 4. Transmission electron micrograph showing internal transformation twins in an Fe-Ni-C alloy martensite

A martensitic transformation is a lattice-distortive, virtually diffusionless structural change having a dominant deviatoric component and associated shape change such that strain energy dominates the kinetics and morphology during the transformation.

Such a definition may be disputed on the grounds that it is too broad by attempting to mix both crystallography and kinetics. As a case in point, Fe-Pt alloys near the composition Fe_3Pt undergo an austenite-martensite transformation irrespective of whether or not the parent phase is ordered (Dunne and Wayman, 1973). No differences in the transformation crystallography can be detected, i.e. the shape strain is the same in both cases, yet the transformation in ordered alloys is completely thermoelastic while that in disordered alloys is non-thermoelastic, like the Fe-Ni alloy shown in Figure 5. In other words the kinetics are vastly different although the crystallography is unchanged. In view of this difficulty, it appears that an earlier description (Clark and Wayman, 1969) may be more appropriate:

A martensitic transformation is in general described by an invariant-plane strain relief effect at a free surface, an irrational habit plane and orientation relationship, a lattice correspondence between substitutional atoms which implies the absence of long-range diffusion, and the presence of an internal inhomogeneity such as twinning, all of these features being uniquely related in accordance with the phenomenological crystallographic theory, according to which this body of information is completely internally consistent.

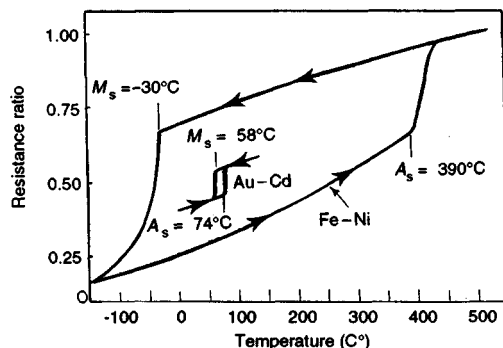


Figure 5. Electrical resistance changes during cooling and heating Fe-Ni (70:30) and Au-Cd (52.5:47.5) alloys, showing the hysteresis of the martensitic transformation on cooling and the reverse transformation on heating, for non-thermoelastic and thermoelastic transformation, respectively (After Kaufman and Cohen, 1957)

In effect, in the above description one uses all aspects of the crystallography and PTMC to define martensite.

3. Kinetics of Martensitic Transformations

It is implied from earlier discussion that martensitic transformations occur during quenching. While this may be the case for steels, it is not so in general. Indeed, martensitic transformations in many materials can occur during 'slow' cooling. Furthermore, they usually occur over a temperature range given by M_s (the martensite start temperature) and M_f (the martensite finish temperature). Although in steels when the martensite is heated it decomposes by tempering, in general a reverse martensitic transformation occurs given by the A_s and A_f temperatures, where A refers to the parent phase generally termed austenite (following steels).

But the thermal hysteresis can vary widely from case to case, as is shown in Figure 5 for Fe-Ni and Au-Cd alloys (Kaufman and Cohen, 1957). The Au-Cd alloy with narrow thermal hysteresis exhibits thermoelastic behavior, where the reverse transformation is essentially the inverse of the forward (cooling) transformation. On the other hand, the Fe-Ni alloy exhibits wide thermal hysteresis, and the reverse transformation occurs by the separate nucleation of the austenite phase. Simply put, in this case the nucleation of the parent phase requires a higher-energy barrier than the shrinkage of plates already there. With reference to Figure 5 it can be said that the Fe-Ni alloy exhibits non-thermoelastic behavior whereas the Au-Cd alloy shows thermoelastic behavior. The magnitude of the hysteresis is, however, not the only difference. Other differences are found in characteristics of both the forward ($P \rightarrow M$) and reverse ($M \rightarrow P$) transformations. In non-thermoelastic transformations during cooling, a martensite plate usually springs full size into existence, and then its interface becomes sessile. In thermoelastic martensites, transformation proceeds by the continuous growth of the plates upon cooling. If the cooling process is stopped, growth ceases; but, if it is resumed, growth continues until the plates eventually impinge upon a grain boundary or another plate. When the specimen is heated the reverse transformation occurs by the 'backward' movement of the martensite/parent interface. The martensite plates revert completely to the parent phase and to the original lattice orientation, i.e. complete crystallographic reversibility. A good analogy here would be to imagine filming the transformation on

cooling, and then running the film backwards to depict the reverse transformation on heating.

4. Nucleation of Martensite

It is generally believed that martensitic transformations cannot be homogeneously nucleated (Cohen and Wayman, 1981), but instead must commence at some lattice defect or inhomogeneity. It has been convincingly shown (Saburi and Nenno, 1986) that dislocations act as preferred sites for martensite nucleation, and accordingly various dislocation-type nucleation models have appeared. In an oversimplified view, one can imagine that the relaxed lattice at the core of a dislocation permits the Bain distortion to 'get started easier'. The literature abounds with cases where martensite is nucleated at grain boundaries, twin boundaries, dislocation clusters, etc., and quite specific nucleation models have appeared (Olson and Cohen, 1976). The evidence for nucleation at imperfections is overwhelming.

5. Stress- and Strain-Induced Martensitic Transformations

As early as the 1930s Scheil (1932) predicted the formation of martensite above M_s by the application of a stress. According to him, the shear stress required to activate the transformation decreases with decreasing temperature (being zero at M_s) whereas the shear stress required for austenite slip increases with decreasing temperature. Thus, at temperatures near M_s , applied stresses should induce plastic deformation by the martensitic mode rather than by slip.

It is observed that the critical stress to form martensite increases linearly with an increase in temperature from M_s up to a temperature M_s^σ above which martensite forms only after plastic deformation of the parent phase. There is another temperature, M_d , above which martensite cannot be mechanically stimulated, no matter what the stress. This behavior is shown in Figure 6 (Olson and Cohen, 1972). Note that between M_s and M_s^σ the stress is below the yield strength of the parent and is thus an elastic stress. Accordingly, the nucleation is stress-assisted and existing nucleating sites are simply aided mechanically. At M_s^σ the stress surpasses the parent yield strength, and because of the plastic deformation new nucleating sites are introduced. Thus, a distinction between elastic stress-induced martensite and plastic strain-induced martensite can be made.

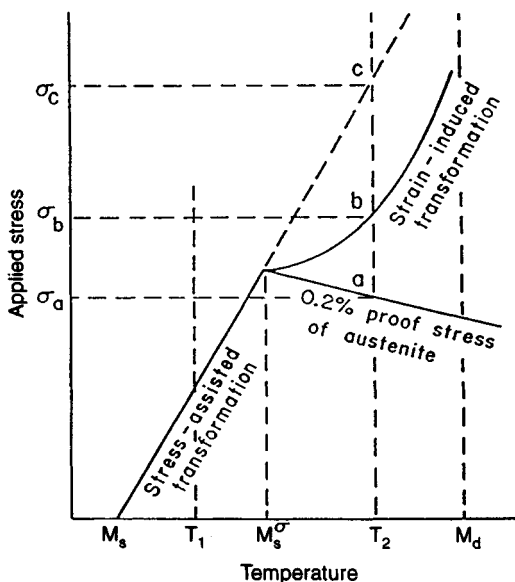


Figure 6. Stress-temperature diagram showing the critical stress for martensite formation in a typical iron alloy as a function of temperature. This diagram is of universal applicability. σ_a , σ_b , and σ_c are discussed in the text (After Olson and Cohen, 1972)

6. Shape-Memory Effects

6.1 Overview

The shape-memory effect (SME) has brought renewed interest that has led to recognition of diverse martensitic transformations. Although discovered in Au-Cd by Chang and Read (1951), activity in the SME field did not really become extensive until Buehler and colleagues (Buehler *et al.*, 1963) found similar behavior in a less exotic alloy, Ni-Ti (Nitinol). Chang and Read studied a Au-47.5Cd alloy with a view to the general features of its cubic-orthorhombic martensitic transformation. Between the SME discoveries in Au-Cd and Ni-Ti came similar findings for β -brass (Reynolds and Bever, 1952) and Cu-Al-Ni alloys (Rachinger, 1958). At present, Cu-Zn-Al, Cu-Al-Ni, and Ni-Ti alloys are all being commercially exploited for their SME.

The SME behavior is basically a consequence of a martensitic transformation. When compared, shape-memory alloys are found to have common characteristics such as atomic ordering, a thermoelastic martensitic transformation that is crystallographically reversible, and a martensite phase that forms in a self-accommodating

manner. The explanation of the shape-memory phenomenon is now universal and well in hand. In addition to the familiar 'one-way' memory, shape-memory alloys can also exhibit a 'two-way' memory, and a 'mechanical' shape memory resulting from the formation and reversal of stress-induced martensite. Some shape-memory alloys also exhibit 'rubber-like' behavior. See also Chapter 26 by Schetky in Volume 2 on applications of shape-memory alloys.

6.2 One-Way Memory

The shape-memory process is schematically illustrated in Figure 7 (Saburi *et al.*, 1979). Upon cooling a single crystal of the parent, typically 24* variants of martensite form. They form in self-accommodating groups of four variants in a diamond-like morphology. As the martensite phase is deformed, some variants grow at the expense of others, and eventually only one variant persists. At this point, the specimen surface is featureless, showing no relief effects. The surviving variant is that whole-shape strain direction that is most parallel to the tensile axis, thus permitting maximum elongation of the specimen. When this resultant single crystal of martensite is heated between A_s and A_f , the original specimen shape and parent single crystal are regenerated.

Because of crystallographic restrictions and the necessity to maintain ordering, the single crystal of martensite has only one way to undergo the reverse transformation. In other words, there are numerous variants of the Bain strain during the forward transformation but only one during reversal. It is to be noted that the 'one-way' memory just described is a one-time-only occurrence, but can be revived by re-forming the martensite, deforming it, etc. Completely recoverable strains of over 10% have been observed.

6.3 Two-Way Memory

A comparison between the one- and two-way shape memories is given in Figure 8. In the two-way shape

*From the observed parent-martensite orientation relationship and other features such as stacking faults in the martensite, the basal plane of martensites (say 18R (or 9R)) can be known to originate from one of the $\{110\}$ basal planes of the parent $D0_3$ (or B2) phase. This inhomogeneous shear (of the phenomenological theory) during transformation is also known to occur on the basal plane. There are six $\{110\}$ planes and two possible shear directions for each $\{110\}$ plane. Hence, there are 12 possible combinations of stacking planes and shear directions. Each combination leads to two possible crystallographically equivalent unrotated and undistorted habit planes, resulting in 24 martensite variants in a parent grain

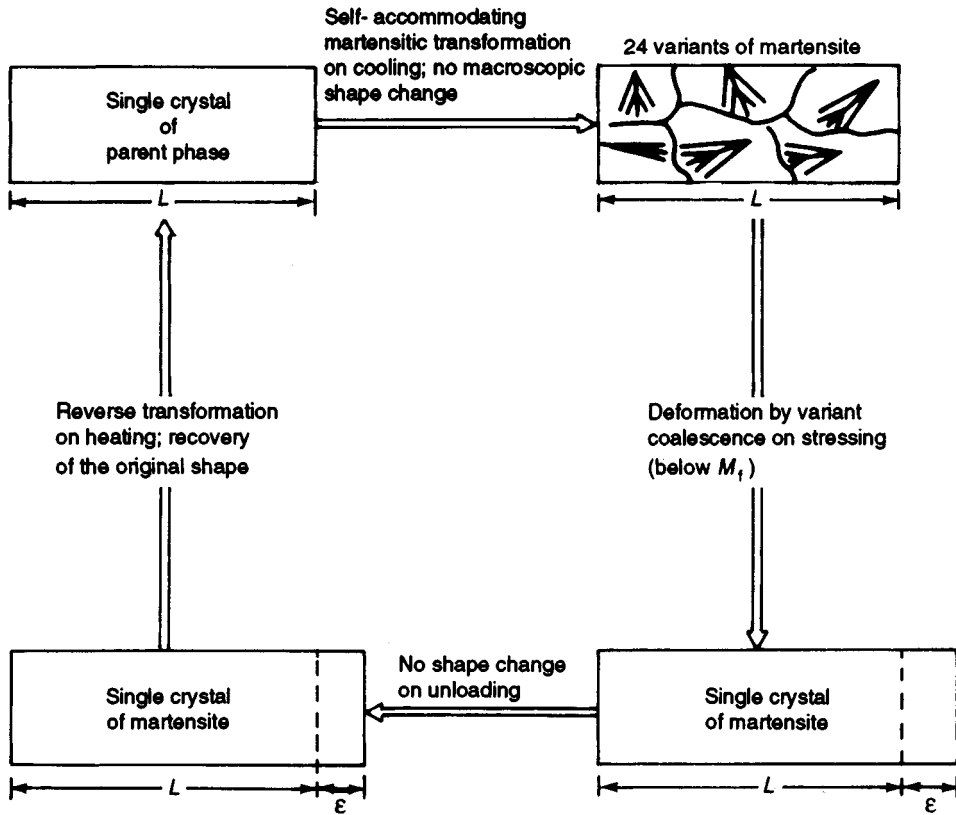


Figure 7. Schematic illustration of the various processes involved in the shape-memory effect (After Saburi *et al.*, 1979)

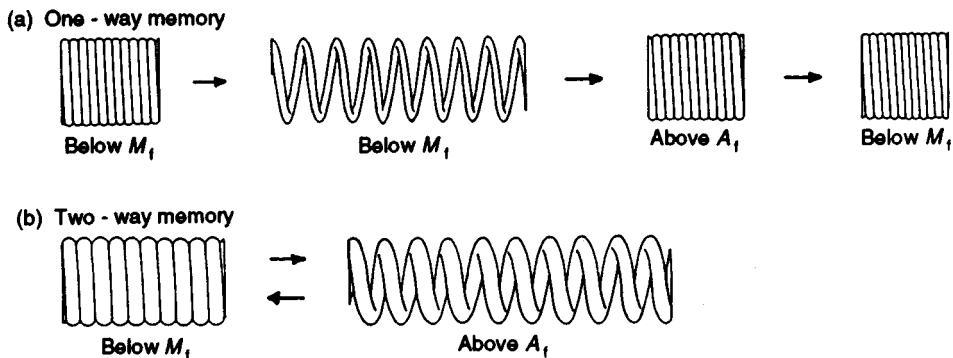


Figure 8. An example using coil springs to compare the differences between the one-way and two-way shape memories

memory the object changes shape upon both cooling and heating. This differs from the one-way memory in two respects: (i) infinite repeatability, and (ii) a shape change during cooling. The two-way memory is

associated with built-in microstresses, which progressively accumulate after appropriate thermomechanical treatment (Schroeder and Wayman, 1977). These microstresses 'program' the object so that during cooling between

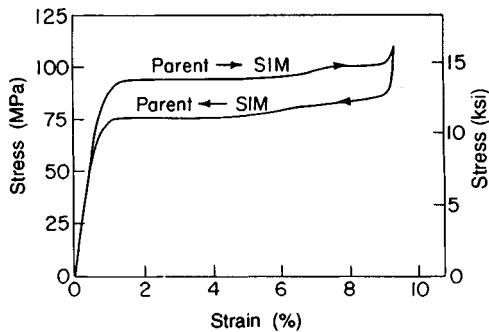


Figure 9. Superelastic stress-strain loop for a Cu-Zn alloy (Cu-39.8Zn) deformed at about 50 °C above the M_s temperature, i.e. $M_s = -125$ °C and transformed at -77 °C (After Schroeder and Wayman, 1979)

M_s and M_f only one variant of the martensite forms—hence the shape change. The shape-change process upon heating is the same as with the one-way memory: a single crystal of the martensite reverts to a single crystal of its parent.

The two-way memory can be brought about by either, or a combination, of two procedures. First, the specimen is subjected to deformation in the martensitic condition, and then heated to above A_f . It is then cooled below M_f and deformed again in exactly the same manner to the same shape, and heated above A_f again. This process is repeated a few times and then the specimen is fully programmed. Alternatively, a specimen can be superelastically stress-cycled above M_s . A stress-induced martensite then forms and in reverse generates the microstress sources.

6.4 Superelasticity

Figure 9 is a stress-strain curve for a single-crystal specimen of a Cu-39.1Zn shape-memory alloy deformed in tension at about 50 °C above its M_s temperature (Schroeder and Wayman, 1979). Yielding at an essentially constant stress (upper plateau) corresponds to the formation of 9R stress-induced martensite (SIM) from the B2 parent. At about 9% strain the specimen becomes fully martensitic. When the stress is released, the strain follows the lower plateau and fully recovers as the SIM reverts to the parent. This behavior corresponds to a mechanical (as opposed to a thermal) shape memory. A stress-strain relationship such as that shown in Figure 9 is frequently referred to as a superelastic stress-strain loop. The stress necessary to

induce the martensite decreases with temperature and falls to zero at M_s .

6.5 Rubber-like Behavior

Rubber-like behavior was first observed for a Au-Cd alloy by Ölander (1932). That is, the alloy deformed like rubber with low effective modulus when loaded but it sprang back to the initial shape when unloaded. This phenomenon was later confirmed by Chang and Read (1951) in a Au-47.5Cd alloy, and by Burkhart and Read (1951), who studied an In-20.7Ti alloy. Both of these systems show shape-memory behavior. Considering the Au-Cd alloy, it is interesting to note that the rubber-like behavior is found only after the martensite is aged at room temperature ($M_s = 60$ °C) for at least a few hours. Freshly transformed specimens exhibit shape-memory behavior and bent rods will not spring back to their initial shape. Chang and Read (1951) attributed the rubber-like behavior to favorably oriented 'regions' growing at the expense of others, based on microscopic observations.

Rubber-like behavior also constitutes a mechanical type of shape memory as does the process of SIM formation. But rubber-like behavior is characteristic of a fully martensitic structure whereas superelastic behavior is associated with formation of martensite under stress. These two types of behavior collectively fall in the category of 'pseudoelasticity', but one should use care in the interest of preciseness. Broadly speaking, Ölander's (1932) report of rubber-like behavior in Au-Cd was the first indication of the existence of a shape-memory effect. It is ironic that even today, 60 years later, the origin of rubber-like behavior remains obscure.

6.6 Summary

Figure 10 is a stress-strain-temperature diagram for a Ni-Ti shape-memory alloy that summarizes its mechanical behavior. At the extreme rear the stress-strain curve shown in the σ - ϵ plane corresponds to the deformation of martensite below M_f . The induced strain, about 4%, recovers between A_s and A_f after the applied stress has been removed and the specimen heated, as seen in the ϵ - T plane. At a temperature above M_s (and A_f) SIM is formed, leading to a superelastic loop with an upper and lower plateau, the middle σ - ϵ plane. At a still higher temperature and above M_d , the front σ - ϵ plane, no SIM is formed. Instead, the parent phase undergoes ordinary plastic deformation.

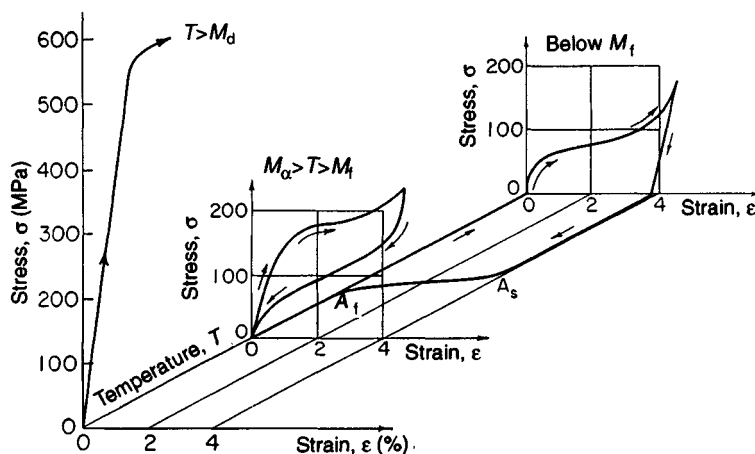


Figure 10. Stress-strain-temperature diagram for a Ni-Ti (Nitinol) shape-memory alloy showing shape-memory and superelastic characteristics and the deformation behavior of the parent phase above the M_d temperature (above which no martensite can form regardless of the magnitude of the stress). Temperature increases from upper right to lower left

7. Martensitic Transformations in Ceramics

Although beyond the scope of the subject matter at hand, it should be noted that martensitic transformations occur in numerous ceramics. An especially interesting case involves zirconia. By proper doping (alloying), tetragonal precipitates of zirconia will form in the cubic matrix. When the matrix is stressed, it will become ductilized by the stress-induced tetragonal-to-monoclinic martensitic transformation in the stress field of advancing cracks; the transforming particles in effect de-energize the cracks by absorbing energy and slowing cracks (Sakuma, 1988). Attempts to improve ductility of intermetallic compounds by utilizing stress-induced martensites have recently been made, which will be described in Section 11.1.

8. Bainite Transformations

Bainite forms isothermally as an intermediate transformation product above M_s but below the temperature of eutectoid decomposition in ferrous alloys. This product is a mixture of ferrite and carbide, which is distinctly different from pearlite (a eutectoid product), and is termed 'bainite' in honor of E. C. Bain who first observed such microstructures in collaboration with Davenport (Davenport and Bain, 1930). Bainite also forms during continuous cooling. Bainite transformations occur not only in ferrous alloys but also in non-ferrous

substitutional alloys including ordered intermetallics, and the product exhibits a plate-like morphology.

8.1 Bainite Transformations in Ferrous Alloys

Bainite transformations in steels are characterized by a C curve on a time-temperature-transformation (TTT) diagram; thereby an incubation period is present during isothermal annealing. Bainite transformations occur with compositional changes, indicative of diffusion-controlled processes. However, they also exhibit surface relief (Ko and Cottrell, 1952; Speich, 1962), a characteristic of a diffusionless (or displacive) reaction. Because of these contradictory characteristics, mechanisms are mainly categorized into two distinctly different models: a diffusionless martensitic transformation (Garwood, 1954) and a diffusion-controlled precipitation phenomenon (Hehemann *et al.*, 1972; Lorimer *et al.*, 1975). Many researchers have been attracted to the former model but some believe in the latter because similar surface relief also accompanies a higher-temperature product, Widmanstätten ferrite (Watson and McDougall, 1973). Ohmori and Maki (1991) have pointed out recently that Widmanstätten ferrite can form displacively if the magnitude of the shape strain and the morphology of surface relief are taken into account. Because of a lack of decisive evidence, whether bainite transformations in ferrous alloys are displacive or diffusion-controlled remains unsolved.

Table 1. Crystal structures of parent and bainite phases at early stages of transformation in Cu- and Ag-based alloys

Alloy	Parent	Bainite	References
Cu-37.8 to 43.3Zn	B2 (cP2)	Disordered 9R	Cornelis and Wayman (1974)
Cu-39.3Zn	B2 (cP2)	Disordered 9R	Sato and Takezawa (1968)
Cu-28.9Zn-6.1Al	B2 (cP2)	Ordered 9R	Takezawa and Sato (1986)
Cu-29.1Zn-6.7Al	B2 (cP2)	Ordered 9R to disordered 9R	Takezawa and Sato (1990)
Cu-24.8Zn-9.0Al	L2 ₁ (cF16)	Ordered 18R to ordered 9R	Wu <i>et al.</i> (1989)
			Hamada <i>et al.</i> (1991)
Cu-24.8Zn-9.0Al	B2 (cP2)	Ordered 9R	Wu <i>et al.</i> (1989)
Cu-40Zn-4Au	B2 (cP2)	Ordered 9R to disordered 9R	Tadaki <i>et al.</i> (1991)
Cu-40Zn-9Au	L2 ₁ (cF16)	Ordered 18R	Tadaki <i>et al.</i> (1991)
Ag-45Cd	B2 (cP2)	Disordered 9R	Wu <i>et al.</i> (1988)
			Tadaki <i>et al.</i> (1989)
Ag-27.0 to 28.1Zn	B2 (cP2)	9R (?)	Kubo and Hirano (1972)

8.2 Bainite Transformations in Ordered Intermetallic Alloys

Bainite transformations occur in many Cu, Ag, and Ti alloys when a metastable phase is aged isothermally at a moderate temperature between the M_s point and the eutectoid temperature after being quenched from a high-temperature β -b.c.c. region. The metastable phase becomes ordered when quenched, and then transforms into a f.c.c.-based, close-packed ordered structure. Ordered intermetallics exhibiting bainite transformations include Cu-Zn (Cornelis and Wayman, 1974), Cu-Zn-Al (Wu and Wayman, 1986), Cu-Zn-Au (Doig and Flewitt, 1983), Cu-Sn (de Bondt and Deruyttere, 1967), Ag-Zn (Kubo and Hirano, 1972), Cu-Al (Moon and Garwood, 1968), and Ag-Cd (Wu *et al.*, 1988). Because ordered intermetallics offer structural advantages over disordered alloys in terms of atomic arrangements and do not contain carbon atoms that cause intricate phenomena related with carbide precipitation as in steels, the change in composition during a bainite transformation can be clearly observed by electron diffraction and microanalysis techniques, and thereby better understanding of the bainite transformation is achieved.

8.3 Crystal Structures of Parent and Bainite Phases

The high-temperature β -b.c.c. (A2, cI2) phase of binary and ternary Cu-Zn alloys and binary Ag-Cd and Ag-Zn alloys transforms when cooled or quenched into a metastable ordered b.c.c. phase that has either a B2 (cP2), D0₃ (cF16) or L2₁ (cF16) structure. This metastable phase undergoes a bainite transformation during isothermal aging into a f.c.c.-based α_1 phase (also called α_b phase) having either a 9R or 18R

structure, similar to that of martensites formed by subzero cooling. The 9R and 18R structures are layered structures and are similar in stacking sequence. In the case of martensites, the former is derived from a B2 parent having a stacking sequence ABCBCACAB, while the latter is from a D0₃ parent with a stacking sequence AB'CB'CA'CA'BA'BC'BC'AC'AB', both being related with the stacking of the parent {110} planes. As seen in Table 1, the α_1 bainite is either ordered or disordered at early stages of growth, although the parent phase is ordered. For example, in a Cu-29.1Zn-6.7Al alloy the B2 phase transforms initially into the bainite phase having an ordered 9R structure and then to a disordered 9R structure during thickening of the plates, while such disordering occurs even at an early stage in Cu-40Zn and Ag-45Cd alloys (Cornelis and Wayman, 1974; Wu *et al.*, 1988; Tadaki *et al.*, 1989). This crystal structural difference in terms of atomic ordering is due to the difference in diffusion rate of solute atoms in bainite plates. Whether the parent phase is of B2, D0₃, or L2₁ is determined by heat-treatment conditions and alloy compositions (Wu *et al.*, 1989; Takezawa and Sato, 1990).

The α_1 phase is a plate-shaped bainite and reveals surface relief, as shown in Figure 11 and 12. A TTT diagram study by Flewitt and Towner (1967) has revealed that, in addition to the α_1 phase, a rod-shaped Widmanstätten product of the equilibrium, disordered f.c.c. α phase forms during isothermal aging in a higher temperature range. Upon prolonged aging, the α_1 bainite becomes the disordered f.c.c. (3R) structure of the equilibrium α phase.

8.4 Shape Change

A shape change occurs in Cu-Zn and Cu-Zn-Al alloys when aged at temperatures above M_s under stress.

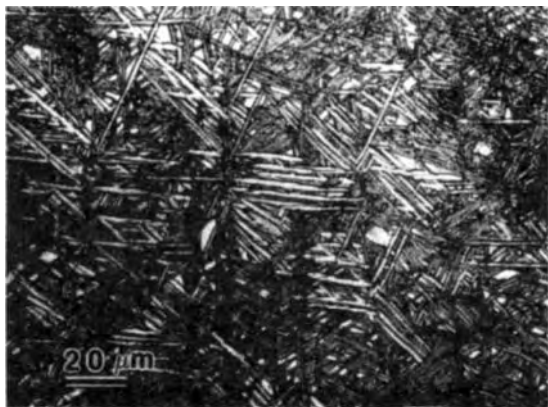


Figure 11. Optical micrograph of α_1 plate-shaped bainite in a Cu-39.3Zn alloy transformed at 450 °C for 90 s (After Cornelis, 1973)

Takezawa and Sato (1986, 1988) observed elongations up to 5.5% in a Cu-28.9Zn-6.1Al alloy upon isothermal aging at various temperatures (above M_s) at a tensile stress of 125 MPa. They attribute the elongation to the formation of particular variants of bainite. The shape change occurred only after an incubation period and followed a curve that represents the kinetics of a diffusion-controlled transformation, with an activation energy corresponding to that for the diffusion of Zn in the matrix. The incubation period and the time necessary to reach the ultimate elongation decrease and the growth rate increases with increasing isothermal temperature. The ultimate shape change is roughly equal to, but not higher than, that of shape recovery with the shape-memory effect of the same alloy. Takezawa and Sato (1986, 1988) think that the shape change results from a martensitic process. They conclude that diffusion is necessary to prepare suitable surrounding conditions for the nucleation and growth of bainite crystals to be formed by a shear process. Figure 13, from their work, shows the incubation period as well as the good agreement of elongations upon the bainite transformation with a theoretical curve based on a diffusion-controlled Austin-Ricketts process (Austin and Ricketts, 1939).

8.5 Microstructure

The microstructure and crystal structure of bainite crystals in Cu-Zn alloys are quite similar to those of diffusionless martensites forming at subzero temperatures in the same alloys (Cornelis and Wayman, 1974; Warlimont and Delaey, 1974). Bainite plates

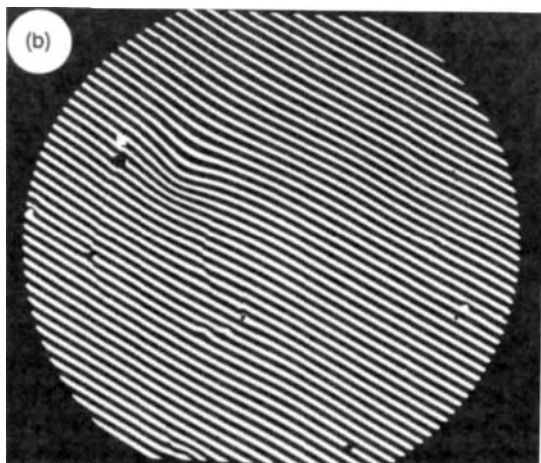
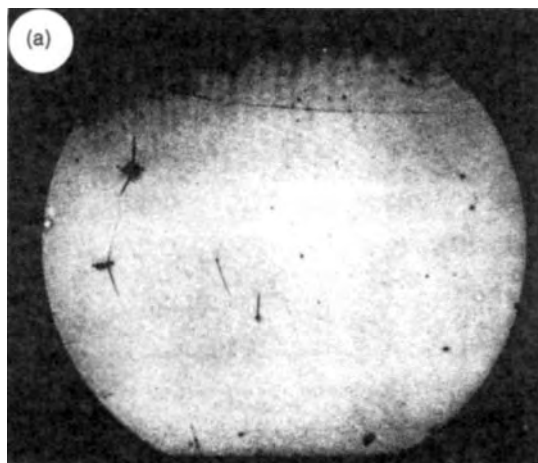


Figure 12. (a) Optical and (b) interference micrographs of α_1 plate-shaped bainite of a Cu-39.6Zn-1.2Ag alloy transformed at 430 °C for 5 s, showing surface relief (After Cornelis, 1973)

contain a fine internal structure consisting of stacking faults parallel to the basal plane of the 9R structure at early stages of transformation (Cornelis and Wayman, 1974). The density of stacking faults is higher at higher aging temperatures. The tips of bainite plates are defect-free (Takezawa and Sato, 1986), similar to very thin martensite plates at an early stage of growth (Saburi *et al.*, 1986).

During prolonged aging, the 9R stacking sequence of the bainite is gradually destroyed and thin bainite plates increase their width concurrently with annihilation

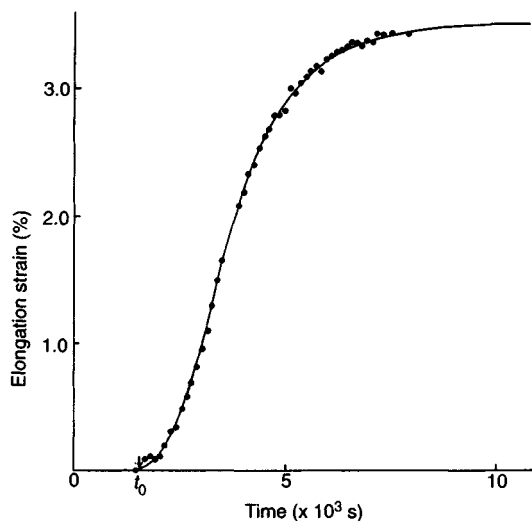


Figure 13. Macroscopic shape change during bainite transformation in a Cu-40Zn alloy subjected to a tensile stress of 98 MPa at 473 K. The curve is theoretical (After Takezawa and Sato, 1986)

of stacking faults. On further aging, the density of stacking faults becomes very low where the crystal structure of the bainite becomes the disordered f.c.c. structure of the equilibrium α phase (Cornelis and Wayman, 1974).

8.6 Habit Plane

The habit plane of the α_1 bainite is $\{2\ 11\ 12\}_{B2\text{ or }L2_1}$ at early stages of transformation in both binary and ternary Cu-Zn alloys (similar to β_1' -9R martensite in binary Cu-Zn alloys) and changes to $\{123\}_{B2\text{ or }L2_1}$ at later stages where the bainite eventually becomes disordered f.c.c. (Cornelis and Wayman, 1974; Flewitt and Towner, 1967). In Cu-Zn-Al alloys the habit plane is reported to be $\{155\}_{L2_1}$, nearly parallel to $\{2\ 11\ 12\}_{L2_1}$ (Takezawa and Sato, 1986). In a Ag-27.1Zn alloy the habit planes are reported to be both $\{235\}_{B2}$ and $\{134\}_{B2}$ (Kubo and Hirano, 1972).

Stress-assisted bainite plates form under stressing at moderate temperatures in Cu-Zn and Cu-Zn-Al alloys. Several variants of stress-assisted bainite occur but all have the $\{2\ 11\ 12\}_{L2_1}$ habit plane (Takezawa and Sato, 1988). Different from 9R martensite, variants having the highest Schmid factor do not always occur predominantly, resulting in the difference in the ultimate shape change under stress comparing bainite and martensite formation.

8.7 Nucleation and Growth

Similar to martensite, bainite plates nucleate at or near structural defects such as dislocations, grain boundaries, precipitate rods, and inclusions. Figure 14 is a set of electron micrographs showing small α_1 bainite plates

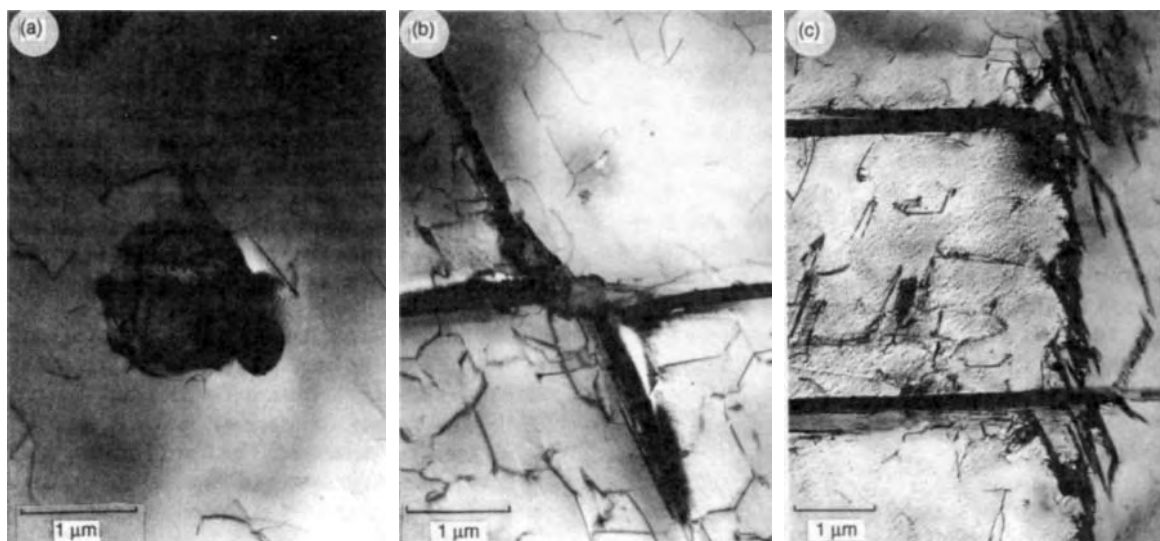


Figure 14. Electron micrographs showing various nucleation sites of bainite plates in a Cu-28.9Zn-6.1Al alloy: (a) oxide particle; (b) α rod; (c) grain boundary (After Takezawa and Sato, 1986)

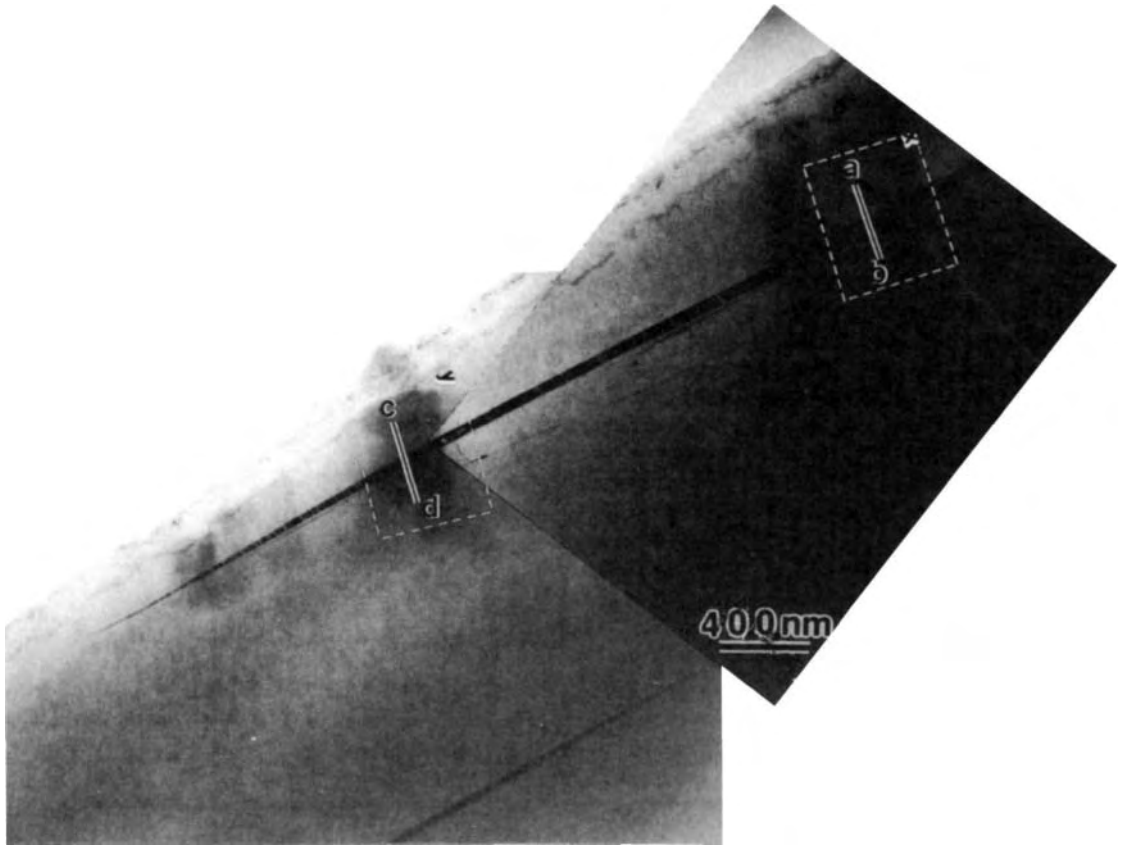


Figure 15. Transmission electron micrograph of an α_1 bainite plate formed after aging at 423 K for 175 ks. Microanalyses along lines a-b and c-d were performed (After Hamada *et al.*, 1991)

formed at various nucleation sites in a Cu-41.0Zn alloy aged at 230 °C (Takezawa and Sato, 1986). These nucleation sites are structurally inhomogeneous and may have Zn concentrations that are almost equal to that of a bainite plate, because such inhomogeneity causes a localized stress gradient that assists diffusion of solute atoms. Substantial changes in composition occur during the bainite incubation period by stress-induced diffusion of solute atoms at dislocations. Figures 15 and 16, from Hamada *et al.* (1991), show that the Zn concentration near dislocations is almost equal to that of a bainite plate in a Cu-Zn-Al alloy.

8.8 Growth Kinetics

The α_1 bainite plates in Cu-Zn and Cu-Zn-Al alloys grow anisotropically, i.e. rapid lengthening and slow thickening. Hornbogen and Warlimont

(1967) studied growth rates and determined that α_1 plates in a Cu-Zn alloy lengthen linearly at a high rate of $1.5 \times 10^{-6} \text{ cm s}^{-1}$ at 250 °C and that the growth ceases at later stages, while plate thickening occurs slowly at a rate of $0.6 \times 10^{-8} \text{ cm s}^{-1}$ at 250 °C. The activation energy obtained from the lengthening rate is nearly equal to that obtained from diffusion coefficients of Zn in the β phase, suggesting that the growth of α_1 plates is controlled by Zn diffusion. Lengthening kinetics were studied by Simonen and Trivedi (1977), and their results indicate that the rapid lengthening can only be rationalized under the two assumptions of a semicoherent interfacial boundary and supersaturation of Zn concentration. The former assumption, however, is not supported by high-resolution transmission electron microscope (HRTEM) studies of the interface, in that there is no semicoherent interfacial boundary between an α_1 plate and the matrix at an early stage

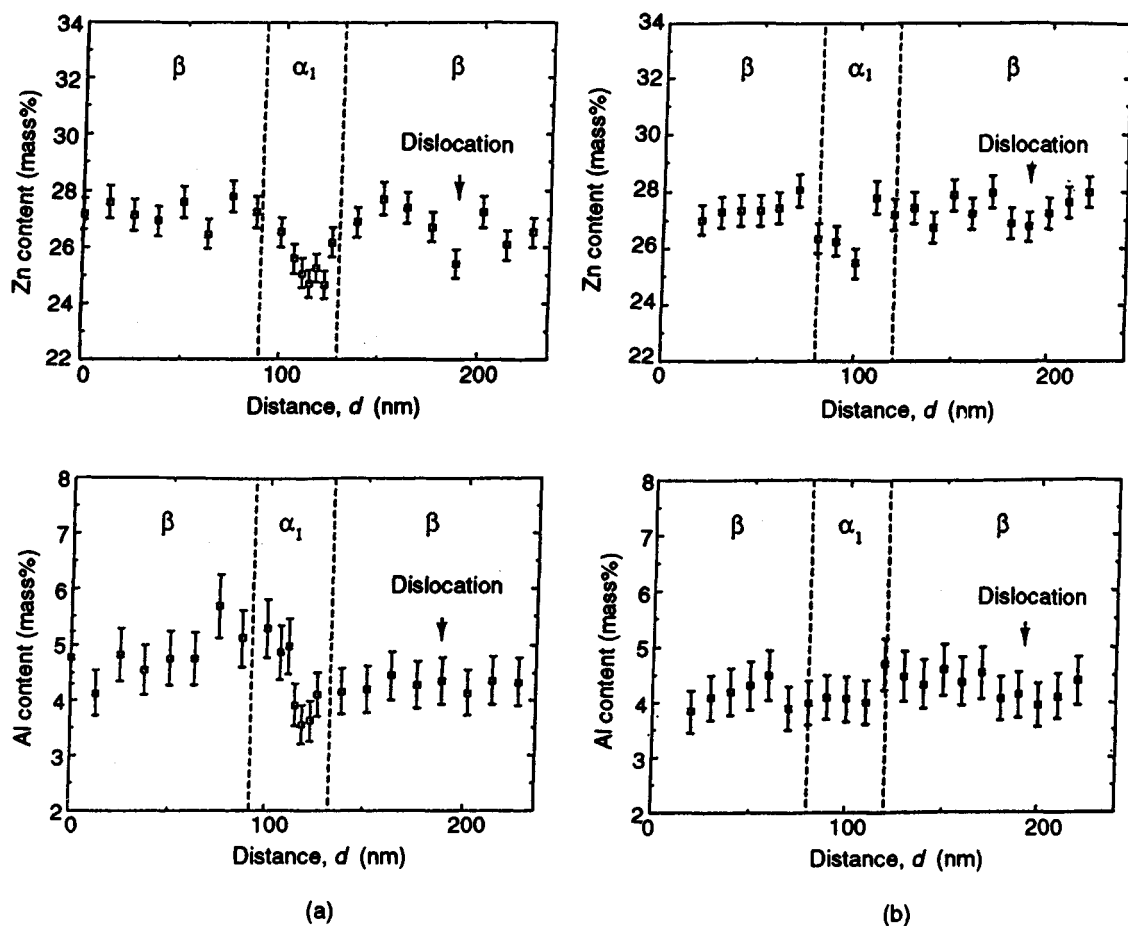


Figure 16. Zn and Al concentrations (a) along line a-b and (b) along line c-d of microanalyses of the α_1 bainite plate in Figure 15 (After Hamada *et al.*, 1991)

of transformation in a Cu-Zn-Al alloy (Hamada *et al.*, 1992). The slow plate-thickening kinetics caused by Zn diffusion also may not agree with recent compositional observations, as described in the following section.

8.9 Compositional Alteration

It has been accepted that a compositional change occurs in association with bainite transformation, but when diffusion actually occurs has been in debate. Recent studies with analytical electron microscopy, which has improved resolution, have revealed that the compositions of an α_1 bainite plate and the surrounding matrix are distinctly different even at a very early stage of growth in Cu-Zn (Cliff *et al.*, 1990), Cu-Zn-Al

(Nakata *et al.*, 1989; Hamada *et al.*, 1991), Cu-Zn-Au (Tadaki *et al.*, 1991), and Ag-Cd (Tadaki *et al.*, 1989) alloys. Although the α_1 bainite shows slightly different aging behavior with respect to disordering, probably due to the difference in diffusion rates of solute atoms in these alloys, the composition in the bainite plate in all alloys remains almost constant upon further aging, and it is nearly equal to that of the α phase.

Contradictory results are found by Doig and Flewitt (1983), who reported that the composition of an α_1 bainite plate was similar to that of the matrix near a tip of the α_1 plate in a Cu-Zn-Au alloy. This discrepancy, however, is probably due to low resolution.

8.10 Atomic Disordering

Whether mechanisms of bainite transformations involve a diffusionless and/or a diffusion reaction can be assessed using the unique structural advantages that ordered structures possess. Wu *et al.* (1989) and Hamada *et al.* (1991) have studied antiphase-domain (APD) structures of α_1 bainite plates and the matrix in a Cu-26.7Zn-4.0Al alloy at different stages of the transformation. The parent β phase of the alloy becomes an ordered $L2_1$ structure via an intermediate B2 structure. The B2 phase possesses only nearest-neighbor (NN) order while the $L2_1$ phase possesses both NN and next-nearest-neighbor (NNN) order. At temperatures below the $B2 \rightarrow L2_1$ ordering temperature, both NN and NNN order and the associated APD structures are inherited by α_1 plates during the initial stage of plate formation and maintained at a subsequent stage of plate thickening. The boundary of both NN and NNN APD structures matches perfectly at interfaces between the matrix and α_1 plates. At later stages, α_1 plates thicken and the NNN order is lost in outer regions, although the NN order and the APD structure are preserved. In inner regions, the NNN order remains. These observations indicate that substantial diffusion occurs at later stages of bainite growth. Taking compositional alterations into account, Hamada *et al.* (1992) have concluded that the transformation is initiated martensitically after diffusion of solute atoms but eventually becomes dominated by diffusion kinetics.

8.11 Interfacial Structure

Hamada *et al.* (1992) studied interfacial structures between an α_1 bainite plate and the $L2_1$ matrix in a Cu-Zn-Al alloy at different growth stages. They observed that there are periodic stacking faults at every third (0018) basal plane of the $18R\text{-}\alpha_1$ plate in early stages of growth. This basal plane maintains complete coherence with the $(0\bar{2}2)_{L2_1}$ plane of the parent phase, although a strain field appears at the interface where these two planes meet at an angle of a few degrees. At later stages, the periodicity loses its regularity, and either ledges or lattice misfits appear at interfacial regions having stacking irregularity. These observations do not fit the rapid lengthening kinetics based on a semicoherent interfacial boundary as suggested by Simonen and Trivedi (1977). Figure 17 is a high-resolution electron micrograph showing an interface between an α_1 plate and the $L2_1$ matrix.

8.12 Models of Bainite Formation

There are basically two different mechanisms describing the bainite transformation. In one type a bainite transformation involves both diffusionless and diffusional processes (Flewitt and Towner, 1967), while in the other it occurs as a diffusion-controlled precipitation process (Lorimer *et al.*, 1975). Recent detailed microanalysis and electron microscope studies appear to rule out the latter and support the former, although in the former case the central issue remains as to when the two processes occur. The models proposed are as follows: (1) A diffusionless martensitic transformation occurs first in the matrix without any compositional alteration, followed by diffusion of solute atoms to approach the composition of the equilibrium α phase with a structural change into a f.c.c. structure (Flewitt and Towner, 1967). (2) Diffusion occurs first at a region of the matrix where the chemical composition is close to that of the equilibrium α phase and then a shear process is triggered by a rise of M_s , followed by further diffusion to approach the composition of the equilibrium phase (Takezawa and Sato, 1986; Wu *et al.*, 1988; Tadaki *et al.*, 1989; Hamada *et al.*, 1991). (3) A martensitic transformation occurs after some compositional change and then diffusion of solute atoms occurs along with structural and morphological changes (Nakata *et al.*, 1989). Thermodynamic approaches by Hsu and Zhou (1989) suggest that a composition-invariant bainite transformation is energetically unfavorable in Cu-Zn alloys. In other words, their calculations suggest that bainite transformation occurs by a shear process if diffusion of solute atoms occurs either before the transformation or concurrently with it. This thermodynamic approach and the microanalysis results appear to rule out model (1).

A mostly descriptive model of the α_1 bainite transformation has been proposed by Takezawa and Sato (1986, 1990). In their model, solute Zn atoms diffuse by a localized stress gradient around defects such as dislocations, resulting in a rise of the M_s temperature, and a nucleus of α_1 bainite that is martensitically triggered. As such a nucleus forms by a martensitic shear process, a new stress field is created in the matrix. The stress promotes diffusion of solute atoms, especially at the tip of the bainite plate, resulting in lengthening of the plate. During thickening, solute atoms diffuse out to the matrix. Since the stable phase of the alloy is disordered f.c.c. at aging temperatures, the bainite plate further transforms into a f.c.c. structure during prolonged aging, both by introduction/annihilation of stacking faults parallel

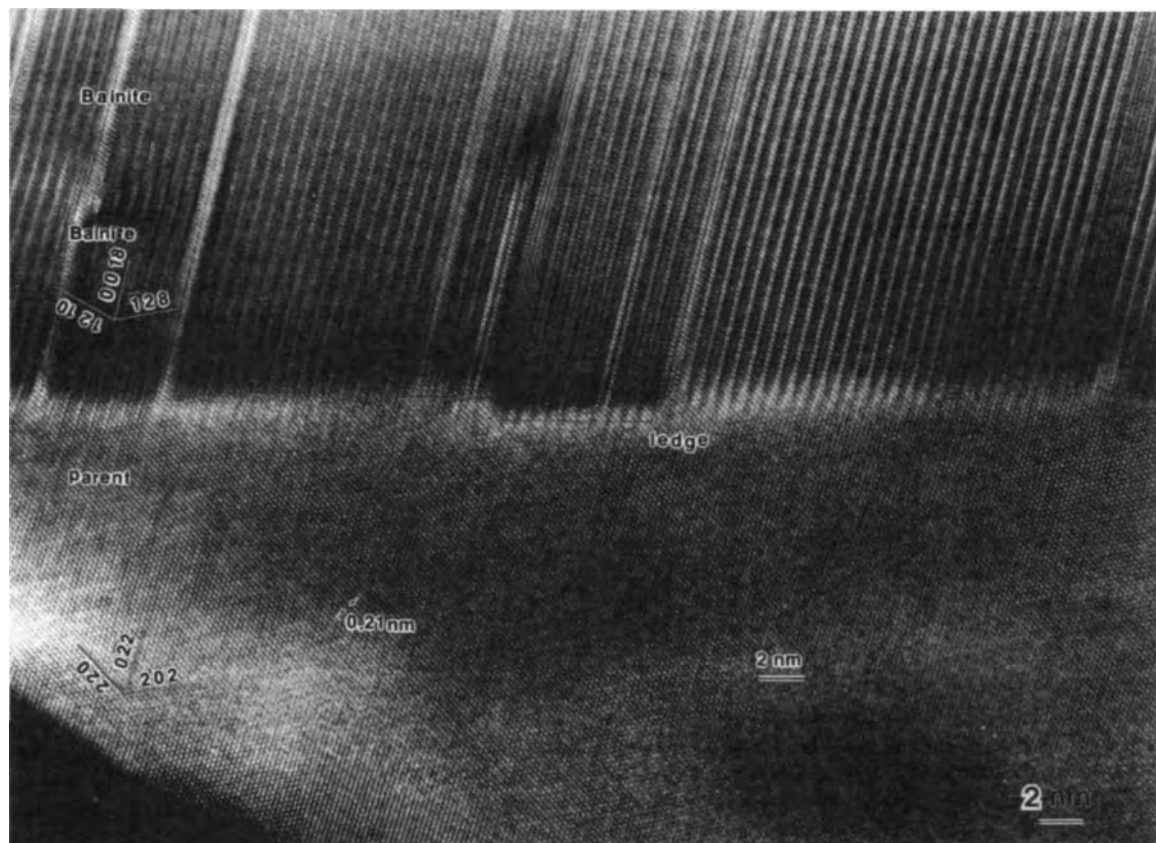


Figure 17. High-resolution electron micrograph of the interface between α_1 18R-bainite plate and $L2_1$ matrix in a Cu-26.7Zn-4.0Al alloy aged at 423 K for 864 ks, showing ledges and misfits (indicated by arrows) formed at interfacial regions where the 18R stacking periodicity loses its regularity (After Hamada *et al.*, 1992)

to the basal plane of the 9R or 18R structure and by atomic disordering to reduce the chemical free energy.

This model appears most plausible in describing certain observations associated with bainite transformation. However, there are some unexplained phenomena, e.g. the observation that the initial composition of bainite plates in Cu-Zn-Al and Cu-Zn-Au alloys is almost equal to that of the equilibrium f.c.c. α phase.

8.13 Summary

Bainite transformations occur in many ordered b.c.c. phases upon isothermal aging above M_s and below eutectoid temperatures. Bainite plates form martensitically either immediately after, or simultaneously with, some compositional change at a local region of the matrix that has lattice defects, whose localized stress fields assist solute atoms to diffuse. Upon prolonged aging, the

composition of bainite plates approaches that of the equilibrium phase (except for bainite in Cu-Sn alloys, where no stable phases have the same structure as the bainite (de Bondt and Deruyttere, 1967)). At an early stage of bainite growth, periodic stacking faults are present and the fault plane maintains complete coherence with the parent phase. At later stages, the periodicity of the stacking faults loses its regularity, and ledges appear at some interfacial regions. It is interesting to note that bainite transformations occur not only in metallic alloys but also in some ceramics such as ZrO_2 - Y_2O_3 and ZrO_2 - CeO_2 (Nakanishi and Shigematsu, 1991).

Detailed structural and chemical analyses of bainite forming in ordered intermetallics have upgraded experimental understanding of bainite transformation. However, a lack of understanding of theoretical aspects remains.

Index

Note: Figures and Tables are indicated [in this index] by *italic page numbers*

<u>Index terms</u>	<u>Links</u>				
A					
A15 compounds					
irradiation effects	182	184	198		
point defects in	150				
superconductors	182				
as superconductors	198				
vacancy migration	151				
<i>Ab initio</i> calculations, antiphase-boundary energies	69	86			
Adiabatic elastic constants	1				
compared with isothermal elastic constants	4				
Ag-Cd system	230				
Ag-Cu-Zn system	231				
Ag-Zn system	230	240			
Al-Co system	14				
Al-Cu-Ni system	226	240			
Al-Cu-Zn system	226	230	231	232	233
	235	236			
Al-Fe-Ni system	53	56	240		
Al-Fe system					
composition dependence of elastic moduli	14				
crystallographic transformation	239				
Alloying additions					
ductility affected by	28				
major	28				
trace-element	28	29			
Al-Mn-Ni system	28	30			
Al-Nb-Ti system	238				
Al-Ni-based alloys					
dislocations in	99				
ductility	240				

Index terms**Links**

Aluminides				
crystal structures	41			
<i>see also</i> Cobalt...; Iron...; Nickel...; Ruthenium...; Titanium...;				
Zirconium aluminides				
Amorphization				
irradiation-induced	181	182	198	215
dose required	201	202	205	
experimental observations	198			
mechanisms	207			
models for	210			
Anisotropic elasticity, dislocation cores affected by	112	113		
Antiphase boundaries (APBs)	67			
amorphization at	206			
chemical effects	68	74		
classification of	68			
in $D0_{22}/D0_{23}/L1_2$ relation	71			
and dislocations	83	115		
and disorder-order transformations	68	72		
dragging of APBs	118			
and grain boundaries	159	161	177	
ideal	68	69	86	
deviations due to chemical effects	68	74		
deviations due to structural effects	68	72		
nearest-neighbor models	72			
residual contrast	73	74		
segregation of alloying elements	76			
segregation of vacancies	75			
structural effects	55	68	72	
surface energy	76			
in two-dimensional AB alloy	67			
Antiphase-boundary (APB)-coupled dipoles	123	124		
Antiphase-boundary (APB) energies	76			
<i>ab initio</i> calculations	69	86	89	
anisotropy	69			
calculations	79			

Index terms**Links**

Antiphase-boundary (APB) energies (<i>Continued</i>)			
and deformation mechanisms	44		
and dissociation of dislocations	97	98	103
effect of long-range order parameter	79		
experimental determination	80		
listed	77		
B2 compounds	78		
D0 ₃ compounds	79		
D0 ₂₂ compounds	78		
L1 ₀ compounds	78		
L1 ₂ compounds	77	89	
L2 ₁ compounds	79		
plot vs. disorder – order transition temperature	80		
and structural stability	71		
temperature dependence	75	112	
Antiphase-boundary (APB) tubes	68	84	122
Antiphase domains (APDs)	67		
in bainite phases	235		
crystallography	81		
disorder-order transition	81	82	
isostructural transformation	81		
morphology	81		
‘Swiss-cheese’ structure	81	82	
in two-dimensional AB alloy	67		
Antisite defects	182	183	
formation of	136	185	
Antistructure atoms	52		
Atomic diffusion, and point defects	146	152	
Atomic images, grain boundaries	158	159	
Atomic packing, diffusivity affected by	51		
Atomistic models, grain boundaries	172	177	
Atom-probe (AP) analysis, grain-boundary chemistry studied using	163	167	168
Au-Cd system	224	225	

Index terms**Links**

Au-Cu system			
twinning in	238		
<i>see also</i> Copper-gold alloys			
AuCu ₃			
antiphase-boundary energies	76	77	89
variation with temperature	75		
elastic properties	3	16	
Au-Cu-Zn system	230	234	
Auger electron spectroscopy (AES)	27	31	163
limitations	27		

B

B2 type compounds			
APB energies	78		
crystal structure	26	92	
defects/dislocations in	107	114	188
dislocations in	95	107	
flow-stress anomaly in	64	95	108
fracture of	34		
grain-boundary structure model	175		
vacancy migration	148		
vacancy migration in	147		
B11 structure	188		
irradiation effects	188		
vacancy migration in	147	149	
Bain deformation	221	222	
Bainite	229		
compositional alteration	234		
crystal habit plane	232		
crystal structure	230		
growth kinetics	233		
interfacial structure	235		
microstructure	231		
nucleation and growth	232		
shape changes	230		

<u>Index terms</u>	<u>Links</u>				
Bainite transformations	229				
and atomic disordering	235				
in ceramics	236				
in ferrous alloys	229				
models describing	235				
in ordered intermetallic alloys	230				
Banerjee-Urban [irradiation-induced ordering/disordering] model	192				
Body-centred cubic (b.c.c.) alloys, dislocation in	107				
Bond directionality					
at grain boundaries	176				
dislocation cores affected by	112				
Bonding, plasticity affected by	49	65			
Boron					
ductility affected by	29	35	36	54	
adverse effect of sulfur	34				
fracture affected by	26				
interstitial boron in AlNi ₃	29				
segregation at grain boundaries	29	31	34	165	166
solubility in Ni ₃ X	165	166			
Boron-doped Al-Ni-based alloys					
ductility	29	35	54		
grain-boundary structures	159	160	174	177	
Bragg-Williams approximation	74	142			
Bragg-Williams LRO model	189				
β -Brass [CuZn]					
dislocations in	108	109	112		
vacancies in	134	136			
Brillouin scattering, amorphous phases studied using	204				
Brittle fracture					
B2 compounds	34				
L1 ₂ compounds	27				
models for	37				
Brittleness	25				
Brittle-to-ductile transition	41	48			

Index terms**Links**

Brittle-to-ductile transition temperature, factors affecting	65	
Bulk modulus		
calculated values	13	
composition dependence	15	
for polycrystals	13	
estimation from single-crystal constants	11	13
C		
C11 _b structure	92	
dislocations in	111	
elastic properties of compounds	5	
point defects in	147	
CANDU nuclear power reactor	181	
Carbides, point defects in	151	
Cauchy relationships	2	
listed for various intermetallics	3	
Ceramics, transformations in	229	236
C-Fe-Ni system	224	
Chalmers-Martius criterion	114	
violations	107	115
Charge transfer, embrittlement caused by	37	
Chemical composition		
and dislocation cores	111	
elastic properties affected by	14	
plasticity affected by	52	65
Chemical disordering, and irradiation effects	207	208
Clapeyron-Clausius equation	244	247
Cleavage fracture	25	
examples	25	
meaning of term	25	
Cluster variation method (CVM)	83	
Coatings, protective	42	
Cobalt aluminides		
elastic properties	13	14

Index terms**Links**

Cobalt aluminides (<i>Continued</i>)			
effect of alloying elements	15		
point-defect formation properties	133		
Cobalt-gallium alloys, vacancy formation in	137		
Coble creep	47	49	64
Co-Fe-V system	43	44	
Coil-spring behavior, shape-memory effects compared	227		
Coincidence-site lattice (CSL) boundaries	158		
Coincidence-site lattice (CSL) model	170	172	
Coincidence-site lattices	158		
Collapse of cascades			
to dislocation loops	197		
to vacancy loops	193		
Collision cascade parameters	201	203	
Collision cascades	151	199	
Composites	56		
Computer models, irradiation-induced amorphization	210		
Copley-Kear model	118		
Copper-gold alloys			
electrical resistivity	139	145	
irradiation effects	184	185	
production of point defects in	132	139	
recovery of point defects	145		
TEM/HRTEM observations of grain boundaries	159	161	
twinning in	238		
vacancy formation in	137		
Copper-titanium alloys, vacancy migration in	147	149	
Corrosion	57		
Coulomb explosion model	211		
Cowley-Warren SRO parameter	193		
Creep <i>see</i> Coble...; Diffusional; Dislocation...; Harper-Dorn...; Inverse...;			
Nabarro-Herring creep			
Creep resistance			
and diffusion coefficient	53		

Index terms**Links**Creep resistance (*Continued*)

effect of second phase 56

temperature dependence 52

Cross-slip 97 101 101 119

Crowdions 142 187 188

Crystalline-to-amorphous transformation, irradiation-induced 181 199 201 206 215

Crystallographic transformations 221

Crystal structures

of aluminides 41

of bainite phases 230

illustrated 92

Crystal symmetry, plasticity affected by 51 65

Cu-Ga system 237 240

Cu-Sn-Ni system 237

Cu-Zn system

bainite phases/transformations 230 232 233 235

superelasticity 228

DD0₃ structure 92

APB energies 79

dislocations in alloys 108

fracture of compounds 37

D0₁₉ structure 92 106

dislocations in alloys 106

elastic properties of compounds 7

D0₂₂ structure 92 101

APB energies 78

dislocations in alloys 101 114 115

elastic properties of compounds 6

fracture of compounds 37

relation to L1₂ structure 71 92 102 102D0₂₃ structure

fracture of compounds 37

<u>Index terms</u>	<u>Links</u>				
D0 ₂₃ structure (<i>Continued</i>)					
relation to L1 ₂ structure	71				
Debye temperature	13				
Decomposition reaction [for dislocation]	99				
examples for various structures	99	105	107	108	109
	111	115			
Defect cascades, collapse of	197				
Defect concentrations, requirement for amorphization	208				
Deformation, role of Kear-Wilsdorf configurations in	116				
Deformation maps	46	48	65		
Deformation twinning	45	64	238		
Density of states (DOS), at grain boundaries	177				
Diffusion					
and creep resistance	51				
factors affecting	51				
Diffusion activation energy, boron in AlNi ₃	166				
Diffusional creep	47	64			
Diffusion coefficients, boron in AlNi ₃	166				
Diffusion mechanisms, jump mechanisms	148				
Directional bonding, at grain boundaries	176				
Directional solidification techniques	42				
Dislocation climb	46				
Dislocation cores					
and alloy composition	111				
effect of anisotropic elasticity	112	113			
effect of bond directionality	112				
factors affecting	111				
mechanical properties affected by	118				
properties in various structures	99				
and slip systems	113				
Dislocation creep	46	49	64		
Dislocation debris	122				
Dislocation locks	97	101	115	117	
conservative locks	117				

Index terms**Links**

Dislocation mechanisms, antiphase boundaries formed	68			
Dislocations	91			
APB-caused	83			
in B2 alloys	95	107	114	188
in b.c.c. alloys	107			
in C11 _b phases	111			
choice of slip directions	114			
in D0 ₃ alloys	108			
in D0 ₁₉ alloys	106			
in D0 ₂₂ alloys	101	114	115	
definitions	91	93		
dissociation of	83			
in D0 ₂₂ alloys	103			
in L1 ₂ alloys	100			
static equilibrium configuration	96			
in various crystal structures	99			
elastic properties affected by	8	11	12	
in L1 ₀ alloys	104	114	117	
in L1 ₂ alloys	95	99	114	117
in L2 ₁ alloys	108			
in Laves phases	109			
mobility	91			
experimental determination of	94			
non-conservative dislocation	118			
observation of fine structure	93			
in ordered structures	91			
and point defects	152			
in quasicrystals	109	110		
sessile	115			
simulation of fine structure	95			
type-a superdislocations	106	107		
Disorder effects, and antiphase boundaries	74			
Disordering, irradiation-induced	181	193		
Disorder-order transition				
antiphase boundaries formed	68	72		

<u>Index terms</u>	<u>Links</u>				
Disorder-order transition (<i>Continued</i>)					
antiphase domains	81	82			
APB energies vs transition temperature	80				
Displacement energies	139	142	184	187	
Displacements per atom	187				
Displacement threshold energies	139	142	184	187	188
	220				
Dissociation climb	118				
Dorn [dislocation creep] equation	46				
Ductility, factors affecting	27	28	48	53	54
Ductility enhancement	54	239			
Dumbbell structure [of interstitials]	139	150	186	188	
E					
EL2 defect [in AsGa]	152				
Elastic-compliance-constant matrix	4	5			
Elastic constants					
<i>ab initio</i> /first-principles calculations	50				
calculated values, binary intermetallic compounds	4				
effect of magnetic transition	17				
effect of order-disorder transition	16				
effect of point defects	152				
first-principles calculation	2				
of single crystals	1	3			
Elastic moduli					
dynamic modulus	1				
magnetic-field dependence	17	18			
and melting temperatures	19				
of polycrystalline intermetallics	10				
static modulus	1				
Elastic properties	1				
anisotropy in single crystals	2	4			
composition dependence	14				
of dislocations	8	11	12		

<u>Index terms</u>	<u>Links</u>				
Elastic properties (<i>Continued</i>)					
orientation dependence	5	5	6	7	8
	9	10			
pressure dependence	18	19			
temperature dependence	15	23			
Elastic stiffness constants	2				
calculated values listed	4				
measured values listed	3				
Electrical resistance, changes during martensitic transformation	224				
Electrical resistivity					
effect of point defects	140	152			
point defects and	134	139			
point defects studied	140	149			
Electronegativity difference, embrittlement affected by	37	38			
Electron irradiation					
amorphous phases produced	201	204			
amorphous phases produced by	203	216			
defects produced	132	139	145	150	183
	184				
effects compared with those of ion irradiation	203	216	217		
order-disorder transformation affected by	193				
recovery after	184	185			
Electron microscopy					
high-resolution					
dislocations	93				
grain boundaries	33	158	176		
weak-beam (WB) technique	68	76	93		
Embedded-atom method (EAM)					
applicability	2	4	79	108	141
	142				
dislocations simulated by	95	108			
irradiation effects modeled using	187				
Embrittlement					
environmental	57	65			
by hydrogen	57				

<u>Index terms</u>	<u>Links</u>			
Embrittlement (<i>Continued</i>)				
by impurities	34	37	38	
Enthalpy of phase formation	50			
Environmental factors				
ductility affected by	57	65		
fracture behavior affected by	27	35		
Eshelby twist	93			
Etch-pitting techniques, dislocation mobility measured using	95			
F				
Fast-neutron irradiation, A15 superconductors affected by	198			
Fe-Ni system	224			
Fe-Pt system	223			
Ferromagnetic martensite phase				
effect of magnetic field on transformation temperatures	244	245		
magnetic field induced	244	246		
Ferrous alloys, bainite transformations in	229			
Fe-Zr compounds, irradiation-induced amorphization of	201	215		
Field ion microscopy (FIM) observations				
with atom-probe analysis (FIM-AP)	167	168		
grain boundaries	162			
Finnis-Sinclair method	95			
Fission-neutron irradiation, effects	194			
Flinn's model	118			
Flow stress				
at low temperatures	121			
temperature dependence	43	45	53	95
Flow-stress anomaly	44	64		
in B2 alloys	95	108		
in B2 phases	64			
and Kear-Wilsdorf locking	116			
in L1 ₀ alloys	104			
in L1 ₂ alloys	44	99	118	
locking of screws				

<u>Index terms</u>	<u>Links</u>				
Flow-stress anomaly (<i>Continued</i>)					
by elongated KW segments	120				
by pinning-point formation	119				
Focusons, energy dissipated by	184				
Fracture	25				
B2 compounds	34				
effect of boron	26	28	36		
and environment	27	35			
and grain size	32	33			
L1 ₂ compounds	26	37			
and processing history	28				
and quantum-mechanical calculations	37				
and stoichiometry	27	34			
Fracture maps	48				
Fracture strength	1				
Frank criterion	96				
Frenkel defect-pairs	182	183	188		
irradiation-induced amorphization affected by	209	210			
Frenkel-pair resistivity	139				
Full-potential linear augmented plane-wave (FLAPW) method,					
applications	2	4	73	77	78
	79	89			
Full-potential linear muffin-tin orbital (FLMTO) method, applications	2	4			
G					
Gallium arsenide, point defects in	151				
GaNi ₃					
antiphase-boundary energies	77				
APB tubes	85				
factors affecting ductility	29	34			
Gas atomization [processing technique]	42				
GeNi ₃					
antiphase-boundary energies	89				
factors affecting ductility	29	34			
fracture of	25	27			

<u>Index terms</u>	<u>Links</u>			
GeNi ₃ single crystal, elastic properties	8			
Giamei dislocation lock	117			
Glass-forming techniques	182			
Grain boundaries				
amorphization at	206			
atomic configurations	170	171		
bonding at	175			
dislocation structures	160			
in disordered alloys	32			
slip transmission across	32			
vacancies at	175			
Grain-boundary chemistry				
AES observations	163	177		
direct observations	163	177		
FIM-AP observations	163	167	177	
TEM-EDX observations	166			
Grain-boundary embrittlement	34	37	38	57
Grain-boundary enrichment factor	166			
Grain-boundary hardening	167			
elimination of	168			
and pest effect	168	169		
Grain-boundary sliding	47	55		
Grain-boundary structure	157			
direct observations	158	176		
by FIM	162			
by TEM	158	176		
effects of boron doping	174			
modeling of	170	177		
computed atomic models	172	177		
geometric/crystallographic models	170			
properties interpreted	167			
stoichiometric effects	172			
Grain size				
tensile properties affected by	55			

Index terms**Links**Grain size (*Continued*)

yield strength affected by	33
Griffith's relation	1
Growth kinetics, bainite	233

H

Hall-Petch relationship	32	55
Hardness, grain-boundary	167	
Hard-sphere models	172	
Harper-Dorn creep	64	
Heat capacity, point defects affecting	134	
Heavy-ion irradiation, effects	211	215 216
Heteropolarity, at grain boundaries	176	
High-resolution electron microscopy observations		
dislocations	93	
grain boundaries	33	158 176
Hill's approximation, elastic constants estimated using	11	12 13
Hirsch [dislocation-locking] model	120	
Hooke's law	2	
Hot forming processes	65	
Hot isostatic pressing (HIP)	42	
Huang X-ray scattering	134	136 145
self-interstitial structure determined by	139	
Hume-Rothery rules	140	
Hydrogen embrittlement	57	
plasticity affected by	57	
Hydrostatic pressure, elastic constants affected by	18	19

I

Initial flow stress, effect of order	43
Intergranular fracture	25
examples	25
meaning of term	25
Interstitial clusters	145

<u>Index terms</u>	<u>Links</u>				
Interstitial defects	131				
migration properties	132	149			
production of	132	138			
structure	132	139	150		
Interstitial energies	189				
In-Ti system	228				
Invariant line strain	223				
Invariant plane strain	222				
Inverse creep	47				
Ion-beam mixing	182				
Ion implantation	182				
Ion irradiation effects					
on amorphization	199				
compared with electron-irradiation effects	203	216	217		
on disordering	196				
Iron aluminides					
elastic properties	8	13			
grain boundaries in	161				
tensile properties	34				
Iron silicides, elastic properties	16				
Irradiation					
alloy stability during	211				
amorphization induced by	181	198	215		
dose required	201	202	205	217	218
experimental observations	198				
mechanisms	207				
temperature effects	203	205			
collision sequence resulting	151				
disordering induced by	181	193			
effects of	181				
theoretical modeling	187				
ordering enhanced by	189				
Ising model	72	76	79		
Isochronal annealing treatments	183				

<u>Index terms</u>	<u>Links</u>				
Isothermal elastic constants	1				
compared with adiabatic elastic constants	4				
J					
Johnston-Gilman etch-pitting techniques	95				
K					
Kear-Wilsdorf (KW) configuration	101	115			
generalized	116				
properties	115				
role in deformation	116				
Kear-Wilsdorf (KW) locks/mechanism	44	84	89	97	100
	101				
and flow-stress anomaly	116				
locking of screw dislocations by	120				
Khantha-Cserti-Vitek (KCV) [dislocation-locking] model	119				
Kinchin-Pease function	189				
Kinetics					
amorphization	202				
bainite growth	233				
martensitic transformation	225				
Kurnakov compounds	54				
L					
L1 ₀ type compounds					
APB energies	78				
crystal structure	92	104			
dislocations in	104	114	117		
debris resulting	123				
flow-stress anomaly in	104				
fracture of	37				
vacancy migration	147				
L1 ₂ type compounds					
antiphase boundaries in	69	70	71		
APB-coupled dipoles	123	124			

<u>Index terms</u>	<u>Links</u>			
L1 ₂ type compounds (<i>Continued</i>)				
APB energies	68	77	89	
variation with temperature	75			
crystal structure	26	69	92	
relation to D0 ₂₂ and D0 ₂₃ structures	71	92	102	
dislocations in	95	99	114	117
debris resulting	123			
elastic properties	7	8		
flow-stress anomaly in	44	99	118	
fracture of	26	37		
fracture modes	27			
grain boundaries	158			
bonding at	175			
grain-boundary structure models	170			
trialuminides	54			
vacancy migration in	146			
L2 ₁ type compounds				
APB energies	79			
crystal structure	92			
dislocations in	108			
Lamellar microstructure	56			
Lattice softening	18			
Laves phases				
dislocations in	109			
temperature dependence of elastic properties	17			
Lindemann [melting] criterion	209			
Linear augmented plane-wave (LAPW) method, applications	2	4		
Linear augmented Slater-type orbital (LASTO) method, applications	38			
Linearized muffin-tin orbital (LMTO) method, applications	77	78	79	
Line compounds	10	27		
Lomer-Cottrell dislocation locks	112	117		
Long-range degree, for various irradiation temperatures	190	191		

Index terms**Links****M**

Magnesium-silver system, grain-boundary hardening in	168	169	
Magnetic field induced martensite	244	256	
Magnetic ordering, elastic moduli affected by	17		
Magnetostatic effect	246		
Magnetostriction	246		
Many-body interactions	175		
Martensites			
crystallography	222	224	
and ductility	239		
formation of			
magnetic field induced	244		
stress-induced	65		
meaning of term	221		
nucleation of	225		
Martensitic transformations			
in ceramics	229		
crystallography	221		
definitions	223		
electrical resistance changes during	224		
kinetics	225		
relationship with massive transformations	237		
and shape-memory effects	226		
stress- and strain-induced	225	226	228
theories	222		
Massive-like transformations	238		
Massive transformations	237		
definition	237		
in intermetallics	237		
and optical-memory applications	240		
relationship with martensitic transformations	237		
Mechanical alloying, synthesis using	42		
Mechanical properties	1		
Mechanical testing	42		

<u>Index terms</u>	<u>Links</u>			
Melting temperatures, and elastic constants	19			
Melt spinning [processing technique]	42			
Memory effects	226			
Microhardness testing	167			
Microstructures				
properties affected by	54			
effect of second phases	55	65		
Miedema's model	141			
Miedema's vacancy-formation relationship	140			
Models				
amorphization	210			
bainite formation	235			
brittle fracture	37			
dislocation-locking	119			
flow-stress anomaly	118			
grain boundaries	170	177		
irradiation damage	190			
triple-defect	131	138	144	147
Molecular dynamics (MD) calculations				
defect structures formation	189			
irradiation-induced amorphization	207	210		
Molybdenum disilicide				
dislocations in	111			
elastic properties	11	13	22	
N				
Nabarro-Herring creep	47	49	64	
Nearest-neighbor models, antiphase boundaries	72			
Neutron irradiation, effects	193	194	203	
Nickel aluminides				
antiphase-boundary energies	77	78	89	
variation with temperature	75			
boron at grain boundaries	165			
brittle-to-ductile transition	41			

Index terms**Links**Nickel aluminides (*Continued*)

commercial developments	58				
creep behavior	46	64			
creep resistance	56				
dislocations in	94	99	100	111	123
ductility improvement	28				
elastic properties	7	8	11	13	
factors affecting ductility	28				
fracture of	25				
irradiation effects	184	206			
plastic deformability	42	45			
point defects in	187	188			
TEM/HRTEM observations of grain boundaries	158	159	160		
tensile properties	34				
vacancies in	136				
vacancy formation in	138				
Nickel silicides, factors affecting ductility	29	34			
Niobium disilicide, elastic properties	22	23			
Ni-Si-Ti system	28	30			
Ni-Sn system	237	240			
Nitinol alloy	226	229			
Ni-Ti system	226	229			
Nitrides, point defects in	151				
Nuclear fission gas bubble formation, factors affecting	205	206			
Nuclear fuel applications	181				
Nuclear reactor structural materials	181				
Nucleation					
bainite	232				
martensite	225				

O

O (orthorhombic) phase

Al-Nb-Ti system	110
dislocations in	110
structure	92

<u>Index terms</u>	<u>Links</u>			
O-lattice [grain-boundary structure] model	170			
One-way shape-memory effect	226	227		
Optical-memory alloys	240			
Order-disorder transition				
at grain boundaries	162			
elastic moduli affected by	16			
Ordering				
irradiation-enhanced	189			
spinodal	193			
Ordering energy, grain-boundary structure studied using	172			
Orowan equation	119			
Orthorhombic phase <i>see</i> O...phase				
Oxidation resistance, oxide layers providing	42			
Oxide dispersion-strengthened (ODS) alloys	55			
P				
Paidar-Pope-Vitek (PPV) [dislocation-locking] model	119	120		
Particulate-reinforced alloys	55			
Peierls stress	1			
Percolation model for amorphization	210			
Pest degradation effect/phenomenon	28	57	168	169
Phase enthalpy	50			
and Young's modulus	50			
Phenomenological theory of martensite crystallography	222			
Pinning, locking of screw dislocations by	119			
Plastic deformation	41			
controlling factors				
composition and stoichiometry	52	65		
crystal symmetry	51	65		
environmental factors	57	65		
microstructural features	54	65		
point defects	152			
factors controlling	49			
bond characteristics	49	65		

Index terms**Links**Plastic deformation (*Continued*)

composition and stoichiometry	52	
crystal symmetry	51	
environmental effects	57	
microstructure and effects of second phases	54	
mechanisms	43	
diffusional creep	47	64
dislocation creep	46	64
slip	43	64
twinning	45	64

Point defects

	131	
in A15 compounds	150	
accumulation during irradiation	207	
clustering of	136	
concentration required for amorphization	208	
and dislocations	152	
and electrical resistivity	149	
experimental investigations	132	183
formation properties		
computation of	141	
experimental determination of	132	
theory	140	
and lattice parameter	133	137
low-temperature retention	145	
migration properties	146	
experimental determination	134	
and ordering energies	136	
physical properties affected by	152	
production of	132	
recovery of	136	
after irradiation or quench	145	
in semiconductors	151	
theoretical modeling	187	
theoretical modeling of	141	
thermodynamics	142	

<u>Index terms</u>	<u>Links</u>			
Point defects (<i>Continued</i>)				
in transition-metal carbides and nitrides	151			
triple-defect model	131	138	144	147
typical examples	131			
Poisson's ratio	4			
composition dependence	15			
orientation dependence	5	6	8	
of polycrystals	13			
estimation from single-crystal constants	12	13		
temperature dependence	16	23		
Polycrystalline intermetallics, elastic moduli	10			
Positron annihilation techniques, vacancies studied using	133	136	152	
Powder metallurgy	42			
techniques				
hot isostatic pressing	42			
reactive sintering	42			
Power-law creep	46	53	64	
Pressure effects, elastic constants	18	19		
Primary creep	47			
Processing	42			
ductility affected by	28			
Proton irradiation, amorphization caused by	207			
Pseudoelasticity	228			
Pseudosymmetrical [atomic] configurations	170	171		
Q				
Quantum-mechanical calculations				
boron bonding	37			
phase-formation enthalpies	50			
Quasicrystals, dislocations in	109	110		
R				
Radiation damage	181			
Rare-earth compounds, temperature dependence of elastic properties	17			

Index terms**Links**

Reactive consolidation/sintering	42				
Rearrangement of atoms, mechanisms for	193				
Recombination mechanisms	193				
Relaxation volumes, interstitial defects	139				
Replacement collisions, effect	193	194			
Replacement-collision sequence mechanism	185				
Resonance ultrasound spectroscopy (RUS), elastic constants determined by	22	23	23		
Reuss's approximation	11	12			
Rubber-like behavior, in shape-memory alloys	228				
Rupture length	41				
Ruthenium aluminides					
antiphase-boundary energies	78				
ductility	36				
elastic properties	13	15			
effect of alloying elements	15				
$\text{Ru}_{11}\text{Ta}_9$					
elastic properties	13	15			
effect of alloying elements	15				
RuTi					
elastic properties	13	15			
effect of alloying elements	15				
S					
Saturation magnetization, effects of fission neutrons	195				
Screw dislocations	44	94			
locking of	119				
Secondary creep	47	99			
Segregation					
at grain boundaries, of boron	29	31	34	165	166
to antiphase boundaries	75				
Self-diffusion activation energy	147				
Self-diffusion coefficients	146	147			
Self-interstitials					
migration of	187				

<u>Index terms</u>	<u>Links</u>			
Self-interstitials (<i>Continued</i>)				
structures determined	139			
Semiconductors, point defects in	151			
Sessile dislocations	115			
Shape-memory alloys	226			
ferromagnetic compounds	242			
crystal structure	242			
effect of magnetic field on transformation temperatures	244	245		
magnetic field induced martensite	244	246		
magnetization behavior	246			
transformation temperature	247			
transformation temperatures	242			
stress-strain diagrams for	228	229		
superelasticity	228	229		
Shape-memory effects	226			
and martensitic transformations	226			
one-way memory	226	227		
processes involved	227			
rubber-like behavior	228			
superelasticity	228			
two-way memory	226			
Shear modulus	4			
changes during amorphization	204			
composition dependence	15			
and melting temperature	19			
of polycrystals	13			
estimation from single-crystal constants	12	13		
temperature dependence	16	23		
Shock densification processes	42			
Shockley partials	93	99	100	101
Simulation methods, dislocation fine structure	95			
Single crystals				
anisotropy of elastic properties	2	4		
elastic constants	1			

Index terms**Links**

Sintering, reactive sintering	42		
Slip directions	114		
Slip mechanisms	43	64	
Slip systems	113		
SnTi ₃ single crystal, elastic properties	9	13	
Sodani-Vitek (SV) [dislocation-locking] model	119		
Solid-solution hardening	53		
Specific gravity, and lattice parameter	133		
Spinodal ordering	193		
Split interstitials	131	150	186
Stacking faults, in L1 ₀ alloys	106		
Staircase-configuration dislocations	104	105	
Stoichiometry, ductility affected by	27	52	65
Strain-hardening behavior	43	55	
Strain-induced martensitic transformation	225	226	
Strength			
effect of APBs	55		
effect of second phase	55		
and grain size	55		
Stress corrosion cracking	57		
Stress-induced martensitic transformation	225	226	228
and ductility improvement	239		
Stress-strain diagrams			
Cu-Zn system	228		
effect of order	44		
serrations in	45		
superelasticity loop	228		
Stress-strain-temperature diagrams, shape-memory alloys	229		
Stress-temperature diagrams, martensitic transformation	226		
Structural stability, and antiphase-boundary energies	71		
Structural vacancies			
detection/determination techniques	132		
empirical prediction	140		
formation of	137		

<u>Index terms</u>	<u>Links</u>	
Subgrain formation	46	55
Sulfur, segregation to grain boundaries	34	
Superalloys, nickel-based	182	
Superconducting critical/transition temperature, effect of point defects	150	152
Superconductors, A15 compounds as	182	198
Superdislocations	43	93
fine structure in relation to crystal structure	95	
Superelasticity	228	
Super-lattice dislocations	43	93
Superlattice extrinsic stacking-fault (SESF) dipoles	106	123
Superlattice intrinsic stacking fault (SISF)	72	
and Superdislocations	100	
Superlattice intrinsic stacking-fault (SISF) energies		
and antiphase boundaries	84	
and APB energies, in dissociation of dislocations	97	98
Superlattice stacking fault (SSF) dipoles	123	
Superplastic forming	55	65
Superplasticity	65	
Supertwinning	239	
Surface energies, antiphase boundaries	68	76
Swelling behavior	181	
irradiation-induced	205	
Symmetrical (atomic) configurations	170	171
Symmetrical tilt boundaries	172	173
Synthesis techniques	42	
T		
Takeuchi-Kuramoto [dislocation-locking] model	119	
Takezawa-Sato [bainite transformation] model	235	
Tensile strength		
Al-Fe alloys	35	
Al-Ni alloys	34	
brittle-to-ductile transition	49	
Thermal expansion, vacancy-affected	133	

<u>Index terms</u>	<u>Links</u>				
Thermal spike model	193	198	211		
Thermoelastic martensitic transformation	225				
III-V compounds, point defects in	151				
Threshold displacement energies <i>see</i> Displacement threshold energies					
Tilt boundaries, atomic structures	172	173			
Time – temperature-transformation (TTT) diagrams	229	230			
Titanium aluminides					
antiphase-boundary energies	77	78			
commercial developments	58				
creep behavior	64				
dislocations in	102	104	105	106	115
	117				
elastic properties	6	13	22	23	
massive-like transformations	238				
plastic deformability	49				
TEM/HRTEM observations of grain boundaries	159				
tensile strength	49				
Toughness improvement	57				
Trace-element alloying additions	28	29			
Transformations					
applications to materials	239				
ductility improvement	239				
optical-memory applications	240				
bainite	229				
crystallographic	221				
martensitic	223				
massive	237				
massive-like	238				
Transition-metal compounds					
bonding characteristics	50				
point defects in	151				
Transmission electron microscopy (TEM) observations					
antiphase boundaries/domains	68	69	73	73	74
	76	80			

Index terms**Links**

Transmission electron microscopy (TEM) observations (<i>Continued</i>)				
with energy-dispersive X-ray analysis (TEM-EDX)	166			
grain boundaries	158			
irradiation effects	196	197	206	215
Triple-defect model	131	138	144	147
TTT diagrams	229	230		
Tungsten silicides, elastic properties	5	13		
Twin boundaries	159	161		
Twinning	45	64	221	238
Two-way shape-memory effect	226			
U				
Ultrasonic wave velocity	1			
Ultrasonic wave velocity measurement, elastic properties determined by	1	10		
Uranium intermetallic compounds, irradiation effects	205			
V				
Vacancies	131			
at grain boundaries	48	175		
dislocations as sources/sinks	48			
formation of	132	136		
energies predicted	140			
volume change	133			
and Hume-Rothery rules	140			
migration properties	132	145		
A15 compounds	151			
B2 compounds	147	148		
B11 compounds	147	149		
L1 ₀ compounds	147			
L1 ₂ compounds	146			
mobility	146	149		
and off-stoichiometry	144			
structural vacancies	132	137	140	
thermal vacancies	133			

<u>Index terms</u>	<u>Links</u>			
Vacancy clusters	146			
Vacancy concentration	143			
Vacancy-energy model	143	144		
Vacancy-ordered phases	138			
Valency difference, grain-boundary structure affected by	176			
Vidoz-Brown dislocation mechanism	84	86		
Voigt approximation	11	12		
Voigt notation	2			
Von Mises criterion	51			
W				
Widmanstätten ferrite	229			
Wrong-pair bonds	171			
Y				
Yield anomaly, and APB energy anisotropy	70			
Yield strength				
Al-Fe alloys	35			
Al-Ni alloys	34			
Young's modulus	4			
composition dependence	14	15		
orientation dependence	5	6	8	
and phase enthalpy	50			
of polycrystals	13			
estimation from single-crystal constants	12	13		
temperature dependence	16	17	23	
Z				
Zeeman effect	246			
Zee-Wilkes [irradiation-induced ordering/disordering] model	190			
Zircaloy alloys	181	203	209	
Zirconium aluminides, irradiation effects	196	199	200	207